

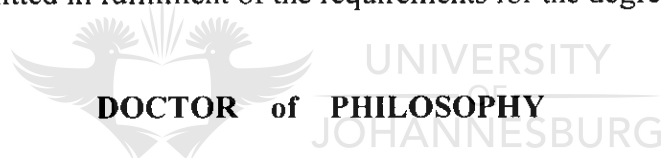
**THE DOORNHOEK GOLD DEPOSIT IN THE LIMPOPO BELT,  
SOUTH AFRICA: AN EXAMPLE OF AN ARCHAEOAN SHEAR ZONE  
HOSTED DEPOSIT FORMED AT HIGH-GRADE METAMORPHIC  
CONDITIONS**

*by*

*LAURENTIU DANIEL STEFAN*

**THESIS**

submitted in fulfilment of the requirements for the degree of



in **GEOLOGY**

**Faculty of Science**

at the

**RAND AFRIKAANS UNIVERSITY**

Promoters: **Prof. D.D. van Reenen, and**

**Dr. C.A. Smit**

**Johannesburg, May 1997**

*To my family, with all my love*



UNIVERSITY  
OF  
JOHANNESBURG

*Science means Knowledge,*

*Knowledge means Wisdom,*

*Wisdom is Power.*



# ACKNOWLEDGEMENTS

## THANKS:

To my promoters, Prof. DD van Reenen and Dr. CA Smit for all the discussions, positive criticism, encouragements, a lot of patience spread over several years, and for their input in the preparation of this thesis.

To my first geological mentor, Prof. E Constantinescu who taught me how to think and how to understand geology, and not only.

To Corina and Mara for colouring my life pink when sometimes it was only grey and for their moral support and continuous encouragement.

To the Foundation for Research and Development for funding this project in the beginning.

To the Department of Geology at the Rand Afrikaans University that made my very first stay in South Africa pleasant and enjoyable

To Shell South Africa (now Billiton) for granting permission to study the Doornhoek gold deposit.

To the Rand Afrikaans University for the award of additional financial support during the early stages of this research project.

To Gold Fields of South Africa for their financial support.

To Mr. J Jonker for his support over many years.

To Mrs. CA Day for her patient assistance with microprobe work at the RAU.

To Dr. JM Huizenga for his very careful and constructive help in finalising the fluid inclusions data and the discussion thereof.

To Mr. S Nicolescu from Natal University, Durban (now in Stockholm, Sweden) for his tremendous help with the REE analyses.

To my mom and dad for being their son and offering a big helping hand with the domestic activities at home during the final stages of the preparation of this thesis.

To Ms. TA Wilkinson for her help with all the figures and diagrams.

To Mrs. L Kemmish for her help with the drawing of diagrams.

To Ms. E de Coq for typing large parts of the thesis.

To Mrs. AR Gaspar for checking parts of the list of references.

To JCI Ltd. for their technical and financial assistance during the final year of editing the thesis.

To Dr. AM Killick for allowing other people to help when I needed it most.

To Mr. J da Silva and Mrs. G Tadford for the last week rush.

To Prof. DD van Reenen and Dr. CA Smit again for not giving up when even I thought that enough is enough.

ACKNOWLEDGEMENTS

CONTENTS

ABSTRACT

LIST OF FIGURES

LIST OF TABLES

<b>1</b>	<b>INTRODUCTION</b>	<b>1</b>
1.1.	Objectives of the present study	1
<b>2</b>	<b>IMPORTANT FEATURES OF ARCHAEOAN LODE-GOLD DEPOSITS</b>	<b>3</b>
2.1.	Introduction	3
2.1.1	History of research	4
2.2.	Gold deposition and occurrences in metamorphic terranes	7
2.3.	The role of fluids in Archaean gold deposition	11
2.3.1.	Fluid activity in greenstone belts and amphibolite facies rocks	12
2.3.2.	Fluid activity in upper-amphibolite - granulite facies conditions	13
2.3.3.	Characteristics of the Archaean gold-related fluids	16
2.3.4.	Concentrated brines as high-grade metamorphic fluids	16
2.4.	Source of gold mineralisation and related fluids in Archaean terranes	20
2.4.1.	Magmatic origin of gold	22
2.4.2.	Metamorphic origin of gold	27
2.4.3.	Discussions	32
<b>3</b>	<b>METHODS OF STUDY</b>	<b>34</b>
3.1	Field mapping	34
3.2	Structural geology	34
3.3	Structural petrology	35
3.4	Petrography	35

3.5	Ore mineralogy	35
3.6	Fluid inclusions	36
3.7	Geochemical data	36
3.8	Isotope studies	37
<b>4</b>	<b>GEOLOGICAL SETTING OF THE DOORNHOEK GOLD DEPOSIT IN THE SOUTHERN MARGINAL ZONE OF THE LIMPOPO BELT</b>	<b>38</b>
4.1	Regional geology of the Southern Marginal Zone of the Limpopo Belt	38
	<b>4.1.1. Structure</b>	40
	<u>4.1.1.1. D<sub>1</sub> fold dominated domains</u>	43
	<u>4.1.1.2. The Southern Marginal Shear System</u>	45
	<u>4.1.1.3. Reactivated shear zones</u>	47
	<u>4.1.1.4. Other features related to the shear zones         of the SMZ</u>	48
	<b>4.1.2. Metamorphism</b>	48
4.2	Structural setting of the Doornhoek Gold Deposit	51
	<b>4.2.1. Large-scale deformational features</b>	51
	<b>4.2.2. Meso-scale deformation</b>	57
	<b>4.2.3. Micro-scale deformation: Structural petrology and     microtectonic study</b>	61
	<b>4.2.4. Conclusion</b>	69
4.3	Importance of the hydration event with respect to gold mineralisation in the SMZ	70
4.4	Age relationship	77

<b>5</b>	<b>PETROGRAPHY OF UNHYDRATED AND HYDRATED GRANULITES</b>	
	<b>OF THE SOUTHERN MARGINAL ZONE AT THE DOORNHOEK LOCALITY</b>	<b>79</b>
5.1	Introduction	79
5.2	Unhydrated rocks	80
	<b>5.2.1. Baviaanskloof Gneiss</b>	80
	<b>5.2.2. Mafic rocks</b>	83
	<b>5.2.3. Ultramafic rocks</b>	83
	<b>5.2.4. Metapelite</b>	85
	<b>5.2.5. Banded Iron Formation (BIF)</b>	85
	<b>5.2.6. Hydration of the initially unhydrated granulite facies rocks</b>	85
5.3	Hydrated lithologies representing the regional host of the Doornhoek Ore	
	Body	88
	<b>5.3.1. The hydrated equivalent of the Baviaanskloof Gneiss</b>	89
	<b>5.3.2. The partly hydrated mafic granulite</b>	92
	<b>5.3.3. The partly hydrated ultramafic lithologies</b>	92
	<b>5.3.4. The hydrated pelitic granulite</b>	93
	<b>5.3.5. The partly hydrated BIF</b>	93
5.4	Highly altered rocks (metasomatised) associated with the Doornhoek Gold	
	Deposit	93
	<b>5.4.1. The highly altered equivalent of the Baviaanskloof Gneiss</b>	94
	<b>5.4.2. The highly altered BIF (mafic granulite)</b>	105
	<b>5.4.3. The highly altered ultramafic granulite</b>	110
	<b>5.4.4. The highly altered felsic granulite</b>	111
	<b>5.4.5. The Mineralised Zone of the Ore Body</b>	116
	<u>5.4.6.1. Metasomatic biotite-garnetiferous formation</u>	118
	<u>5.4.6.2. Quartz veins</u>	120



<b>6</b>	<b>MINERALOGY OF THE ORE BODY</b>	<b>128</b>
6.1	Mineral chemistry of the gangue	128
	Plagioclase	128
	K-feldspar	129
	Garnet	129
	Biotite	131
	Orthopyroxene	133
	Clinopyroxene	134
	Amphiboles	135
	Tourmaline	137
	Carbonates	137
6.2	Chemical zonation of silicates and related textures	139
	6.2.1. Baviaanskloof Gneiss	139
	6.2.2. Doornhoek Ore Body	142
	<u>6.2.2.1. Reactions reflecting resorbition (retrogression) of</u>	
	<u>garnet</u>	143
	<u>6.2.2.1.1. Garnet</u>	143
	<u>6.2.2.1.2. Orthopyroxene</u>	148
	<u>6.2.2.1.3. Biotite</u>	149
	<u>6.2.2.2. Prograde pattern reactions and textures</u>	150
	<u>6.2.2.2.1. Garnet</u>	150
	<u>6.2.2.2.2. Biotite</u>	159
	<u>6.2.2.2.3. Orthopyroxene</u>	160
	6.2.3. Conclusion	165
6.3	Mineral chemistry of ore minerals	166
	Löllingite	166
	Arsenopyrite	166
	Pyrrhotite	166
	Chalcopyrite	166

	<b>Sphalerite</b>	167
	<b>Ni-Co minerals</b>	167
	<b>Gold</b>	167
	<b>Pyrite</b>	168
<b>7</b>	<b>MINERALISATION</b>	<b>169</b>
7.1	Introduction	169
7.2	Mineralisation associated with quartz veins	170
	<b>7.2.1. Oxides</b>	177
	<b>7.2.2. Sulphides and Arsenides</b>	180
	<b>7.2.3. Native elements</b>	188
	<b>7.2.4. Evolution of the mineralisation associated with quartz veins</b>	191
7.3	Mineralisation entrapped in metasomatic garnet porphyroblasts	196
	<b>7.3.1. Zoning of garnet</b>	196
	<b>7.3.2. Mineralisation trapped within prograde garnet porphyroblast</b>	196
	<b>7.3.3. Oxides</b>	199
	<b>7.3.4. Sulphides and Arsenides</b>	200
	<b>7.3.5. Native elements</b>	202
	<b>7.3.6. Thermal zonation of mineralisation entrapped in the zoned garnet porphyroblast</b>	203
7.4	Similarities between mineralisation deposited within quartz veins and trapped in the garnet porphyroblast in the biotite-garnetiferous formation	205
<b>8</b>	<b>RELATIONSHIP BETWEEN DEFORMATION, HYDRATION AND METASOMATISM IN THE DOORNHOEK ORE BODY</b>	<b>207</b>
8.1	Suggested protolites and mechanism of formation of the prograde pattern lithologies at Doornhoek	207

8.2	Mineralisation in veins and in prograde pattern garnets	212
8.3	Summary	215
<b>9</b>	<b>FLUID INCLUSIONS</b>	<b>218</b>
9.1	Data	218
9.2	Discussion	227
9.3	Summary	228
<b>10</b>	<b>THERMOBARIC CALCULATIONS</b>	<b>231</b>
10.1	Thermobarometry	231
	<b>10.1.1. Retrograde assemblages</b>	232
	<b>10.1.2. Prograde assemblages</b>	235
10.2	P-T conditions for the retrograde assemblages	237
	<b>10.2.1. P-T constraints in the felsic granulite</b>	237
	<b>10.2.2. P-T constraints in the mafic granulite</b>	238
10.3	P-T conditions for the prograde assemblages	242
<b>11</b>	<b>P-T CONDITIONS OF MINERALISATION</b>	<b>246</b>
<b>12</b>	<b>GEOCHEMISTRY</b>	<b>251</b>
12.1	Proton microprobe analyses	252
	<b>12.1.1. Manganese distribution</b>	252
	<b>12.1.2. Iron distribution</b>	253
	<b>12.1.3. Germanium distribution</b>	254
	<b>12.1.4. Arsenic distribution</b>	255
	<b>12.1.5. Yttrium distribution</b>	256
	<b>12.1.6. Zirconium distribution</b>	257
	<b>12.1.7. Nickel distribution</b>	258

	<b>12.1.8. Gold distribution</b>	<b>258</b>
12.2	Rare Earth Elements (REE)	260
12.3	Major element geochemistry	264
12.4	Trace element geochemistry	268
12.5	Conclusion	274
12.6	Stable isotope geochemistry	276
	<b>12.6.1. Reconstruction of peak-temperatures</b>	<b>277</b>
	<b>12.6.2. Conditions of retrogression</b>	<b>280</b>
	<b>12.6.3. Nature and source of retrograde fluids</b>	<b>284</b>
	<b>12.6.4. Conclusion</b>	<b>286</b>
	<b>12.6.5. Concentrated brines as high-grade metamorphic fluids</b>	<b>286</b>
<b>13</b>	<b>RELATIONSHIP BETWEEN DEEP CRUSTAL DEFORMATION AND FLUID ACTIVITY AT THE DOORNHOEK GOLD DEPOSIT: A THEORETICAL MODEL</b>	<b>291</b>
13.1	Pervasive circulation of fluids (porous media flow)	294
13.2	Mass transport	297
13.3	Channelised circulation of fluids (fracture flow)	298
13.4	Source of metamorphic fluids	301
13.5	Deep crustal embrittlement and fluid flow during granulite facies in the SMZ of the LB and fluid:rock conditions at Doornhoek	303
<b>14</b>	<b>CONCLUSIONS</b>	<b>307</b>
	REFERENCES	<b>310</b>
	APPENDICES	

## ABSTRACT

Lode-gold deposits usually occur in granite-greenstone terranes of low- to medium-grade of metamorphism. Such deposits are well studied in terms of their petrogenesis, ore mineralogenesis and structural control. Gold occurrences associated with high-grade terranes are, however, also known from the Yilgarn Block in Australia (Griffin's Find) and Northern Marginal Zone of the Limpopo Belt in Zimbabwe (Renco), but the genesis of these deposits are not as well understood as that of their lower grade counterparts. The Doornhoek lode-gold deposit, situated in the granulite terrane of the Southern Marginal Zone of the Limpopo Belt in South Africa displays an important sequence of structural and metamorphic events that proved to be very useful in understanding the formation of metamorphic gold deposits formed under upper-amphibolite - granulite facies conditions.

Structurally the Doornhoek gold deposit is situated in a large low-angle  $D_1$  fold plunging towards the west at  $10-15^\circ$ . The fold structure and the mineralised zone are affected by  $D_2$ -strike-slip shear zones which occur both within and along the outer contacts of the ore zone. The gold deposit is also affected by southward verging  $D_3$  shear zones which thrust Baviaanskloof Gneiss over and onto the Doornhoek Ore Body.

The Doornhoek Gold Deposit is also situated in a highly altered zone of metasomatised rocks within the zone of rehydration of the Southern Marginal Zone. The actual Ore Body is represented by a remnant of BIF, mafic and ultramafic rocks surrounded by Baviaanskloof Gneiss. The alteration process, caused by high-temperature fluids channeled along the  $D_2$

shear zones was responsible for the formation of the different metasomatic lithologies. These altered rocks initially experienced a regional hydration event followed by the high-temperature metasomatic event.

The very intense metasomatic activity was synchronous with the growth of prograde-zoned garnet and gold mineralisation associated with quartz veins. This scenario is suggested by the fact that gold associated with Zn, Ge, As, Y, Zr and Ni was trapped in the mineralised inner-ring of the zoned garnet, by the REE pattern and presence of Th<sup>232</sup> and U<sup>238</sup> in the biotite-garnetiferous formation, and by the mobility of major elements such as Al<sub>2</sub>O<sub>3</sub>, K<sub>2</sub>O, SiO<sub>2</sub> and TiO<sub>2</sub> associated with the metasomatic activity. The alteration is probably related to externally derived magmatic fluids mixed with metamorphic aquitards that were active in both open and close system conditions along deep seated D<sub>2</sub> shear zones. These fluids are characterised by the presence of high-density CO<sub>2</sub>-rich and high salinity fluid inclusions. The gold mineralisation is closely associated with pyrrhotite, magnetite, löllingite, arsenopyrite, chalcopyrite, ilmenite, pentlandite, sphalerite and gold. The gold has a very low fineness (520), typical of gold precipitated from hydrothermal solutions at high-grade conditions. The textural relationships of the ore minerals hosted by the quartz veins, furthermore demonstrate a prograde pattern of mineralisation, similar as in the case of mineralisation trapped within different zones of the zoned garnet porphyroblast. The dark inner-ring of the garnet is characterised by high concentrations of sulphides, oxides and gold. The mineralising event initially deposited sphalerite and arsenopyrite at low temperatures of up to 569°C with temperatures increasing to 673°C, and even up to 750°C when löllingite was formed. Most of the gold is related to As-rich arsenopyrite, löllingite and graphite at temperatures ranging from upper-amphibolite facies to lower-granulite facies metamorphic conditions.

The Doornhoek gold deposit is an example of a high-grade lode-gold deposit formed during a prograde hydrothermal event and demonstrates unequivocally the possibility of economic gold mineralisation during granulite facies conditions. This observation has important implications for gold exploration in high-grade geological terranes that to date have been mostly ignored by the gold mining industry.



## List of figures

- Figure 2.1: Changes in the composition of the metamorphic fluid associated with medium- to high-grade metamorphic rocks. CO<sub>2</sub>-rich fluids dominate in the high-grade metamorphic terranes, regardless of rock composition (*from Touret, 1981*).
- Figure 2.2: At pressures above 3-4 kbar, the H<sub>2</sub>O activity drops precipitously from values nearly equal to the H<sub>2</sub>O mole fractions, to activities near the squares of the mole fractions in the deep-crustal pressure range. Thus, concentrated brines may have low enough H<sub>2</sub>O activities (0.2-0.4) under deep-crustal conditions to coexist with the assemblage *orthopyroxene+K-feldspar* in charnockites, and that the low H<sub>2</sub>O activities in such brines protect the rocks against melting even at temperatures >750°C (*from Newton et al., 1996*).
- Figure 2.3: Composite crustal section illustrating the elements of an Archaean gold genetic model (*from Colvine et al., 1988*). The vertical scale is not defined. Crustal cratonization culminates with the addition of mafic magma to the base of and also into the existing lower crust. Crustal thickening is accomplished in part by the addition of diapiric mass to the base of the crust, which grows downward to form a subvolcanic keel. Granulitisation of the lower crust results from the introduction of magma, heat and volatiles, principally CO<sub>2</sub>. A compositional spectrum of silicate magmas is generated by partial melting of the upper mantle and lower crust in the presence of fluids with varying CO<sub>2</sub>/H<sub>2</sub>O ratios. Fluids originating by exsolution from silicate magmas anywhere between the upper mantle and upper crust, may evolve compositionally as a result of reaction with rock (granulitisation) and due to immiscible separation. Chemical mass transfer from the mantle, lower and middle crust to the upper crust is done by silicate magma and fluids, which migrate along zones of crustal weaknesses (penetrative at least to the Conrad discontinuity). Gold concentration in the upper crust is a consequence of this late crustal magmatic, tectonic and thermal history.
- Figure 2.4: Solubility of CO<sub>2</sub>, H<sub>2</sub>O and S in a tonalitic-granitic melt, as a function of temperature and pressure. Sulphur data from Carroll and Rutherford (1985), solubility for dacite melt at 1025°C and fO<sub>2</sub> of the hematite-magnetite buffer. Data for CO<sub>2</sub> from Holloway and Lewis (1974), solubility for binary CO<sub>2</sub>-H<sub>2</sub>O fluids in albite liquid, X<sub>CO<sub>2</sub>(fluid)</sub> = 0.75. Data for H<sub>2</sub>O from Burnham and Ohmoto (1980). Diagram from Colvine et al., 1988.
- Figure 2.5: Cartoon illustrating a possible cratonisation model of the Archaean crust, which accounts for the late plutonism and metamorphism of the crust and the coeval differentiation of the upper mantle. Mantle diapirism supplies magma, heat and volatiles to the base of the crust, which induces granulitisation and crustal thickening (*from Colvine et al., 1988*).
- Figure 4.1: Map of the Southern Marginal Zone of the Limpopo Belt showing the major tectonic and metamorphic elements (*after Smit and Van Reenen, 1997*).
- Figure 4.2: The location of the Doornhoek Gold Deposit in the central part of the SMZ, related to the main shear zones in the area. Note the variation of the structural elements foliation and lineations in different zones in the SMZ. In the Doornhoek domain the lineation is subhorizontal showing strike-slip movements along D<sub>2</sub> which is almost E-W and very steep (*after CA Smit, personal communication, 1997*).
- Figure 4.3: The Doornhoek Gold Deposit is located between the small transfer fault NW-SE striking Klipbank Shear Zone, the major NE striking N'Tabalala and Doornfontein shear zones.



- Figure 4.4:** Simplified *P-T* diagram showing the *P-T* evolution of the granulite facies metamorphic rocks in the SMZ of the LB and illustrating the conditions of the  $M_1$ ,  $M_2$  and  $M_3$  metamorphic events (from Stevens and van Reenen, 1992).
- Figure 4.5:** Sliced block-diagram showing the morphology of the Doornhoek Ore Body and the thrust over Baviaanskloof Gneiss. As a result of drilling, the Ore Body can be followed for about 800m along strike. Note the sheath-like fold appearance of the ore body and the mode in which the fold was cut due to the overthrusting of the Baviaanskloof Gneiss.
- Figure 4.6:** Sketch showing the internal folding inside the Doornhoek Ore Body at the contact with the Baviaanskloof Gneiss. The  $D_3$  folds are enveloped by the  $D_2$  folds but have a variable wave-length and locally display mylonitic features (vertical cross-section, 1cm=1m).
- Figure 4.7:** Fibrous anthophyllite in a hydrated ultramafic granulite (sample DH-2136).  
1cm=400 $\mu$ m
- Figure 4.8:** Sample DH-1073: Calcite augens in a felsic granulite. Note the tails of these fish-like structures and the presence of deformation lamellae in quartz showing a dextral displacement. The similar rheological behaviour of the carbonate augens and the quartz host shows that the deformation at the time of augen formation was ductile.  
1cm=400 $\mu$ m
- Figure 4.9:** Stereograms showing the structural elements foliation and lineation inside the Doornhoek Ore Body (Schmidt projection). Average strike direction is 174°8' with a 88°3' angle of dip towards north. Mean lineation direction is 85°2' dipping at 3° towards east.  
 a) *Foliation (dip direction data)*: 403 poles to plane (contours at 20%, 5%, 3% and 1% per 1% area)  
 b) *Lineation plunge data*: 110 lineation data (contours at 12%, 5%, 3% and 1% per 1% area)  
 c) *Quartz boudins*: 39 measurements of long axis boudines (contours at 15%, 3%, 2% and 1% per 1% area).
- Figure 4.10:** Stereograms of plots of orientation of optic axes for minerals which occur within the Doornhoek Ore Body. Samples were cut perpendicular to the fabric, along lineation direction (kinematic direction). Projections are made on the horizontal plane. S is the vertical projection of the foliation plane. N is the true north direction.  
 a) *Hornblende*: 237 [010] axes (contours at 12%, 5%, 3% and 1% per 1% area; L represents the *c* axis)  
 b) *Biotite*: 93 {001} poles of biotite (contours at 25%, 10%, 5% and 1% per 1% area)  
 c) *Plagioclase (An<sub>35</sub> in average)*: 29 [100] axes of plagioclase (contours at 18%, 10%, 5% and 1% per 1% area)  
 d) *Quartz*: 336 [0001] axes (contours at 8%, 5%, 3% and 1% per 1% area)  
 e) 123 poles of shear fractures (no tension) in 27 garnet porphyroblasts (contours at 20%, 10% 5% and 1% per 1%)
- Figure 4.11:** Stereograms of plots of orientation of optical axes for minerals which occur within the Baviaanskloof Gneiss, tectonically thrust over the Doornhoek Ore Body. Projections are made normal to the foliation of the gneiss. S is the vertical projection of the foliation plane. N is the north direction.  
 a) *Fabric of the banded Baviaanskloof Gneiss*: black is biotite, mesh-twinned is microcline, dashed is quartz and without fabric is plagioclase  
 b) *Biotite*: 157 {001} poles of biotite (contours at 8%, 5%, 3%, 2% and 1% per 1% area)  
 c) *Quartz*: 276 [0001] axes (contours at 5%, 3%, 2% and 1% per 1% area)  
 d) *Plagioclase*: 197 [100] axes in plagioclase (contours at 12%, 5%, 3% and 1% per 1% area)

e) *Microcline* : 97 {001} axes in plagioclase (contours at 12%, 5%, 3% and 1% per 1%)

f) No representation

- Figure 4.12: An illustration of the relationship between the Kaapvaal Craton and the two zones of the SMZ, as suggested by Stevens (1995). In the scenario proposed by Stevens, the ortho-amphibole isograd is represented by a fault boundary and is not related to the grade of metamorphism. Escaping hydrated fluids may have blurred this relationship slightly by interacting to a minor degree with the overlying granulite zone. This would depend on synretrogression thrusting. Open arrows indicate melt migration, filled arrows indicate fluid migration (*after Stevens, 1995*).
- Figure 4.13: Schematic crustal section of the terrane boundary of the granite-greenstone terrane of the KVC and the SMZ of the LB.
- Figure 5.1: Untwinned plagioclase crystals (Pl) and xenomorphic grains of quartz crystalloblasts (Qz) occurring as main constituents in the Baviaanskloof Gneiss (sample DH-L7).  
1 cm = 400  $\mu$ m
- Figure 5.2: Microphotograph of biotite (Bi) being replaced by muscovite (Mu). The core of the biotite is highly chloritised. The opaque mineral occurring along the biotite cleavage is ilmenite (arrow).  
1 cm = 400  $\mu$ m
- Figure 5.3: Vertical leucocratic (anatectic?) veins that crosscut the banded Baviaanskloof Gneiss. The grey host gneiss is trondhjemitic in composition.
- Figure 5.4: Microphotograph of a mafic granulite interlayered with the Baviaanskloof Gneiss near Doornhoek: hornblende (Ho) replaces orthopyroxene (Opx). A quartz-magnetite augen occurs in the center. Biotite (Bi) and Ca-amphibole (Tr = tremolite) are also present.  
1cm=200 $\mu$ m
- Figure 5.5: Unhydrated grey metapelite with lenses of quartz and feldspar. The primary paragenesis of this rock is plagioclase, biotite, garnet, quartz, cordierite and hypersthene (photo taken at Petronella locality, north of the orthoamphibole isograd).
- Figure 5.6: An idioblastic garnet (Ga) surrounded by cordierite (arrow). This is a metamorphic reaction which documents the  $M_1$  decompression north of the isograd ( $ga+qz=crd+hy$ ).
- Figure 5.7: Baviaanskloof Gneiss (folded and grey) with pinkish neosome composed mainly of microcline-perthite and albite.
- Figure 5.8: Typical tonalitic Baviaanskloof Gneiss at Doornhoek. The gneiss host (grey) reflects the regional hydration event. The hydrated gneiss is crosscut by a pinkish vein, which is the product of metasomatic alteration. It consists mainly of microcline-perthite, albite and quartz. Quartz (Qz) is already forming boudins, due to its different rheological behaviour.
- Figure 5.9: Baviaanskloof Gneiss. Relic plagioclase crystals (Pl) with deformed twinning planes. The plagioclase is replaced by newly formed albite (Ab) and microcline-perthite as the result of the intense alteration that affected the Doornhoek area.  
1cm=100 $\mu$ m
- Figure 5.10: Baviaanskloof Gneiss. Relic plagioclase crystals (Pl), still displaying deformation lamellae, replaced by newly formed albite (Ab).  
1cm=100 $\mu$ m

- Figure 5.11:** Newly formed metasomatic vein material, consisting mainly of microcline-perthite. Note the presence of relic plagioclase crystals (Pl). 1cm=100µm
- Figure 5.12:** Relic plagioclase (Pl) replaced by both microcline-perthite (M) and quartz (Qz). 1cm=50µm
- Figure 5.13:** Sub-solidus replacement of plagioclase (Pl) by microcline-perthite (M). 1cm=50µm
- Figure 5.14:** Boundary between leucocratic vein and Baviaanskloof Gneiss: anhedral grain of microcline-perthite penetrating through intercrystalline discontinuities into the Baviaanskloof Gneiss. Part of the quartz has been remobilised as very thin channelets into the initial plagioclase (Pl) at the edges of the crystals forming real myrmekitic textures (arrow). 1cm=100µm
- Figure 5.15:** Albite (thick black stripes) hosted by the K-feldspar (grey host) as channelets along the perthitic planes. 1cm=25µm
- Figure 5.16:** Albite and K-feldspar substitute for each other along perthitic planes rather than albite being the product of exsolution in microcline-perthite (M). One can also see the newest crystallised pure albite (Ab), replacing the microcline-perthite. Myrmekitic structures (arrow) also occur in the albite. 1cm=50µm
- Figure 5.17:** Same as photo 5.16 but slightly rotated in order to better see the myrmekitic structure. 1cm=50µm
- Figure 5.18:** Microcline-perthite (M) is the main component of the newly formed metasomatic veins. Albite (Ab) replaces deformed plagioclase. 1cm=50µm
- Figure 5.19:** The metasomatic corrosion exercised by the microcline-perthite (M) was so intense that even the preexisting quartz (Qz) from the initial paragenesis of the tonalitic gneiss has been almost completely consumed by microcline-perthite. 1cm=100µm
- Figure 5.20:** Blow-up of photo 5.20 in order to better see the quartz relics within the newly introduced microcline-perthite. 1 cm=25µm
- Figure 5.21:** Field-image of photos 5.19 and 5.20 in order to have a better understanding of the relationships between quartz and microcline. 1 cm=100µm
- Figure 5.22:** Biotite relic (arrow) in a K-feldspar-rich metasomatic vein in the Baviaanskloof Gneiss. 1cm=400µm
- Figure 5.23:** Highly corroded biotite crystal in newly formed microcline-perthite. A weak Fe contamination of the microcline-perthite is noticed at the contact. 1cm=25µm
- Figure 5.24:** Muscovite (Mu) formed as a result of Fe-depletion of the chloritised biotite (arrow). 1cm=400µm
- Figure 5.25:** Muscovite in veins (arrow) crosscutting the microcline-perthite. 1cm=200µm
- Figure 5.26:** Photograph of drill core showing altered and sheared calc-silicate facies BIF. Note the presence of quartz boudines in the foliation (borehole DD7, 55.50-55.68m).

- Figure 5.27:** Photograph of drill core samples of the magnetite-free calc-silicate facies BIF. Note the presence of quartz boudines, some of them mineralised with gold (borehole DD7, 58.00-60.00m).
- Figure 5.28:** Slightly altered magnetite-bearing mafic rock: ferrohypersthene +salite + magnetite.  
1cm=400µm
- Figure 5.29:** Microphotograph showing the initial retrogression of the magnetite-bearing BIF, in which ferrohypersthene (Opx) is rimmed by ferrogedrite (arrow). Metasomatic biotite (Bi) changed its rim composition due to an interactive chemical exchange with the orthopyroxene, and became marginally very Fe-rich.  
1cm=200µm
- Figure 5.30:** Microphotograph showing gedrite-ferrogedrite (G-Fg - intense green) which completely replaced the initial Opx in the magnetite-free paragenesis of the BIF.  
1cm=400µm
- Figure 5.31:** Microphotograph illustrating the replacement of salite (Sa) by Fe-rich hornblende (Ho) in the magnetite-rich assemblage of the BIF.  
1cm=400µm
- Figure 5.32:** Microphotograph illustrating garnet (Ga) intergrown with ferrohypersthene (Opx) at the boundary between the magnetite-rich and the magnetite-free BIF. This specific lithological sequence was intensely altered by the mineralising fluids.  
1cm=200µm
- Figure 5.33:** Microphotograph illustrating the completely retrogressed ultramafic granulite, now consisting mainly of anthophyllite (sample DH-2120).  
1cm=400µm
- Figure 5.34:** Drill core sample from borehole DD-2 (89.75-89.90m). Felsic granulite (probably an altered metapelite) which usually occurs as thin layers in BIF.
- Figure 5.35:** Microphotograph of sample DD2-13. Relics of garnet (high relief mineral - arrows), probably belonging to the M<sub>2</sub> metamorphic event (typical retrograde zoning pattern) occur in a matrix consisting mainly of quartz, newly introduced K-feldspar and albite.  
1cm=400µm
- Figure 5.36:** Large retrograde garnet poikiloblast (Ga) associated with interstitial cordierite (colourless). Newly formed biotite (arrow) occurs in the finely crystallised felsic granulite. Due to the intense metasomatism, the matrix now consists of albite and K-feldspar (translucent) (sample DH-2028). Albite, cordierite and K-feldspar can be separated only by electron microprobe.  
1cm=400µm
- Figure 5.37:** At the boundary between the BIF and the felsic granulite, relics of plagioclase (Pl = An<sub>90</sub>) from the former paragenesis still occur. This early plagioclase is intensely twinned (arrow) (sample DH-2008).  
1cm=200µm
- Figure 5.38:** Newly crystallised tourmaline crystals (arrow) occurring in the highly metasomatised felsic granulite (sample DD-2-13).  
1cm=200µm
- Figure 5.39:** Photograph of a drillcore sample showing the relationship between the metasomatic biotite-garnetiferous formation (red arrow) and the quartz veins (blue arrow). Both the garnetiferous formation and the quartz veins are mineralised (borehole DD2, 68.90-69.25m).
- Figure 5.40:** A close-up of the relationship between the biotite-garnetiferous formation and the quartz veins. The garnets are usually idioblastic, zoned, mineralised and display a prograde

zonation pattern. In this sample quartz appears brecciated (borehole DD2, 69.31-69.44m).

- Figure 5.41: Microphotograph showing the boundary between the newly formed metasomatic biotite-garnetiferous formation (BiGF) and the BIF. Sample DH-2034.  
1cm=1000µm
- Figure 5.42: Microphotograph of a large zoned euhedral garnet (Ga) associated with biotite (Bi) and also containing biotite inclusions (arrow). The biotite-garnetiferous metasomatic rock is closely associated with mineralised quartz veins (Qz). Sample DH-2035.  
1cm=1000µm
- Figure 5.43: Drill core (74 cm length) showing the relationship between quartz veins (Qz) and the biotite-garnetiferous formation (BiGF). Thin horizons of fine grained felsic granulite (arrows), also intensely metasomatised (K-feldspar and albite), occur interlayered with the mineralised horizons.
- Figure 5.44: A sketch map illustrating the relationships between quartz-veins (yellow), the metasomatic biotite-garnetiferous formation (red) and the BIF, felsic granulite or mafic granulite (wall-rock, white). The observed structural relationships suggest that the newly formed mineralised horizons (yellow and red) represent the filling of quasi-vertical deep crustal channels. The main mineralisation precipitated with the hydrothermal quartz veins (yellow). The fluid which carried and precipitated the huge amount of silica strongly interacted (metasomatically) with the BIF and formed the biotite-garnetiferous formation, which is also mineralised. The mineralisation occurring in the quartz veins is identical to the mineralisation in the metasomatic garnet.
- Figure 5.45: Sketch of textural relationship in drill core DD-35. The metasomatic biotite-garnetiferous formation (black) envelopes the mineralised quartz veins (yellow). These two altered sequences are hosted by previous lithologies such as felsic granulite (white) and granulitic BIF granulite (horizontal dashes).
- Figure 5.46: Microphotograph showing relics (laminae) of cpx-opx, "assimilated" from the wall-rock and cemented by the highly deformed quartz veins. (Sample DH-2037).  
1cm=400µm
- Figure 5.47: Microphotograph showing highly deformed fragments of ga-opx xenoblasts retrogressed into amphibole and orientated parallel to the vein margin and wall-rock foliation. The composition of the wall-rock in this case is identical to the fragments assimilated during the D<sub>2</sub> shear event within the newly formed shear zones and quartz veins. Sample DH 2067.  
1cm=400µm
- Figure 5.48: The same image as fig. 5.47, but with X-Nicols. The shear fabric is better highlighted. Sample DH 2067.  
1cm=400µm
- Figure 5.49: Brecciated character of a quartz vein (Qz) that hosts gold-related mineralisation and contains relics of opx, garnet and amphiboles from the wall-rock (WR). Borehole DD-2, sample DD2-11.
- Figure 5.50: Brecciated features of a weakly mineralised quartz vein system (Qz). Note how the quartz "infiltrated" the wall-rock (WR). Borehole DD-2, Sample DD2-24.
- Figure 6.1: Microprobe traverses of two garnet porphyroblasts showing the variation in the pyrope, grossular and spessartine contents. *a.* typical retrograde pattern displayed by very small (< 1mm) garnet grains that occur as inclusions in large orthopyroxene. The core to rim increase in the spessartine content and the core to rim decrease in the pyrope content is clear. The grossular pattern is quite irregular. *b.* typical prograde zoning pattern

displayed by large garnet crystals (8mm) that form part of the metasomatic biotite-garnetiferous formation. The increase in the pyrope content from core to rim and the decrease in the spessartine content from core to rim is clear. The grossular variation is quite erratic.

**Figure 6.2:**  $Ti^{4+}(\%)$  versus  $Fe^{2+}(tot)/Mg^{2+}$  (microprobe analyses) for biotite compositions in the highly altered (metasomatised) lithologies (prograde lithologies - red) compared with biotite from the pervasively hydrated lithologies (retrograde lithologies - blue). Biotite associated with the prograde zoned garnet shows a higher Ti content than biotite associated with the retrograde zoned garnet. Furthermore, the cores of biotite from the prograde zoned lithologies show a higher Fe/Mg ratio than the core of biotite associated with the retrograde lithologies, which usually shows enrichment in Mg.

**Figure 6.3:** Nomenclature of pyroxenes in the system  $CaMgSi_2O_6$ - $CaFeSi_2O_6$ - $Mg_2Si_2O_6$ - $Fe_2Si_2O_6$  (modified after Poldervaart and Hess, 1951, in order to include the spatial distribution of the orthopyroxenes). Both orthopyroxene and clinopyroxene compositions are plotted on the same graph ( $\Delta$  represents orthopyroxene;  $\circ$  represents clinopyroxene; the red arrow indicates the chemical evolution of the opx during retrogression and alteration; the green arrow shows the chemical evolution of the cpx during retrogression and alteration).

**Figure 6.4:** A Mg- $Fe^{2+}$ -Ca diagram for amphiboles in the absence of alkali metals and trivalent elements (after Whittaker, 1960). Symbols as in the legend. There are mainly three types of amphiboles in all rock types:

$\Delta$  ferrogdrite-grunerite and anthophyllite

\* actinolite-tremolite.

[ ] Al-rich amphiboles which do not plot accurately in this type of diagram.

Due to the intense alteration suffered by lithologies at Doornhoek, and the intimate transition between lithologies with very different bulk chemistries, a continuous transition in the amphibole composition occurs.

**Figure 6.5:** Ternary diagram showing the composition of calcite present in some of the quartz veins. The carbonate is a ferroan calcite with up to 6.87 per cent FeO.

**Figure 6.6:** Sample 2101: Baviaanskloof Gneiss outcropping at Doornhoek Farm. Photograph showing newly formed folded metasomatic leucocratic veins consisting of microcline-perthite and albite, crosscutting the grey tonalitic Baviaanskloof Gneiss.

**Figure 6.7:** Sample DH 2106, Baviaanskloof Gneiss outcropping at Doornhoek Farm. Microphotograph showing a garnet porphyroblast (Ga) surrounded by orthopyroxene (Opx). The orthopyroxene is replaced by biotite (blue arrows) and later introduced quartz (Qz).

1cm=100 $\mu$ m

**Figure 6.8:** Sample DD-2-2014: BIF. Microphotograph showing a small relic of garnet (Ga) included in a large orthopyroxene crystal. This garnet typically displays retrograde zoning probably due only to diffusion (Fe/Mg exchange).

1cm=50 $\mu$ m

**Figure 6.9:** a) Pyrope, spessartine and grossular distribution within a partially resorbed garnet showing retrograde zoning (microphotograph in fig. 6.8). The garnet is predominantly almandine in composition. Although the  $Fe/(Fe+Mn+Mg+Ca)$  ratio is relatively high, the pyrope, spessartine and grossular ratios are still highly variable. The  $Mg/(Mg+Fe)$  ratio shows a decrease from core to rim, from 2.2 per cent to 1.2 per cent;

Figure 6.9.b: The  $Mn/(Mn+Mg+Fe+Ca)$  ratio increases from a low of 5.6 per cent in the core of the garnet to a high of 8 per cent towards the rim of the porphyroblast. This variation of the Mn content within the garnet porphyroblast is typical retrograde.

Figure 6.9.c: The  $Ca/(Ca+Mn+Mg+Fe)$  ratio shows a *positive ridge* of almost 18 per cent in the middle of the crystal. The grossular ratio decreases softly to a minimum of 17 per cent and then increases sharply to more than 20 per cent.

Figure 6.10: Photograph of borehole DD-7, 47.23-47.30 m showing retrograde zoned and elongated garnets in a felsic granulite. This garnet is clearly pre-tectonic, being deformed during the deformational event that accompanied metasomatism.

Figure 6.11: Sample DH-2139: Highly altered felsic granulite. The microphotograph displays elongated garnets (Ga) from fig. 6.10 under the polarising microscope. One can see a system of shear joints developed within the rods-like garnets, a close association between garnet and Ti-rich biotite, and a relatively high amount of graphite (opaque).

1cm=400 $\mu$ m

Figure 6.12: Sample DH-7-23: Highly altered felsic granulite at the boundary with magnetite-rich BIF. The microphotograph shows biotite replacing garnet (yellow arrow). Both the garnet and the biotite display a typical retrograde pattern, excepting a very thin contact between the two reacting minerals. The garnet in contact with biotite is more Fe-rich than the garnet core, while the biotite shows the opposite. But when the biotite is not in direct contact with garnet, the Mg/Fe ratio in the core of the biotite is always higher than in the rims, as well as the  $TiO_2$ -content. This red biotite shows a very high Ti-content, indicative of initial high-grade metamorphism undergone by the rock.

1cm=400 $\mu$ m

Figure 6.13: Photograph of borehole DD-2, 67.30-67.52m, sample DD2-35. Folded layers of the biotite-garnetiferous formation representing the product of intense potassic metasomatism.

Figure 6.14: Sample DD-2-35: Biotite-garnetiferous formation. Microphotograph of the borehole chip displayed in fig. 6.13. These prograde zoned garnets are surrounded by biotite and smaller amounts of quartz. The dark core is characterised by the presence of numerous very fine grained inclusions consisting of ilmenite, magnetite, graphite, sulphides, arsenides and gold.

1cm=750 $\mu$ m

Figure 6.15: Sample DD-2-35: Biotite-garnetiferous formation. Microphotograph of a large euhedral zoned porphyroblast of garnet. Both the garnet and the associated biotite display a typical prograde growth zoning pattern. The garnet consists of four concentric zones which are better illustrated in fig. 6.16: a mineralised core (yellow), an inner zone (red), an inner black ring (pink) and a wide rim (white). Mineralisation is mainly present within the core and the inner ring, and it also displays a prograde pattern (see text). Biotite inclusions (arrows) coloured black in fig. 6.16 occur throughout the garnet, from core to edge. The gold mineralisation is associated with arsenides and graphite, usually in the inner zone and inner ring.

1cm=1000 $\mu$ m

Figure 6.16: The prograde zonation pattern of this garnet is best shown by a) the pyrope  $[Mg/(Mg+Fe)]$  ratio and by b) the spessartine distribution  $[Mn/(Mn+Mg+Fe+Ca)]$ . These molar distributions are based on 800 microprobe point analyses.

a)  $Mg/(Mg+Fe)$  increases from core to rim, from 3 to 10 per cent.

b) Spessartine molar ratio decreases from 7 per cent in the core to 1wt per cent to the very edge.

Figure 6.16.c: Grossular molar ratio displays a relative random distribution from 14 per cent in the core, decreasing to 12 per cent towards the inner ring, increasing to 19 per cent and decreasing again sharply to 13 per cent towards the edge.

Figure 6.17: a) Different alteration patterns that can occur after various lithologies have presumably undergone hydrothermal alteration at the time of gold introduction. Note that the sketch does not indicate neither the scale nor the metamorphism or alteration intensity. Four different lithological types are illustrated: a) basalts; b) calc-silicate-oxide facies BIF; c) ultramafic and komatiitic; d) silica-saturated and -undersaturated granitoid rocks (from Colvine *et al.*, 1988).

The sketch above illustrates the schematic representation of the field of occurrence of important minerals in progressively altered and metamorphosed basaltic rocks in gold-bearing systems. Hornblende is the main mineral for high-grade metamorphic conditions and low fluid:rock ratios. Garnet is characteristic for high-grade metamorphic condition and intense alteration (high fluid:rock ratio).

Possible prograde reactions that occurred at Doornhoek (after Colvine *et al.*, 1988):

- a1 - Quartz + Calcite + Chlorite = Hornblende
- a2 - Quartz + Calcite + Chlorite = Actinolite
- a3 - Chlorite + Quartz + Magnetite + K<sup>+</sup> = Biotite
- a4 - Chlorite + Quartz + H<sub>2</sub>S = Anthophyllite + Cordierite + Pyrrhotite
- a5 - Chlorite + Quartz + Dolomite + K<sup>+</sup> = Garnet + Pargasite

Figure 6.17b: Schematic representation of the fields of occurrence of important minerals in progressively altered and metamorphosed calc-silicate facies BIF in gold-bearing systems. Hedenbergite and Fe-rich olivine (fayalite) is the alteration product characteristic for high PT conditions and low alteration intensity. Garnet and pyrrhotite+arsenopyrite are the minerals formed under high-grade metamorphic condition and high fluid-rock ratio.

Possible prograde reactions that occurred at Doornhoek:

- b1 - Chlorite + Quartz + Dolomite + K<sup>+</sup> = Stilpnomelane + Calcite
- b2 - Magnetite + Quartz = Grunerite
- b3 - Grunerite-gedrite + H<sub>2</sub>S = Gedrite + Pyrrhotite + Quartz
- b4 - Chlorite + Quartz + Magnetite + K<sup>+</sup> = Biotite
- b5 - Chlorite + Quartz + Dolomite + K<sup>+</sup> = Garnet + Pargasite

Figure 6.18: Sample DD-2-2035: Microphotograph of the contact between the retrograde opx-bearing BIF (green) and the prograde biotite-garnetiferous formation (brown). The contact is characterised by ilmenite-magnetite-pyrrhotite-pentlandite-chalcopyrite mineralisation. Biotite associated with garnet also displays variation in chemistry (Mg-rich rims, Mg-poor cores).

1cm=1000µm

Figure 6.19: Sample DD-2-2035: Biotite-garnetiferous formation. This microphotograph shows tiny inclusions of biotite (Bi) in the dark inner-ring zone of the prograde garnet porphyroblast. The inner-ring zone is highly mineralised (opaque minerals).

1cm=25µm

Figure 6.20: Sample DD-2-2020: Wall-rock BIF. Microphotograph showing a large orthopyroxene crystal crosscut perpendicular to the [010] cleavage planes by narrow veinlets consisting of pyrrhotite-magnetite-chalcopyrite-löllingite-gold (opaque). The epigenetic introduction of sulphide-oxide mineralisation has been made under high deformation conditions, resulting in the ductile behaviour of a normally brittle mineral.

1cm=100µm



- Figure 6.21:** Same view as fig. 6.20 but under X Nicols for a better visualisation of the kink-band deformation in birefringent colours.
- Figure 6.22:** Sample DD-2-2020. Wall-rock BIF. Blow up of microphotograph 8.15. The angle between the direction of the mineralised veinlets (opaque) and the direction of the cleavage planes in opx (arrows) is obvious. Mineralisation is therefore clearly unconformable and epigenetic with reference to the peak metamorphic assemblage.  
1cm=25µm
- Figure 6.23:** Sample DD-2-2020. Wall-rock BIF. Microphotograph showing introduction of mineralised veinlets (opaque) parallel to the cleavage direction of the opx.  
1cm=25µm
- Figure 6.24:** Sample DD-2-2020. Wall-rock BIF. Microphotograph showing mineralisation infiltrating both unconformably and conformably into the opx. The infiltration of sulphides and oxides took place under pressure, as shown by tiny fragments of brecciated opx (arrows). These tiny, highly deformed and corroded pieces of opx are part of the main opx crystal which was fragmented by the infiltration of ore minerals.  
1cm=25µm
- Figure 7.1:** Intimate association between the syn-tectonic quartz veins (Qz) and biotite-garnetiferous formation (BiGF). Both mineralised formations were deformed and folded during D<sub>3</sub>. Borehole DD-7, 46.60-49.70m.
- Figure 7.2:** Drillcore sample showing a quartz-calcite vein with material still left "undigested" from the wall-rock BIF. Borehole DD-5, 81.55-82.75m.
- Figure 7.3:** Microphotograph of the coarse grained calcite-quartz vein macroscopically shown in fig. 7.2. Orthopyroxene (opx) occurs as remnants of the wall-rock BIF (the interference colours are high due to the thick thin section). The carbonate is ferroan calcite (Cc). Sample DH-2114.  
1cm=400µm
- Figure 7.4:** Microphotograph of a highly sheared quartz-calcite vein displaying highly sigmoidal shaped calcite augens. Sample DH-1073.  
1cm=400µm.
- Figure 7.5:** Photograph of a drillcore sample showing boudinaged syn-tectonic quartz veins. The quartz boudines are hosted by mineralised calc-silicate facies BIF. Sample DH-2135 from borehole DD-5, 90.33-90.38m.
- Figure 7.6:** Relics of garnet and opx, identical in composition to similar minerals from the wall-rock, and orientated parallel to the edges of the quartz vein. Sample DH-1073.  
1cm=400µm.
- Figure 7.7:** Microphotograph in reflected light of the high-temperature mineral paragenesis: löllingite (Lo) associated with magnetite (Mt) and pyrrhotite (Po). The host is orthopyroxene. Sample DH-2114.  
1cm=200µm
- Figure 7.8:** Microphotograph in reflected light showing arsenopyrite (Aspy) and pyrrhotite (Po) that are part of the medium-temperature ore mineral association. Sample DH-2025.  
1cm=100µm
- Figure 7.9:** Microphotograph in reflected light of chalcopyrite (Cpy) and arsenopyrite (Aspy), part of the medium-temperature ore mineralisation. Sample DH-2025.  
1cm=100µm

- Figure 7.10:** Microphotograph in reflected light of sphalerite with chalcopyrite exsolutions (tiny yellow specks). This association is also part of the medium-temperature ore mineralisation. Sample DH-2025. 1cm=50µm
- Figure 7.11:** Microphotograph in reflected light of gold (actually electrum - arrow) hosted by löllingite veins (white). Sample DH-2011. 1cm=25µm
- Figure 7.12:** Microphotograph in reflected light of a tiny grain of gold (blue arrow) that together with sphalerite+chalcopyrite (red arrow) and magnetite (Mt), are hosted by a thin quartz vein (yellow arrow). Note that sphalerite includes chalcopyrite exsolutions and is also rimmed by a thin shell of chalcopyrite. Sample DH-2017. 1cm=25µm
- Figure 7.13:** Microphotograph (reflected light) of euhedral/subhedral magnetite crystals (Mt) intergrown with pyrrhotite (Po) (sample DH-2138). 1cm=400µm
- Figure 7.14:** Microphotograph (reflected light) of schlieren of pyrrhotite and magnetite orientated parallel to the shearing direction and replacing shear microfolds. Sample DH-2030. 1cm=400µm
- Figure 7.15:** Microphotograph in transmitted light of magnetite (Mt-opaque) that corrodes orthopyroxene (Opx). This brecciated type of mineralisation is preserved in relatively unshered portions of the ore body. 1cm=400µm
- Figure 7.16:** Microphotograph in reflected light showing replacement of orthopyroxene (opx) by magnetite (Mt). This reaction started along cleavage planes or irregularities and represents a frozen stage of the replacement reaction of opx by magnetite. Pyrrhotite (Po) is also present in the field of this photograph. Sample DD-2-2. 1cm=25µm
- Figure 7.17:** Photograph of a drillcore sample showing the pre-existent mineral assemblage almost totally replaced by pyrrhotite (yellow). Sample DH-2221, borehole DD-19, 113.50-113.60m.
- Figure 7.18:** Microphotograph (reflected light) showing the partial replacement of the silicate assemblage by pyrrhotite (Po) and löllingite (Lo). Sample DH-2113. 1cm=200µm
- Figure 7.19:** Microphotograph showing thin veinlets of chalcopyrite (red arrows) crosscutting pyrrhotite. Sample DH-2113. 1cm=100µm
- Figure 7.20:** Microphotograph showing an occurrence of very late chalcopyrite (Cpy) in crosscutting veinlets. Sample DH-2115. 1cm=200µm
- Figure 7.21:** Microphotograph showing porous pyrite (Py) after pyrrhotite (Po). Sample DH-2097. 1cm=400µm
- Figure 7.22:** Microphotograph showing löllingite (Lo) associated with the highest temperature ore paragenesis at the Doornhoek gold-deposit. It is corroded by pyrrhotite (Po). Sample DH-2030. 1cm=200µm
- Figure 7.23:** Microphotograph showing löllingite (Lo) associated with both magnetite (arrow) and pyrrhotite (Po) in crosscutting veins. Sample DH-2030. 1cm=400µm

- Figure 7.24:** Microphotograph showing gold grains included in löllingite (red arrow) and free gold associated with graphite (blue arrow). The microprobe analyses demonstrated that this type of löllingite displays inclusions of arsenopyrite. Magnetite (Mt) also occurs. Sample DH-2039. 1cm=50µm
- Figure 7.25:** Microphotograph showing crystals of gersdorffite (arrow) included within the prograde garnet porphyroblast (Ga). This gersdorffite is very unusual: instead of the normal formula (Fe,Ni)AsS<sub>3</sub>, it contains up to 6wt% Zn, suggesting the formula (Fe,Ni,Zn)AsS<sub>3</sub> - probably a new mineral phase. Sample DH-2038. 1cm=100µm
- Figure 7.26:** Microphotograph showing an isolated skutterudite crystal (arrow) associated with a pyrrhotite (Po) - gersdorffite (Gs) veinlet. Sample DH-2039. 1cm=50µm
- Figure 7.27:** Microphotograph showing graphite crystals (red arrows) at the edge of a large prograde garnet porphyroblast (Ga). A system of thin quartz veinlets (yellow arrows) displays gold (electrum) mineralisation (Au). Sample DH-2047. 1cm=50µm
- Figure 7.28:** Gold crystals intimately associated with graphite (G) in a quartz (Qz) - calcite (Cc) vein. Arsenopyrite occurs in the corner of the microphotograph (arrow). Sample DH-2047. 1cm=25µm
- Figure 7.29:** Microphotograph showing gold crystals (yellow arrow) associated with arsenopyrite (red arrow) and large graphite crystals (G). Sample DH-2047. 1cm=25µm
- Figure 7.30:** The four stages of mineralisation described in the text. Mineralisation started with a low-temperature paragenesis (step 1), consisting mainly of arsenopyrite-sphalerite-chalcopyrite and pyrrhotite. The deposition continued with medium-temperature mineralisation (step 2), consisting mainly of arsenopyrite, Ni-bearing minerals, pyrrhotite and gold. A time gap followed after step 2. Mineralisation then continued with a high-temperature paragenesis (step 3) consisting of löllingite-pyrrhotite-magnetite and electrum. These three stages of ore mineral deposition occurred during a prograde metamorphic event. Step 4 was represented by the remobilisation of the initial Fe sulphides, mainly as pyrite and secondary pyrrhotite and small amounts of gersdorffite during a retrograde event.
- Figure 7.31:** Microphotograph showing sulphides hosted by the core of a large, progradely zoned garnet porphyroblast (see fig. 6.15). This mineralisation consists of chalcopyrite (yellow arrow), pyrrhotite (blue arrow), arsenopyrite (red arrow) and tiny sphalerite crystals (black arrow). A large sphalerite crystal also occurs. Sample DH-2035. 1cm=25µm
- Figure 7.32:** Microphotograph showing graphite crystals (beige rods) and As-rich arsenopyrite (red arrow) trapped in the inner zone of the prograde garnet porphyroblast. Their actual host is quartz also trapped inside the garnet. Sample DH-2035. 1cm=25µm
- Figure 7.33:** Microphotograph showing löllingite (Lo) and tiny magnetite and ilmenite crystals (arrows) trapped in the dark inner-ring zone of the prograde garnet porphyroblast. Sample DH-2035. 1cm=25µm
- Figure 7.34:** Microphotograph showing a tiny gold crystal (red arrow) associated with pyrrhotite (yellow arrow) and gersdorffite (blue arrow) in the inner zone of the prograde, zoned garnet porphyroblast. Magnetite is relatively abundant (mauve arrow). Graphite is also present as very small crystals. Sample DH-2035. 1cm=25µm

**Figure 7.35:** Microphotograph showing a high density of tiny crystals of Fe and Ti oxides entrapped in the dark inner-ring zone of the prograde zoned garnet porphyroblast. Sample DH-2035. 1cm=25µm

**Figure 8.1:** a) Different alteration patterns that can occur after various lithologies have presumably undergone hydrothermal alteration at the time of gold introduction. Note that the sketches do not indicate the scale and neither the metamorphism or alteration intensity. Four different lithological types are illustrated: a) basalts; b) calc-silicate-oxide facies BIF; c) ultramafic and komatiitic; d) silica-saturated and -undersaturated granitoid rocks (from Colvine et al., 1988).

The sketch above illustrates the schematic representation of the field of occurrence of important minerals in progressively altered and metamorphosed basaltic rocks in gold-bearing systems. Hornblende is the main mineral for high-grade metamorphic conditions and low fluid:rock ratios. Garnet is characteristic for high-grade metamorphic condition and intense alteration (high fluid:rock ratio).

Possible prograde reactions that occurred at Doornhoek (after Colvine et al., 1988):

- a1 - Quartz + Calcite + Chlorite = Hornblende
- a2 - Quartz + Calcite + Chlorite = Actinolite
- a3 - Chlorite + Quartz + Magnetite + K<sup>+</sup> = Biotite
- a4 - Chlorite + Quartz + H<sub>2</sub>S = Anthophyllite + Cordierite + Pyrrhotite
- a5 - Chlorite + Quartz + Dolomite + K<sup>+</sup> = Garnet + Pargasite

**Figure 8.1b:** Schematic representation of the fields of occurrence of important minerals in progressively altered and metamorphosed calc-silicate facies BIF in gold-bearing systems. Hedenbergite and Fe-rich olivine (fayalite) is the alteration product characteristic for high PT conditions and low alteration intensity. Garnet and pyrrhotite+arsenopyrite are the minerals formed under high-grade metamorphic condition and high fluid-rock ratio.

Possible prograde reactions that occurred at Doornhoek:

- b1 - Chlorite + Quartz + Dolomite + K<sup>+</sup> = Stilpnomelane + Calcite
- b2 - Magnetite + Quartz = Grunerite
- b3 - Grunerite-gedrite + H<sub>2</sub>S = Gedrite + Pyrrhotite + Quartz
- b4 - Chlorite + Quartz + Magnetite + K<sup>+</sup> = Biotite
- b5 - Chlorite + Quartz + Dolomite + K<sup>+</sup> = Garnet + Pargasite

**Figure 8.1c:** Schematic representation of the fields of occurrence of important minerals in progressively altered and metamorphosed ultramafic and komatiitic rocks in gold-bearing systems. Anthophyllite is the main alteration mineral and it can be associated with tremolite under low alteration condition and biotite under high alteration condition (high fluid:rock ratio).

Possible prograde reactions that occurred at Doornhoek:

- c1 - Serpentine + CO<sub>2</sub> = Talc + Magnesite
- c2 - Talc + Chlorite + K<sup>+</sup> = Anthophyllite + Biotite

**Figure 8.1d:** Schematic representation of the fields of occurrence of important minerals in progressively altered and metamorphosed silica-saturated and -undersaturated granitoid rocks in gold-bearing systems. Biotite and orthoclase represent the alteration minerals characteristic for the entire spectrum of high-grade metamorphic condition, for both low and high alteration intensity. Scapolite is also part of the mineral paragenesis associated with very high fluid:rock ratios.

Possible prograde reactions that occurred at Doornhoek, and also at Klipbank and Petronella:

d1 - Albite + K<sup>+</sup> = Orthoclase

d2 - Chlorite + Albite + Quartz + K<sup>+</sup> = Orthoclase + Biotite

d3 - Garnet + K<sup>+</sup> = Biotite + Sillimanite + Quartz

- Figure 8.2:** Sample DD-2-2014: Mineralised quartz vein. Microphotograph showing fragments of garnet (Ga), and orthopyroxene (Opx), assimilated from the wall rock into the mineralised quartz vein (QV). This process of assimilation is a result of intense shearing that occurred simultaneously with precipitation of mineralisation.  
1cm=400µm
- Figure 8.3:** Sample DD-2-2008. Boundary between the quartz vein (QV) and the wall-rock. Microphotograph showing tourmaline needles (arrows) inside a quartz vein, orientated parallel to the wall-rock.  
1cm=100µm
- Figure 9.1:** Sample DH-2035: Microphotograph showing trails of fluid inclusions crosscutting grain boundaries, an indication for entrapment after the peak-metamorphic event.  
1cm=25µm
- Figure 9.2:** Homogenisation temperature (Th) for all CO<sub>2</sub>-fluid inclusions (n=282). Typical bimodal distribution showing high-density fluid inclusions (aprox. 1.15g/cm<sup>3</sup>, at Th=-48°C) and low-density fluid inclusions (aprox. 0.50g/cm<sup>3</sup>, at Th=28°C).
- Figure 9.3:** Final melting temperature (Tmf) and homogenisation temperature (Th) for the low-density CO<sub>2</sub>-rich fluid inclusions. The final melting temperature lower than -56.6°C (pure CO<sub>2</sub>) is probably due to the presence of methane and/or nitrogen.
- Figure 9.4:** Sample DH-2033: Microphotograph showing high-density CO<sub>2</sub>-rich fluid inclusions hosted by quartz veins. The inclusions, at room temperature, usually host a single CO<sub>2</sub> phase.  
1cm=25µm
- Figure 9.5:** Sample 2035: Microphotograph showing clusters of relatively isolated high-density CO<sub>2</sub>-rich fluid inclusions (arrow) hosted by the prograde garnet porphyroblast. Note the high relief of the inclusions, a typical feature of the high-density type.  
1cm=25µm.
- Figure 9.6:** Sample DH-2035: Microphotograph showing low-density CO<sub>2</sub>-rich fluid inclusions (arrows) along healed cracks hosted by a quartz vein. The liquid/vapour ratio of these inclusions is variable, probably due to leakage of liquid from the fluid inclusions.  
1cm=25µm.
- Figure 9.7:** Sample 2035: Microphotograph showing low-density CO<sub>2</sub>-rich fluid inclusions (yellow arrow) in a trail associated with tiny tourmaline crystals (green arrow). There is a close relationship between gold mineralisation related, to CO<sub>2</sub>-fluid activity and other volatiles, such as boron.  
1cm=25µm
- Figure 9.8:** Sample DH-2033C: Microphotograph of low-density CO<sub>2</sub>-rich fluid inclusions associated with graphite (arrow). The black spots are graphite crystals.  
1cm=25µm.
- Figure 9.9:** Sample DH-2035: Microphotograph showing the presence of rounded graphite crystals (red-arrow) hosted by quartz inclusions in the mineralised dark inner-ring of the prograde garnet porphyroblast. Graphite is associated with low-density CO<sub>2</sub>-rich fluid inclusions (yellow arrow).  
1cm=25µm
- Figure 9.10:** Mechanism of trapping the high-density fluid inclusions in the dark inner-ring and rim of the prograde garnet porphyroblast along the same isochor of 1.16g/cm<sup>3</sup>, during the

prograde metasomatism at Doornhoek. During isothermal decompression, the  $fO_2$  changed and  $CO_2$  broke down into  $O_2$  and C, with the formation of graphite. Data derived from Doornhoek Ore Body.

**Figure 10.1:** P-T diagram displaying all the P-T calculations obtained from petrologic data and from two isochors derived from the fluid inclusions data.

- Point A ( $T=712^\circ C$ ;  $P=7.21\text{kbar}$ ): intersection of  $Keq Px(T)$  and  $Px(P)$ , based on the orthopyroxene-bearing assemblage of the felsic granulite (Bohlen et.al., 1983; Ellis and Green, 1979)
- Point B ( $T=849^\circ C$ ;  $P=8.38\text{kbar}$ ): intersection of  $Keq Bi(T)$  and  $Bi(P)$ , based on biotite-bearing assemblage from the BIF-mafic granulite (Ellis and Green, 1979; Harley and Green, 1982; Hodges and Spear, 1982; Ganguly and Saxena, 1984)
- Thermo-Keq R ( $580^\circ C$ ) represents the isotherm obtained from the equilibration of retrograde garnet with the large orthopyroxene host in the BIF-mafic granulite (Ellis and Green, 1979)
- Thermo-Keqs Core ( $500^\circ C$ ), Md ( $570^\circ C$ ) and Rim ( $720^\circ C$ ) represent isotherms derived from Ga-Bi pairs in the core, middle zone and rim of the prograde garnet porphyroblast in the metasomatic biotite-garnetiferous formation (Ganguly and Saxena, 1984)
- Thermo-Keq Tu represents the isotherm obtained from biotite-tourmaline pairs in felsic granulite intensely affected by metasomatic reactions (Colopietro and Frieberg, 1987)
- Curve labelled 1.15 represents the isochor derived from high-density  $CO_2$ -rich fluid inclusions. Point D represents the intersection between the  $1.15\text{g/cm}^3$  isochor and the isotherm Rim derived from the prograde garnet porphyroblast where most of the high-density fluid inclusions are located. Point D reflects  $T = 745^\circ C$  and  $P = 8.32\text{ kbar}$ .

**Figure 10.2:** Sample DH-2024: BIF. Microphotograph showing resorbed garnet (arrow - Ga) hosted by orthopyroxene (Opx). The resorption of the garnet took place uniformly, preserving the euhedral shape, due to similar diffusion rates of Fe and Mg in both garnet and host ferrohypersthene. Garnet displays a typical retrograde zoning pattern, being part of the assemblage that underwent peak-metamorphic condition during  $M_1$  and retrogression during  $M_2$ .

1cm=100 $\mu$ m

**Figure 10.3:** Sample DH-2008. Felsic granulite affected by metasomatic alteration. Microphotograph showing a deformed large garnet porphyroblast (Ga). Tourmaline (yellow - arrow) has been introduced along fractures into the garnet.

1cm=400 $\mu$ m

**Figure 11.1:** Scott diagram (Scott, 1983) showing the composition of arsenopyrite plotted against the temperature of arsenides precipitation. The composition of arsenopyrite from Doornhoek suggests precipitation temperatures ranging from  $569$  to  $673^\circ C$ , while the gold-free arsenopyrite precipitated at temperatures ranging between  $428$  to  $569^\circ C$ . However, the precipitation temperature of the gold mineralisation probably occurred at higher conditions considering the presence of löllingite (l $\ddot{o}$ ) as the main arsenide associated with gold (see text for explanations).

**Figure 11.2:** P-T diagram used to determine the pressure conditions of mineralisation based on temperature obtained from the Scott diagram (fig. 11.1). The T data ( $\Delta T=569^\circ-673^\circ C$ ) derived from the Scott diagram were plotted against the isochores obtained from the fluid inclusions study. These  $CO_2$ -rich fluid inclusions probably represent fluid inclusions associated with arsenopyrite and gold mineralisation. The resulting P data ( $\Delta P=7.11-8.01\text{kbar}$ ) suggests the pressure conditions at which the gold mineralisation was entrapped in the garnet porphyroblasts and precipitated into the quartz veins. The real entrapping pressures should be higher considering the fact that most of the gold is associated with löllingite.

**Figure 12.1:** a. Mn distribution in the prograde garnet porphyroblast displays a typical prograde pattern with high values in the core that decreases towards the rim;

*b.* Fe distribution reaches a maximum value in the vicinity of the mineralised inner-ring that is also characterised by the presence of numerous magnetite and ilmenite inclusions.

- Figure 12.1: *c)* Ge distribution in the prograde garnet porphyroblast (see text for explanations);  
*d)* As distribution in the prograde garnet porphyroblast (see text for explanation).
- Figure 12.1: *e)* Y distribution in the prograde garnet porphyroblast (see text for explanations);  
*f)* Zr distribution in the prograde garnet porphyroblast (see text for explanation).
- Figure 12.1: *g)* Ni distribution in the prograde garnet porphyroblast (see text for explanations);  
*h)* Au distribution in the prograde garnet porphyroblast (see text for explanation).
- Figure 12.2: Normalised REE trend in the Doornhoek lithologies. *a)* Normalised REE trend for the retrogressed lithologies which occur at Doornhoek (felsic granulite, BIF and ultramafic granulite). As a general trend, one can see positive Sm and Tm peaks as a characteristic for this lithologies. *b)* Normalised REE distribution in metasomatic lithologies (biotite-garnetiferous formation, massive sulphide mineralisation from a quartz vein, pure quartz vein material and calcite vein material). These prograde lithologies are characterised by Eu positive peak.
- Figure 12.3: Geochemical variation of several major elements across the wall-rock contact of BIF with the biotite-garnetiferous formation (Bi-GaF) and back into BIF (wall-rock). The enrichment in SiO<sub>2</sub>, Al<sub>2</sub>O<sub>3</sub>, K<sub>2</sub>O and TiO<sub>2</sub> (*a*) and the depletion in FeO and MnO (*b*) that characterise the biotite-garnetiferous formation is clear.
- Figure 12.4: Geochemical variation of several major elements across the contact of Baviaanskloof gneiss with pink metasomatic vein material. The strong enrichment of K and depletion in Ca and Na in the pink vein is clear.
- Figure 12.5: Geochemical variation of chalcophile elements in the Doornhoek lithologies, illustrated across a generalised lithostratigraphic column. See text for details.
- Figure 12.6: Geochemical variation of lithophile elements in Doornhoek lithologies. See text for details.
- Figure 12.7: Geochemical variation of Nb, Mo and W in Doornhoek lithologies. A weak increase in Mo content in the biotite-garnetiferous formation and the strange enrichment of W in the BIF is apparent.
- Figure 12.8: Geochemical variation of Ni, Co, Cr and V in Doornhoek lithologies. A major surprise is the high concentration of Cr and V in the felsic granulite, raising question about the real nature of this lithological type.
- Figure 12.9: FCD graphical representation for isotopic equilibria in a sample of metasomatic aplitic band. The O-isotope fractionation is defined by garnet-core, sillimanite and K-feldspar and represents the peak-temperature of alteration of 890°C, under closed-system conditions (from Mokgatla, 1995).
- Figure 12.10: FCD diagram of metapelites from the SMZ derived from whole-rock/garnet fractionations. Data from Vennemann and Smith (1992). Example of near-peak temperature of 820°C defined by plagioclase, whole rock and garnet. Orthoamphibole, whole rock and quartz define a secondary linear array with a flatter slope corresponding to the formation temperature of orthoamphibole (635°C). The modal content of anthophyllite is 40% (from Hoernes et al., 1995).

- Figure 12.11:** FCD diagram of a metasomatically altered gneiss from Klipbank. Although the equilibrium is not so well defined, the fractionation pattern is remarkably different, in that it shows a tendency to equilibrate at lower temperatures. This is caused by infiltration of a new fluid. Note the correspondence of this temperature to that of orthoamphibole formation (fig. 12.10) (from Hoernes et al., 1995).
- Figure 12.12:** FCD diagrams representative for open-system conditions outside shear zones, proving the fluid-influx model of the SMZ. Data from Vennemann and Smith (1992).  
*a.* The linear array defined by quartz, plagioclase, whole rock and orthopyroxene corresponds to a temperature of 670°C - at which new fluid entered the system. Garnet represented a closed system at the time of fluid infiltration, yielding thus to an extremely small whole-rock/garnet fractionation.  
*b.* Vertical alignment of plagioclase, whole-rock, clinopyroxene and orthoamphibole can only be reached by interaction with fluid during a larger temperature interval (open system) (from Hoernes et al., 1995).
- Figure 12.13:** Whole rock O-isotopic (per mil) compositional changes plotted against increasing alteration (from Mokgatla, 1995). One can see a very weak increase of the <sup>18</sup>O with the increasing of the alteration intensity, although it is also possible due to the mineral composition of the analysed material.
- Figure 12.14:** At pressures above 3-4 kbar, the H<sub>2</sub>O activity drops precipitously from values nearly equal to the H<sub>2</sub>O mole fractions, to activities near the squares of the mole fractions in the deep-crustal pressure range. Thus, concentrated brines may have low enough H<sub>2</sub>O activities (0.2-0.4) under deep-crustal conditions to coexist with the assemblage *orthopyroxene+K-feldspar* in charnockites, and that the low H<sub>2</sub>O activities in such brines protect the rocks against melting even at temperatures >750°C (from Newton et al., 1996).
- Figure 13.1:** Large orthopyroxene crystal (opx) crosscut by epigenetic mineralisation (opaque). Due to the introduction of mineralisation into the Doornhoek system under ductile conditions, the opx underwent kink-band type of deformation (note the angle made by the cleavage direction at the top (red arrow) and bottom (yellow arrow) of the photo). Sample DD-2-2. 1cm=50µm
- Figure 13.2:** As fig. 13.1 but under crossed nicols. The kink-band type of deformation in the opx is better displayed, due to the variation of birefringency colours. Sample DD-2-2. 1cm=50µm
- Figure 13.3:** Pressure-depth relations for litho- and hydro-static gradients. The transition zone observed in oil-wells in sedimentary basins is from Fyfe et al. (1978) and Wood and Walther (1986) for fluids from the deep Kola Borehole from (Kozlovsky, 1987). The focal depth ranges of earthquakes in continental interiors of different tectonic-age is from Chen and Molnar (1983) and show deeper brittle behaviour in older and colder lithosphere (from Colvine et al. 1988).
- Figure 13.4:** Heat production ( $Hu$ ,  $\mu Wm^{-3}$ ) from advected fluids for various fluid-flux rates ( $q_p$ ,  $m^3m^{-2}s^{-1}$ ) for  $\rho C_p = 3.5 \times 10^6 J/m^3$  and  $dT/dz = 10-100^0 K/km$ . Knowing that the radiogenic heat production for the crust ranges between 0.03 and  $2.3 \mu W/m^3$ , values of  $q_r$  higher than  $10^{-10} m^3/m^2s^{-1}$  are required for advective heat production to exceed radiogenic heat production (from Thompson and Conolly, 1992).
- Figure 13.5:** Transport distances for heat and mass transfer as a function of fluid-flux rates, for advective events of  $10^4$  a, 1 Ma and  $10^8$  a duration (modified from Bickle and McKenzie, 1987). Simple thermal and chemical Peclet numbers are defined as  $Pe_T = zW_0/k$  and  $Pe_C = zW_0/D$ , where  $z$  is lengthscale (m),  $W_0$  = fluid velocity ( $ms^{-1}$ ),  $k$  is a typical thermal



diffusivity ( $10^{-6} \text{ m}^2 \text{ s}^{-1}$ ), and  $D = 10^{-11} \text{ m}^2 \text{ s}^{-1}$  is a simple chemical diffusivity ( $10^{-8} \text{ m}^2$ ) for a porosity of  $10^{-3}$ . Such Peclet numbers are smaller by a factor of  $\pi^2$  (approx. 10) than those defined by Bickle and McKenzie (1987) (from Thompson and Conolly, 1992).

**Figure 13.6:** Variation of volumetric fluid-rock ratios required to cause crustal heating, for different initial values for  $T_{crust}$ . Various values of initial  $T_{fluid}$  are shown for selected values of  $T_{final}$  of  $700^\circ$ ,  $500^\circ$  and  $300^\circ$ . Heat conservation was assumed to be given by:  $C_p^{fluid}/C_p^{rock} = \text{Volume}^{(fluid/rock)} \cdot \Delta T^{fluid}/\Delta T^{rock}$ , with equal values from volumetric heat-capacities (from Thompson and Connolly, 1992).



## **List of tables**

**Table 10.1a:** Microprobe analyses of minerals used for P-T calculations in the retrograde pattern rocks

**Table 10.1b:** Microprobe analyses of garnet and biotite used for P-T calculations in the prograde pattern rocks (metasomatic biotite-garnetiferous formation)

**Table 11.1:** Representative microprobe analyses of löllingite and arsenopyrite



# 1. INTRODUCTION

## 1.1. OBJECTIVES OF THE PRESENT STUDY

Several small gold deposits occur in both the Southern (SMZ) and Northern Marginal Zones (NMZ) of the Limpopo Belt (LB) of Southern Africa. Five of these are located in the SMZ of the LB in South Africa. Whereas gold deposits in the low-grade greenstone belts of the Kaapvaal and Zimbabwean Craton are well studied (Weilers, 1956; Fripp, 1976; Pearton, 1984; Nisbet et al., 1981; Viljoen, 1984; Potgieter and de Villiers, 1986; Nisbet, 1987; Pretorius et al., 1988; Foster, 1989; van Reenen et al., 1994a; Gan and van Reenen, 1995) less is known about similar deposits in the high-grade metamorphic terrane of the LB. These deposits in the high-grade metamorphic terrane display a lower ore grade (e.g. Renco in the NMZ in Zimbabwe - Bohmke and Vardell, 1986 - and Fumani in the SMZ in South Africa - Pretorius et al., 1988) but offers an excellent opportunity for petrologists, mineralogists, structural geologists and economic geologists to study the occurrence, deposition and characteristics of Archaean lode-gold deposits in higher grade metamorphic terranes.

A study of the high-grade gold deposits also offers an excellent opportunity for the exploration geologist to understand and apply his theoretical and academical knowledge in the prospecting and exploration for gold deposits in such areas. The present study involves an investigation of the Doornhoek gold deposit, situated on the farm Doornhoek about 11km WNW of Soekmekaar in the *hydrated zone of the SMZ of the LB (fig. 4.1)*.

The objective of this study is to develop a genetic model for lode-gold deposits in high-grade metamorphic terranes and to establish a possible genetic link between fluid circulation in the deep crust, ore deposition and the often controversial source of the fluids. The physical conditions and structural framework for the emplacement of the gold mineralisation will also be addressed.

Since *lode-gold deposits* can be either magmatic or metamorphic in origin and can occur in low-, medium- or high-grade gneiss terranes, a short review of the different types of gold deposits and a discussion of the lode-gold problem is necessary.



## 2. IMPORTANT FEATURES OF ARCHAEOAN LODE-GOLD DEPOSITS

### 2.1. INTRODUCTION

Gold is the mineral most closely associated with the Archaean, although other valuable mineral deposits ( e.g. Platinum Group Elements, nickel, chrome, asbestos, iron, copper, lead, zinc, tin, tungsten, lithium, semi-precious stones and numerous industrial minerals) are also intimately identified with Archaean shields.

From a production point of view, the world's gold deposits can be grouped into two classes:

#### **Witwatersrand gold versus the rest!**

From a genetic point of view gold deposits can be classified as *i) paleoplacer* (or sedimentary) and *ii) lode* (or hydrothermal) deposits (Nisbet, 1987).

Both varieties occur in Archaean terranes:

*i) paleoplacer gold deposits*, such as the Witwatersrand paleoplacer (gold and Fe sulphides), or the Tarkwa paleoplacer in Ghana (gold and Fe oxides) (Nisbet, 1987), and

*ii) lode gold deposits*, such as the Au deposits located in the greenstone belts of the Kaapvaal and Zimbabwean Cratons (South Africa, Zimbabwe and Botswana), the Yilgarn Block in Western Australia, the Abitibi greenstone belt in Canada (Colvine et al., 1988), etc.

A prominent feature of these deposits is their "*gold only*" nature, with silver present only in subordinate amounts. Other characteristics are the affinity between gold and uranium in paleoplacer deposits.

Gold also occurs as a co-product in Archaean Cu-Zn massive sulphide deposits (Noranda, Superior Province, Canada) (Nisbet, 1987).

In general, a variety of classification schemes can be considered in order to characterise Archaean lode-gold deposits, such as the host rock, the mineralogy of the ore deposit, the timing of formation and structural setting of the ore deposit as well as the personal prejudice of the researcher who made the classification.

Several important questions arise from the widespread studies of the Archaean lode-gold deposits:

- i.* what was the original source of gold,
- ii.* what mechanism was responsible for the concentration of gold, and
- iii.* are Archaean gold deposits somehow different from later aeons, i.e. why was gold deposition more common during the Archaean?

### **2.1.1 History of research**

In a recent paper, Kerrich (1993) emphasised that Archaean greenstone belts represent the main host of lode-gold deposits, although similar deposits are also present in Proterozoic, Palaeozoic and Mesozoic metamorphic terranes. These types of deposits have broadly similar structural, mineralogical, ore metal and geochemical characteristics, implying a singular, rather than multiple, genetic process (Kerrich, 1989a; Kerrich and Wyman 1990; Groves et al., 1992; Kerrich, 1993). These lode gold vein systems, however, have been attributed to diverse ore forming processes including lateral diffusion; syngenetic exhalation; multistage

exhalative remobilisation; derivation variously from komatiites, granitoids or lamprophyres; granulitisation; metamorphic replacement; meteoric water circulation, and most recently metamorphism at collisional boundaries (Kerrick, 1993).

Arguably, the most fundamental constraint on lode gold deposits is their ubiquitous setting in metamorphic terranes. A feature which is also important is their distribution in belts of great geological complexity (Kerrick, 1993). In the 1970's there was an attempt to link syngensis to lode gold deposits, following the renaissance of the syngenetic model for the volcanic-hosted massive sulphides (VHMS) and sedimentary-exhalative base-metal sulphides (SEDEX). Fripp (1976) considered the presence of chemical sedimentary units, especially gold-rich sulphide facies BIF in Archaean metamorphic terranes as evidence for a syngenetic model. Furthermore, Hodgson and MacGeehan (1982) considered the giant quartz vein lode systems as subseafloor hydrothermal feeders to gold-rich chemical sediments. Phillips and Groves (1983), on the other hand argued that lode gold deposits are sited in some BIF simply because epigenetic sulphidation reactions with concomitant gold deposition are favoured in iron-rich rocks.

Fyfe and Henley (1973) made a major contribution in understanding the lode gold deposits. They envisaged gold-bearing quartz veins precipitating in shear zones that focused metamorphic fluids generated at depth (Kerrick, 1993). This new approach to the role of metamorphic fluids explained the interrelationship between structurally hosted veins, focused fluid advection, large source reservoirs and regional heat flow. Another important step ahead was made by Robert and Brown (1986) and Sibson et al., (1988) who established that the banded veins, characteristic of many lode gold deposits, formed syn-kinematically in the

seismogenic zone, during pulsed discharge of ore solutions in a suprahydrostatic to supralithostatic fluid pressure cycle - the fault valve model (Kerrich, 1993).

The next contribution in developing an integrated model for lode gold deposits was the recognition that these deposits occurred in a specific geodynamic environment - convergent margin tectonics (Fyfe and Kerrich, 1985). Wyman and Kerrich (1988) and Kerrich and Wyman (1990) refined the model, explaining that these deposits are associated with lithological, structural and metamorphic complexity because these are the consequences of terrane-terrane collisions. It also explained the distribution of lode gold deposits mostly abundant in the late Archaean, lower Palaeozoic and Mesozoic, because these are the times of extensive Cordilleran style terrane accretion in the earth history. Actually, the giant Archaean deposits are only abundant in the late Archaean, during the first global onset of collisional accretionary tectonics, and are scarce or absent in early and mid Archaean terranes (Wyman and Kerrich, 1988; Kerrich and Wyman, 1990; Colvine, 1989). Barley and Groves (1990) applied this model to the lode gold deposits in Western Australia and demonstrated that the ore-forming fluids are most likely to be of metamorphic origin, evolved as a result of dehydration reactions at depth in the collision zone and focused up into the terrane boundary structures. Hence, the source bed model has been supplemented by the concept of large source volumes from which gold is extracted and concentrated into the deposits (Kerrich, 1989a; Groves et al., 1992; Kerrich, 1993). There is always textural and radiogenic evidence that after the primary deposition mineralisation was remobilised within the depositional site. Even where the timing of gold mineralisation is well constrained, the precipitation event closely follows accretion and the peak metamorphism (Kerrich and Wyman, 1993).



Colvine (1989) and Foster (1989) provided major overviews of the field characteristics of lode gold deposits in the Archaean Superior Province and Archaean Zimbabwe Craton, respectively. They synthesised the variety of structural styles of the ores into a single scheme from deeper level ductile shear zones in amphibolite facies environments through a brittle-ductile regime, to shallow level brittle vein stockworks in lower-, to sub-greenschist facies environments. Barnicoat et al. (1991) provided the first documentation of a lode gold deposit formed under granulite facies conditions.

Building continuously on all these recent observations, Groves et al. (1992), working in the western Yilgarn Block, have described lode gold deposits in granulite, amphibolite and sub-greenschist facies metamorphic environments, together with counterparts in greenschist environments. They demonstrated that the deposits collectively share several fundamental properties, such as a common ore-forming fluid and developed coevally in a PTt regime where peak metamorphism was diachronous in the vertical crustal dimension.

## 2.2. GOLD DEPOSITION AND OCCURRENCES IN METAMORPHIC TERRANES

The concentration of gold is a multistage process involving *i)* the liberation of gold from the source rock by a leaching fluid of some sort (metamorphic, magmatic or mixed in origin), *ii)* the transport of gold in the fluid, *iii)* the precipitation of gold, usually at another site than that of the rock source, *iv)* followed by one or more repetitions of the process, *v)* subsequently followed by erosion and sedimentary reconcentration of the eroded material (Nisbet, 1987).

The first episode involves the extraction of gold from some source rock, which is usually a country rock sited in the very close vicinity of a heat source, e.g., a lava pile around a subvolcanic pluton or intrusion; an older intrusion around a new intrusion; a thick pile of rocks undergoing metamorphism, etc. This process of *gold leaching* would not be possible without large amount of fluids being involved. Fyfe and Kerrich (1984) for example calculate that the gold deposits in the Timmins area, Canada, where more than 100 million ounces of gold have been produced up to date, may have been concentrated by leaching of up to 5000 km<sup>3</sup> of rock by anything up to 750 km<sup>3</sup> of fluid.

Most hydrothermal, *or lode, gold deposits appear to have formed in the temperature range 175-450°C*. Archaean gold bearing quartz veins typically formed toward the upper end of this temperature range, at 320-480°C (Fyfe and Kerrich, 1984). Starting from 1987 researchers described gold deposits with textural and mineral equilibria data that suggested gold was deposited well above 500°C (amphibolite facies conditions) or even at 600-700°C (upper amphibolite facies to granulite facies conditions) (Groves et al., 1989, van Reenen et al., 1993).

Apart from the metamorphic grade at which gold was transported and deposited, Archaean gold deposits are worldwide associated with two major tectonic events that occurred at about 3.5 Ga and 2.7 Ga. A short overview of typical Archaean gold-lode deposits from all over the world clearly shows that most of the known deposits of this kind occur in Southern Africa (South Africa, Zimbabwe, Botswana), Australia and Canada.

**Southern Africa:** Epigenetic auriferous veins ranging from a few cm to 20 m thick and with strike distances of a few meters to several kilometres occur both on the Kaapvaal and the Zimbabwe Cratons. Gold deposits in the Barberton, Murchinson and Guyani greenstone belts occur in lithologies with a simple mineralogy (predominantly composed of quartz with minor carbonates) hosted by shear zones. The main host rock of the quartz veins are often komatiitic basalts (Viljoen, 1984) which, despite the fact that it is now altered, metamorphosed and poor in gold, were presumably a principal factor for delivering the Au from the mantle to the site of deposition (Viljoen, 1984). Sulphide minerals are often disseminated in the veins, while the gold occurs as massive ore, disseminated ore or in microfractures. The wallrocks are often intensely altered close to the veins. The carbonate-bearing rocks also played an important role with regard to transport and precipitation of the gold. Pearton (1984) and Viljoen (1984) have emphasised the importance of carbonate-bearing rocks in gold mineralisation in the Barberton Mountain Land. The carbonate-rich material is the alteration product of ultramafic flows or tuffs, as a result of ultimate hydrothermal alteration. It is assumed that the CO<sub>2</sub> is derived directly from the mantle (Newton et al., 1980). This is suggested by the pseudomorphic replacement of spinifex-textured olivine by carbonates (Pearton, 1984).

Other gold deposits, often considered to be syngenetic or *strata-bound*, are hosted by BIF. Such deposits occur mainly in Zimbabwe, but also in South Africa (Nisbet, 1987).

**Australia:** Most of the gold production in Western Australia is from quartz veins, or from vein-related alteration zones. Although many of these deposits exhibit a vein character, Groves et al. (1984) considered the main type of vein deposit to be typically discordant, in that the distribution of the veins is controlled by local faults and shear zones. Thus, although many gold veins may seem to be strata-bound they are nevertheless *epigenetic*, i.e. *formed at*

*a time later than the formation of the host country rock* (Groves et al., 1984). Approximately half of the gold production in Western Australia comes from the Kalgoorlie area, where the host rock is tholeiitic metabasalts or metadolerites. Some of the Australian deposits are also associated with BIF, felsic volcanics, metasediments or ultramafics, but in the Kalgoorlie area these are of minor significance in terms of gold production. The Pilbara Block in NW Australia demonstrates the gold being hosted by ultramafic rocks, BIF, mafic rocks and metasediments.

**Canada:** The controversy of whether all gold deposits are syngenetic or epigenetic, or magmatic/metamorphic in origin was more of an issue in Canada (Colvine, 1989). Although *strata-bound* does not always mean *syngenetic*, and *non-strata-bound* (mainly *crosscutting veins*) does not necessarily mean *epigenetic*, the controversy raged for a long period of time (Colvine, 1989). Despite this controversy, the Timmins area alone produced about 100 million ounces of gold, thus emphasising a true exploration observation, namely that gold occurs wherever it is found! Many of the Canadian gold mines are located in lodes or, to use the terminology of Lindgren (1928), in *large fractures filled with ore and partially replaced country rock*. Many of the gold-bearing quartz veins are limited to specific stratigraphic horizons, although, from a structural point of view, the veins display a discordant relationship.

The ore bodies are mainly hosted by rocks of low to middle greenschist facies, in terranes composed predominantly of mafic and ultramafic sequences with minor felsic volcanics and epiclastics (Hodgson and MacGeehan, 1982). Extensive zones of carbonate-rich altered rocks are associated with many of the gold deposits, especially where the deposits are associated

with felsic volcanic rocks (Hodgson and MacGeehan, 1982). A good example are the lode-gold carbonate-bearing deposits of the Timmins/Kirk Lake districts which are considered to be strata-bound (Karvinen, 1982). Historically gold in the Timmins district is strongly associated with carbonate alteration (Nisbet, 1987; Hodgson and MacGeehan, 1982). A review of the Canadian gold deposits (Nisbet, 1987; Colvine et al, 1988) clearly shows that both conformable and discordant gold veins are present in the Canadian deposits and that the gold was later remobilised to some extent.

### 2.3. THE ROLE OF FLUIDS IN ARCHAEOAN GOLD DEPOSITION

The term *hydrothermal fluid*, as defined by Niggli (1926), represents a volatile phase derived from igneous, metamorphic or sedimentary rocks during either the late stage of the magmatic activity or liberated from metamorphic/sedimentary rocks during tectonic processes or diagenesis. The term does not only apply to igneous hydrothermal processes, as it was used for a long period of time, but to any geological process which could generate fluids. Derivation of hydrothermal fluid by prograde devolatilisation reactions has been proposed as the main process responsible for the generation of the Archaean auriferous fluids (Kerrick and Fyfe, 1981; Groves and Phillips, 1987; Colvine et al., 1988). In this chapter, and further on, several characteristics of *gold-related metamorphic fluids* will be reviewed and discussed. Although no attempt will be made to present a complete review of reactions that might generate fluids during prograde metamorphism, the main characteristics and composition of metamorphic fluids as a function of metamorphic grade will be presented.

Metamorphic fluids relevant to Archaean gold metallogeny have the following characteristics (Colvine et al., 1988):

*i)* fluids generated by dehydration reactions up to and including the amphibolite grade are compositionally variable, but tend to be H<sub>2</sub>O-rich,

*ii)* ambient fluids associated with the granulite facies or with anatexis are CO<sub>2</sub>-rich, regardless of host rock composition, and

*iii)* fluids generated within a lithological sequence, at a particular metamorphic grade, are in equilibrium with the mineralogy of the host rock, but are not necessarily in equilibrium with a different rock assemblage under the same metamorphic conditions, or the same rock assemblage at lower metamorphic conditions.

*iv)* hypersaline fluids, presumable emanating from volatile-rich alkaline basalts emplaced in the deep crust during metamorphic episodes, may have played a very important role in mobilising metals and redepositing them at a later stage (Newton et al., 1996)

### **2.3.1. Fluid activity in greenstone belts and amphibolite facies rocks.**

Gold occurs in a widespread variety of settings, but usually in different types of structurally controlled veins. The transport medium of gold must therefore have been a fluid, either metamorphic or igneous, or a mixture of both (Kerrick, 1989a). In low- to medium-grade metamorphic terranes, metamorphic rocks are dominated by the presence of H<sub>2</sub>O-rich fluid, which is usually generated by dehydration reactions or by mobilisation of pore fluids and intergranular fluid films (Fyfe et al., 1978). The volume of the liberated fluids is related to the thermal gradient and the bulk composition of the rock (Fyfe et al., 1978). Variable, but small amounts of CH<sub>4</sub> and CO<sub>2</sub> directly related to the composition of the immediate country rock

may be generated during low-grade, prograde metamorphism. Above the staurolite isograd, liberated metamorphic fluids should contain between 10 and 60 mole percent of CO<sub>2</sub> (Colvine et al., 1988).

The most significant characteristic of metamorphic fluids in the upper crust (from greenschist to amphibolite facies metamorphic conditions) is the compositional dependency, thereof on the bulk composition of the source rock that is undergoing devolatilisation reactions (e.g., CH<sub>4</sub>-rich fluids in carbonaceous sediments, or NaCl-rich brines related to evaporites, Rich, 1979). This suggests that the fluid composition is strongly dependent on and buffered by the composition of the country rock (Touret and Dietvorst, 1983). The composition of the metamorphic fluids become richer in CO<sub>2</sub> as the metamorphic grade increases to the upper part of the amphibolite facies. However, the localised, intensive alteration of the country rock into carbonate and Al-rich assemblages at the contact with the gold-bearing quartz veins is evidence that the gold-related fluids were not in equilibrium with the country rock during the gold mineralising event. This suggests that the gold-bearing fluid was not generated within the metamorphic domain of the country rock (greenschist or amphibolite facies), but under higher grade metamorphic conditions (the granulite facies), if the hydrothermal fluid was metamorphic in origin.

### **2.3.2. Fluid activity in upper-amphibolite - granulite facies conditions**

The transition from the amphibolite to the granulite facies, where partial melting may occur, corresponds to a major change in the composition of the ambient metamorphic fluid, from H<sub>2</sub>O-dominant to CO<sub>2</sub>-dominant (Touret, 1981; Colvine et al., 1988). Fig. 2.1 demonstrates

this change in the composition of the metamorphic fluid (Touret, 1981). In granulites, the ambient fluid during peak metamorphism consists of high density (up to  $1.23 \text{ g/cm}^3$ )  $\text{CO}_2$ , regardless of the local host rock composition (Touret and Dietvorst, 1983). Contamination of the main  $\text{CO}_2$  fluid with  $\text{H}_2\text{O}$ -,  $\text{CH}_4$ - or  $\text{N}_2$ -bearing fluid is often reported from the literature, although this is often related to post-peak retrograde metamorphic events (Touret, 1981).

The fact that granulitic rocks always display a high  $\text{CO}_2$  fluid content points to an external control of the fluid composition (*external buffering*) in contrast to *internal buffering* that is characteristic for low to medium grade metamorphic rocks (Colvine et al, 1988).

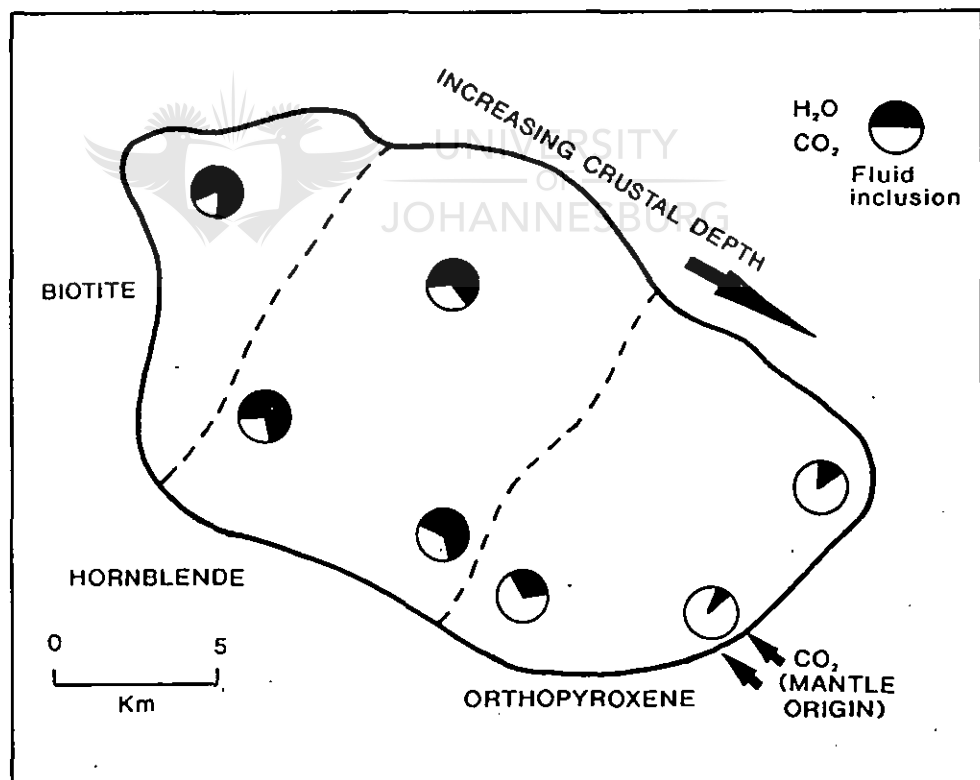


Figure 2.1: Changes in the composition of the metamorphic fluid associated with medium- to high-grade metamorphic rocks.  $\text{CO}_2$ -rich fluids dominate in the high-grade metamorphic terranes, regardless of rock composition (from Touret, 1981).



Two main mechanisms were proposed to explain the external buffering of fluids in high-grade metamorphic rocks.

1) CO<sub>2</sub>-rich fluids were introduced into the lower crust from a deep-seated source, thereby decreasing the activity of H<sub>2</sub>O (Newton et al, 1980), and

2) CO<sub>2</sub> was omnipresent in the lower crust, but it was concentrated in the fluid due to the fact that H<sub>2</sub>O was preferentially partitioned into and removed by silicate partial melts (Touret and Dietvorst, 1983). The problem with this second mechanism is that CO<sub>2</sub>-rich fluids are often described in high grade terranes that did not undergo partial melting (Touret and Dietvorst, 1983; Colvine et al, 1988).

Although the concept is very new, Newton et al., (1996) proposed the third mechanism of buffering for hypersaline fluids in high-grade metamorphic rocks, as follows:

3) Alkalic magmatism was probably present during ancient continental disruption. The magmatic emanations may split into concentrated brines and immiscible CO<sub>2</sub> during ascent. The alkalic basalts transport heat and alkalis upwards in the crust.

Ambient metamorphic fluids associated with high-grade metamorphic mineral assemblages (granulite facies condition) are therefore compositionally uniform, regardless of the rock composition (Colvine et al., 1988). Similarly, the composition of gold-related hydrothermal fluids is also uniform, regardless of the depositional site or the bulk chemistry of the country rock. This may indicate that the composition of the gold-bearing fluid is somehow related to the process of granulite facies metamorphism in the lower crust.

### 2.3.3. Characteristics of the Archaean gold-related fluids

The fluid characteristics of the Archaean gold-related hydrothermal systems are as follows (Colvine et al., 1988; Kerrich, 1989b):

*i)* the fluid is aqueous, of relatively uniform composition, and containing variable amounts of CO<sub>2</sub> depending on the grade of metamorphism,

*ii)* the fluid is derived from a source external to the immediate depositional site,

*iii)* a large volume of fluid is involved,

*iv)* extensive alteration at the depositional site indicates that the fluid was not in equilibrium with the rock assemblage at the depositional site, and

*v)* the gold-transporting fluid was also not in equilibrium with the rock assemblage in the metamorphic domain where gold was deposited.



### 2.3.4. Concentrated brines as high-grade metamorphic fluids

The role apparently played by hypersaline fluids, although not clearly understood yet, is presented in this chapter. Since the development of modern fluid inclusions studies three decades ago, concentrated aqueous salt inclusions have been identified in a great diversity of igneous and metamorphic settings (Touret, 1995; Newton et al., 1996). Hypersaline fluids are now believed to have played a major role in the evolution of alkaline volcanic rocks (Lowenstern, 1994), carbonatites (Samson et al., 1995), several gabbroic rocks (Pasteris et al., 1995), Alpine eclogites (Philippot and Selverstone, 1991) and the super high-pressure coesite-bearing metasediments (Philippot et al., 1995). Aranovich et al. (1987) suggested that concentrated brines as a high-grade metamorphic fluid could satisfy the requirement of

low-H<sub>2</sub>O activity combined with alkali mobility. Some recent studies (Touret, 1995; Newton et al., 1996) of brine-rock interactions at high temperatures and pressures demonstrate additional properties of concentrated NaCl-rich solutions which support renewed consideration of such fluids as important agencies in the evolution of the continental crust.

These properties include (Newton et al., 1996):

1. Immiscibility with CO<sub>2</sub> at high pressures and temperatures

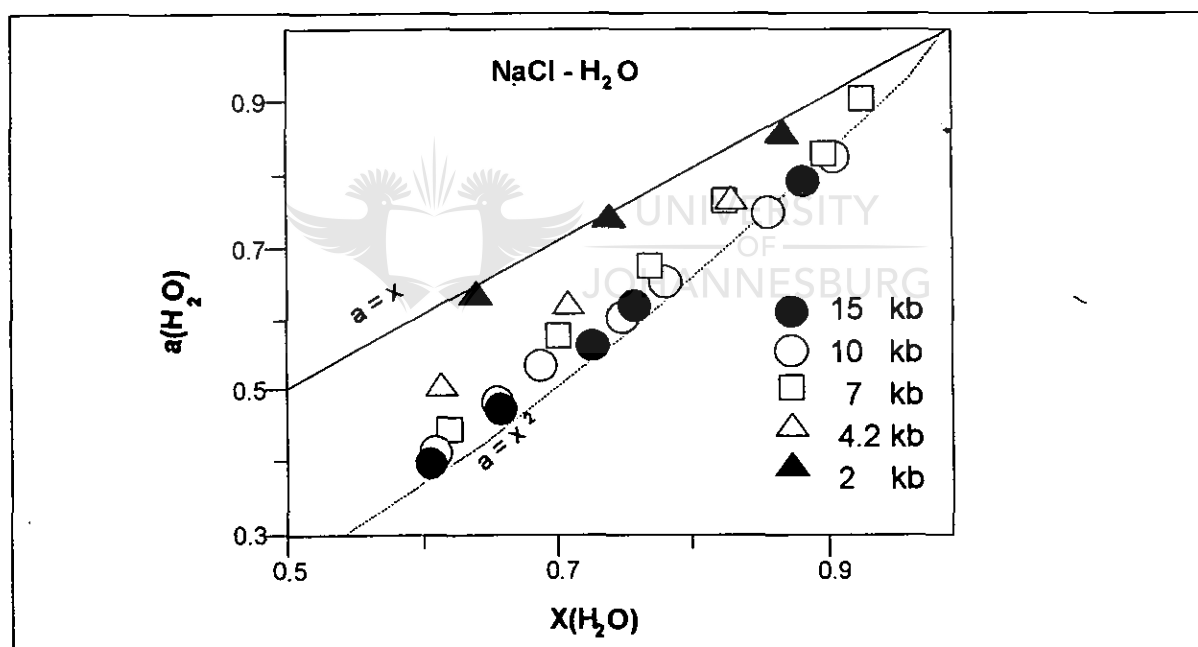
2. Ability to infiltrate grain boundaries of silicate rocks of low permeability, in contrast to dense CO<sub>2</sub>.

3. Low H<sub>2</sub>O activity in concentrated brines at pressures above 5kbar, by virtue of pressure-induced ionic dissociation of NaCl.

4. High affinity of Rb relative to biotite and K-feldspar, in contrast to granitic melts.

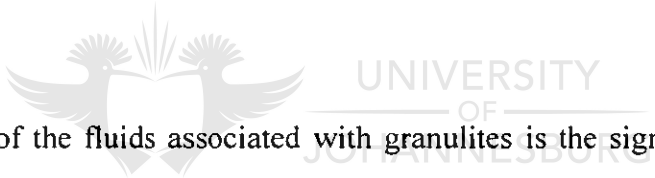
Thermodynamics-based reconstructions of the NaCl-H<sub>2</sub>O-CO<sub>2</sub> system (Bowers and Helgeson, 1983; Duan et al., 1995) show that concentrated brines with small CO<sub>2</sub> content coexist stably with a nearly pure CO<sub>2</sub> phase at temperatures in the deep-crustal T and P range (500<sup>o</sup>-900<sup>o</sup> and pressures from 2 to 10kbar). Although infrequently reported, brine solutions in granulites are increasingly recognised (Rollinson and Berger, 1995; Touret, 1995; Smit and van Reenen, 1997), and fluid immiscibility is generally accepted and cited as a basis for apparently coeval suites of hypersaline and CO<sub>2</sub> inclusions in granulites (Crawford and Hollister, 1986; Touret, 1985). The much more abundant CO<sub>2</sub> inclusions in granulites, reported by many authors, may result from greater propensity for capture in silicate minerals. Watson and Brenan (1987) experimentally showed that disseminated pure CO<sub>2</sub> at elevated T and P forms high contact angles (>60<sup>o</sup>) in quartz aggregates and hence has low infiltration ability and greater tendency to be captured in secondary arrays along healed fractures. Water, in contrast, generally forms lower contact angles, and concentrated salt solutions have extraordinary wetting ability.

Watson and Brenan (1987) stated that brines would have a very low tendency to be captured as fluid inclusions in the high-grade metamorphic regime. This property quite plausibly accounts for the rarity of the brines relative to CO<sub>2</sub>-rich inclusions. The importance of brines in high-grade metamorphic reactions is therefore likely to have been underestimated from the fluid inclusion evidence. Aranovich and Newton (1995) measured H<sub>2</sub>O activities in concentrated NaCl solutions at deep crustal temperatures and pressures by depression of the brucite dehydration equilibrium. Their results are shown in **fig. 2.2**.



**Figure 2.2:** At pressures above 3-4 kbar, the H<sub>2</sub>O activity drops precipitously from values nearly equal to the H<sub>2</sub>O mole fractions, to activities near the squares of the mole fractions in the deep-crustal pressure range. Thus, concentrated brines may have low enough H<sub>2</sub>O activities (0.2-0.4) under deep-crustal conditions to coexist with an assemblage such as *orthopyroxene+K-feldspar* in charnockites, and that the low H<sub>2</sub>O activities in such brines protect the rocks against melting even at temperatures >750°C (from Newton et al., 1996).

Within the pressure range 4 to 15 kbar, the  $H_2O$  activity drops precipitously from values nearly equal to the  $H_2O$  mole fractions, to activities near the squares of the mole fractions in the deep-crustal pressure range (**fig. 2.2**). This behaviour is almost independent of temperature in the range  $600^{\circ}$ - $900^{\circ}C$  and is undoubtedly the result of pressure-induced ionic dissociation of NaCl as fluid densities approach those of condensed liquids. Predictable consequences are that concentrated brines may have low enough  $H_2O$  activities (0.2-0.4) under deep-crustal conditions. The low  $H_2O$  activity allows the brines to coexist with the assemblage orthopyroxene+K-feldspar in quartzofeldspathic rocks. At the same time the low  $H_2O$  activities in the brines protect the rocks against melting even at temperatures  $>750^{\circ}C$ , although hyperfusible components (such as F) may provoke limited anatexis (Newton et al., 1996).



An important feature of the fluids associated with granulites is the significant solubility of silica with high alkali mobility. It is likely that quartz is substantially more soluble in alkaline aqueous solutions than in nearly pure  $CO_2$ . The K-feldspar veining phenomenon in charnockites is understood by simple exchange of  $K^+$  for  $Na^+$  in plagioclase, with the other major components being inert. A concentrated brine could most plausibly provide the observed high alkali mobility, as well as the high volatile mobilities. Thus, dehydration reactions and consequently the widespread LILE depletion in Precambrian granulite terranes would be favoured by elevated pressure in middle- to high-grade metamorphic rocks in the presence of saline pore solutions. If Rb, U and Th extraction is accompanied by upward migrating brines during deep-crustal metamorphism, the fluids must have been fairly voluminous and pervasive and really extensive sources must be considered (Newton et al., 1996). Several possible sources of brines for deep crustal metamorphism may be imagined,

including connate waters in metasediments, meta-evaporite deposits and exhalations from deep-crustal mafic intrusions (Newton et al., 1996). The first possibility may be discounted because there are many Precambrian terranes with limited occurrences of metasediments. For the second possibility, to the general knowledge, metamorphosed halite deposits are never found in granulite facies terranes. Mechanical buoyancy and high solubilities of salt beds prevent evaporites from reaching the deep crustal milieu. Regarding the third possibility, it seems the most reasonable (Newton et al., 1996) considering that some basaltic magmas, notably the alkalic suite, are inferred to be very rich in volatiles, alkalis and halogens (Bailey, 1980).

#### 2.4. SOURCE OF GOLD MINERALISATION AND RELATED FLUIDS IN ARCHAEOAN TERRANES

Colvine et al. (1988) suggested that hydrothermal  $\text{CO}_2$  -  $\text{H}_2\text{O}$ -bearing fluids are generated by exsolution from silicate magmas in the mantle and lower crust. This fluid which may be contaminated to a variable degree, may evolve compositionally in response to changing redox conditions in the granulite zone and may pass directly into the upper crust along permeable structural systems. The gold is introduced into structural zones of deformation by fluids which percolated through very large volumes of rock on their way to the depositional site. Both magmatic and metamorphic sources for the gold are consistent with the available data. In the low-grade greenstone belts different processes of dissolution, transport, concentration and precipitation of gold are proposed by different authors (Kerrick and Fyfe, 1981; Fyon and Crocket, 1982; Viljoen, 1984; Groves et al., 1984;) and were discussed by Colvine et al.

(1988). In the higher grade terranes, the lower crust undergoing granulite facies metamorphism is considered to be a possible source for gold mineralising fluids. A very good example of such a study was done during 1976 in the Bahia State granulites, Brazil (see Colvine et al., 1988). This phenomenon is illustrated in fig. 2.3.

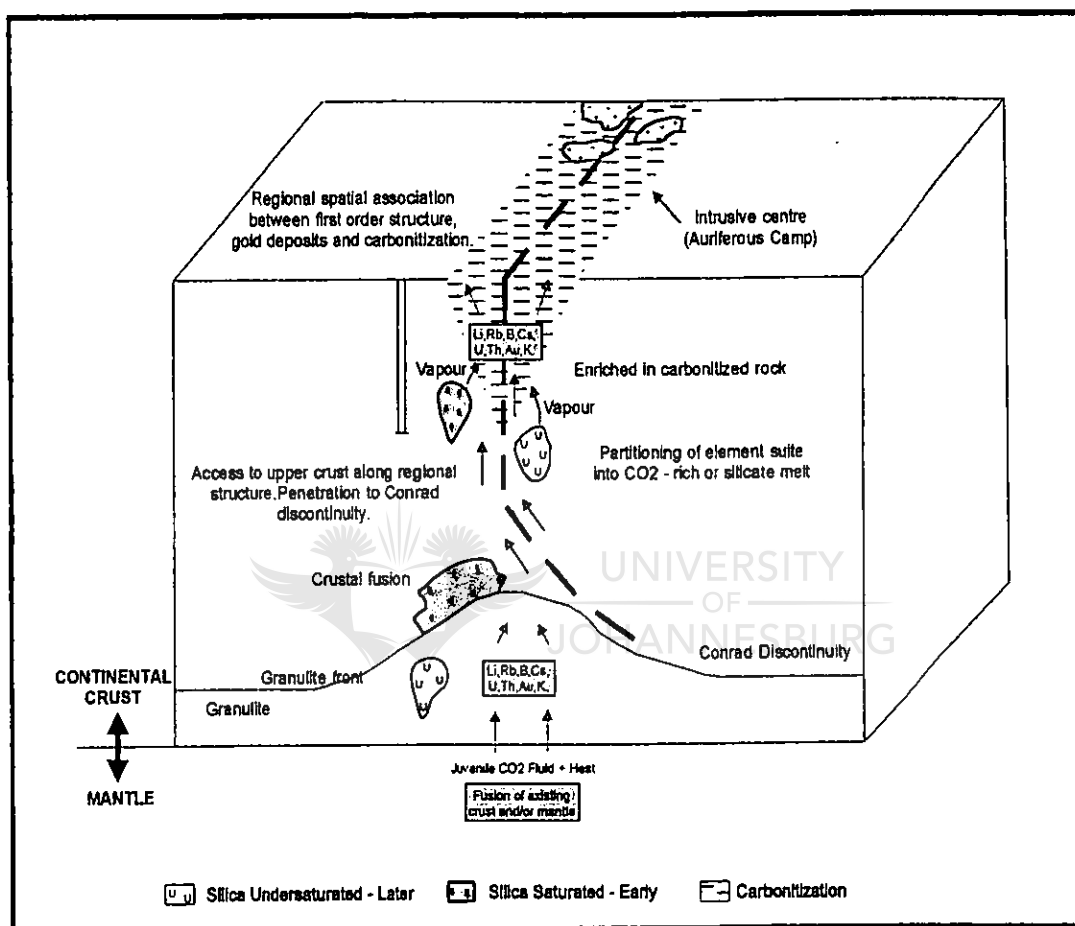


Figure 2.3: Composite crustal section illustrating the elements of an Archaean gold genetic model (from Colvine et al., 1988). The vertical scale is not defined. Crustal cratonisation culminates with the addition of mafic magma to the base of and also into the existing lower crust. Crustal thickening is accomplished in part by the addition of diapiric mass to the base of the crust, which grows downward to form a subvolcanic keel. Granulitisation of the lower crust results from the introduction of magma, heat and volatiles, principally CO<sub>2</sub>. A compositional spectrum of silicate magmas is generated by partial melting of the upper mantle and lower crust in the presence of fluids with varying CO<sub>2</sub>/H<sub>2</sub>O ratios. Fluids originating by exsolution from silicate magmas anywhere between the upper mantle and upper crust, may evolve compositionally as a result of reaction with rock (granulitisation) and due to immiscible separation. Chemical mass transfer from the mantle, lower and middle crust to the upper crust is done by silicate magma and fluids, which migrate along zones of crustal weaknesses (penetrative at least to the Conrad discontinuity). Gold concentration in the upper crust is a consequence of this late crustal magmatic, tectonic and thermal history.

### 2.4.2. Magmatic origin of gold

Fluid inclusion and stable isotope studies of Archaean gold-related fluids suggest the involvement of either a magmatic or a metamorphic process for the gold transport and deposition. Classical, magmatic-hydrothermal models of gold mineralisation were many times reviewed (Macdonald, 1984; Mason and Melnik, 1986; Wood et al., 1984, 1986; Spooner et al., 1985; Groves and Phillips, 1987; Colvine et al., 1988), the main reason being the association between plutons and the gold depositional environment but also because of fluid inclusion and the isotopic constraints. However, two main critics remain against the magmatic model:

*i)* is it possible for such a classical model of magmatic fluid generation, involving silicate magma formation, fluid exsolutions and mineral precipitation, to generate fluids compatible with those attributed to the Archaean gold-related fluids?

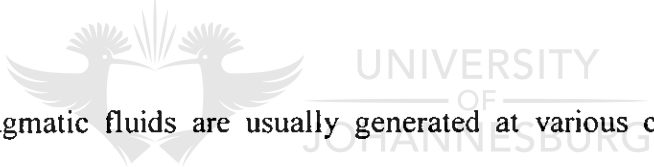
*ii)* it has been demonstrated, especially in the Superior Province, Canada, where the igneous activity supposed to play an important role, that early emplacement of intrusive bodies or syn-volcanic tonalite-trondhjemitic plutonism was a very prominent characteristic of Late Archaean greenstone belt development (Paradis et al., 1988). Despite this very long history of plutonism, significant gold mineralisation developed only during late stages of tectonism and plutonism, after the termination of calc-alkaline volcanism and consanguineous plutonism (Colvine et al., 1988). Similar arguments against the model were used by Ojala et al. (1993), Wang et al. (1993) and McCuaig et al. (1993) in Western Australia.

*iii)* if gold mineralisation is attributed to only magmatic processes, a very rare and quite unique process must have operated during the igneous process that generated the



plutons and their magmatic fluid evolution, otherwise many other volcanic/plutonic bodies should have formed similar gold deposits at various times in the Earth's history, and not only within tectonically cratonised shields.

Magmatic fluids are usually produced when a crystallising magma reaches vapour saturation with the exsolution of the vapour phase from the melt and the already solidified crystalline system. In the case of Archaean auriferous systems, CO<sub>2</sub> is a fundamental component of the hydrothermal fluids, but CO<sub>2</sub> did not play the same important role in Phanerozoic magmatic ore-forming fluids (Colvine et al., 1988). As an example, Nash (1976) reported that fluids associated with porphyry copper systems generally contain less than 3 mole % CO<sub>2</sub>, although concentrations of up to 30 mole % have been recorded.

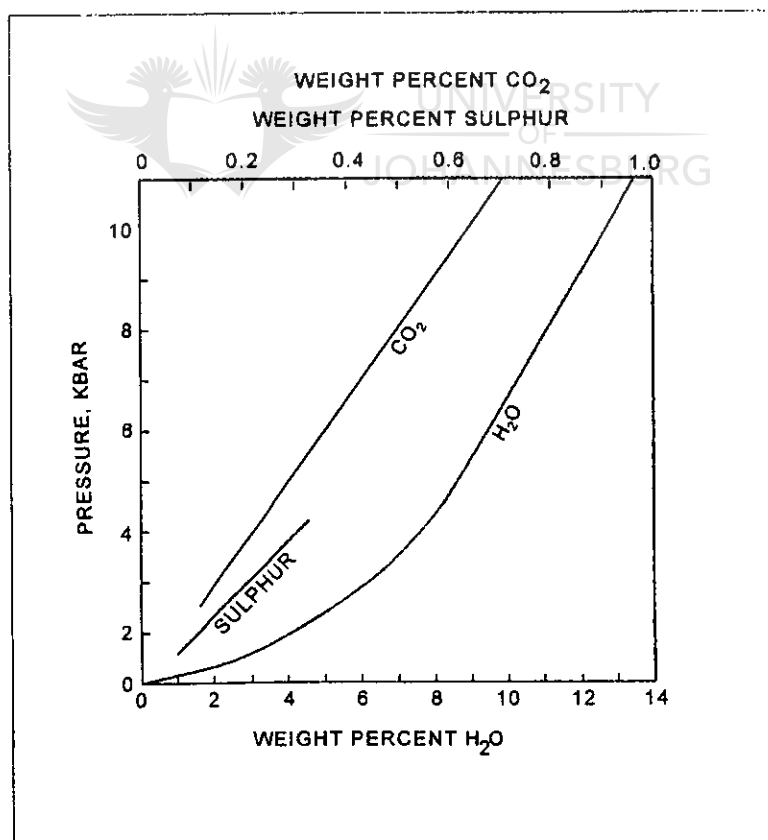


CO<sub>2</sub>-rich, aqueous magmatic fluids are usually generated at various crustal levels by the crystallisation of tonalite-granitic magmas, if the magma contained both H<sub>2</sub>O and CO<sub>2</sub> (Newton et al., 1980). CO<sub>2</sub> solubility in silicate melts is dependent on melt composition, temperature and pressure, and is lower than that of H<sub>2</sub>O (**fig. 2.4**; e.g. Kadik and Eggler, 1975; Mysen, 1976).

Due to the low solubility of CO<sub>2</sub> in the magma, silicate melts need only small amounts of CO<sub>2</sub> to become saturated in CO<sub>2</sub>. Taking into account the higher CO<sub>2</sub> solubility at higher pressures and temperatures (**fig. 2.4**), magmas generated under upper mantle conditions and which evolved further in the upper crust will quickly become CO<sub>2</sub>-saturated, long before the same magma reached H<sub>2</sub>O saturation conditions. Thus, the melt phase will coexist with a CO<sub>2</sub>-saturated vapour phase (Wells, 1979). As a result, melts will continuously evolve CO<sub>2</sub> (plus minor H<sub>2</sub>O) vapour during their ascent into the upper crust. Such magmas will

crystallise at higher temperature conditions than H<sub>2</sub>O-saturated magmas, if the CO<sub>2</sub> vapour remains in equilibrium with melt and with the crystalline component of the melt. If vapour is slowly distilled during a near-isothermal ascent, the magma will remain molten to lower temperatures.


At pressures of about 4 to 7 kbar the CO<sub>2</sub>:H<sub>2</sub>O ratio of the evolved vapour reaches a maximum value (Holloway and Lewis, 1974; Wells, 1979). Under such conditions, and if the tonalitic melt crystallised at pressures greater than 5 kbar, most of the H<sub>2</sub>O dissolved in the melt will be absorbed in the lattice of the crystallising silicates, such as micas (biotite, muscovite) and amphiboles (hornblende, alkaline amphiboles). The resulting composition of the final vapour phase will therefore be very CO<sub>2</sub>-rich (Stern et al., 1975).



**Figure 2.4:** Solubility of CO<sub>2</sub>, H<sub>2</sub>O and S in a tonalitic-granitic melt, as a function of temperature and pressure. Sulphur data from Carroll and Rutherford (1985), solubility for dacite melt at 1025°C and  $f_{O_2}$  of the hematite-magnetite buffer. Data for CO<sub>2</sub> from Holloway and Lewis (1974), solubility for binary CO<sub>2</sub>-H<sub>2</sub>O fluids in albite liquid,  $X_{CO_2}(\text{fluid}) = 0.75$ . Data for H<sub>2</sub>O from Burnham and Ohmoto (1980). Diagram from Colvine et al., 1988.

Thus, it is clear that for a silicate magma to become vapour saturated at a higher temperature early in its ascent, and to evolve a CO<sub>2</sub>-rich vapour, it is necessary for the anatectic source area to contain some CO<sub>2</sub> (Colvine et al., 1988). When CO<sub>2</sub> is absent in the source area, vapour saturation is achieved at a higher crustal level (lower temperature) and the vapour is H<sub>2</sub>O-dominated with only small amounts of CO<sub>2</sub>.

An important conclusion follows from this discussion: if igneous fluids are the source for the CO<sub>2</sub>-dominated Archaean fluids, in the shallower and medium crustal levels (greenschist and amphibolite facies conditions), the deeper levels of the crust (upper amphibolite and granulite facies conditions), dominated by crustal thickening and ductile tectonic processes, probably interact with CO<sub>2</sub>-rich fluids of metamorphic origin.



In the case of the magmatic model of gold deposition, the gold mineralising fluid either evolved from *mafic or ultramafic magmas* or from *tonalitic melts* also of mantle parentage, otherwise the fluids would not display the CO<sub>2</sub>-rich character associated with gold deposition (Nisbet, 1987). Other possible sources include granitic melts derived from partial melting of the lower crust which scoured the deep continental crust of gold. Another solution, although improbable, is that the gold has resided in the upper crust since the Earth's primordial differentiation, and has been simply redistributed since (Nisbet, 1987).

A suitable source for gold mineralising fluids remains the high magnesian lavas (komatiites, komatiitic basalts, picrites) that display high PGE's and Au-contents in comparison with other lithologies in greenstone belts. Magnesium-rich lavas become saturated in sulphur at high crustal levels, just prior to eruption, because they are much hotter than normal basaltic or

felsic magmas. S, Au and PGE's are therefore carried to much higher crustal levels, and even to extrusion (Keays, 1984).

On eruption, massive heat exchange with sea water takes place, giving rise to hydrothermal circulation throughout the hot volcanic pile (Seward, 1984). This may produce strata-bound syngenetic or epigenetic gold deposits, depending on the time of major hydrothermal movement and redeposition of the gold (Nisbet, 1987). Late stage metamorphic fluids associated with the alteration of the magnesian lavas, may reconcentrate the gold (Fyfe and Kerrich, 1984). Viljoen (1984) studied the association of Archaean lode-gold deposits with komatiites and came to the conclusion that they played an important role in delivering the gold from the mantle. Groves et al., (1984) suggested that, although the concentration factors from source to depositional site are so high that differences in absolute Au content of the source may not be significant, a source enriched in gold is obviously helpful. An alternative view proposed by Kerrich and Fyfe (1981) is that komatiites may be preferential sinks for gold rather than sources, given their high bivalent metal inventory for carbonisation. Ultramafic rocks may therefore act as preferred source or preferred sink.

Fyon and Crocket (1982) emphasised an interesting aspect of the geometry of different volcanic/intrusive rocks with relationship to the position of the gold veins (quartz veins or stratabound deposits). Although the main initial concentrating process probably took place as a result of hydrothermal circulation, the depositional site is often closely associated with felsic volcanic centres that overlie mafic or komatiitic lavas. Thus, felsic hydrothermal systems penetrating hot magnesian lavas could potentially flush the Au from a fertile source region within the mafic lava piles and transport it upward.

In conclusion, different magmatic fluid evolutionary paths can be expected, depending in part on initial magma composition, redox conditions and the presence of CO<sub>2</sub>-H<sub>2</sub>O in the magmatic chamber. The gold-related fluids should be chemically similar to the fluids produced by classic magmatic exsolutions, if they are derived from a magma source. A wide spectrum of fluids might evolve, as a result of different depths of exsolutions, different degrees of equilibrium between the evolved fluid and the generating magmas, or whether fluid immiscibility occurred (Colvine et al., 1988).

#### 2.4.3. Metamorphic origin of gold

Derivation of hydrothermal fluids by prograde devolatilisation reaction has been proposed as a process responsible for the formation of Archaean auriferous fluids (Hutchinson et al., 1980; Kerrich and Fyfe, 1981; Groves and Phillips, 1987; Colvine et al., 1988). The characteristic features of Au-bearing fluids related to the Archaean metallogeny were presented in **Chapter 2.3**. The variability in the composition of such fluids due to different controlling conditions were also emphasised (**Chapters 2.3.1.** and **2.3.2.**). As asserted before, the introduction of large volumes of CO<sub>2</sub> into low-grade greenstone belts is an inherent characteristic of the Au-related Archaean metallogenetic event. Large volumes of ankerite, dolomite or manganoan calcite were introduced into regional structures, penecontemporary to the gold deposition.

Finely dispersed calcite, precipitated during sea-water alteration of the volcano-sedimentary assemblage, may provide some CO<sub>2</sub> to a metamorphic fluid (Colvine et al., 1988). However, the carbon isotopic data are not consistent with this model (Schidlowski et al., 1975). Recent

papers, written mostly in the 90's demonstrate that the CO<sub>2</sub> could not be generated by the process of decarbonisation of carbonated greenstone successions (Kerrick, 1990; Groves et al, 1992; Groves, 1993; Mikucki and Ridley, 1993). Other sources for CO<sub>2</sub> must be found in order to explain the  $\delta^{13}\text{C}$  composition of the gold-bearing mineralised fluids. A mixture between a magmatic and metamorphic fluid might be an answer to this problem.

A prominent feature of the gold metallogenetic provinces in the Abitibi Belt (Canada), Yilgarn Block (Australia) and the Barberton Mountain Land (South Africa) is the fact that gold is concentrated into regional zones of deformation (shear zones). Both ductile and brittle deformation occurred at the time of gold deposition (Percival and Krogh, 1983; Groves et al., 1989). Rocks metamorphosed under highly variable metamorphic conditions, although predominantly mafic in composition, ranging from greenschist facies rocks to granulites, represent the regional or local country rock of the gold-bearing veins. Bancroft and Jean (1982) and Groves et al. (1992) submitted the idea that the gold deposition should be a continuous process, concentrated along crustal shear zones, spanning the entire range of metamorphic facies from the granulite facies to the greenschist facies. Crustal scale depositional mechanism is therefore needed to explain the widespread features of the gold deposits, regardless of the style of deformation or the metamorphic grade.

It is also important to emphasise that at a depth suitable for granulite facies metamorphism, it is difficult to distinguish a pure magmatic process from a pure metamorphic process. Thus, it is much more reasonable to speculate that the late Archaean granulitic facies metamorphism that affected the lower crust, and the emplacement of magmas of diverse composition into the lower crust were triggered by a process external to the crust (Colvine et al., 1988). Such a

process could involve crustal thickening due to primitive Archaean tectonism, the ancestor of modern global tectonics.

Beside the magmatic/metamorphic link, the granulitisation process appears to require the presence and generation of CO<sub>2</sub>-rich metamorphic fluids (Touret and Dietvorst, 1983). This observation could be explained as follows:

*i)* granulites represent a residuum from which a felsic melt has been removed (Fyfe and Henley, 1973; Pride and Muecke, 1980), or

*ii)* granulites were produced by the reaction between amphibolitic rocks and CO<sub>2</sub>-bearing fluids, a process which could involve partial melting (Hamilton et al., 1979; Newton et al., 1980).

Many granulites are depleted in certain LILE, such as K, Rb, Cs, U, Th, Y, heavy REE and have high Ba/Rb, Ba/Sr, Ce/Yb, K/Cs and K/Rb ratios, relative to inferred and adjacent protolites (Rollinson and Windley, 1980; Kerrich, 1989b). Taking into account these geochemical features, the derivative melt separated from the granulitic residuum, should be geochemically complementary, and would be characterised by low K/Rb, Ba/Rb ratios and relatively enriched in Rb, because Rb is preferentially depleted from granulites, with respect to K and Ba (Kerrich, 1989).

Regarding the source of Au, a very pertinent study was done by Sighinolfi and Santos (in Colvine et al., 1988). In their view, a potentially very large gold reservoir is provided by that part of the lower crust undergoing granulitisation. They found that granulites from Bahia State, Brazil, contained an average of 0.8 ppb gold. If the anomalous values are also considered (about a maximum of 8 ppb), the average rises to 0.9 ppb. This data suggest that

the Bahia granulites are depleted in gold by a factor of at least 2 with respect to either crustal igneous rocks or their lower metamorphic grade equivalents lithologies. This might suggest that gold can be removed from the lower crust during granulitisation. Furthermore, the incompatible element suite (K, Rb, Li, B, Ba, REE) defines a dispersion halo around many Archaean gold systems (Colvine et al., 1988; Kerrich, 1989b), that is identical to the depletion of many granulites. Thus, gold and associated elements, may have been mobilised from the lower crust during the late Archaean granulitisation event, and concentrated in supracrustal domains (Colvine et al., 1988).

The gold could have been transported in a vapour phase of metamorphic origin from the source area to the depositional site, without passing through a silicate magma stage (pure metamorphic affiliation). Because of such a mechanism, large amounts of CO<sub>2</sub> could play an important role in the late Archaean magmatic-metamorphic history of the crust and of the gold-carbonate association. In this way, abundant CO<sub>2</sub> (manifested as carbonate) was introduced into the regional shear zones (**fig. 2.5**), before and during gold precipitation. If the redox conditions of the crustal environment changed during the channelling of the fluids, the ambient fluid might have been transformed into an oxidised, CO<sub>2</sub>-rich, S-bearing (SO<sub>2</sub>?) fluid, capable of scavenging and transporting gold from a large rock reservoir (Colvine et al., 1988). This influx of CO<sub>2</sub>-bearing vapour along major crustal structures into the upper crustal rocks culminated with intense carbonisation of susceptible lithologies and generation of nearly pure carbonate veins within regionally extensive deformation zones.

4

The oxidising conditions mentioned above may have changed and enhanced the solubility of gold and sulphur. Incompatible elements cited previously (LILE, U, Th, Zr, Au, REE) were



probably transferred from the zone of granulitisation to the upper crust by the vapour phase, the so-called *magmatic-metamorphic fluid*. Specific depositional factors controlled the gold precipitation in structurally and geochemically controlled zones of permeability.

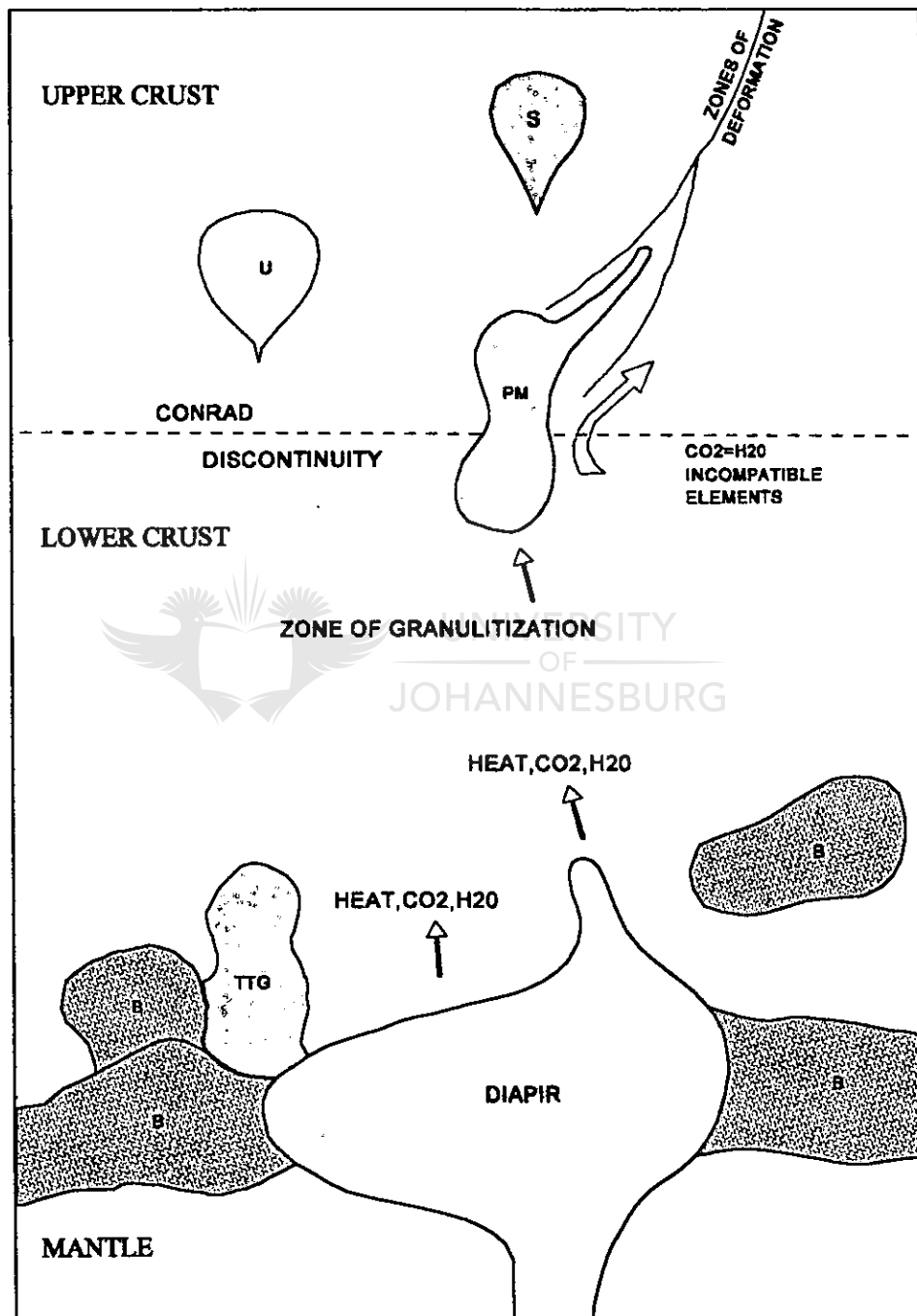


Figure 2.5: Cartoon illustrating a possible cratonisation model of the Archaean crust, which accounts for the late plutonism and metamorphism of the crust and the coeval differentiation of the upper mantle. Mantle diapirism supplies magma, heat and volatiles to the base of the crust, which induces granulitisation and crustal thickening (from Colvine et al, 1988).

#### 2.4.4. Discussions

A clear-cut distinction between magmatic (silicate magma derived fluids) and metamorphic (vapour phase) processes is not possible at present (Colvine et al., 1988). However, the Archaean gold metallogenic episode must be considered in the context of the totality of the late Archaean cratonisation events.

Considering one or the other end member of the hypothesis as the unique model may prove simplistic, as it is evidenced from all over the world, namely that both processes played symbiotic roles in concentrating gold during the climax of the cratonisation event (Colvine et al., 1988). Radiogenic data showed that multiple sources contributed to the hydrothermal fluid (Kerrick, 1989b). Multiple mantle (magmatic) and crustal sources (metamorphic) are probably required. In some cases one fluid or another was predominant and played the dominant role. In other cases the fluid represented a real mixture between the two end members. Remaining uncertainties regarding such a gold-mineralising fluid include the evolution of the fluid present in the lower crust during and following peak granulite metamorphism.  $^{40}\text{Ar}/^{39}\text{Ar}$  data recorded by hydrothermal white micas (Masliwec et al., 1986) in the upper crust, and by U-Pb ages of monazite and rutile (Corfu and Muir, 1988) in granulites from the lower crust showed that gold was deposited in the upper crust slightly later than the time when granulitisation occurred in the lower crust. The time gap probably represents the time interval when the fluids were channelled from the lower toward the upper crust. In other words, the contemporaneity between the relatively oxidising lower crustal hydrothermal activity, which post-dated peak-granulite facies metamorphism, and the hydrothermal activity within the auriferous system where gold was deposited, suggests that a

component of hydrothermal activity at the depositional site was derived from the lower crust. These fluids infiltrated the upper crust during a period of no magmatic activity (Colvine et al., 1988). Late, post-peak metamorphic fluid activity in the lower crust is supported by the age relationships between titanite, monazite and rutile (Corfu, 1987; Corfu, 1988; Krogh et al., 1988). The role of such a fluid is more difficult to demonstrate, but it was coeval with fluid activity in the upper, auriferous, depositional sites. In other words, it is highly possible that the fluids associated with auriferous zones have been coupled with similar activity in the lower crust (Corfu, 1988). Only through detailed studies, including structural, petrographical, mineralogical, chemical and isotopic studies will it be possible to arrive at a better understanding of the late magmatic, metamorphic and tectonic history of Archaean cratonised areas and the related Archaean gold metallogeny. This is the main topic of the present study.



### 3. METHODS OF STUDY

#### 3.1. FIELD MAPPING

Grid surface mapping of the Doornhoek gold deposit, and the adjacent host rocks, including mapping of trenches and shallow shafts were carried out during 1991 and 1992. The area mapped is about 1.5 km by 0.52km. Detailed logging of more than 30 boreholes was carried out during April-May 1991 and more than 200 borecore samples were collected for petrographical studies. An additional 50 samples were collected from percussion drilled boreholes (rock chips) and from the surface. The results of the mapping, integrated with data made available by Shell Minerals (now Gengold) is shown in a sliced block-diagram (**fig. 4.5**) in chapter 4.2.

#### 3.2. STRUCTURAL GEOLOGY

A detailed sliced block-diagram (**fig. 4.5**) was constructed (**Chapter 4**) on the basis of all the available structural and petrographical data obtained during the mapping of the surface and trenches, and especially from the logging of both diamond and percussion borehole cores. The structural data were collected from almost fresh outcrops in the close vicinity of the Doornhoek exploration camp and from the highly weathered rocks in the exploration trenches. About a thousand measurements of foliation, mineral lineations, fissures and strikes of leucocratic injections were used for a microtectonic study.

### 3.3. STRUCTURAL PETROLOGY

A detailed structural petrological study was carried out on six orientated thin sections, prepared from granite-gneiss, felsic granulite and mafic granulite. The mineral orientation data obtained using a Fedorov universal stage were correlated with the local structural features of Doornhoek gold deposit and with the regional tectonic features of the SMZ of the LB.

### 3.4. PETROGRAPHY

A detailed petrographical description of the various rock types of the Doornhoek gold deposit and adjacent lithologies was undertaken. Modal mineral analyses in highly altered coarser-grained rocks were established using point counting in thin sections of 100 x 80 mm stained for K-feldspar. Where possible, established nomenclature was used for rock classification, but in the case of highly metasomatised rocks generic names such as *calc-silicate facies rocks* were used.

### 3.5. ORE MINERALOGY

A detailed ore petrological study was carried out on polished sections and polished thin sections. Relevant features of the ore minerals and their relationship with the silicate host

minerals are described in **Chapter 7** (Mineralisation) and **Chapter 8** (Mineral reactions and textures).

### 3.6. FLUID INCLUSIONS

Preliminary fluid inclusion studies were carried out on 10 double polished wafers. The samples were only exploratorily investigated in order to confirm the existing types of fluid inclusions. A USGS gas flow fluid inclusion stage adapted for a Nikon polarising microscope was used to record homogenisation and melting temperatures of the fluid inclusions. The recorded fluid inclusions data are discussed in **Chapter 9**.



Major and trace elements analyses were done by RockLab in Pretoria and Gold Fields Laboratories in Johannesburg for the volumetrically significant lithologies of the Doornhoek gold deposit and adjacent high grade rocks. A comparison was also made between the unhydrated and highly altered (hydrated) granulites. REE analysis were done at the University of Natal, Durban for representative samples of the highly altered lithologies (hydrated rocks). Microprobe analyses, using the Cameca Camebax Electron Microprobe in the Department of Geology, Rand Afrikaans University, were collected for all the major rock forming minerals and ore minerals of the volumetrically significant lithologies of the Doornhoek gold deposit and the associated lithologies. Important metamorphic minerals (such as garnet) were studied in detail in order to develop models to explain the observed

compositional zoning. Highly accurate trace element analyses were also carried out at the National Accelerator Centre, based at the Atomic Energy Corporation in Cape Town, South Africa, on several garnets from the mineralised zone using the neutronic microprobe.

### 3.8. ISOTOPE STUDIES

C and O stable isotopes studies were not done on samples from Doornhoek, but a large set of isotopic data from the RAU Geology library was used for comparison and for a better understanding of the isotopical exchange that took place in areas showing similar alteration patterns, namely at Klipbank (Mokgatla, 1995) and Petronella (Du Toit, 1994) localities.



## 4. GEOLOGICAL SETTING OF THE DOORNHOEK GOLD DEPOSIT IN THE SOUTHERN MARGINAL ZONE OF THE LIMPOPO BELT

### 4.1. REGIONAL GEOLOGY OF THE SOUTHERN MARGINAL ZONE OF THE LIMPOPO BELT

The granulite facies Limpopo Belt (LB) of southern Africa, bounded in the north by the Zimbabwe Craton and in the south by the Kaapvaal Craton, developed as a result of a late Archaean orogeny (2.70 Ga) (van Reenen et al., 1990). The LB displays a threefold subdivision in which the similar SMZ and NMZ, composed of reworked granulite-grade equivalents of the adjacent granite-greenstone terranes, are distinguished from the predominantly supracrustal Central Zone (CZ) (e.g. Mason, 1973; van Reenen et al., 1990, 1995). These terranes are separated from one another and from the surrounding cratons, by prominent terrane boundaries (Van Reenen et al., 1987, 1990, 1995). The NMZ is separated from the Zimbabwean Craton by the southward dipping Umlali Thrust Zone (Coward et al., 1976; Coward, 1983; Roering et al., 1992a; van Reenen et al., 1995). The SMZ is separated from the Kaapvaal Craton by the northward dipping Hout River Shear Zone with down-dip lineations (van Reenen et al., 1988; Smit et al., 1992; Smit and van Reenen, 1997) (**fig. 4.1**).

The Doornhoek gold deposit is situated in the SMZ of the LB, relatively close to the Doornhoek Shear Zone (**fig. 4.1**). It is therefore necessary to discuss the regional geology of the northern Kaapvaal Craton and the SMZ of the LB as an introduction to the geological setting of the gold deposit.



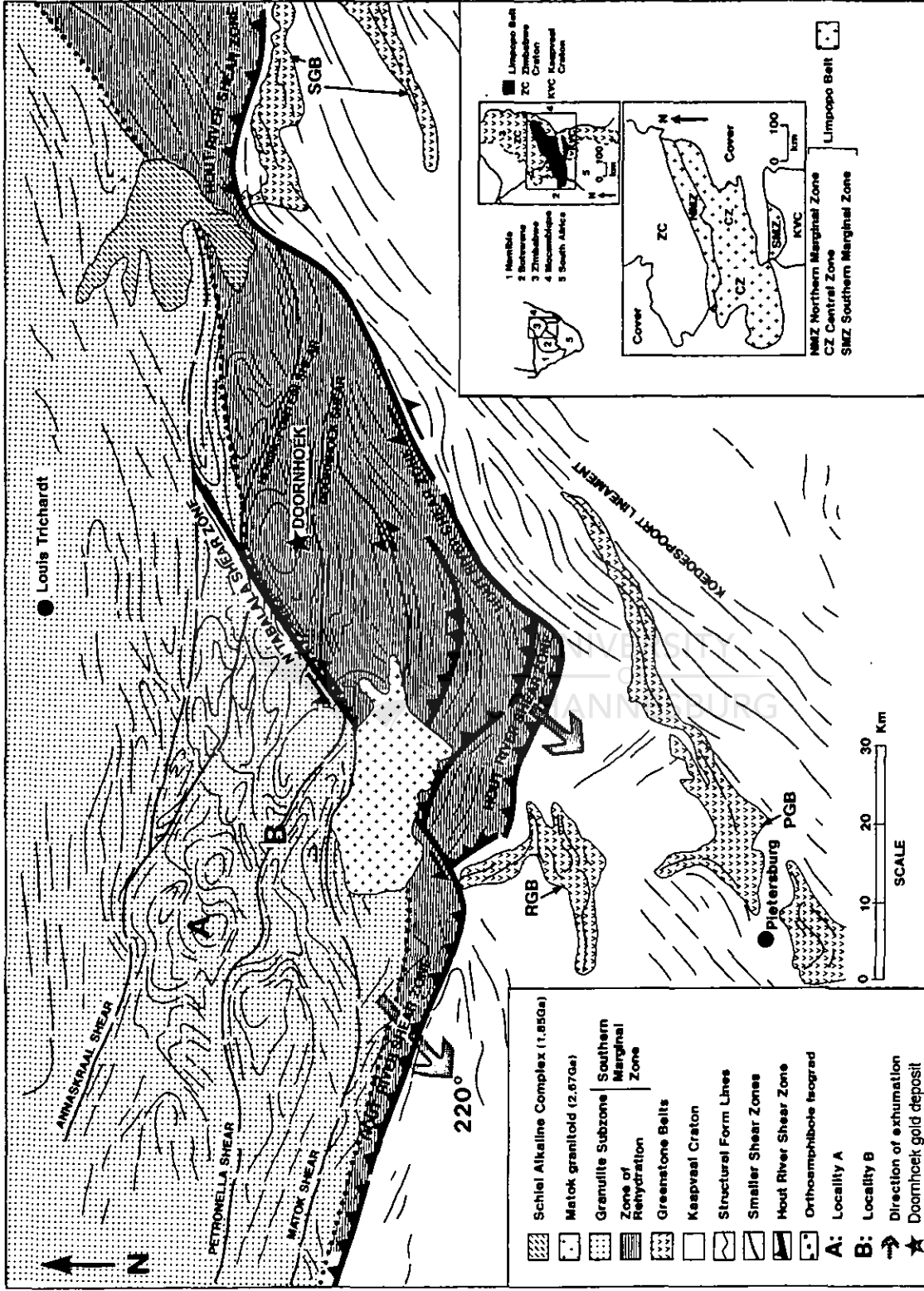


Figure 4.1: Map of the Southern Marginal Zone of the Limpopo Belt showing the major tectonic and metamorphic elements (after Smit and Van Reenen, 1997).

#### 4.1.1. Structure

Recent studies (van Reenen et al., 1990; Roering et al., 1992 a and b; Smit et al., 1992; Smit and van Reenen, 1997) showed that the structural and metamorphic pattern of the SMZ developed through the interaction of deep crustal folding and faulting as the result of crustal thickening related to the late-Archaean collision of the Kaapvaal and Zimbabwe Cratons during the Limpopo Orogeny. This style of deep-crustal deformation and metamorphism portrayed by intense attenuated granulite-grade granite-greenstone lithologies differs markedly from that of the adjacent granite-greenstone terranes of the two adjacent cratons. The style of deformation on the two cratons during the early  $D_1$  phase of deformation was less intense and at greenschist to amphibolite grade of metamorphism (**fig. 4.1**), whereas in the SMZ both  $D_1$  and the shear-dominated  $D_2$  event are very well developed (van Reenen, 1986; van Reenen et al., 1990; Roering et al., 1992a and b; Smit et al., 1992; Smit and van Reenen, 1997).

The Sutherland (SGB) and Rhenosterkoppies greenstone belts (RGB) straddle the southern boundary of the SMZ of the Kaapvaal Craton (KVC) (**fig. 4.1**). These two greenstone remnants are separated from the high-grade terrane by the northward dipping Hout River Shear Zone. This major tectonic boundary separates areas defined by continuous greenstone belts on the KVC from highly tectonised high-grade equivalents in the SMZ of the LB (**fig. 4.1**). At the same time, the ultramafic, mafic and metapelitic granulite-grade rocks of the Bandelierkop Formation in the SMZ occur as tectonically dismembered slivers intimately mixed with the tonalitic-trondhjemitic Baviaanskloof Gneiss (du Toit et al., 1983; Barton et al., 1992; Smit et al., 1992; Smit and van Reenen, 1997).

a) **Kaapvaal Craton:** the internal structure of the greenstone belts along the northern boundary of the KVC all have a similar ENE-WSW trending structural grain and reveal a history of thin-skin contractional faulting which truncated them at depth, rendering them allochthonous (de Wit et al., 1992). The faults have a general north-westward vergence and movement vectors are generally down-dip to oblique.

**The Sutherland Greenstone Belt:** this belt is located along the eastern contact between the LB and the KVC (**fig. 4.1**). It consists of northerly verging tectonically stacked thrust sheets which rest on a granitoid footwall (de Wit et al., 1992). Amphibolite rocks in the Sutherland greenstone belt typically consist of hornblende + plagioclase + quartz + sphene + magnetite/ilmenite, while garnet-bearing varieties are restricted to the northern contact with the LB. Rare pelitic schists in the southern part of the belt comprise mainly muscovite + biotite + quartz + feldspar, while similar rocks in the northern part consist of garnet + muscovite + biotite + kyanite + staurolite. Ultramafic rocks are mainly composed of anthophyllite + tremolite + chlorite with olivine restricted to the northern part of the belt. On a regional scale the belt is characterised by a south-to-north increase in the grade of metamorphism, from lower to middle amphibolite facies. The highly tectonised nature of the rocks is especially apparent near the contact with the SMZ which is characterised by intermixed tectonic slices of prograde greenstone assemblages with retrogressed metapelitic granulites belonging to the SMZ (McCourt and van Reenen, 1992). Coarse-grained prograde kyanite is also restricted to the northern contact zone.

**The Rhenosterkoppies Greenstone Belt:** this belt is also situated at the contact with the SMZ, but in the central part of the area (fig. 4.1). It consists mainly of mafic and ultramafic schists and banded iron formation (BIF), and is also characterised by a south-to north increase in the grade of metamorphism from upper greenschist facies to middle and upper amphibolite facies (Miyano and van Reenen, 1987; Miyano et al., 1990). Ultramafic rocks from the northern limb of the greenstone belt, adjacent to the Hout River Shear Zone are characterised by the assemblage olivine + anthophyllite + tremolite + chlorite. Olivine clearly overgrows an earlier fabric defined by chlorite (van Schalkwyk and van Reenen, 1992). Prograde kyanite also occurs in quartzitic rocks close to the contact with the Hout River Shear Zone.

**b) Southern Marginal Zone:** the SMZ is characterised by a prominent east-west orientated deformation pattern that also displays a complex fold pattern referred to as the  $D_1$  phase of deformation (random structure trend) (Smit et al., 1992; Smit and van Reenen, 1997). Superimposed on the  $D_1$  folded trend is a regional system of roughly E-W trending major ductile shear zones ( $D_2$ ), which clearly transpose and therefore post-date the early  $D_1$  gneissic banding (Smit et al., 1992; Smit and van Reenen, 1997). The system of  $D_2$  shear zones are collectively referred to as the Southern Marginal Shear Systems (Smit and van Reenen, 1997). This  $D_2$  system of shear zones displays different geometries and different orientations with respect to the regional trend of the Limpopo Belt. Some are strike-slip and others dip-slip faults. Previous work in the SMZ has emphasised the important relationship of deep crustal shear zones which formed at about 2.67 Ga (Barton and van Reenen, 1992), with the distribution of the zone of high-grade retrogression (see section 4.1.2) and gold mineralisation along the southern boundary of the SMZ (fig. 4.1) (van Reenen et al., 1994; Gan and van Reenen, 1995). The  $D_2$  shear zones were later reactivated along  $D_3$  shear zones,

still under ductile conditions (Smit and van Reenen, 1997), although in certain places, such as Doornhoek, brittle deformation was also recorded.

Four major structural elements have been identified in the SMZ (Smit and van Reenen, 1997)

(fig. 4.1):

*i)* domains with strongly foliated, folded and intensely attenuated granite-greenstone lithologies

*ii)* terrane bounding shear zones

*iii)* shear zones situated within the granulite terrane and having a strong influence on the regional structural pattern of the SMZ

*iv)* reactivated shear zones with dominant strike-slip movement, discordant with the regional fabric and with the older shear zones.

#### 4.1.1.1. D<sub>1</sub> fold dominated domains

This domain is characterised by large, oval-shaped closed-fold structures (fig. 4.2) related to an earlier (D<sub>1</sub>) phase of deformation (Smit and van Reenen, 1997).

The oval-shaped closed-folds are also present in the CZ, and have previously been described as sheath-like folds (Roering et al., 1992a).

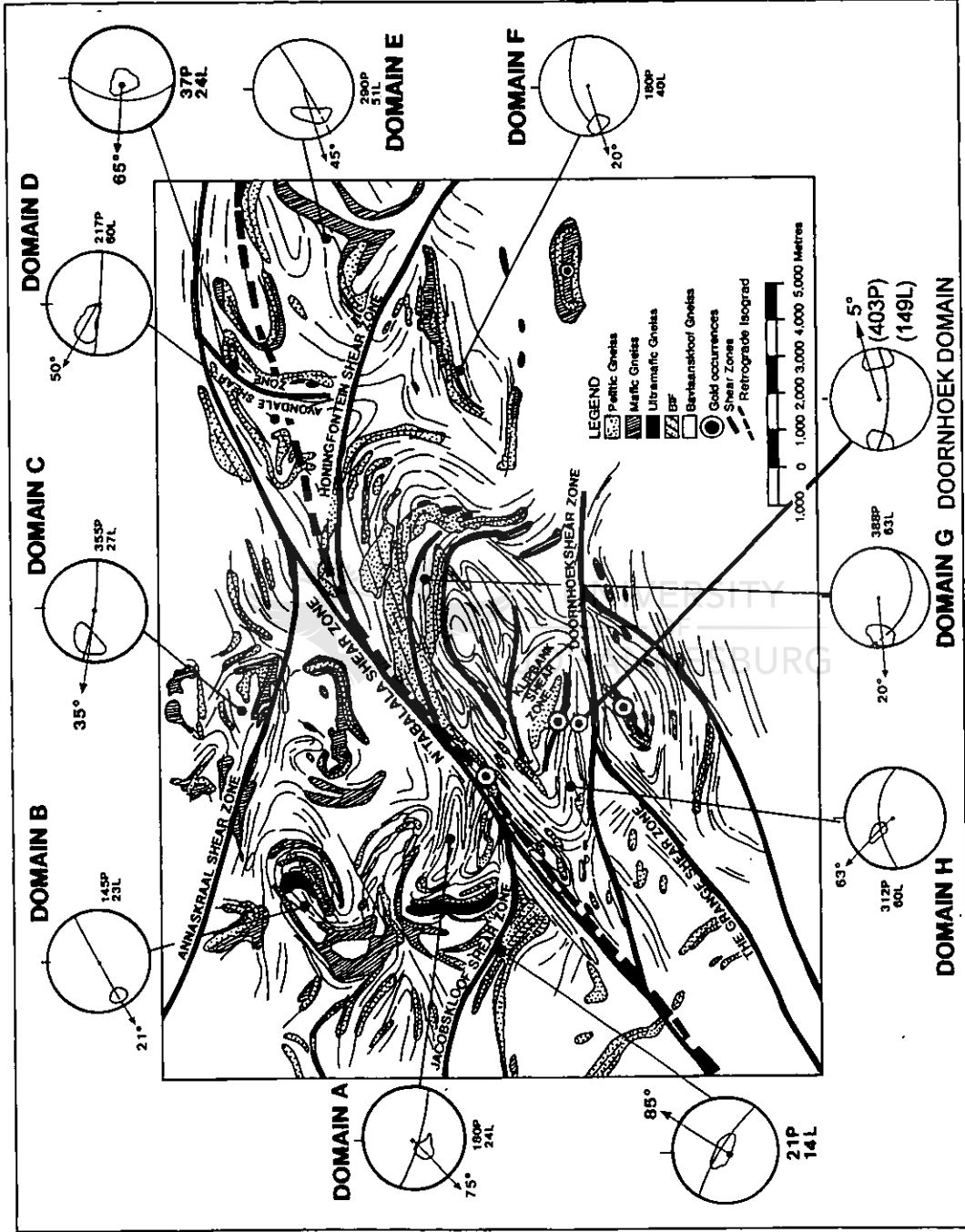


Figure 4.2: The location of the Doornhoek Gold Deposit in the central part of the SMZ, related to the main shear zones in the area. Note the variation of the structural elements and lineations in different zones in the SMZ. In the Doornhoek domain the lineation is subhorizontal showing strike-slip movements along  $D_2$  which is almost E-W and very steep (after CA Smit, personal communication, 1997).

#### 4.1.1.2. The Southern Marginal Shear System

This domain is characterised by anastomosing ductile ( $D_2$ ) shear zones that bound the  $D_1$  structural domains (Smit and van Reenen, 1997) (fig. 4.2.). In contrast, the  $D_2$  shear zones are narrow zones of intense deformation characterised by  $D_2$  deformation fabrics (Smit and van Reenen, 1997).

The SMZ Shear System can be subdivided into two systems: the terrane bounding Hout River Shear Zone and an E-W system of smaller thrust and strike slip faults that are developed within the SMZ.

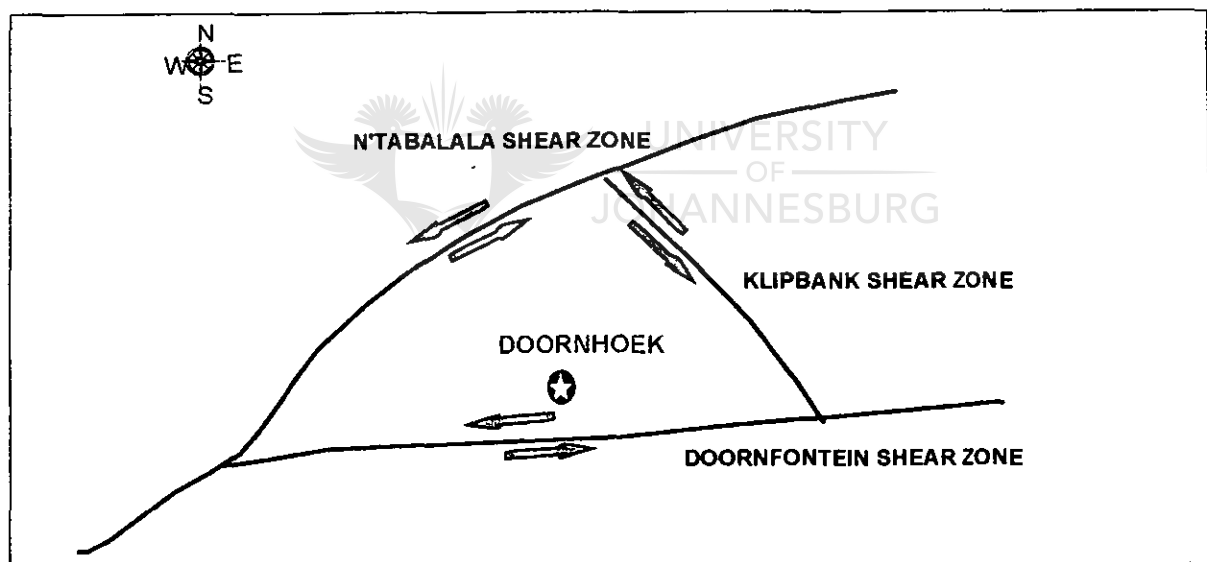


Figure 4.3: The Doornhoek Gold Deposit is located between the small transfer fault, NW-SE striking Klipbank Shear Zone, the major NE striking N'Tabalala and Doornfontein shear zones.

**The Hout River Shear Zone (HRSZ).** This composite structure, up to 4km wide (Smit et al., 1992; Smit and van Reenen, 1997) has been mapped as individual segments over a distance of more than 200km and bounds the SMZ in the south (de Wit et al., 1992; McCourt and van

Reenen, 1992; Roering et al., 1992a; Smit et al., 1992; Ruygrok, 1992; Gan and van Reenen, 1995). It consists of EW trending, steeply dipping reverse fault segments and several near-vertical NE trending strike-slip faults. The strike-slip faults acted as transfer zones linking the different thrust segments to form a zig-zag pattern of lateral and frontal ramps (**fig.4.1**).

The Doornhoek Gold Deposit is located close to a transfer structure, along a secondary shear zone (Doornfontein Shear Zone) which links two prominent shear zones in the area (Klipbank and N'Tabalala Shear Zones) (**fig. 4.3**). The Klipbank Shear Zone probably acted as a transfer shear zone between the two major shears and as a result was able to channelise and focus a major fluid event which produced the Doornhoek Gold Deposit on it.

Geo-electrical data and seismic reflection data, collected across the HRSZ (de Beer and Stettler, 1992), confirmed that the high-grade rocks of the SMZ were thrust southwards over the low-grade cratonic rocks along this steeply northward dipping shear zone (van Reenen et al., 1987; de Wit et al., 1992; McCourt and van Reenen, 1992; Roering et al., 1992b; Smit et al., 1992; Gan and van Reenen, 1995). Geobarometric studies likewise showed that the vertical displacement across the HRSZ was in the order of 15km (Miyano et al., 1990), and that significant vertical displacement also occurred across various  $D_2$  shear zones within the granulite subzone of the SMZ (Tsunogae et al., 1992).

**Smaller Shear Zones.** The SMZ Shear System is also characterised by an EW system of smaller thrusts (e.g. the Petronella and Matok Shear Zones in the granulite subzone) and by strike-slip faults (e.g. the Doornhoek Shear Zone in the rehydrated zone) (**fig. 4.1**). To the



northwest of the N'Tabalala Shear Zone (**fig. 4.1**), steeply northward dipping thrusts bound the  $D_1$  crustal sheets of the granulite subzone juxtaposing high-grade rocks against low-grade rocks. The area to the southeast of this strike-slip fault is characterised by a complex system of smaller closely spaced and roughly E-W trending strike-slip duplexes and southward verging thrust-faults that define a major transpressional jog structure (**fig. 4.1** and **4.2**). The jog of rhomb-horst (Aydin and Nur, 1982) also hosts the main development of the zone of rehydration due to enhanced fluid flow along the strike-slip faults (Roering et al., 1995). The retrograde ortho-amphibole isograd (**fig. 4.1**) clearly follows the Matok thrust in the western part of the area, and the N'Tabalala Shear Zone in the central part (Roering et al., 1992b; Smit et al., 1992; van Reenen et al., 1990; Roering et al., 1995), but cut across fold structures in the eastern part of the area.



UNIVERSITY  
OF  
JOHANNESBURG

#### 4.1.1.3. Reactivated shear zones

Some of the  $D_2$  shear zones in the SMZ Shear System are also characterised by discrete mylonite zones up to 100m wide which mainly occupy the central parts of  $D_2$  structures. These younger faults are post Matok Pluton (2.67 Ga) in age and characterised by a mylonitic fabric that is clearly superimposed onto the main straight gneiss fabric (Smit and van Reenen, 1997).

The N'Tbalala Shear Zone is a major structure which displays a sinistral strike-slip geometry (**fig. 4.2**) demonstrated by the lateral displacement (up to 12 km) of distinctive lithological units and structures (Smit et al., 1992). The Matok Pluton, which intruded this shear zone, does not show any  $D_2$  displacement but exhibits displacement along mylonitic faults (**see fig. 4.1**). This might be explained by the fact that the pluton was probably intruded after the  $D_2$

deformation, and were only affected by younger and relatively unimportant reactivation of the shear zone (Bohlender et al., 1992).

Some of the frontal ramp portions of the HRSZ also show reactivation with down-slip lineations similar to that of the N'Tabalala Shear Zone. Although the age of the reactivation is difficult to be established it is probably pre-Bushveld in age.

#### 4.1.1.4. Other features related to the shear zones of the SMZ

Shear zones in the SMZ reveal a spatial relationship to:

- post-tectonic granitoids which intrude the shear zones (Matok type with an age of 2.67 Ga, Barton et al., 1983)
- gold-bearing deposits (Bochum and Harlequin Deposits, Sieber, 1991; Doornhoek Deposit, this study)
- chromite-bearing deposits with Alpine characteristics (Smit, 1983)
- the development of charnockite (Bohlender et al., 1992)
- the position of the retrograde ortho-amphibole isograd (there is a very close spatial relationship between the isograd and the HRSZ - **fig. 4.1** and **4.2**).

#### **4.1.2. Metamorphism**

The SMZ is subdivided into a northern granulite subzone and a southern zone of rehydrated granulites by a well established retrograde ortho-amphibole isograd (**fig.4.1**) (van Reenen et al., 1990). The zone of hydrated granulites is situated in the hanging wall area of the HRSZ (e.g. van Reenen, 1986; **fig. 4.1**). The metamorphic evolution of the SMZ of the LB has been discussed in various publications (e.g. Stevens and van Reenen, 1992) and is best

documented by a series of well preserved reactions in metapelite. Three distinct metamorphic phases have been identified as part of a continuous clockwise P-T evolution (fig. 4.4). A period of prograde heating ( $M_1$ ) resulted in the establishment of granulite facies conditions and the formation of the peak-metamorphic assemblage Ga + Hy + Bi + Qz + Plag + Ksp in metapelites. Maximum P-T conditions during this prograde phase were about 9.5 kbar and above 840°C (fig. 4.4) (Stevens and van Reenen, 1992).

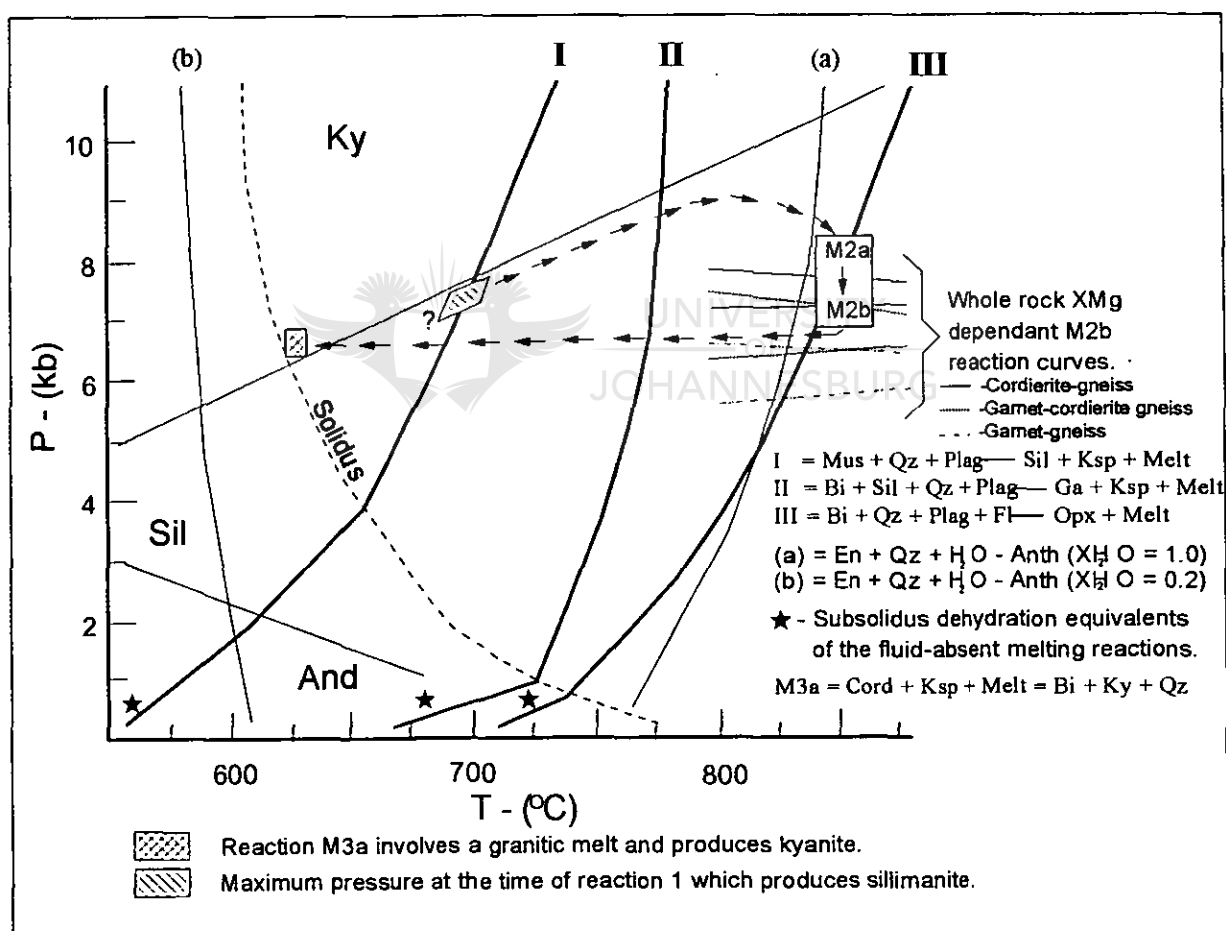
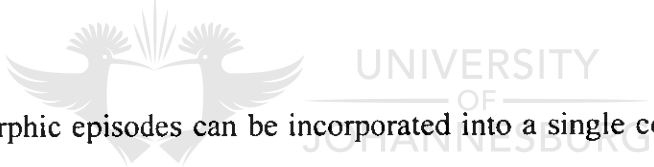


Figure 4.4: Simplified P-T diagram showing the P-T evolution of the granulite facies metamorphic rocks in the SMZ of the LB and illustrating the conditions of the  $M_1$ ,  $M_2$  and  $M_3$  metamorphic events (from Stevens and van Reenen, 1992).

This event was followed by a period of rapid decompression and cooling ( $M_2$ ) to about 6 kbar. During this decompression event the southern part of the Southern Marginal Zone was subjected to the introduction of a  $H_2O$ -bearing  $CO_2$ -rich fluid phase into lithologies still at high grade ( $M_3$ ;  $P=6$ kbar,  $T=600-620^\circ C$ , van Reenen, 1986). This event established the retrograde ortho-amphibole isograd which separates the Southern Marginal Zone into a granulite subzone in the north and a zone of retrogression in the south. The isograd is only expressed in the metapelitic rocks. Associated lithologies (mafic, ultramafic, BIF) have been variously affected by the hydration (Roering et al., 1995). Van Reenen and Hollister (1988) suggested that the retrograde fluids infiltrated rocks still at granulite grade along shear zones and only interacted with the southern part of the granulite terrane at lower temperatures because of a N-S temperature gradient that was established across the high-grade terrane.



These distinct metamorphic episodes can be incorporated into a single continuous clockwise P-T-t path which implies that heating occurred after tectonic loading during the Limpopo Orogeny. The fact that the zone of retrogression, in its most elementary form, is confined to the hanging wall of the HRSZ and its associated system of shear zones, is of importance and will be discussed later.

The post-peak metamorphic evolution of the SMZ was previously considered to reflect a near total re-equilibration during the high-grade cooling portion of the P-T path, and as a result reflects P-T conditions considerably lower than those of peak metamorphism. The results of the present study, however, suggest that in certain areas, closely associated with shear zones, the post peak-metamorphic history of the SMZ could have reached temperature and pressure conditions similar, or even higher than what has previously been reported for the granulite

terrane. These events, which are probably related to the regional  $D_2$  shearing and  $M_3$  hydration events, were preserved in restricted tectonic, mineralogical and geochemical environments such as the Doornhoek Gold Deposit. The main features of the regional  $M_3$  hydration event will, because of its importance with reference to the gold mineralisation, be discussed later (see **section 4.3**).

## 4.2. STRUCTURAL SETTING OF THE DOORNHOEK GOLD DEPOSIT.

The Doornhoek Gold Deposit is located in the zone of rehydration, about 5 km south of the retrograde ortho-amphibole isograd in the SMZ of the LB (**fig. 4.1**). The ore body occurs in a strongly deformed area that shows elements of both  $D_1$  folding and  $D_2$  shear deformation (**fig.4.2**).



### 4.2.1 Large-scale deformation

The Doornhoek Gold Deposit is not directly located on one of the major  $D_2$  shear zones in the area (**fig. 4.2**), but is hosted in a large-scale  $D_1$  fold that was subsequently reworked during the  $D_2$  shear event. The structural pattern of the ore body therefore conforms to a history of early  $D_1$  folding with subsequent transposition and shearing during the younger  $D_2$  event, a common scenario that is observed throughout the SMZ.

Several other gold occurrences are present in the vicinity of Doornhoek, but working gold mines are located in the most eastern part of the area. These mines occur both within the high grade hanging wall section (e.g. Osprey and Louis Moore) and the lower grade footwall

section of the HRSZ (e.g., Franke, Klein Letaba and Fumani Mines) (Van Reenen et al., 1993). The mines in the high grade portion of the fault are structurally very similar to Doornhoek and are all shear zone hosted gold deposits in a high grade metamorphic setting.

The Doornhoek Gold Deposit is hosted in a large  $D_1$  fold structure that plunges gently ( $12^\circ$ ) towards the east ( $\pm 80^\circ$ ) (fig. 4.5). The fold structure which is defined mainly by detailed drilling can be followed for about 800 m along strike. This type of complex fold patterns can be observed throughout the SMZ (Smit et al., 1992) and even in the CZ (Roering et al., 1992a) where they represent the early phase of deformation that developed during the crustal thickening event of the LB. These folds were subsequently deformed and dismembered by intense shearing that took place during the exhumation stage of the LB. The  $D_2$  shear zones, up to 5 km wide (Smit et al., 1992) caused intense shear deformation and transposition of the early folding resulting in large sheath folds that plunge parallel to the transport direction of the  $D_2$  shear zones. This scenario is probably also applicable to the Doornhoek setting.

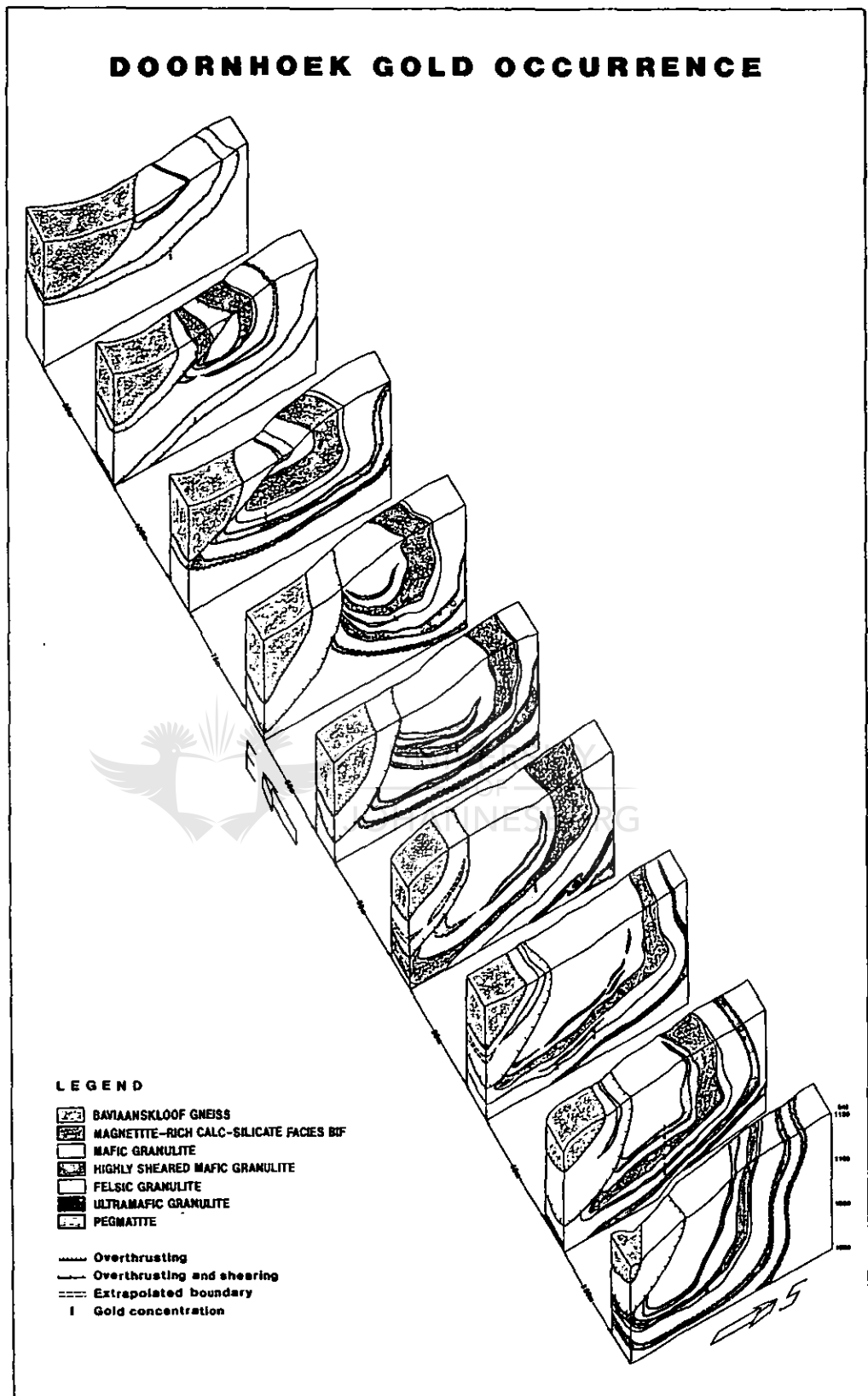


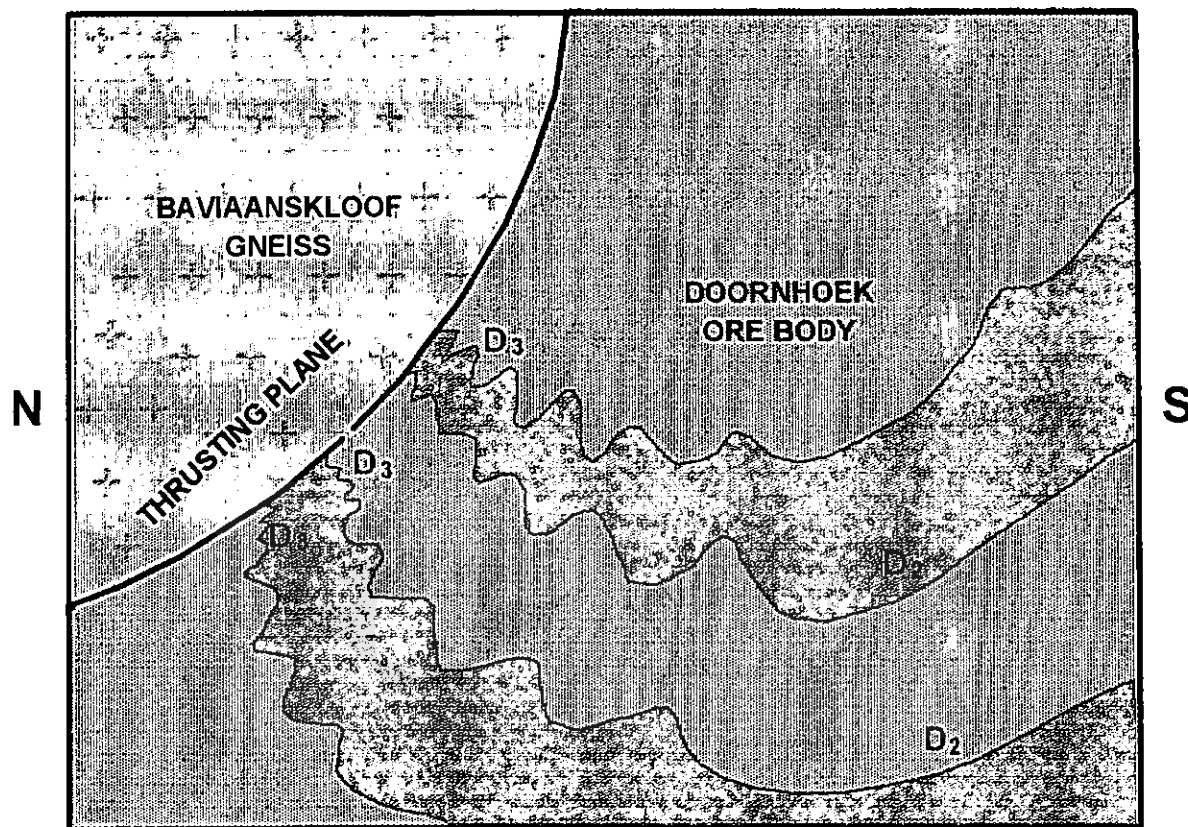
Figure 4.5: Sliced block-diagram showing the morphology of the Doornhoek Ore Body and the thrusts over Baviaanskloof Gneiss. As a result of drilling, the Ore Body can be followed for about 800m along strike. Note the sheath-like fold appearance of the ore body and the mode in which the fold was cut due to the overthrusting of the Baviaanskloof Gneiss.

The ore body, structurally situated in a large low-angle plunging  $D_1$  fold is bounded by three  $D_2$  shear zones (i.e. the N'Tabalala, Doornhoek and Klipbank Shear Zones, **fig. 4.2**) but is not located on a specific structure.  $D_2$  shear deformation is however evident along the contact of the ore body and also as shear zones occurring within the deposit which all have a common strike-slip geometry. Kinematic indicators such as prismatic minerals and winged strain insensitive structures (**fig. 4.7** and **4.8**) suggest a general E-W transport direction of shearing, parallel to the long axis of the large  $D_2$  fold. Augen are commonly observed in the felsic granulite, the augen amphibolite and in sheared mineralised quartz-calcite veins (**fig. 4.8**). The area surrounding the ore body is therefore characterised by a pronounced parallelism between the  $D_2$  shear fabric, the shape and strike of the ore body, the orientation of the contact with the wall rock, and the structures present within the mineralised zones. The shear deformation is also preserved in shear related features in mineralised quartz veins developed parallel to the fabric. The close relationship between the different structural elements occurring at the Doornhoek ore body is also emphasised by the parallelism of the shear fabric with mineralised quartz veins and with well-developed biotite-garnetiferous metasomatic sequences in the ore body.

The mineralised zone plunges towards the west at  $10^\circ$  to  $15^\circ$  and was identified in boreholes over a distance of about 800m to the west. Although borehole data are not continuously present, it is assumed that the mineralised structure dips towards the west beneath the overthrust Baviaanskloof Gneiss. Outcrops in the area are extremely poor and geological observations are mainly based on drillcore available from about 100 boreholes as well as from a network of trenches and shallow shafts. The strike length of the reef could be followed



continuously for more than 800 m and the borehole intersections indicate a minimum depth of 250 m (fig. 4.5).



**Figure 4.6:** Sketch showing the internal folding inside the Doornhoek Ore Body at the contact with the Baviaanskloof Gneiss. The D3 folds are enveloped by the D2 folds but have a variable wave-length and locally display mylonitic features (vertical cross-section, 1cm = 1m).

The gold deposit is also deformed by a southward-verging  $D_3$  shear zone along which Baviaanskloof Gneiss was thrust over the Doornhoek Ore Body (fig. 4.5 and 4.6). The Baviaanskloof Gneiss at Doornhoek is a banded gneiss with planar fabric that strikes north-south, in contrast to the Doornhoek structure which strikes west-southwest to

east-northeast. Meso-scale  $D_3$  folds are well developed along the footwall section of the fault but wanes with distance towards the south and sub-parallel to the older  $D_2$  folds that also occur within the ore body.

The shear zone on the contact between the Baviaanskloof Gneiss and the ore body is a typical mylonitic fault as opposed to the deep crustal  $D_2$ , characteristic of shear zones within the ore body. It is therefore considered that the Baviaanskloof Gneiss has been thrust onto the ore body after mineralisation. This observation is further supported by the fact that the Baviaanskloof Gneiss is not mineralised in the Doornhoek area.



Figure 4.7: Fibrous anthophyllite in a hydrated ultramafic granulite (sample DH-2136).

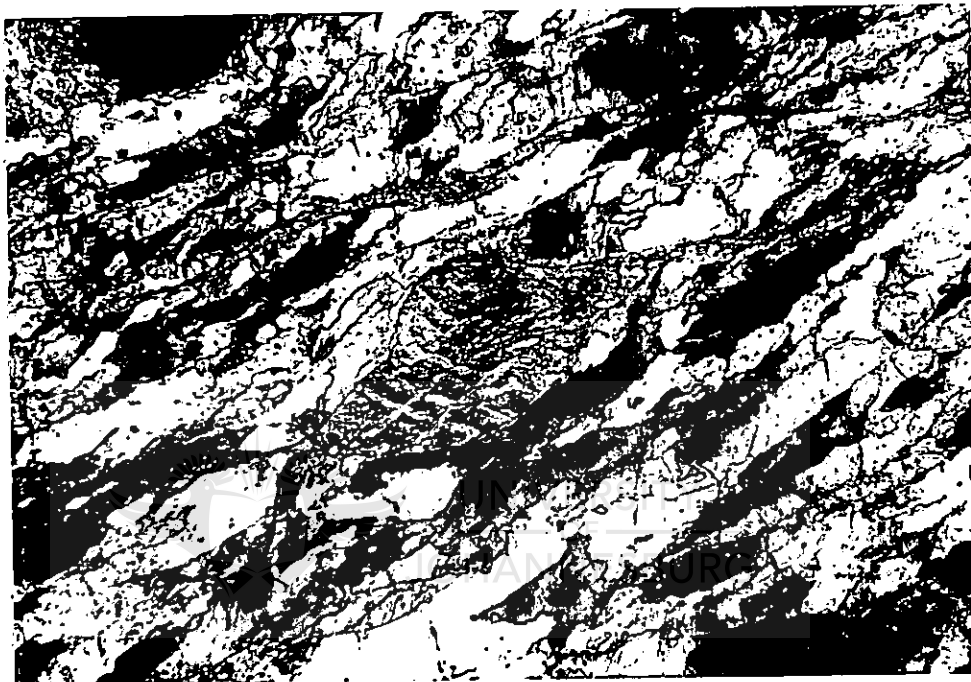
1cm=400 $\mu$ m

#### 4.2.2 Meso-scale deformation

Unsheared rocks associated with the Doornhoek ore body often occur in close proximity to highly sheared varieties, a structural pattern related to the anastomosing character of most of the  $D_2$  shear zones. This same alternating structural pattern can also be observed on a regional scale in the entire SMZ where early  $D_1$  folds are transected by  $D_2$  shear zones (Smit et al., 1992). The fault rocks of the ore body vary from highly sheared "amphibolite" without augen textures which actually represent highly sheared silicate-facies BIF, to augen-bearing rocks which represent the intermediate phase of stretching of the silicate-facies BIF. The transition from "augen-amphibolite" (highly deformed silicate facies BIF) to unsheared "amphibolite" is accompanied by the transformation of anhydrous mineral phases (pyroxene) into hydrous phases (amphibole). The mafic granulitic BIF, consisting mainly of orthopyroxene, quartz and magnetite is usually a massive rock while the sheared and retrogressed equivalent consists mainly of ortho-amphibole. The retrogressed and sheared ultramafic granulite is characterised by similar features (the presence of fibrous anthophyllite is responsible for the development of a strong linear structural fabric **fig. 4.7**). In other words, deformation is accompanied by hydration and the development of a linear fabric.

Highly deformed zones within the gold deposit are usually defined by the presence of augen, while the intensely hydrated horizons are characterised by the presence of K-feldspar and traces of carbonates (ferroan calcite). This suggests that mineral replacement and metasomatism have been the main processes within the active shear zone system. In contrast, pervasive alteration has been the dominant process occurring in areas between the active shear zones. If the intensity of both deformation and hydration was very high, augen of

calcite or K-feldspar occur. The textural relationship between the carbonate-augen and the foliation, as shown in fig. 4.8, demonstrates that the deformation was ductile. However, neither K-feldspar nor calcite is in chemical equilibrium with the precursor granulite-facies mineralogy of the BIF, mafic or ultramafic rock.



**Figure 4.8:** Sample DH-1073: Calcite augen in a felsic granulite. Note the tails of these fish-like structures and the presence of deformation lamellae in quartz showing a dextral displacement. The similar rheological behaviour of the carbonate augen and the quartz host shows that the deformation at the time of augen formation was ductile.

1cm=400 $\mu$ m

The above mentioned petrographic types (silicate-facies granulite BIF, now called opx-bearing BIF), ultramafic granulite, felsic granulite and their hydrated equivalents) are associated with the ore body (fig. 4.5).

A number of 403 measurements of foliation planes in the Doornhoek Ore Body show an almost E-W orientation of the strike (fig. 4.9a). The dip direction stereogram (poles to plane)

exhibits a very steep mean S plane. The lineation plunge data (**fig. 4.9b**) based on 110 measurements inside the Doornhoek Ore Body, show an almost E-W direction ( $85^{\circ}$  mean lineation azimuth) with a subhorizontal plunge ( $0^{\circ}$  to  $37^{\circ}$ ). A mechanism of strike-slip movement is suggested by these structural data. These observations are further supported by the 39 measurements of orientation of long axis of quartz boudines (**fig. 4.9c**). Their mean lineation azimuth is  $83^{\circ}$  with a subhorizontal mean lineation plunge of  $5^{\circ}$ .

The relationship between the crystallographic orientation of the minerals in different lithologies, and the low-plunge host fold is next discussed.



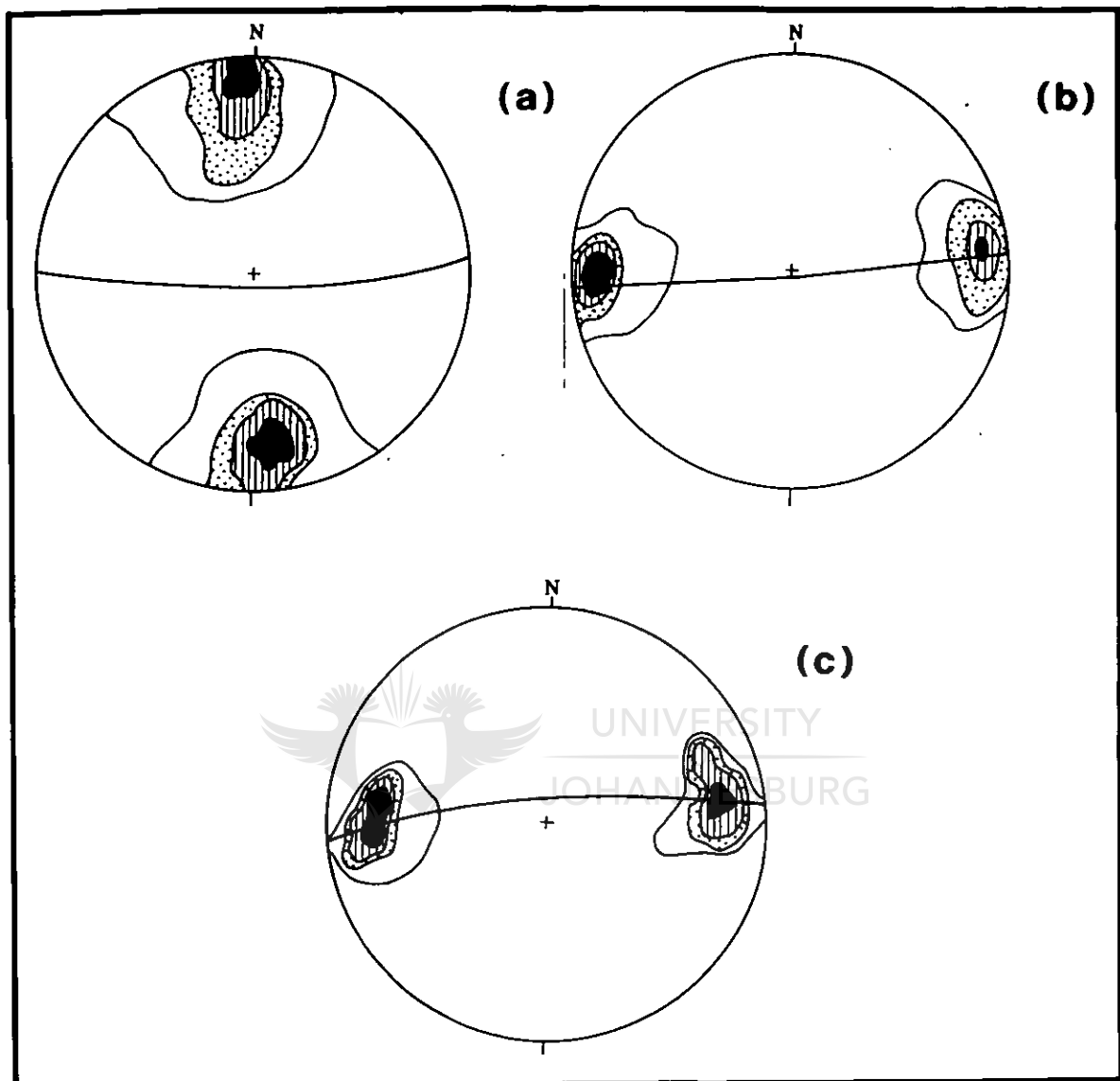


Figure 4.9: Stereograms showing the plot of the structural elements foliation and lination inside the Doornhoek Ore Body (Schmidt projection). Average strike direction is  $174^{\circ}8'$  with a  $88^{\circ}3'$  angle of dip towards north. Mean lination direction is  $85^{\circ}2'$  dipping at  $3^{\circ}$  towards east.

a) *Foliation (dip direction data)*: 403 poles to plane (contours at 20%, 5%, 3% and 1% per 1% area)

b) *Lination plunge data*: 110 lination data (contours at 12%, 5%, 3% and 1% per 1% area)

c) *Quartz boudines*: 39 measurements of long axis of boudines (contours at 15%, 3%, 2% and 1% per 1% area).

### 4.2.3. Micro-scale deformation: Structural petrology and microtectonic study

Almost 1500 crystallographic orientation measurements were done with an Universal Stage attached to a Nikon petrographic microscope. The data are presented in **fig. 4.10.** and **4.11** as stereograms of axes orientation. From the sliced block-diagram (**fig. 4.5**) it is clear that the ore body (green) strikes almost E-W, while the long axis of the sheath-like fold plunges at a low angle to the west. The Baviaanskloof Gneiss (pink), which is thrust over the mafic lithologies of the Doornhoek ore body, displays a weakly developed N-S striking foliation with an almost vertical dip.

#### *I Data of structural petrology in the ore body*

*a. Amphibole* The stereogram of **fig. 4.10.a** shows the orientation of 237 [010] axes of amphibole in the mafic lithologies. The amphibole (hornblende, gedrite and anthophyllite) is orientated with the long axis (*c*) parallel to the E-W direction of stretching (the main foliation is vertical and is represented as the diameter of the stereogram). Under conditions of strong ductile strain amphiboles therefore orientate themselves with their long axis [001] parallel to the direction of shearing, according to the theory of mineral flow (Ramsay, 1960; Ramberg, 1963; Turner and Weiss, 1963). A number of 9 tourmaline crystals were also analysed, but not shown due to the small number of measurements, and exhibit a similar orientation, parallel to the general direction of flow.

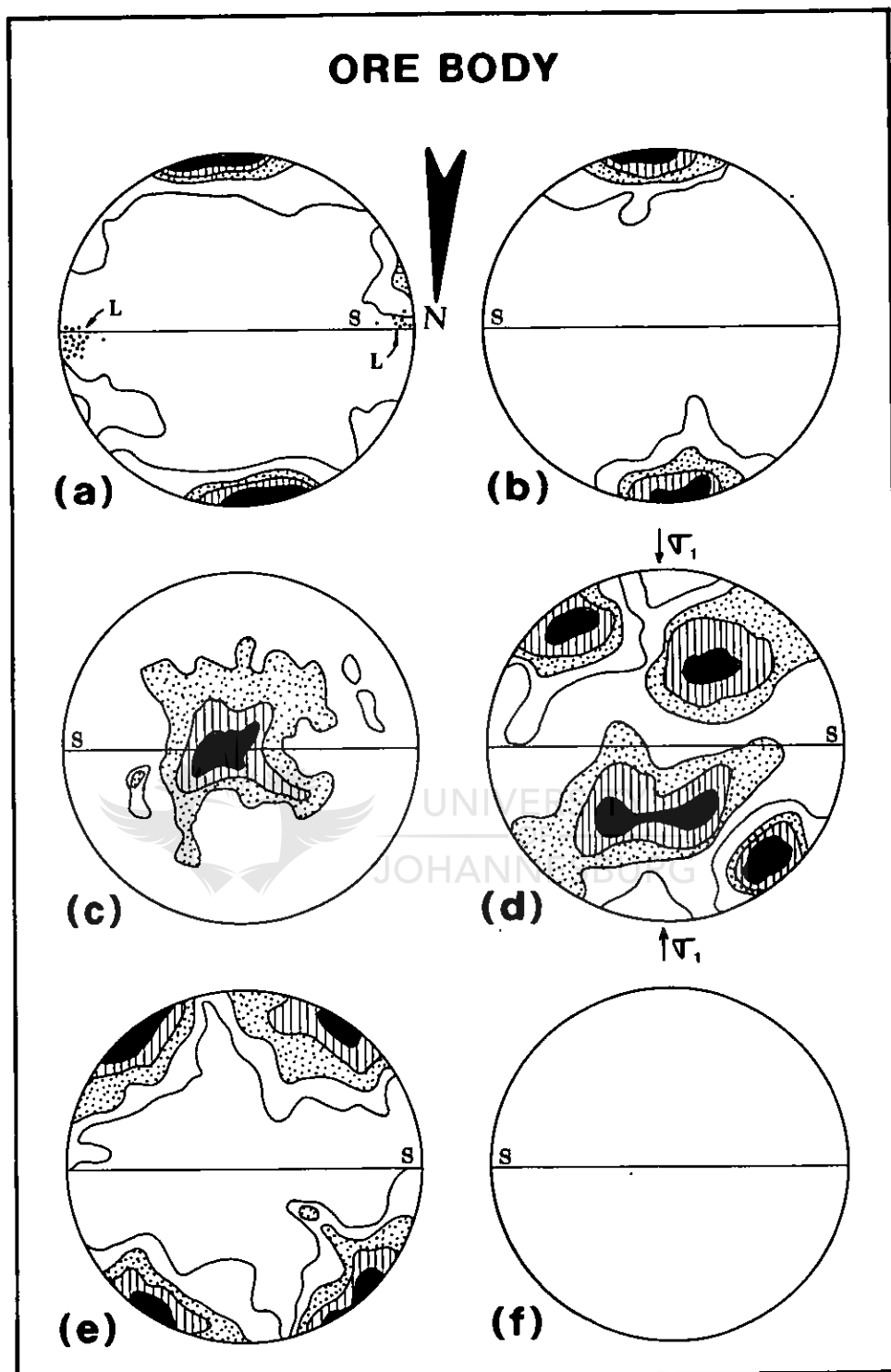


Figure 4.10:

Stereograms of plots of orientation of optic axes for minerals which occur within the Doornhoek Ore Body. Samples were cut perpendicular to the fabric and along lineation direction (kinematic direction). S is the vertical projection of the foliation plane. N is the true north direction.

a) Hornblende: 237 [010] axes (contours at 12%, 5%, 3% and 1% per 1% area; L represents the c axis )

b) Biotite: 93 (001) poles of biotite (contours at 25%, 10%, 5% and 1% per 1% area)

c) Plagioclase ( $An_{33}$  in average): 29 [100] axes of plagioclase (contours at 18%, 10%, 5% and 1% per 1% area)

d) Quartz: 336 [0001] axes (contours at 8%, 5%, 3% and 1% per 1% area)

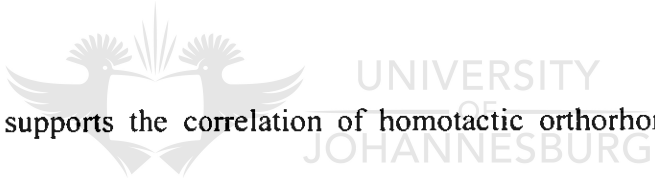
e) 123 poles of shear fractures (no tension) in 27 garnet porphyroblasts (contours at 20%, 10% 5% and 1% per 1%)



b. Biotite **Figure 4.10b** is a stereogram that shows the plots of the orientation of 93 (0001) poles of biotite crystals from the metasomatised garnetiferous formation (the main gold host) and the felsic granulite. The axes normal to the basal face (0001) of the biotite crystals are orientated NNW-SSE. The biotite crystals therefore grew under a stress field with the basal face (0001) orientated parallel to the foliation. Biotite crystals deformed by sliding along the basal cleavage planes parallel to the shearing direction, therefore accommodating the strain perpendicular to the (0001) faces and dissipating it through ductile sliding on the basal (0001) faces. They also orientate perpendicular to the maximum compression direction ( $\sigma_1$ ) and therefore define the fabric at that time of metasomatic alteration, knowing that biotite was not recrystallised but formed during the intense alteration that affected the Doornhoek Ore Body.

Plagioclase **Figure 4.10.c** displays plots of 29 [100] axes of plagioclase ( $An_{35}$ ) which is assumed to represent the plagioclase present in the felsic granulite before the mineralising event. The axes to the (100) faces define a major pole in the foliation plane. Keeping in mind that the (010) crystallographic faces define the polysynthetic twinning of the plagioclase, it is clear that plagioclase crystals orientated themselves with the twinning plane parallel to the shearing direction and direction of escape. This deformation process produced new twinning lamellae, called *deformational lamellae*, that mimic the polysynthetic twinning. The new lamellae represent the planar faces along which the plagioclase crystals started to slide under intense strain. The strain energy is dissipated within the crystal, forming new planes of mechanical discontinuity through twinning, without destroying the crystallographic shape. A very ingenious way to adapt to stress!

Quartz **Figure 4.10.d** represents plots of 336 [0001] axes of quartz crystals from the felsic granulite and the mineralised quartz veins. Four distinct clusters of poles are produced which probably represent the orientation of the quartz crystals during the E-W orientated shearing. This orthorhombic symmetry is typical for quartz in metamorphic rocks from low-grade up to the granulite grade (Sahama, 1936; Sander, 1950; Turner and Verhoogen, 1960; Turner and Weiss, 1963). This type of tectonite is therefore also characteristic of high-grade rocks, in which a simple foliation is defined, not only by the orientation of micas, but also by the parallel alignment of flat lenses of coarsely crystalline quartz (as is often the case in granulites). Such fabrics are widely prevalent among quartzo-feldspathic granulites and quartzites such as those from Saxony, Finland, Northwest Scotland, etc. (Turner and Weiss, 1963).



The quartz symmetry supports the correlation of homotactic orthorhombic fabrics with a geometrically concordant orthorhombic system of pure strain and stress. From the nature of the relationship between the foliation and the orthorhombic symmetry of the quartz crystals,  $\sigma_1$  is much more likely to be normal, than parallel to the foliation plane (S), so that S could also be identified as the AB plane of the strain ellipsoid (Turner and Weiss, 1963). This scenario is also compatible with simple shearing described in the Limpopo Belt (Smit et al., 1992) based on the fact that the planar fabric defined by the east-west orientated  $D_2$  shear zones dips very steeply. This is also an indicator of foliation attributable to compression (Turner and Weiss, 1963).

*Shear fractures in garnets* **Fig. 4.10.e** represents the projection of 123 poles of tension fractures in 27 elongated garnet porphyroblasts (probably stretched during  $D_2$ ). These

fractures are extremely regularly distributed throughout the garnet grains. The experimental deformation of garnet porphyroblasts associated with lamellae deformation in quartz (Turner and Weiss, 1963) suggests that these tension fractures are orientated normal to  $\sigma_3$  of the stress system. In actual fact pure shear deformation is characterised by shear fractures oriented at an angle of 30-45° to  $\sigma_3$  (Means, 1963), once more emphasising the pure shear features of the D<sub>2</sub> deformation in the LB.

*Conclusion:* The results of the textural petrological study of five different minerals which form part of the ore body of the Doornhoek mineralised structure suggested that most of these minerals crystallised during or adapted to, a structural regime of pure shear, characterised by a predominant E-W deformational trend of material escaping parallel to the E-W shearing direction. This is in contrast with most of the escaping directions in the SMZ which are mostly subvertical.



## ***II. Data of structural petrology in the Baviaanskloof Gneiss***

*Microphotograph of the gneiss* **Figure 4.11a**, which is a sketch after a microphotograph of the gneiss, shows the main fabric of the banded Baviaanskloof Gneiss that is thrust over the Doornhoek ore body (**fig. 4.5**). Flakes of biotite define the N-S orientated weak foliation. The biotite is associated with coarse grained xenomorphic porphyroblasts of plagioclase, quartz and microcline. Taking into account that the SMZ is characterised by a general E-W trend this atypical N-S fabric demonstrates that the Baviaanskloof Gneiss was rotated during the event which resulted in it being thrust over the predominantly mafic lithologies of the Doornhoek Ore Body.

Biotite A number of 157 poles of the (0001) crystallographic face of biotite (**fig. 4.11b**) show the orientation of the basal face to be parallel to the weak foliation expressed mostly by itself. Secondary biotite poles show some evidence of a very weak rotation towards the E-W trend displayed by the Doornhoek ore body. However this transposition is displayed only by a few biotite crystals.

Quartz A number of 276 [0001] axes of quartz crystals (**fig. 4.11c**) show the same orthorhombic symmetry displayed by quartz crystals deformed under conditions of pure stress and strain during granulite facies metamorphism (Sander, 1950; Turner and Weiss, 1963). The fact that five clusters of poles developed and not only four, and that their positions are not exactly equidistant at  $45^{\circ}$  as is the case with pure shearing (Turner and Weiss, 1963; Hobbs et al., 1976), but quite random, demonstrate the progressive rotation and transposition of the quartz crystalloblasts towards the E-W trend. The initial structural characteristics of the Baviaanskloof Gneiss, before rotation and thrusting over the Doornhoek ore body, therefore still dominate.

Plagioclase **Figure 4.11d** shows the plots of the crystallographic orientation of 197 [100] axes of plagioclase crystals, mainly oligoclase, which characterise the Baviaanskloof Gneiss. An unique cluster of poles in the center of the stereogram and within the foliation plane is defined. Plagioclase crystals therefore slid with the polysynthetic twinning planes [010] orientated parallel to the main N-S trend. Three secondary clusters of poles at 5% demonstrate the same transposition, rotation and possible sliding due to newly formed deformational lamellae during overthrusting, as was the case for other minerals in the Baviaanskloof Gneiss.

Microcline Figure 4.11e demonstrates a deformation pattern for microcline very similar to that of quartz crystals (fig. 4.11c). A number of 97 [001] axes are grouped in four highly distorted clusters of poles, which in the perfect theoretical case should be orientated  $45^{\circ}$  from each other (Turner and Weiss, 1963; Hobbs et al., 1976). This difference in the behaviour of microcline in comparison with plagioclase is probably due to the absence of polysynthetic twinning and therefore also of *deformational lamellae*. Due to its characteristic mesh-like twinning, the microcline would display a brittle behaviour under stress, with the development of deformational features very similar to that of quartz (Turner and Weiss, 1963). However, the imperfect orientation of the [001] axes is probably also related to the rotation of the Baviaanskloof Gneiss block over the Doornhoek Ore Body, after the development of  $D_2$  structures.

Conclusion: The crystallographic orientation of minerals in the Baviaanskloof Gneiss define the weakly developed N-S foliation. This N-S fabric in the Baviaanskloof Gneiss is orientated perpendicular to the  $D_2$  fabric in the Doornhoek Ore Body which trends E-W. Both blocks were probably defined by the same fabric during  $D_2$ , but disruption occurred during a later  $D_3$  event, during which crustal blocks once belonging to the same structural unit were thrust over one other. As a result, these two units, the Doornhoek ore body and the Baviaanskloof Gneiss, are rotated at almost  $90^{\circ}$  relative to each other.

Minerals occurring in rocks within the two blocks are crystallographically orientated relative to the main  $D_2$  deformational fabric. The late  $D_3$  rotation and overthrusting weakly affected some of the minerals in the Baviaanskloof Gneiss, but the main crystallographic orientation relative to the initial E-W  $D_2$  fabric, now orientated N-S, has remained almost unchanged.

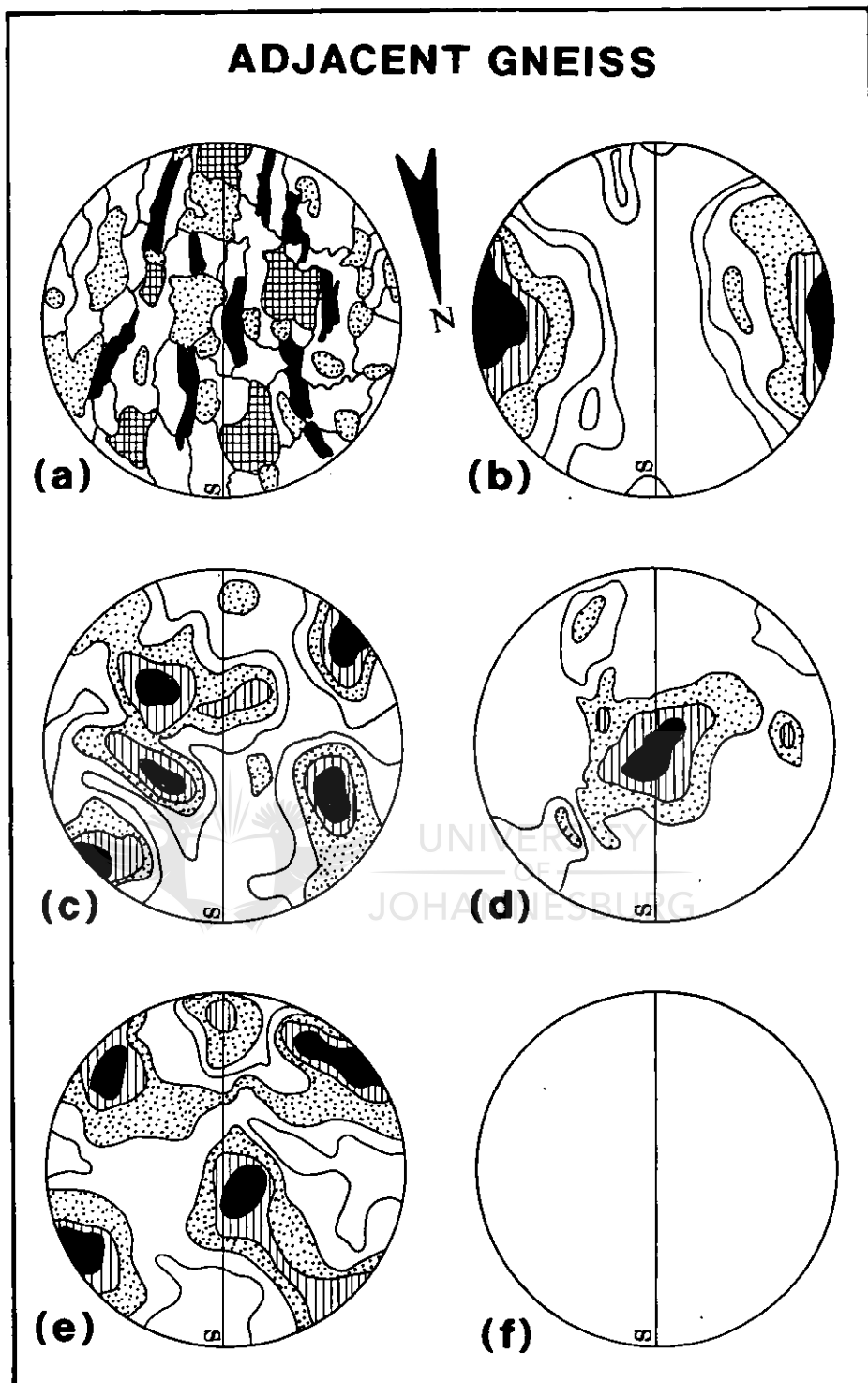


Figure 4.11:

Stereograms of orientation of optical axes for minerals which occur within the Baviaanskloof Gneiss, tectonically thrust over the Doornhoek Ore Body. Projections are made normal to the foliation of the gneiss. S is the vertical projection of the foliation plane. N is the north direction.

a) Fabric of the banded Baviaanskloof Gneiss: black is biotite, mesh-twinned is microcline, dashed is quartz and without fabric is plagioclase

b) Biotite: 157 (001) poles of biotite (contours at 8%, 5%, 3%, 2% and 1% per 1% area)

c) Quartz: 276 [0001] axes (contours at 5%, 3%, 2% and 1% per 1% area)

d) Plagioclase : 197 [100] axes in plagioclase (contours at 12%, 5%, 3% and 1% per 1% area)

e) Microcline : 97 [001] axes in plagioclase (contours at 12%, 5%, 3% and 1% per 1%)

f) No representation

#### 4.2.4. Conclusion

The regional structural setting of the Doornhoek deposit suggests that the ore body is located within a gently eastward dipping  $D_1$  fold structure. This early fold pattern was subsequently strongly influenced by  $D_2$  shearing although the ore body cannot directly be linked to one specific shear zone. The detail study of the ore body should therefore reflect to some extent the influence of  $D_2$  shearing on the development and distribution of the ore body at Doornhoek.

From the detail structural data described under 4.2.2 (**fig. 4.9**) it can be demonstrated that the constant E-W trending shear fabric in the ore body is accompanied by a near horizontal E-W trending mineral stretching lineation which could be linked to E-W strike-slip shearing. This shear trend coincides well with the regional structural pattern of roughly E-W trending strike-slip  $D_2$  shear zones in the eastern part of the SMZ. This suggests that the orientation and lateral extent of the early  $D_1$  fold, and therefore of the ore body, can be linked to the transport direction of subsequent shear deformation that transposed the large fold structures into parallelism with the shear direction. Evidence from other parts of the SMZ suggest that the  $D_2$  shear zones also acted as conduits for mineralising and rehydrating fluids. It can therefore be assumed that mineralisation in the Doornhoek deposit is also related to fluids that were conduited along  $D_2$  shear zones.

### 4.3. IMPORTANCE OF THE HYDRATION EVENT WITH RESPECT TO GOLD MINERALISATION IN THE SOUTHERN MARGINAL ZONE

Many previous studies attempted to characterise the fluid composition during both peak granulite conditions and during the subsequent shear related hydration event in the SMZ of the LB (van Reenen, 1986; van Reenen and Hollister, 1988; Baker et al, 1992; Hoernes and van Reenen, 1992; Hollister, 1992; van Schalkwyk and van Reenen, 1992; Venneman and Smith, 1992; Du Toit, 1994; Mokgatla, 1995; Hoernes et al., 1995). The available data appear to support a hypothesis that relatively small amounts of a CO<sub>2</sub>-rich fluid infiltrated the SMZ at high (but subsolidus) temperatures and participated in retrograde reactions.

Several hypothesis for the origin of these fluids were suggested:

**1. A model for the introduction of high-temperature retrograde fluids from an external source** was supported by van Reenen (1978), van Reenen and Hollister (1988), van Schalkwyk and van Reenen (1992), Baker et al. (1992) and Hoernes et al. (1995). Van Schalkwyk and van Reenen (1992) considered that the fluids were derived from the upper mantle or from mantle melts underplated to the lower crust. Van Reenen and Hollister (1988) considered that the emplacement of the hot granulite-facies rocks of the SMZ over the cooler low-grade greenschist facies rocks of the KVC caused devolatilisation of the underlying rocks and hydration of the overlying granulites. These authors concluded, on the basis of field, petrographic, petrological and stable oxygen isotope studies that the high-grade rocks of the SMZ interacted with an externally derived H<sub>2</sub>O-bearing CO<sub>2</sub>-rich fluid. Direct petrographic evidence for a CO<sub>2</sub>-rich fluid was documented by van Schalkwyk and van Reenen (1992) on



the basis of the observed replacement of olivine in ultramafic granulite by the assemblage magnesite and hypersthene (olivine + CO<sub>2</sub> = magnesite + hypersthene). Baker et al. (1992) showed, on the basis of thermodynamic arguments that metapelitic rocks were retrogressed in the presence of a fluid with less than 60 mole per cent H<sub>2</sub>O.

## **2. A model for the release of hydrating fluids during the solidification of anatectic melts**

was proposed by Vennemann and Smith (1992) using an impressive number of stable isotope data and concluded that temperatures of about 740°C prevailed at the time of the hydration. This temperature is in contrast with that determined by van Reenen (1986) using cation exchange thermometry. The latter author concluded that the temperature of the equilibrium between anthophyllite and enstatite was too low, and the activity of H<sub>2</sub>O also too low for melt to have been present during the time of hydration. A similar conclusion was highlighted by Baker et al. (1992) who, relying on phase equilibria arguments to estimate P-T-aH<sub>2</sub>O (a much more reliable method than either cation exchange or isotopic exchange thermometries) calculated low water activities and temperatures just above 600°C, also inconsistent with partial melting. Subsequent oxygen isotope studies (Hoernes et al., 1995) also suggested that the formation of anthophyllite occurred at about 600°C.

Since the question of the source of the CO<sub>2</sub>-rich fluids is still unresolved, two observations need to be made. Firstly, there is a very sharp boundary between hydrated and unhydrated granulites (van Reenen and Hollister, 1988). The retrograde fluid apparently moved through large portions of the granulites (van Reenen and Hollister, 1988) but hydration only occurred where the granulites were cool enough for the retrograde reactions to have taken place (the orthopyroxene was altered into ortho-amphibole, due to the reaction: Hy+Qz+H<sub>2</sub>O = Anth;

and the cordierite was transformed into gedrite plus kyanite due to the reaction:  $\text{Cord} + \text{H}_2\text{O} = \text{Ged} + \text{Ky} + \text{Qz}$  - **fig. 4.4**). Where the granulites were still too hot these retrograde hydration reactions did not occur (van Reenen and Hollister, 1988).

The second observation is that the oxygen isotopic exchange between rocks of the SMZ and a common fluid was minor to non-existent (Hoernes and van Reenen, 1992; Vennemann and Smith, 1992). Hoernes and Van Reenen (1992) concluded that only a small amount of fluid passed through the granulite and as a result there is still a high oxygen-isotopic heterogeneity between different rock types in the SMZ (Vennemann and Smith, 1992). However, using O-isotope data from shear zone samples and wall-rock metapelites, Hoernes et al. (1995) concluded that the fluid in the shear zones samples is probably magmatic in origin and in the metapelites has a slightly more enriched magmatic-metamorphic signature, supporting even further the external source for the retrograde fluids. Even with these new data, the exact origin of the fluids in the SMZ is not completely solved. The exact origin can probably be solved using He-isotopes (Hoernes et al., 1995).

**3. A model that attempted to explain the inconsistencies of the two previous models was proposed by Stevens (1995): both fluid and melt migration did exist.** Fluid migration was very active towards the greenstone belts of the Kaapvaal Craton or within the well expressed  $D_2$  shear zones of the SMZ. Melt migration has been extremely active in the lower zones of the SMZ which underwent, at that time, intense granulitic metamorphism (**fig. 4.12**).

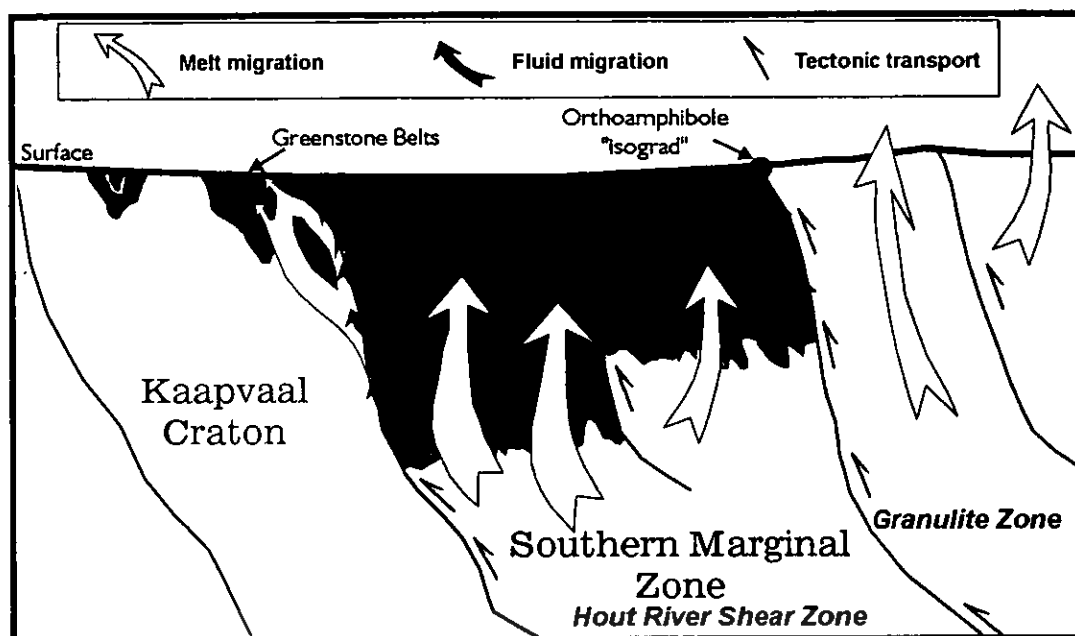


Figure 4.12: An illustration of the relationship between the Kaapvaal Craton and the two zones of the SMZ, as suggested by Stevens (1995). In the scenario proposed by Stevens, the ortho-amphibole isograd is represented by a fault boundary and is not related to the grade of metamorphism. Escaping hydrated fluids may have blurred this relationship slightly by interacting to a minor degree with the overlying granulite zone. This would depend on synretrogression thrusting. Open arrows indicate melt migration, filled arrows indicate fluid migration (after Stevens, 1995).

In his study, Stevens (1995) concluded that rocks did interact with an extensive, pervasive,  $H_2O$  undersaturated fluid, but suggested that the fluid was internally derived, as a result of crystallising melts and thus, the isotope systematics carry no record of fluid infiltration. His petrographic study of the hydration reactions suggested that the disequilibrium assemblages are preserved simply because there was insufficient fluid with which to react, according to Stevens (1995). According to the model fluid availability has controlled the retrogression. Melt migration out of the granulite zone, probably at conditions approaching the

peak-metamorphic conditions, but for some reason it was more active than in the hydrated zone. Consequently, much of the  $H_2O$ , partitioned into the leucosomes during prograde melting, was released back into the rocks during cooling. This occurred through reactions between melt, high-grade phases and reactive fluid. In the hydrated zone, the fluid was recycled effectively between fluid-absent equilibria on the prograde path and crystallisation hydration equilibria on the retrograde path (Stevens, 1995). Stevens (1995) considers that the ortho-amphibole retrograde isograd does not represent a reaction front resulting from a change in grade (P-T), but rather proposed that it represents a fault boundary between two high-grade SMZ blocks with different  $H_2O$  contents, due to different degrees of melt loss.

This last observation is not supported by the field data. **Fig. 4.1** clearly shows that the isograd *cuts across* fold structures without any evidence of any displacement. This suggests that the hydrated fluids emerged from regionally expressed shear zones and migrated upwards and laterally to a certain level that is referred to as the hydration front, after the main  $D_2$  structure has been emplaced (**fig. 4.1** and **4.13**). The hydration front actually represents the boundary between the hydrated and the unhydrated lithologies. The distance from the emerging shear zones at which the fluids were still active is variable and depended on the time of hydration by local parameters such as fluid/solid flow ratio, different lithologies, intensity of shearing etc.

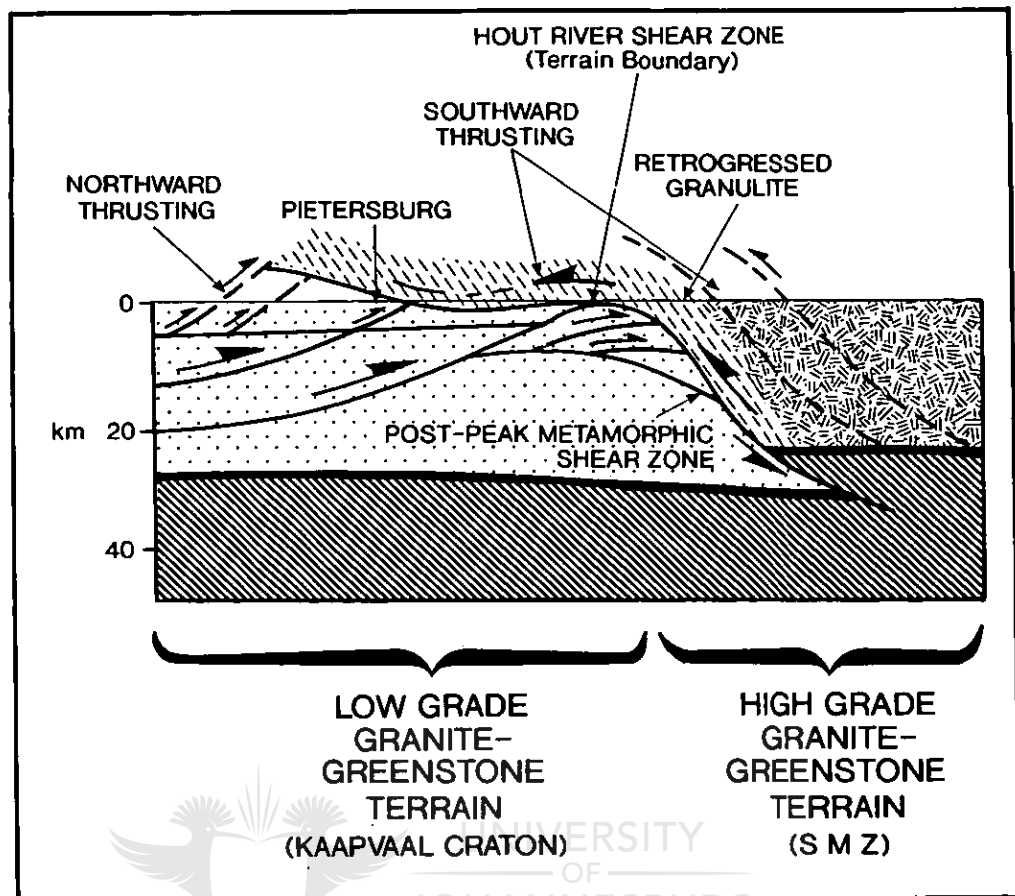


Figure 4.13: Schematic crustal section of the terrane boundary of the granite-greenstone terrane of the KVC and the SMZ of the LB.

A fault boundary is also not supported by the observed N-S temperature gradient across the SMZ (van Reenen and Hollister, 1988). Furthermore, JM Huizenga (personal communication, 1996) calculated that the fluids in the SMZ which, according to Stevens (1995), interacted with graphite to form  $\text{CO}_2$  could never have formed nearly pure  $\text{CO}_2$  under the suggested PT conditions (as has been described as fluid inclusions trapped in these rocks by van Reenen and Hollister in 1988). A simple percolation of water through greenschists would also not produce a  $\text{CO}_2$ -pure liquid, but rather a  $\text{CO}_2\text{-H}_2\text{O}\pm\text{CH}_4$  fluid. Furthermore, the

amount of primary graphite in the SMZ is not volumetrically sufficient to produce the CO<sub>2</sub>-dominated fluids which are relatively abundant in the SMZ.

Previous discussions on the nature of the retrograde fluids were based on the assumption that a CO<sub>2</sub>-rich fluid infiltrated the still hot granulite during a pervasive alteration event (porous fluid-flow). The presence of gold deposits and other base metal sulphides, within the zone of hydrated and retrogressed granulite of the SMZ (Gan and van Reenen, 1995), actually demonstrates that in certain places the fluids were channelled through and along regional shear zones (van Reenen et al., 1994; Roering et al, 1995), and deposited their metallic load in specific depositional sites due to complex chemical interactions between the carrying fluid and the infiltrated rock. How the transition from a pervasive flow to a channelised flow was made and under what conditions, is still uncertain. A comprehensive explanation for fluid activity in the SMZ should try to explain the contradictions between the two models of fluid movement throughout the SMZ. The Doornhoek Gold Deposit might be one of the keys to this problem. Unexplained inconsistencies based on the results of petrological studies versus stable isotopic studies have to some extent been solved (Hollister, 1992; Hoernes et al., 1995). These authors concluded that the retrogression of the SMZ granulites was probably triggered by the influx of external fluids into an existing north-to-south temperature gradient in the SMZ. Partial O-isotopic equilibria suggests that ortho-amphibole formation (establishment of the retrograde isograd) has occurred at temperatures close to 600°C whereas at higher temperatures the granulite-facies paragenesis, specially hypersthene, remained stable. The quantity of fluids which penetrated the high-grade terrane differed, depending on the porosity of the rocks. In the case of shear zones, fluid flux was accompanied by complete re-equilibration, whereas in most rocks outside the shear zones only partial isotopic

re-equilibration was reached. Fluid/rock ratios in metapelites were in most cases very small, resulting in fractionation patterns typical for closed-system exchange. However, the exact source of the retrograde fluids still remains an unsolved problem.

A fact which is very clear, based on both field and microscopical observations, is that the ortho-amphibole isograd really does exist and that there is a clear-cut boundary between the hydrated and the unhydrated granulite. The inconsistency that still exists is *how the hydration event occurred?*

#### 4.4. AGE RELATIONSHIP

The high-grade rocks of the SMZ are intruded by late-tectonic granitoid plutons of varying ages (**fig. 4.1.**). The Matok Complex (2.67Ga) intruded the D<sub>2</sub> Matok shear zone and thus postdates the D<sub>2</sub> deformational event (Barton et al., 1983; Barton et al., 1992), but is affected by the reactivation of the D<sub>2</sub> shear zones during the D<sub>3</sub> event, still under ductile conditions (Smit et al., 1992; Smit and van Reenen, 1997). The post-tectonic Palmietfontein Granite intruded as small bodies and dykes throughout the Southern Marginal Zone at about 2.45 Ga (Barton et al., 1983). The Schiel Alkaline Complex was implaced at about 1.957 Ga (JM Barton, personal communication, 1996, unpubl. data).

The reactivation of the N'Tabalala Shear Zone during D<sub>3</sub> predates the emplacement of the Schiel Alkaline Complex (1957 Ma), but clearly deformed the Matok Granitoid (Bohlender et al., 1992). Reactivation of the N'Tabalala Shear Zone therefore occurred between about 2.70

and 1.975Ga, and is associated with mylonitisation. Although Du Toit (1979) showed that the Palmietfontein type granite (2.45Ga) intruded the N'Tabalala Shear Zone, its relationship to the reactivation and mylonite formation has yet to be established.

Although radiogenic data to establish the exact age of the Doornhoek Gold Deposit are not yet available, the close structural relationship with the regional structural pattern of the SMZ indicates a possible 2.67 Ga age for the mineralisation. However, muscovite replacing sillimanite at the Klipbank locality about 3 km from the Doornhoek Gold Deposit (Mokgatla, 1995), gave an age of about 2.2 Ga which might be considered a minimum age for the regional metamorphic retrogression and gold mineralisation of the SMZ.





## 5. PETROGRAPHY OF UNHYDRATED AND HYDRATED GRANULITES OF THE SOUTHERN MARGINAL ZONE AT THE DOORNHOEK LOCALITY

### 5.1. INTRODUCTION

The Doornhoek Gold Deposit is located in a zone of highly altered (metasomatised) rocks that occur in the hydrated zone of the SMZ south of the retrograde isograd (**fig. 4.1**). The wall-rocks to the alteration zone are represented by weakly (mafic and ultramafic gneisses) to completely (pelitic lithologies and the Baviaanskloof Gneiss) hydrated former granulite facies lithologies that also include banded iron formation (BIF). In discussing the petrography of the major lithologies of the Doornhoek deposit, the following must be kept in mind:

- i*) the wall-rock lithologies consist of partly or completely hydrated granulites, and
- ii*) extremely altered (metasomatised) lithologies host the gold mineralisation;
- iii*) the intense metasomatic alteration is superimposed on the hydrated or partially hydrated rocks.

Thus, a distinction has to be made between *hydration* (which occurred during the establishment of the ortho-amphibole isograd and which resulted in the formation of the regional zone of hydration that is located in the hanging-wall of the northward dipping HRSZ and *metasomatic alteration* (that is confined to well defined shear zones). Whereas hydration of the granulites is regionally expressed, metasomatic alteration was highly channelised and restricted to shear zones. The highly channelised metasomatic alteration is therefore closely related to the regional hydration event as has been discussed in **section 4.2-**

dealing with oxygen isotope data that showed that all rocks in the SMZ interacted with a similar externally derived fluid (Hoernes et al., 1995). Furthermore, the isograd is only expressed in a specific lithology (metapelite), while the associated rock types (mafic, ultramafic and BIF) are only variably affected by the hydration event. The wall-rocks of the Doornhoek deposit (mafic, ultramafic, BIF) are therefore partly to completely hydrated.

## 5.2. UNHYDRATED ROCKS

Although completely unhydrated lithologies do not occur within the Doornhoek area, such lithologies, representing the precursors of lithologies exposed at Doornhoek, are described in this chapter. This is done in order to obtain a better understanding of their hydrated and metasomatised equivalents. The term *hydration*, as used here, refers to a process that did not change the major element composition of the rock, resulting only in hydration reactions. *Metasomatism*, on the other hand, is related to the depletion and addition of chemical components, thereby changing the bulk chemical composition of the rock.

**5.2.1. Baviaanskloof Gneiss:** A sequence of banded tonalitic to trondhjemitic gneisses, often migmatic, and varying from light to dark grey in colour. This lithology in the vicinity of Doornhoek, consists only of plagioclase (oligoclase), biotite and quartz (**figures 5.1 and 5.2**) with small amounts of hornblende. Biotite is the dominant ferromagnesian mineral (**fig. 5.2**). Cross-cutting leucocratic (anatectic?) veins (**fig. 5.3**) consist of quartz and feldspar. Apatite, sphene, magnetite, epidote, zircon, muscovite and seldomly also carbonate (calcite), occur as accessory minerals.

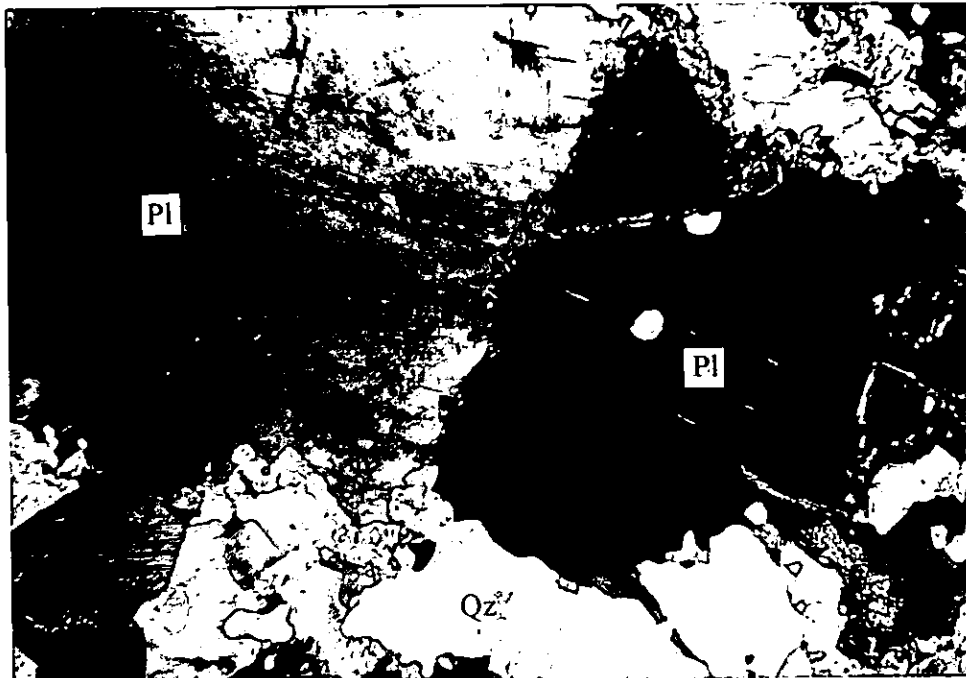


Figure 5.1: Untwinned plagioclase crystals (Pl) and xenomorphic grains of quartz crystalloblasts (Qz) occurring as main constituents in the Bavianskloof Gneiss (sample DH-L7). 1 cm = 400  $\mu$ m



Figure 5.2: Microphotograph of biotite (Bi) being replaced by muscovite (Mu). The core of the biotite is highly chloritised. The opaque mineral occurring along the biotite cleavage is ilmenite (arrow). 1 cm = 400  $\mu$ m



Figure 5.3: Vertical leucocratic (anatectic?) veins that crosscut the banded Baviaanskloof Gneiss. The grey host gneiss is trondhjemitic in composition.

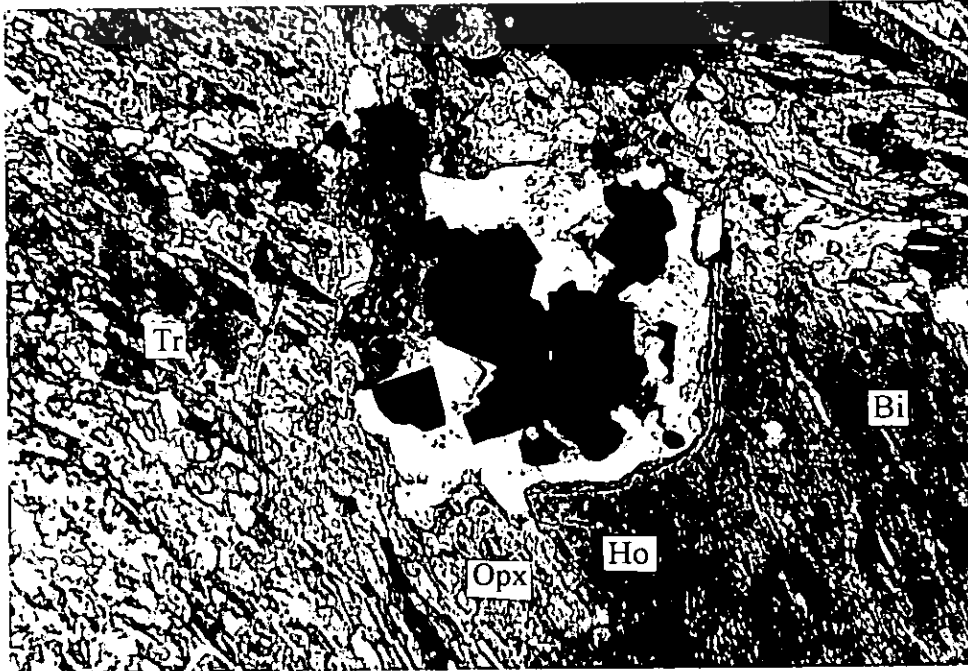
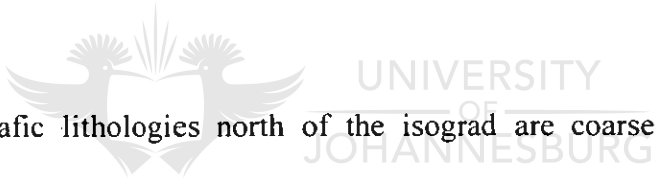


Figure 5.4: Microphotograph of a mafic granulite interlayered with the Baviaanskloof Gneiss near Doornhoek: hornblende (Ho) replaces orthopyroxene (Opx). A quartz-magnetite augen occurs in the center. Biotite (Bi) and Ca-amphibole (Tr = tremolite) are also present.  
1cm=200µm

The unhydrated precursor of this rock (occurring north of the isograd) is represented by the orthopyroxene-bearing banded Baviaanskloof Gneiss which is light to dark grey in colour, depending on the intensity of alternating bands of mafic and felsic minerals. The bands vary in thickness from a few millimetres to centimetres, being sometimes discontinuous, with irregular schlieren shapes. Evidence for late deformation is offered by biotite kink-bands and by deformed plagioclase lamellae. The rock consists of quartz, oligoclase-andesine, biotite, hypersthene (and sometimes also augite), with subordinate magnetite, ilmenite, orthoclase and hornblende, as well as accessory apatite, zircon and traces of pyrite, chalcopyrite and rutile. Biotite, hypersthene, augite and opaques are concentrated in the mafic bands. Biotite is mostly orientated parallel to the banding. The lithology can also be described as a banded enderbite (Bohlender et al., 1992).



**5.2.2. Mafic rocks:** Mafic lithologies north of the isograd are coarse-grained, weakly banded rocks composed of hypersthene, augite, plagioclase and magnetite, with accessory quartz and hornblende. The partly hydrated equivalent in the vicinity of the Doornhoek locality is a well-foliated rock composed of plagioclase, hornblende, magnetite and quartz, with relics of ferrohypersthene, salite and augite, partly replaced by hornblende (**fig. 5.4**).

**5.2.3. Ultramafic rocks:** Ultramafic granulite north of the isograd is mainly composed of olivine, orthopyroxene, pargasitic hornblende and spinel, usually displaying a coarse granoblastic texture (van Schalkwyk and van Reenen, 1992). The partly to highly hydrated equivalent in the vicinity of Doornhoek is characterised by the presence of chlorite and carbonates that partly replace the high-grade assemblage (van Schalkwyk and van Reenen, 1992).

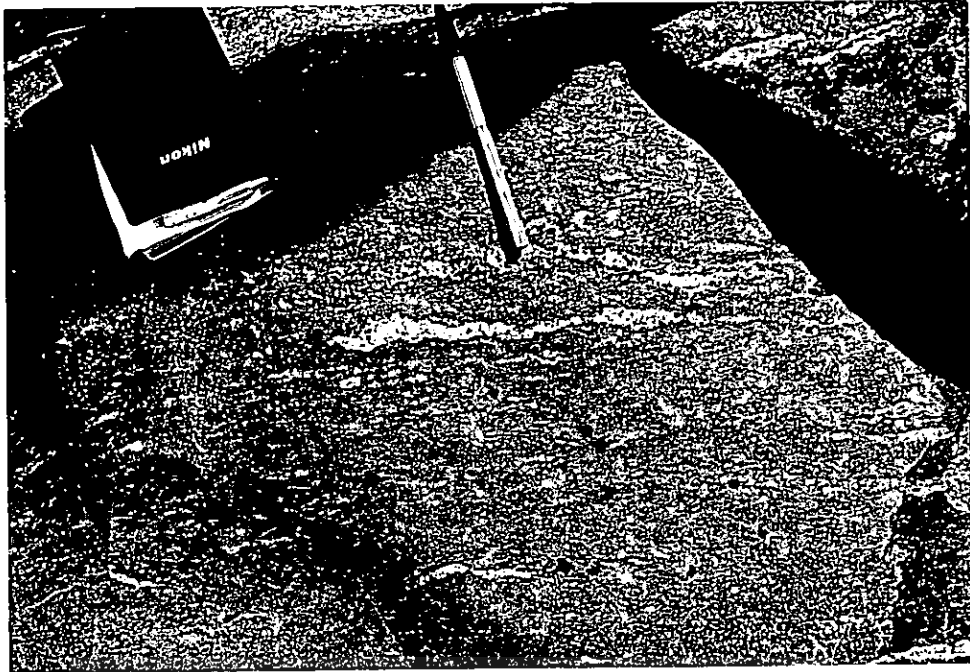


Figure 5.5: Unhydrated grey metapelite with lenses of quartz and feldspar. The primary paragenesis of this rock is plagioclase, biotite, garnet, quartz, cordierite and hypersthene (photo taken at Petronella locality, north of the orthoamphibole isograd).

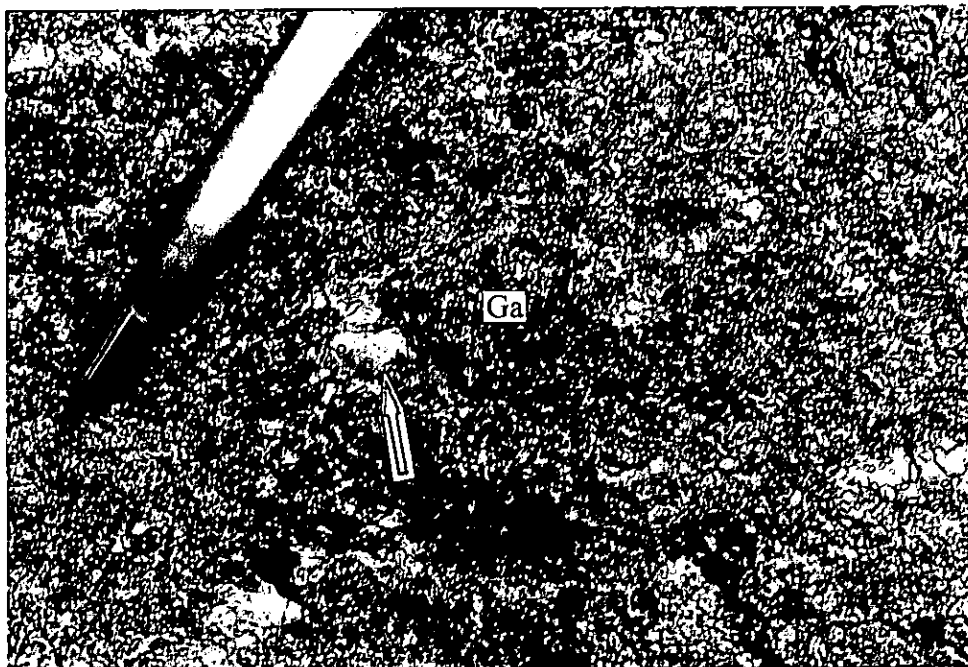
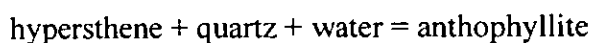


Figure 5.6: An idioblastic garnet (Ga) surrounded by cordierite (arrow). This is a metamorphic reaction which documents the  $M_2$  decompression north of the isograd ( $ga+qz=crd+hy$ ).

**5.2.4. Metapelite:** The highly foliated gneiss in the vicinity of Doornhoek consists mainly of garnet, biotite, ortho-amphibole, quartz and plagioclase, with accessory kyanite. The precursor (unhydrated granulite north of the isograd) is composed of the same minerals, but with cordierite and hypersthene instead of ortho-amphibole and kyanite (van Reenen, 1986). Cordierite and hypersthene were involved in the following two hydration reactions as a result of the event that established the retrograde isograd and zone of hydrated granulite (van Reenen, 1986) (**fig. 5.5 and 5.6**).



**5.2.5. Banded Iron Formation (BIF):** This lithology north of the isograd can be subdivided into two major assemblages: pyroxene-bearing and pyroxene-free. The pyroxene-free assemblage is composed of quartz and magnetite with quartz boudins a common feature. The pyroxene-bearing assemblage also contains almandine-rich garnet and orthopyroxene. In the vicinity of the Doornhoek locality, the same lithology is also characterised by the presence of grunerite partly replacing hypersthene.

**5.2.6 Hydration of the initially unhydrated granulite facies rocks:** The different lithologies in the vicinity of the alteration zone at Doornhoek display evidence of retrograde alteration after the peak granulite facies metamorphic event. The hydration of pelitic granulites in the southern part of the SMZ of the LB (**fig. 4.1**) is marked by the presence of a relatively sharp transition from orthopyroxene-cordierite-bearing assemblages to

anthophyllite- and gedrite-bearing assemblages. This transition is defined by the position of the retrograde orthoamphibole isograd. Ortho-amphibole along the isograd can be observed in various arrested stages of replacing orthopyroxene and cordierite. Van Reenen (1986) concluded that these textural relationships indicate that the orthoamphibole crystallised during the infiltration of externally derived fluids, and thus, the presence of anthophyllite and/or gedrite marks the front of the hydration event.

The same regional hydration event which established the isograd and regional zone of hydration produced plagioclase+hornblende+quartz+sphene assemblages, with relics of augite and sometimes hypersthene in the mafic lithologies.

As an example of hydration, forsterite in ultramafic granulites was replaced first by magnesite+enstatite, and then by chlorite+dolomite suggesting that these assemblages interacted with a CO<sub>2</sub>-rich fluid during hydration (van Schalkwyk and van Reenen, 1992). Petrographic observations at the Doornhoek locality showed that Fe-rich pyroxenes (ferrohypersthene and sallite), in extremely hydrated BIF, were transformed into Fe-rich amphiboles: ferrogedrite, grunerite or Fe-rich hornblende. The Fe-rich character of the rocks was kept unchanged even after hydration, although the initial assemblages were completely removed, sometimes even without any relics remaining.

This regional hydration event was followed by a metasomatic alteration event that is restricted to the vicinity of shear zones (e.g. the Doornhoek locality). This channelised alteration event completely transformed the already hydrated or partially hydrated lithologies into intensely metasomatised rocks.



The alteration process at Doornhoek was so intense that evidence for the regional hydration event is completely obliterated. In conclusion, on a regional level, three processes can be distinguished:

i) unhydrated granulites that occur north of the regional isograd, which are not affected by the regional hydration event (described in **chapter 5.2**).

ii) partly to completed hydrated granulites occurring south of the isograd (described in **chapter 5.2.6**) representing the regional host of the Doornhoek gold deposit, and

iii) intensely altered (metasomatised) lithologies in alteration zones associated with gold mineralisation (the Doornhoek ore body). These lithologies also experienced the regional hydration event.



### 5.3. HYDRATED LITHOLOGIES REPRESENTING THE REGIONAL HOST OF THE DOORNHOEK ORE BODY

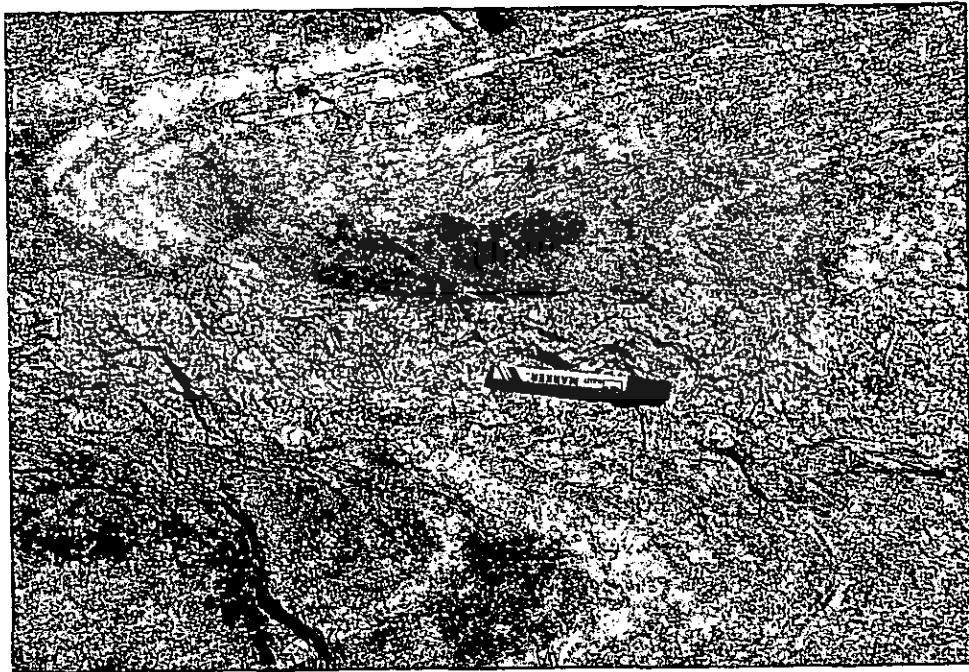
The hydrated lithologies that underlie the entire area south of the retrograde isograd record the influx of a H<sub>2</sub>O-bearing CO<sub>2</sub>-rich fluid. In the immediate vicinity of Doornhoek these hydrated lithologies display the same mineralogical compositions as in the rest of the hydrated zone of the SMZ (van Reenen, 1986). Minerals such as olivine, garnet, plagioclase, pyroxene and cordierite were transformed into *hydrous minerals*, such as amphiboles and phyllosilicates, still under high-grade metamorphic conditions.

Garnet zoning profiles in hydrated metapelitic granulite displays strong retrograde patterns that developed under upper-amphibolite metamorphic conditions (van Reenen, 1986). The completely hydrated granulites (e.g. former pelitic granulites) south of the isograd are composed only of assemblages that re-equilibrated under amphibolite facies condition, whereas the partially hydrated granulites (e.g. the mafic, ultramafic and BIF rocks) still preserve relics of the granulite facies assemblages. These lithologies represent the wall rock to the Doornhoek alteration zone.

The hydrated Bavianskloof Gneiss is thrust over the predominantly mafic lithologies (BIF and mafic gneisses) that dominates the Doornhoek Ore Body (**fig. 4.5**).

### 5.3.1. The hydrated equivalent of the Baviaanskloof Gneiss

Outcrops of the hydrated Baviaanskloof Gneiss occur in the eastern part of the Farm Doornhoek and is excellently displayed on the Farm Klipbank, about 2.5km NNE of Doornhoek (**fig. 4.1**). The Baviaanskloof Gneiss is often characterised by the presence of neosomes consisting of pinkish material, made up mainly of microcline-perthite and albite. The composition and petrographic features of the neosome reflect the initial stages of the metasomatic alteration of the Baviaanskloof Gneiss (**fig. 5.7 and 5.8**).



**Figure 5.7:** Baviaanskloof Gneiss (folded and grey) with pinkish neosome composed mainly of microcline-perthite and albite.

The hydrated Baviaanskloof Gneiss occurring at Doornhoek is a coarse grained, equigranular and slightly banded rock consisting of plagioclase (An 18-34 per cent), quartz, biotite (usually orientated parallel to the banding) and small amounts of muscovite and traces of apatite, zircon, ilmenite and rutile. The fact that plagioclase displays curved twinning planes,

especially at the contact with pygmatic veins (**fig. 5.9** and **5.10**), demonstrates the ductile conditions during the emplacement of the leucocratic material. Sericite replaces plagioclase.

The crosscutting pink veins consist mainly of microcline-perthite and albite. Small amount of quartz is also present, but usually as a late reaction product or as relic boudines from the host gneiss (**fig. 5.8**). Plagioclase is always absent from the metasomatic veins. The metasomatic alteration process that affected the gneiss (and resulted in the formation of the pink veins) is characterised by the domination of K-feldspar.

Considering the mineralogical composition of the leucocratic veins (microcline-perthite and albite) in comparison to the Baviaanskloof Gneiss host, it may be concluded that the metasomatic process represents a chemical alteration event consisting of enrichment in  $K_2O$ ,  $Al_2O_3$ ,  $SiO_2$  and  $Na_2O$ .



The mechanical disturbance displayed by the plagioclase in the gneiss at the contact with the pinkish veins suggests that the veins were introduced during intense shearing conditions. The veins are orientated parallel to the  $D_2$  direction in the Baviaanskloof Gneiss.



**Figure 5.8:** Typical tonalitic Baviaanskloof Gneiss at Doornhoek. The gneiss host (grey) reflects the regional hydration event. The hydrated gneiss is crosscut by a pinkish vein, which is the product of metasomatic alteration. It consists mainly of microcline-perthite, albite and quartz. Quartz (Qz) is already forming boudins, due to its different rheological behaviour.



**Figure 5.9:** Baviaanskloof Gneiss. Relic plagioclase crystals (Pl) with deformed twinning planes. The plagioclase is replaced by newly formed albite (Ab) and microcline-perthite as the result of the intense alteration that affected the Doornhoek area. 1cm=100µm



Figure 5.10: Baviaanskloof Gneiss. Relic plagioclase crystals (Pl), still displaying deformation lamellae, replaced by newly formed albite (Ab). 1cm=100 $\mu$ m



UNIVERSITY  
OF  
JOHANNESBURG

### 5.3.2. The partly hydrated mafic granulite

The hydrated mafic granulite is a well foliated rock consisting of plagioclase, hornblende, quartz, sphene, magnetite and relics of salite, augite and hypersthene. In certain places and especially in the vicinity of the highly metasomatised and mineralised lithologies, magnetite is quite abundant, and might be related to the mineralising event.

### 5.3.3. The partly hydrated ultramafic lithologies

The hydrated ultramafic granulite consists mainly of enstatite, olivine, hornblende, chlorite and dolomite while newly formed sphene is quite abundant. More intensely hydrated

varieties are also characterised by the presence of anthophyllite as a retrograde product after enstatite and olivine, while the amount of chlorite and dolomite also increases drastically.

#### **5.3.4. The hydrated pelitic granulite**

This rock type has not been identified in the Doornhoek Ore Body, but outcrops in the immediate vicinity. It consists of orthoamphibole, kyanite, quartz, garnet, biotite and plagioclase. The orthoamphibole can be either anthophyllite and/or gedrite.

#### **5.3.5. The partly hydrated BIF**

The BIF lithologies at the Doornhoek locality are characterised by two varieties: magnetite-rich and magnetite-free. The magnetite-rich rock consists of magnetite, quartz, ferropseudobrookite and grunerite. Weakly hydrated varieties display a high amount of ferropseudobrookite and salite, and very small amounts of almandine garnet, while highly hydrated lithologies are characterised by high amounts of grunerite and Fe-rich hornblende that replaced orthopyroxene (ferropseudobrookite) and clinopyroxene (salite).

### **5.4. HIGHLY ALTERED ROCKS (METASOMATISED) ASSOCIATED WITH**

#### **DOORNHOEK GOLD DEPOSIT**

The Doornhoek gold deposit is located in an alteration zone (shear zone) associated with a suite of altered (metasomatised) metamorphic rocks that include highly metasomatised

Baviaanskloof Gneiss, partially or completely hydrated mafic granulite, silicate facies BIF, narrow sequences of completely altered felsic granulite and altered ultramafic granulite. The alteration event that accompanied mineralisation followed on the regional hydration event described by van Reenen (1986).

#### 5.4.1. The highly altered equivalent of the Baviaanskloof Gneiss

The already hydrated Baviaanskloof Gneiss (described in **chapter 5.3.1**) is almost completely altered in the Doornhoek alteration zone that is related to a system of shear zones which probably acted as channelways infiltrating metasomatic fluids. Newly percolating hot fluids described in the close vicinity, at Klipbank, by Mokgatla (1995), were K-, Na-, Ca-, Al- and Si-rich and produced mainly microcline-perthite, albite and minor quartz. The alteration process displayed little or no evidence of deformation in the gray Baviaanskloof Gneiss and the macroscopic appearance of the grey gneiss, although altered, is almost unchanged. Plagioclase is only present as highly deformed relics (**fig. 5.11, 5.12 and 5.13**). This type of transformation is similar to the incipient alteration which affected the coarse leuco zones at Klipbank (Mokgatla, 1995).

The alteration process is mostly clearly visible in late leuco veins (**fig. 5.8**), with a pinkish appearance, the result of channelised metasomatic fluids. In the leuco zones microcline-perthite occurs as large anhedral crystals consisting of microcline with typical extinction (**fig. 5.14**) hosting albite along perthitic planes which can be very wide (**fig. 5.15**).





Figure 5.11: Newly formed metasomatic vein material, consisting mainly of microcline-perthite. Note the presence of relic plagioclase crystals (Pl). 1cm=100µm



Figure 5.12: Relic plagioclase (Pl) replaced by both microcline-perthite (M) and quartz (Qz). 1cm=50µm



Figure 5.13: Sub-solidus replacement of plagioclase (Pl) by microcline-perthite (M).  
1cm=50µm



Figure 5.14: Boundary between leucocratic vein and Baviaanskloof Gneiss: anhedral grain of microcline-perthite penetrating through intercrystalline discontinuities into the Baviaanskloof Gneiss. Part of the quartz has been remobilised as very thin channelets into the initial plagioclase (Pl) at the edges of the crystals forming real myrmekitic textures (arrow).  
1cm=100µm

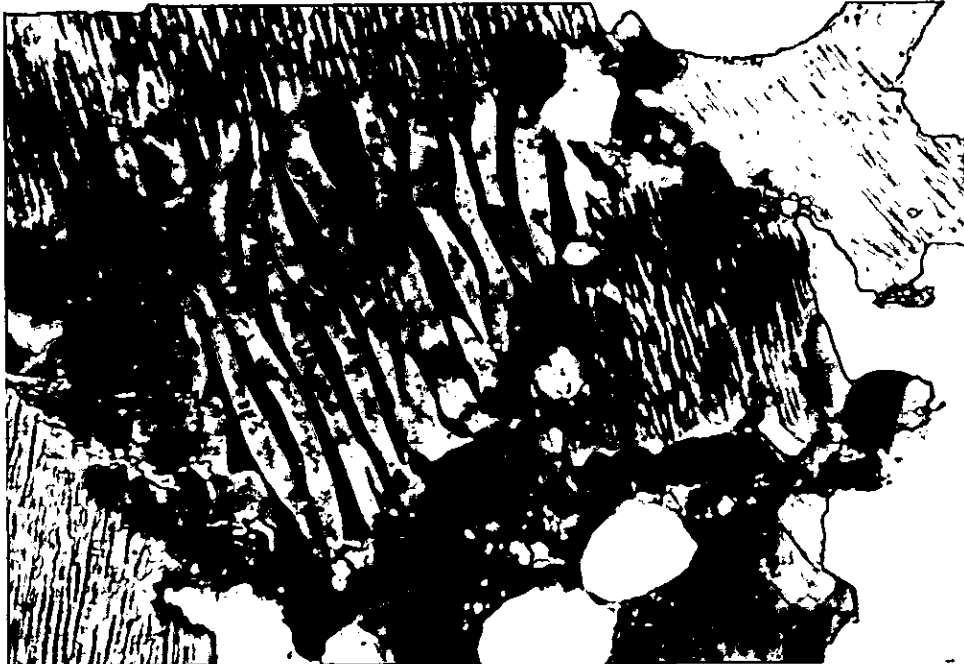


Figure 5.15: Albite (thick black stripes) hosted by the K-feldspar (grey host) as channelets along the perthitic planes. 1cm=25 $\mu$ m

This relationship between the microcline-perthite host and the hosted albite is rather related to a process of mutual substitution than to exsolution (fig. 5.16 and 5.17). This is suggested by the fact that microcline is quite homogenous in composition (almost pure with less than 4wt per cent Ab) displaying a slight increase in albite marginal to the perthitic structures. Microcline-perthite was probably introduced in large amounts from the sub-solidus metasomatising fluid into the vein. Microcline-perthite is the main newly introduced component into the Baviaanskloof Gneiss and it corrodes all the preexistent minerals (especially plagioclase - fig. 5.18 - and to a smaller extent also quartz - fig. 5.19 and 5.20).

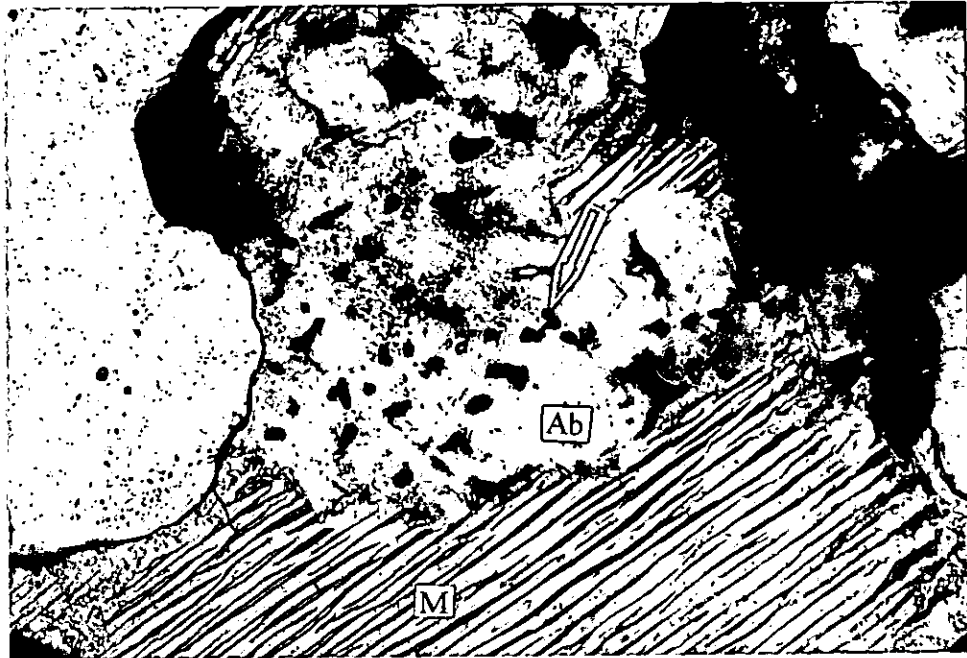


Figure 5.16: Albite and K-feldspar substitute for each other along perthitic planes rather than albite being the product of exsolution in microcline-perthite (M). One can also see the newest crystallised pure albite (Ab), replacing the microcline-perthite. Myrmekitic structures (arrow) also occur in the albite. 1cm=50 $\mu$ m

Quartz is anhedral and mainly related to the initial granulite facies event. However, quartz was also newly introduced during the alteration event which produced the gold and associated mineralisation. (fig. 5.21).

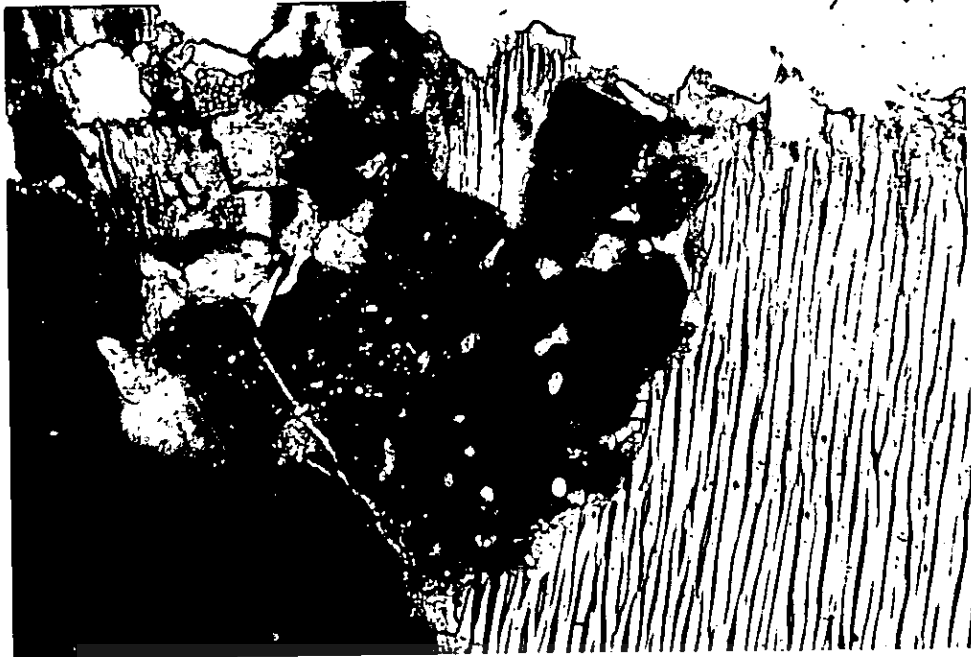


Figure 5.17: Same as photo 5.16 but slightly rotated in order to better see the myrmekitic structure.

1cm=50µm



Figure 5.18: Microcline-perthite (M) is the main component of the newly formed metasomatic veins. Albite (Ab) replaces deformed plagioclase.

1cm=50µm

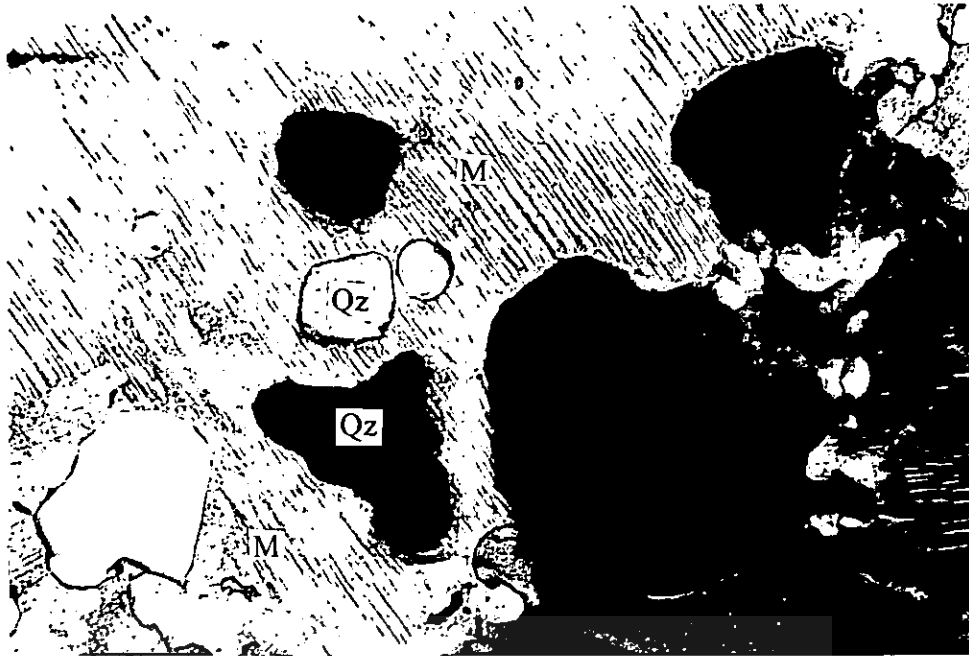


Figure 5.19: The metasomatic corrosion exercised by the microcline-perthite (M) was so intense that even the preexisting quartz (Qz) from the initial paragenesis of the tonalitic gneiss has been almost completely consumed by microcline-perthite. 1 cm=100 $\mu$ m

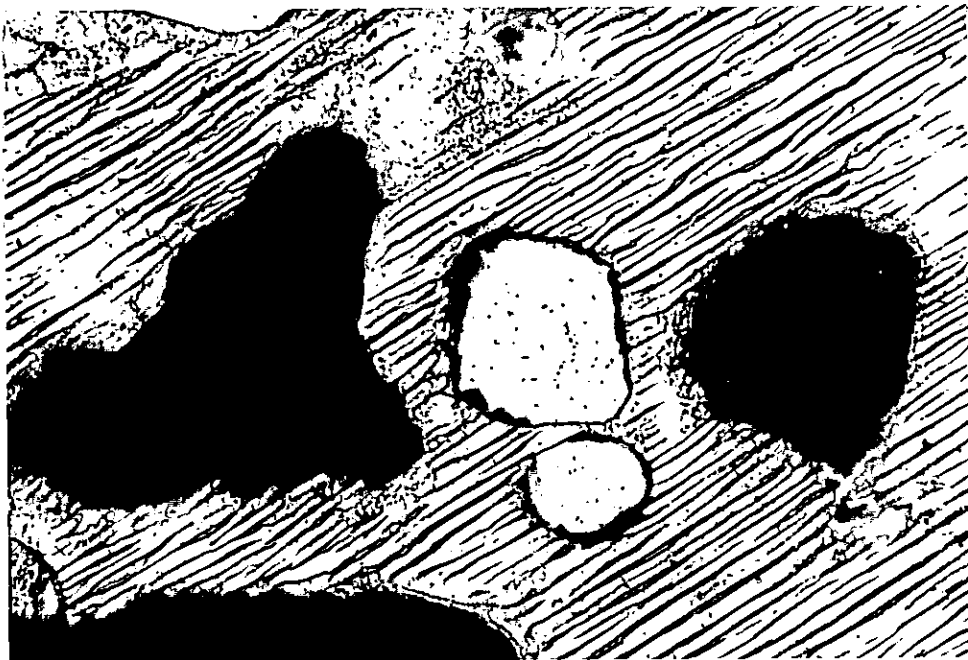


Figure 5.20: Blow-up of photo 5.20 in order to better see the quartz relics within the newly introduced microcline-perthite. 1 cm=25 $\mu$ m

An interesting occurrence of quartz is in the form of myrmekitic (graphic) textures (fig. 5.17). Part of the quartz was remobilised as very thin channellets into the newly formed albite or into the initial plagioclase of the gneiss, usually at the edges of the crystals, forming real myrmekitic textures (fig. 5.14, 5.16 and 5.17). The fact that the quartz channelets in myrmekites always crosscut the twinning planes in albite (fig. 5.13) demonstrates that the quartz was remobilised after the introduction of the pinkish veins, due to later reactions between microcline, albite and highly corroded plagioclase. The fact that a high amount of albite and K-feldspar was introduced into all the lithologies that form the Doornhoek ore body, suggests that these reactions probably occurred during the late alteration process related to the mineralisation event.



Figure 5.21: Field-image of photos 5.19 and 5.20 in order to have a better understanding of the relationships between quartz and microcline. 1 cm=100µm

Plagioclase (An 18-34 per cent) occurs only as relics in the Baviaanskloof Gneiss, being intensely corroded by microcline (fig. 5.11 and 5.13), and it is always rimmed by a very thin shell of hematite, probably exsolved from the plagioclase lattice.

Albite occurs as small anhedral or subhedral crystals, always marginal to the microcline-perthite, displays a very high purity (An < 2 per cent) and is intensely twinned.

Biotite occurs as chloritised relics in the Baviaanskloof Gneiss (fig. 5.22, 5.23 and 5.24). During the chloritisation reaction, part of the Fe and Ti from the biotite lattice were exsolved along the cleavage planes as tiny ilmenite crystals (fig. 5.2). An important aspect is that biotite is highly chloritised only when it occurs within the pinkish veins.

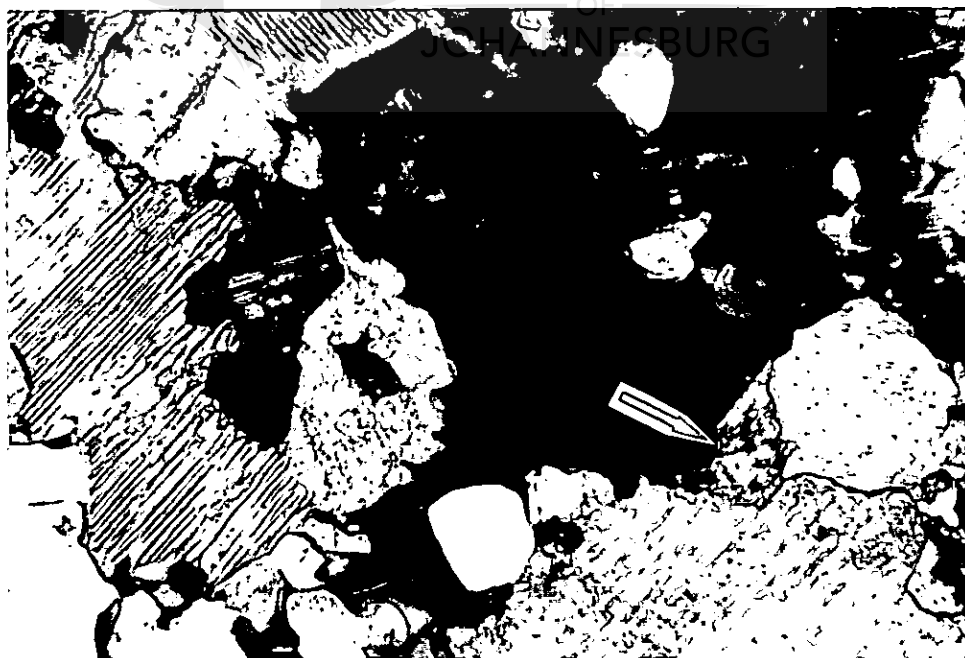


Figure 5.22: Biotite relic (arrow) in a K-feldspar-rich metasomatic vein in the Baviaanskloof Gneiss.  
1cm=400µm



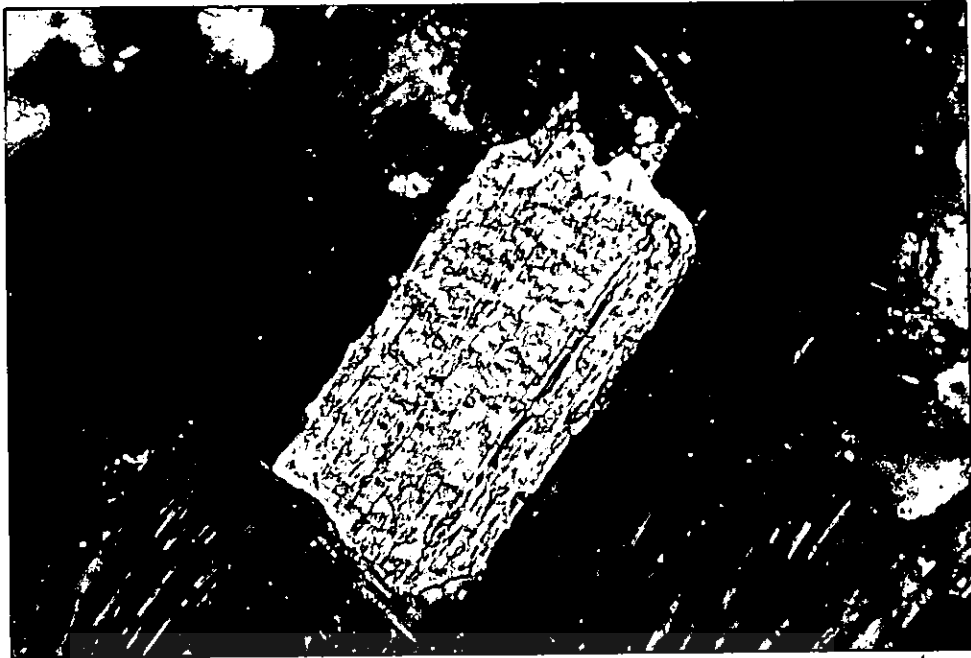


Figure 5.23: Highly corroded biotite crystal in newly formed microcline-perthite. A weak Fe contamination of the microcline-perthite is noticed at the contact.

1cm=25 $\mu$ m

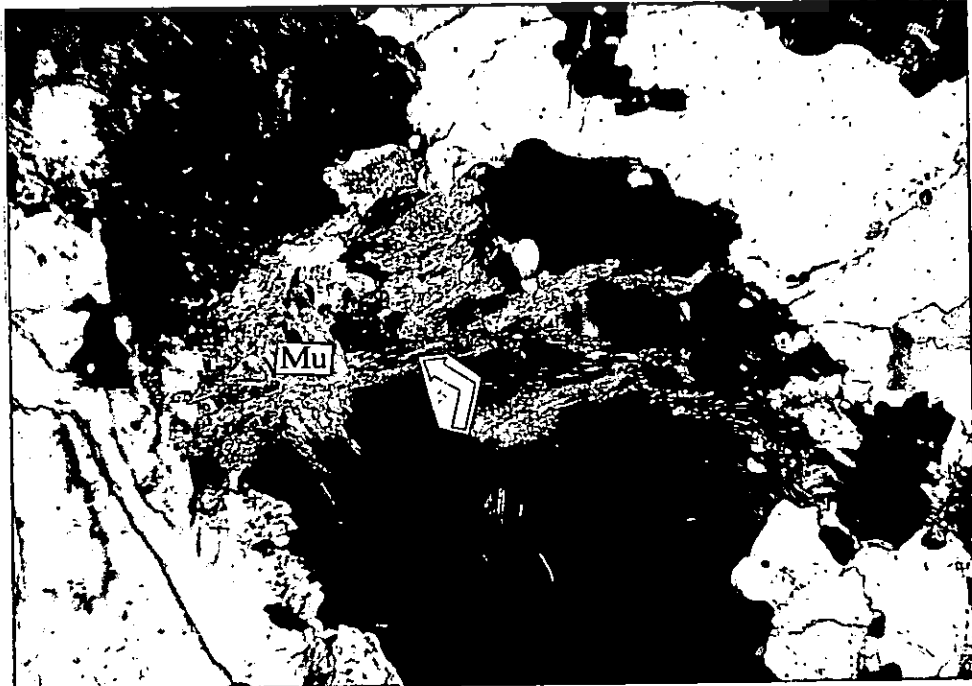


Figure 5.24: Muscovite (Mu) formed as a result of Fe-depletion of the chloritised biotite (arrow).

1cm=400 $\mu$ m

Muscovite occurs associated with the chloritised biotite (fig. 5.24) or along the perthitic planes in the microcline-perthite (fig. 5.25). There is much more muscovite present in the newly formed K-rich metasomatic product than in the grey Baviaanskloof Gneiss host. This is probably due to the high influx of K-rich solutions into Baviaanskloof Gneiss. This is the very evidence of the alteration phenomenon that probably introduced the mineralisation, but within the gneissic lithologies and not affecting the mafic or BIF lithologies.

Sericite occurs as a late alteration product after plagioclase and seldomly after microcline.

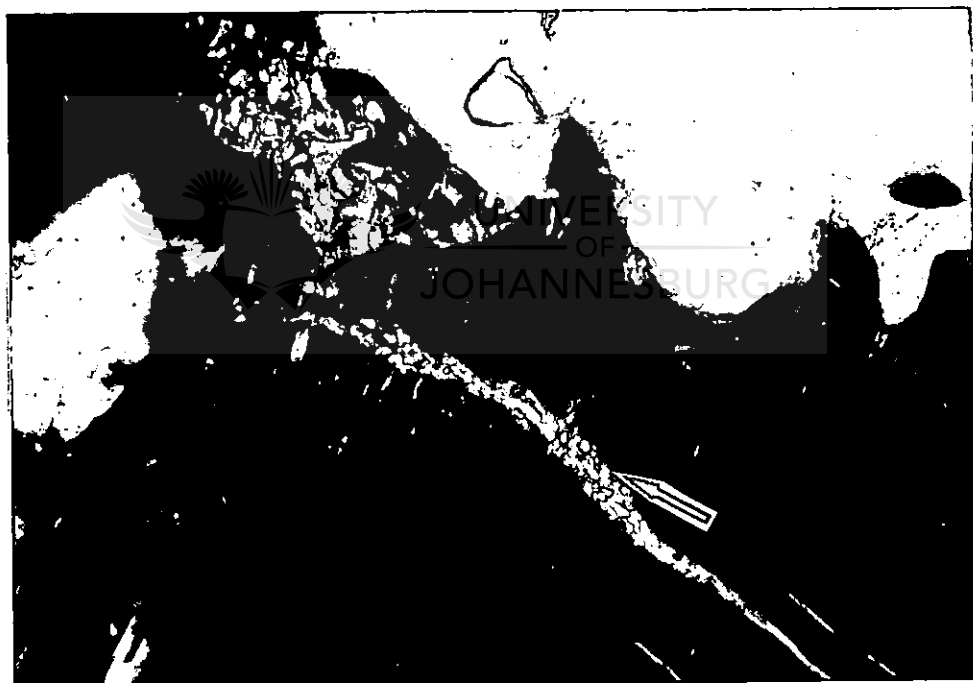


Figure 5.25: Muscovite in veins (arrow) crosscutting the microcline-perthite. 1cm=200 $\mu$ m

The described mineral textures might also suggest a migmatitic provenience for these substitutions, thus involving a super-solidus process associated with partial melting. A sub-solidus process, however, is only possible at much higher temperature conditions,

whereas the alteration process preserved at Doornhoek only occurred at temperatures close to 600°C (Hoernes et al., 1995).

#### 5.4.2. The highly altered BIF (mafic granulite)

This rock prior to the alteration event consisted mainly of ferrohypersthene, salite, hornblende, quartz, possible plagioclase and sphene. Magnetite could also have been present in certain amounts. As a result of the intense alteration, presumably no plagioclase was left in the rock. Probably, all the pre-existing plagioclase affected by hydrothermal alteration was transformed into albite and some plagioclase relics. However, no plagioclase relic was encountered in this rock type. The presence of two pyroxenes and hornblende suggest a mafic origin of the rock. However, similar rocks in Canada (Colvine et al., 1988) are described as starting life as Fe-rich sediments (BIF type) and due to high-grade metamorphism today display the above mentioned mineralogical composition. This petrographic type will be called calc-silicate facies BIF, or simple BIF in this thesis, although in certain places its mafic origin can not be disputed.

This high-grade calc-silicate facies BIF rock type displays evidence of shearing that varies from almost unshered rocks through augen-bearing rocks and finally into intensely altered, highly stretched tectonites. The general appearance of the BIF rock at Doornhoek gold deposit is illustrated in **fig. 5.26** and **5.27**.



**Figure 5.26:** Photograph of drill core showing altered and sheared calc-silicate facies BIF. Note the presence of quartz boudines in the foliation (borehole DD7, 55.50-55.68m).



**Figure 5.27:** Photograph of drill core samples of the magnetite-free calc-silicate facies BIF. Note the presence of quartz boudines, some of them mineralised with gold (borehole DD7, 58.00-60.00m).

The hydrated paragenesis suffered retrogression under low granulite - upper amphibolite facies conditions, in order to produce a rock with an amphibolitic composition in which relics of the unaltered assemblages are still preserved in the unsheared portions (fig. 5.28). As a result, pre-existent pyroxene was transformed into highly zoned amphibole. The ferrohypersthene was first rimmed by ferrogedrite, under essentially static conditions (fig. 5.29). This static hydration process recognised at Doornhoek graded into a more dynamic event with increased intensity of deformation. This resulted in the formation of a dynamically retrogressed rock consisting mainly of orientated bands of amphibole (fig. 5.30). At the same time, the mineralisation event associated with the alteration introduced high amounts of magnetite into the system. Due to the different influx of fluids related to the different intensities of shearing, the altered calc-silicate facies BIF can be magnetite-rich or magnetite-free. The magnetite-rich variety is referred to as BIF in this study.

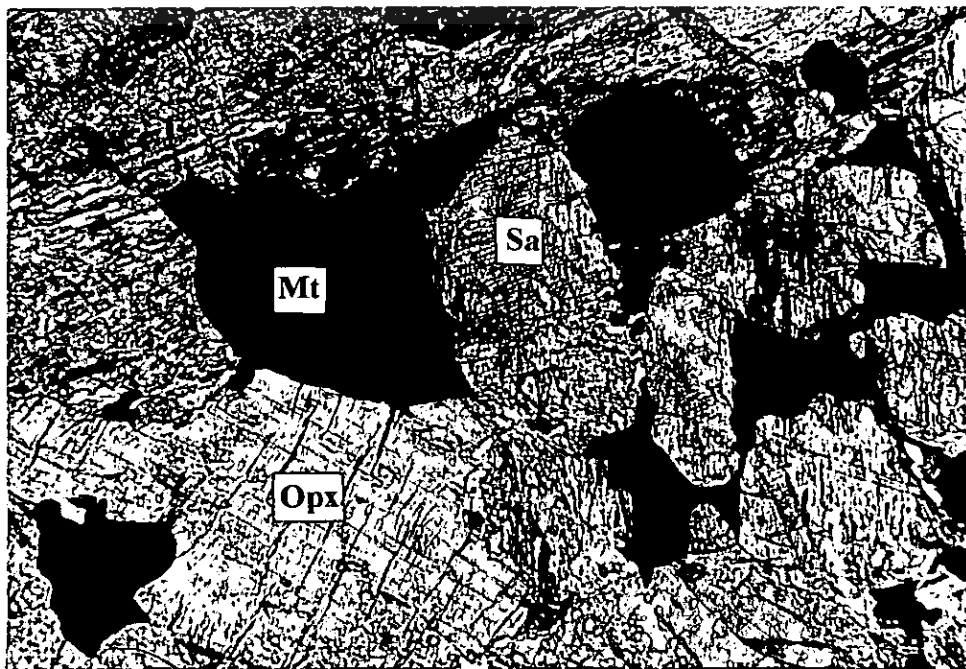


Figure 5.28: Slightly altered magnetite-bearing mafic rock: ferrohypersthene (Opx) + salite (Sa) + magnetite (Mt). 1cm=400µm

The composition of the amphibole varies (core-to-rim) from gedrite to ferrogedrite in the magnetite-free assemblage (fig. 5.30), and from grunerite to a dark Fe-rich hornblende (bergamasikite?) in the magnetite-rich assemblage (BIF) (fig. 5.31). Whenever the Fe-rich hornblende is the main mineral the rock is transformed into a typical Fe-rich amphibolite. At the boundaries with the BIF, garnet is also present, probably as a reaction product between the interlayered sequence of magnetite-rich and magnetite-free BIF and the newly introduced metasomatic fluids (fig. 5.32).



Figure 5.29: Microphotograph showing the initial retrogression of the magnetite-bearing BIF, in which ferrohypersthene (Opx) is rimmed by ferrogedrite (arrow). Metasomatic biotite (Bi) changed its rim composition due to an interactive chemical exchange with the Opx, and became marginally very Fe-rich. 1cm=200µm

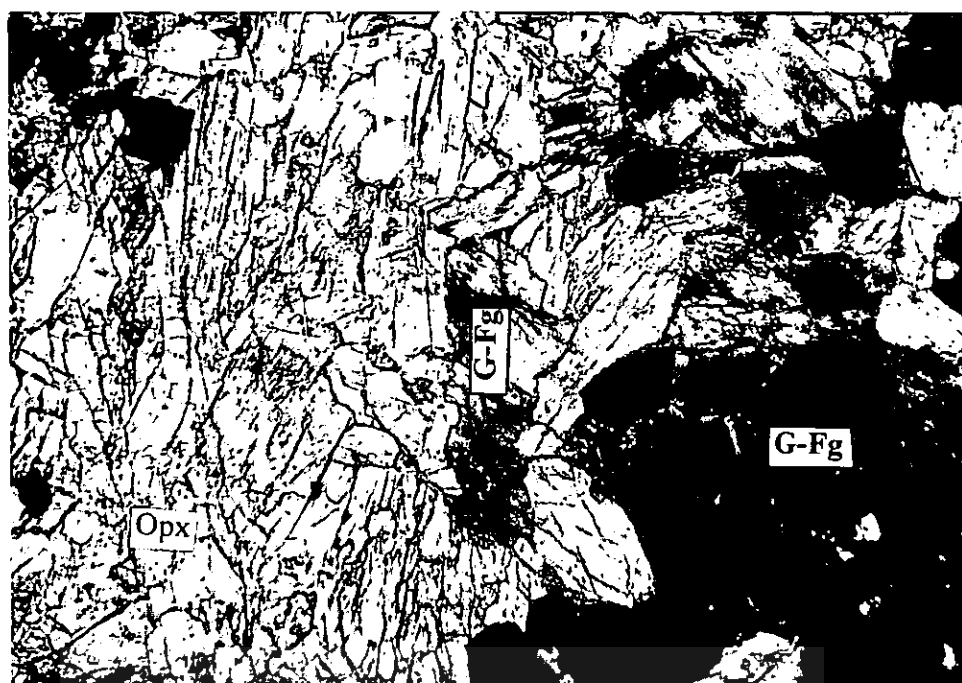


Figure 5.30: Microphotograph showing gedrite-ferrogedrite (G-Fg - intense green) completely replacing the initial Or x in the magnetite-free paragenesis of the BIF.

1cm=400µm

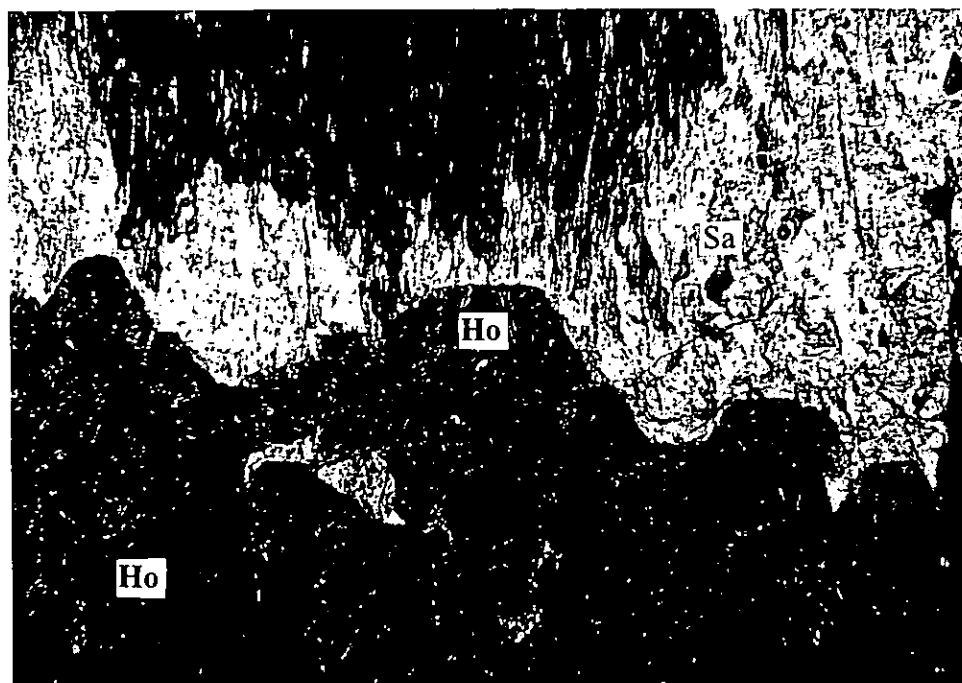


Figure 5.31: Microphotograph illustrating the replacement of salite (Sa) by Fe-rich hornblende (Ho) in the magnetite-rich assemblage of the BIF.

1cm=400µm



Figure 5.32: Microphotograph illustrating garnet (Ga) intergrown with ferrohypersthene (Opx) at the boundary between the magnetite-rich and the magnetite-free BIF. This specific lithological sequence was intensely altered by the mineralising fluids.

1cm=200µm

#### 5.4.3. The highly altered ultramafic granulite

The ultramafic granulite occurring in the alteration zone at Doornhoek presently consists mainly of anthophyllite (fig. 5.33). Olivine which probably represented the primary assemblage only occurs as isolated relics surrounded by newly formed anthophyllite. In contact with the hydrated BIF, anthophyllite changes into a mainly gedrite-pargasitic hornblende composition and finally into grunerite. The sharp transition of the amphibole from a Mg-rich mineral (anthophyllite) through gedrite and finally into grunerite is probably the result of the interaction of the channelised mineralised metasomatic fluid with Fe from



the BIF during ductile shearing. Later generations of talc, serpentine and Mg-rich chlorite were formed in addition to the initial paragenesis.

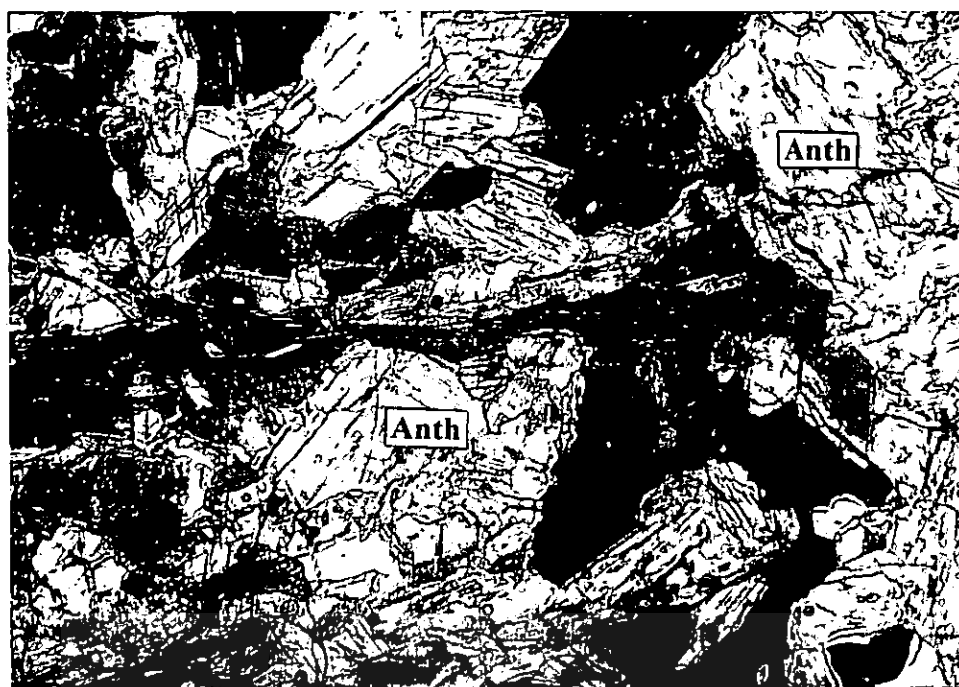


Figure 5.33: Microphotograph illustrating the completely retrogressed ultramafic granulite, now consisting mainly of anthophyllite (sample DH-2120). 1cm=400µm

#### 5.4.4. The highly altered felsic granulite

This petrographic type represents an extremely metasomatised rock. The present mineral composition is more than 75 wt per cent K-feldspar and albite with smaller amounts of quartz, biotite, garnet, plagioclase ( $An_{21}-An_{49}$ ), ferrohypersthene, tourmaline and Fe-rich cordierite. This so-called felsic granulite (altered metapelite?) occurs as thin zones intimately associated with the BIF (fig. 5.34). The presence of Fe-rich cordierite (table 5.1) is unusual, but similar cordierite has been described from a hornfels in Angus, Scotland (Chinner, 1962).

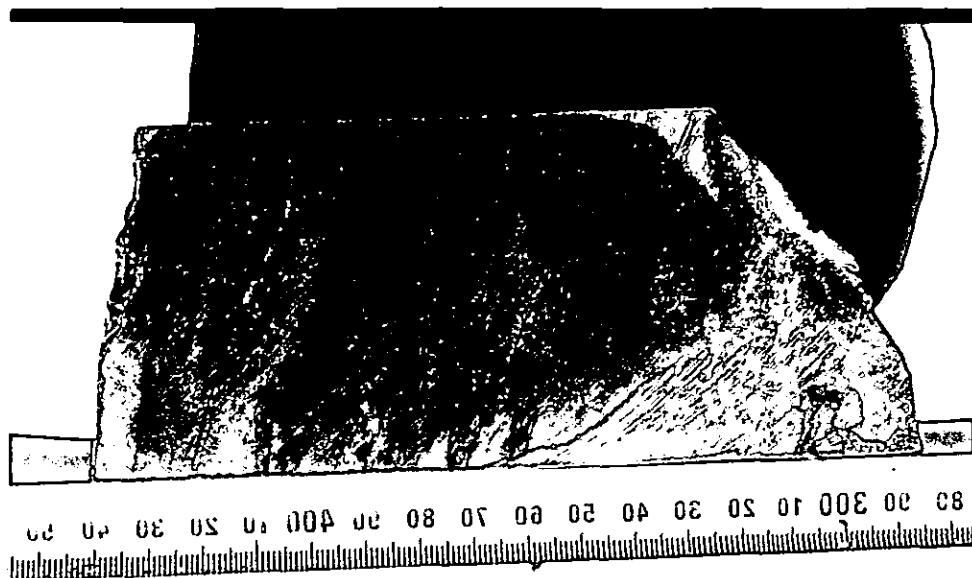


Figure 5.34: Drill core sample from borehole DD-2 (89.75-89.90m). Felsic granulite (probably altered metapelite) that usually occurs as thin layers in BIF.

The altered felsic granulite at Doornhoek is mainly composed of fine grained crystals of albite and K-feldspar. The newly crystallised feldspars occur as a late groundmass (fig. 5.35 and 5.36) or in tiny veinlets. The late veinlets are mainly albitic. While albite and K-feldspar coexists in equal amounts in the groundmass, textural and chemical evidence (zonation of feldspars based on microprobe analyses) indicate that the felsic granulite was metasomatised during two distinct events:

*i)* the first event was characterised by the introduction of K-feldspar with a very low albite content (almost pure microcline). The process of K-feldspar enrichment of the initial felsic granulite also produced albite from the breakdown of the plagioclase. But the amount of albite in the rock is too high to assume that all of it is the result of plagioclase alteration.

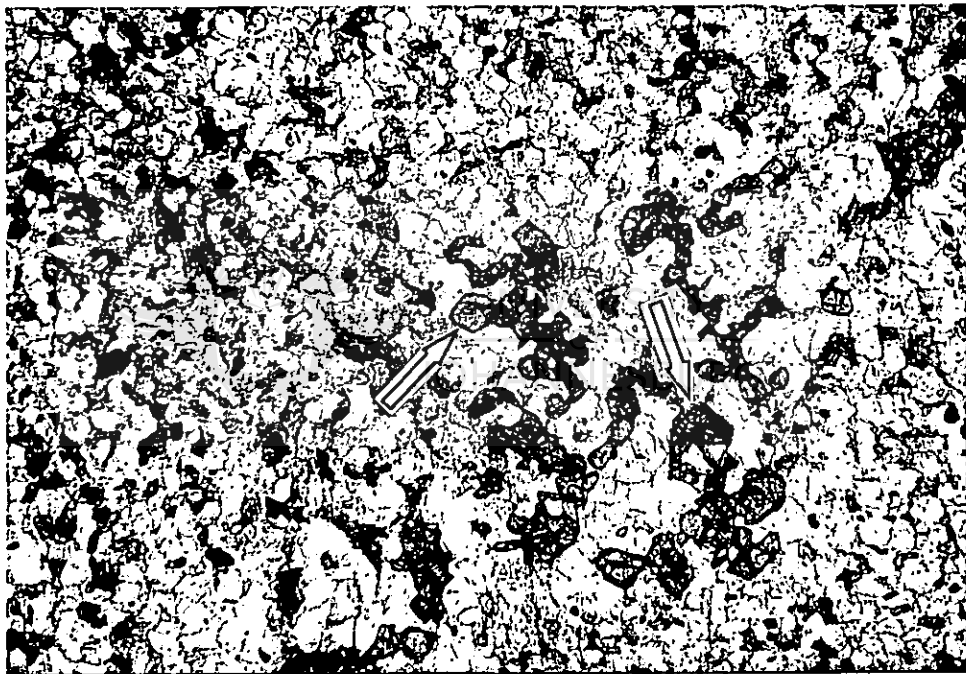
*ii)* therefore, some of the albite must also have been introduced into the system as was the microcline. Furthermore, textural relationships demonstrate that part of the microcline was subsequently replaced by abundant late albite and tourmaline (**fig. 5.38**), during the second alteration event. The replacement of microcline by albite is very difficult to identify optically, but can clearly be documented with an electron microprobe.

Textural relationship with sulphides and magnetite show that albite and especially tourmaline form veinlets cutting the ore minerals. Thus, albite and tourmaline were introduced after the deposition of the sulphides and oxides, therefore, post-mineralisation as opposed to microcline that predates mineralisation. The late character of the tourmaline is displayed by its crosscutting textural features. Tourmaline cuts retrogressed garnet and is the main mineral that occur in pressure shadows of garnet porphyroblasts, an indicator for a late, metasomatic-deformational event. Both microcline and albite occur as small crystals (**fig.5.35**), superimposed upon the initial metamorphic paragenesis.

The initial paragenesis of the so-called felsic granulite is difficult to establish but is probably represented by quartz-biotite-garnet-plagioclase ( $An_{21}-An_{49}$ ) (**fig. 5.35, 5.36 and 5.37**). The present mineral assemblage suggests a metapelitic precursor such as an Al-, Fe-rich chamosediment, finely interlayered with a BIF (**fig. 5.37**). Its nature is even further complicated by the geochemical features of the rock (Cr- and V-rich) (**Chapter 12**). If the rock had some pelitic component prior to granulitisation and metasomatism, it can be assumed that during the  $M_2$  decompression event Fe-rich cordierite and ferrohypersthene replaced garnet. During the later  $M_3$  hydration event ferrohypersthene was replaced by

Fe-rich gedrite which later evolved into highly zoned Fe-rich hornblende-grunerite associations.

It is likely that this rock type is the product of intense metasomatism which occurred during the  $M_3$  rehydration event. It only occurs in zones of intense alteration and has never been described from the wall rock.



**Figure 5.35:** Microphotograph of sample DD2-13. Relics of garnet (high relief mineral - arrows), probably belonging to the  $M_2$  metamorphic event (typical retrograde zoning pattern) occur in a matrix consisting mainly of quartz, newly introduced K-feldspar and albite.  
1cm=400 $\mu$ m

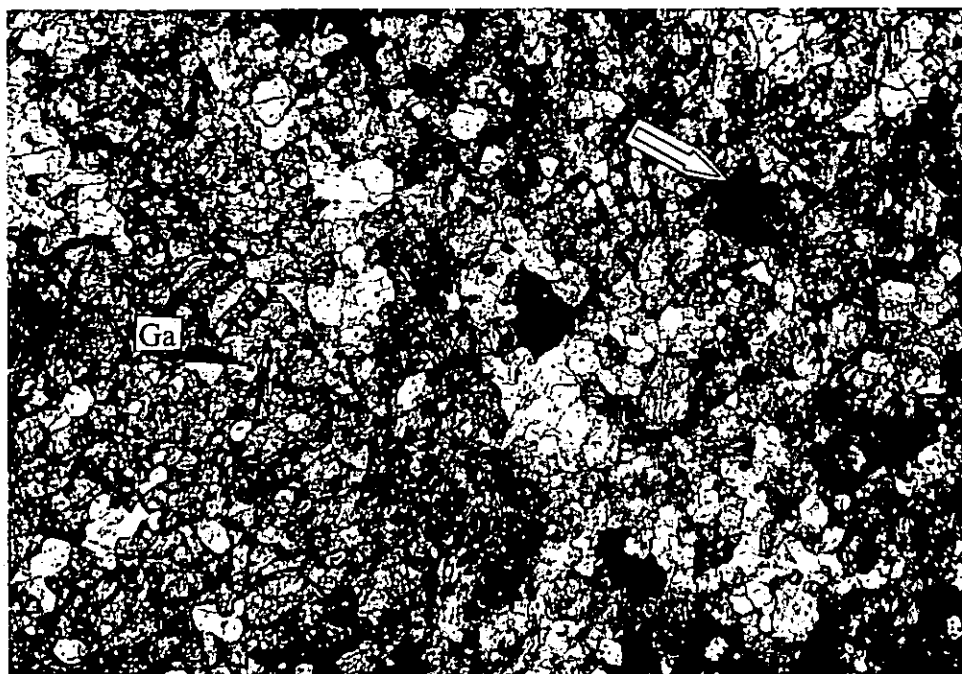


Figure 5.36: Large retrograde garnet poikiloblast (Ga) associated with interstitial cordierite (colourless). Newly formed biotite (arrow) occurs in the finely crystallised felsic granulite. Due to the intense metasomatism, the matrix now consists of albite and K-feldspar (translucent) (sample DH-2028). Albite, cordierite and K-feldspar can be separated only by electron microprobe. 1cm=400 $\mu$ m

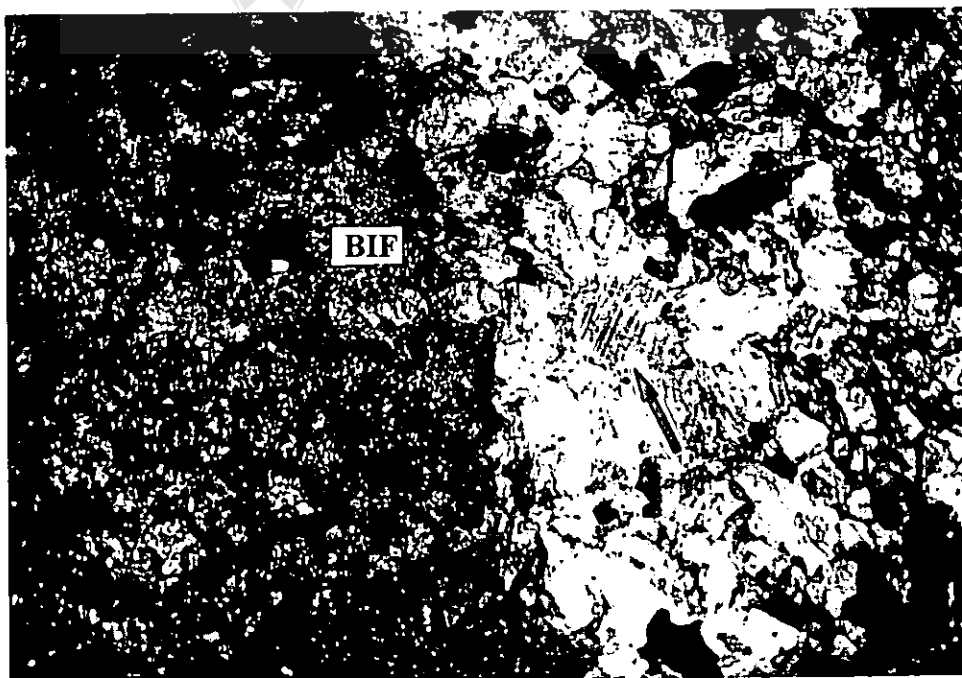


Figure 5.37: At the boundary between the BIF and the felsic granulite, relics of plagioclase (Pl = An<sub>49</sub>) from the former paragenesis still occur. This early plagioclase is intensely twinned (arrow) (sample DH-2008). 1cm=200 $\mu$ m

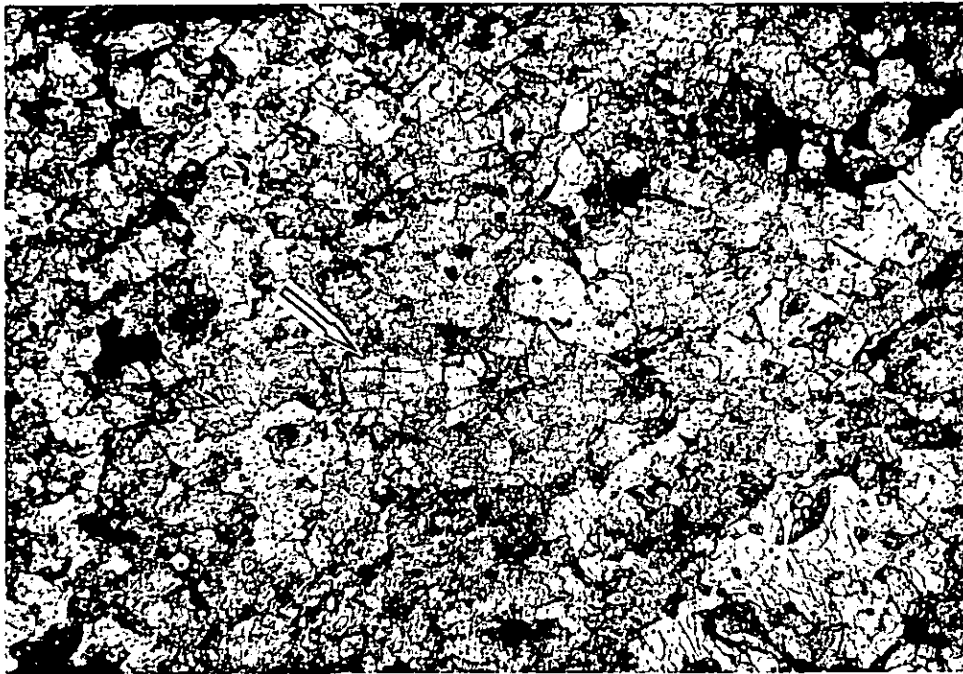


Figure 5.38: Newly crystallised tourmaline crystals (arrow) occurring in the highly metasomatised felsic granulite (sample DD-2-13). 1cm=200μm



UNIVERSITY  
OF  
JOHANNESBURG

#### 5.4.5. The Mineralised Zone of the Ore Body

Although the previously described lithologies are also mineralised to some extent, the metasomatised BIF represents the most intensely mineralised section of the Doornhoek Ore Body. Mineralisation is not only abundant in this Fe-rich lithology, displaying Au grades of up to almost 10g/t Au (1m samples), but the alteration style is also different from the rest of the alteration zone. The alteration style demonstrates the transformation of the precursor BIF, and also of the felsic granulite (**Chapter 5.2**), due to fluid flow that was presumably channelised along shear zones.

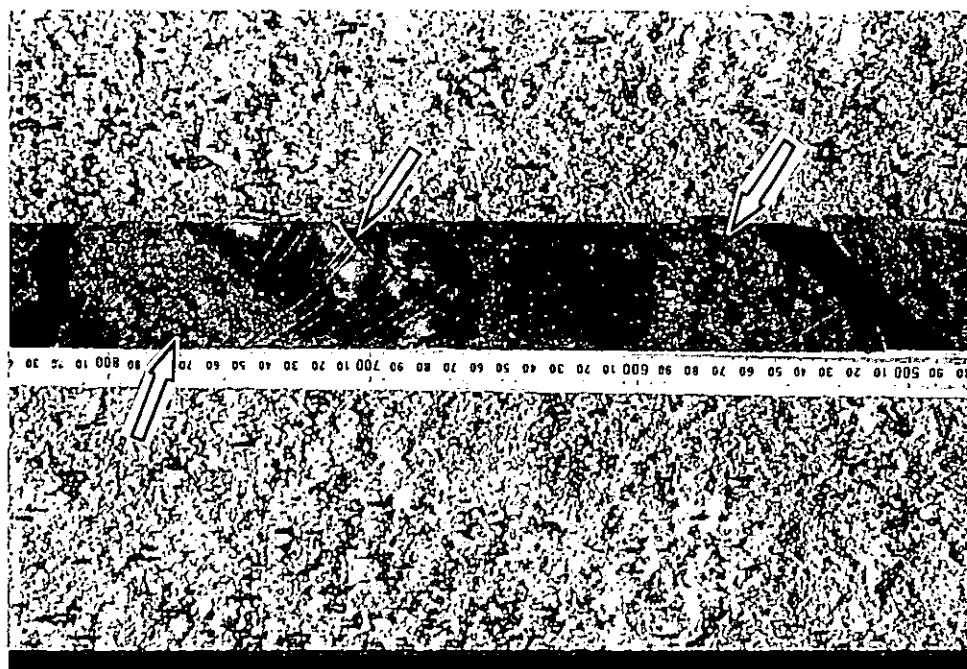


Figure 5.39: Photograph of a drillcore sample showing the relationship between the metasomatic biotite-garnetiferous formation (red arrow) and the quartz veins (blue arrow). Both the garnetiferous formation and the quartz veins are mineralised (borehole DD2, 68.90-69.25m).

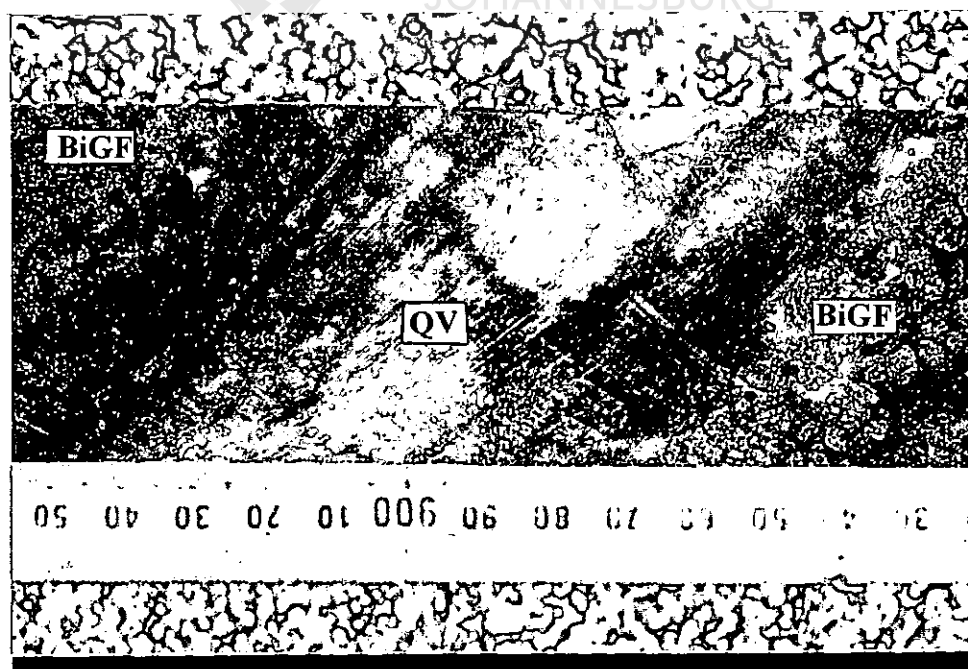


Figure 5.40: A close-up of the relationship between the biotite-garnetiferous formation and the quartz veins. The garnets are usually idioblastic, zoned, mineralised and display a prograde zonation pattern. In this sample quartz appears brecciated (borehole DD2, 69.31-69.44m).

The final products of this highly channelised metasomatic alteration, that defines the Doornhoek Ore Body, are as follows: *i) mineralised quartz veins* that were introduced syntectonically and probably almost simultaneously with the alteration process (fig. 5.39 and 5.40); *ii) mineralised metasomatic biotite-garnetiferous formation* formed as the result of in-situ transformation of the BIF and of the interlayered felsic granulite (fig. 5.39 and 5.40).

**5.4.6.1. Metasomatic biotite-garnetiferous formation:** this metasomatic lithology is always closely associated with the boudinaged quartz veins where it occurs as centimetre to decimetre wide sequences (fig. 5.39 and 5.40). This unusual rock type is dark-brown in colour, and consists mainly of garnet, biotite and quartz and is entirely restricted to the boundary between the quartz veins and the wall-rock (the magnetite-bearing BIF or the felsic granulite - fig. 5.41). Although the felsic granulite can also border the biotite-garnetiferous formation, the principal wall-rock of this metasomatic formation is represented by a dark-green rock, magnetite-bearing calc-silicate facies BIF, composed of grunerite, Fe-rich hornblende, magnetite, quartz and relics of ferrohypersthene and salite. Tiny garnet crystals also occur as relics in the relic ferrohypersthene.



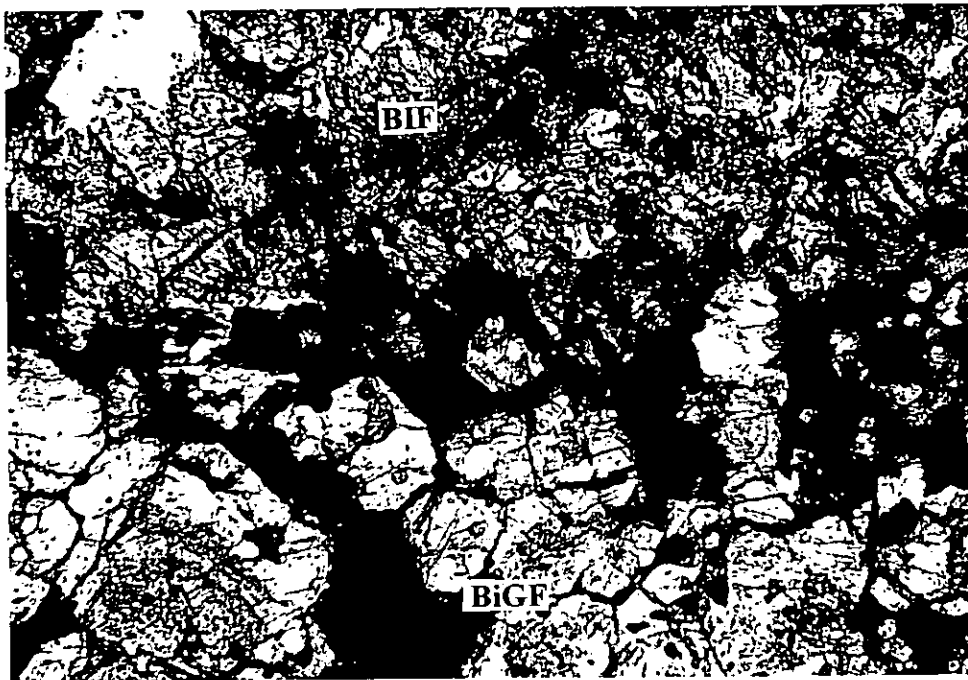


Figure 5.41: Microphotograph showing the boundary between the newly formed metasomatic biotite-garnetiferous formation (BiGF) and the BIF. Sample DH-2034.

1cm=1000 $\mu$ m

The garnet in the metasomatic biotite-garnetiferous formation occurs as euhedral garnet porphyroblasts with well developed zoning (fig. 5.42). The garnet is mineralised with arsenopyrite concentrated in the core and löllingite concentrated in the rim. Weakly zoned zircon-bearing biotite is also intimately associated with the garnet. The garnet in the biotite-garnetiferous formation contains inclusions of the same ore minerals that are also present in the mineralised quartz veins. Graphite is a major phase of this metasomatic sequence, and occurs either as large flakes intimately intergrown with biotite or as rounded inclusions or smaller flakes within the garnet porphyroblast. Quartz is a minor constituent of the biotite-garnetiferous formation, usually filling the space between the garnet porphyroblasts. Newly introduced magnetite and pyrrhotite occur disseminated in the biotite-rich zones.

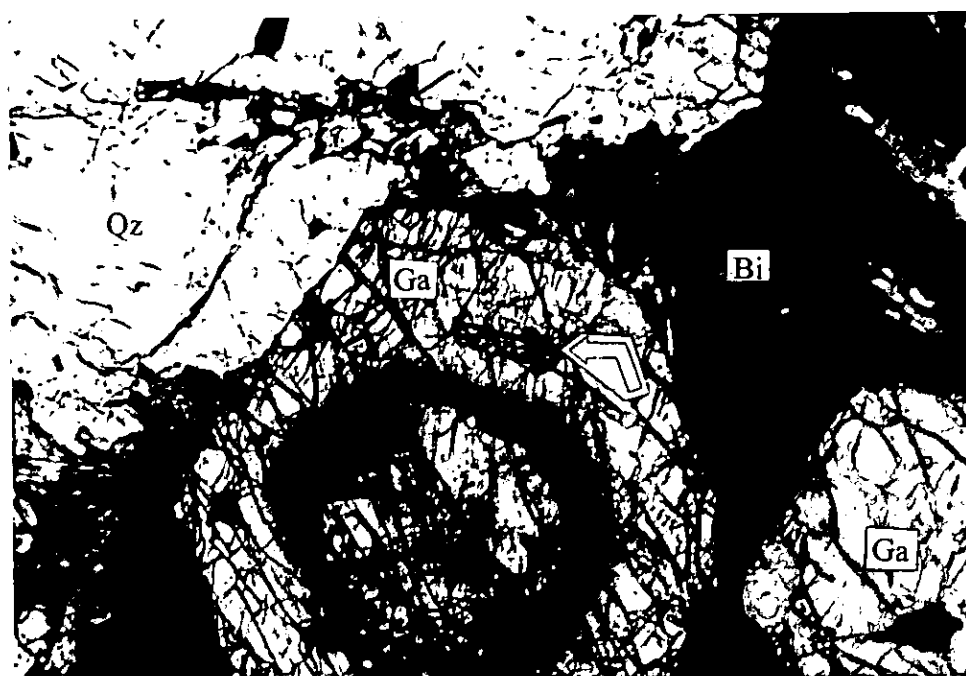


Figure 5.42: Microphotograph of a large zoned euhedral garnet (Ga) associated with biotite (Bi) and also containing biotite inclusions (arrow). The biotite-garnetiferous metasomatic rock is closely associated with mineralised quartz veins (Qz). Sample DH-2035.

1 cm=1000μm

5.4.6.2. **Quartz veins:** Syntectonic quartz veins occur conformable to the foliation (fig. 5.43 and 5.44) that is orientated parallel to the regional  $D_2$  structural elements (Chapter 4.4.). Veining is directly related to the gold mineralisation: only very seldomly does mineralisation occur in vein-free or weakly altered rocks. The quartz veins are sometimes highly laminated (fig. 5.45) and also boudinaged. The long axis of the boudines are orientated parallel to the regional  $D_2$  lineation. The laminated veins often contain bands of relic wall-rock material (fig. 5.46). Where the quartz veins are highly laminated, material defining the laminae is identical to that of the wall-rock and is also orientated parallel to both the vein margin and the foliation of the wallrock (fig. 5.47 and 5.48). Thus, veining occurred penecontemporaneously with the development of the  $D_2$  extensional shear bands or folds. The  $D_3$  deformation affected the *quartz veins and the metasomatic*

*biotite-garnetiferous formation* (i.e. the mineralised horizon of the ore body discussed above) as well as the rest of the deposit (the unmineralised ore body) (fig. 5.44 and 5.45).

In areas of less deformation the syntectonic quartz veins are also developed parallel to the  $D_2$  fabric and display evidence of corrosion of the wall-rock with the development of a local brecciated character (fig. 5.49 and 5.50). The vein quartz consists of white and greenish quartz that hosts the sulphide-arsenide-oxide-gold mineralisation and also contains small amount of calcite and relics of orthopyroxene, garnet and amphibole (fig. 5.49). The quartz veins therefore represent the product of a sub-solidus alteration process, channelised along dynamic shear zones.

The vein quartz is also filled with numerous generations of  $\text{CO}_2$ -rich fluid inclusions that occur in trails orientated parallel to the direction of schlieren of pyrrhotite and magnetite (see Chapter 9). The textural features of the quartz veins are similar to those described from shear zone-hosted lode gold deposits in greenstone belts (Colvine et al., 1988; Vearncombe, 1992) and clearly demonstrate a link with percolating channelised fluids (Groves et al., 1992).

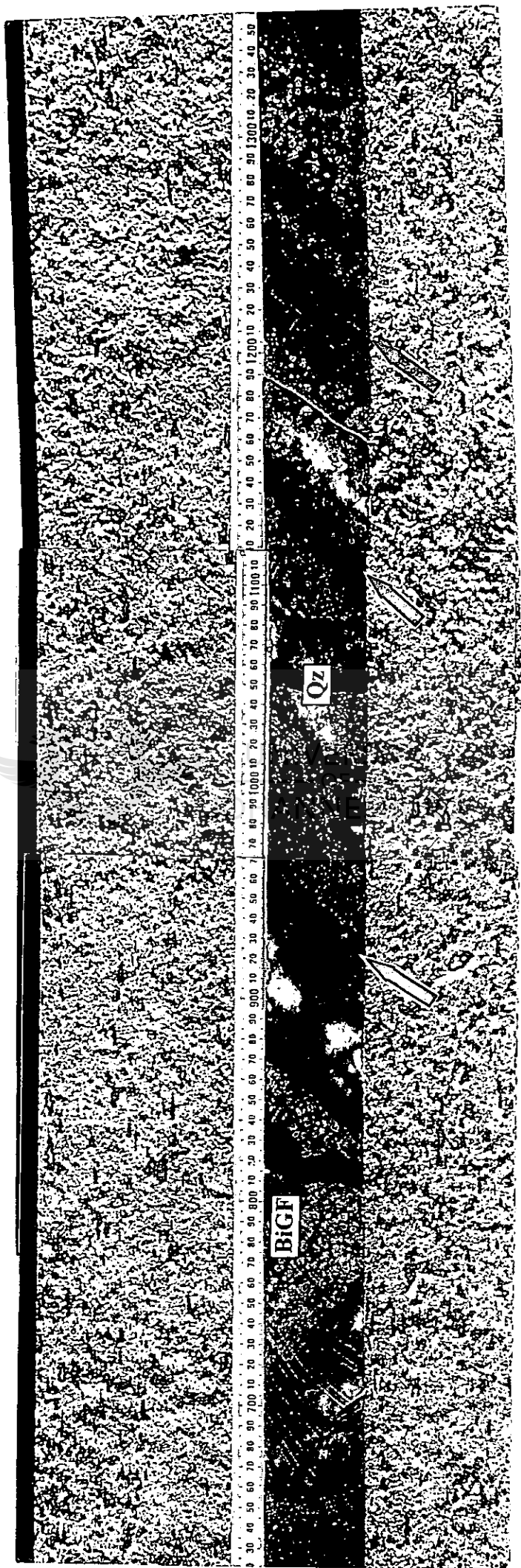


Figure 5.43: Drill core (74 cm length) showing the relationship between quartz veins (Qz) and the biotite-garnetiferous formation (BiGF). Thin horizons of fine grained felsic granulite (arrows), also intensely metasomatised (K-feldspar and albite), occur interlayered with the mineralised horizons.

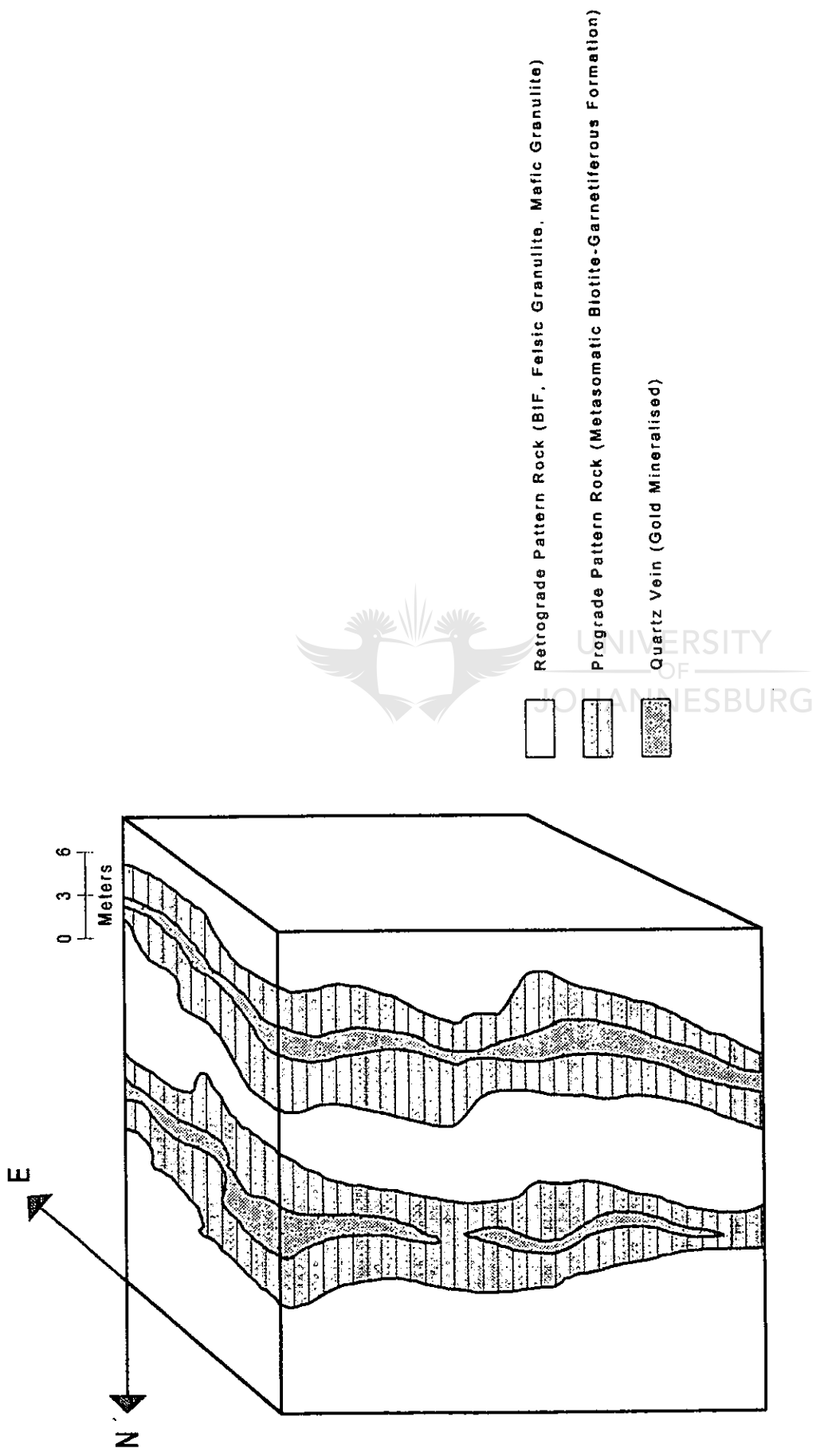


Figure 5.44 A sketch map illustrating the relationships between quartz-veins (yellow), the metasomatic biotite-garnetiferous formation (red) and the BIF, felsic granulite or mafic granulite (wall-rock, white). The observed structural relationships suggest that the newly formed mineralised horizons (yellow and red) represent the filling of quasi-vertical deep crustal channels. The main mineralisation precipitated with the hydrothermal quartz veins (yellow). The fluid which carried and precipitated the huge amount of silica strongly interacted (metasomatically) with the BIF and formed the biotite-garnetiferous formation, which is also mineralised. The mineralisation occurring in the quartz veins is identical to the mineralisation in the metasomatic garnet. "Prograde "and" retrograde pattern" refer to the zoning exhibited by garnet

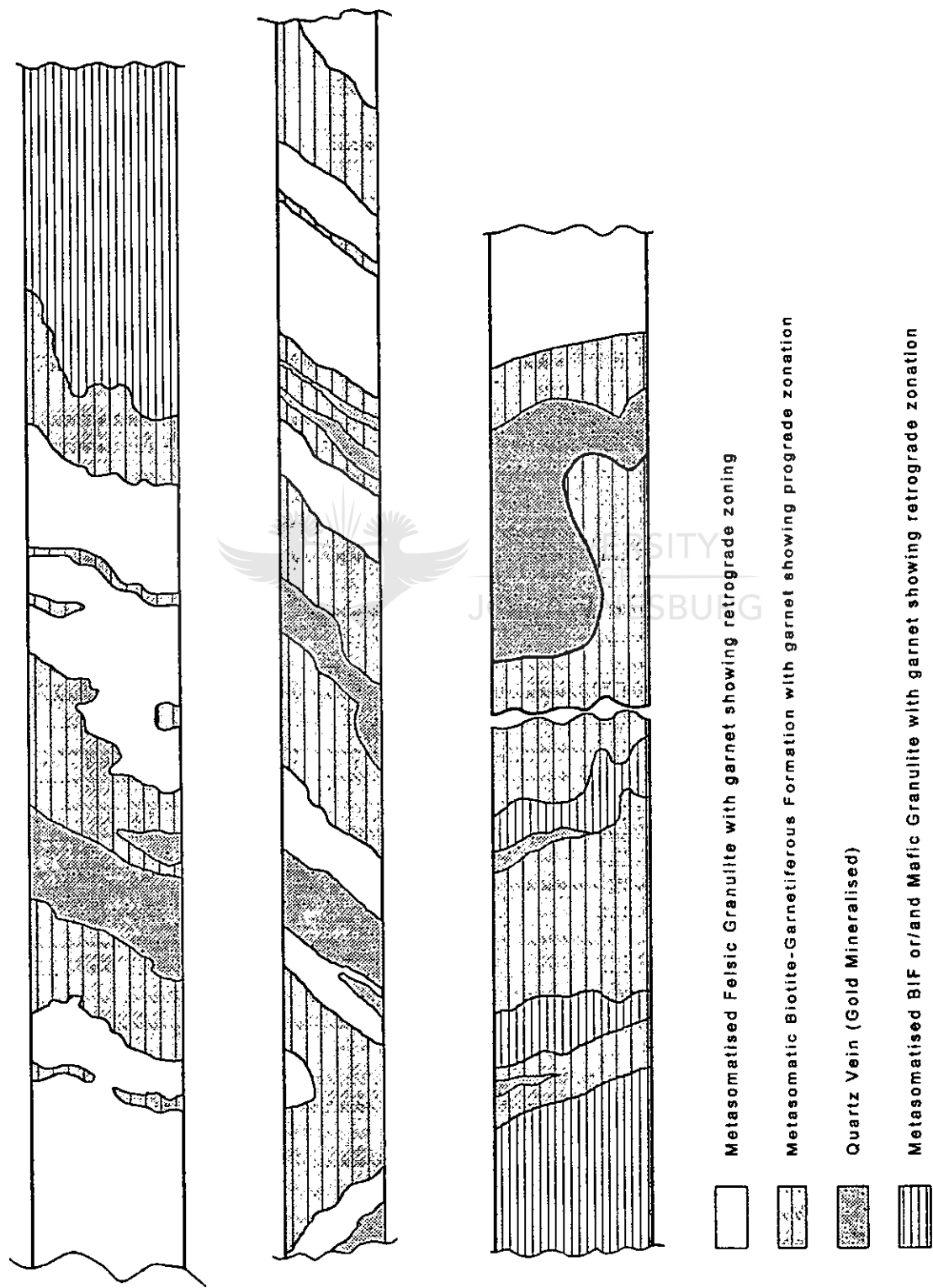


Figure 5.45 Sketch of textural relationship in drill core DD-35. The metasomatic biotite-garnetiferous formation (red) envelopes the mineralised quartz veins (yellow). These two altered sequences are hosted by previous lithologies such as felsic granulite (white) and granulitic BIF (horizontal dashes)

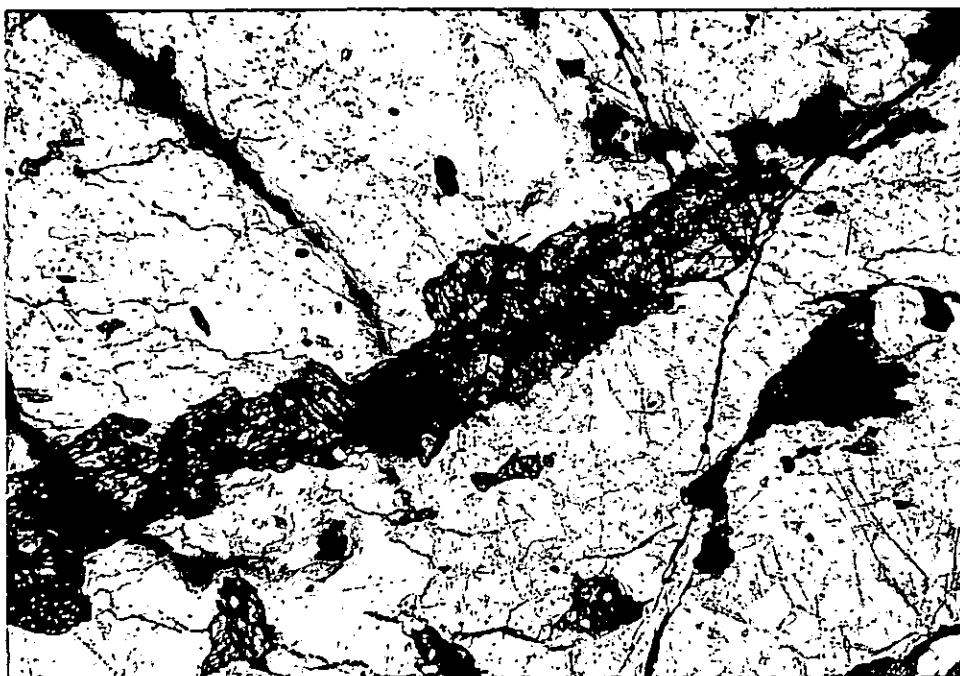


Figure 5.46: Microphotograph showing relics (laminae) of cpx-opx, "assimilated" from the wall-rock and cemented by the highly deformed quartz veins. (Sample DH-2037).

1cm=400 $\mu$ m

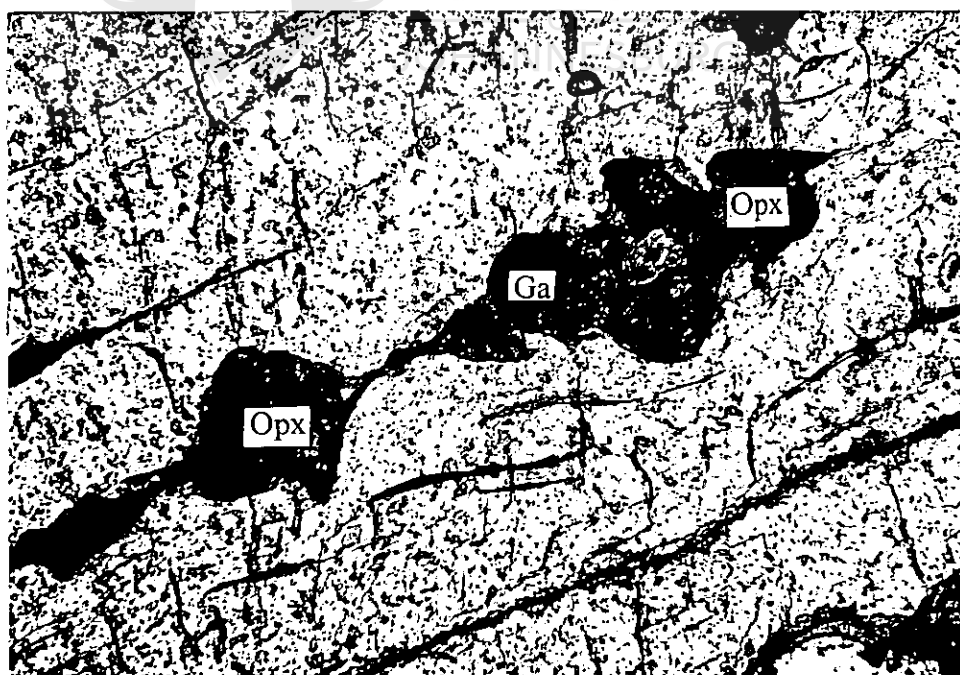


Figure 5.47: Microphotograph showing highly deformed fragments of ga-opx xenoblasts retrogressed into amphibole and orientated parallel to the vein margin and wall-rock foliation. The composition of the wall-rock in this case is identical to the fragments assimilated during the D<sub>2</sub> shear event within the newly formed shear zones and quartz veins. Sample DH 2067.

1cm=400 $\mu$ m



Figure 5.48: The same image as fig. 5.47, but with X-Nicols. The shear fabric is better highlighted. Sample DH 2067. 1cm=400µm

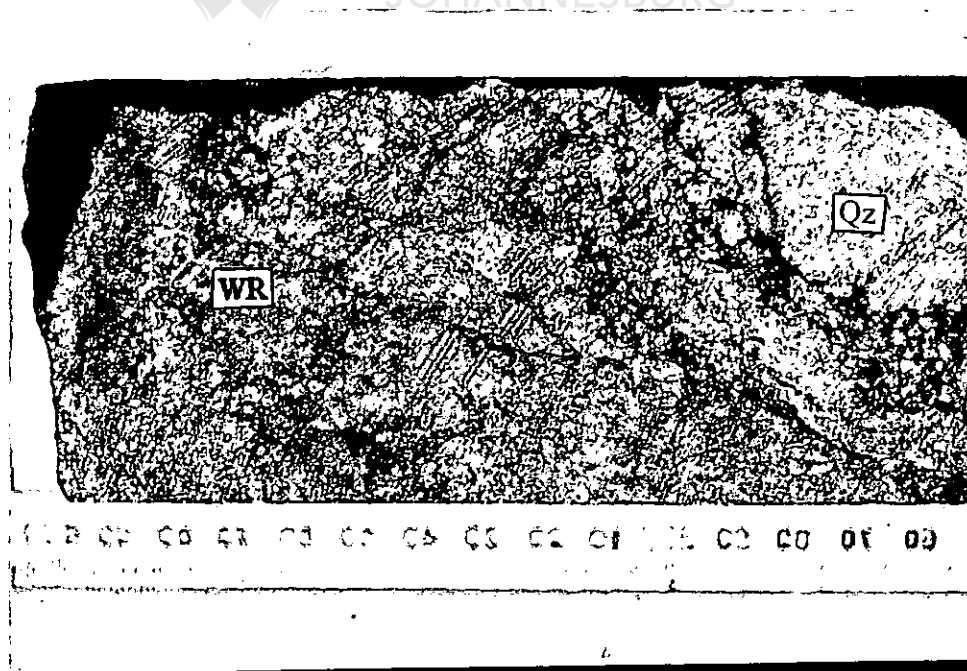


Figure 5.49: Brecciated character of a quartz vein (Qz) that hosts gold-related mineralisation and contains relics of opx, garnet and amphiboles from the wall-rock (WR). Borehole DD-2, sample DD2-11.



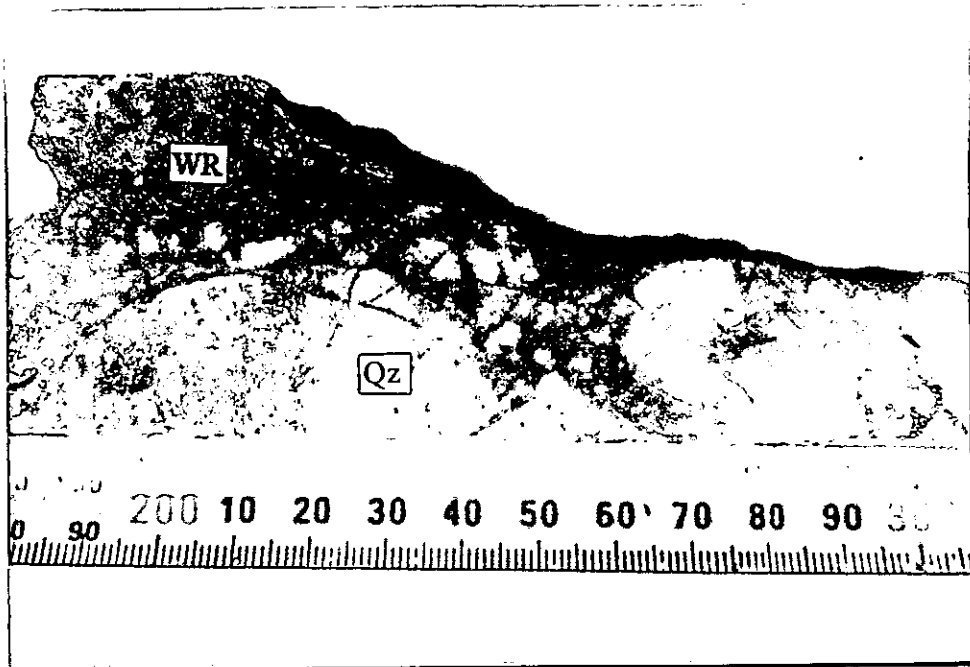


Figure 5.50: Brecciated features of a weakly mineralised quartz vein system (Qz). Note how the quartz "infiltrated" the wall-rock (WR). Borehole DD-2, Sample DD2-24.



## 6. MINERALOGY OF THE ORE BODY

The chemical composition of the minerals which are part of both the retrograde and prograde pattern rocks of the ore body and of the overthrust Baviaanskloof Gneiss varies drastically from unit to unit. The chemical features of the minerals reflect the bulk chemistry of the host lithologies. A comparison is also made between the composition of the same mineral in various lithologies, in order to obtain a better understanding of the chemical exchanges that occurred between minerals, during the evolution of the shear zone.

### 6.1 MINERAL CHEMISTRY OF THE GANGUE



**Plagioclase:** the plagioclase composition of the volumetrically significant Baviaanskloof Gneiss ranges between albite and andesine ( $An_6$ - $An_{38}$ ). The K-feldspar (orthoclase) content in the plagioclase varies from  $Or_0$  to  $Or_{11}$ . The An-content of the plagioclase gradually decreases towards the contact with the migmatic veins, where a higher Or-content is prevalent. Zoning of the plagioclase is within a limited range of +3.5 to -3 per cent An towards the rim for most of the samples analysed. This very limited range suggests a slow cooling rate.

In the ore body the plagioclase composition of the felsic granulite varies between  $An_0$ - $An_{60}$  (from almost pure albite to labradorite). The Ca-rich value of  $An_{60}$  is restricted to rare relic plagioclase that probably represents the composition of the initial plagioclase, before the rocks underwent metasomatic alteration. However, most of the relic plagioclase has a

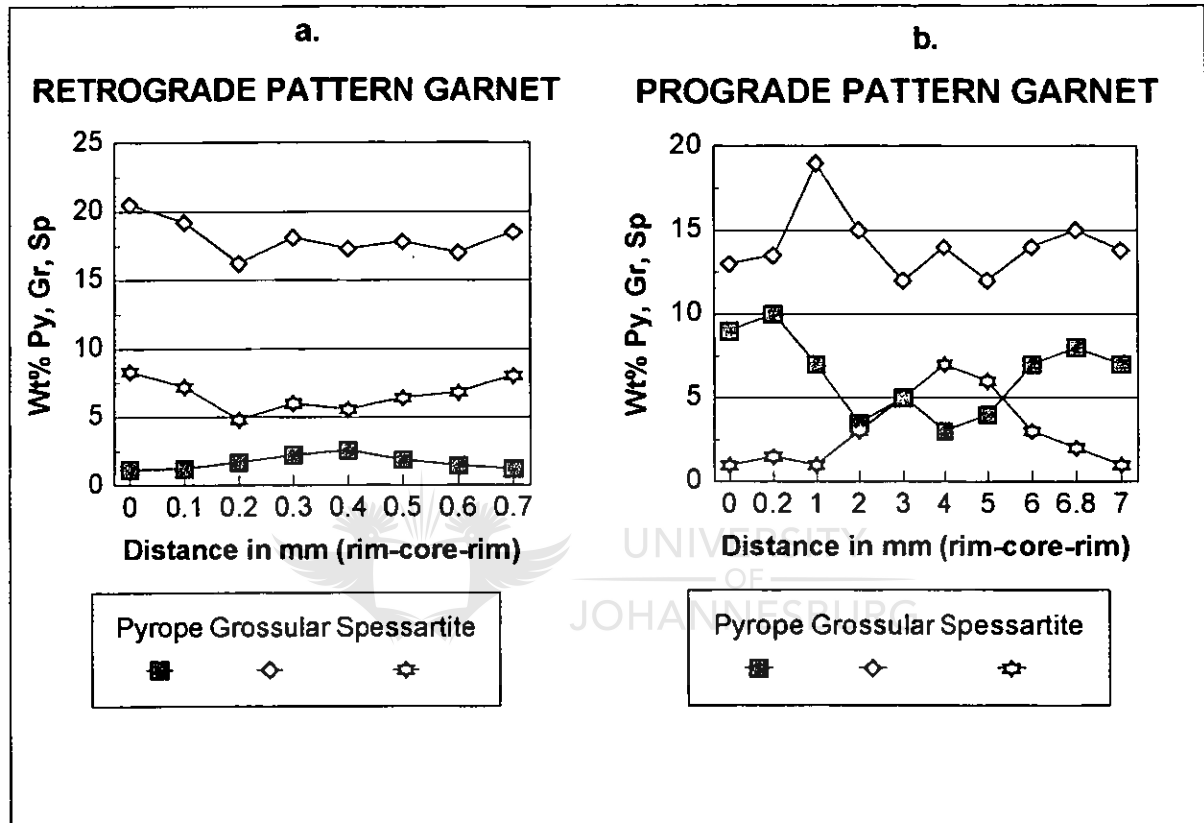
composition in the  $An_{46}-An_{48}$  range. During metasomatism the initial plagioclase was replaced by almost pure albite ( $Ab_{99.6}An_{0.1}Or_{0.3}$ ). Up to 40 per cent of the plagioclase in the matrix of the altered felsic granulite is almost pure albite, some of it resulted after the breakdown of plagioclase, and some newly introduced by the mineralising fluids.

**K-feldspar:** microcline-perthite is a major component of both the pink leucocratic veins and of the Baviaanskloof Gneiss associated with the Ore Body. This is an additional indicator of the intense metasomatism undergone locally by the Baviaanskloof Gneiss, because the gneiss, either hydrated or unhydrated, contains virtually no K-feldspar. The Or-content ranges from 87 to 94wt per cent and the Ab content from 5 to 11wt per cent. The An component is very low and varies from detection limit to a maximum of 3.3wt per cent. There is no major compositional variation from the Baviaanskloof Gneiss to the pink metasomatic veins, showing once more that K-feldspar is part of the same unique metasomatic alteration process. The high Si-Al ordering is an indication of either slow cooling or of metasomatic reactions. At the contact with the resorbed biotite a weak contamination with Fe is noticed in the perthite composition.

Orthoclase which occurs as a metasomatic alteration product in the felsic granulite is very pure. It ranges in composition from  $Or_{100}$  to  $Or_{93}Ab_6An_1$ . A very weak contamination by Fe and Mg is noticed in very close vicinity to resorbed biotite or garnet.

**Garnet:** Garnet in both the mafic and felsic granulite (retrograde pattern rocks) and in the biotite-garnetiferous formation (prograde pattern rocks) is almandine-rich (average formula  $Alm_{75}Pyr_{15}Spess_4Gr_6$ ). Two types of garnet were recognised (**fig. 6.1**):

- i) *partially resorbed (retrogressed) garnet* that occurs in the altered BIF and in the altered felsic granulite, and
- ii) *prograde garnet*, that formed in the biotite-garnetiferous formation as a result of metasomatic interaction between the mineralised fluids and the Fe-rich protolite.



**Figure 6.1:** Microprobe traverses of two garnet porphyroblasts showing the variation in the pyrope, grossular and spessartine contents.

**a.** typical retrograde pattern displayed by very small (< 1mm) garnet grains that occur as inclusions in large orthopyroxene. The core to rim increase in the spessartine content and the core to rim decrease in the pyrope content is clear. The grossular pattern is quite irregular.

**b.** typical prograde zoning pattern displayed by large garnet crystals (8mm) that form part of the metasomatic biotite-garnetiferous formation. The increase in the pyrope content from core to rim and the decrease in the spessartine content from core to rim is clear. The grossular variation is quite erratic.

Although these two type of garnet formed at different times and are characterised by different zoning patterns, they have very similar overall chemical compositions. This is probably due to the fact that the geochemical evolution of the metasomatic system was controlled by (Fe-rich) BIF-mafic lithologies.

**Biotite:** Biotite in the prograde biotite-garnetiferous formation shows a gradational variation of the Ti-content and the  $\text{Fe}^{2+}(\text{tot})/\text{Mg}$  ratio (**fig. 6.2**). The highest Ti-content was recorded in biotite included in the rim of the progradely zoned garnet porphyroblast. This biotite is red-brown in colour, reflecting the high Ti-content of up to 5.1 per cent (**appendix II, table II F, Biotite**). The colour is consistent with Hayama's study (1959) in which it was concluded that Ti and Fe are the elements that determine the pleochroic colour scheme of the biotite: high Ti-contents are responsible for a reddish-brown colour while high ferric ion results in a green pleochroism. However, it is the ratio of these two elements rather than the absolute values that determines the colour. Thus, a biotite with low Ti-contents might still be brown, provided that the  $\text{Fe}_2\text{O}_3$ -content is low.

It was found that the Mg/Fe ratio of biotite in the retrogressed rocks is different from the same ratio in the prograde biotite-garnetiferous formation. Biotite in both the altered felsic granulite and in the altered BIF is characterised by an increase in the Fe/Mg ratio from the core to the rim (**fig. 6.2**). The opposite pattern is shown by biotite in the prograde biotite-garnetiferous formation where the Fe/Mg ratio decreases from the core to the rim. This is probably due to the resorbtion of biotite and garnet in rocks with a retrograde zoning pattern of the garnet. In rocks with a prograde zoning pattern of the garnet the zonation of the Fe/Mg ratio is due to the growth of biotite and garnet (Woodsworth, 1977; Yardley, 1977). At

the same time Ti displays higher concentrations in biotite from the prograde lithologies compared with biotite from the retrograde lithologies.

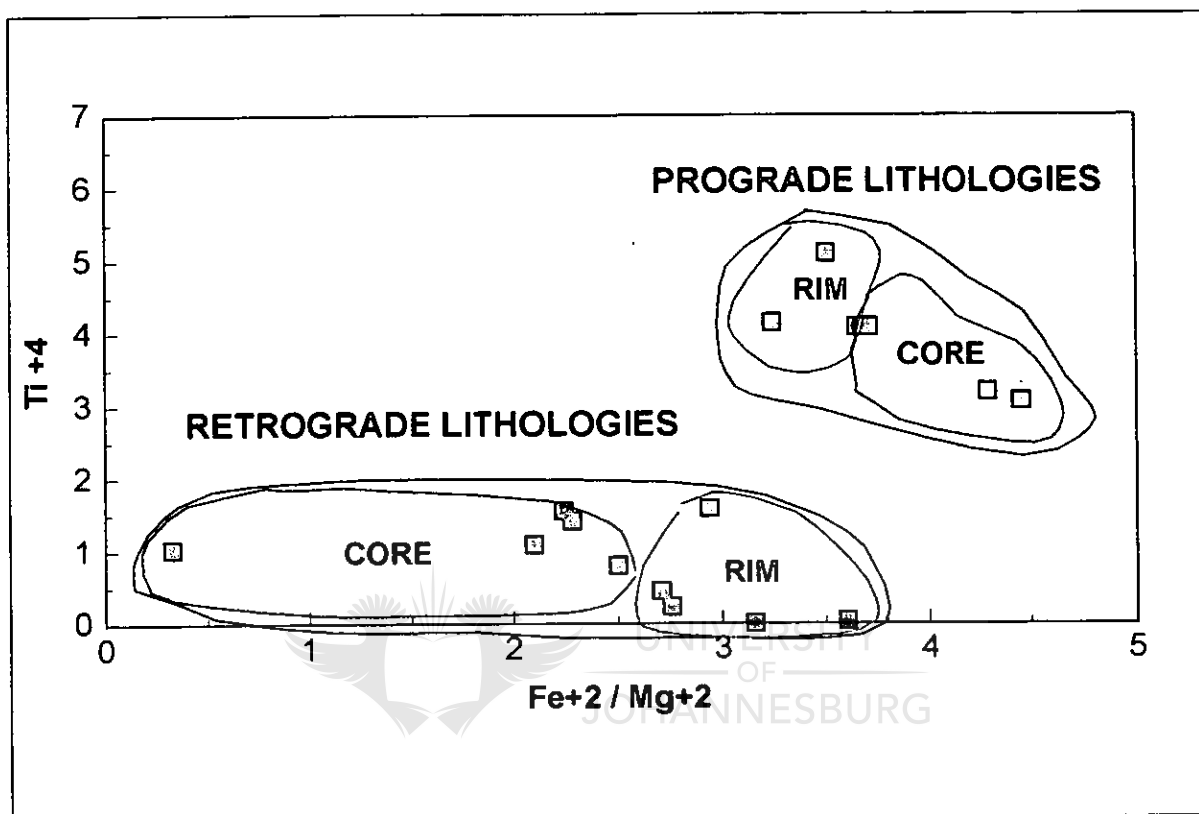


Figure 6.2:  $Ti^{4+}$ (%) versus  $Fe^{2+}(tot)/Mg^{2+}$  (microprobe analyses) for biotite compositions in the highly altered (metasomatised) lithologies (prograde lithologies - red) compared with biotite from the pervasively hydrated lithologies (retrograde lithologies - blue). Biotite associated with the prograde zoned garnet shows a higher Ti-content than biotite associated with the retrograde zoned garnet. Furthermore, the cores of biotite from the prograde zoned lithologies show a higher Fe/Mg ratio than the core of biotite associated with the retrograde lithologies, which usually shows enrichment in Mg.

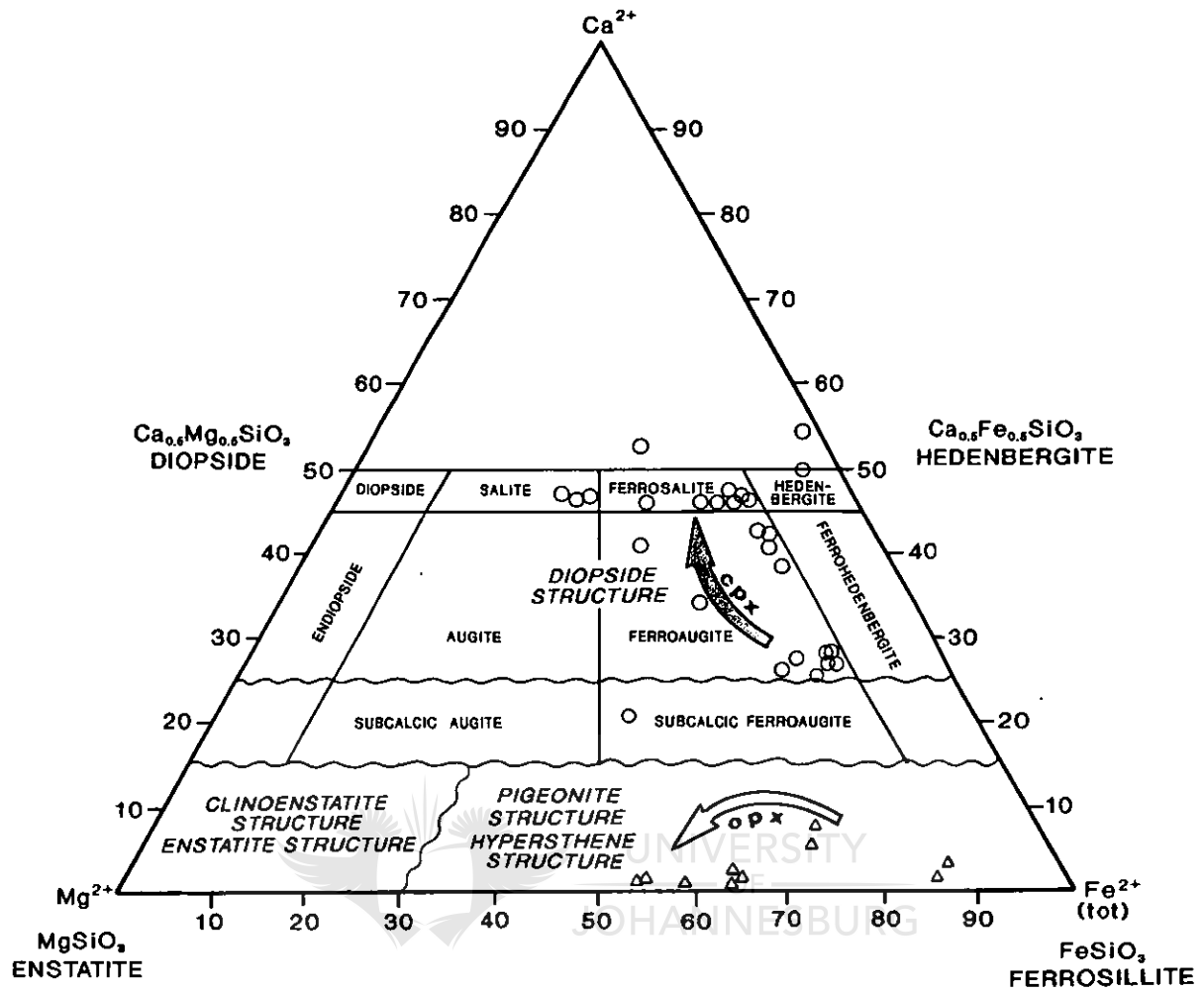
Biotite therefore reflects:

- i) the high-grade metamorphism undergone by the Doornhoek lithologies, as well as
- ii) the same zoning patterns as the rest of the lithologies, namely:

*the regional retrograde pattern* reflected by the hydrated lithologies not affected by channelised fluid flow, and *the local prograde pattern* in already hydrated lithologies that were also affected by intense fluid infiltration (metasomatic alteration).

**Orthopyroxene:** Orthopyroxene occurs as relics in the altered felsic granulite and as main phase in the granulite facies BIF. Orthopyroxene in the felsic granulite is a ferrohypersthene with a rather homogenous composition ( $En_{35}Fs_{65}$ ). In zones not much affected by channelised fluid flow the variation in the composition of orthopyroxene is very limited (ranging from  $En_{14}Fs_{86}$  to  $En_{27}Fs_{73}$ ). At the boundary with the prograde biotite-garnetiferous formation, most affected by the channelised fluid flow, the initial composition of the orthopyroxene, reflected by the core compositions, was in the ferrosilite-ferrohypersthene field  $En_{14}Fs_{86}$  (**fig. 6.3**). Due to metasomatic interaction with the mineralised fluids the orthopyroxene was enriched in Mg so that the composition moved towards the enstatite field ( $En_{45}Fs_{55}$ - $En_{35}Fs_{65}$ ) (**fig. 6.3**).

The composition of the orthopyroxene drastically varies according to the classification of Poldervaart and Hess (1951) (**fig. 6.3**). The wide variation in composition can be explained by the complex lithological composition of the Doornhoek Ore Body (Fe-rich opx in BIF, Fe-Mg amphiboles in the other lithologies). The initial variable composition of the orthopyroxene (due to differences in the chemical composition of the parental material) has been further changed as a result of interaction between the highly channelised mineralised fluids and the pre-existent silicate assemblage. Drastic rim-core-rim variations of the mineral composition have been recorded and preserved by orthopyroxene.



**Figure 6.3:** Nomenclature of pyroxenes in the system  $\text{CaMgSi}_2\text{O}_6$ - $\text{CaFeSi}_2\text{O}_6$ - $\text{Mg}_2\text{Si}_2\text{O}_6$ - $\text{Fe}_2\text{Si}_2\text{O}_6$  (modified after Poldervaart and Hess, 1951, in order to include the spatial distribution of the orthopyroxenes). Both orthopyroxene and clinopyroxene compositions are plotted on the same graph ( $\Delta$  represents orthopyroxene;  $o$  represents clinopyroxene; the red arrow indicates the chemical evolution of the opx during retrogression and alteration; the green arrow shows the chemical evolution of the cpx during retrogression and alteration).

**Clinopyroxene:** Cpx only occurs in lithologies of the granulite facies BIF and represents a primary pyroxene that crystallised together with opx. This suggests that the initial BIF-mafic lithologies, prior to the granulite metamorphic event that affected the SMZ, probably consisted of interlayering of BIF and mafic lava. The clinopyroxene also displays a sharp



variation in the core-to-rim composition, as follows: ferroaugite in the core (**fig. 6.3**) changing towards ferrosalitic-hedenbergitic in the rim. The average composition of the core is  $En_{14}Fs_{60}Wo_{26}$  and that of the rim  $En_{12}Fs_{42}Wo_{46}$ . In other words, the cpx reflects a strong depletion in Fe, a weak enrichment in Mg and a major enrichment in Ca. The Ca enrichment might be due to the breakdown of the initial Ca-rich plagioclase into albite, but some of it could be a result of the metasomatic interaction with the mineralised fluids.

This can be explained by the fact that the channelised fluids were probably rich in K, Na, Si and probably Ca, based on the composition of the mineralised veins and the observed mineral reactions.

**Amphiboles:** Amphiboles represent a major component related to the rehydration event that affected the southern margin of the SMZ of the LB (van Reenen, 1986). An example is the hydration reaction described by van Reenen (1986) in which gedrite and kyanite formed after cordierite, and anthophyllite after hypersthene as a result of the introduction of  $H_2O$  into the system. Three different types of amphibole occur at Doornhoek:

i) The main amphibole that formed as a retrograde product after Fe-rich pyroxene in the BIF lithologies of the Doornhoek Ore Body is Fe-rich: grunerite-ferrogedrite. (**fig. 6.4**).

ii) A second amphibole, anthophyllite formed in Mg-rich ultramafic lithologies as a replacement product of olivine.

iii) A third amphibole only formed in the case of intense alteration of precursor granulitic rocks. This type of actinolite represents a Ca-rich amphibole, formed probably as a result of residual enrichment in Ca (breakdown of initial plagioclase) and presumably introduction of Ca-rich fluids into the system.

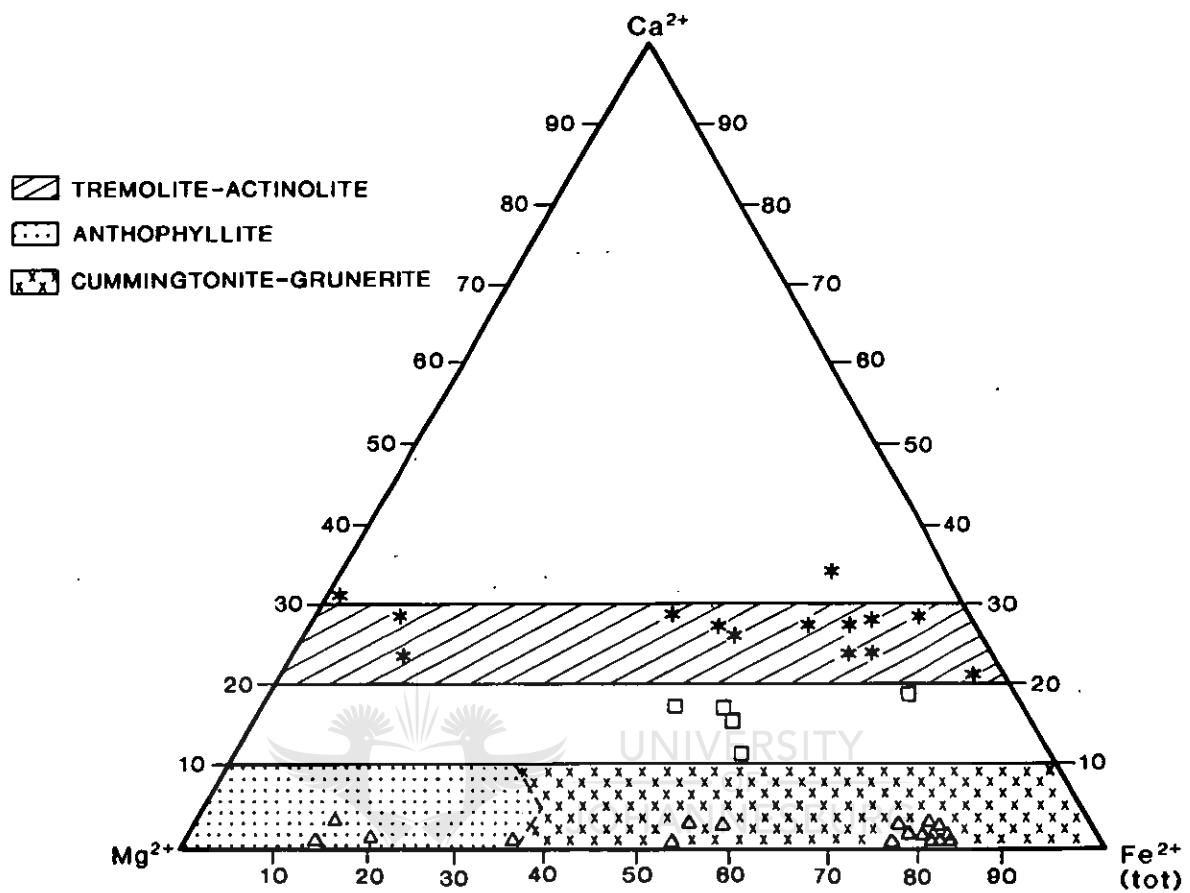


Figure 6.4: A Mg-Fe<sup>2+</sup>-Ca diagram for amphiboles in the absence of alkali metals and trivalent elements (after Whittaker, 1960). Symbols as in the legend. There are mainly three types of amphiboles in all rock types:

Δ ferrogedrite-grunerite and anthophyllite

\* actinolite-tremolite.

[ ] Al-rich amphiboles which do not plot accurately in this type of diagram.

Due to the intense alteration suffered by lithologies at Doornhoek, and the intimate transition between lithologies with very different bulk chemistries, a continuous transition in the amphibole composition occurs.

If present, hornblende is very Fe-rich and varies from ferroedenitic to a very Fe-rich type, probably bergamasikite(?). At the boundary between the ultramafic granulite and the BIF, grunerite-ferrogedrite in the BIF changes in composition towards a gedrite (Mg enrichment)

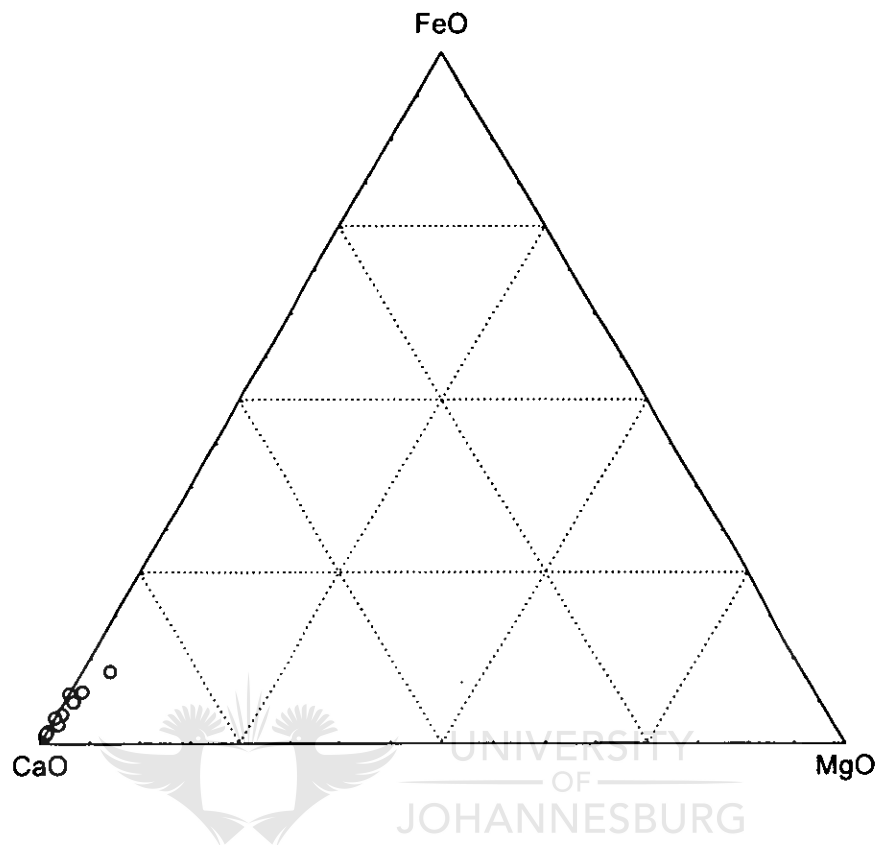
while anthophyllite in the ultramafic granulite also changes towards gedrite (Fe and Al enrichment relative to anthophyllite) (**fig. 6.4**).

The amphiboles are highly zoned from core to rim. Gedritic amphibole changes to ferrogedrite in the rim in the magnetite-free lithologies, while grunerite becomes a Fe-rich hornblende in the magnetite-bearing lithologies. This last type of alteration is very unusual, requiring enrichment in both Fe and Al.

**Tourmaline:** Tourmaline present in the Doornhoek Gold Deposit is a product of boron metasomatism. The fact that tourmaline is always associated with K-feldspar and albite suggests that the boron alteration is part of the major metasomatic event that affected the entire deposit. The composition of the tourmaline is weakly alkaline with moderate amounts of Na (1.85-2.67wt per cent  $\text{Na}_2\text{O}$ ) and K (up to 0.67wt per cent  $\text{K}_2\text{O}$ ) which complements the chemical nature of the Doornhoek alteration. The tourmaline is geochemically a mixture of dravite (Mg-rich) and schörl (Fe-rich). The colour of the tourmaline (very dark blue, **fig.10.3**) also reflects the composition of the mineral: dravite is brown and schörl is black.

**Carbonates:** The carbonate that very seldomly occurs in the quartz veins is always a ferroan calcite, with FeO ranging from 0.66 to 6.87wt per cent (**fig.6.5**). This is the normal composition of hydrothermal calcite associated with gold deposition in greenstone belts (either ferroan or manganoan calcite) (Colvine et al., 1988). Taking into account that Doornhoek represents a high metamorphic grade gold deposit it is clear that the same type of carbonate did not precipitate continuously from granulite facies to greenschist facies conditions. The primary carbonate that only very seldomly crystallised from the high-grade

mineralised fluids was probably calcite. This calcite was contaminated by Fe liberated from the BIF that represents the main rock type at Doornhoek.



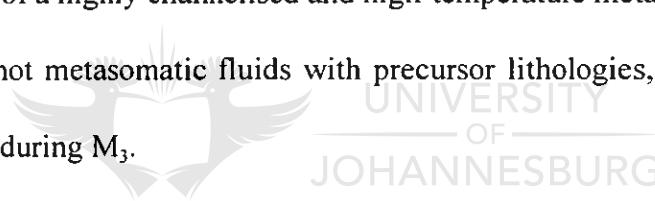
**Figure 6.5:** Ternary diagram showing the composition of calcite present in some of the quartz veins. The carbonate is a ferroan calcite with up to 6.87wt per cent FeO.

## 6.2. CHEMICAL ZONATION OF SILICATES AND RELATED TEXTURES

Two major structural units occur within the area of the Doornhoek Gold Deposit:

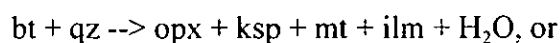
- i) the predominantly BIF-mafic lithologies that include the Ore Body and
- ii) the overthrust Baviaanskloof Gneiss.

From a metamorphic point of view the ore body consists of a mixture of metamorphic rocks characterised by retrograde features and metasomatic rocks characterised by prograde features. The retrograde rocks suffered peak metamorphic conditions during  $M_1$  and subsequently underwent retrogression during  $M_2$  and  $M_3$ . These lithologies therefore participated in the entire metamorphic history of the SMZ. The prograde rocks on the other hand are the products of a highly channelised and high-temperature metasomatic event related to the interaction of hot metasomatic fluids with precursor lithologies, next to the  $D_2$  shear zones, most probably during  $M_3$ .



### 6.2.1 Baviaanskloof Gneiss

This grey tonalitic gneiss is characterised by the presence of pinkish leucocratic veins, that consist mainly of microcline-perthite and albite. In the vicinity of the Doornhoek Gold Deposit the Baviaanskloof Gneiss very seldomly preserve relics of prograde mineral reactions such as:



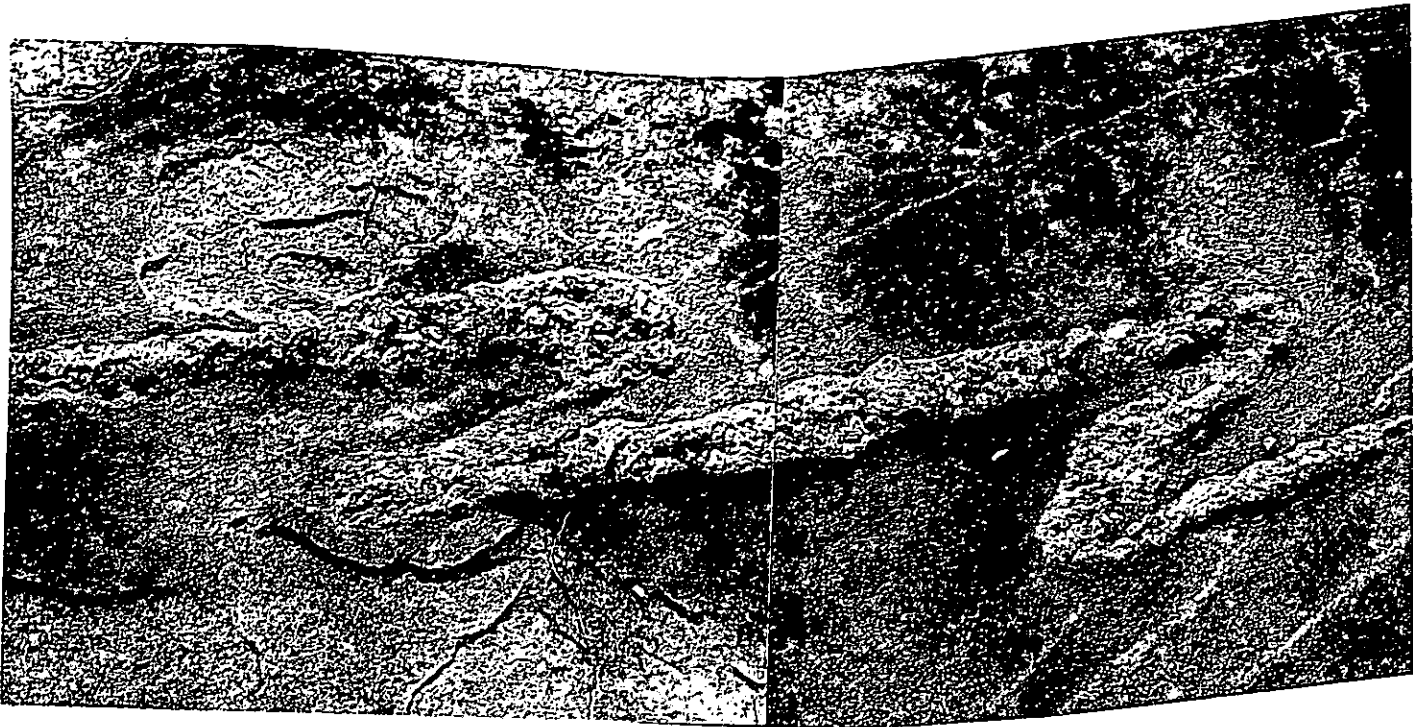


Figure 6.6: Sample 2101: Baviaanskloof Gneiss outcropping at Doornhoek Farm. Photograph showing newly formed folded metasomatic leucocratic veins consisting of microcline-perthite and albite, crosscutting the grey tonalitic Baviaanskloof Gneiss.

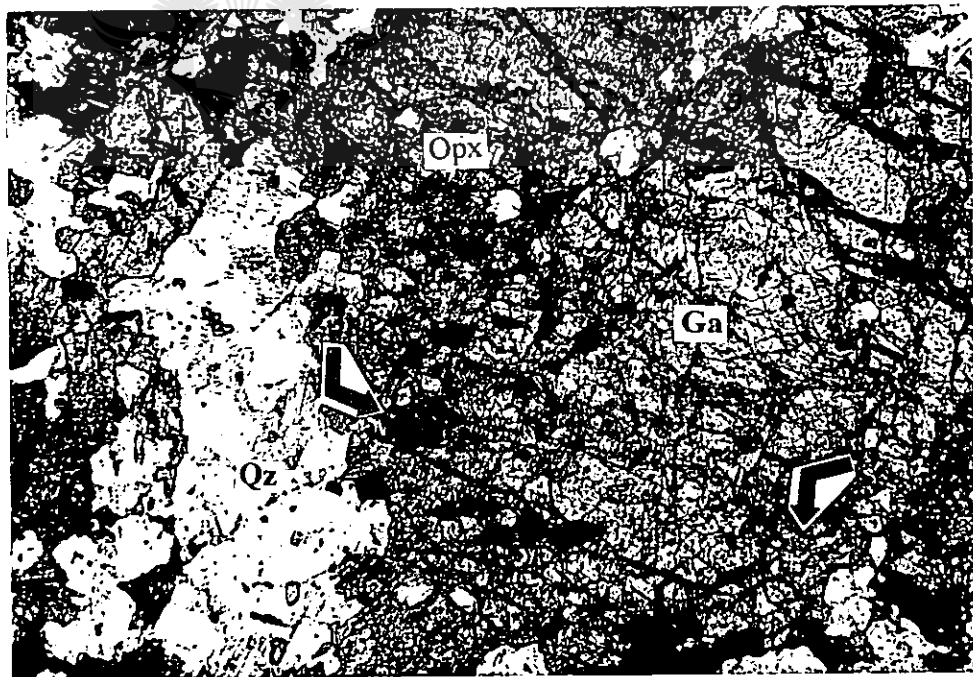


Figure 6.7: Sample DH 2106, Baviaanskloof Gneiss outcropping at Doornhoek Farm. Microphotograph showing a garnet porphyroblast (Ga) surrounded by orthopyroxene (Opx). The orthopyroxene is replaced by biotite (blue arrows) and later introduced quartz (Qz).

1cm=100 $\mu$ m

in which orthopyroxene formed at the expense of biotite and quartz. Additional evidence for relic prograde reactions are the presence of tiny inclusions of plagioclase in magnetite, which may indicate that the same reactions which produced magnetite and/or ilmenite also produced plagioclase. But indications of these types of prograde mineral reactions are never encountered within the Doornhoek area.

Biotite in the banded gneiss is orientated parallel to the banding and this preferred orientation becomes even more prominent towards the shear zones, where the  $D_2$  fabric is well expressed.

The prograde formation of orthopyroxene in a metamorphic rock requires a very low activity of water. One possible way of achieving this condition is through the infiltration of  $CO_2$ -rich fluids which initiate dehydration reactions of biotite to produce orthopyroxene and the subsequent dilution of the released water with the  $CO_2$  could stabilise anhydrous minerals (e.g. Frost and Frost, 1987). The fact that the Baviaanskloof Gneiss was so highly migmatized **fig. 6.6** (Stevens and Van Reenen, 1992) indicates that granulite metamorphism and migmatization were closely associated. In order to avoid wide-spread melting reactions during granulite metamorphism (absent in the SMZ), the activity of water must have been very low, such as the 0.1-0.3 estimated for the amphibolite-to-granulite transition in the Archaean terrain of south-west Greenland (Wells, 1979).

The reverse of the prograde reactions during the retrograde P-T path of the LB history is documented by the replacement of orthopyroxene by biotite and quartz (**fig. 6.7**). The absence of K-feldspar in these retrograde reaction textures indicates that it was largely consumed

during formation of retrograde (and sometimes prograde!) biotite and that the replacement of orthopyroxene by biotite was limited by the amount of K-feldspar present in the rock (Bohlender, 1992). Locally hornblende, formed mostly after clinopyroxene, occurs as a reaction product during the same retrogressed event.

### 6.2.2 Doornhoek Ore Body

The Doornhoek Ore Body was formed during the retrograde stage of the evolution of the SMZ as the result of metasomatic fluids that were channelled along shear zones. Lithologies associated with the Ore Body therefore demonstrate evidence for two distinct stages of this evolution:

i) the first stage is regional retrograde metamorphism associated with the establishment of the retrograde isograd within the zone of retrogressed granulites that bound the SMZ in the south (fig. 4.1.). These reactions involved the replacement of hypersthene by anthophyllite ( $\text{Opx} + \text{Qz} + \text{H}_2\text{O} = \text{Anth}$ ), and cordierite by gedrite and kyanite ( $\text{Cord} + \text{H}_2\text{O} = \text{Ged} + \text{Ky} + \text{Qz}$ ) in pelitic granulites, as well as the replacement of both orthopyroxene and clinopyroxene by amphibole in mafic and ultramafic granulites.

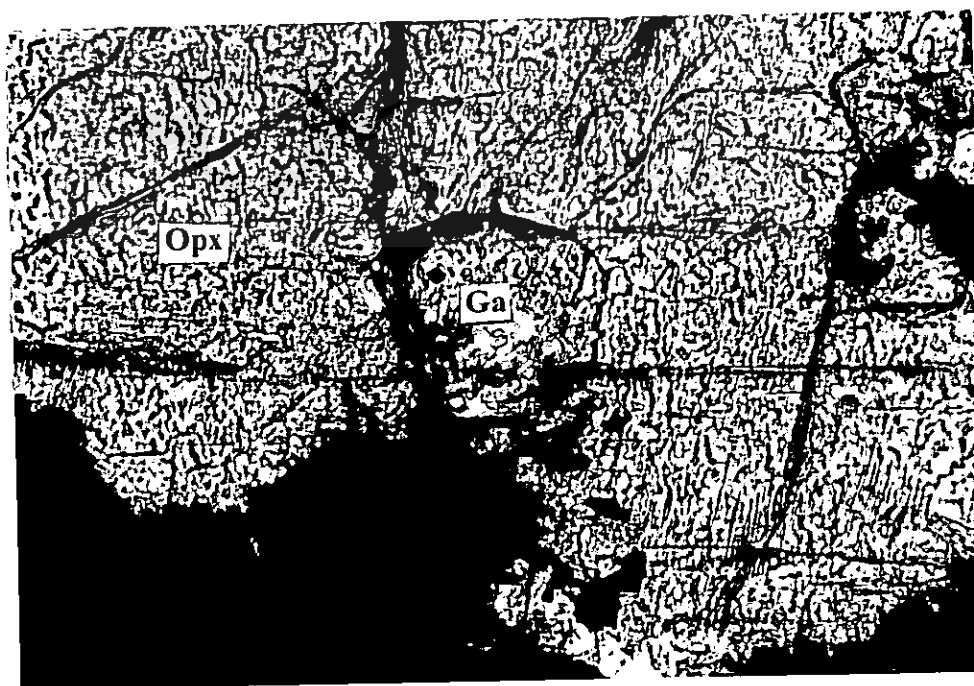
ii) the second stage is represented by prograde reactions associated with highly channelised metasomatic fluids and resulted in the formation of the zoned metasomatic garnet in the *biotite-garnetiferous formation*. This garnet displays clear evidence for prograde growth zoning. Associated with the metasomatic growth of garnet is the introduction of mineralised quartz veins in which the presence of arsenides (arsenopyrite and löllingite) suggests that the deposition of gold-related mineralisation also occurred during prograde growth.



### 6.2.2.1. Reactions reflecting resorbtion (retrogression) of garnet

#### 6.2.2.1.1. Garnet

The best example of resorbed garnet is illustrated by the presence of relic garnet included in large orthopyroxene crystals in the highly altered BIF-mafic granulite (fig. 6.8). These garnets are usually very small in size and almost completely resorbed by the orthopyroxene. Due to diffusion, intense Fe/Mg exchange with the host orthopyroxene took place during the retrograde cooling. Geochemical distribution maps of these garnets shows typical retrograde zoning patterns (fig. 6.9.a, b and c).



**Figure 6.8:** Sample DD-2-2014: BIF. Microphotograph showing a small relic of garnet (Ga) included in a large orthopyroxene crystal. This garnet typically displays retrograde zoning probably due only to diffusion (Fe/Mg exchange).

1cm=50µm

The analysed garnet was mapped with a Cameca Camebax Electron Microprobe in the Geology Department at Rand Afrikaans University, and the results are as follows:

i) *Pyrope distribution*: the garnet is predominantly almandine in composition. To obtain a decent variation of Mg distribution within the garnet crystals the molar ratio  $Mg/(Mg+Fe)$  was used. This calculation procedure is also used by other authors for highly almandinic garnets (Tucillo et al., 1990).

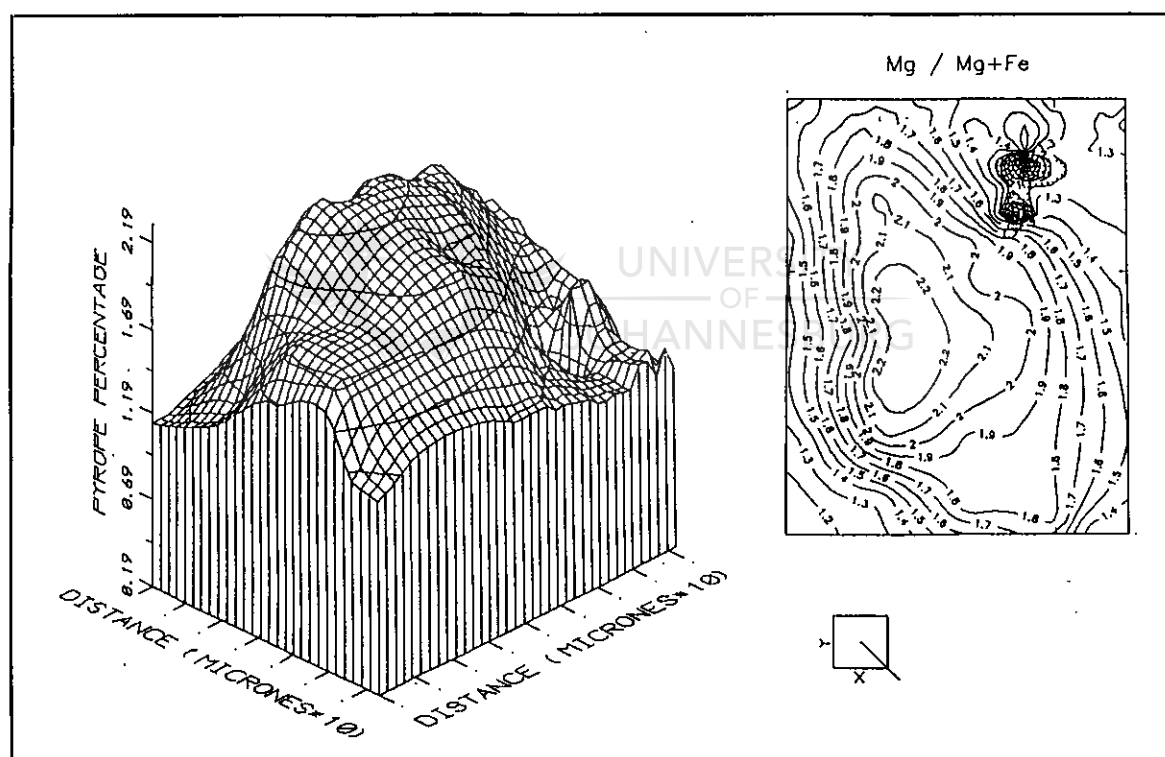


Figure 6.9: a) Pyrope, spessartine and grossular distribution within a partially resorbed garnet showing retrograde zoning (microphotograph in fig. 6.8). The garnet is predominantly almandine in composition. Although the  $Fe/(Fe+Mn+Mg+Ca)$  ratio is relatively high, the pyrope, spessartine and grossular ratios are still highly variable. The  $Mg/(Mg+Fe)$  ratio shows a decrease from core to rim, from 2.2 to 1.2 per cent;

The pyrope distribution  $[Mg/(Mg+Fe)]$  (fig. 6.9a) shows a slight decrease of 1 per cent from core to rim. The  $Mg/(Mg+Fe)$  ratio decreases from 2.2 per cent (rim) to 1.2 per cent (core). The decrease from the core to the rim is continuous and sharp, showing the Fe/Mg exchange of the garnet with the orthopyroxene host during cooling. Thus, the garnet becomes Fe-rich and the orthopyroxene Mg-rich during the retrograde cooling.

ii) *Spessartine distribution*: the spessartine molar distribution  $[Mn/(Mn+Mg+Fe+Ca)]$  increases with 2.4 per cent from the core (5.6 per cent Sp) to the rim (up to 8 per cent Sp) (fig. 6.9b). The distribution is not homogenous, certain parts of the rim showing only 6.2 per cent Sp (the NW corner of the mapped garnet). However the 5.6 per cent Sp is not the minimum value, there are two areas of minimum spessartine distribution, lower than 5 per cent, towards the NE corner of the garnet.

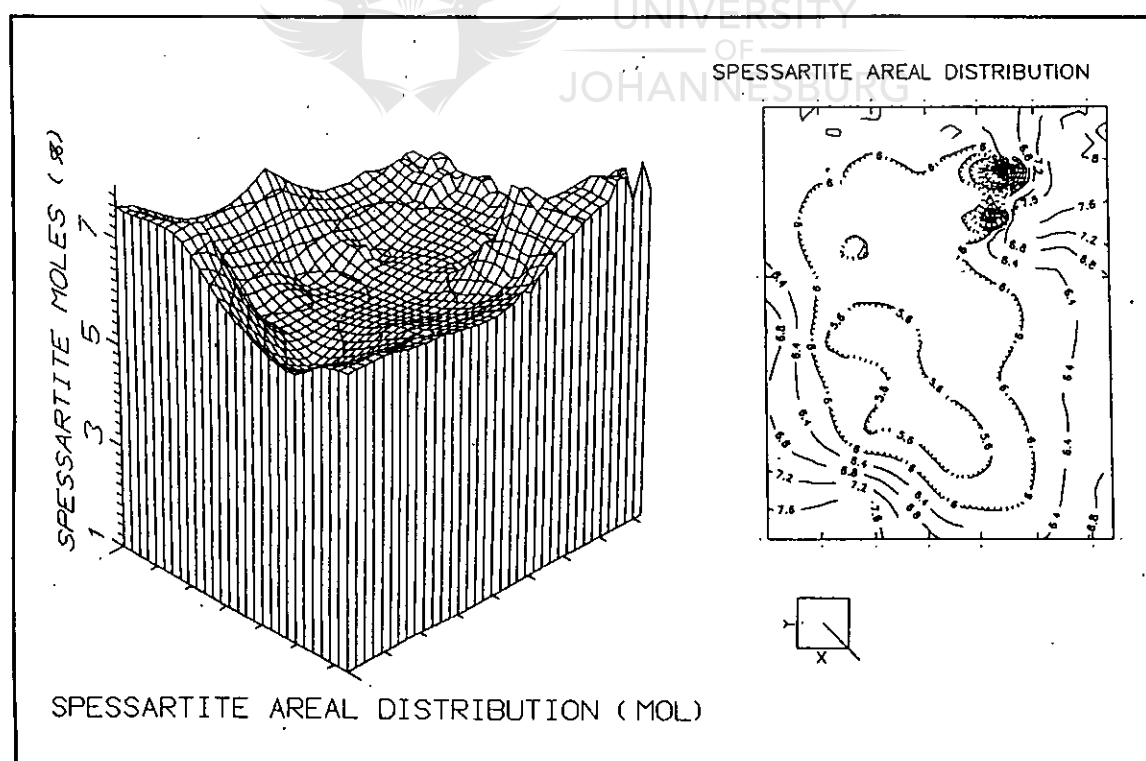


Figure 6.9.b: The  $Mn/(Mn+Mg+Fe+Ca)$  ratio increases from a low of 5.6 per cent in the core of the garnet to a high of 8 per cent towards the rim of the porphyroblast. This variation of the Mn content within the garnet porphyroblast is typical retrograde.

iii) *Grossular distribution*: the grossular molar distribution  $[Ca/(Mn+Mg+Fe+Ca)]$  is less regular in comparison with that of pyrope and spessartine. There are three areas of minimum grossular distribution: one in the NE corner (15 per cent Gr), one in the SE corner (17 per cent Gr) and a larger area in the W side of the garnet (also 17 per cent Gr) (fig. 6.9c). There is a *ridge* of maximum grossular molar concentration (almost 18 per cent Gr) between the two minimal values of 17 per cent Gr, and a continuous increase towards the rims of the garnet, where the maximum value reached is 20 per cent grossular. In other words, there is a variation of 5 per cent Gr between the minimum and the maximum values. The grossular distribution is more erratic, probably due to the slower diffusion of the Ca ion within the garnet lattice during retrograde reactions (Tucillo et al., 1990).

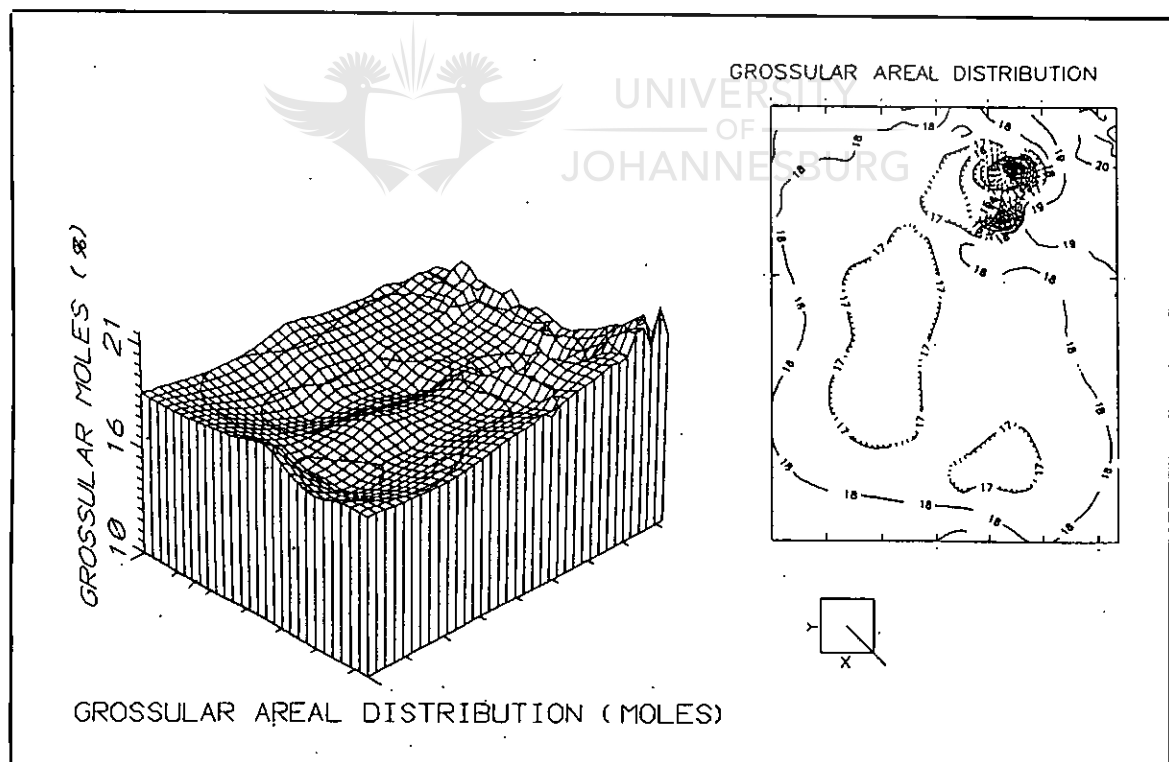


Figure 6.9.c: The  $Ca/(Ca+Mn+Mg+Fe)$  ratio shows a *positive ridge* of almost 18 per cent in the middle of the crystal. The grossular ratio decreases softly to a minimum of 17 per cent and then increases sharply to more than 20 per cent.

A similar retrograde zoning pattern is shown by garnets which are not included in orthopyroxene crystals in the magnetite-bearing BIF, but hosted by felsic granulite at the boundary with BIF. This lithological boundary was highly deformed under high-grade conditions (fig. 6.10 and 6.11).

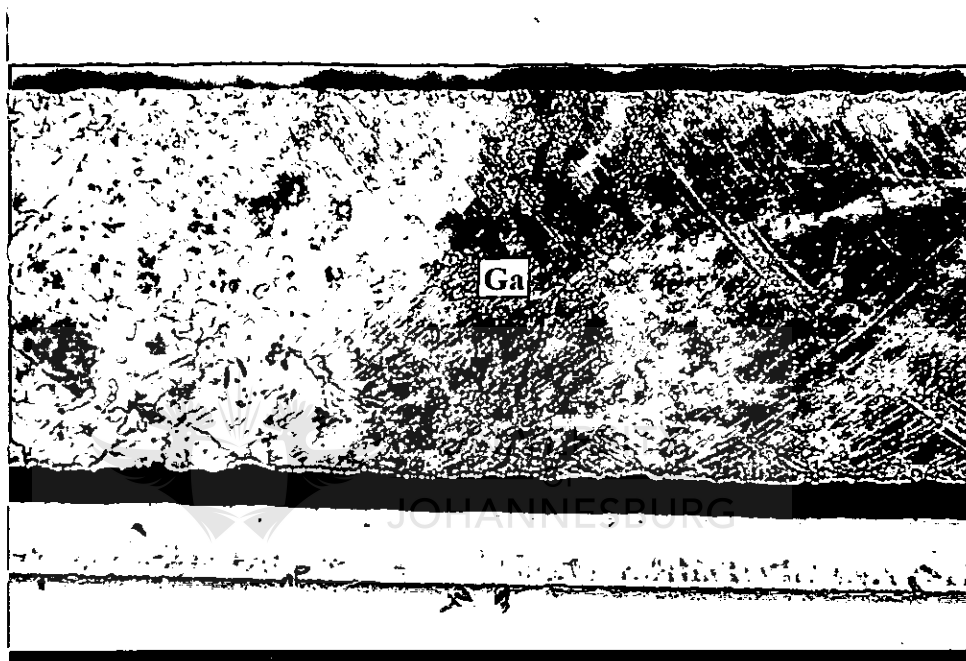


Figure 6.10: Photograph of borehole DD-7, 47.23-47.30 m showing retrograde zoned and elongated garnets in a felsic granulite. This garnet (Ga) is clearly pre-tectonic, being deformed during the deformational event that accompanied metasomatism.

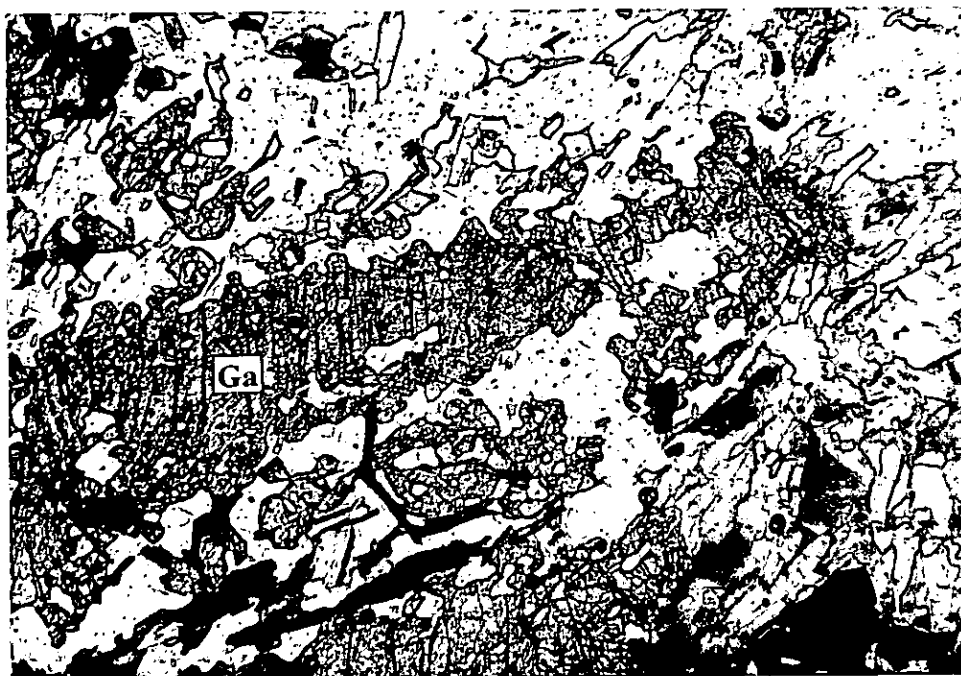


Figure 6.11: Sample DH-2139: Highly altered felsic granulite. The microphotograph displays elongated garnets (Ga) from fig. 6.10 under the polarising microscope. One can see a system of shear joints developed within the rods-like garnets, a close association between garnet and Ti-rich biotite, and a relatively high amount of graphite (opaque).

1cm=400μm

JOHANNESBURG

#### 6.2.2.1.2. Orthopyroxene

Another example of retrogression is shown by orthopyroxene in both the calc-silicate facies BIF granulite (fig. 6.8) and the felsic granulite. Usually the orthopyroxene displays Mg-richer cores than rims ( $En_{26}Fs_{74}$  in the core and  $En_{14}Fs_{86}$  in the rims). The  $Al_2O_3$ -content of the orthopyroxene is very low and as a result the Al variation is of little importance. But when opx is in direct contact with garnet, the opx has a very thin rim more Mg-rich than the rest of the edge of the crystal. Therefore, it was suggested that the same diffusion mechanism of the Mg and Fe ions that occurred in the retrogressed garnets also occurred in the pyroxenes.

### 6.2.2.1.3 Biotite

Biotite from the highly altered felsic and mafic granulite (usually lithologies displaying retrograde pattern) always shows a higher Mg/Fe ratio in the cores than in the rims. But where biotite directly replaces garnet, a very thin edge of the biotite is always more Mg-rich than the rest of the rim of the biotite crystal. Therefore, garnet exchanged Fe/Mg with the newly formed biotite due to diffusion mechanism, but for a short period of time, considering that textural relationships demonstrate the replacement of garnet by biotite (**fig. 6.12**) and not a continuous, simultaneous crystallisation. The TiO<sub>2</sub>-content is higher in the core than in the rim of the same analysed biotite crystals. This pattern is probably due to the general retrogression of biotite, as well as garnet and orthopyroxene (**fig. 6.12**) in the retrograde pattern lithologies.



Figure 6.12:

Sample DH-7-23: Highly altered felsic granulite at the boundary with magnetite-rich BIF. The microphotograph shows biotite replacing garnet (yellow arrow). Both the garnet (Ga) and the biotite (Bi) display a typical retrograde pattern, excepting a very thin contact between the two reacting minerals. The garnet in contact with biotite is more Fe-rich than the garnet core, while the biotite shows the opposite. But when the biotite is not in direct contact with garnet, the Mg/Fe ratio in the core of the biotite is always higher than in the rims, as well as the TiO<sub>2</sub>-content. This red biotite shows a very high Ti-content, indicative of initial high-grade metamorphism undergone by the rock.

1cm=400µm

#### 6.2.2.2. Prograde pattern reactions and textures

The main feature of the Doornhoek Ore Body is the presence of retrogressed granulite that was completely metasomatised. These zones include mineralised quartz veins and the so-called biotite-garnetiferous formation (**fig. 6.13** and **6.14**). Their textural features, relationship with adjacent lithologies (**fig. 5.43, 5.44** and **5.45**) and mineralogical composition show that these rocks were mainly formed due to the interaction between already retrogressed BIF granulite and hot metasomatic solutions.

##### 6.2.2.2.1. Garnet

Garnet in the biotite-garnetiferous formation occurs as euhedral porphyroblasts in a matrix consisting mainly of biotite and quartz (**fig. 6.13** and **6.14**). Biotite also occurs as inclusions in the garnet. The euhedral garnet porphyroblasts display a very well preserved prograde zonation pattern with a distinct black inner ring (**fig. 6.14**) that consists of numerous inclusions of sulphides, Ti and Fe oxides and gold. Graphite is always present in this rock type, either intergrown with biotite in the matrix, or as inclusions in the garnet.

The prograde zonation of this garnet consists of the following zones that can be optically identified (**fig. 6.15** and **6.16a, b** and **c**):

*a core (yellow),*

*an inner zone (red), marking the transition from the core to the dark inner ring,*

*a dark inner ring (pink and dashed), and*

*a wide edge zone (white).*



All these zones are part of the prograde zonation pattern exhibited by the garnet porphyroblast. The pyrope (Mg) and spessartine (Mn) distribution (mol%) within the garnet porphyroblast shows the following:

*core (yellow)*: Mg slowly increases from 3 to 4 per cent, while Mn decreases from 7 to 5 per cent

*inner zone (red)*: Mg slowly increases from 4 to 5 per cent while Mn decreases from 5 to 4 per cent

*dark inner ring (pink)*: Mg slowly decreases from 5 to 3.5 per cent, while Mn remains almost constant, varying around 4 per cent

*edge zone (white)*: Mg sharply increases from 3.5 to 10 per cent, while Mn sharply decreases from 4 to 1 per cent.

It is suggested that the decrease in the Mg content within the black inner ring can be explained by the energy consumption (heat) during the crystallisation of the very numerous and very fine crystals of sulphides and oxides in the zone. For a similar reason, the Mn content remains almost constant.

Mineralisation that occurs in the core zone and in the inner ring zone, also shows a prograde pattern outwards (i.e. arsenopyrite in the core and löllingite in the inner zone, or As-poor arsenopyrite in the core and As-rich arsenopyrite towards the external part of the inner zone) (Chapter 7).

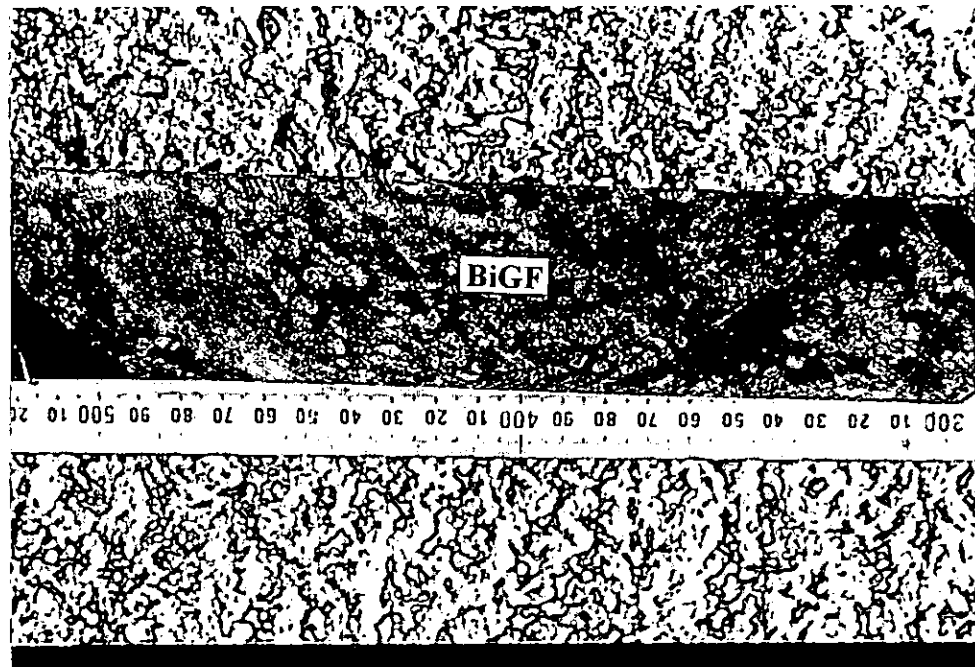


Figure 6.13: Photograph of borehole DD-2, 67.30-67.52m, sample DD2-35. Folded layers of the biotite-garnetiferous formation (BiGF) representing the product of intense potassic metasomatism.



Figure 6.14: Sample DD-2-35: Biotite-garnetiferous formation. Microphotograph of the borehole chip displayed in fig. 6.13. These prograde zoned garnets are surrounded by biotite and smaller amounts of quartz. The dark core is characterised by the presence of numerous very fine grained inclusions consisting of ilmenite, magnetite, graphite, sulphides, arsenides and gold.

1cm=750 $\mu$ m



Figure 6.15:

Sample DD-2-35: Biotite-garnetiferous formation. Microphotograph of a large euhedral zoned porphyroblast of garnet. Both the garnet and the associated biotite display a typical prograde growth zoning pattern. The garnet consists of four concentric zones which are better illustrated in fig. 6.16: a mineralised core (yellow), an inner zone (red), a black inner-ring (pink) and a wide rim (white). Mineralisation is mainly present within the core and the inner-zone, and it also displays a prograde pattern (see text). Biotite inclusions (arrows) coloured black in fig. 6.16 occur throughout the garnet, from core to edge. The gold mineralisation is associated with arsenides and graphite, usually in the inner zone and inner-ring.

JOHANNESBURG

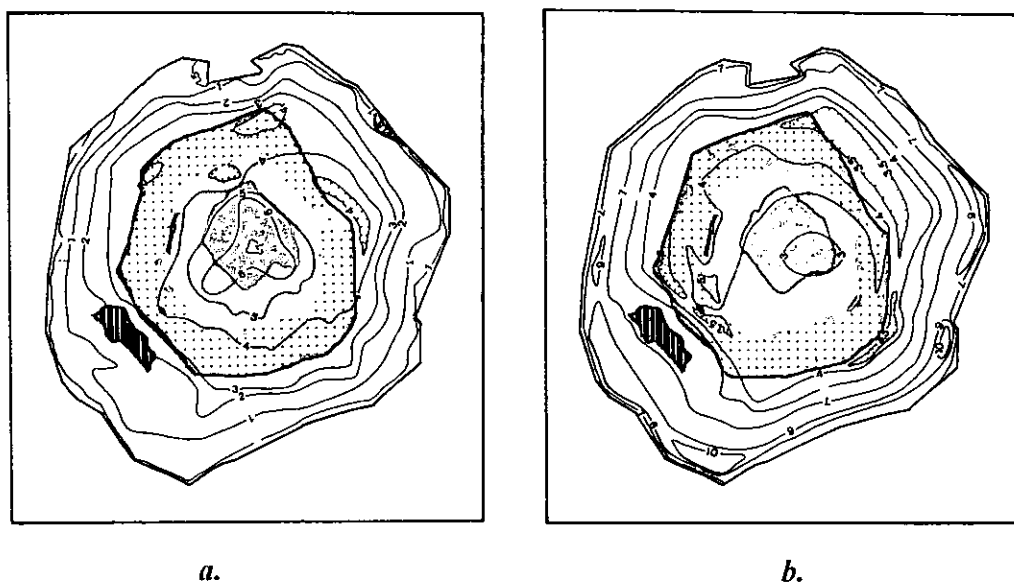
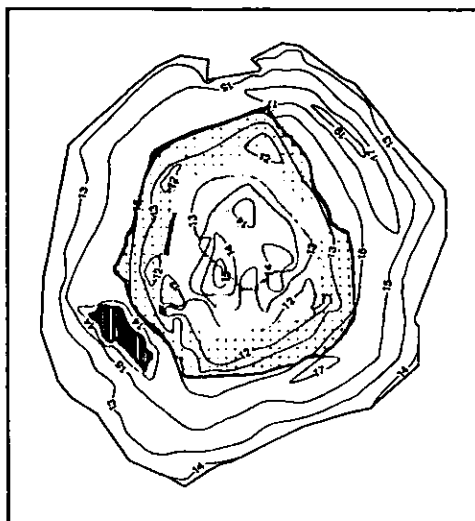
1cm=1000 $\mu$ m

Figure 6.16:

The prograde zonation pattern of this garnet is best shown by *a*) the pyrope  $[Mg/(Mg+Fe)]$  ratio and by *b*) the spessartine distribution  $[Mn/(Mn+Mg+Fe+Ca)]$ . These molar distributions are based on 800 microprobe point analyses.

a)  $Mg/(Mg+Fe)$  increases from core to rim, from 3 to 10wt per cent.

b) Spessartine molar ratio decreases from 7wt per cent in the core to 1wt per cent to the very edge.



**Figure 6.16.c:** Grossular molar ratio displays a relative random distribution from 14 per cent in the core, decreasing to 12 per cent towards the inner ring, increasing to 19 per cent and decreasing again sharply to 13 per cent towards the edge.

*i) Pyrope distribution:* the  $Mg/(Mg+Fe)$  ratio increases from 3 per cent in the core to more than 10 per cent to the rim (**fig. 6.16a**). The increase in the pyrope ratio inside the core is gradational, from 3 to 4 per cent. The same slow increase in the pyrope ratio continues inside the inner zone, from 4 to 5 per cent. The increasing trend is discontinued inside the black inner ring, where the pyrope ratio decreases from 5 to 3.5 per cent, being relatively constant at about 4 per cent pyrope. From the inner ring towards the edge zone, the pyrope ratio increases very sharply from 3.5-4 per cent to 10 per cent. The maximum content of 10 per cent pyrope is not reached all over the rim but only in certain places (the southern and the western edge of the garnet - **fig. 6.16a**). There is a very thin retrogressed zone at the very edge of the garnet, which displays a sharp decline from 10 to 7 per cent  $Mg/(Mg+Fe)$ .

The increase in the Mg/(Mg+Fe) ratio is therefore not continuous. As already described the zone in which the Mg/(Mg+Fe) ratio decreases coincides with the black inner ring - (fig. 6.15 and 6.16a). This zone might be interpreted as a slow growth zone, probably due to the fact that the heat liberated by the metasomatising fluids during the crystallisation of the garnet has been used for the precipitation of the sulphides and oxides and not for the garnet growth. Thus, although garnet continued the process of crystallisation at that stage, its growth pattern shows retrogression due to losses of lattice energy at the time when mineralisation was entrapped. After mineralisation was entrapped in the garnet, the heat liberated by the metasomatising fluids was probably very high in order to produce such a sharp increase in pyrope towards the rim.

A very important conclusion follows from the observed zonation of garnet: the fluids transporting the mineralisation precipitated most of their metallic load during the early stages of the shearing-mineralisation process. Although the shearing and fluid percolation continued well after the mineralising stage, no more ore minerals, but only gangue minerals, were deposited. The mineralising activity of this high-grade metasomatic process was therefore probably concentrated during the early part.

ii) *Spessartine distribution*: the spessartine molar ratio  $[Mn/(Mn+Mg+Fe+Ca)]$  displays a similar prograde growth pattern, with spessartine decreasing from 7 per cent Sp in the core to 1 per cent in the rim. The decrease of the spessartine ratio is gradational in the core (from 7 to 5 per cent). The spessartine molar ratio decreases further in the inner zone from 5 to 4 per cent. In the black inner ring, where most of the mineralisation was deposited, the spessartine molar ratio displays a very flat trend ( $\pm 4$  per cent spessartine). This slower change in the

spessartine distribution coincides with the retrograde pattern of pyrope. The reason is probably mineralisation trapped during the prograde growth of the garnet. The edge zone of the garnet porphyroblast exhibits a sharp decrease from 4 to 1 per cent spessartine. The very edge of the garnet displays the same very narrow retrogressed pattern, expressed by a weak increase in the spessartine molar content from 1 to 1.5 per cent and back to 1 per cent Sp.

*iii) Grossular distribution:* the grossular distribution is more erratic (**fig. 6.16c**). The core of the garnet displays about 14 per cent  $[Ca/(Mn+Mg+Fe+Ca)]$ . The grossular-content increases to a maximum of 15 per cent just before the mineralised inner ring is reached, and afterwards decreases to 12 per cent for most of the width of the inner ring. This decrease and the subsequent flat Ca-profile in the mineralised zone of the garnet is probably due to the consumption of Ca somewhere else in the metasomatically active system. Considering that the mineralised veins are actually quartz veins with very small amounts of ferroan calcite, and that mineralisation in the veins was precipitated penecontemporaneously with the entrapment of the ore minerals in the growing garnet, it can be assumed that some of the Ca has been used for the formation of calcite crystals within the mineralised vein system.

The garnet subsequently recorded an increase in the grossular content of up to 19 per cent. The grossular content decreases sharply from 19 to 13 per cent Gr and then increases again with 1 per cent to 14 per cent Gr at the extreme edge of the grain. This distribution pattern is less regular probably due to the slower rate of Ca diffusion within the garnet porphyroblast. This is in response to changes that occurred in the high-temperature metasomatic system as a result of deposition of ore minerals at different stages. It is known that  $Ca^{++}$  has a slower diffusion rate within the silicate lattice than  $Mg^{++}$  or  $Fe^{++}$  (Tucillo et al., 1990).

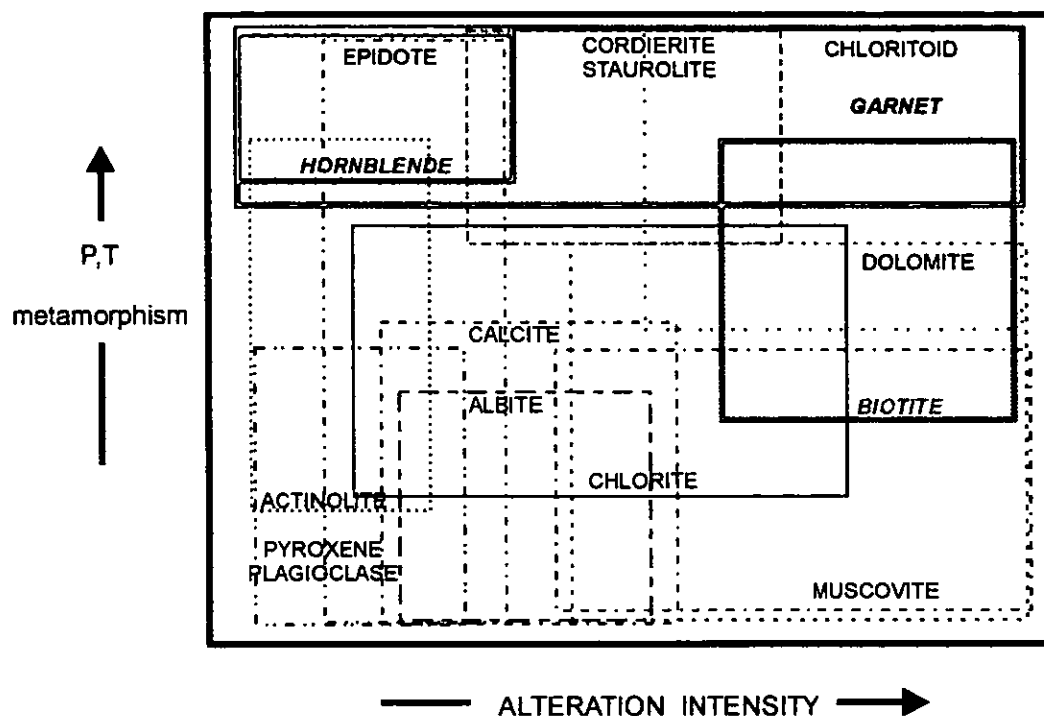


Figure 6.17a: Different alteration patterns that can occur after various lithologies have presumably undergone hydrothermal alteration at the time of gold introduction. Note that the sketch does not indicate neither the scale nor the metamorphism or alteration intensity. Four different lithological types are illustrated: a) basalts; b) calc-silicate-oxide facies BIF; c) ultramafic and komatiitic; d) silica-saturated and -undersaturated granitoid rocks (from Colvine *et al.*, 1988).

The sketch above illustrates the schematic representation of the field of occurrence of important minerals in progressively altered and metamorphosed basaltic rocks in gold-bearing systems. Hornblende is the main mineral for high-grade metamorphic conditions and low fluid:rock ratios. Garnet is characteristic for high-grade metamorphic condition and intense alteration (high fluid:rock ratio).

Possible prograde reactions that occurred at Doornhoek (after Colvine *et al.*, 1988):

- a1 - Quartz + Calcite + Chlorite = Hornblende
- a2 - Quartz + Calcite + Chlorite = Actinolite
- a3 - Chlorite + Quartz + Magnetite +  $K^+$  = Biotite
- a4 - Chlorite + Quartz +  $H_2S$  = Anthophyllite + Cordierite + Pyrrhotite
- a5 - Chlorite + Quartz + Dolomite +  $K^+$  = Garnet + Pargasite

The presence of euhedral garnet porphyroblast with prograde zonation pattern is, at first glance, rather unusual in an environment that suffered the same retrograde history as the rest of the SMZ of the LB. The growth of prograde garnet, however, is a relatively common phenomenon in BIF and mafic rocks as the result of the introduction of high-temperature fluids into Fe- and Fe+Mg-rich systems (Colvine *et al.*, 1988) (see figure 6.17). The mineral

reactions recognisable in the Doornhoek lithologies are compared with the multiple possibilities of mineral association described by Colvine et al., 1988 (fig. 6.17a and b):

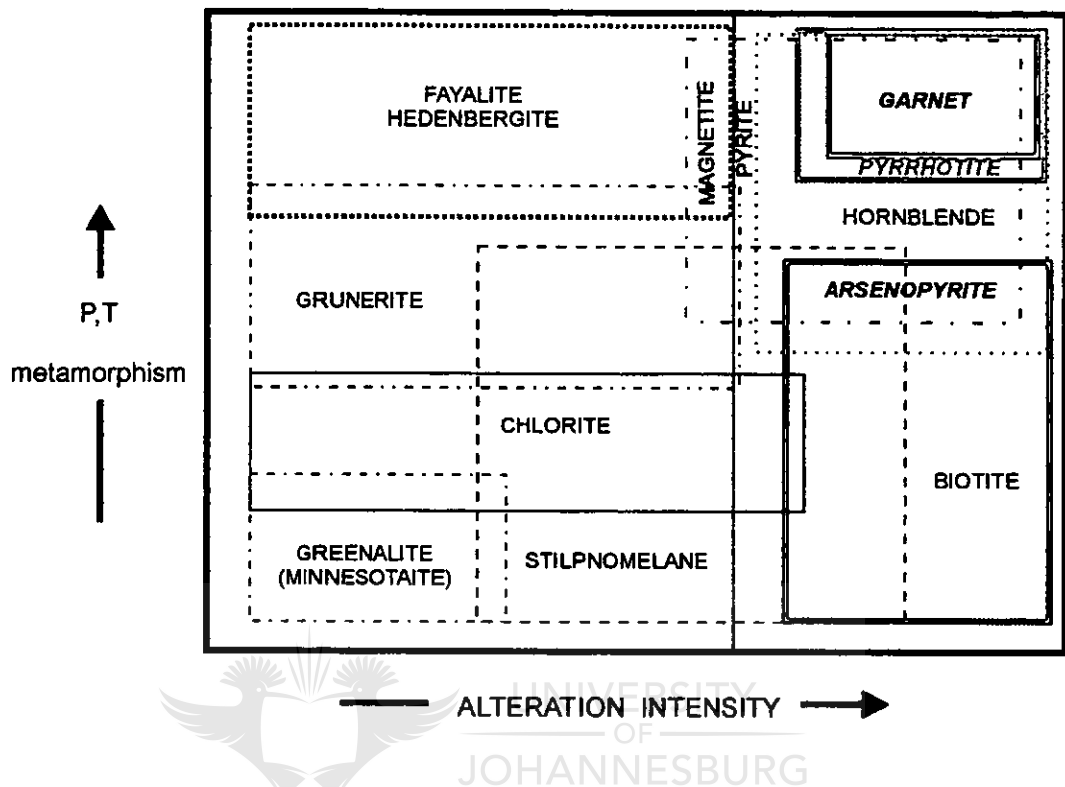


Figure 6.17b: Schematic representation of the fields of occurrence of important minerals in progressively altered and metamorphosed calc-silicate facies BIF in gold-bearing systems. Hedenbergite and Fe-rich olivine (fayalite) is the alteration product characteristic for high PT conditions and low alteration intensity. Garnet and pyrrhotite+arsenopyrite are the minerals formed under high-grade metamorphic condition and high fluid-rock ratio.

Possible prograde reactions that occurred at Doornhoek:

- b1 - Chlorite + Quartz + Dolomite + K<sup>+</sup> = Stilpnomelane + Calcite
- b2 - Magnetite + Quartz = Grunerite
- b3 - Grunerite-gedrite + H<sub>2</sub>S = Gedrite + Pyrrhotite + Quartz
- b4 - Chlorite + Quartz + Magnetite + K<sup>+</sup> = Biotite
- b5 - Chlorite + Quartz + Dolomite + K<sup>+</sup> = Garnet + Pargasite

Therefore, mafic and BIF lithologies may display the type of prograde reactions encountered in the Doornhoek Ore Body that include the formation of garnet and biotite. The introduction of K-rich fluids into the system is crucial for both discussed lithologies. On the other hand the K-rich solutions also affected the felsic lithologies and this process is beautifully expressed at Klipbank (Mokgatla, 1995). At Klipbank, about 2km north of Doornhoek, the grey tonalitic



Baviaanskloof Gneiss is highly metasomatised and characterised by the presence of K-feldspar, sillimanite and zoned garnet (Mokgatla, 1995). Mineralisation is absent at this locality due to absence of suitable lithologies to act as a geochemical and rheological trap (BIF or mafic rocks). This metasomatic process at Klipbank occurred at temperatures ranging from about 890°C to less than 600°C (Mokgatla, 1995; Hoernes et al., 1995). A similar alteration phenomenon, characterised by the sub-solidus replacement of oligoclase by orthoclase, also affected Baviaanskloof Gneiss at Petronella, a locality in the granulite subzone, and is described by du Toit (1994). The process of metasomatism at this locality also occurred at temperatures in excess of 700°C.

#### 6.2.2.2. Biotite

The biotite associated with garnet in the prograde biotite-garnetiferous formation also displays a prograde growth pattern (fig. 6.18):

- the Mg-content in biotite increases towards the rim but where in contact with prograde garnet porphyroblast the Mg content is even higher.

- the Mg-content also varies in matrix biotite (about 1.5 per cent less MgO in the core than in the rim of the biotite from the biotite-garnetiferous formation)

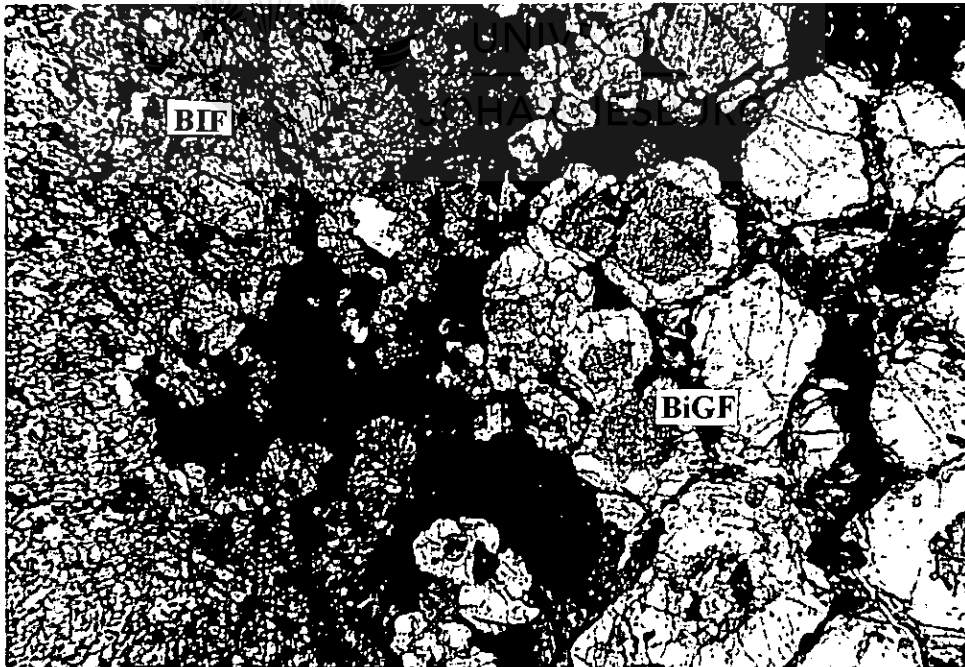
- the composition of different biotite grains included at different positions in the garnet porphyroblast also vary (i.e. the biotite included in the core of the garnet displays a lower Mg- and Ti-content than the biotite included in the edge of the garnet; the Ti-content can show a major difference of up to 3 per cent TiO<sub>2</sub> between biotite included in the core - 2 per cent TiO<sub>2</sub> - and in the edge - 5 per cent TiO<sub>2</sub> - of the garnet porphyroblast) (fig. 6.19).

This change in the chemistry of biotite is probably due to continuous re-equilibration between garnet and the included biotite as the garnet porphyroblast grew during a continuous

temperature increase. The temperature increase is probably related to the heat liberated by the hot metasomatising fluids.

#### 6.2.2.2.3. Orthopyroxene

Orthopyroxene closely associated with the prograde biotite-garnetiferous formation (**fig. 6.18**) belongs to the retrograde pattern lithologies that suffered the same general retrograde history as the rest of the SMZ of the LB. The orthopyroxene-bearing rock therefore represents the wall-rock of the prograde biotite-garnetiferous formation. Orthopyroxene in this rock displays interesting textures that may be clues to the way of formation of mineralisation at Doornhoek. The orthopyroxene (**fig. 6.20 and 6.21**) is crosscut, almost perpendicular to the 010 cleavage plane, by thin veins consisting of pyrrhotite+magnetite±chalcopyrite±löllingite ±gold.

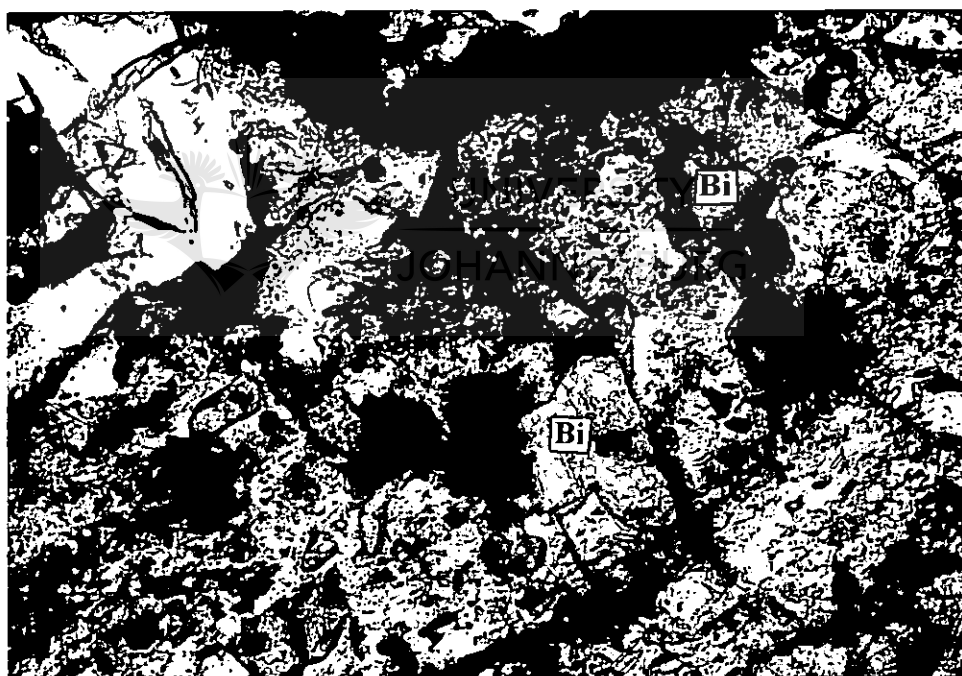


**Figure 6.18:** Sample DD-2-2035: Microphotograph of the contact between the retrograde opx-bearing BIF (green) and the prograde biotite-garnetiferous formation (brown). The contact is characterised by ilmenite-magnetite-pyrrhotite-pentlandite-chalcopyrite mineralisation. Biotite associated with garnet also displays variation in chemistry (Mg-rich rims, Mg-poor cores).

1cm=1000µm

The deformation was so intense and occurred at such high-metamorphic grade, that orthopyroxene, normally a very brittle silicate, here exhibits a high ductility demonstrated by the presence of real kink-bands (fig. 6.20 and 6.21).

At a higher magnification the angle between the direction of the mineralised veinlets and the direction of the cleavage planes in the orthopyroxene is better illustrated (fig. 6.22, 6.23 and 6.24). As the infiltration of the mineralising fluids increased in intensity the mineralisation penetrated the directions of weak mechanical resistance in orthopyroxene both conformably and unconformably (fig. 6.20, 6.21, 6.22, 6.23 and 6.24).



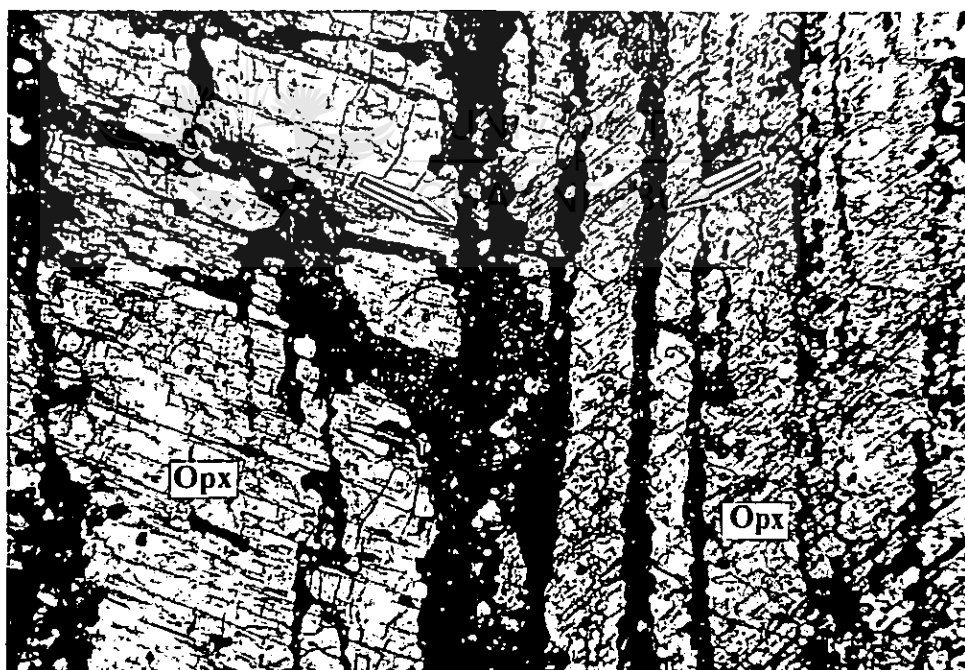
**Figure 6.19:** Sample DD-2-2035: Biotite-garnetiferous formation. This microphotograph shows tiny inclusions of biotite (Bi) in the dark inner-ring zone of the prograde garnet porphyroblast. The inner-ring zone is highly mineralised (opaque minerals).

1cm=25 $\mu$ m

Textural evidence that the mineralisation was introduced into the system (epigenetically or metamorphic) and that Doornhoek does not represent a metamorphosed deposit is as follows:

- mineralisation was introduced along veinlets in orthopyroxene, parallel to the direction of the main mineralised quartz veins
- the mineralisation is mainly hosted by syntectonic quartz veins
- the direction of crosscutting veinlets in orthopyroxene (fig. 6.20 and 6.21) is perpendicular to the cleavage of the pre-existent retrograde BIF-dominant lithologies
- these textural features demonstrate that this type of mineralisation is epigenetic and not syngenetic.

This suggestion is further supported by the fact that the same mineralisation was also trapped in the newly formed metasomatic garnet porphyroblasts.



**Figure 6.20:** Sample DD-2-2020: Wall-rock BIF. Microphotograph showing a large orthopyroxene crystal (Opx) crosscut perpendicular to the [010] cleavage planes by narrow veinlets consisting of pyrrhotite-magnetite-chalcopyrite-löllingite-gold (opaque - red arrows). The epigenetic introduction of sulphide-oxide mineralisation has been made under high deformation conditions, resulting in the ductile behaviour of a normally brittle mineral.

1cm=100µm



Figure 6.21: Same view as fig. 6.20 but under X Nicols for a better visualisation of the kink-band deformation in birefringent colours.



Figure 6.22: Sample DD-2-2020. Wall-rock BIF. Blow up of microphotograph 8.15. The angle between the direction of the mineralised veinlets (opaque) and the direction of the cleavage planes in opx (arrows) is obvious. Mineralisation is therefore clearly unconformable and epigenetic with reference to the peak metamorphic assemblage.

1cm=25 $\mu$ m



Figure 6.23: Sample DD-2-2020. Wall-rock BIF. Microphotograph showing introduction of mineralised veinlets (opaque) parallel to the cleavage direction of the opx (arrows).  
1cm=25 $\mu$ m

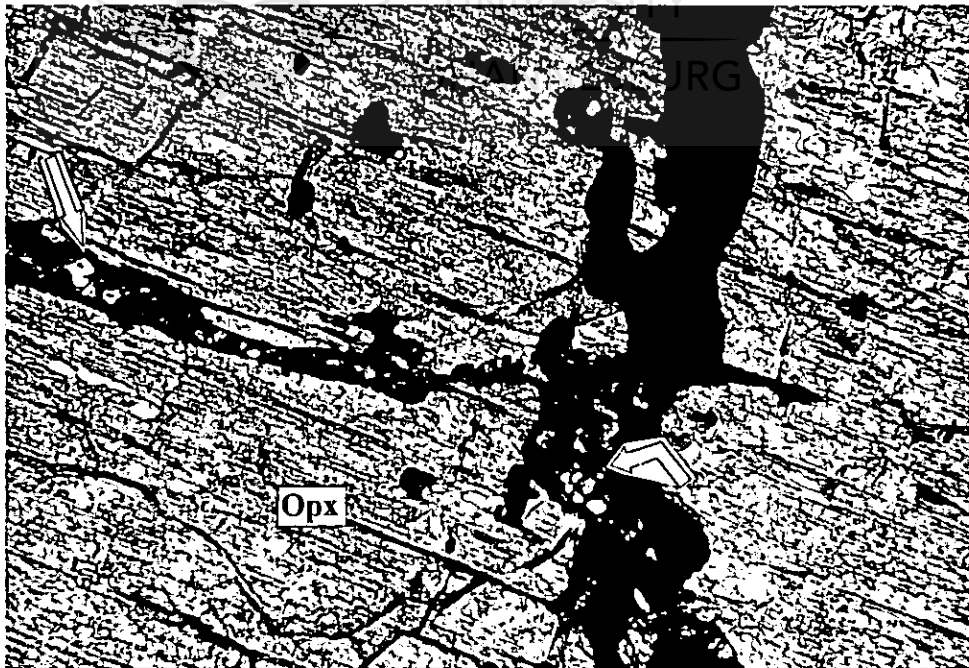


Figure 6.24: Sample DD-2-2020. Wall-rock BIF. Microphotograph showing mineralisation infiltrating both unconformably and conformably into the orthopyroxene (Opx). The infiltration of sulphides and oxides took place under pressure, as shown by tiny fragments of brecciated opx (arrows). These tiny, highly deformed and corroded pieces of opx are part of the main opx crystal which was fragmented by the infiltration of ore minerals.

1cm=25 $\mu$ m

### 6.2.3 Conclusion

The data presented in this chapter suggest the following:

- i) the co-existence of a retrograde pattern lithology with a prograde pattern lithology
- ii) the prograde pattern lithology was formed later than the retrograde pattern lithology, as a result of intense metasomatic alteration. Textural data suggest an epigenetic source for the mineralised veins that are part of the prograde pattern lithology
- iii) mineralisation occurred within the metasomatic lithologies in several stages that clearly exhibit a prograde pattern (the last stage of ore minerals precipitation occurred at a higher temperature than the first stage: arsenopyrite occurs in the core and lollingite in the dark inner ring of the prograde garnet porphyroblast)
- iv) the newly formed prograde pattern lithology consists of a mineralised quartz vein system and a metasomatic biotite-garnetiferous formation. The same type of mineralisation occurs in both formations, suggesting a penecontemporaneous deposition in both the quartz veins and in the garnet porphyroblasts.
- v) The boundaries between the prograde and retrograde lithologies are, with a few exceptions, very sharp. The only way to explain the intimate co-existence of these two very different lithological formations is by calling upon the action of highly channelised fluid flow along deep-crustal shear zones.

### 6.3 MINERAL CHEMISTRY OF ORE MINERALS

**Löllingite:** This is the main arsenide associated with the gold mineralisation and reflects the high-grade metamorphic conditions (Colvine et al., 1988; Groves et al., 1991) of the mineralisation at Doornhoek. Löllingite displays the formula  $\text{Fe}_{33}\text{As}_{61}\text{S}_4$ . However the amount of S is variable, ranging from 2.43 to 4.40 atomic concentration. Löllingite that occurs at Doornhoek usually displays a higher As-content than normal, probably due to the very high PT conditions of mineralisation.

**Arsenopyrite:** Arsenopyrite is also associated with gold, but as part of a lower temperature sulphide assemblage. Two types of arsenopyrite occur:

- i) the first type shows a low As-content, ranging from 31.67 to 35.58wt per cent As.

This arsenopyrite is not associated with the gold mineralisation

- ii) the second type displays a higher As-content which varies from 35.91 to 38.33wt per cent As and is always part of the gold-bearing assemblages.

**Pyrrhotite:** This Fe sulphide is part of the high-temperature sulphide paragenesis. It displays a major deficit in Fe (as low as 46.88wt per cent Fe) and a variable Ni-content which can be as high as 5.56wt per cent Ni.

**Chalcopyrite:** This mineral has a normal composition with a very small amount of Pb (0.12wt per cent Pb) or Zn (0.07wt per cent Zn).



**Sphalerite:** This Zn sulphide has a relative high Fe-content (7.21-11.34wt per cent Fe) and also contains some Ag (up to 130 ppm Ag). The relatively high Ag-content might be explained by the presence of Ag in the hydrothermal system (the gold is actually electrum with up to 40.75wt per cent Ag).

**Ni-Co minerals:** Several Ni-Co arsenides and sulphides have been identified as part of the ore assemblage at Doornhoek. These are as follows:

- **pentlandite**  $(\text{Fe,Ni})_5\text{S}_8$  which usually occurs as flames in the highest temperature pyrrhotite. The Ni content is about 27.74wt per cent Ni.

- **gersdorffite** with variable Ni-, Co-, Fe- and S-contents. Ni is quite constant in the range 11.03-12.46wt per cent Ni while Co ranges from 0 to 18.05wt per cent Co. Fe varies from 7.23 to 21.97wt per cent Fe. S is also relatively constant in the range 18.30-20.57wt per cent S. The presence of Zn in some of the analysed gersdorffite, however, is very uncommon. The maximum Zn content recorded is 6.10wt per cent, which is more than enough to affect the lattice of the mineral. In other words, it can be assumed that this type of mineral is either a product of the gersdorffite-ullmanite isomorphous series, or a new mineral. The formula of this mineral is  $(\text{Fe}_{0.4}\text{Ni}_{0.4}\text{Zn}_{0.2})\text{AsS}$ .

- **niccolite**  $(\text{NiAs})$  and **skutterudite**  $(\text{Co,Ni,Fe})\text{As}_3$  are two very rare minerals.

**Gold:** Gold that occurs at Doornhoek is actually electrum. The composition is AuAg with small amounts of Fe and Cu. Au ranges in content from 56.27 to 69.71wt per cent, while Ag varies from 8.06 to 40.75wt per cent, Fe from 1.18 to 24.10wt per cent, and Cu from nil to 1.65wt per cent. The ratio Au/Ag is normal for high-grade Au occurrences (upper-amphibolite to granulite facies conditions), e.g. as at Renco (Zimbabwe) or Griffins's

Find (Western Australia) (Groves et al., 1991). Very unusual, however, is the high Fe-content of two of the analysed samples. This is probably due to some contamination from the prograde zoned garnet porphyroblast host. At the time of crystallisation, the gold probably absorbed some of the Fe from the metasomatic garnet, due to the high-grade conditions of the gold precipitation.

**Pyrite:** This very common Fe sulphide is very rare at Doornhoek and is not related to the Au depositional event, but is a late, retrograde product displaying small amounts of Cu and As. The absence of pyrite is also indicative for the high-grade metamorphic conditions of mineralisation deposition at Doornhoek. Cu is usually in the range 0.04-0.40wt per cent, but can be as high as 1.99wt per cent. As is usually low (0.01-0.09wt per cent As), but can also be higher (0.83wt per cent As). The Ni-content varies from 0.04wt per cent to as high as 4.04wt per cent Ni. The unusual high amount of trace elements in the pyrite from the Doornhoek deposit can be explained by the late introduction of pyrite in the system. Pyrite precipitated from late residual solutions percolating the already mineralised system, dissolved some of the earlier formed minerals and at a later stage precipitated as pyrite.

## 7. MINERALISATION

### 7.1. INTRODUCTION

The Archaean lode-gold deposit at Doornhoek in the SMZ of the LB offers an excellent opportunity for a detailed study of a gold deposit formed under high-pressure-temperature conditions.

Petrographical evidence presented in **Chapter 5** suggests at Doornhoek intense metasomatism related to highly channelised fluids that evolved at high temperatures, deposited gold and associated sulphide mineralisation in the syn-tectonic quartz veins and metasomatised biotite-garnetiferous formation. Large amounts of mineralised syn-tectonic quartz veins developed in the ductile shear zones, due to a process of continuous hydraulic micro-pumping and precipitation. As a result the granulitic host has been penetrated, metasomatised and mineralised by the channelised fluids. The mineralised shear zones were probably characterised by very high fluid:rock ratios, in order to allow such an event to evolve under lower-granulite facies conditions.

Mineralisation occurs in both the syntectonic quartz veins and in the biotite-garnetiferous formation and displays similar mineralogical and geochemical features in both hosts.

## 7.2. MINERALISATION ASSOCIATED WITH QUARTZ VEINS

Quartz (**fig. 7.1**) and seldomly quartz-carbonate veins (**fig. 7.2**) occur as syn-tectonic veins, representing the main host of the mineralisation. Veining is directly related to gold mineralisation with the result that mineralisation only occurs in quartz veins and in the associated mineralised biotite-garnetiferous formation. No mineralisation was observed in vein-free unaltered rocks. Most quartz veins are orientated parallel to the foliation of the wall-rock and display textures ranging from coarse-grained with antitaxial quartz and very rare ferroan calcite (**fig. 7.3**), to finer grained, recrystallised veins with sutured grain boundaries. Highly sheared quartz veins with a laminated character also occur (**fig. 7.4**); these veins may be boudinaged (**fig. 7.5**). Relics of orthopyroxene, garnet, hornblende and laminae identical to that of the wall-rock orientated parallel to the edge of the veins (probably mechanically transposed from the wall-rock), demonstrate the syn-tectonic nature of the veining (**fig. 7.4** and **7.6**). Mineralisation (oxides, sulphides, arsenides and gold) also occur in the veins characterised by sutured grain boundaries. Two types of mineralisation can be recognised: *i*) a *high temperature paragenesis* consisting of pyrrhotite, magnetite, ilmenite and löllingite (with pyrrhotite displaying exsolution lamellae of pentlandite) (**fig. 7.7**) and, *ii*) a *medium-temperature ore mineralisation* composed of arsenopyrite, chalcopyrite, pyrrhotite, sphalerite, gersdorffite and skutterudite (**figures 7.8, 7.9** and **7.10**). Gold is associated with both löllingite- (**fig. 7.11**), and with the arsenopyrite-associated paragenesis (**fig. 7.12**). Gold is actually a typical electrum (consisting of up to 45wt per cent Ag, with small amounts of Fe and traces of Cu). Gold-free pyrite crystals occur in late, cross cutting low-temperature veinlets. This association is very late and probably not related to the main gold mineralisation.

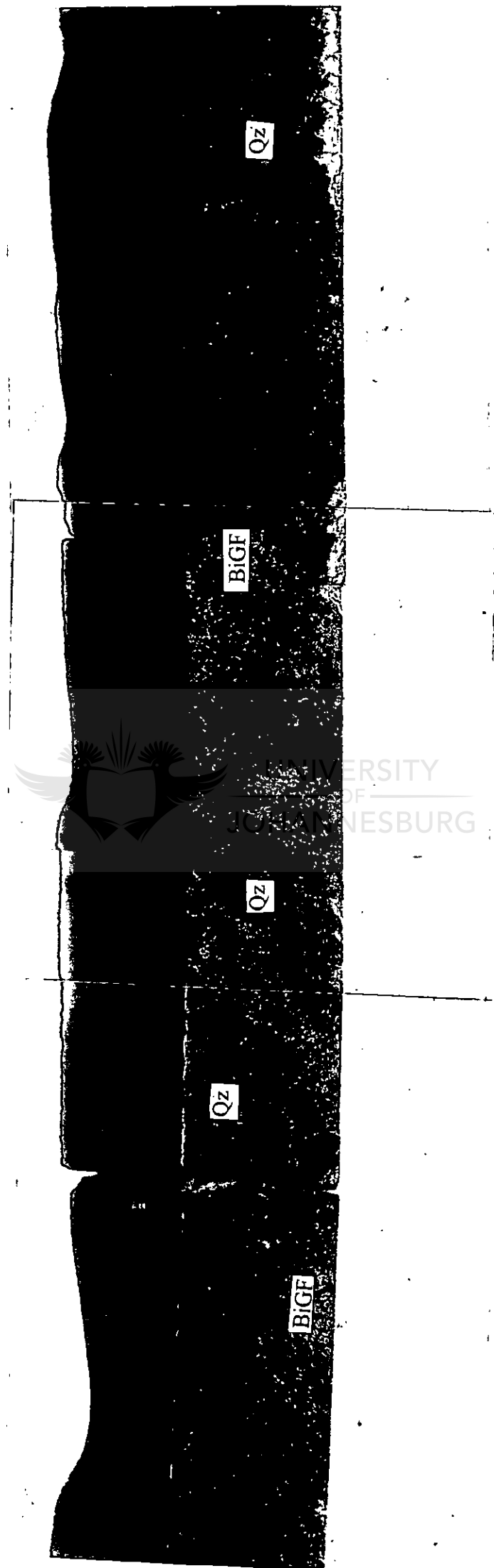


Figure 7.1: Intimate association between the syn-tectonic quartz veins (Qz) and biotite-garnetiferous formation (BiGF). Both mineralised formations were deformed and folded during D<sub>3</sub>. Borehole DD-7, 46.60-49.70m.

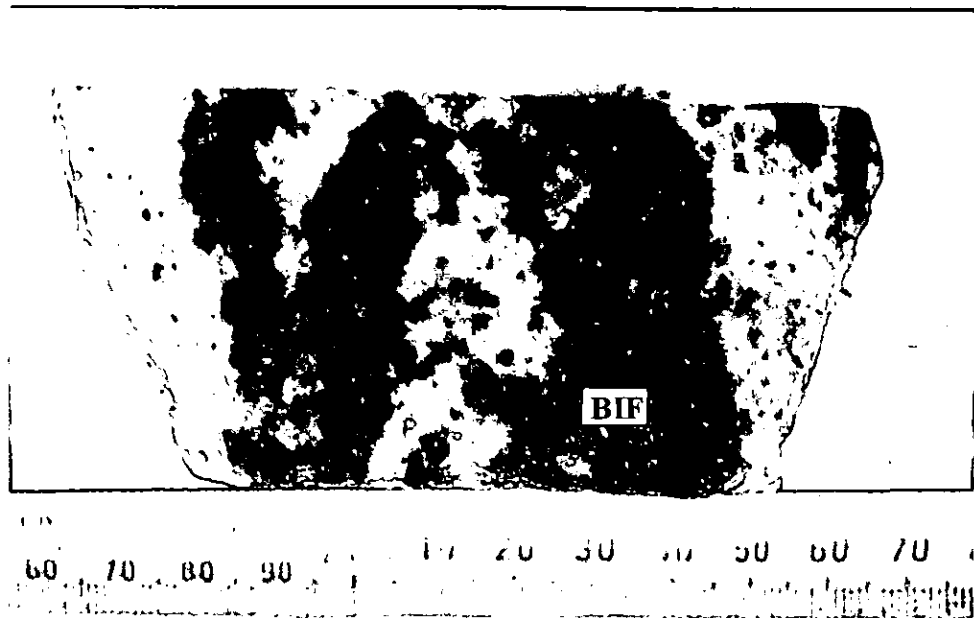


Figure 7.2: Drillcore sample showing a quartz-calcite vein with material still left "undigested" from the wall-rock BIF. Borehole DD-5, 81.55-82.75m.

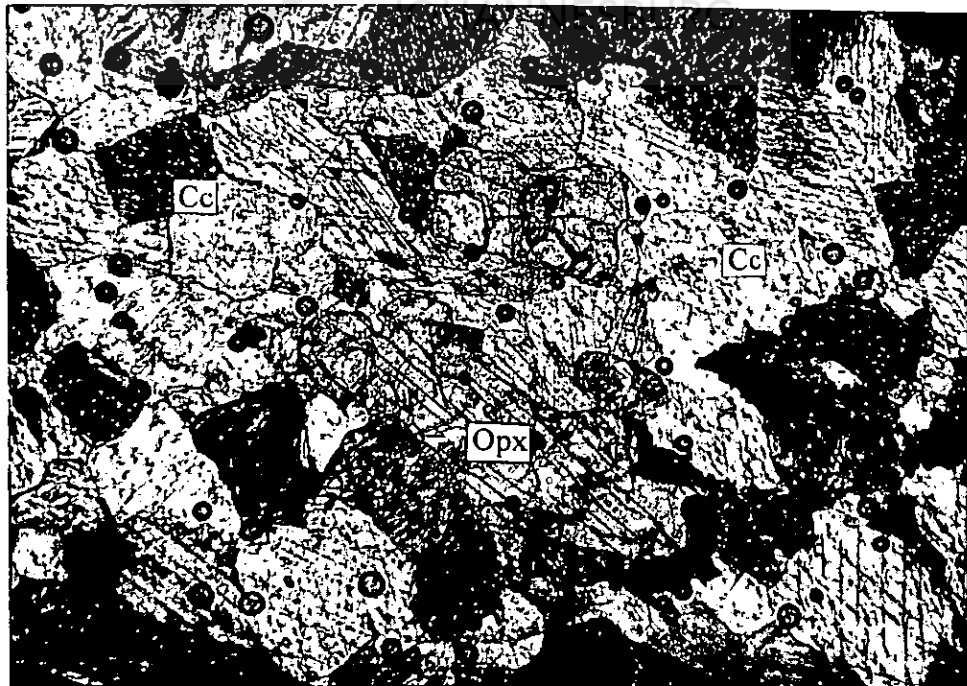


Figure 7.3: Microphotograph of the coarse grained calcite-quartz vein macroscopically shown in fig. 7.2. Orthopyroxene (opx) occurs as remnants of the wall-rock BIF (the interference colours are high due to the thick thin section). The carbonate is ferroan calcite (Cc). Sample DH-2114. 1cm=400µm



Figure 7.4: Microphotograph of a highly sheared quartz-calcite vein displaying highly sygmoidal shaped calcite augens. Sample DH-1073. 1cm=400µm.



Figure 7.5: Photograph of a drillcore sample showing boudinaged syn-tectonic quartz veins. The quartz boudines are hosted by mineralised calc-silicate facies BIF. Sample DH-2135 from borehole DD-5, 90.33-90.38m.

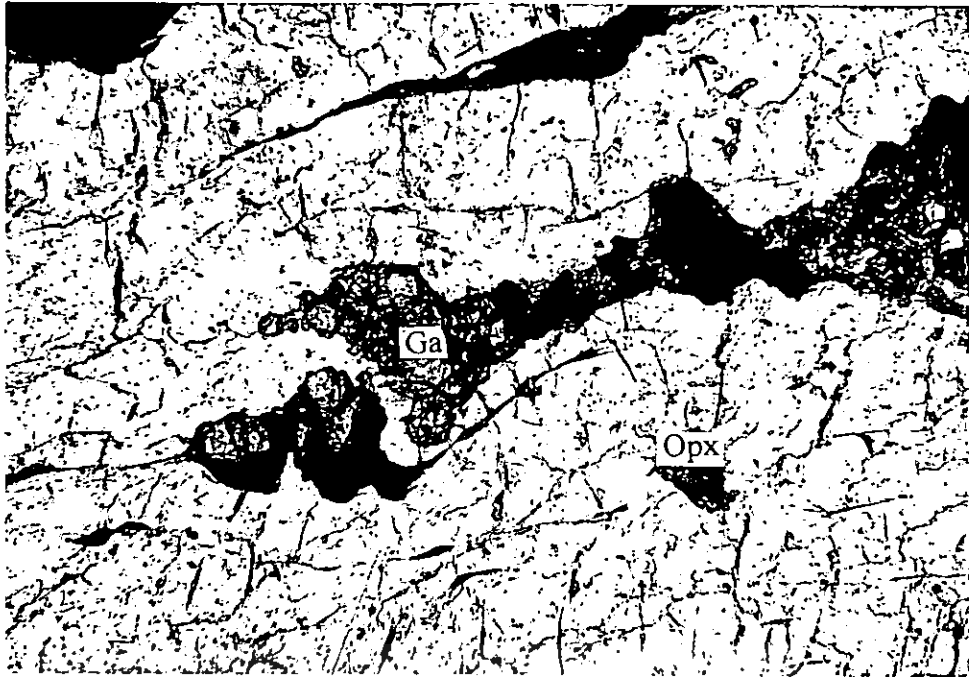


Figure 7.6: Relics of garnet and opx, identical in composition to similar minerals from the wall-rock, and orientated parallel to the edges of the quartz vein. Sample DH-1073.  
1cm=400 $\mu$ m.

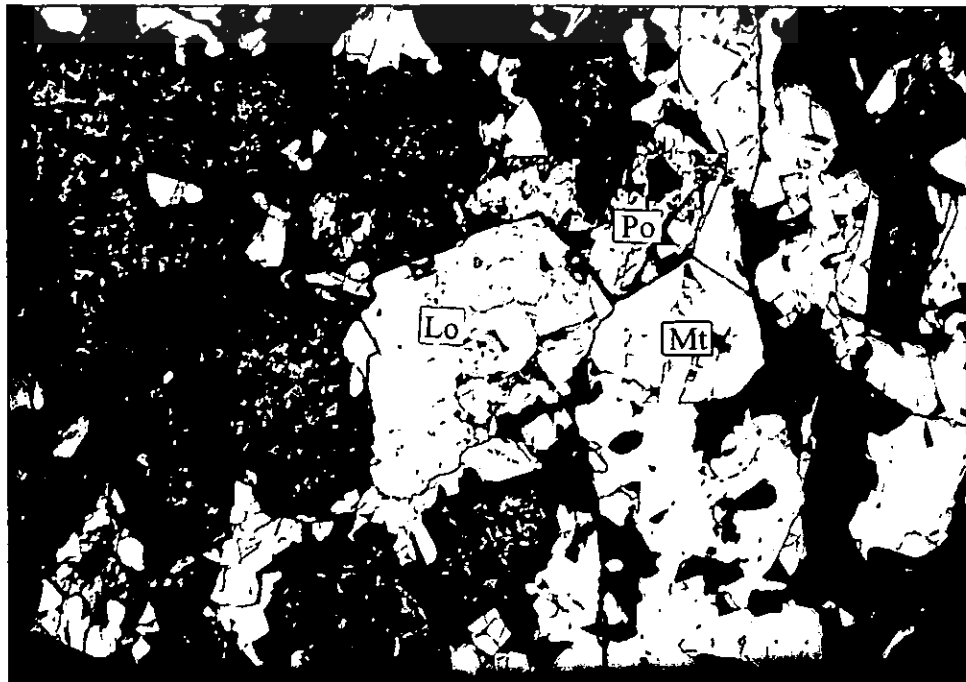


Figure 7.7: Microphotograph in reflected light of the high-temperature mineral paragenesis: löllingite (Lo) associated with magnetite (Mt) and pyrrhotite (Po). The host is orthopyroxene. Sample DH-2114.  
1cm=200 $\mu$ m





Figure 7.8: Microphotograph in reflected light showing arsenopyrite (Aspy) and pyrrhotite (Po) that are part of the medium-temperature ore mineral association. Sample DH-2025. 1cm=100µm

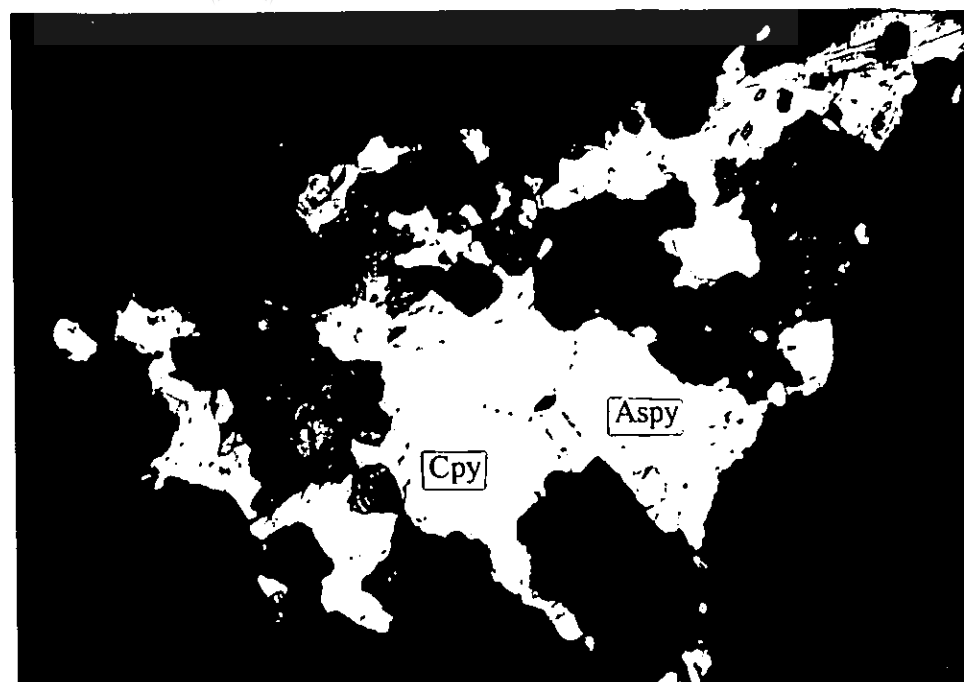


Figure 7.9: Microphotograph in reflected light of chalcopyrite (Cpy) and arsenopyrite (Aspy), part of the medium-temperature ore mineralisation. Sample DH-2025. 1cm=100µm

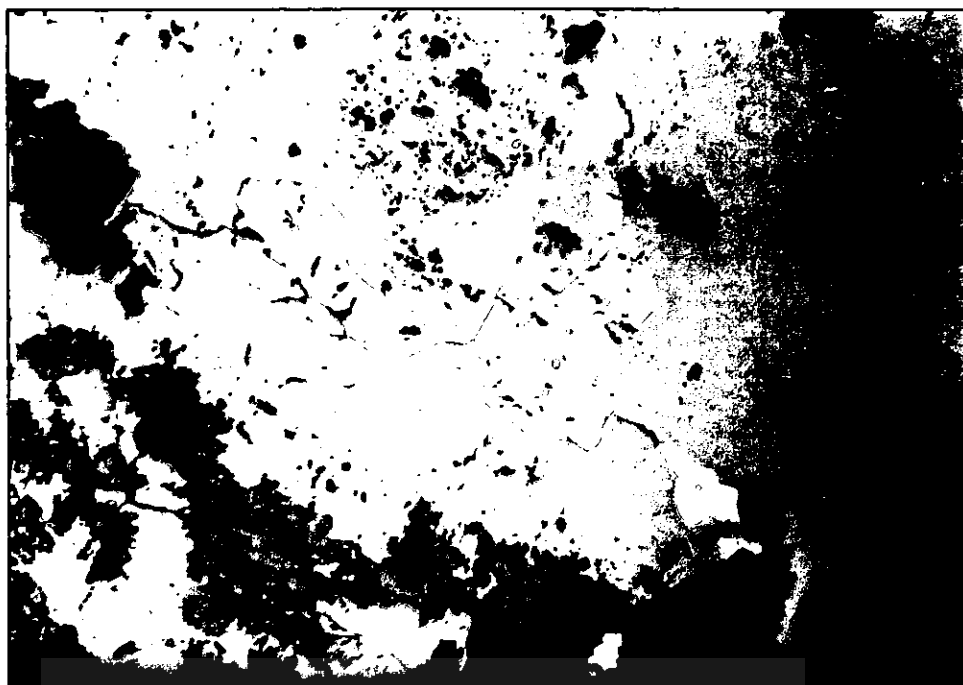


Figure 7.10: Microphotograph in reflected light of sphalerite with chalcopyrite exsolutions (tiny yellow specks). This association is also part of the medium-temperature ore mineralisation. Sample DH-2025. 1cm=50µm

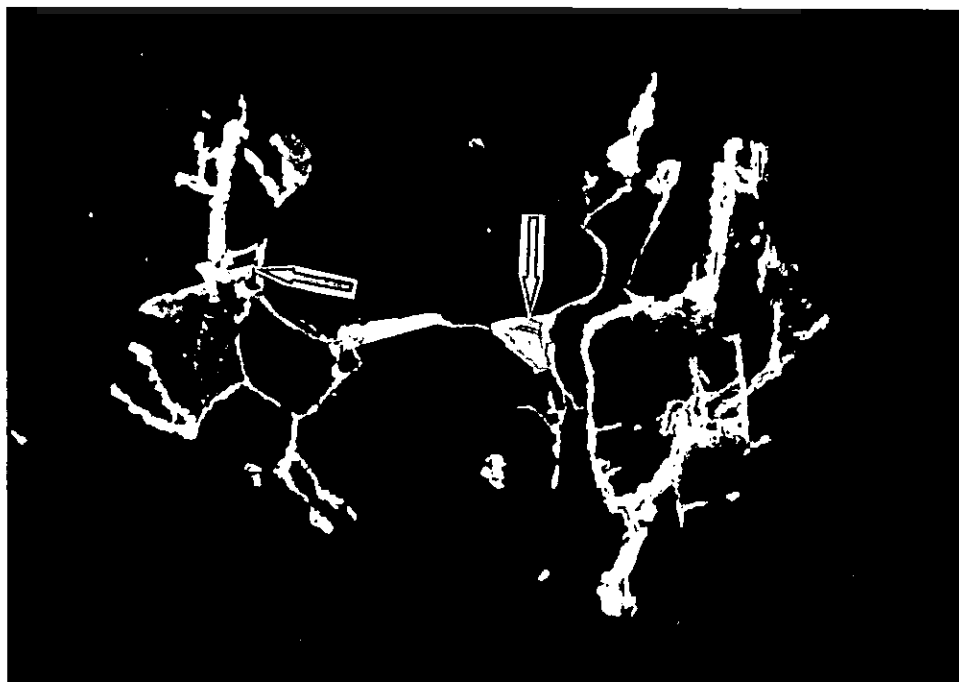


Figure 7.11: Microphotograph in reflected light of gold (actually electrum - arrow) hosted by lollingite veins (white). Sample DH-2011. 1cm=25µm



**Figure 7.12:** Microphotograph in reflected light of a tiny grain of gold (blue arrow) that together with sphalerite+chalcopyrite (red arrow) and magnetite (Mt), are hosted by a thin quartz vein (yellow arrow). Note that sphalerite includes chalcopyrite exsolutions and is also rimmed by a thin shell of chalcopyrite. Sample DH-2017.

1cm=25µm

### 7.2.1. Oxides

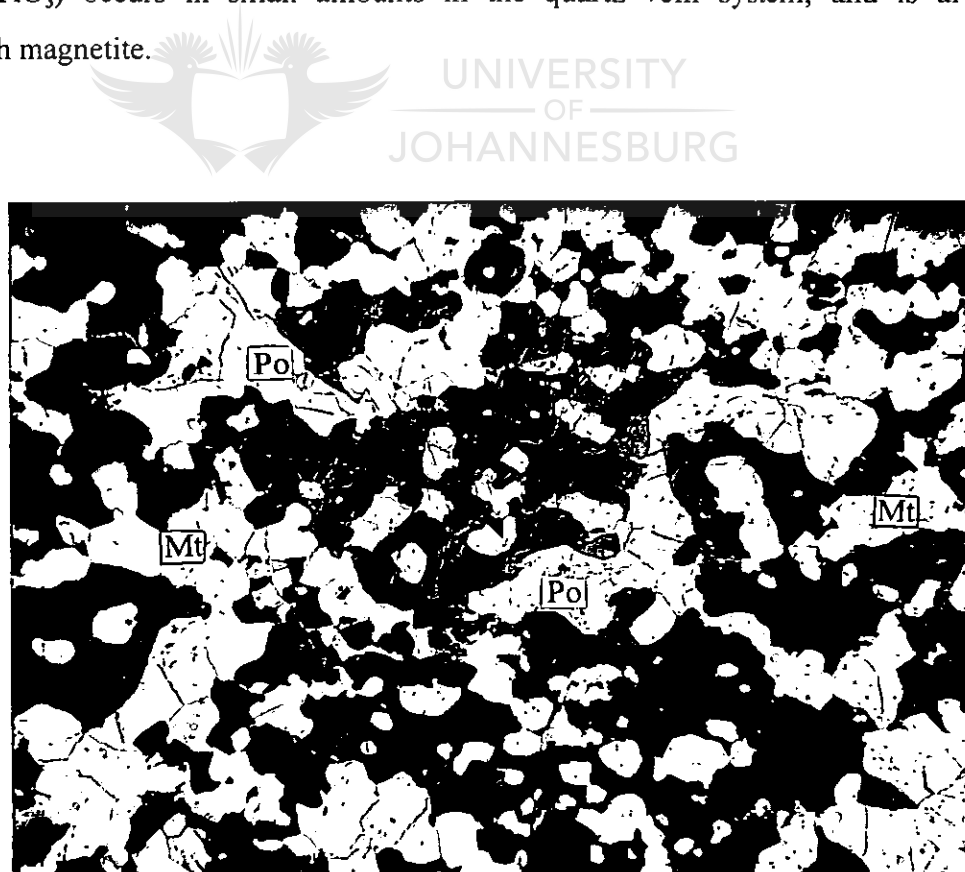
**Magnetite ( $\text{Fe}_3\text{O}_4$ ):** Magnetite is the main oxide that occurs in the mineralised part of the ore body. It occurs as euhedral to subhedral crystals (**fig. 7.13**) intimately associated with pyrrhotite in schlieren-like textures. The schlieren are orientated parallel to the shearing direction (**fig. 7.14**), sometimes displaying a brecciated character (**fig. 7.15**) due to the late, epigenetic character of the mineralisation. Relics of pyroxene are cemented by magnetite (**fig. 7.15**). The introduction of magnetite by the mineralising system was so intense that very often magnetite does not only crosscut the pre-existing minerals such as pyroxene (**fig. 7.15**),

but also infiltrated the pyroxene crystals along the tiniest mechanical discontinuities such as cleavage planes. This results in the formation of replacement textures (graphic/mirmekitic overgrowths including ferrohypersthene, grunerite or garnet (fig. 7.16). The textural data therefore suggests that the mineralisation was introduced during a period of intense deformation. Furthermore, pyroxene in contact with magnetite or pyrrhotite is transformed into a variety of Fe-rich hornblende, suggesting

i) that re-equilibration of the granulite paragenesis occurred at lower temperature conditions, and

ii) that chemical reactions occurred between the granulitic precursor and the newly introduced fluids.

**Ilmenite ( $\text{FeTiO}_3$ )** occurs in small amounts in the quartz vein system, and is always associated with magnetite.



**Figure 7.13:** Microphotograph (reflected light) of euhedral/subhedral magnetite crystals (Mt) intergrown with pyrrhotite (Po) (sample DH-2138). 1cm=400µm

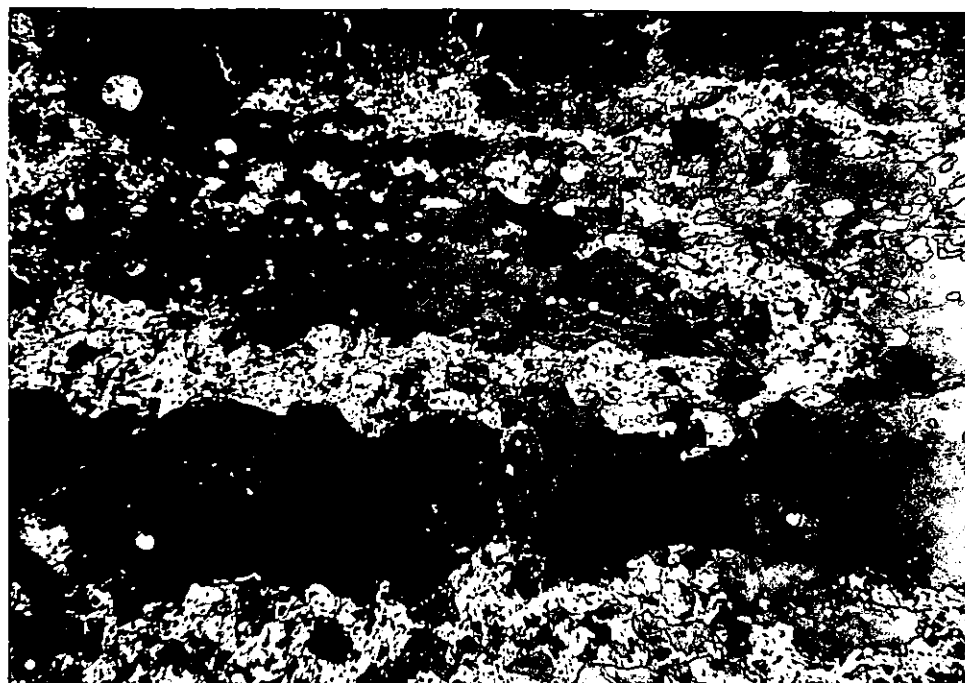


Figure 7.14: Microphotograph (reflected light) of schlieren of pyrrhotite and magnetite orientated parallel to the shearing direction and replacing shear microfolds. Sample DH-2030. 1cm=400µm

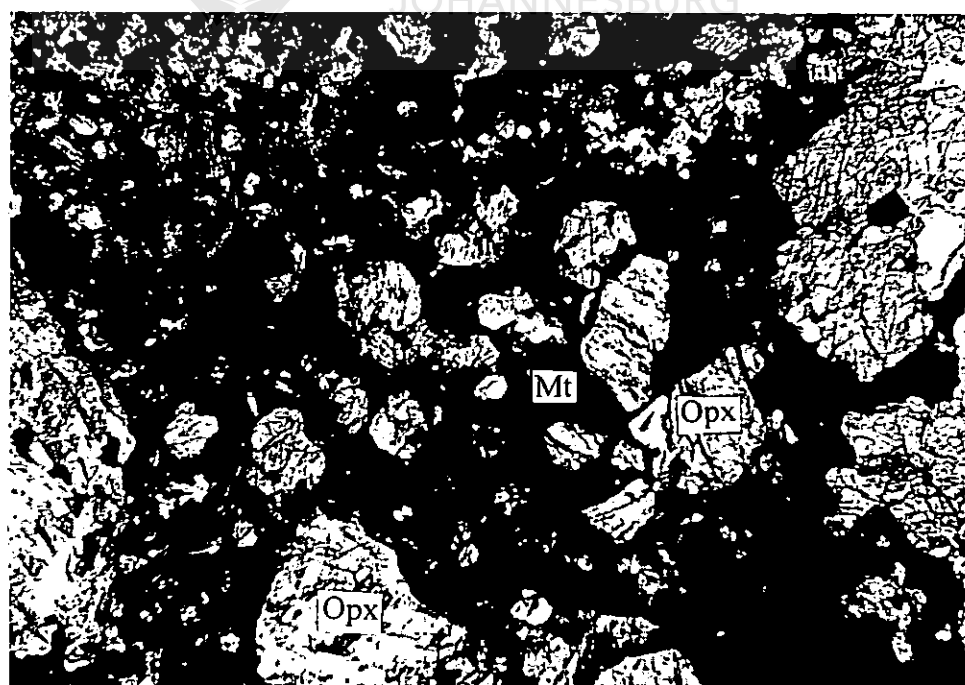


Figure 7.15: Microphotograph in transmitted light of magnetite (Mt-opaque) that corrodes orthopyroxene (Opx). This brecciated type of mineralisation is preserved in relatively unshered portions of the ore body. 1cm=400µm

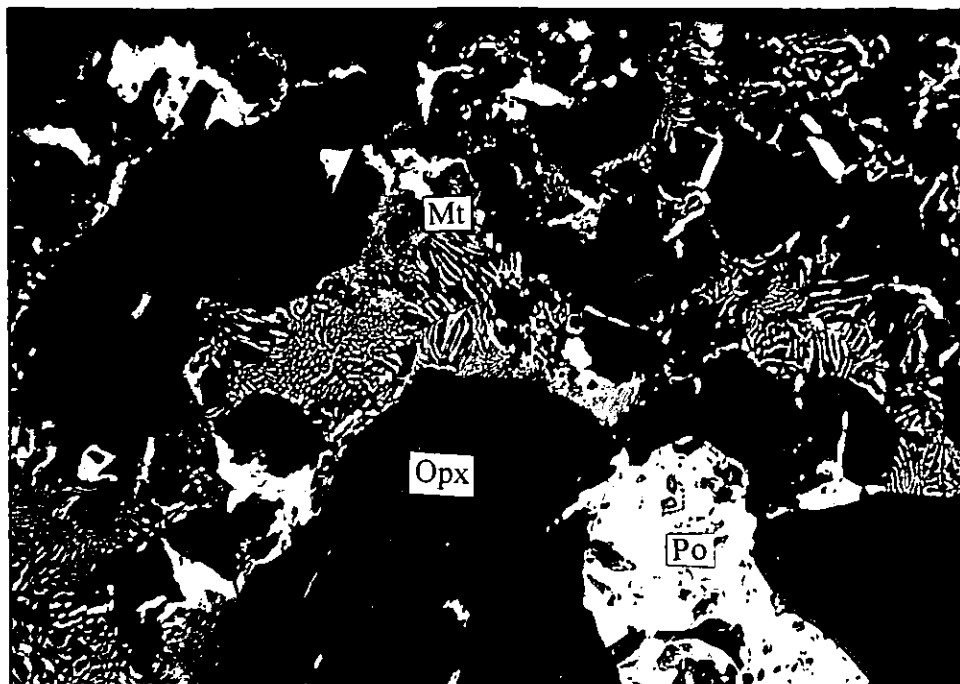


Figure 7.16: Microphotograph in reflected light showing replacement of orthopyroxene (opx) by magnetite (Mt). This reaction started along cleavage planes or irregularities and represents a frozen stage of the replacement reaction of opx by magnetite. Pyrrhotite (Po) is also present in the field of this photograph. Sample DD-2-2.

1cm=25 $\mu$ m

### 7.2.2. Sulphides and Arsenides

Pyrrhotite ( $\text{Fe}_{1-x}\text{S}$ ) is the main sulphide that occurs in the quartz veins system. It precipitated just after the crystallisation of magnetite, sometimes corroding the magnetite crystals (fig. 7.14). It occurs in schlieren textures together with magnetite and seldomly with chalcopyrite. Pyrrhotite is sometimes severely stretched due to its very high plasticity. Brecciation-like textures are also very frequently observed (fig. 7.17 and 7.18), demonstrating the late character of the mineralisation with reference to the main granulitic paragenesis. The mineralisation is therefore epigenetic and not syngenetic.

Pentlandite  $[(\text{Fe},\text{Ni})_9\text{S}_9]$  occurs as deformed flames in pyrrhotite.

**Pentlandite** [(Fe,Ni)<sub>8</sub>S<sub>9</sub>] occurs as deformed flames in pyrrhotite.

**Chalcopyrite** (CuFeS<sub>2</sub>) is the second most frequently occurring sulphide, nearly always associated with pyrrhotite, but sometimes also associated with lower temperature sulphides and arsenides. In the high-temperature paragenesis, two types of chalcopyrite are present:

- i) Cpy I is present in very small amounts preceding the crystallisation of pyrrhotite
- ii) Cpy II represents the main phase and corrodes, crosscuts or replaces magnetite and pyrrhotite. It crystallised just after pyrrhotite (**fig. 7.19**).

Chalcopyrite was later remobilised together with the low-temperature sulphide and sulpho-arsenide paragenesis. It is also possible that the chalcopyrite represents a new wave of Cu-rich solutions that percolated throughout the system. This type of chalcopyrite can be labelled as Cpy III (**fig. 7.20**).

**Sphalerite** (ZnS) with small amounts of Fe rarely occurs in the quartz veins, and is always associated with the low-temperature paragenesis (arsenopyrite-pyrrhotite-chalcopyrite III). Actually only two small sphalerite crystals (15µm) were encountered in quartz veins. It always hosts chalcopyrite exsolutions in the form of tiny bubbles.

**Pyrite** (FeS<sub>2</sub>) is rarely present in the quartz vein system but is absent from the biotite-garnetiferous formation. It occurs as xenoblastic, slightly porous crystals (**fig. 7.21**) in crosscutting veinlets or as a late alteration product of pyrrhotite related to the main pyrrhotite-dominated mineralisation that consists of pyrite, altered pyrrhotite and gersdorffite. Pyrite is never related to the gold mineralisation. It is suggested that pyrite represents the very late remobilisation of the iron sulphides under slightly higher sulphur fugacity, or possibly even a supergene enrichment of the main ore mineralogy.

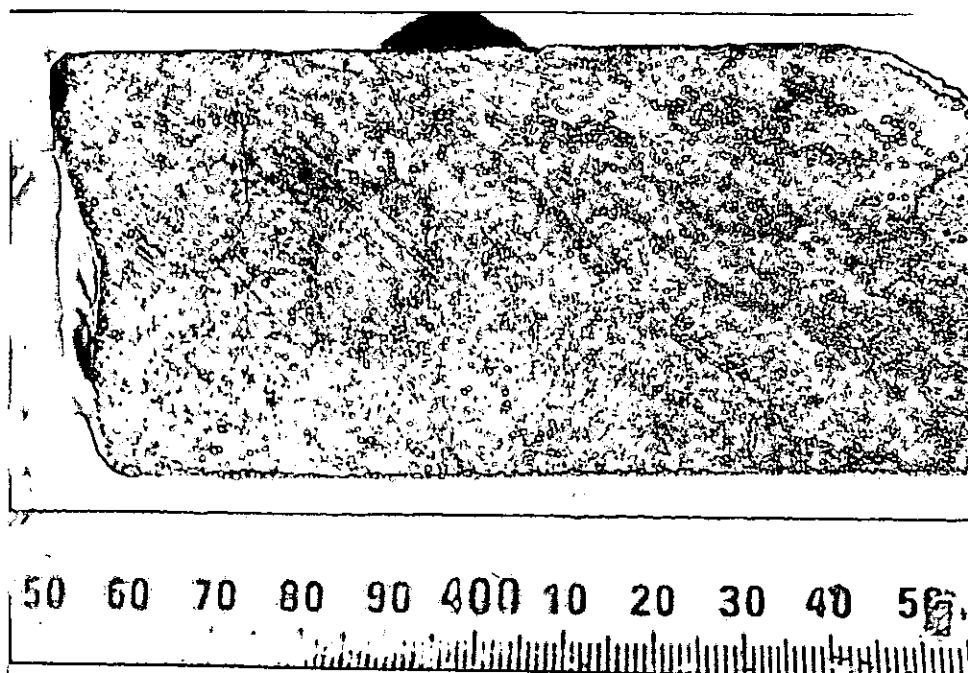


Figure 7.17: Photograph of a drillcore sample showing the pre-existent mineral assemblage almost totally replaced by pyrrhotite (yellow). Sample DH-2221, borehole DD-19, 113.50-113.60m.

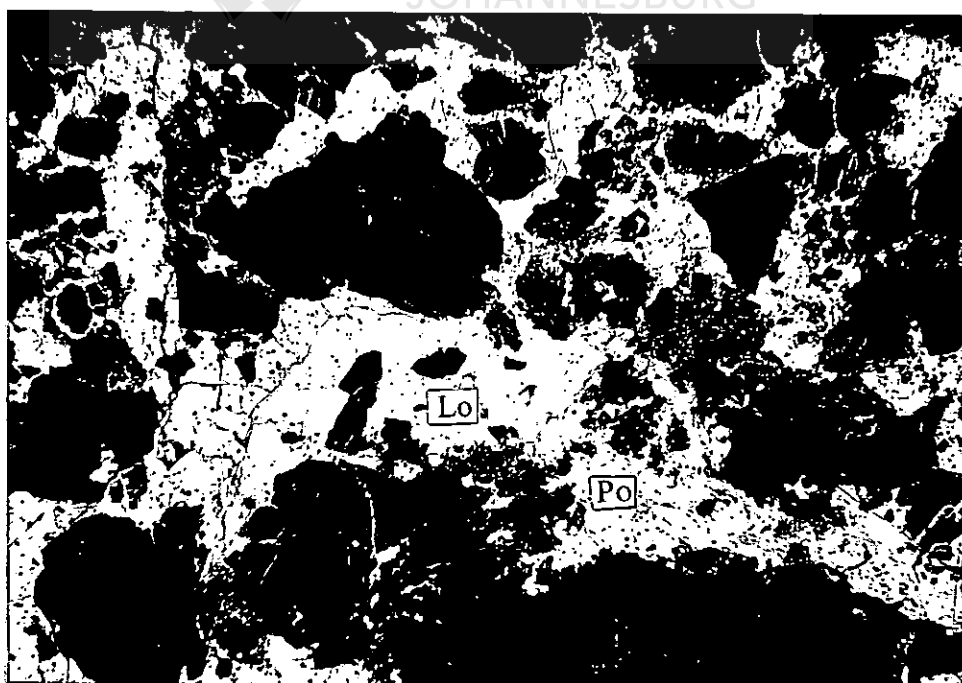


Figure 7.18: Microphotograph (reflected light) showing the partial replacement of the silicate assemblage by pyrrhotite (Po) and löllingite (Lo). Sample DH-2113.

1cm=200 $\mu$ m



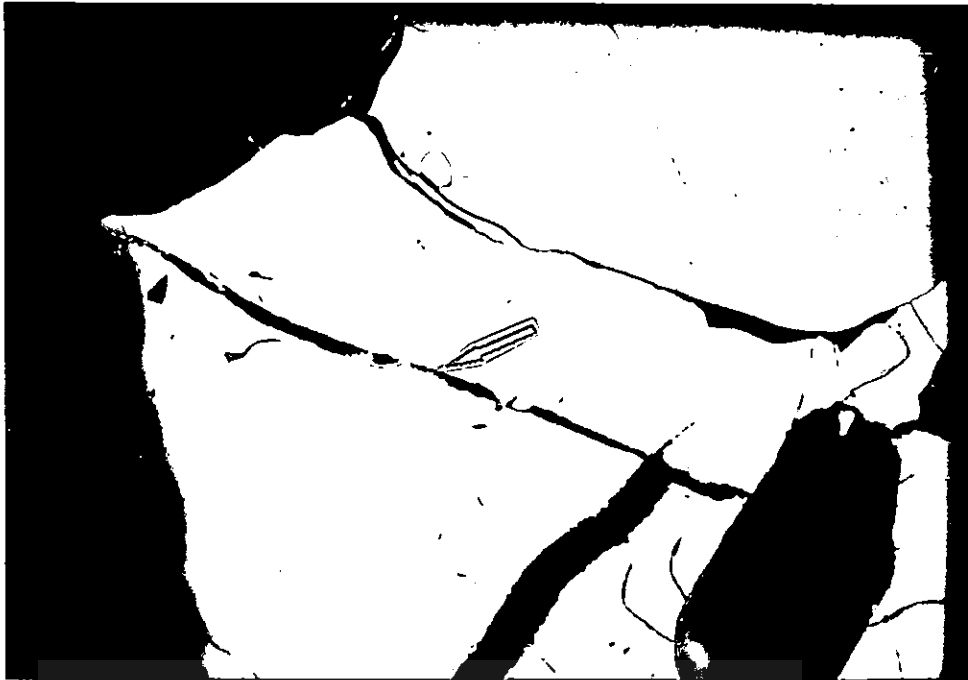


Figure 7.19: Microphotograph showing thin veinlets of chalcopyrite (red arrows) crosscutting pyrrhotite. Sample DH-2113. 1cm=100 $\mu$ m



Figure 7.20: Microphotograph showing an occurrence of very late chalcopyrite (Cpy) in crosscutting veinlets. Sample DH-2115. 1cm=200 $\mu$ m

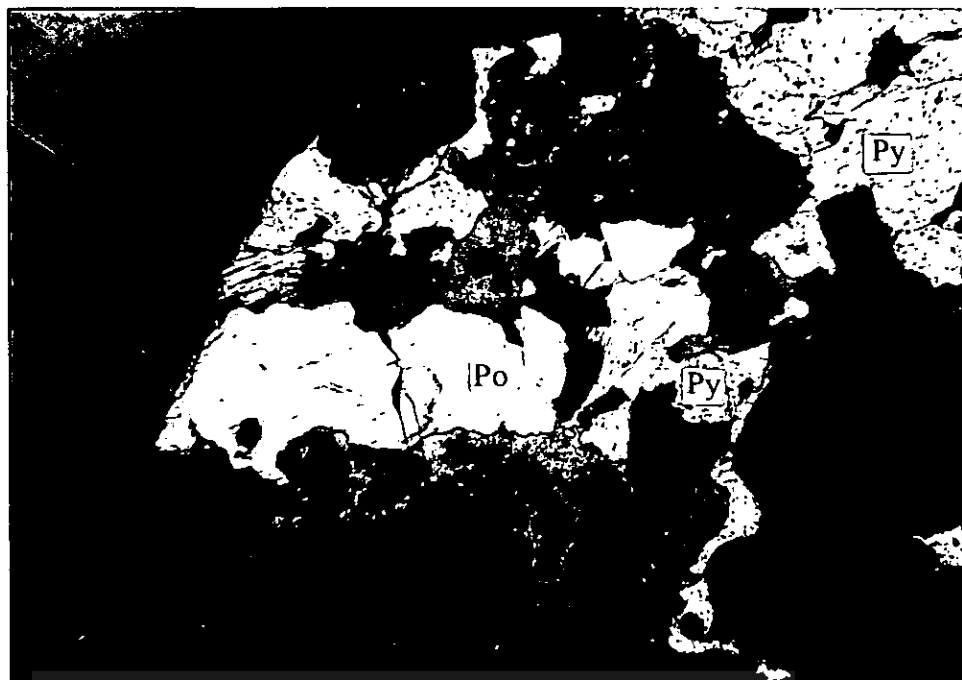


Figure 7.21: Microphotograph showing porous pyrite (Py) after pyrrhotite (Po). Sample DH-2097. 1cm=400 $\mu$ m

**Löllingite (FeAs)** with small amounts of S is always associated with pyrrhotite and magnetite (fig. 7.22). It is usually cemented by pyrrhotite and sometimes intimately intergrown with magnetite (fig. 7.23). Löllingite was therefore formed at the same time as magnetite, or just preceding magnetite, and just before pyrrhotite was introduced into the system. Löllingite is almost always closely associated with gold, and it is sometimes intergrown with it (fig. 7.11). A relationship therefore exists between the high-temperature gold and the precipitation of the Fe-arsenide. The same type of relation between gold and löllingite was also described by Fare (1989), Barnicoat et al. (1991) and by Groves et al. (1992) from a similar high-temperature gold deposit (Griffins Find) from the Yilgarn Craton in Western Australia.

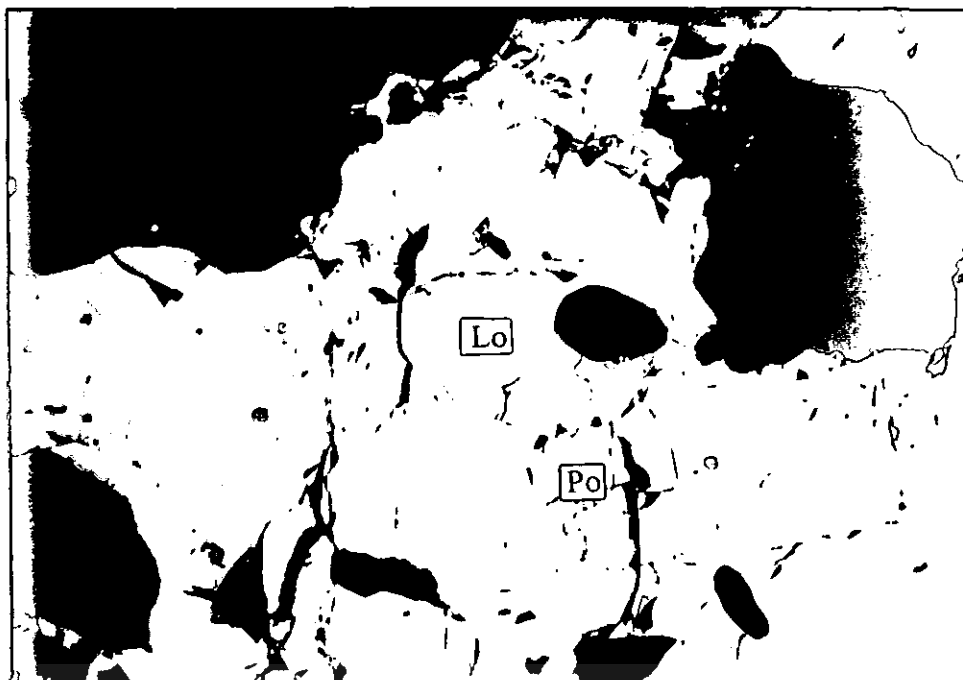


Figure 7.22: Microphotograph showing löllingite (Lo) associated with the highest temperature ore paragenesis at the Doornhoek gold-deposit. It is corroded by pyrrhotite (Po). Sample DH-2030. 1cm=200µm

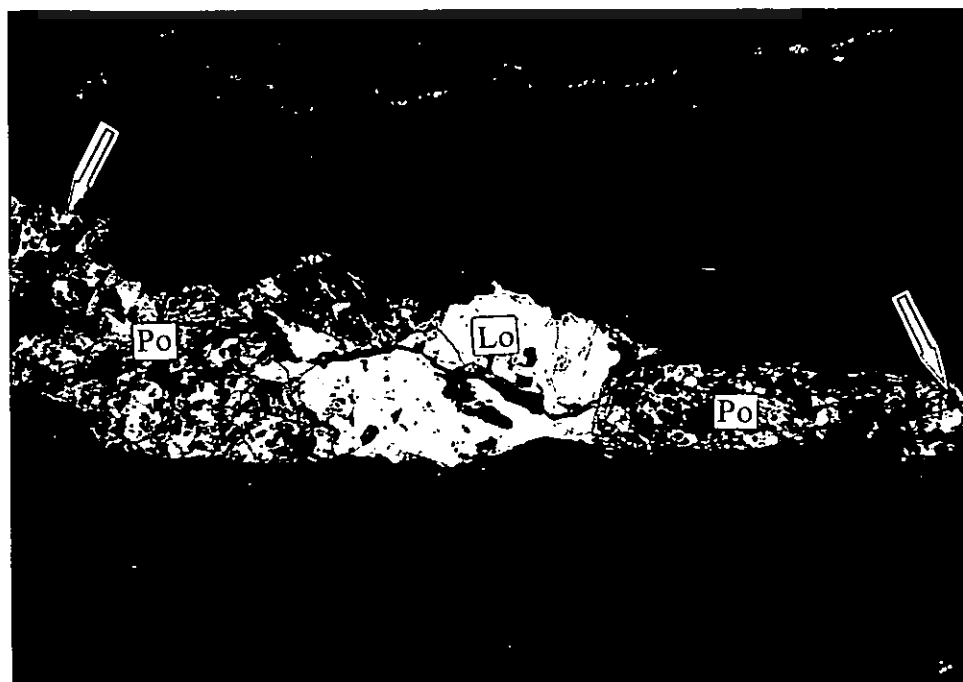


Figure 7.23: Microphotograph showing löllingite (Lo) associated with both magnetite (arrow) and pyrrhotite (Po) in crosscutting veins. Sample DH-2030. 1cm=400µm

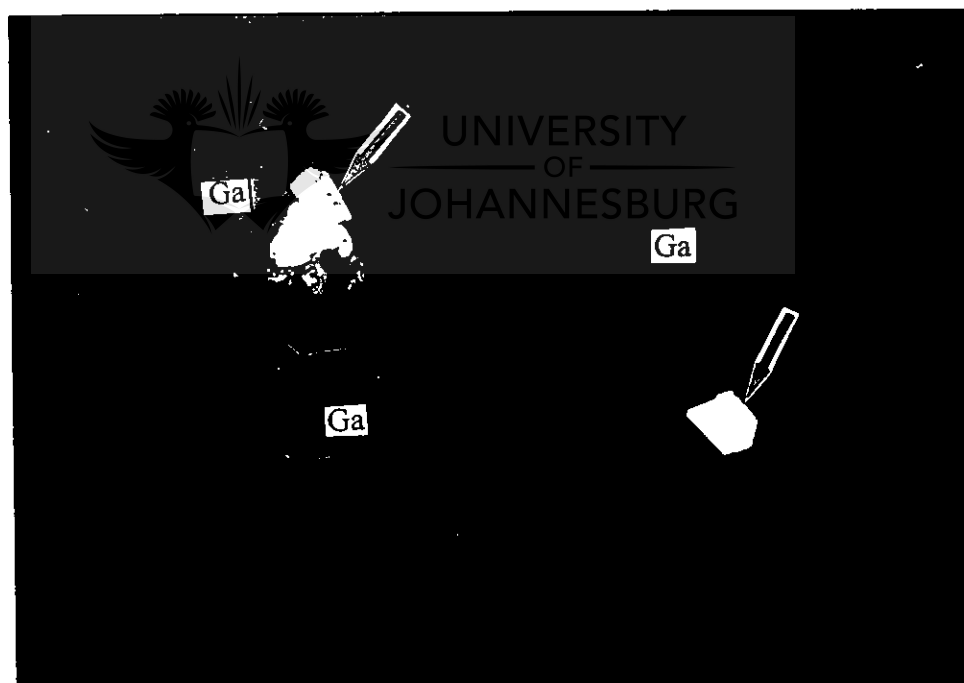
**Arsenopyrite (FeAsS)** occurs mainly with gold, graphite and chalcopyrite, and sometimes also with pyrrhotite and magnetite (**fig. 7.24**). It is usually euhedral to subhedral and occurs both as isolated grains or as crystals corroded by chalcopyrite/pyrrhotite. The typical association of gold-arsenopyrite-graphite (**fig. 7.24**) and the association gold-löllingite-pyrrhotite-magnetite suggests that two different temperature-related paragenesis occur in the same quartz vein. Textural data show that the low-temperature arsenopyrite-gold paragenesis was first formed, followed by the high-temperature löllingite-gold paragenesis. In other words, gold mineralisation at the Doornhoek gold deposit is prograde with reference to the associated metamorphic event. This suggestion is strongly supported by the concentric pattern of mineralisation that is trapped within the zoned garnet porphyroblasts that formed in the metasomatic biotite-garnetiferous formation (**Chapter 6.2**).



**Figure 7.24:** Microphotograph showing gold grains included in löllingite (red arrow) and free gold associated with graphite (blue arrow). The microprobe analyses demonstrated that this type of löllingite displays inclusions of arsenopyrite. Magnetite (Mt) also occurs. Sample DH-2039. 1cm=50µm

**Gersdorffite** [(Fe,Ni)AsS] with very unusual Zn content (up to 6wt per cent Zn) very rarely occurs in the quartz vein system (**fig. 7.25**). It always accompanies the arsenopyrite-related low-temperature type paragenesis. One crystal of gersdorffite was also encountered with the very late (gold unrelated) pyrite dominated mineralisation.

**Skutterudite** (Fe,Ni,Co)As<sub>3</sub> is the rarest ore mineral encountered at the Doornhoek deposit. Only one crystal associated with gersdorffite and pyrrhotite (**fig. 7.26**) was microscopically identified in the quartz vein system. Abundant arsenopyrite crystals in close vicinity to this mineral might suggest that skutterudite is part of the low-temperature mineral association.



**Figure 7.25:** Microphotograph showing crystals of gersdorffite (arrow) included within the prograde garnet porphyroblast (Ga). This gersdorffite is very unusual: instead of the normal formula (Fe,Ni)AsS<sub>3</sub> it contains up to 6wt per cent Zn, suggesting the formula (Fe,Ni,Zn)AsS<sub>3</sub> - probably a new mineral phase. Sample DH-2038.

1cm=100μm

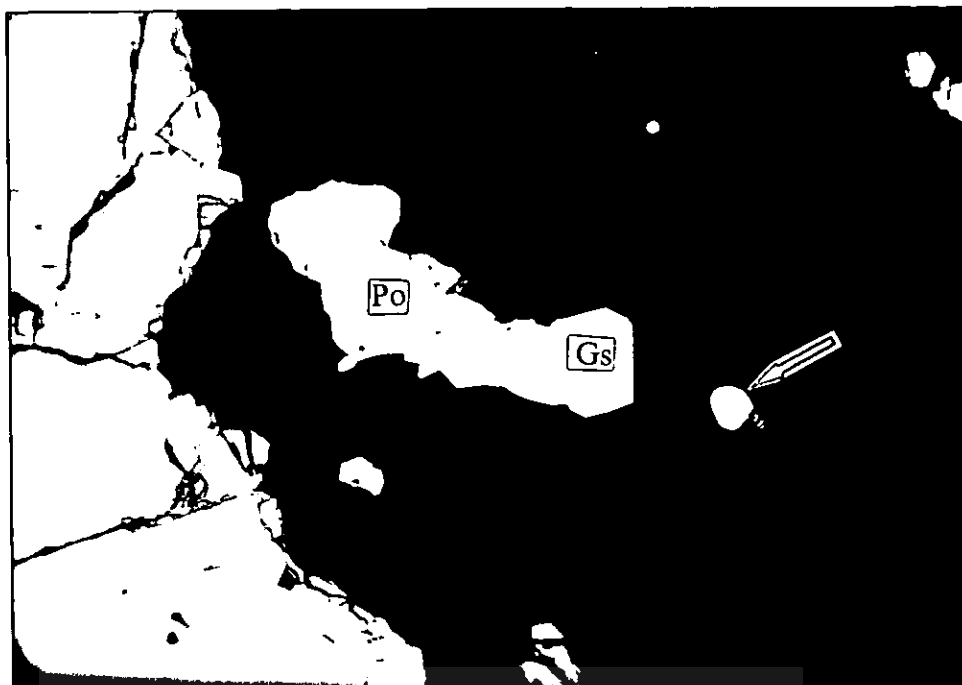


Figure 7.26: Microphotograph showing an isolated skutterudite crystal (arrow) associated with a pyrrhotite (Po) - gersdorffite (Gs) veinlet. Sample DH-2039. 1cm=50µm

### 7.2.3. Native elements

**Graphite (C)** is invariably present in the deposit. Three types of graphite occur: **i)** large crystals intergrown with biotite in the metasomatic biotite-garnetiferous formation (**fig. 7.27**) or associated with quartz in the quartz vein system, **ii)** small crystals, usually associated with gold (**fig. 7.24**) and arsenopyrite, and seldomly with pyrrhotite and magnetite in the quartz vein system, and **iii)** tiny graphite crystals included in the low-density fluid inclusions (**Chapter 9**).

**Gold (Au)** occurs in the quartz veins system as anhedral, usually hackly-shaped grains, ranging in size from 1 to 40 µm. It is always associated with löllingite or arsenopyrite (**fig. 7.11, 7.24 and 7.27**) while graphite is invariably also present (**fig. 7.24, 7.27, 7.28 and 7.29**).



**Figure 7.27:** Microphotograph showing graphite crystals (red arrows) at the edge of a large prograde garnet porphyroblast (Ga). A system of thin quartz veinlets (yellow arrows) displays gold (electrum) mineralisation (Au). Sample DH-2047. 1cm=50µm

Whenever gold is entrapped within garnet porphyroblasts, it usually occurs in the core or in the mineralised dark inner-ring (**Chapter 6.2**). In some cases gold also occurs in tiny quartz veinlets hosted by the edge of the garnet porphyroblasts. But these quartz veinlets actually emerge from the main quartz vein system and represent later remobilisation from the main mineralised system. Such a situation is displayed in **fig. 7.27** where gold is clearly hosted by a late quartz veinlet crosscutting the edge of a large garnet porphyroblast. The gold present within the Doornhoek deposit is highly alloyed with silver (up to 45wt per cent Ag), being a real electrum. As a result gold appears yellow-silverish, especially when it is associated with intense white minerals, such as arsenopyrite, löllingite or gersdorffite.

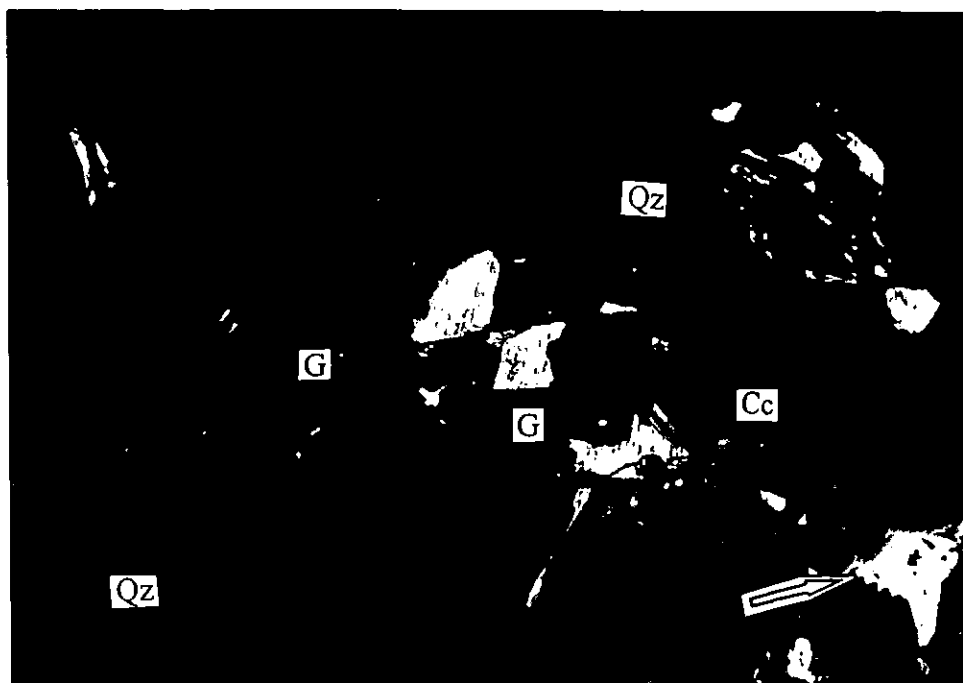


Figure 7.28: Gold crystals intimately associated with graphite (G) in a quartz (Qz) -calcite (Cc) vein. Arsenopyrite occurs in the corner of the microphotograph (arrow). Sample DH-2047. 1cm=25µm



Figure 7.29: Microphotograph showing gold crystals (yellow arrow) associated with arsenopyrite (red arrow) and large graphite crystals (G). Sample DH-2047. 1cm=25µm



#### 7.2.4. Evolution of the mineralisation associated with quartz veins

The mineralisation encountered within the quartz vein system could not have precipitated altogether at the same time because of the large temperature gap between the stability fields of the paragenesis löllingite-pyrrhotite-chalcopyrite and arsenopyrite-gersdorffite-sphalerite (Scott, 1983). The different ore mineral paragenesis were therefore precipitated at different times during the evolution of the mineralised shear zone.

The following observations can be used to establish the evolution of the mineralisation:

i) the same mineral associations were trapped in the growing garnet porphyroblast (see **next Chapter 7.3**) in the metasomatic biotite-garnetiferous formation and in the quartz veins, suggesting that the order of ore mineral precipitation inside the quartz vein system should be the same as that for the zoned garnet. This also suggests that both types of mineralisation (in the quartz vein and included within the garnet porphyroblast) were deposited during the same event.

ii) ore minerals were trapped in different zones of the garnet during its prograde growth (core, inner ring, edge) - see **Chapter 7.3**. This suggests that mineralisation within the quartz-vein system was also deposited during the same prograde event, namely starting with a low-temperature paragenesis (mainly arsenopyrite-sphalerite-gersdorffite) that was followed by a high-temperature paragenesis (mainly löllingite-pyrrhotite-chalcopyrite). A medium-temperature paragenesis (mainly consisting of Ni-bearing minerals) might be located in time between the low- and the high-temperature paragenesis.

There are no clear textural data preserved in the mineralised quartz veins to prove the order of crystallisation of the ore minerals. However, scarce as they may be, the discussed crosscutting textural features, corroborated with data from the literature (Scott, 1983) and other references (Barnicoat et al., 1991; Groves et al., 1992) can be used to deduce an order of crystallisation. Observations at Griffins Find in the Yilgarn Block, Western Australia (Groves et al., 1992) allowed the style of mineralisation at Doornhoek to be divided into two distinct paragenesis with a transitional type between them. These paragenesis and their order of crystallisation are described below and demonstrated in **fig. 7.30**:

**Step 1:** a low-temperature paragenesis consisting of arsenopyrite, chalcopyrite, pyrrhotite without pentlandite exsolutions and sphalerite was precipitated during step 1. Arsenopyrite displays a low As-content, being an As-poor FeAsS (32wt per cent As). Arsenopyrite and sphalerite are among the first minerals to crystallise and occur as isolated crystals surrounded by pyrrhotite. Chalcopyrite is also associated with sphalerite, being among the first ore minerals to precipitate, but it also corrodes and crosscuts pyrrhotite, suggesting remobilisation during the late stage 1. Pyrrhotite, the main mineral that precipitated during stage 1, is pentlandite-free. Pyrrhotite post-dates arsenopyrite and sphalerite but the two types of chalcopyrite (Cpy I and Cpy II) respectively predates and post-dates pyrrhotite. Although magnetite is present in large amounts in the mineralised quartz veins, its association with the pentlandite-rich pyrrhotite suggests that magnetite was introduced into the veins system, as an oxide, at a later stage.

**Step 2:** the second wave of mineralising solutions (the medium temperature paragenesis) precipitated As-rich arsenopyrite, pyrrhotite (with some exsolutions of pentlandite), small

amounts of chalcopyrite and Ni-bearing minerals such as: gersdorffite, skutterudite and niccolite. Gold and graphite were also deposited during this event. As-rich arsenopyrite (with up to 38wt per cent As) is quite abundant and is one of the first ore minerals that crystallised during step 2. Pyrrhotite probably continued its precipitation from step 1, starting to exsolve Ni in the form of pentlandite flames. Although the textural relationships between the Ni-bearing minerals (gersdorffite, niccolite, skutterudite) and the rest of the mineralisation are not very clear it can be assumed that the end of stage 2 of ore mineralisation was also characterised by a Ni-rich event. Gold is mainly associated with arsenopyrite and graphite and is usually surrounded by pyrrhotite. It can therefore be suggested that both gold and graphite crystallised at the beginning of the stage 2 event and continued to crystallise towards the middle part of stage 2. Pyrrhotite is the most abundant ore mineral and crystallised continuously during step 2. It is highly probable that a time gap occurred in the ore mineral deposition after step 2, because the step 3 event consists mainly of much higher temperature ore mineralisation in comparison with the typical mesothermal mineralisation that characterised the step 2 event.

**Step 3:** this is a high-temperature paragenesis consisting of löllingite, magnetite, pyrrhotite (with pentlandite exsolutions), chalcopyrite, ilmenite and gold. Graphite is also present in this paragenesis and is associated with both gold and löllingite. These high-temperature solutions primarily deposited löllingite. The cores of the löllingite crystals consist of arsenopyrite (with anomalous high As-content) transformed immediately into löllingite. Magnetite surrounds most of the löllingite grains and occur as crosscutting schlieren. Pyrrhotite (with pentlandite exsolutions) cements most of the magnetite, being precipitated just after magnetite. In areas where the silicate matrix is highly deformed pyrrhotite is highly stretched. Finally,

chalcopyrite, ilmenite and again gold were precipitated. Gold (actually electrum) is definitely one of the last minerals that precipitated because gold-bearing quartz veinlets crosscut the edges of the mineralised garnet porphyroblast (**fig. 7.27**).

**Step 4:** re-equilibration of the ore minerals during subsequent cooling was probably dominated by remobilisation of part of the iron sulphides and sulphur in crosscutting veinlets consisting of pyrite and pyrrhotite. Pyrite is very porous and usually transformed into marcasite, indicative of very low temperature conditions. The very narrow pyrite veinlets crosscut all the preexistent mineral associations, also suggesting a very late event, that probably took place during cooling, if not even supergene. Gersdorffite was also precipitated during this late, but relatively minor event (step 4).



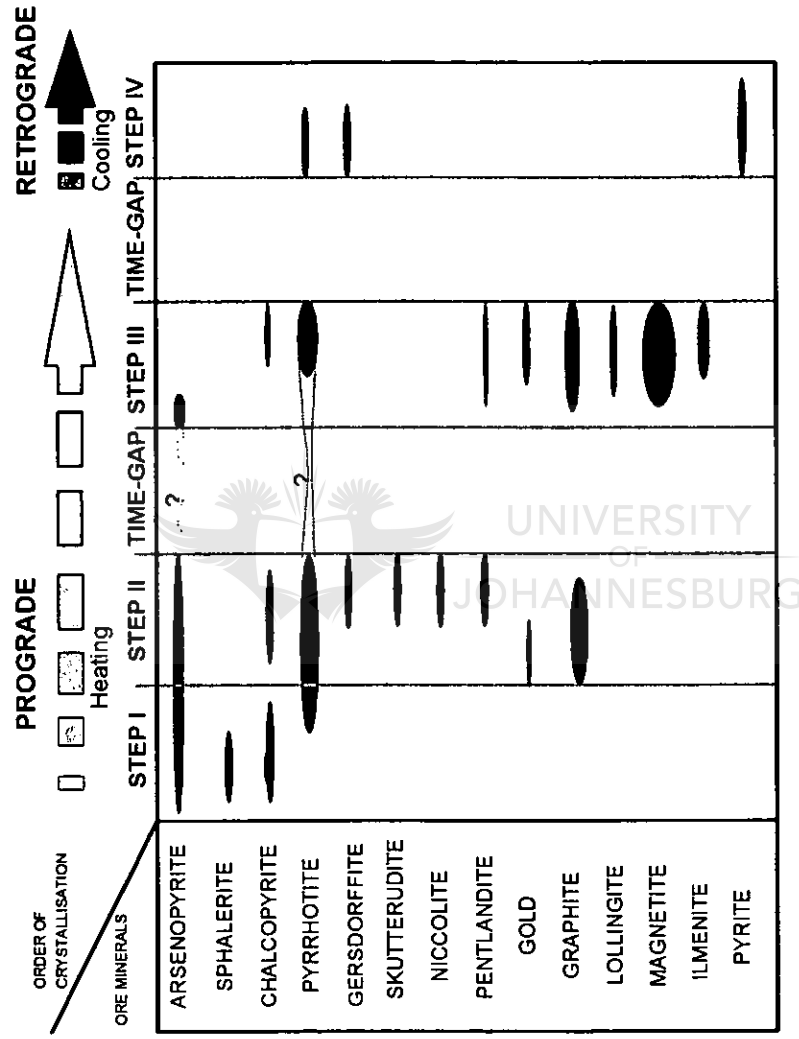


Figure 7.30: The four stages of mineralisation described in the text. Mineralisation started with a low-temperature paragenesis (step 1), consisting mainly of arsenopyrite-sphalerite-chalcopyrite and pyrrhotite. The deposition continued with medium-temperature mineralisation (step 2), consisting mainly of arsenopyrite, Ni-bearing minerals, pyrrhotite and gold. A time gap followed after step 2. Mineralisation then continued with a high-temperature paragenesis (step 3) consisting of illingite-pyrrhotite-magnetite and electrum. These three stages of ore mineral deposition occurred during a prograde metamorphic event. Step 4 was represented by the remobilisation of the initial Fe sulphides, mainly as pyrite and secondary pyrrhotite and small amounts of gersdorffite during a retrograde event.

### 7.3. MINERALISATION ENTRAPPED IN METASOMATIC GARNET PORPHYROBLASTS

#### 7.3.1. Zoning of garnet

The metasomatised biotite-garnetiferous formation and the quartz veins both formed at the same time as a result of shearing and fluid infiltration. The euhedral garnet porphyroblast that characterises the biotite-garnetiferous formation displays a distinct concentric prograde growth pattern that clearly reflects the changing PT-fluid characteristics during the mineralisation event (**Chapter 6.2.2.2**). The growth pattern displayed by the garnet porphyroblast consists of a **core, an inner zone, a dark inner-ring and an unmineralised edge (fig. 6.15)**. The  $Mg/(Mg+Fe)$  ratio increases gradually from the core to the inner-ring zone and then sharply (with more than 6wt per cent) to the edge (**fig. 6.16**; see detailed description of the garnet in **Chapter 6.2.2.2**). The  $Mn/(Mn+Mg+Fe+Ca)$  ratio exhibits the reverse pattern and decreases slowly (with 2wt per cent) from the core to the inner-ring zone and then sharply (4wt per cent) to the unmineralised edge. The  $Ca/(Mn+Mg+Fe+Ca)$  ratio varies between 12 and 19wt per cent but the zoning pattern is irregular, probably due to a slower rate of diffusion of the Ca ion within the garnet lattice (Anderson and Buckley, 1973).

#### 7.3.2. Mineralisation trapped within prograde garnet porphyroblasts

As already discussed (**Chapter 6.2.2.2**) the garnet porphyroblasts (**fig. 6.15 and 6.16**), which together with biotite represent the main component in the metasomatic biotite-garnetiferous

formation, display a well preserved prograde zonation pattern. The different zones developed in the garnet porphyroblast each hosts a different mineralisation type:

**Core:** sphalerite with exsolutions of chalcopyrite, pyrrhotite, and arsenopyrite (with a lower As-content than normal - 32 wt per cent As) was trapped in the core of the growing garnet (**fig. 7.31**). Very small amounts of chalcopyrite also occur in the core, while no gold was trapped.

**Inner Zone:** gold (actually electrum) is always associated with an As-rich arsenopyrite (up to 38 wt per cent As) and with graphite (**fig. 7.32** and **7.34**), while niccolite, an unusual Zn-bearing gersdorffite from the sulpho-arsenides mineral group (19 per cent Fe, 15 per cent Ni, 1 per cent Zn, 30 per cent S and 35 per cent As - **fig. 7.26**), skutterudite and pyrrhotite with exsolutions of pentlandite also occur. Small amounts of chalcopyrite were also identified.

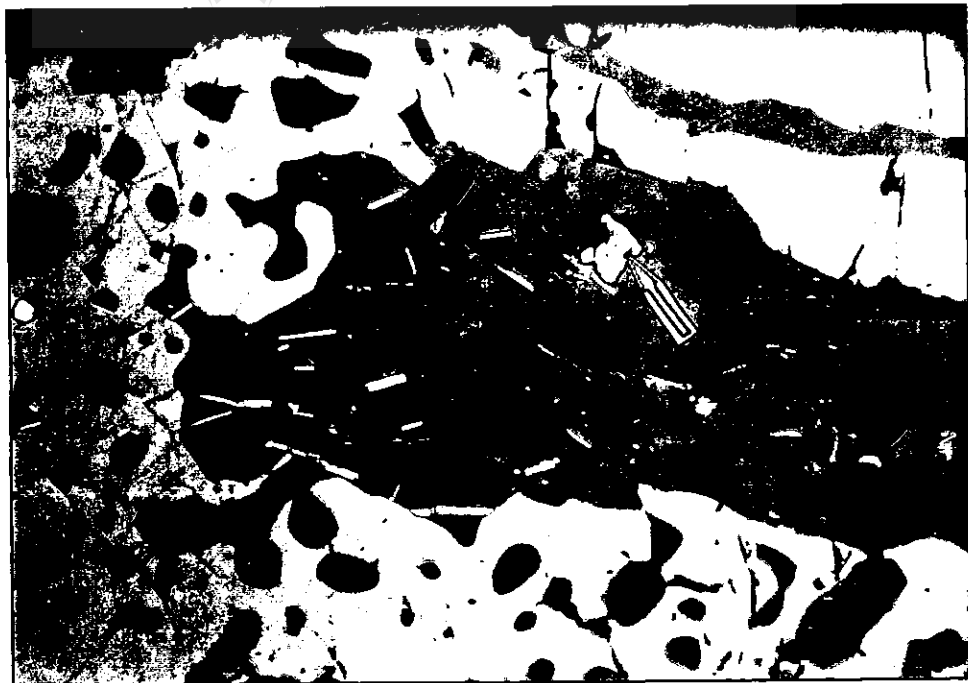
**Dark inner-ring zone:** löllingite (**fig. 7.33**), pyrrhotite (also with exolutions of pentlandite) and chalcopyrite. Magnetite and ilmenite is present in all the zones (**fig. 7.35**).

**Edge:** the edge of the garnet porphyroblast is usually unmineralised, suggesting that the final stages in the evolution of the mineralised shear zone were generally not associated with mineralised fluids. This can possibly be explained by the very high temperature at which the edge of the garnet crystallised from hot metasomatic fluids (720°C, see **Chapter 10**). Therefore, these mineralised fluids, being probably too hot, inhibited the precipitation of the gold and associated metals during the formation of the edge of the garnet porphyroblast.



**Figure 7.31:** Microphotograph showing sulphides hosted by the core of a large, progradely zoned garnet porphyroblast (see fig. 6.15). This mineralisation consists of chalcopyrite (yellow arrow), pyrrhotite (blue arrow), arsenopyrite (red arrow) and tiny sphalerite crystals (black arrow). A large sphalerite crystal also occurs. Sample DH-2035.

1cm=25 $\mu$ m



**Figure 7.32:** Microphotograph showing graphite crystals (beige rods) and As-rich arsenopyrite (red arrow) trapped in the inner zone of the prograde garnet porphyroblast. Their actual host is quartz also trapped inside the garnet. Sample DH-2035.

1cm=25 $\mu$ m





Figure 7.33: Microphotograph showing löllingite (Lo) and tiny magnetite and ilmenite crystals (arrows) trapped in the dark inner-ring zone of the prograde garnet porphyroblast. Sample DH-2035. 1cm=25µm

### 7.3.3. Oxides

**Ilmenite and magnetite** occur as a very fine pigment in the garnet porphyroblast but also as slightly bigger crystals, especially towards the outer zone of the mineralised dark inner-ring. Both minerals occur as anhedral, sometimes completely rounded tiny crystals (**fig. 7.33**) entrapped during the garnet growth in almost all the zones of the host mineral, but generally concentrated within the dark inner-ring. The inner-ring, due to the high concentration of Fe and Ti oxides frequently appears opaque (**fig. 6.15 and 7.35**). Ilmenite is frequently elongated, but also displays rounded margins.

#### 7.3.4. Sulphides and arsenides

**Sphalerite** mainly occurs within the core of the garnet porphyroblasts, although one crystal was also encountered in the inner-ring zone. The crystals are anhedral, usually rounded and always display exsolutions of chalcopyrite (**fig. 7.31**). In one case sphalerite is rimmed by gold.

**Pyrrhotite** (pentlandite-free) occurs as large anhedral crystals (up to 250  $\mu\text{m}$ ) in the core of the garnet, or as small, rounded crystals of pentlandite-bearing pyrrhotite in the dark inner-ring and inner zones of the garnet (**fig. 7.31** and **7.34**). The modal abundance decreases towards the inner-ring zone.

**Chalcopyrite** forms part of the ore mineral association entrapped within the dark inner-ring and inner zones of the garnet porphyroblast (**fig. 7.31**). It also occurs as exsolutions in sphalerite trapped in the core zone. Chalcopyrite seldomly occurs in bubbles with a triple composition: chalcopyrite, pyrrhotite and löllingite, hosted by the heavily mineralised inner-ring zone of the garnet porphyroblast.

**Niccolite** ( $\text{NiAs}$  - with small amounts of Fe, Co and S) is very rarely present in the inner zone of the mineralised garnet, the only zone where it occurs. The niccolite crystals are completely rounded.

**Löllingite** was entrapped at the external margin of the dark inner-ring of the garnet porphyroblast, near the unmineralised zone and even in the unmineralised edge, within the

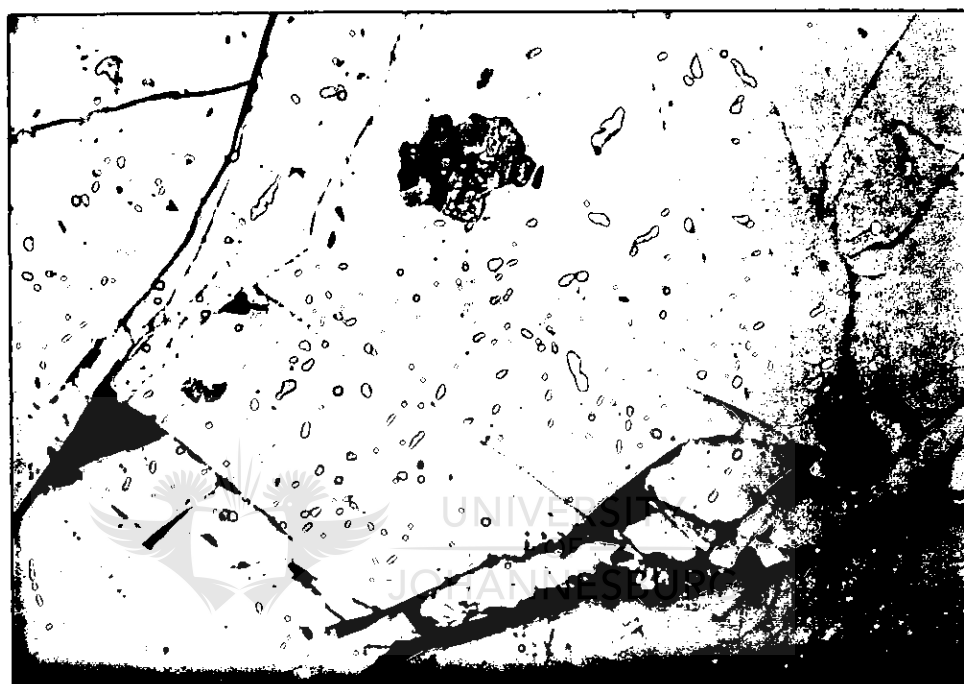
zone that displayed the highest equilibration temperature for the pair garnet-biotite (see **Chapter 11**). In the highly mineralised inner-ring zone of the garnet porphyroblast löllingite occurs as tiny crystals, almost always associated with gold-graphite or with pyrrhotite-chalcopyrite (**fig. 7.33**). There appear to be a genetical relationship between löllingite, gold and graphite within the dark inner-ring of the garnet porphyroblast.

**Arsenopyrite** was entrapped into the core zone of garnet as an As-poor arsenopyrite and in the inner zone as an As-rich arsenopyrite. This difference in chemistry is probably due to the different temperatures at which the mineral was formed during the prograde growth of the garnet porphyroblast. It occurs as subhedral to almost euhedral crystals (**fig. 7.31 and 7.32**), and is associated with gold and graphite within the inner zone.



**Figure 7.34:** Microphotograph showing a tiny gold crystal (red arrow) associated with pyrrhotite (yellow arrow) and gersdorffite (blue arrow) in the inner zone of the prograde, zoned garnet porphyroblast. Magnetite is relatively abundant (mauve arrow). Graphite is also present as very small crystals. Sample DH-2035. 1cm=25µm

**Gersdorffite** and very rare **skutterudite** occur together within the inner zone. Gersdorffite is quite common within the inner zone of the garnet porphyroblast, but it is a very unusual mineral species (6 wt per cent Zn, although the usual Zn content is only 1-2 wt per cent). This unusual high Zn content is quite odd taking into account that Zn is not a chemical component of gersdorffite (Ramdohr, 1980).



**Figure 7.35:** Microphotograph showing a high density of tiny crystals of Fe and Ti oxides trapped in the dark inner-ring zone of the prograde zoned garnet porphyroblast. Sample DH-2035. 1cm=25 $\mu$ m


### 7.3.5. Native elements

**Gold** (actually electrum) is concentrated within the inner zone and inner-ring zone of the garnet porphyroblast. It occurs as tiny, either hackly shaped or rounded crystals, always associated with graphite (**fig. 7.34**) or with an arsenide (arsenopyrite in the inner zone and löllingite in the dark inner-ring zone). Electrum is sometimes geometrically associated with

the Fe and Ti oxides in the inner-ring zone. Very often gold is present in quartz veinlets or as inclusions within the garnet (fig. 7.27 and 7.29), but always closely associated with graphite.

**Graphite** occurs in all zones of the garnet porphyroblast (except in the core). Two types of graphite was recognised: needles or rods, usually included towards the edge of the garnet, and rounded crystals, usually included within the dark inner-ring zone. Gold is always closely associated with graphite, while there is also a close association of tiny graphite crystals with low-density CO<sub>2</sub>-rich fluid inclusions (see **Chapter 9**).

#### **7.3.6. Thermal zonation of mineralisation entrapped in the zoned garnet porphyroblast**



Mineralisation entrapped in the garnet porphyroblast is zoned from the core to the edge, with a lower temperature paragenesis trapped in the core and a higher temperature paragenesis trapped towards the edge. This matter was discussed in detail in **Chapter 6.2.2.2.** and summarised below.

Mineralisation within the prograde zoned garnet was trapped during a gradually increasing temperature gradient. This temperature gradient was probably established as a result of hot hydrothermal solutions that were channelised through the active shear zone system at Doornhoek. As a result, mesothermal sulphides and arsenides were trapped in the core of the garnet: sphalerite (with chalcopyrite exsolutions), pyrrhotite and As-poor arsenopyrite. The deposition of minerals continued during garnet growth, with As-rich arsenopyrite, graphite,

niccolite, gersdorffite, skutterudite, pyrrhotite (with pentlandite exsolutions) and electrum (up to 45wt per cent Ag) being trapped in the inner zone.

Magnetite and ilmenite, together with löllingite, pyrrhotite (with pentlandite exsolutions), chalcopyrite and electrum (poorer in Ag: only up to 36wt per cent Ag) were precipitated when the metasomatic system reached temperatures conditions equivalent to the lower-granulite facies. At this stage the mineralising metasomatic solutions deposited the main part of their metallic load. The density of oxides, sulphides, arsenides and native elements is so high that the garnet porphyroblast actually displays a black inner-ring, due to the high concentration of ore minerals (**fig. 6.15**).

The edge of the garnet porphyroblast is unmineralised, probably suggesting the following:

- i) the peak temperature reached by the hydrothermal solutions was too high to allow ore minerals to precipitate, or
- ii) the main metallic load was precipitated during the early stage of the evolution of the shear zone, and from there onward only silicate minerals were formed or redistributed within the hydrothermal shear system.

#### 7.4. SIMILARITIES BETWEEN MINERALISATION DEPOSITED WITHIN QUARTZ VEINS AND TRAPPED IN THE GARNET PORPHYROBLAST IN THE BIOTITE-GARNETIFEROUS FORMATION

The same mineralisation characterises both the quartz-vein system and the prograde zoned garnet porphyroblasts. The order and timing of mineralisation in the quartz vein system is very similar to that of the mineralisation trapped in the growing garnet porphyroblast (**Chapters 7.2 and 7.3**). Both the quartz veins and the garnet porphyroblasts are therefore characterised by three successive prograde mineralising events:

**Step 1:** sphalerite, chalcopyrite, As-poor arsenopyrite and pyrrhotite (without pentlandite exsolutions) - trapped in the core of the garnet and in the quartz veins. In the quartz veins sphalerite and As-poor arsenopyrite are usually corroded by pyrrhotite and stoichiometrically equilibrated arsenopyrite

**Step 2:** gersdorffite (with an unusually high Zn content), skutterudite, niccolite, gold, chemically equilibrated arsenopyrite, chalcopyrite and pyrrhotite - trapped in the inner zone of the garnet and in quartz veins. In the quartz veins this step 2 ore paragenesis usually corroded step 1 ore paragenesis and it is corroded by magnetite, ilmenite, pyrrhotite (with pentlandite exsolutions) and löllingite

**Step 3:** As-rich arsenopyrite followed shortly by löllingite, magnetite, pyrrhotite (with pentlandite exolutions), ilmenite and gold - trapped in the dark inner-ring of the garnet and the latest precipitated within the quartz veins.

Several small differences do exist. Niccolite, for instance, was only identified in the garnet, and never in the quartz veins. There is also a larger amount of ilmenite trapped in garnet porphyroblasts compared with the quartz veins. Sphalerite is also much more abundant in garnet. Pentlandite occurs more frequently as exsolutions in pyrrhotite entrapped in garnet than in pyrrhotite in the quartz veins. Ni-bearing minerals, such as pentlandite, niccolite, skutterudite and gersdorffite are usually concentrated in garnet porphyroblasts. This preference of the Ni-ion for the garnet structure is probably controlled by crystal-chemical considerations. Furthermore, the zonation of Ni-minerals within garnet demonstrates that Ni was precipitated predominantly at higher temperatures, during step 2 (niccolite, skutterudite, gersdorffite, pentlandite) and even during step 3 (only pentlandite).

Another important observation is that the Zn-bearing gersdorffite occurs at the boundary between the core and the inner zone of the garnet porphyroblast, therefore defining the transition between the mesothermal phase of mineralisation (sphalerite main phase) and the hypothermal phase (with Ni-bearing minerals as main phases).

However, despite the differences, mineralisation in both the quartz veins and in the garnet porphyroblast displays similar features, due to the fact that both were probably precipitated/trapped by the same mineralising fluids during the same event.



## 8. RELATIONSHIP BETWEEN DEFORMATION, HYDRATION AND METASOMATISM IN THE DOORNHOEK ORE BODY

### 8.1 SUGGESTED PROTOLITES AND MECHANISM OF FORMATION OF THE PROGRADE PATTERN LITHOLOGIES AT DOORNHOEK

The following features characterise the mineralised zone of the Ore Body:

*i)* the same sulphide-arsenide-oxide-gold mineralisation occurs in both the quartz veins and in the metasomatic biotite-garnetiferous formation (**Chapter 7**)

*ii)* euhedral metasomatic garnet is the main alteration product of the silicate facies BIF and it hosts the same mineralisation as the quartz veins and probably reflects a high fluid:rock ratio (**fig. 8.1a, b**) (Colvine et al., 1988)

*iii)* the garnet displays a prominent prograde zoning pattern and occurs as perfect euhedral porphyroblasts, typically of metasomatic growth as the result of very high fluid:rock ratios (Colvine et al., 1988)

*iv)* CO<sub>2</sub>-rich fluid inclusions occur both in quartz from the quartz veins and in quartz inclusions in garnet in the biotite-garnetiferous formation (see **Chapter 9**).

The textural features of the biotite-garnetiferous formation and of the quartz veins, as well as the association between different minerals, namely garnet+biotite in the BIF and mafic volcanics (**fig. 8.1a and b**); anthophyllite+biotite in ultramafic lithologies (**fig. 8.1c**); and orthoclase+biotite+tourmaline in the granite-gneisses (**fig. 8.1d**), suggest that the

metasomatic biotite-garnetiferous formation represents the product of interaction between highly channelised fluids and the Fe-rich host rock (fig. 8.1).

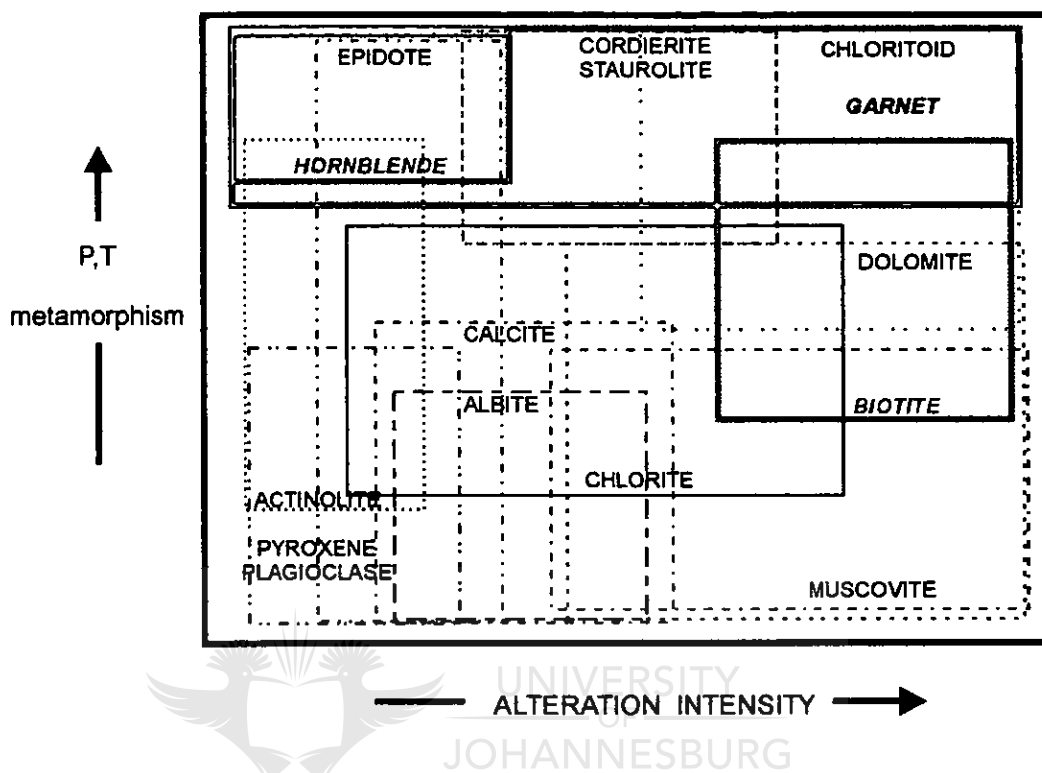


Figure 8.1:

a) Different alteration patterns that can occur after various lithologies have presumably undergone hydrothermal alteration at the time of gold precipitation. Note that the sketches do not indicate the scale and neither the metamorphism or alteration intensity. Four different lithological types are illustrated: a) basalts; b) calc-silicate-oxide facies BIF; c) ultramafic and komatiitic; d) silica-saturated and -undersaturated granitoid rocks (from Colvine et al., 1988).

The sketch above illustrates the schematic representation of the field of occurrence of important minerals in progressively altered and metamorphosed basaltic rocks in gold-bearing systems. Hornblende is the main mineral for high-grade metamorphic conditions and low fluid:rock ratios. Garnet is characteristic of high-grade metamorphic condition and intense alteration (high fluid:rock ratio).

Possible prograde reactions that occurred at Doornhoek (after Colvine et al., 1988):

- a1 - Quartz + Calcite + Chlorite = Hornblende
- a2 - Quartz + Calcite + Chlorite = Actinolite
- a3 - Chlorite + Quartz + Magnetite + K<sup>+</sup> = Biotite
- a4 - Chlorite + Quartz + H<sub>2</sub>S = Anthophyllite + Cordierite + Pyrrhotite
- a5 - Chlorite + Quartz + Dolomite + K<sup>+</sup> = Garnet + Pargasite

The presence of euhedral garnet porphyroblast with prograde zonation pattern is, at first glance, rather unusual since lithologies in the Doornhoek environment were all affected by the retrograde history that characterises this part of the SMZ of the LB. The growth of

prograde garnet, however, is a relatively common phenomenon in BIF and mafic rocks as the result of the introduction of high-temperature fluids into Fe- or Mg-rich systems (Colvine et al., 1988) (see figures 8.1). The mineral reactions recognisable in the Doornhoek lithologies, compared with the multiple possibilities of mineral association described by Colvine et al., 1988, are summarised below (fig. 8.1a, b, c and d):

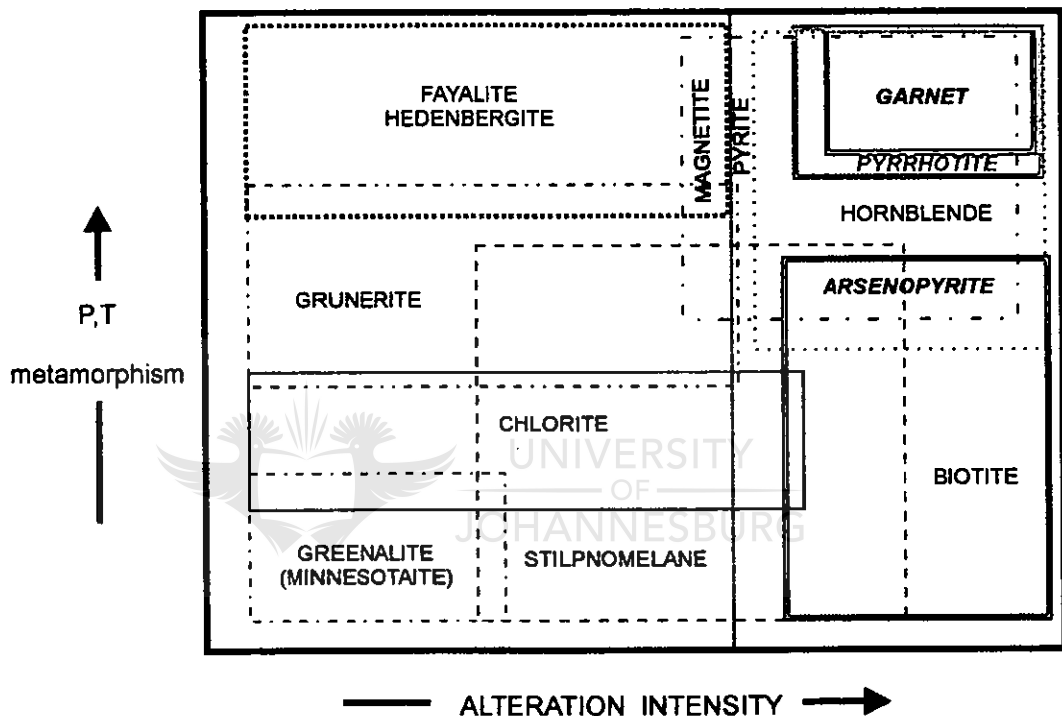


Figure 8.1b: Schematic representation of the fields of occurrence of important minerals in progressively altered and metamorphosed calc-silicate facies BIF in gold-bearing systems. Hedenbergite and Fe-rich olivine (fayalite) is the alteration product characteristic for high PT conditions and low alteration intensity. Garnet and pyrrhotite+arsenopyrite are the minerals formed under high-grade metamorphic condition and high fluid-rock ratio.

Possible prograde reactions that occurred at Doornhoek:

- b1 - Chlorite + Quartz + Dolomite +  $K^+$  = Stilpnomelane + Calcite
- b2 - Magnetite + Quartz = Grunerite
- b3 - Grunerite-gedrite +  $H_2S$  = Gedrite + Pyrrhotite + Quartz
- b4 - Chlorite + Quartz + Magnetite +  $K^+$  = Biotite
- b5 - Chlorite + Quartz + Dolomite +  $K^+$  = Garnet + Pargasite

Therefore, only mafic, BIF and to a lesser extent ultramafic lithologies display the type of prograde reactions encountered in the Doornhoek Ore Body that include the formation of

garnet, biotite and anthophyllite. The introduction of K-rich fluids into the system is typical of all four lithologies. On the other hand, the K-rich solutions also affected the felsic lithologies, as described by the above reactions and in **fig. 8.1**. This process is beautifully expressed at Klipbank (Mokgathla, 1995) and also at Doornhoek (the intense K-feldspar enrichment of the Baviaanskloof Gneiss and of the felsic granulite - see **Chapters 5 and 6**).

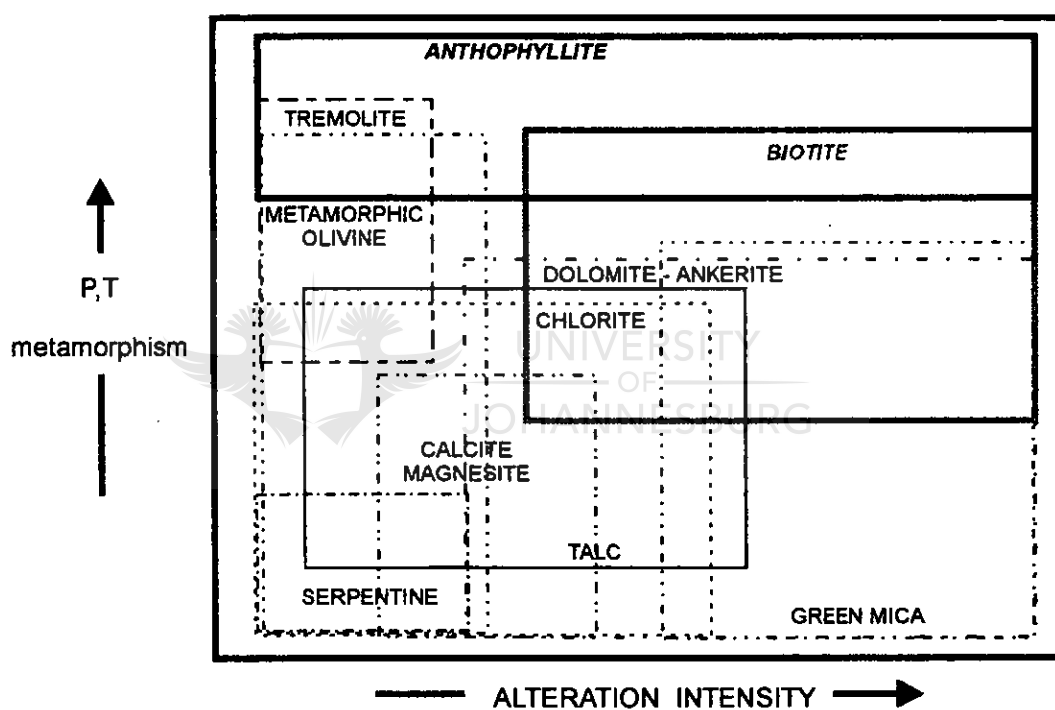
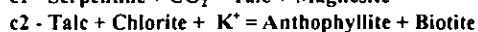
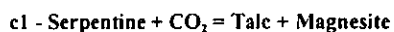


Figure 8.1c:

Schematic representation of the fields of occurrence of important minerals in progressively altered and metamorphosed ultramafic and komatiitic rocks in gold-bearing systems. Anthophyllite is the main alteration mineral and it can be associated with tremolite under low alteration condition and biotite under high alteration condition (high fluid:rock ratio).

Possible prograde reactions that occurred at Doornhoek:



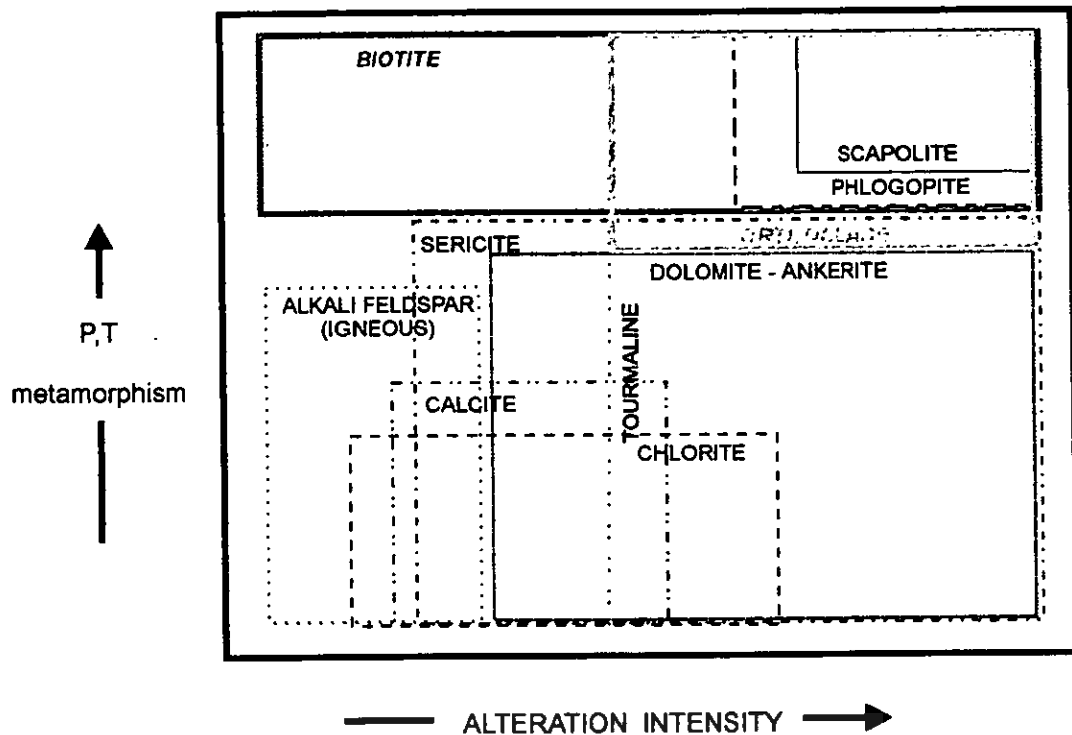


Figure 8.1d:

Schematic representation of the fields of occurrence of important minerals in progressively altered and metamorphosed silica-saturated and -undersaturated granitoid rocks in gold-bearing systems. Biotite and orthoclase represent the alteration minerals characteristic for the entire spectrum of high-grade metamorphic condition, for both low and high alteration intensity. Scapolite is also part of the mineral paragenesis associated with very high fluid:rock ratios.

Possible prograde reactions that occurred at Doornhoek, and also at Klipbank and Petronella:

- d1 - Albite + K<sup>+</sup> = Orthoclase
- d2 - Chlorite + Albite + Quartz + K<sup>+</sup> = Orthoclase + Biotite
- d3 - Garnet + K<sup>+</sup> = Biotite + Sillimanite + Quartz

Because of rheological differences the BIF and interlayered felsic granulite deformed in a more brittle fashion than the other lithologies present at Doornhoek and were therefore more easily penetrated by the channelised fluids. The overpressurised fluids microfractured the BIF (e.g. Roering et al., 1995) and this resulted in syn-tectonic quartz crystallising from the solution. Although deformation was ductile within the lower-granulite facies condition, the process of quartz crystallisation and boudinage is the result of a continuous process of microhydraulic pumping due to the overpressurised solutions that penetrated the BIF (Roering et al., 1995). As a result, this metasomatic biotite-garnetiferous formation is closely

associated with the BIF, and also explains the reason for 90 per cent of the gold mineralisation being hosted by the same highly metasomatised BIF. The close geometric and genetic association of the mineralised quartz veins with the mineralised biotite-garnetiferous formation is also explained by this process. Garnet from the biotite-garnetiferous formation always exhibits prograde zonation, in sharp contrast with the garnet hosted by the calc-silicate facies BIF that is always retrograde (**Chapter 7**). It can, therefore, be assumed that the metasomatic biotite-garnetiferous formation actually represents the fossil channelways of the high-temperature infiltrating fluids. As a result of the interaction between the hot fluids and the BIF, the BIF was transformed into a rock composed of garnet+biotite+quartz. The garnet porphyroblast started growing as a result of the metasomatic process and continuously adapted to the temperature of the channelised fluids, as is illustrated by the preserved prograde zonation (detailed described in **Chapter 7**). Garnet in the host rock BIF that was not in contact with the channelised fluid completely re-equilibrated during subsequent cooling and exhibits a typical retrograde zoning pattern. The retrograde pattern is similar to that of garnet throughout the zone of retrogression in the SMZ (van Reenen, 1986). The metasomatic garnet must have crystallised very slowly in order to preserve the prograde zoning profile.

## 8.2. MINERALISATION IN VEINS AND IN PROGRADE PATTERN GARNETS

In **Chapter 7** it was demonstrated that the same ore mineral associations that occur in the quartz veins were also trapped in the prograde garnet porphyroblasts. Furthermore, the ore minerals trapped in the prograde garnet demonstrates a prograde sequence of crystallisation from the core to the dark inner-ring.

The mineralised quartz veins occurring at Doornhoek are orientated parallel to the regional  $D_2$  direction of shearing and presumably were formed at the time when the SMZ of the LB was emplaced in the mid-crust (time of quasi-isobaric cooling). This is demonstrated by fragments of wall-rock and fragments of retrograde pattern garnet, orthopyroxene and clinopyroxene from the wall-rock (**fig. 8.2**) that were assimilated by the quartz veins. The actual quartz veins were presumably, at the time of mineralisation, extensional fractures that have been filled and healed with quartz, ore minerals and fragments of wall-rock.

Textural relationships in the quartz vein system also suggests that mineralisation was deposited in stages clearly demonstrating a prograde order of crystallisation: löllingite rims As-rich arsenopyrite, while chalcopyrite with pentlandite exolutions crystallised later than pentlandite-free chalcopyrite.

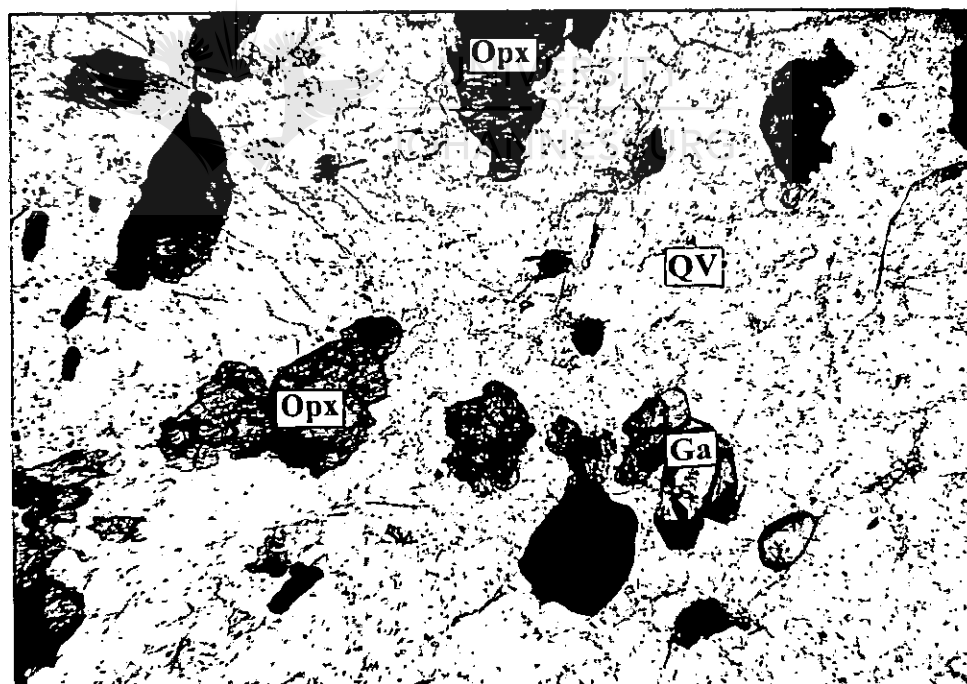


The most compelling argument, however, is given by the zoning demonstrated by the ore minerals entrapped in the growing garnet porphyroblasts: As-poor arsenopyrite in the core, As-rich arsenopyrite in the inner zone and löllingite in the dark inner-ring.

Another important mineral present during the first stages of mineralisation is tourmaline. Tourmaline occurs in both the mineralised quartz veins (**fig. 8.3**) and in the biotite-garnetiferous formation. Tourmaline in the quartz veins occurs as schlieren, developed parallel to the wall-rock. In the garnet porphyroblast, tourmaline occurs as inclusions entrapped only in the dark inner-ring, at a stage when the activity of the mineralised fluids probably reached a climax. This type of tourmaline-garnet association can be used for geothermometric calculations (see **Chapter 11**). The presence of tourmaline further

demonstrates a high fluid activity at the time when mineralisation was entrapped within the garnet porphyroblast or deposited within the quartz vein. Tourmaline also reflects the presence of volatiles (boron) associated with the K- and Na-type of alteration.

The fineness of the gold (actually electrum) is extremely low (as low as 590). This is also characteristic for gold that precipitated from fluids at very high temperature, a process similar to the precipitation of gold in Cu-rich hydrothermal systems. In the porphyry-copper environment, gold displays a very low fineness. The fineness increases in the mesothermal zone and becomes very high in the epithermal zone (Nisbet, 1987; Colvine et al., 1988).



**Figure 8.2:** Sample DD-2-2014: Mineralised quartz vein. Microphotograph showing fragments of garnet (Ga), and orthopyroxene (Opx), assimilated from the wall rock into the mineralised quartz vein (QV). This process of assimilation is a result of intense shearing that occurred simultaneously with precipitation of mineralisation.

1cm=400 $\mu$ m





Figure 8.3: Sample DD-2-2008. Boundary between the quartz vein (QV) and the wall-rock. Microphotograph showing tourmaline needles (arrows) inside a quartz vein, orientated parallel to the wall-rock. 1cm=100µm

### 8.3 SUMMARY

The Archaean lode-gold deposit at Doornhoek in the SMZ of the LB is located along a secondary  $D_2$  shear-zone that forms part of the system of shear zones that controlled the exhumation of the granulite facies terranes of the LB (Smit et al., 1992; Smit and van Reenen, 1997). Later  $D_3$  folding was responsible for the formation of an eastward plunging subhorizontal fold (**Chapter 4.4**), that actually represents the Ore Body consisting of highly metasomatised silicate facies BIF, mafic and ultramafic gneisses. The mineralised horizon is represented by syn-tectonic quartz veins and metasomatic biotite-garnetiferous formation.

These two lithologies represent the result of the strong interaction between the highly channelised metasomatic fluids and the silicate facies BIF (**Chapter 6.2**). During the same event large amounts of ore minerals were precipitated into the quartz vein system or entrapped in zoned porphyroblastic garnet in the biotite-garnetiferous formation.

The metamorphic history of the SMZ is reflected by a continuous clockwise P-T-loop and can be summarised as follows (**fig. 4.4**).

- a) Maximum P-T conditions reached during the prograde part of the loop ( $M_1$ ) were between 8 and 9 kbar and at about 870°C (Stevens and van Reenen, 1992)
- b) This was followed by rapid decompression and cooling ( $M_2$ )
- c) Pervasive hydration ( $M_3$ ) at about 6 kbar and roughly 600°C established the retrograde orthoamphibole isograd and the zone of retrogression that bound the SMZ in the south (van Reenen, 1986).

The P-T loop ended in the stability field of kyanite reflecting the growth of this mineral as a replacement product of cordierite in the pelitic granulite. The CO<sub>2</sub>-rich, H<sub>2</sub>O-bearing fluid responsible for this pervasive regional hydration event was characterised by low fluid:rock ratio (van Reenen, 1986; van Reenen and Hollister, 1988; Hoernes and van Reenen, 1992). The CO<sub>2</sub>-rich nature of the fluid is furthermore confirmed by the replacement of forsterite by enstatite and magnesite in associated ultramafic rocks from the zone of hydration (van Schalkwyk and van Reenen, 1992).

This history reflects a pervasive alteration event that occurred during the  $M_3$  event and at temperatures slightly higher than 600°C. The data obtained from the study of the Doornhoek

gold deposit documents evidence for intense metasomatism associated with highly channelised fluids that probably evolved at higher temperatures than the fluids related to the regional  $M_3$  event (**Chapter 11**). These highly channelised fluids deposited gold and associated arsenide-oxide-sulphide mineralisation in quartz veins and in the metasomatic biotite-garnetiferous formation.

Large amounts of mineralised syn-tectonic quartz veins developed in the ductile shear zones due to a process of continuous hydraulic pumping and precipitation, that allowed the granulitic host to be penetrated, metasomatised and mineralised by the channelised fluids. The mineralised shear zones were probably characterised by very high fluid:rock ratios in order to allow such an event to evolve within lower-granulite facies conditions.

Mineralisation occurs in both the syn-tectonic quartz veins and in the biotite-garnetiferous formation, and displays similar mineralogical and geochemical features.



## 9. FLUID INCLUSIONS

The purpose of this study was to establish the qualitative nature of the fluids associated with the gold mineralisation. All samples of quartz used for the fluid inclusion study were obtained from samples containing up to 10ppm Au. The quartz chips were sampled from mineralised veins or from quartz inclusions in the mineralised garnet porphyroblast from the metasomatic biotite-garnetiferous formation. Several inclusions trapped in the garnet porphyroblast were also analysed.



The fluid inclusion study was carried out on four 0.5 mm thick, double polished wafers prepared from samples that were first studied in ordinary polished thin sections. Heating and freezing experiments were done using the adapted USGS nitrogen gas flow stage in the Department of Geology (RAU), calibrated at low temperatures using the triple points of CO<sub>2</sub> (-56.6°C) and H<sub>2</sub>O (0°C) in synthetic inclusions. The error for Th is about ±2°C. The homogenisation temperature (Th) and final melting temperature (T<sub>mf</sub>) were measured for all selected fluid inclusions.

Quartz in samples from the Doornhoek gold deposit exhibits irregular grain boundaries and is invariably deformed. Where the process of recrystallisation severely affected the quartz veins,

and specifically at the laminated contacts with the wall-rock, quartz is fluid inclusion-free.

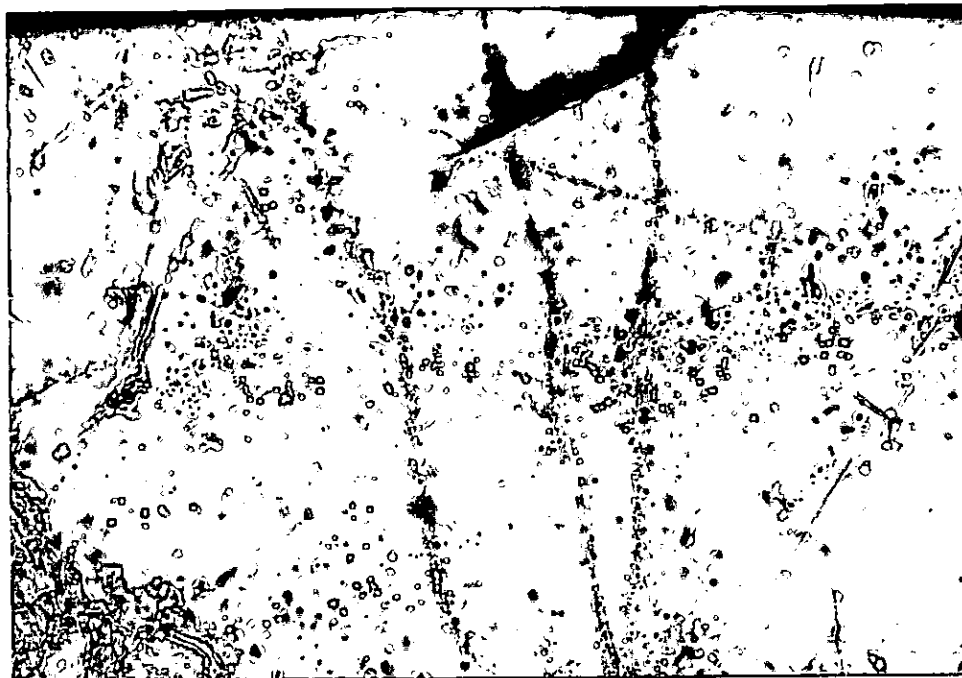
The following three fluid inclusions types were found in all the studied samples:

- *type 1*: CO<sub>2</sub>-rich fluid inclusions with a few showing slight depression of the triple point due to presence of impurities (e.g., CH<sub>4</sub> and N<sub>2</sub>)

- *type 2*: mixed CO<sub>2</sub>-H<sub>2</sub>O inclusions, sometimes of very high salinity in pyrite-bearing paragenesis. The pyrite-bearing association is always late in the paragenetic sequence (**Chapter 7**).

- *type 3*: low-salinity H<sub>2</sub>O-rich fluid inclusions. These type of fluid inclusions were not systematically measured due to the fact that they do not appear to be closely associated with the main mineralisation.

A petrographic study of the fluid inclusions trapped in quartz showed that trails of several types of inclusions often cross grain boundaries, suggesting that these inclusions are secondary. They were therefore, probably trapped during a post-peak metamorphic event, following the peak-deformation\shearing\mineralisation event responsible for the introducing of the gold-related mineralisation (**fig. 9.1**).



**Figure 9.1:** Sample DH-2035: Microphotograph showing trails of fluid inclusions crosscutting grain boundaries, an indication for entrapment after the peak-metamorphic event.

1cm=25 $\mu$ m

A number of 282 fluid inclusions were analysed. The fluid inclusions associated with the gold mineralisation exhibit a bimodal distribution as related to Th. (fig. 9.2). Although the Tm is generally about  $-56.6^{\circ}\text{C}$  (pure  $\text{CO}_2$ ), sometimes lower values (up to  $-60^{\circ}\text{C}$ ) suggests the presence of either methane or/and nitrogen (van der Kerkhof, 1990) (fig. 9.3).

*Type 1 a)* The high-density  $\text{CO}_2$ -rich fluid inclusions occur in trails (fig. 9.4) or as clusters, and/or as even isolated inclusions (fig. 9.5). Their shape is always almost perfectly rounded and may vary in size between 7 to  $45\mu\text{m}$  with an average size of about  $15\mu\text{m}$ . Due to the high concentration of  $\text{CO}_2$  a gas bubble with high relief is well visible (fig. 9.4 and 9.5). The Th varies between  $-26^{\circ}$  and  $-56^{\circ}\text{C}$  and Tm between  $-56.6^{\circ}$  and  $-59.9^{\circ}\text{C}$ , indicating the presence of  $\text{CH}_4$  and/or  $\text{N}_2$  (van den Kerkhof, 1990). The calculated density range derived from the total Th range varies from  $1.06$  to  $1.16\text{g}/\text{cm}^3$  (fig. 9.2) (Brown, 1989; Saxena and Fei, 1987).

Similar high-density fluid inclusions were described in metamorphic rocks by Touret (1981) and Touret and Hansteen (1988).

Larger (up to 45 $\mu\text{m}$ ), isolated CO<sub>2</sub> fluid inclusions are rare and occur in the centres of quartz grains. This fluid inclusion type is considered to represent primary inclusions. The term primary as used here does not refer to primary in the sense of peak-metamorphic condition, but primary relative to the introduction of the mineralising fluid into the Doornhoek ore body (Roedder, 1984). The high-density CO<sub>2</sub> fluid inclusions usually occur whenever graphite is not present. Therefore, the paragenesis *type 1a sulphides+arsenides+gold and without graphite* (Chapter 7) is characterised by the presence of high-density CO<sub>2</sub>-rich fluid inclusions (1.06-1.16 g/cm<sup>3</sup>).

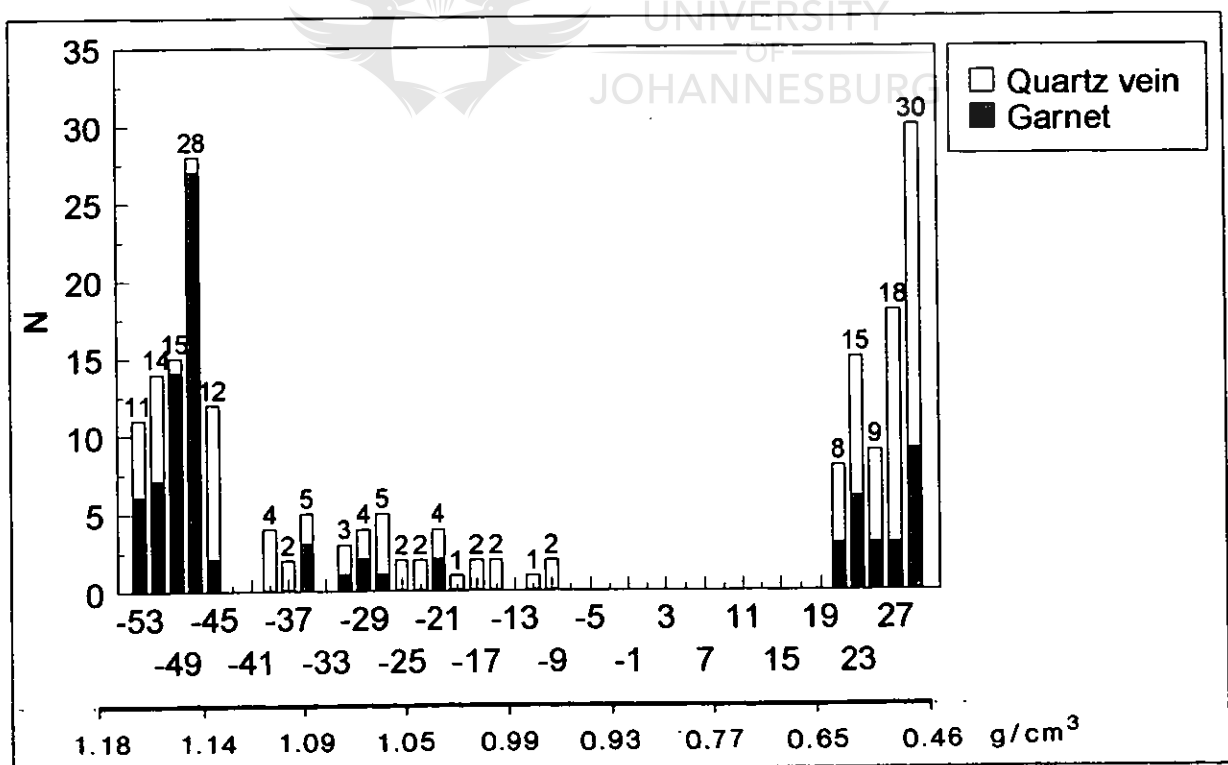
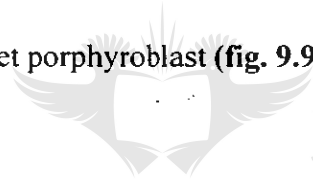


Figure 9.2: Homogenisation temperature (Th) for all CO<sub>2</sub>-fluid inclusions (n=282). Typical bimodal distribution showing high-density fluid inclusions (aprox. 1.15g/cm<sup>3</sup>, at Th=-48°C) and low-density fluid inclusions (aprox. 0.50g/cm<sup>3</sup>, at Th=28°C).

**Type 1 b)** low-density CO<sub>2</sub>-rich fluid inclusions always occur in trails (**fig. 9.6** and **9.7**). Their shape is irregular and a tiny CO<sub>2</sub> vapour bubble is visible (**fig. 9.6** and **9.7**). This type of fluid inclusions vary in size between 12 to 77 μm, with an average size of about 25μm. The Th varies between 19° and 31°C, while Tm varies between -56.2° and -59.1°C (**fig. 9.3**). The calculated density range derived from the total Th range varies from 0.46 to 0.76g/cm<sup>3</sup> (**fig. 9.2**) (Brown, 1989).

The low-density CO<sub>2</sub>-rich fluid inclusions are usually associated with graphite (**fig. 9.8**). Furthermore, the complete *type 1b* association of *gold+sulphides+arsenides±graphite* (**Chapter 7**) is characterised by the presence of low-density CO<sub>2</sub>-rich fluid inclusions (0.4-0.8 g/cm<sup>3</sup>). Although very rare, tiny, round graphite crystals can also be identified inside, or in the close vicinity of the CO<sub>2</sub> fluid inclusions, especially within the mineralised dark inner-ring of the garnet porphyroblast (**fig. 9.9**).





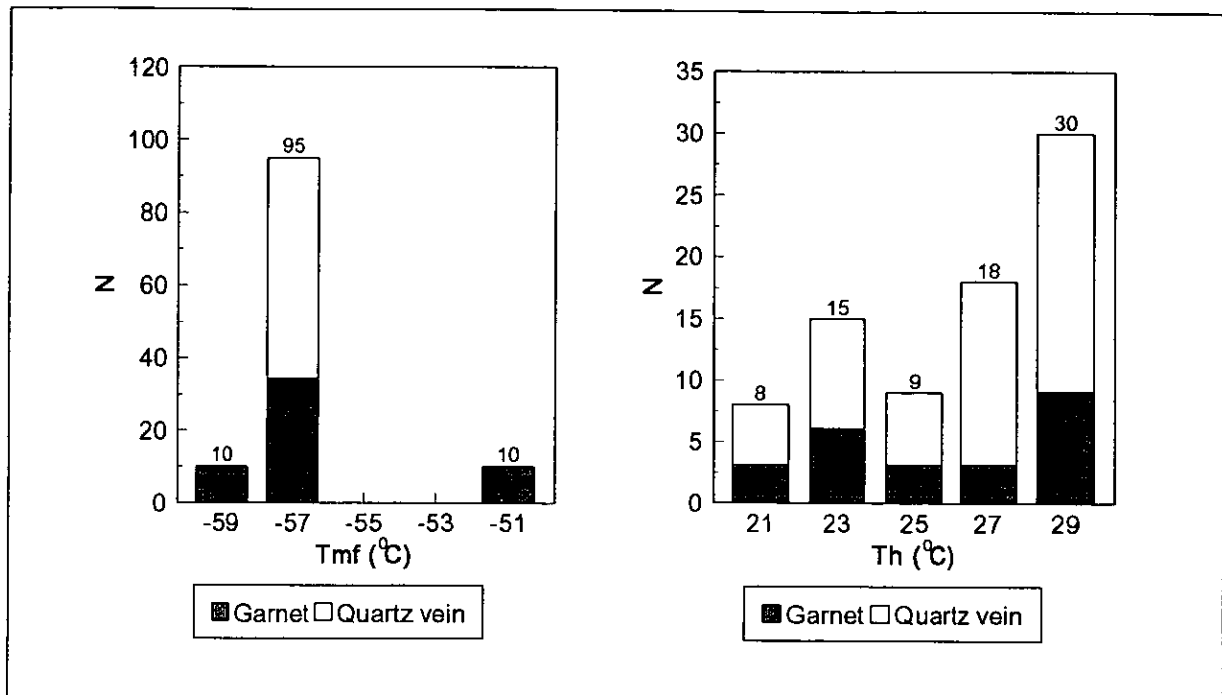


Figure 9.3: Final melting temperature (Tmf) and homogenization temperature (Th) for the low-density CO<sub>2</sub>-rich fluid inclusions. The final melting temperature lower than -56.6°C (pure CO<sub>2</sub>) is probably due to the presence of methane and/or nitrogen.

*Type 2&3*) high salinity mixed H<sub>2</sub>O-CO<sub>2</sub> fluid inclusions belonging to type 2 (with halite daughter minerals) or aqueous inclusions of low salinity (type 3) appear not to be geometrically associated with the gold-bearing assemblage. These fluid inclusions have been measured but not graphically represented because they occur in fluid inclusion trails that always crosscut the textural trend of mineralisation and is therefore considered to be late. Furthermore, these types of fluid inclusions are also associated with the very late pyrite mineralisation, also suggesting that they are not related to the gold deposition.



Figure 9.4: Sample DH-2033: Microphotograph showing high-density  $\text{CO}_2$ -rich fluid inclusions hosted by quartz veins. The inclusions, at room temperature, usually host a single  $\text{CO}_2$  phase. 1cm=25 $\mu\text{m}$

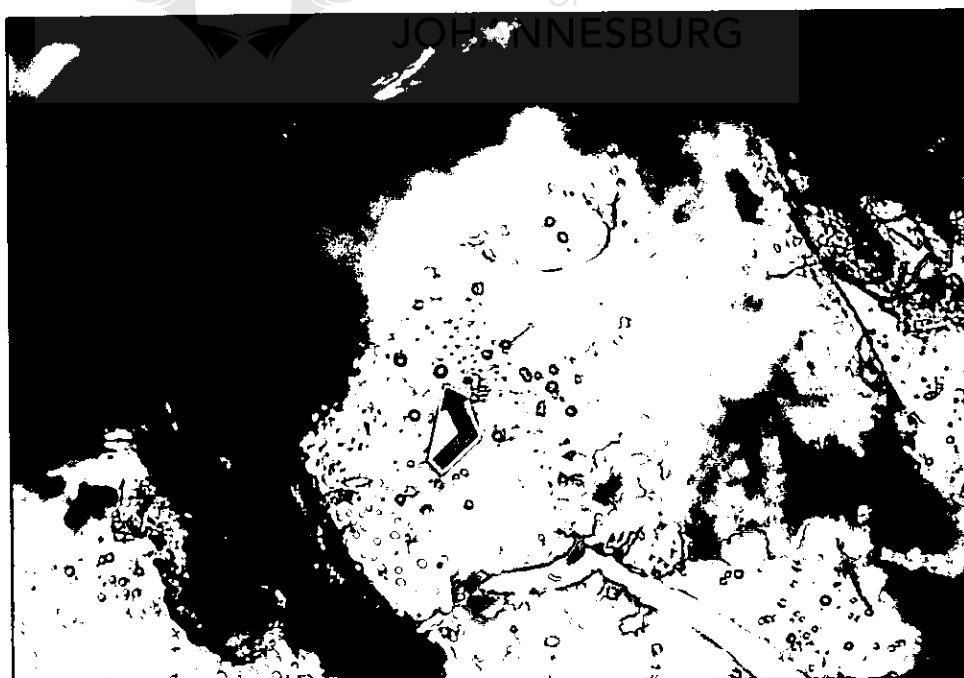


Figure 9.5: Sample 2035: Microphotograph showing clusters of relatively isolated high-density  $\text{CO}_2$ -rich fluid inclusions (arrow) hosted by the prograde garnet porphyroblast. Note the high relief of the inclusions, a typical feature of the high-density type. 1cm=25 $\mu\text{m}$ .



Figure 9.6: Sample DH-2035: Microphotograph showing trails of low-density CO<sub>2</sub>-rich fluid inclusions (arrows) along healed cracks hosted by a quartz vein. The liquid/vapour ratio of these inclusions is variable, probably due to leakage of liquid from the fluid inclusions. 1cm=25µm.

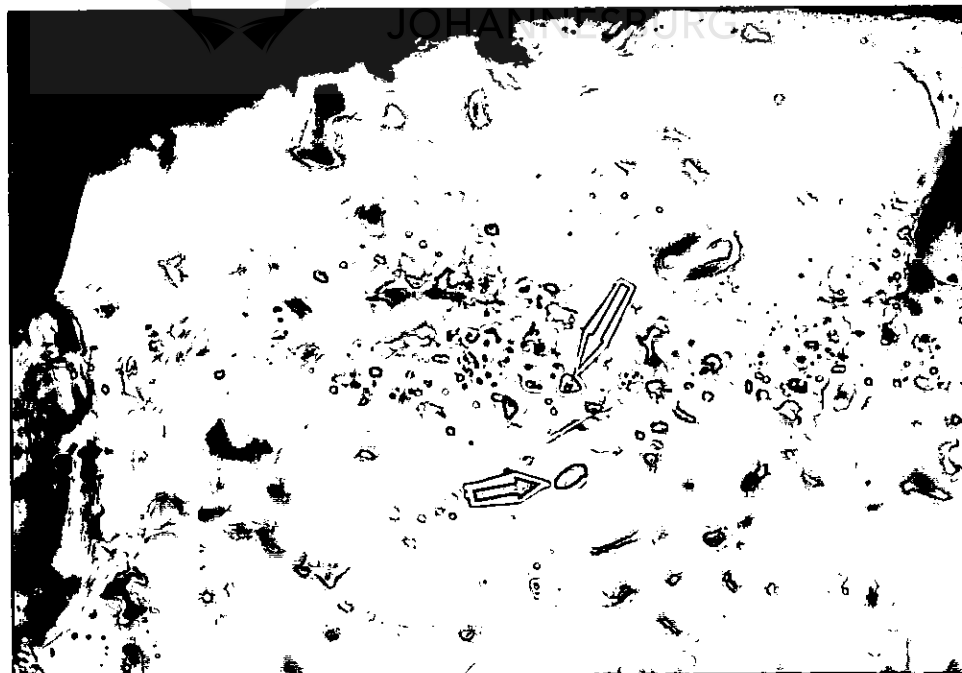


Figure 9.7: Sample 2035: Microphotograph showing low-density CO<sub>2</sub>-rich fluid inclusions (yellow arrow) in a trail associated with tiny tourmaline crystals (green arrow). There is a close relationship between gold mineralisation related, to CO<sub>2</sub>-fluid activity and other volatiles, such as boron. 1cm=25µm



Figure 9.8: Sample DH-2033C: Microphotograph of low-density CO<sub>2</sub>-rich fluid inclusions associated with graphite (arrow). The black spots are graphite crystals. 1cm=25μm.

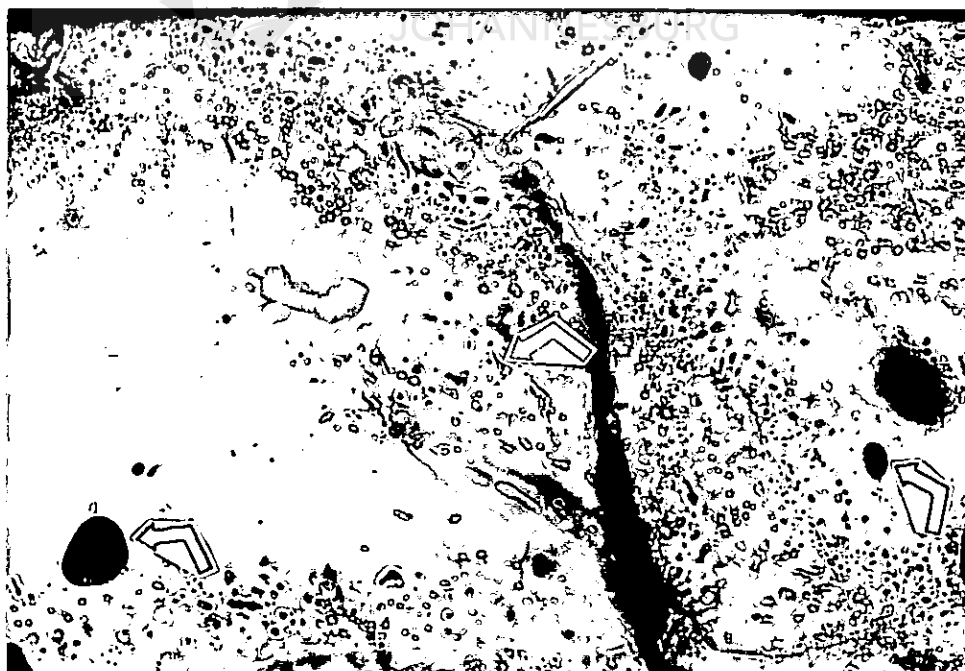


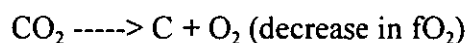
Figure 9.9: Sample DH-2035: Microphotograph showing the presence of rounded graphite crystals (red-arrow) hosted by quartz inclusions in the mineralised dark inner-ring of the prograde garnet porphyroblast. Graphite is associated with low-density CO<sub>2</sub>-rich fluid inclusions (yellow arrow). 1cm=25μm

## 9.2 DISCUSSION

Gold is usually associated with graphite-bearing assemblages and to a lesser extent with graphite-free assemblages. Low-density CO<sub>2</sub>-rich fluid inclusions, however, are restricted to graphite-bearing associations. An important conclusion from the fluid inclusions study, therefore, is that there appear to be a clear association between gold, graphite and the low-density CO<sub>2</sub> fluid inclusions. Although gold is associated with both high and low-density CO<sub>2</sub>-rich fluid inclusions, it appears that most of the gold is associated with low-density fluid inclusions and *paragenesis type 1b: gold+sulphides+arsenides±graphite (see Chapter 7)*.

The bimodal distribution of the homogenisation temperature (Th) for both the low- and high-density inclusions (**fig. 9.2**), with a large gap between the two types demonstrates entrapment of the fluid inclusions at different PT conditions, or due to a different post-entrapment evolution. The high-density inclusions occur both in the rim and in the core (rare) of the zoned garnet. The only way to explain the presence of high-density CO<sub>2</sub> fluid inclusions trapped in the core and the rim of the prograde zoned garnet is that they must have been trapped along the same isochor of 1.16g/cm<sup>3</sup> during the prograde part of the PT evolution (**fig. 9.10**) (Touret, 1981). The low-density fluid inclusions, on the other hand, must have formed at (constant) high temperature during decompression. This is the only plausible way to explain the presence of both low-density and high-density CO<sub>2</sub>-rich fluid inclusions, in the rim of the zoned garnet. The data from Doornhoek processed in **fig. 9.10** suggest that the entire prograde metamorphic event and decompression occurred during a continuous influx of CO<sub>2</sub>-rich fluids. During decompression, the conditions changed from oxidising to

more reducing in order to explain the presence of graphite. CO<sub>2</sub> breaks down into O<sub>2</sub> and C according to the following reaction:



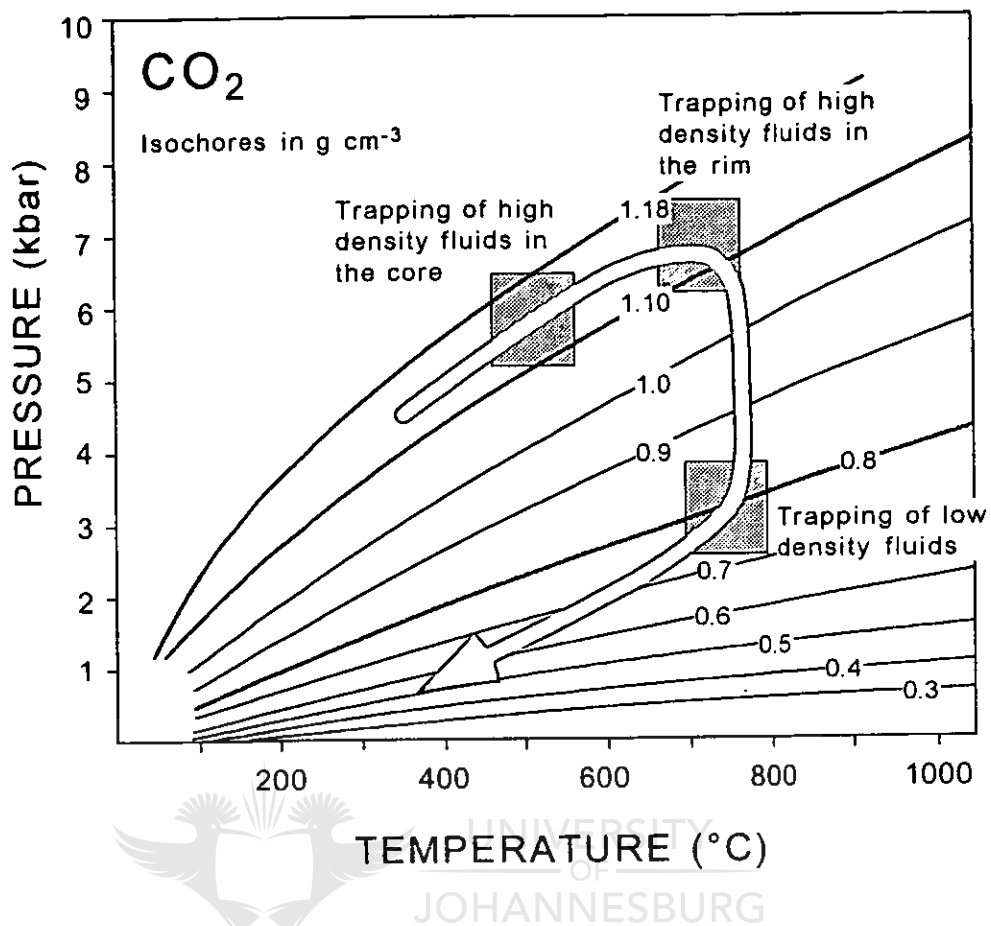
### 9.3 SUMMARY

There is no evidence for leakage of the primary fluid inclusions (Bakker and Jansen, 1990) or for entrapment of the fluids in two stages, one at high P conditions and a second one at much lower P conditions. Therefore, the only way to explain the existence of two populations of CO<sub>2</sub>-rich fluid inclusions with very different densities is to link their evolution to the mineralising event:

- it is known that mineralisation at Doornhoek mainly occurred during a prograde event, initially at lower temperature and later at higher temperatures (**Chapter 7**).

- where graphite is present the density of the fluid inclusions is low, while the absence of graphite is an indicator for high-density fluid inclusions.

- the chemical composition of the garnet porphyroblast, the presence of the dark mineralised inner-ring and the absence of mineralisation in the rim of the garnet suggest that gold started to be trapped during the first stages of mineralisation, but that most of the gold was entrapped towards the final stages of the mineralising event (**Chapter 7**). However, the final stage of fluid evolution, that occurred at very high PT metasomatic conditions, were not associated with mineralisation (**Chapters 6 and 7**).



**Figure 9.10:** Mechanism of trapping the high-density fluid inclusions in the dark inner-ring and rim of the prograde garnet porphyroblast along the same isochor of  $1.16\text{g/cm}^3$ , during the prograde metasomatism at Doornhoek. During isothermal decompression, the  $f\text{O}_2$  changed and  $\text{CO}_2$  broke down into  $\text{O}_2$  and  $\text{C}$ , with the formation of graphite. Data derived from Doornhoek Ore Body.

- the trapped "primary" fluid inclusions probably reflect the composition of the mineralising fluid at the time of ore deposition, but fluids trapped during the first phases of mineralisation might have been affected by subsequent processes.

- it is therefore assumed that the measured  $T_h$  for the low-density fluid inclusions does not reflect the initial fluid density at the time of entrapment, but a modified density.

- due to the reduction of  $\text{CO}_2$  to pure graphite, some of the carbon in the initial fluid inclusions was consumed for graphite formation and, as a result, the entrapped fluid drastically changed its characteristics.

- it can, therefore, be assumed that when high-density CO<sub>2</sub>-rich fluid inclusions were reduced to produce graphite at the time of gold precipitation, the density of the fluid decreased with the result that low-density fluid inclusions were trapped. The fluid inclusions entrapped during earlier and peak-phases of gold mineralisation, therefore continuously changed their density through graphite precipitation. The fluid inclusions trapped during the final stages of gold mineralisation preserved the composition and density of the fluid active at that stage of high PT conditions (thus high density), as shown by the edge of the garnet porphyroblast (**fig. 9.10**). A similar process was described by Hollister (1990) for an opposite phenomenon: the enrichment of CO<sub>2</sub> in fluid inclusions through removal of H<sub>2</sub>O as the result of leaking during crystal-plastic deformation.





## 10. THERMOBARIC CALCULATIONS

### 10.1. THERMOBAROMETRY

The mineral assemblages used for thermobarometric calculations and the methods used are as follows:

**a) retrograde assemblages:**

(i) *felsic granulite*: orthopyroxene+garnet+plagioclase+quartz (P and T; Bohlen et al., 1983)

garnet+orthopyroxene (T; Ellis and Green, 1979)

(ii) *mafic granulite*: garnet+orthopyroxene (T; Ellis and Green, 1979; P; Harley and Green, 1982)

garnet+biotite (T; Hodges and Spear, 1982; Ganguly and Saxena, 1984)

**b) prograde assemblages:**

(i) *metasomatic biotite-garnetiferous formation*: garnet+biotite (T; Ganguly and Saxena, 1984)

(ii) *felsic granulite adjacent to the metasomatic biotite-garnetiferous formation*: tourmaline+biotite (T; Colopietro and Frieberg, 1987)

In order to determine the PT constraints of the Doornhoek prograde and retrograde mineral assemblages, the following assumptions were made:

- the core composition of zoned plagioclase was in equilibrium with either the core or the outer core of the zoned porphyroblastic garnet during peak metamorphic/or alteration conditions.

- biotite replaces garnet in the retrograde lithologies with the result that the outer rim composition of garnet is probably in equilibrium with retrograde biotite

- garnet and orthopyroxene crystallised almost penecontemporaneously in the BIF lithologies, therefore it is assumed their cores were in equilibrium

- garnet and biotite crystallised penecontemporaneously in the metasomatic biotite-garnetiferous formation, therefore where in contact they re-adjusted their composition together.

- the core composition of garnet is in equilibrium with matrix biotite, since biotite in contact with garnet can easily re-adjust its composition during changes in P-T conditions (Loomis, 1983; Tucillo et al., 1990)

- tourmaline that crosscuts garnet and occur in contact with biotite in pressure-shadows areas of the deformed garnet from felsic granulite probably reflects Mg-Fe exchanges with the biotite. This probably reflects the last re-equilibration event in the Doornhoek system.

### 10.1.1. Retrograde assemblages

**Orthopyroxene (ferrohypersthene)** used for pressure and temperature calculations is a ferrohypersthene and occur in both the felsic and mafic granulite. In the felsic granulite orthopyroxene occurs as tiny crystals in the predominantly quartz-K-feldspar-biotite matrix, sometimes in direct contact with retrogressed garnet. In the calc-silicate facies BIF

orthopyroxene is also a ferrohypersthene, sometimes intimately associated with clinopyroxene (salite) and often including resorbed garnet grains. The rims of the hypersthene are very often retrogressed into amphiboles. Magnetite is present in the BIF lithologies.

**Garnet** used for temperature calculations in the felsic granulite is an almandine that displays a retrograde zonation pattern and occurs as resorbed, usually elongated porphyroblasts in the highly altered matrix that consists mainly of quartz and K-feldspar. Biotite is very often intimately associated with this garnet. Garnet in the granulite BIF is always included in large orthopyroxene crystals as small resorbed grains.

**Biotite** used for temperature calculations is a red-brown Ti-rich biotite (with up to 4.6% Ti) and occurs as small crystals in the matrix of the highly altered felsic granulite in direct contact with the resorbed garnet.

**Plagioclase** only occurs as relicts in the unmineralised felsic granulite and has a composition in the range  $An_{36}$ - $An_{55}$ . The associated orthopyroxene used for barometry is a ferrohypersthene.

The microprobe analyses of these minerals are given in **table 10.1.a**.

TABLE 10.1a MICROPROBE ANALYSES OF MINERALS USED FOR P-T CALCULATIONS IN THE RETROGRADE PATTERN ROCKS

	1	2	3	4	5	6	7	8	9	10	11	12	13	14	15	16	17	18	19
Oxide (wt%)	Opx1	Opx2	Plagioclase Matrix	Plagioclase	Cordierite	Cordierite	Garnet 1 Core	Garnet 2 Core	Opx3 Core	Opx4 Rim	Garnet 2 Core	Garnet 2 Rim	Opx 5 Core	Opx 5 Rim	Biotite 1 Core	Biotite 1 Rim	Biotite 2 Core	Biotite 2 Rim	Tourmalin
SiO <sub>2</sub>	50.01	50.08	57.60	56.39	46.11	47.11	38.47	38.02	51.00	50.23	37.01	37.48	49.08	49.28	35.7	35.12	37.34	35.16	35.04
Al <sub>2</sub> O <sub>3</sub>	0.68	0.35	26.51	25.78	31.12	30.22	21.35	21.60	0.34	0.31	20.32	20.46	0.30	0.36	20.21	21.23	18.26	19.28	30.65
FeOTot.	33.64	40.01	-	0.08	12.35	15.12	31.50	33.30	36.44	37.23	32.90	32.00	25.15	24.28	16.5	21.15	20.10	23.15	8.06
MnO	0.69	1.11	-	-	0.11	-	0.74	0.89	0.39	0.41	1.99	2.52	0.39	0.44	0.03	0.18	0.07	0.10	0.11
MgO	13.09	6.23	-	-	6.13	5.79	2.11	1.90	10.60	11.21	0.88	0.60	4.11	5.17	11.12	6.18	9.17	7.13	5.85
CaO	1.48	1.18	8.60	10.87	0.12	0.08	5.54	4.31	0.79	0.34	6.87	7.45	21.18	20.43	-	0.03	-	-	1.81
TiO <sub>2</sub>	0.98	1.07	-	-	0.09	-	-	-	0.02	0.01	-	-	0.12	-	4.50	3.15	4.15	2.98	1.05
Cr <sub>2</sub> O <sub>3</sub>	0.04	0.22	-	-	-	-	0.24	0.17	-	-	0.01	-	-	-	0.11	-	0.85	0.15	1.84
K <sub>2</sub> O	-	-	0.11	0.19	0.89	0.13	-	-	-	-	-	-	-	-	10.19	9.56	9.00	9.01	0.02
Na <sub>2</sub> O	-	-	6.72	5.77	0.15	0.18	-	-	-	-	-	-	-	-	0.20	0.10	-	-	2.00
Total	100.61	100.25	99.60	100.08	98.07	98.63	99.95	100.20	99.99	99.74	99.98	100.51	100.34	99.96	98.56	96.6	98.94	96.95	96.43

\* Note: All Fe assumed FeOTot.

- 1: Ferrohypersthene from the felsic granulite, surrounded by quartz, associated with plagioclase 3 and garnet 7 and cordierite 5 and 6
- 2: Ferrohypersthene (core) from BIF in contact with a small garnet. Associated with plagioclase 3
- 3: Matrix plagioclase in the felsic granulite
- 4: Plagioclase surrounded by quartz, at the boundary between the felsic granulite and BIF
- 5: Matrix cordierite from the felsic granulite
- 6: Cordierite from the felsic granulite in contact with resorbed garnet
- 7: Garnet from the felsic granulite in contact with opx 1 and plagioclase 3
- 8: Garnet from the felsic granulite in contact with biotite 15
- 9, 10: Ferrohypersthene from the felsic granulite, at the contact with mafic granulite
- 11, 12: Small garnet crystals hosted by large orthopyroxene crystals (13 and 14) in the mafic granulite
- 13, 14: Large orthopyroxene crystals in BIF, with inclusions of retrogressed garnet (11 and 12)
- 15, 16: Biotite from the felsic granulite in contact with resorbed garnet 8
- 17, 18: Biotite from the felsic granulite crystallised in pressure shadows of elongated garnet, in contact to biotite 19
- 19: Tourmaline from the felsic granulite in contact with both garnet and biotite (17 and 18)

### 10.1.2. Prograde assemblages

**Biotite** selected for microprobe analysis in the metasomatic biotite-garnetiferous formation occurs as tiny inclusions in the core, the mineralised dark inner-ring and the edge of the prograde garnet porphyroblast, or in the matrix of the biotite-garnetiferous formation. Biotite used for temperature calculations together with tourmaline in the felsic granulite occurs as larger crystals at the boundary with the mineralised metasomatic biotite-garnetiferous formation.

**Garnet** used for temperature calculations represent the large, mineralised and progradely zoned almandine porphyroblasts with numerous inclusions of biotite. This type of garnet represents the main and most characteristic constituent of the metasomatic biotite-garnetiferous formation.

**Tourmaline** used for temperature calculations is a very dark variety and cuts across intensely flattened garnet. Tourmaline is in direct contact with biotite hosted in the pressure shadow of the flattened garnet. This type of assemblage is usually encountered at the boundary between the felsic granulite and the metasomatic biotite-garnetiferous formation. The microprobe analyses of these minerals are presented in **table 10.1.b**.

The P-T estimates are determined by the intersection of the lines of constant equilibrium ( $K_{eq}$  lines) for thermometers and barometers for each analysis in each sample, using the selected coexisting minerals (**tables 10.1.a and b**).

**TABLE 10.1b MICROPROBE ANALYSES OF GARNET AND BIOTITE USED FOR P-T CALCULATIONS IN THE PROGRADE PATTERN ROCKS (METASOMATIC BIOTITE-GARNETIFEROUS FORMATION)**

	1	2	3	4	5	6
Oxide (wt%)	Garnet Core	Garnet Middle	Garnet Rim	Biotite Core	Biotite Middle	Biotite Rim
SiO <sub>2</sub>	37.41	37.51	37.05	32.14	33.78	31.99
Al <sub>2</sub> O <sub>3</sub>	20.68	21.30	21.66	17.26	17.99	16.49
FeO	32.65	33.18	31.19	24.47	26.53	24.12
MnO	2.59	1.81	0.32	0.24	0.19	0.12
MgO	0.95	1.06	2.83	10.70	5.94	10.76
CaO	5.48	4.89	5.52	0.06	0.10	0.08
TiO <sub>2</sub>	0.11	0.08	-	1.42	3.07	1.56
Cr <sub>2</sub> O <sub>3</sub>	0.05	0.27	0.12	0.19	0.17	0.14
K <sub>2</sub> O	-	-	-	9.02	8.21	9.22
Na <sub>2</sub> O	-	-	-	-	-	-
Total	99.88	100.09	99.68	95.50	96.00	94.55

**Note: All Fe assumed FeO. All six analyses are from the same garnet porphyroblast, sample DH-2035, metasomatic biotite-garnetiferous formation. Biotite occurs as tiny inclusions in garnet.**

## 10.2. P-T CONDITIONS FOR THE RETROGRADE ASSEMBLAGES

Calc-silicate facies BIF and felsic granulite evolved together within the Doornhoek Ore Body. Therefore these two lithologies should show similar PT constraints.

### 10.2.1. P-T constraints in the felsic granulite

Taking into account that the felsic granulite is the only lithology that contains plagioclase, this rock-type was selected to determine the peak-pressure and temperature conditions reached by the altered Doornhoek lithologies.

The geobarometer Opx-Ga-Plag-Qz (Bohlen et al., 1983) was used to determine the P-T pairs for cores of relic garnet, orthopyroxene and relic plagioclase (**fig. 5.35, 5.36 and 5.37**). The calculated P-T value is  $T=712^{\circ}\text{C}$  and  $P=7.21$  kbar (**point A**) in **fig. 10.1**. This value define the intersection of Keq lines  $P_x(P)$  and  $P_x(T)$  [where  $P_x(P)$  is the baro-Keq and  $P_x(T)$  is the thermo-Keq, based on orthopyroxene-bearing lithologies ( $P_x$ )]. **Fig. 10.1** displays all the calculated P-T data in order to compare the P-T evolution of various lithologies and the various methods of calculation used.

The Ga-Opx geothermometer (Ellis and Green, 1979) was used in the case of felsic granulite that did not contain any biotite (**fig. 5.35**). This method produced temperatures identical to those obtained from the Opx-Ga-Plag-Qz thermometer and is therefore not represented in **fig. 10.1**.

### 10.2.2. P-T constraints in the BIF-mafic granulite

The calc-silicate facies BIF granulite does not contain plagioclase and can therefore not be used to establish the pressure of equilibration. The high Fe-content and deficit in Mg of BIF lithologies can also lead to inaccuracies in the P-T calculations (Bohlen et al., 1983; Hodges and Spear, 1982; Ganguly and Saxena, 1984). As a result several sets of methods were used in order to obtain a reliable P-T pair that mirrored the peak-metamorphic conditions reached by the BIF-mafic lithologies.

Biotite is very rare in the BIF-mafic granulite but where it was in contact with garnet it was used to calculate temperature. Therefore, only the biotite-bearing assemblages in the mafic granulite were used for P-T calculations (fig. 5.29). The Bi(P) baro-Keq was determined based on the less confident Ga-Opx geobarometer (Ga-Opx: Harley and Green, 1982), the only way to calculate the pressure curve in the absence of plagioclase in the BIF-mafic granulite (fig. 5.32).

The Bi(T) thermo-Keq represented in fig. 10.1 represents the average of several calculations: Ga-Opx (Ellis and Green, 1979) and Ga-Bi (Hodges and Spear, 1982; Ganguly and Saxena, 1984). The Bi(T) thermo-Keq was averaged and is not the result of a single calculation because the above four authors did not write software programs for mafic-BIF lithologies, and therefore all of them produced probably some inaccuracies. In order to minimize the error, the slopes of several thermo-Keq curves resulting from the above mentioned thermometry methods were averaged. The result is the Bi(T) Keq curve. The intersection between the Keqs Bi(P) and Bi(T) produced the pair  $T=849^{\circ}\text{C}$  and  $P=8.38$  kbar (**point B**) in



fig. 10.1, which should mirror the peak-metamorphic condition reached by the mafic-BIF lithologies at Doornhoek.

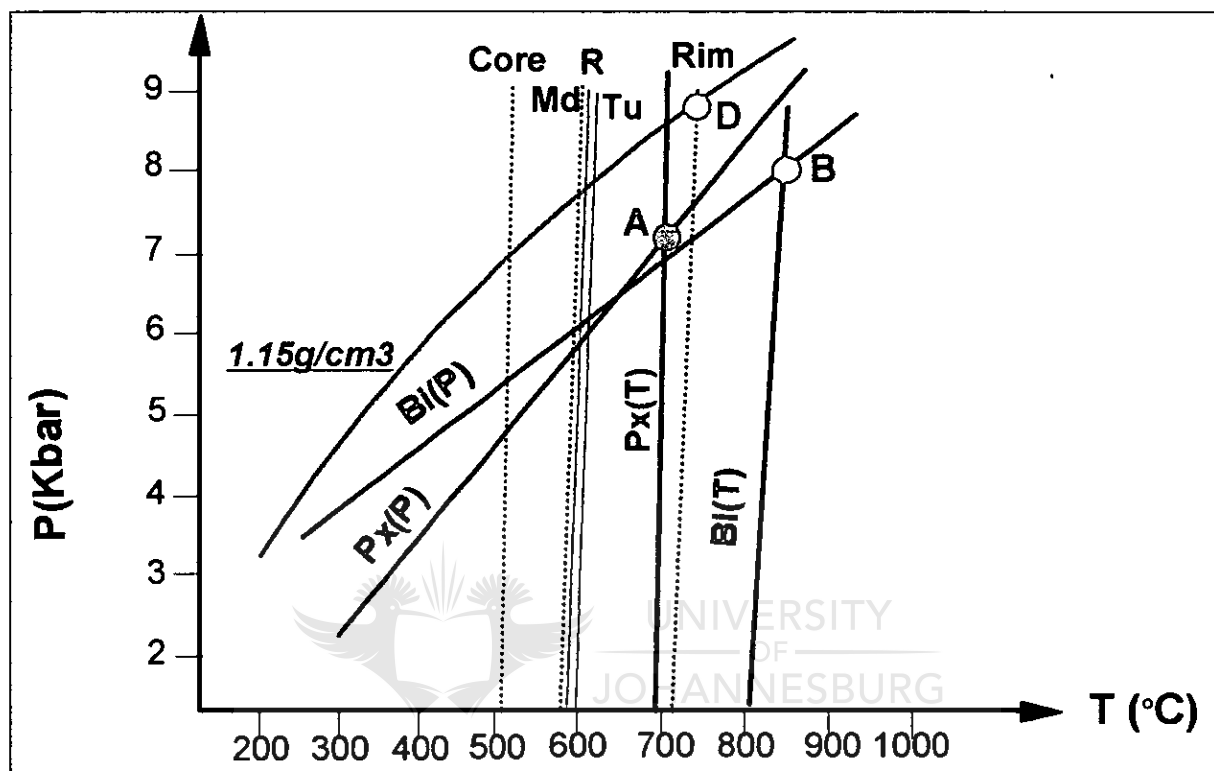


Figure 10.1: P-T diagram displaying all the P-T calculations obtained from petrologic data and from two isochors derived from the fluid inclusions data.

- Point A ( $T=712^{\circ}\text{C}$ ;  $P=7.21\text{kbar}$ ): intersection of Keq Px(T) and Px(P), based on the orthopyroxene-bearing assemblage of the felsic granulite (Bohlen et al., 1983; Ellis and Green, 1979)
- Point B ( $T=849^{\circ}\text{C}$ ;  $P=8.38\text{kbar}$ ): intersection of Keq Bi(T) and Bi(P), based on biotite-bearing assemblage from the BIF-mafic granulite (Ellis and Green, 1979; Harley and Green, 1982; Hodges and Spear, 1982; Ganguly and Saxena, 1984)
- Thermo-Keq R ( $580^{\circ}\text{C}$ ) represents the isotherm obtained from the equilibration of retrograde garnet with the large orthopyroxene host in the BIF-mafic granulite (Ellis and Green, 1979)
- Thermo-Keqs Core ( $500^{\circ}\text{C}$ ), Md ( $570^{\circ}\text{C}$ ) and Rim ( $720^{\circ}\text{C}$ ) represent isotherms derived from Ga-Bi pairs in the core, middle zone and rim of the prograde garnet porphyroblast in the metasomatic biotite-garnetiferous formation (Ganguly and Saxena, 1984)
- Thermo-Keq Tu represents the isotherm obtained from biotite-tourmaline pairs in felsic granulite intensely affected by metasomatic reactions (Colopietro and Frieberg, 1987)
- Curve labelled 1.15 represents the isochor derived from high-density  $\text{CO}_2$ -rich fluid inclusions. Point D represents the intersection between the  $1.15\text{g/cm}^3$  isochor and the isotherm Rim derived from the prograde garnet porphyroblast where most of the high-density fluid inclusions are located. Point D reflects  $T = 745^{\circ}\text{C}$  and  $P = 8.32\text{ kbar}$ .

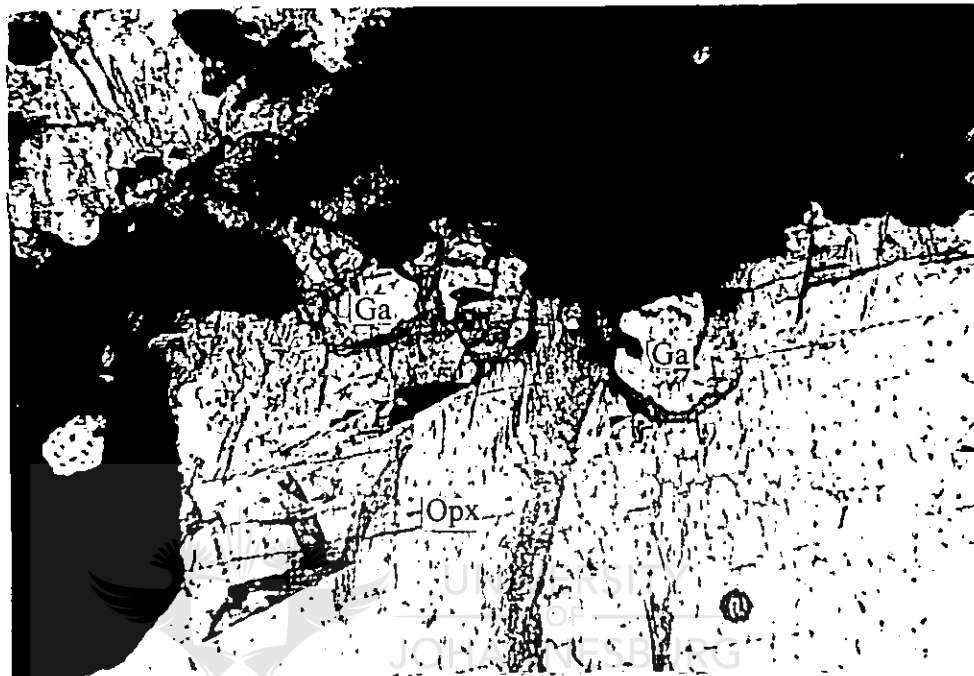
One can see that the Keq lines for the felsic granulite (**point A**) have steeper slopes than the Keq lines for the BIF granulite (**point B**). This situation as well as the higher P-T conditions obtained for BIF-mafic than for felsic lithologies can be explained by:

- incomplete re-equilibration of the core and outer rim of the garnet during cooling, complicated by the prograde effect of the alteration process (**Chapter 6.2**).
- less confidence in the P-T data obtained from the mafic lithologies due to very high Fe/Mg ratios.
- it is probable that the exact P-T peak conditions could not be determined from the present mineral assemblages. The peak conditions were probably slightly higher than A and lower than B.

Another attempt was made to determine the last petrological event recorded by the rim of resorbed garnet surrounded by opx (**fig. 10.2**). The chemical composition of the rim of the resorbed garnet and the contact of the ferrohypersthene host (**fig. 6.8 and 10.2**) were selected for this purpose, using the geothermometer of Ellis and Green (1979). This event probably records the retrograde cooling of the system which occurred just above 600°C (thermo-Keq curve R, **fig.10.1**). The attempt to calculate the pressure of this last recorded cooling gave unrealistic data (>8.05kbar) using the method of Harley and Green (1982), probably due to the incomplete re-equilibration of the garnet rims with the surrounding orthopyroxene, or simply due to the very Fe-rich composition used.

The P-T values that characterised the peak-metamorphic conditions of the felsic and BIF granulites (**points A and B, fig. 10.1**) are slightly higher than those determined by Mokgatla (1995) at the Klipbank locality, about 2 km north of Doornhoek (up to 680°C and 6.8kbar).

Even closer are the P-T estimations of du Toit (1994) at Petronella, based mainly upon metapelitic compositions (770°C and 7kbar). This data is also in accordance with P-T conditions for the M<sub>2</sub> decompressional event published by Stevens and van Reenen (1992) (T = between 780° and 850°C, P = between 6 and 9 kbar).



**Figure 10.2:** Sample DH-2024: BIF. Microphotograph showing resorbed garnet (arrow - Ga) hosted by orthopyroxene (Opx). The resorption of the garnet took place uniformly, preserving the euhedral shape, due to similar diffusion rates of Fe and Mg in both garnet and host ferrohypersthene. Garnet displays a typical retrograde zoning pattern, being part of the assemblage that underwent peak-metamorphic condition during M<sub>1</sub> and retrogression during M<sub>2</sub>.

1cm=100µm

### 10.3. P-T CONDITIONS FOR THE PROGRADE ASSEMBLAGES

In **Chapters 5-8** it was demonstrated that the metasomatic biotite-garnetiferous formation formed as the result of intense channelised metasomatism that affected the BIF and felsic granulite at the Doornhoek locality. The absence of plagioclase in this lithology means that it was not possible to calculate the pressure of formation of the mineralised prograde garnet porphyroblast. However, the temperatures of equilibration could be calculated using the biotite-garnet pair (**fig. 6.15** and **6.19**). More precisely, by using the garnet compositions of the different concentric rings and the composition of biotite inclusions within these zones in the prograde garnet porphyroblast the following temperatures could be calculated (Ganguly and Saxena, 1984):

- T of about 500<sup>0</sup>C for the garnet core
- T of about 600<sup>0</sup>C for the middle zone of the garnet, and
- T greater than 720<sup>0</sup>C for the unmineralised edge of the garnet (Keqs **Core**, **Md** and

**Rim**, **fig.10.1**).

It is important to note that the temperature recorded by the euhedral prograde zoned garnet during its metasomatic growth is slightly higher than the temperature recorded by the partially resorbed retrograde garnet in the felsic granulite during cooling and rehydration (Keq **Px(T)** compared to Keq **Rim**).

If the isochors provided by the fluid inclusion data (**Chapter 9**) are also taken into account (the intersection between the isochor 1.15g/cm<sup>3</sup> calculated from data provided by high-density fluid inclusions hosted by the rim of the garnet porphyroblast and Keq **Rim** - **point D** - **fig. 10.1**) even higher P-T conditions are suggested: T = 745<sup>0</sup>C and P = 8.32 kbar.

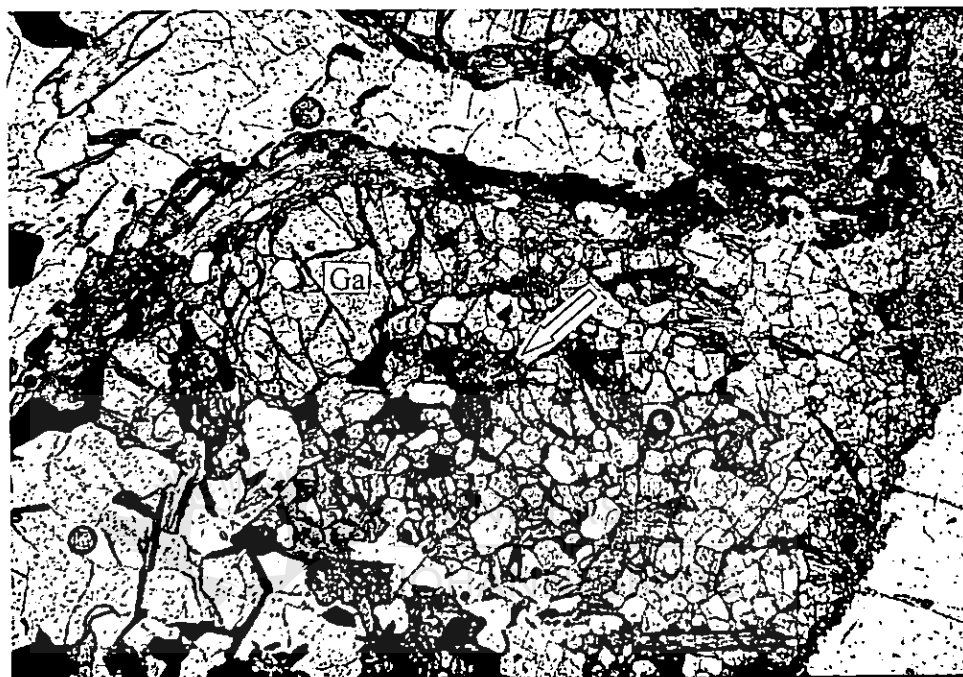
These locally high P-T conditions can be related to the heat introduced into the system by the mineralising metamorphic fluid.

A similar alteration process was described at the Klipbank locality about 2km north of Doornhoek by Mokgatla (1995). The peak temperature obtained from petrologic calculations at this locality (680°C) however, is much lower than the temperature derived from stable isotope studies (710<sup>0</sup>-890<sup>0</sup>C) (Mokgatla, 1995; Hoernes et al., 1995).

A conclusion at this stage is that P-T conditions reached during channelised fluid activity along deep-seated shear zones in the SMZ of the LB were higher than the P-T conditions recorded from the surrounding lithologies.

Evidence of late fluid activity at Doornhoek is suggested by the presence of newly introduced tourmaline crystals that crosscut highly flattened garnet in the sheared (D<sub>3</sub>?) "augen amphibolites" and associated quartz boudins (**fig. 10.3**). The "augen amphibolites" represent highly stretched retrogressed mafic-BIF granulite. The tourmaline crystals are orientated parallel to the D<sub>3</sub> shearing direction (oblique to D<sub>2</sub>) and either fill the pressure shadows of the pre-tectonic garnets or various cavities inside the garnet (**fig. 10.3**). This suggests volatile activity at lower temperatures and under conditions when the garnet was flattened. It can be assumed that the tourmaline and the associated flattened garnet were to some extent affected by cationic Fe-Mg exchange. However, the presence of biotite in garnet pressure shadows, suggests that the compositions of coexisting tourmaline and biotite should reflect the conditions of deformation. The rim of tourmaline in contact with rims of biotite should therefore document the last recorded fluid event which produced the metasomatic

biotite-garnetiferous formation (fig. 5.38 and 10.3). Not surprisingly, the tourmaline-biotite geothermometer (Colopietro and Frieberg, 1987) displays a temperature of 590°C (Tu, fig. 10.1) almost identical to the temperature recorded by the general retrogression of the BIF country rock (curve R, T = 580°C) (fig.10.1).



**Photo 10.3:** Sample DH-2008. Felsic granulite affected by metasomatic alteration. Microphotograph showing a deformed large garnet porphyroblast (Ga) . Tourmaline (yellow - arrow) has been introduced along fractures into the garnet. 1cm=400µm

The metamorphic evolution of the SMZ (fig. 4.4) is considered to reflect a near total re-equilibration during the high-grade cooling portion of the P-T path and at P-T conditions considerably lower than those of peak metamorphism. Recent studies, however (Mokgatlha, 1995; Hoernes et al., 1995) demonstrated that P-T conditions during alteration associated with highly channelised fluid flow along shear zones can be higher than the conditions experienced by the surrounding lithologies. The present study supports these conclusions and

further demonstrates the very close geometric association (sometimes only centimetres apart) between older retrograde garnet in the wall-rock, and newly formed prograde garnet in the metasomatic lithology. Furthermore, at Doornhoek, the well preserved metasomatic biotite-garnetiferous formation is also mineralised, demonstrating the direct relationship between metasomatic activity and mineralisation. This feature is preserved where the wall-rock displayed a suitable chemical composition (mafic, BIF, ultramafic lithologies). This is in contrast with the situation at Klipbank (Mokgatla, 1995), where the absence of rocks of suitable chemical composition (e.g. BIF or mafic lithologies) only resulted in the metasomatic alteration of the Baviaanskloof Gneiss, with no mineralisation.

An explanation for the close geometric association between prograde and retrograde lithologies, so splendidly preserved at Doornhoek, is that the metasomatic fluids were highly channelised and that the actual channelways are represented by the metasomatic biotite-garnetiferous formation as well as by the syn-tectonic quartz veins. This type of highly channelised fluid flow occurred:

- at temperatures close to and within the granulitic domain
- at high fluid:rock ratios, and
- at high infiltration velocities compared to the very slow fluid flow displayed by the percolation of fluid during the regional  $M_3$  hydration event.

## 11. P-T CONDITIONS OF MINERALISATION

Thermobarometric calculations based on coexisting minerals in both the retrograde pattern lithologies and the prograde pattern metasomatic rocks (**Chapter 10**) showed that P-T conditions of lower granulite facies probably prevailed during the metamorphic evolution of the Doornhoek Gold Deposit.

An attempt was also made to calculate the P-T conditions of mineralisation based on the chemistry of the ore minerals. A number of 136 microprobe analysis of sulpho-arsenides (arsenopyrite and löllingite) that are either intimately related to gold, or form part of the gold-free paragenesis were run and used for thermometric calculations (representative chemical analyses of the ore minerals are given in **table 11.1**).

Arsenopyrite in the gold-bearing association has an As-content that ranges from 35.91 to 38.33wt pe cent As. The gold-free association contains arsenopyrite with an As-content that varies from 31.67 to 35.58wt per cent As (**fig 11.1**). As-rich arsenopyrite is always associated with the gold mineralisation.

These As values are plotted on a Scott diagram (Scott, 1983) (**fig 11.1**) that suggests As-rich arsenopyrite, and therefore also gold, was introduced into the Doornhoek deposit at temperatures ranging from 569°C to 673°C, and even higher than 700°C considering that gold is mainly associated with löllingite in the quartz veins.



**TABLE 11.1 REPRESENTATIVE MICROPROBE ANALYSES OF LÖLLINGITE AND ARSENOPIRYRITE**

**LÖLLINGITE MICROPROBE ANALYSES**

WEIGHT % CONCENTRATION									
SAMPLE	DH 2033-17	DH 2033-18	DH 2033-19	DH 2033-20	DH 2033-21	DH 2033-22	DH 2033-23	DH 2033-24	DH 2033-25
ELEMENT									
Fe	30.35	30.37	30.23	31.66	28.56	30.59	29.23	29.94	30.27
S	1.77	1.89	1.94	1.49	4.11	1.62	1.69	1.74	1.87
As	67.73	67.36	67.44	66.00	67.33	68.18	69.44	68.52	67.30
TOTAL	99.85	99.62	99.61	99.15	100.00	100.39	100.36	100.00	99.44

ATOMIC CONCENTRATION									
Fe	35.89	35.61	35.77	38.23	35.74	36.23	34.76	35.76	35.87
S	3.54	3.73	3.87	3.13	13.19	3.33	3.50	3.53	3.73
As	60.34	60.36	60.15	58.50	50.93	60.17	61.55	60.45	60.12
TOTAL	99.77	99.70	99.79	99.86	99.86	99.73	99.81	99.74	99.72

**ARSENOPIRYRITE MICROPROBE ANALYSES**

WEIGHT % CONCENTRATION									
SAMPLE	DH 2005C-1	DH 2005C-2	DH 2005C-3	DH 2005C-11	DH 1026-1	DH 1026-2	DH 2038-1	DH 2038-2	DH 2038-3
ELEMENT									
Fe	35.80	36.61	35.37	35.44	35.53	32.46	36.26	36.41	35.62
S	19.62	19.22	20.04	16.36	20.39	20.21	18.89	20.06	20.24
Cu	-	-	-	-	0.43	0.17	0.12	0.44	0.24
Ni	0.08	-	-	0.06	0.10	0.04	0.47	0.41	0.07
As	44.84	44.56	44.50	48.32	44.04	46.94	44.33	42.91	44.10
TOTAL	100.34	100.39	99.91	100.18	100.49	99.82	100.07	100.23	100.27

ATOMIC CONCENTRATION									
Fe	35.49	36.80	34.43	36.02	33.40	31.06	34.54	34.19	34.83
S	32.08	31.10	31.85	29.10	32.47	33.67	29.69	33.33	31.80
Cu	-	-	-	-	0.35	0.14	0.09	0.34	0.19
Ni	0.07	-	-	0.06	0.08	0.03	0.40	0.34	0.41
As	32.07	31.55	33.65	34.64	33.42	34.18	35.21	31.63	32.34
TOTAL	99.71	99.45	99.93	99.82	99.72	99.08	99.93	99.83	99.57

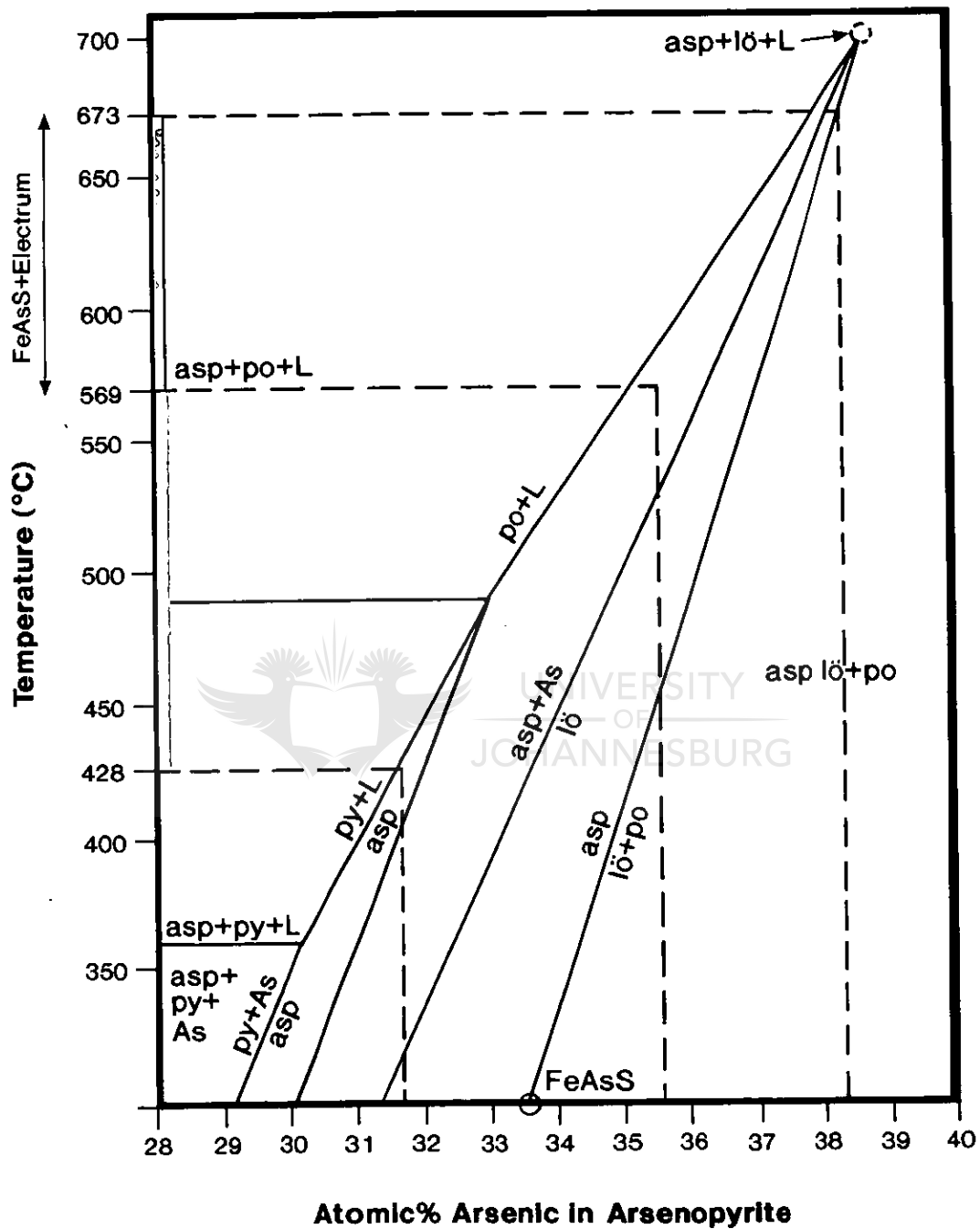
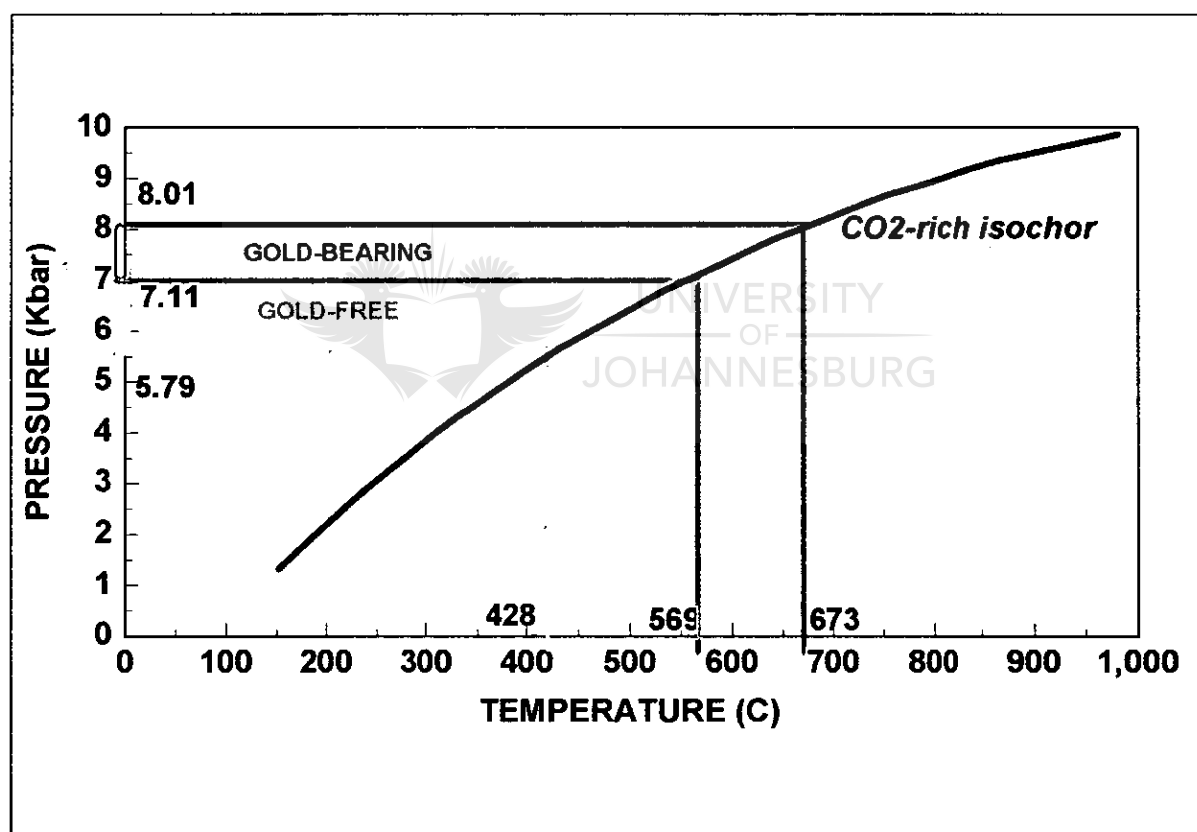


Figure 11.1: Scott diagram (Scott, 1983) showing the composition of arsenopyrite plotted against the temperature of arsenides precipitation. The composition of arsenopyrite from Doornhoek suggests precipitation temperatures ranging from 569 to 673°C, while the gold-free arsenopyrite precipitated at temperatures ranging between 428 to 569°C. However, the precipitation temperature of the gold mineralisation probably occurred at higher conditions considering the presence of löllingite (lö) as the main arsenide associated with gold (see text for explanations).

The pressure conditions of mineralisation was established (fig.11.2) by using the temperature interval (569°C-673°C) derived from the chemical composition of the gold-bearing arsenides in the Scott diagram (fig.11.1), in conjunction with fluid inclusion isochors (Chapter 9) derived from CO<sub>2</sub>-rich fluid inclusions trapped in the mineralised zone of the prograde-zoned garnet porphyroblasts. This approach suggests that mineralisation was trapped at pressures ranging from 6.80 to 8.01 kbar (fig.11.2). The gold-free paragenesis started to crystallise from 5.79 to 6.80 kbar at equivalent temperatures of 428°C-569°C (fig.11.2).



**Figure 11.2:** P-T diagram used to determine the pressure conditions of mineralisation based on temperature obtained from the Scott diagram (fig. 11.1). The T data ( $\Delta T=569^{\circ}\text{C}-673^{\circ}\text{C}$ ) derived from the Scott diagram were plotted against the isochores obtained from the fluid inclusions study. These CO<sub>2</sub>-rich fluid inclusions probably represent fluid inclusions associated with arsenopyrite and gold mineralisation. The resulting P data ( $\Delta P=7.11\text{-}8.01\text{kbar}$ ) suggests the pressure conditions at which the gold mineralisation was entrapped in the garnet poprhyroblasts and precipitated into the quartz veins. The real entrapping pressures should be higher considering the fact that most of the gold is associated with löllingite.

As discussed in **Chapters 7 and 10** the edge of the garnet porphyroblast is unmineralised but still contains fluid inclusions (**Chapter 9**). In order to estimate the T at which the edge of the garnet porphyroblast crystallised, isochors derived from fluid inclusions trapped within the unmineralised edge of the garnet porphyroblast are also plotted on the same P-T diagram (not shown in **fig. 11.2**), with thermo-barometric calculations obtained from the Ga-Bi and Ga-Opx pairs (**Chapter 10**). In this case, temperatures well above 800°C were obtained (**fig.10.1, point D**), suggesting once more that the rim of the garnet porphyroblast is unmineralised probably due to the high temperature of the metasomatic fluid which inhibited the precipitation of ore minerals.

Calculated P-T conditions therefore reflected granulite facies metamorphic conditions for both the mineralising event and the metasomatic process that affected the host rock of the Doornhoek Gold Deposit. Therefore, the deep-crustal shearing event that controlled the highly channelised flow of the hot metasomatic fluids were active during granulite facies conditions. The main conclusion of this study therefore focus on the possibility of gold deposition in metamorphic rocks under conditions close to that of granulite facies. This enhances the possibility for gold exploration in high-grade terranes with low metallogenic prognosis to date.

## 12. GEOCHEMISTRY

Geochemical data is essential in understanding and highlighting several features of the Doornhoek Ore Body discussed in the previous chapters. Major and trace element analyses were done in order to characterise the main geochemical features of various lithological units. The results of this study highlighted the enrichment/depletion of various lithologies in order to visualise the transfer of mass within the Doornhoek Ore Body. Rare earth elements (REE) analyses identified the relative enrichment and depletion of various light or heavy REE with implication for the parental provenance of various lithologies. The REE also emphasised the different alteration patterns of the retrograde lithologies relative to that of the metasomatic biotite-garnetiferous formation. Protonic microprobe analyses of the prograde pattern garnet porphyroblasts were done in order to characterise the distribution of elements such as Au, Y, Zr, Ge, Zn and As in garnet.

Stable isotope analyses were not done but the main conclusions of a whole rock/mineral stable isotope study of the metasomatised lithologies at the Klipbank locality (Mokgatla, 1995; Hoernes et al., 1995) are summarised.

## 12.1 PROTON MICROPROBE ANALYSES

A large prograde zoned metasomatic garnet porphyroblast was selected for proton microprobe analyses (sample DD-2-2035). The distribution of major elements in this garnet was also mapped with the electron microprobe in the Geology Department at Rand Afrikaans University (see **Chapter 6.2**), and the same sample was also used for fluid inclusion studies (see **Chapter 9**). The proton microprobe analyses were made at the National Accelerator Centre in Cape Town. Major elements analysed are Mn, Fe and Ca. Trace elements analysed are Ni, Zn, Ge, As, Y, Zr and Au.

There is a slight difference in the absolute concentration of the major elements (Fe, Mn and Ca) between the analyses done with the electron microprobe and those done with the proton microprobe. This difference is probably due to the differences in software and standards used with different methods.

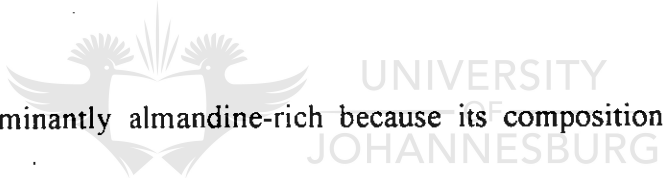
### 12.1.1 Manganese distribution

Rim-core-rim profiles of Mn, Fe, Ge, As, Y, Ni, Zr and Au are shown in **fig. 12.1a-g**. The Mn distribution shows a continuous decrease from core to rim (**fig. 12.1a**), reflecting the prograde growth of the garnet (see **Chapter 6.2**). It is clear that the geometrical core of the garnet does not coincide with the metamorphic core, due to the fact that the thin section did not intersect the exact garnet core. One rim shows a Mn content of 1.23 percent Mn, which increases constantly to 4.46 percent in the core. A narrow plateau of constant Mn distribution

(about 1.5 percent Mn) coincides with the inner-ring zone of intense mineralisation in the garnet porphyroblast. The Mn-content then decreases to 0.42 percent in the other edge of the garnet.

### 12.1.2 Iron distribution

The Fe distribution in garnet is shown in **fig. 12.1b**. The value increases from 29.9 percent Fe in one rim to 32.2 percent in the inner-ring. The Fe value then decreases sharply to a minimum value of 29.1 percent in the core. It then again increases to a maximum value of 32.3 percent in the symmetric side of the mineralised inner-ring. From there it declines to a low value of 28.4 percent Fe in the rim.



The garnet is predominantly almandine-rich because its composition reflects the Fe-rich nature of the BIF lithological environment. The sharp increase in the Fe-content from the core to the rim with the maximum value reached in the mineralised inner-ring probably reflects an increase of the Fe activity during the trapping of the mineralisation at the time when the other chemical components of the garnet (Mg and Ca) displayed a lower chemical activity. This is substantiated by the presence of numerous inclusions of magnetite-ilmenite trapped in the inner-ring of the zoned garnet (**fig. 7.35**).

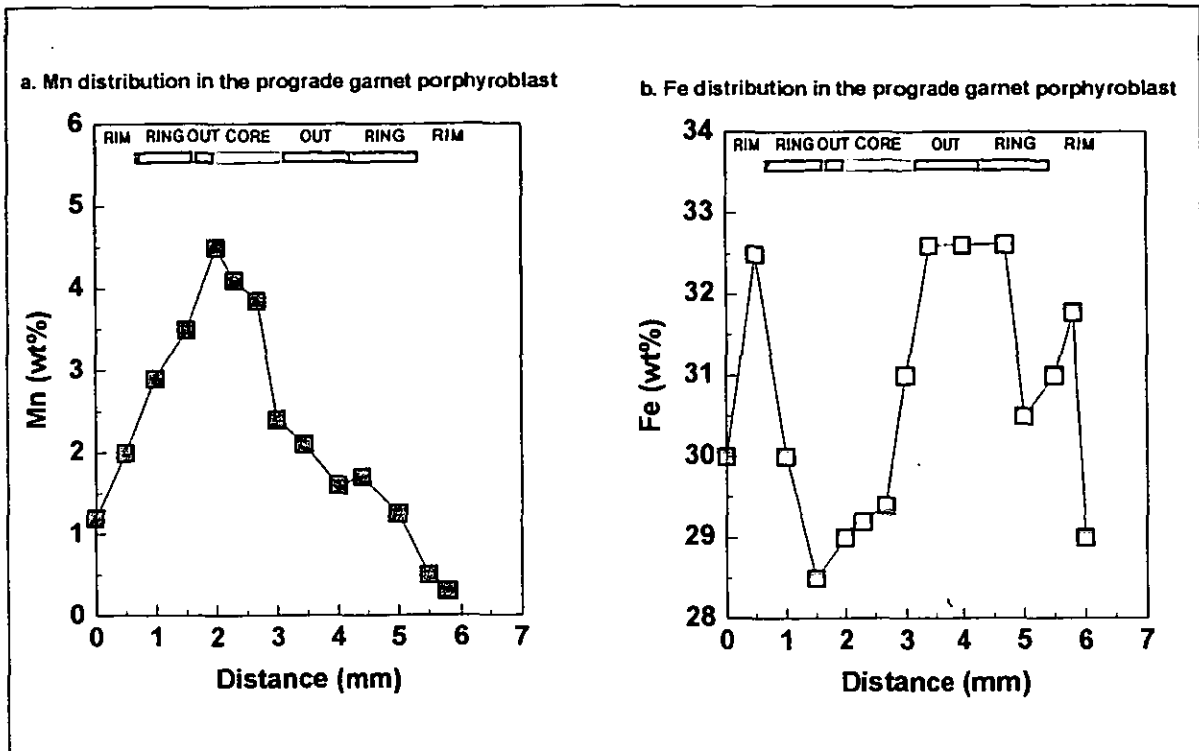


Figure 12.1: *a.* Mn distribution in the prograde garnet porphyroblast displays a typical prograde pattern with high values in the core that decreases towards the rim; *b.* Fe distribution reaches a maximum value in the vicinity of the mineralised inner-ring that is also characterised by the presence of numerous magnetite and ilmenite inclusions.

### 12.1.3 Germanium distribution

Ge-content increases from the rim (20.1 ppm Ge) to the inner-ring where it reaches a maximum value of 83.1 ppm Ge (fig. 12.1c), and then decreases to a minimum value of 4.22 ppm in the core. From here it again increases symmetrically towards the other intersection with the mineralised inner-ring (22.6 ppm Ge) from where it decreases to the rim (3.52 ppm Ge). The profile is asymmetrical, but the trend is quite clear. The asymmetry of the zoning profile is probably due to the way in which the thin section intersects the garnet grain.

Ge thus displays low values in the edges and again in the core of the garnet porphyroblast and high values (20 times higher than the background) in the mineralised inner-ring. This



demonstrates the high activity of the mineralised fluids at the time when the ore minerals were trapped in the garnet porphyroblast and precipitated in the quartz vein system.

#### 12.1.4 Arsenic distribution

As distribution displays three peaks: two high peaks and a very tiny peak (much higher than the background). A maximum value of 2000 ppm As is reached at one intersection with the mineralised inner-ring while a value of 1200 ppm As was recorded with the other intersection of the same mineralised inner-ring (**fig.12.1.d**). The core of the garnet displays the third and much smaller peak of about 200 ppm As. The background value of the As content along the profile through the rest of the garnet grain is extremely low. This As distribution pattern is to be expected since arsenopyrite is concentrated in the core of the garnet while löllingite is the main ore mineral trapped in the mineralised inner-ring of the prograde garnet porphyroblast.

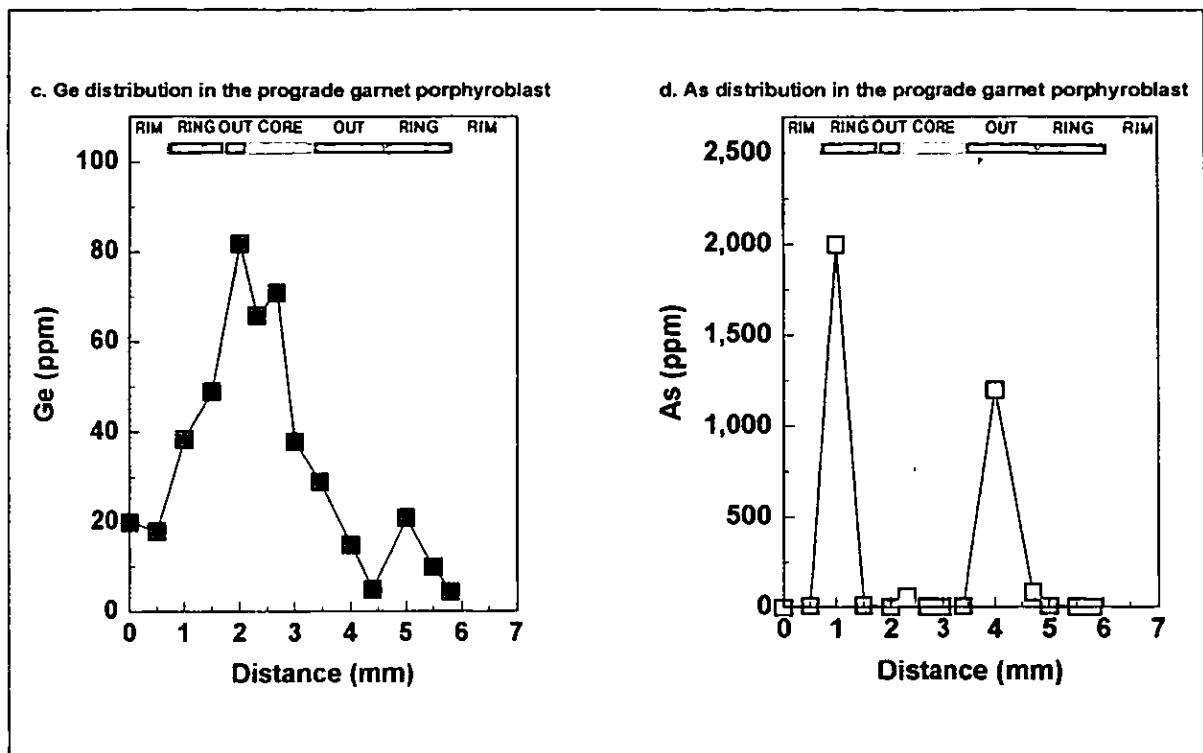


Figure 12.1: *c*) Ge distribution in the prograde garnet porphyroblast (see text for explanations); *d*) As distribution in the prograde garnet porphyroblast (see text for explanation).

### 12.1.5. Yttrium distribution

The Y distribution (**fig.12.1.e**) varies from 3.62 ppm Y at the very edge of the garnet porphyroblast to an intermediate value of 114 ppm Y close to the rim and finally to a value of 627 ppm Y in the mineralised inner-ring. From there it decreases to a value of 25.8 ppm Y in the core. From the core the Y value again increases sharply to another peak of 364 ppm Y in the mineralised inner-ring and then decreases sharply to 3.98 ppm Y at the other edge of the garnet porphyroblast. High Y values are again restricted to the mineralised inner ring with the rest of the garnet porphyroblast characterised by very low Y values.

### 12.1.6. Zirconium distribution

The distribution of Zr displays two high peaks and a third smaller peak similar to that of As distribution. Zr reaches values of 170 ppm Zr in one intersection with the mineralised inner-ring and a value of 364 ppm with the other intersection (fig.12.1.f). The mineralised core of the garnet porphyroblast is characterised by a third peak with a value of 67 ppm Zr. The rest of the garnet displays low Zr values which are still anomalously high at 20 ppm Zr. Zr, therefore also shows a preference for the mineralised zones of the garnet porphyroblast.

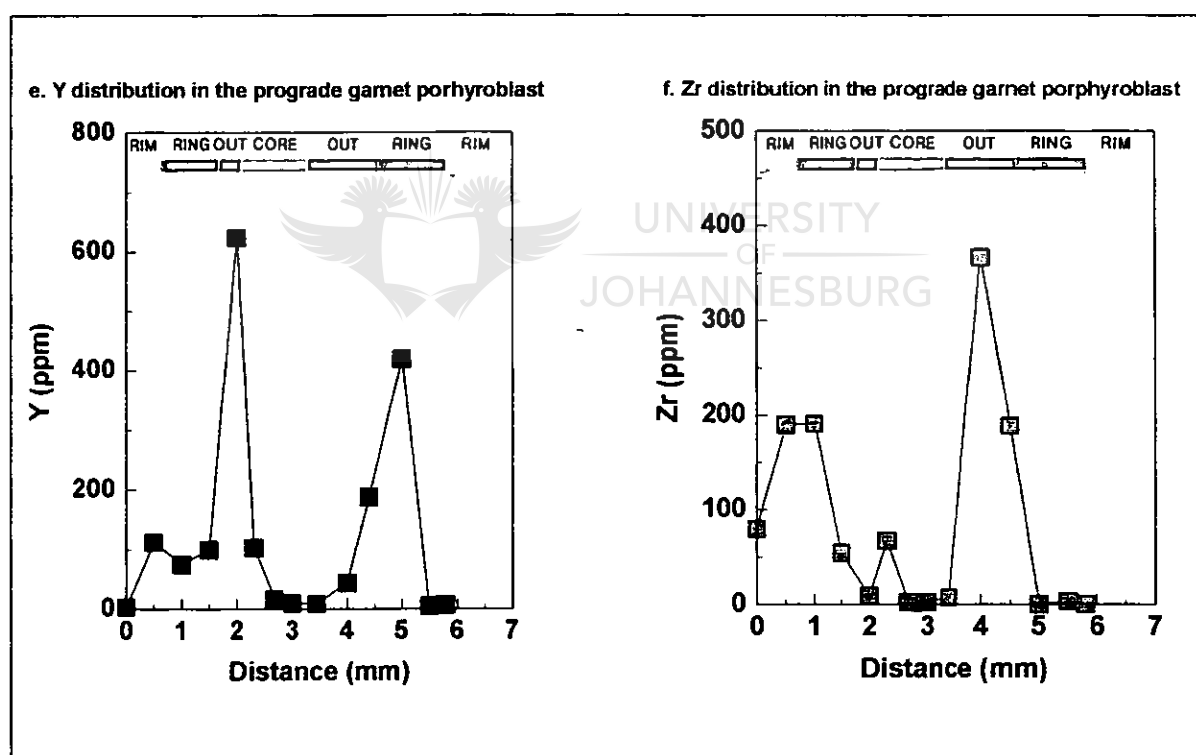
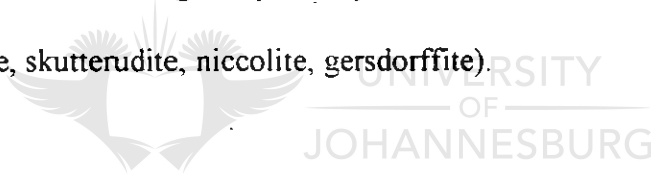


Figure 12.1: *e*) Y distribution in the prograde garnet porphyroblast (see text for explanations);  
*f*) Zr distribution in the prograde garnet porphyroblast (see text for explanation).

### 12.1.7. Nickel distribution

Ni shows a very sharp increase from 44.5 ppm Ni in one rim to 462 ppm Ni in the mineralised inner-ring of the garnet porphyroblast (**fig.12.1.g**). The Ni-content then drops to a value of 22 ppm Ni in the core of the garnet and then increases again to almost 100 ppm Ni in the mineralised inner-ring. It then drops to 18.5 ppm Ni at the very edge of the garnet porphyroblast.

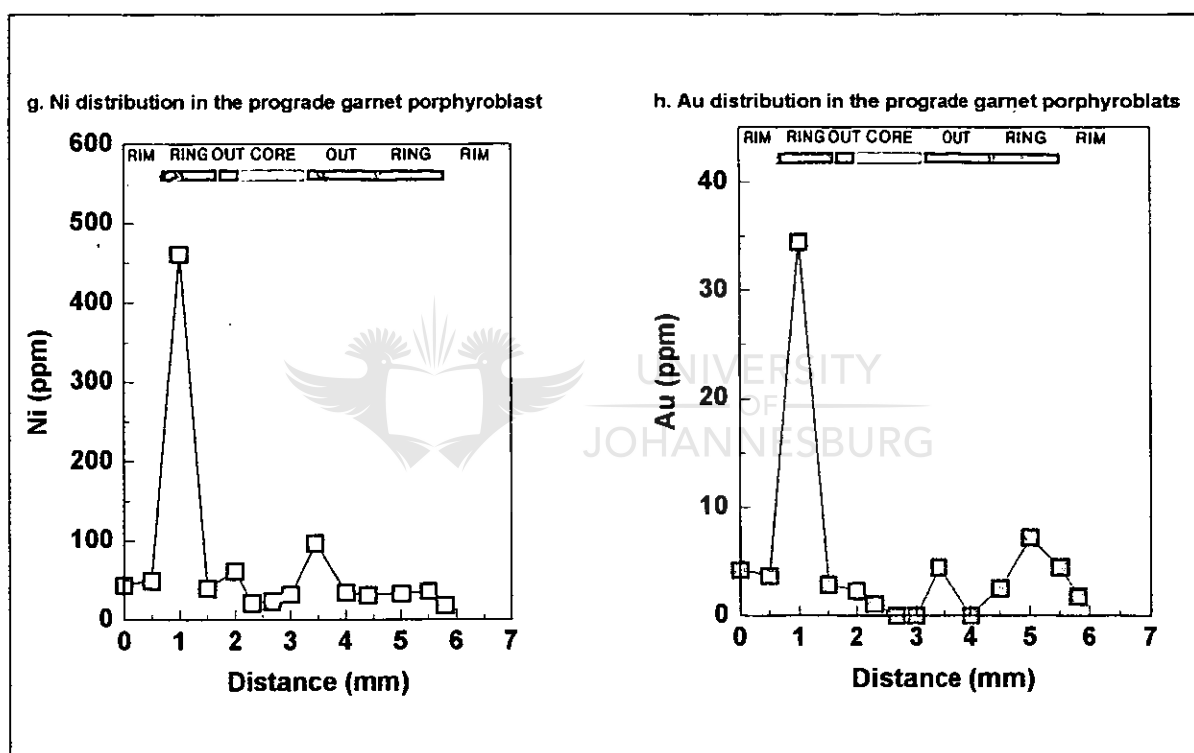
The Ni distribution, therefore, displays the same high values in the inner-ring of the garnet porphyroblast and lower values (background values) in the rest of the garnet. The high Ni values in the mineralised inner-ring are probably linked to the Ni-mineralisation present in the garnet (pentlandite, skutterudite, niccolite, gersdorffite).



### 12.1.8. Gold distribution

The distribution of Au values is the most interesting aspect of the zoned garnet porphyroblast (**fig.12.1.h**). It increases from 4.19 ppm Au in the rim to about 34.5 ppm Au in the mineralised inner-ring - quite a high value. The Au value then decreases from 34.5 ppm in the inner-ring to a low value of 1.06ppm Au in the core and then to zero. A smaller peak value of about 4 ppm Au was also recorded in the core of the garnet porphyroblast. The Au-content increases again to 7.21 ppm Au in the mineralised inner-ring and then decreases to 1.74 ppm Au in the other rim of the garnet.

It is therefore clear that although gold has been identified in both the core and the mineralised inner-ring, the highest gold concentration is in the inner-ring of garnet. This suggests that gold was preferentially precipitated at P-T conditions that coincides with the formation of the inner-ring of the garnet, i.e. lower granulite facies (see **Chapters 10 and 11**). This observation also demonstrates that the Doornhoek gold deposit was formed during granulite facies metamorphic conditions.



**Figure 12.1:** *g)* Ni distribution in the prograde garnet porphyroblast (see text for explanations);  
*h)* Au distribution in the prograde garnet porphyroblast (see text for explanation).

In conclusion, it is clear that anomalous high concentrations of Ni, Zn, Ge, As, Y, Zr and Au were detected in the idiomorphic garnet porphyroblast from the metasomatic biotite-garnetiferous formation. Most of these elements display high concentrations in the mineralised inner-ring of the garnet porphyroblast (up to 34.5 ppm Au, 462 ppm Ni, 840 ppm Zn, 83 ppm Ge, 0.2 percent As, 627 ppm Y, 364 ppm Zr). Some of the elements also display a multi (three) peak distribution, also exhibiting anomalous high values in the core of the garnet (As, Zr, Ge). These values, however, are still much lower than those measured from the mineralised inner-ring. The data demonstrates that the mineralising fluids at Doornhoek were responsible for the intense metasomatism that affected all lithologies that form the ore body. The biotite-garnetiferous formation and the gold mineralisation are therefore closely related.



Representative rock samples (biotite-garnetiferous formation, felsic granulite, BIF-mafic granulite, ultramafic granulite, quartz vein material, mineralised quartz vein material and calcite vein) were analysed for fourteen REE (La, Ce, Pr, Nd, Sm, Eu, Gd, Tb, Dy, Ho, Er, Tm, Yb and Lu) as well as for Pb, U and Th with the ICP-MS at the University of Natal at Durban by Dr. Stefan Nicolescu.

It is difficult to identify any geochemical trends based on the Pb, Th and U values. It appears that only the metasomatic garnetiferous formation displays higher values than the rest of the other lithologies (3.68ppm Th<sup>232</sup> against an average of 0.55ppm Th<sup>232</sup> for the rest of the

other lithologies; 43.98ppm U235 versus 15.68ppm U238; and 1.26ppm U238 versus 0.25ppm U235). Thus, the metasomatic biotite-garnetiferous formation displays the following enrichment factors in comparison with the other lithologies:


- 6.6 for Th232,
- 2.7 for U235
- 5.0 for U238.

In conclusion, one can say that there is a consistent additional source of heat in radioactive elements in the metasomatic lithologies in comparison with the retrogressed country rock.

The REE trend normalised to chondrite values is shown in **fig. 12.2a** and **12.2b**. Positive anomalies for Ce are displayed by the BIF lithologies and the quartz vein samples. Quite a prominent positive Sm peak is shown by the ultramafic granulite and the BIF that also display a negative Eu peak. The opposite trend is exhibited by the metasomatic biotite-garnetiferous formation, the mineralised quartz vein and the calcite vein, all displaying a strong positive Eu peak. Tm shows a strong positive peak for the ultramafic granulite, BIF, felsic granulite, biotite-garnetiferous formation, calcite vein and the quartz vein. The only negative Tm peak is displayed by the mineralised quartz vein material. It is possible that the highly sulphidised environment is depleted in Tm.

**Figure 12.2a** shows the REE trend for the rocks that underwent moderate to high pervasive alteration (felsic granulite, ultramafic granulite and BIF). The general metamorphic pattern of these lithologies is retrograde. **Figure 12.2b** shows the REE trend for rocks that were produced as the result of intense channelised alteration (biotite-garnetiferous formation, quartz vein, mineralised quartz vein and ferroan-calcite vein). The general metamorphic pattern of these lithologies is prograde. The retrogressed lithologies (felsic granulite, BIF and

ultramafic granulite) (fig.12.2) display positive Sm and Tm peaks and negative Nd, Eu and Yb peaks. The metasomatised lithologies show a positive Eu peak (except in the quartz vein which is too pure and depleted in any geochemical elements in order to display any consistent trend), and a positive Tm peak (except in the sulphide-rich quartz vein). Ca and Eu ions display almost identical ionic radius. As a result, the almost pure calcite vein will display a high Eu anomaly. The mineralised vein also contains some ferroan-calcite responsible for the positive Eu peak. The biotite garnetiferous formation is characterised by the presence of the Ca-rich prograde garnet porphyroblast (with up to 15 percent grossular mole). As a result it will also show some Eu enrichment. The absence of Ca-bearing minerals in the retrograde pattern lithologies (felsic granulite, ultramafic granulite, BIF) might explain the negative Eu anomalies in these lithologies.



The metasomatised lithologies also display a relative enrichment in light rare earth elements (LREE), i.e. La, Ce, Pr. There is no consistent negative peak for the metasomatised lithologies.



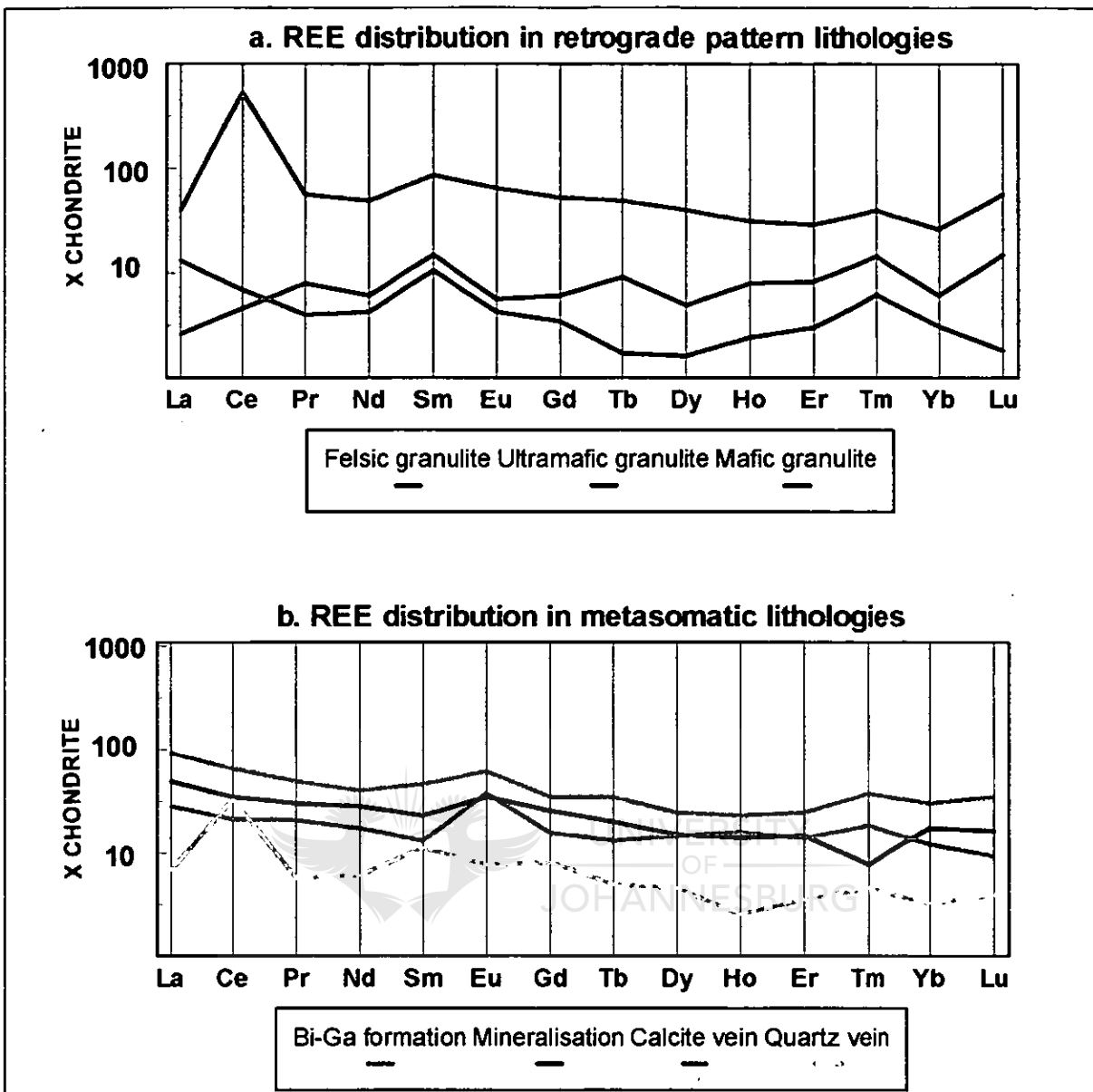


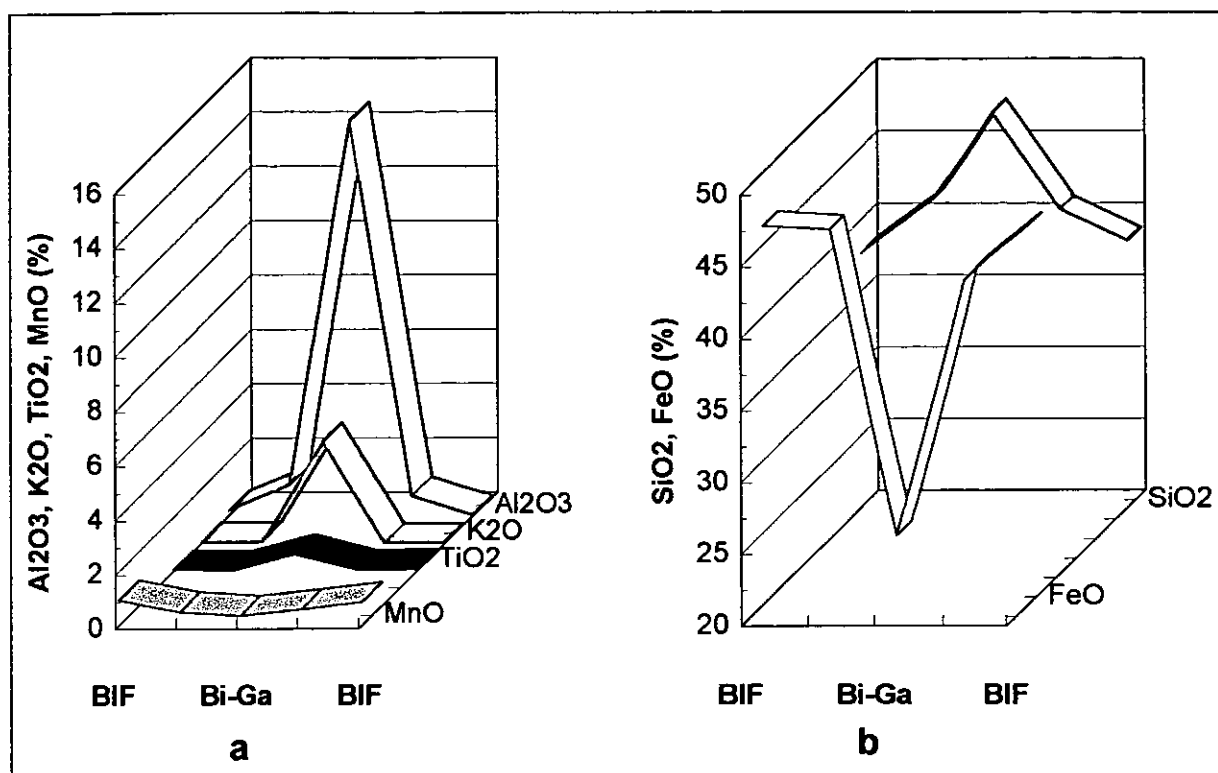
Figure 12.2: Normalised REE trend in the Doornhoek lithologies. *a)* Normalised REE trend for the retrogressed lithologies which occur at Doornhoek (felsic granulite, BIF and ultramafic granulite). As a general trend, one can see positive Sm and Tm peaks as a characteristic for this lithologies. *b)* Normalised REE distribution in metasomatic lithologies (biotite-garnetiferous formation, massive sulphide mineralisation from a quartz vein, pure quartz vein material and calcite vein material). These prograde lithologies are characterised by Eu positive peak.

### 12.3 MAJOR ELEMENT GEOCHEMISTRY

Major element geochemical data have also been obtained for ten samples representative of the major lithologies at the Doornhoek deposit (analyst: Rocklabs, Pretoria). An additional 13 samples were subsequently analysed at the Gold Fields Laboratories in Johannesburg. A total of 23 samples were therefore analysed for major element geochemistry. The analysed lithologies included the following: felsic granulite, BIF, ultramafic granulite, metasomatic biotite-garnetiferous formation, mineralised quartz vein, ferroan-calcite vein, the Baviaanskloof Gneiss and the metasomatic pink veins that occur in the Baviaanskloof Gneiss (fig. 6.6).

These rock types represent lithologies that underwent retrograde metamorphism and lithologies that are the product of highly channelised metasomatic processes.

Previous discussions showed that the newly formed lithologies (metasomatic biotite-garnetiferous formation, mineralised quartz veins and calcite veins) reflect healed shear zones within wall rock that mainly consists of retrogressed BIF and felsic granulite. For example, fig. 12.3.a and b show a geochemical profile from the wall-rock (BIF) through the metasomatic biotite-garnetiferous formation and back into the wall rock (BIF).



**Figure 12.3:** Geochemical variation of several major elements across the wall-rock contact of BIF with the biotite-garnetiferous formation (Bi-GaF) and back into BIF (wall-rock). The enrichment in SiO<sub>2</sub>, Al<sub>2</sub>O<sub>3</sub>, K<sub>2</sub>O and TiO<sub>2</sub> (a) and the depletion in FeO and MnO (b) that characterise the biotite-garnetiferous formation is clear.

- Al<sub>2</sub>O<sub>3</sub> increases from less than 1 percent in the BIF to a maximum value of 14.54wt percent in the biotite-garnetiferous formation (fig. 12.3a).

- K<sub>2</sub>O increases from less than 0.06 percent in the wall rock (BIF) to a maximum value of 3.75wt percent in the biotite-garnetiferous formation (fig. 12.3a)

- SiO<sub>2</sub> also increases from 35.38 percent in the wall rock (BIF) to a maximum of 54.11wt percent in the biotite-garnetiferous formation (fig. 12.3b).

- TiO<sub>2</sub> increases from less than 0.02 percent in the wall rock (BIF) to more than 0.60wt percent in the biotite garnetiferous formation (fig. 12.3a).

- The oxides displaying a real decrease from the parental material (wall rock) to the newly formed biotite-garnetiferous formation are FeO and MnO. The FeO-content decreases

from about 46 percent in the wall rock (BIF) to less than 20wt percent in the biotite-garnetiferous formation (**fig. 12.3b**).

- MnO decreases from a maximum of 0.94 percent in the wall rock (BIF) to less than 0.40wt percent in the biotite-garnetiferous formation (**fig. 12.3a**).

- CaO and MgO do not display major variations if the BIF wall-rock is compared with the metasomatic biotite-garnetiferous formation.

- The almost 14 fold increase in the  $\text{Al}_2\text{O}_3$ -content of the metasomatised biotite-garnetiferous formation, from an initial low content in the BIF which probably represented the parental material prior to metasomatism, is due to the presence of garnet and biotite. Both these minerals are Al-rich. Some of the Al could have been introduced into the system by the hot mineralising fluids, but most of the Al-enrichment is probably due to residual enrichment. Similar mechanisms of Al enrichment due to fluid channelling during ductile shearing at depths of 35-40 km was also described in the Eastern Alps (Selverstone et al., 1991). The biotite-garnetiferous formation therefore marks the healed channels through which hot fluids infiltrated the BIF.

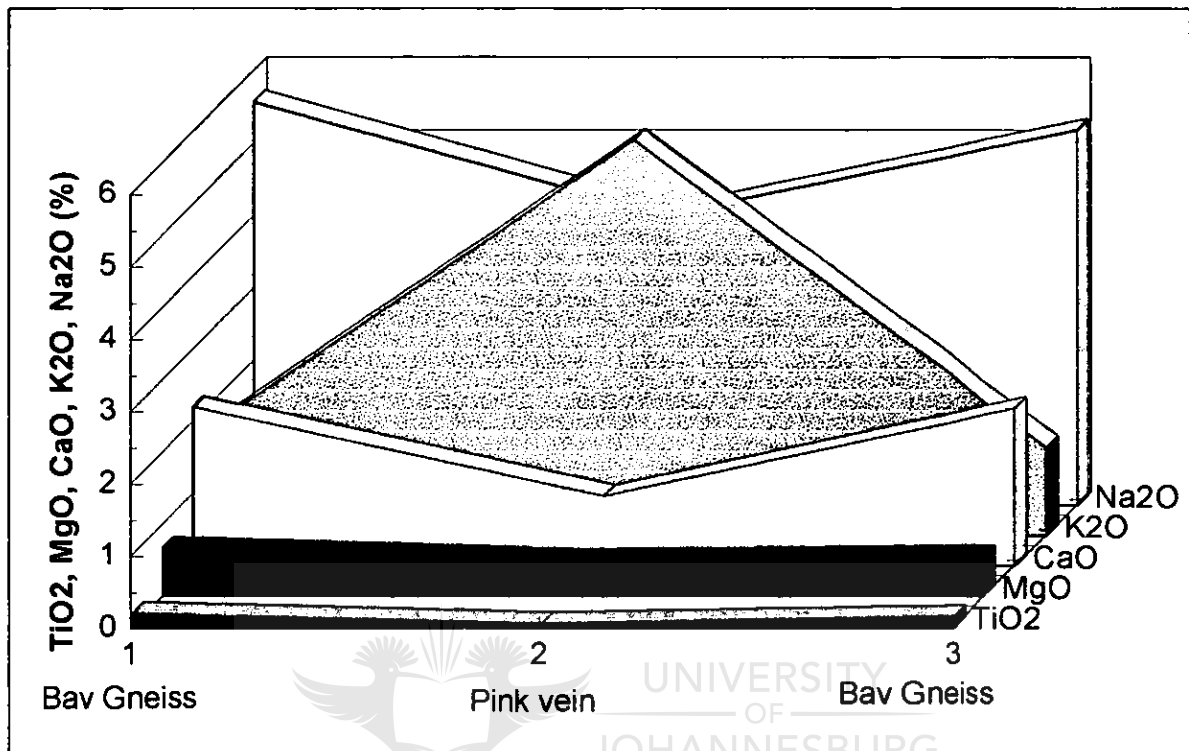
- $\text{K}_2\text{O}$  increases in the biotite-garnetiferous formation due to the presence of biotite.

- $\text{SiO}_2$  increases as a result of the presence of free quartz in the metasomatic formation.

- $\text{TiO}_2$  is high as a result of the presence of ilmenite and rutile as hydrothermal minerals included in garnet and biotite.

- Both FeO and MnO decrease from the BIF to the biotite-garnetiferous formation due to a relative increase in the proportion of other oxides as a result of the introduction of Al, K, Si and Ti.

Fig.12.4 demonstrates the geochemical variation between the hydrated Bavianskloof Gneiss and the altered pink veins that are related to channelised metasomatic fluids.



**Figure 12.4:** Geochemical variation of several major elements across the contact of Bavianskloof gneiss with pink metasomatic vein material. The strong enrichment of K and depletion in Ca and Na in the pink vein is clear.

The only notable geochemical change from the gneiss to the vein is in the K<sub>2</sub>O-content, that increases from 1.23 to 5.48wt percent (a 4.5 fold increase). The enrichment in K is accompanied by the depletion in FeO (from 3.71 to 0.15wt percent), CaO (from 2.21 to 0.97wt percent), Na<sub>2</sub>O (from 5.20 to 4.03wt percent) and in MgO (from 0.67 to 0.50wt percent). The relative high enrichment in K is due to the crystallisation of microcline-perthite in the pinkish veins. The depletion in Ca and Na is due to a decrease in the plagioclase content due to the formation of albite rather than andesine in the metasomatic vein. The depletion of Fe and Mn from the parental Bavianskloof Gneiss to the newly formed

metasomatic pink veins is due to the absence of mafic minerals such as pyroxene and amphibole in the veins.

#### 12.4 TRACE ELEMENT GEOCHEMISTRY

The following trace elements were analysed at Gold Fields Laboratories, using a Phillips X-ray fluorescence machine: Y, Rb, Sr, Zr, Cu, Ba, Ni, Co, Zn, Pb, W, Mo, As, Cr and V. Au was analysed at Gold Fields Laboratories, using fire assay techniques. The same samples analysed for major elements were also analysed for trace elements. The distribution of the trace elements was plotted with reference to a generalised lithostratigraphic column (**fig. 12.5, 12.6, 12.7 and 12.8**) suggested by a real geological situation encountered in borehole DD-2,

as follows:

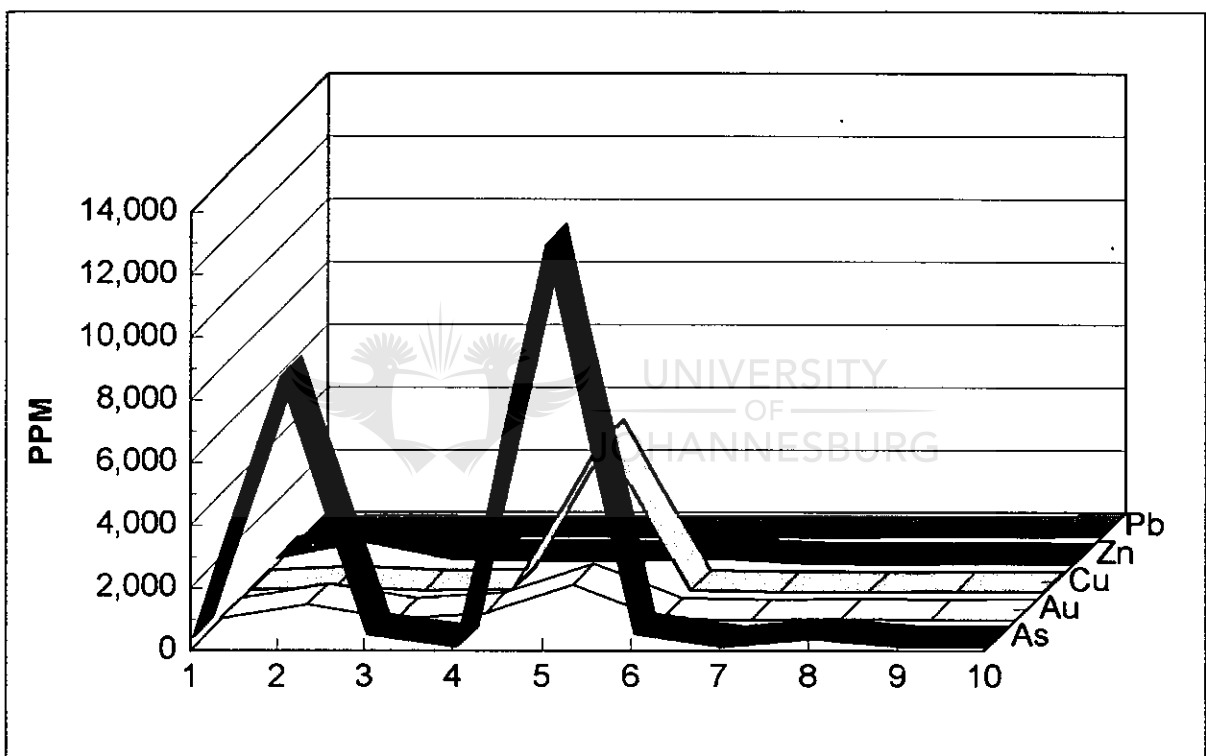
- 1-BIF
- 2-Metasomatic biotite-garnetiferous formation
- 3-BIF
- 4-Felsic granulite
- 5-Mineralised quartz vein
- 6-BIF
- 7-Ultramafic granulite
- 8-Calcite vein
- 9-Baviaanskloof Gneiss
- 10-Metasomatic pinkish vein in Baviaanskloof. Gneiss

The geochemical trend of the chalcophile elements is illustrated in **fig. 12.5**.

- High As enrichment occurs in the metasomatic garnetiferous formation (>8000ppm) and in the mineralised quartz vein (>12.000ppm), where most of the mineralisation is concentrated. As occurs as arsenopyrite and löllingite.

- Au follows the As values with kicks of up to 13ppm in the mineralised vein and 8ppm in the biotite-garnetiferous formation.

- Cu shows a relative enrichment in the biotite-garnetiferous formation (187ppm) but goes up to 0.5% in the mineralised vein. Cu usually occurs as chalcopyrite.
- Zn shows an anomalous concentration in the mineralised vein (118ppm) and is relatively enriched in the biotite-garnetiferous formation (726ppm). Zn occurs as sphalerite.
- Pb does not show any anomalous behaviour or concentration in any of the lithologies presented in the Doornhoek area.



**Figure 12.5:** Geochemical variation of chalcophile elements in the Doornhoek lithologies, illustrated across a generalised lithostratigraphic column. See text for details.

Fig. 12.6 shows the variation of lithophile elements in the Doornhoek lithologies.

- Zr shows relative enrichment in the felsic granulite (131ppm), in the biotite-garnetiferous formation (112ppm) and in the Baviaanskloof Gneiss (81ppm). The almost similar Zr values in the Baviaanskloof Gneiss and in the felsic granulite might suggest a similar origin for both rocks prior to the intense alteration. The anomalous high Zr value in the biotite-garnetiferous formation suggests a possible hydrothermal/metasomatic enrichment due to the presence of numerous tiny inclusions of zirconium crystals in the metasomatic biotite. Similar metasomatic biotite was described by Groves (1993) from the Yilgarn Block, Western Australia.

- Y shows low concentration, although the biotite-garnetiferous formation is relatively enriched in this element.

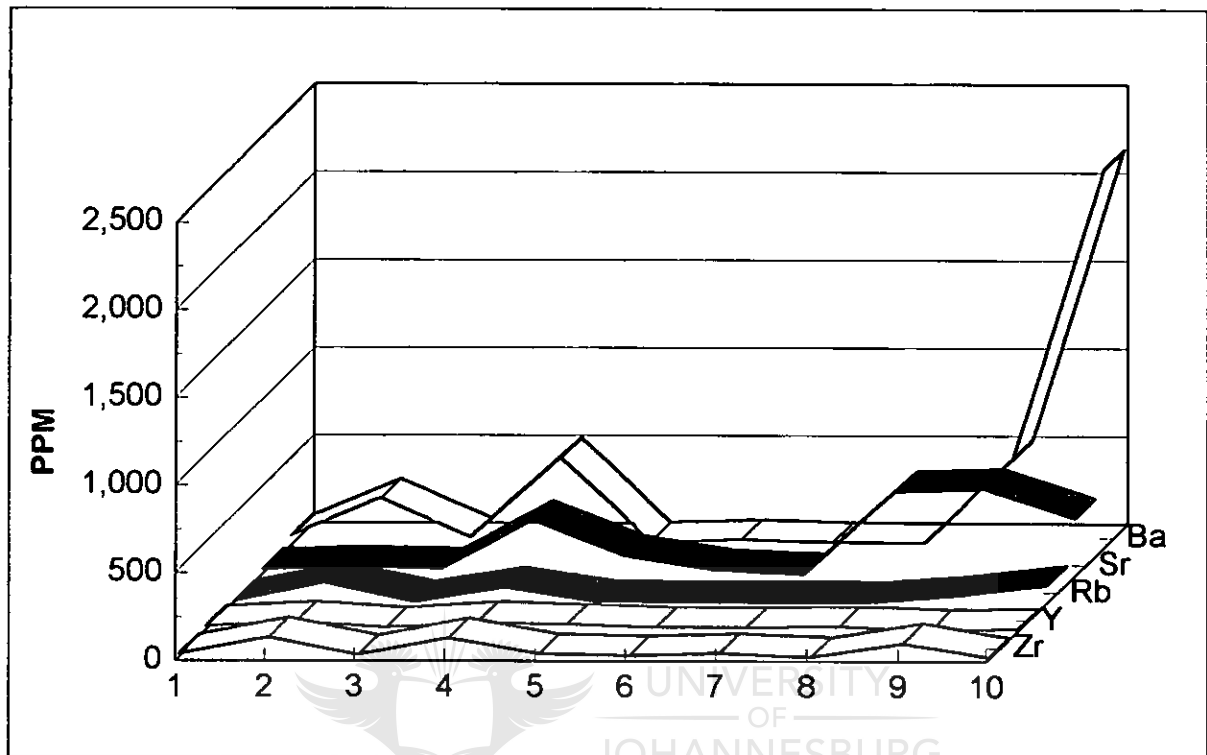
- Rb is weakly enriched in the biotite-garnetiferous formation (hosted probably by the biotite lattice) and in the felsic granulite (hosted probably by potassic feldspar). A weak Rb enrichment is shown by the pink vein (100ppm) in comparison with the parental Baviaanskloof Gneiss (49ppm).

- Surprisingly, Sr shows no enrichment in the biotite-garnetiferous formation but is relatively enriched in the felsic granulite (312ppm, occurring mainly in the metasomatic potassic feldspar). Sr is also enriched in the calcite vein (479ppm) where it replaces Ca orbital positions in the calcite lattice, in the Baviaanskloof Gneiss (612ppm) and the pinkish vein (326ppm) where it replaces K in microcline-perthite.

- Ba, a clear indicator of hydrothermal activity, is concentrated in the biotite-garnetiferous formation (279ppm), in the felsic granulite (533ppm), in the Baviaanskloof Gneiss (499ppm) and shows an extreme enrichment in the pink vein. In other



words, all the lithologies affected by hydrothermal or metasomatic alteration display Ba enrichment.

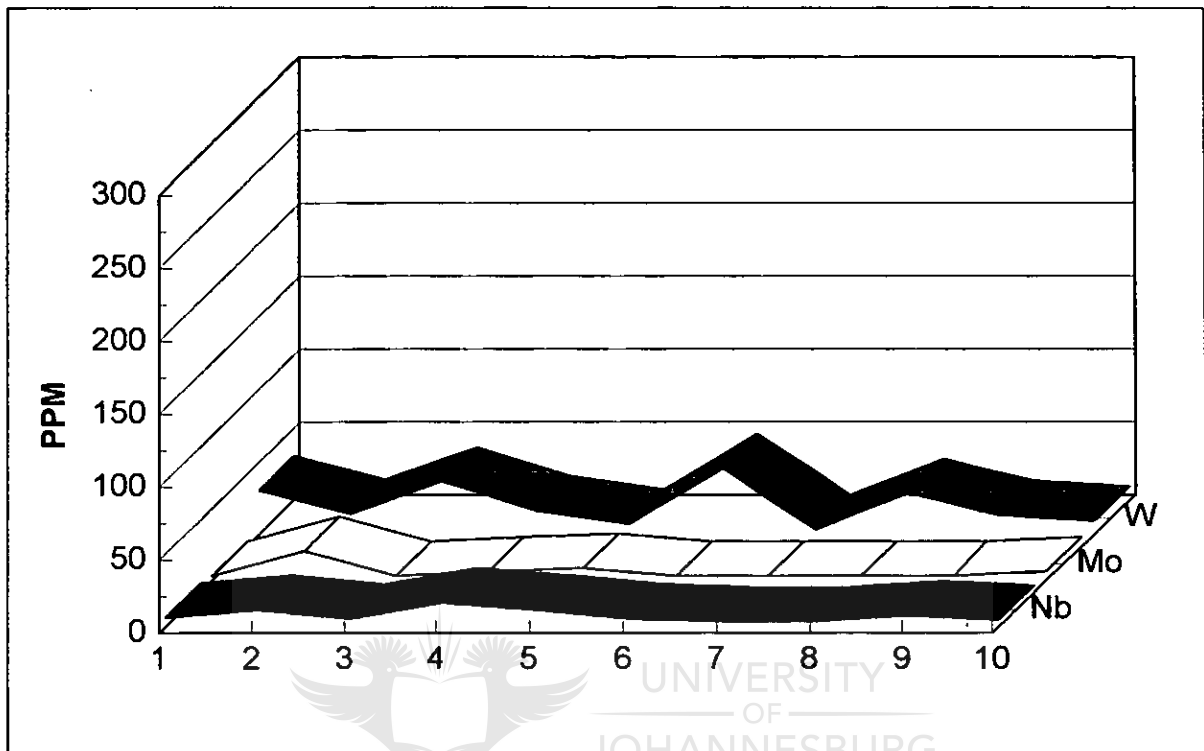


**Figure 12.6:** Geochemical variation of lithophile elements in Doornhoek lithologies. See text for details.

Fig 12.7 shows the distribution of Nb, Mo and W in the lithologies of the Doornhoek deposit. All these elements display concentrations lower than 50ppm.

- Nb shows a small kick in the biotite-garnetiferous formation and in the felsic granulite.
- Mo shows a weak enrichment (21ppm) in the biotite-garnetiferous formation.
- W is surprisingly enriched in the BIF (up to 46ppm) and also shows a small kick in the calcite vein (W in very limited amounts can replace Ca). The relative enrichment of W in

BIF is not common and might be explained by the preference of W for the wall-rock alteration rather than for the proper metasomatic or hydrothermal alteration.



**Figure 12.7:** Geochemical variation of Nb, Mo and W in Doornhoek lithologies. A weak increase in Mo content in the biotite-garnetiferous formation and the strange enrichment of W in the BIF is apparent.

Fig. 12.8 shows the distribution of the mafic/ultramafic elements (Ni, Co, Cr and V) in the Doornhoek lithologies.

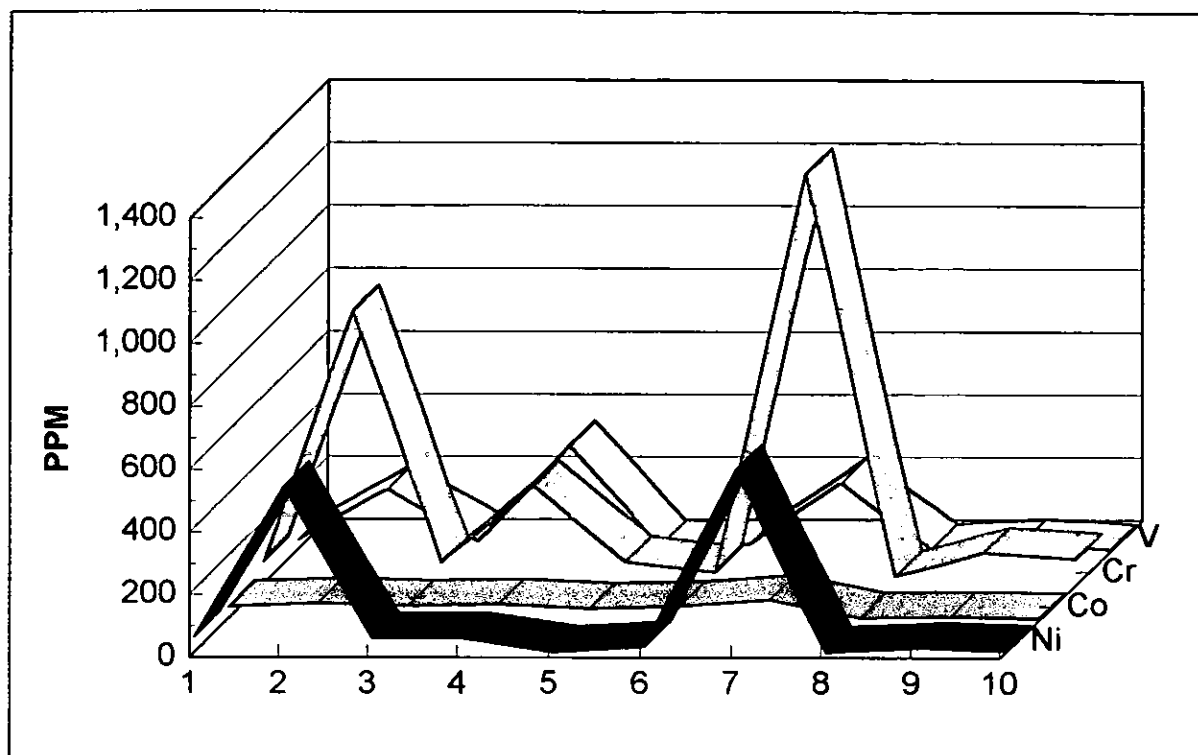
- Ni displays two kicks, one in the biotite-garnetiferous formation (531ppm) and one in the ultramafic granulite (676ppm). The biotite-garnetiferous formation shows an anomalous Ni-content due to the Ni mineralisation hosted by the prograde garnet porphyroblast (gersdorffite, skutterudite, niccolite). The high Ni-content of the ultramafic

granulite is due to the presence of initial olivine, that prior to retrogression hosted Ni in its lattice.

- The highest Co-content is in the ultramafic granulite (61ppm), a relatively low concentration.

- Cr is relatively enriched in the biotite-garnetiferous formation (up to 872ppm), in the ultramafic granulite (1312ppm) and, surprisingly also, in the felsic granulite (313ppm). Cr in the biotite-garnetiferous formation is probably hosted by the lattice of the prograde garnet porphyroblast (the uwarovite component of the garnet). The Cr-content of the felsic granulite is a surprise and raises questions about the origin of this rock prior to the intense metasomatic alteration.

- V follows the Cr trend, showing anomalous values in the biotite-garnetiferous formation (193ppm), in the ultramafic granulite (212ppm) and, surprisingly again also in the felsic granulite (345ppm). The felsic granulite recorded the highest V value of all the Doornhoek lithologies. This again raises questions about the nature of the precursor of the "felsic granulite".



**Figure 12.8:** Geochemical variation of Ni, Co, Cr and V in Doornhoek lithologies. A major surprise is the high concentration of Cr and V in the felsic granulite, raising question about the real nature of this lithological type.

### 12.5 CONCLUSION

The geochemical characteristics of the lithologies present in the Doornhoek area can be summarised as follows:

- i) The proton microprobe analyses emphasised the prograde growth pattern displayed by the euhedral garnet porphyroblast from the biotite-garnetiferous formation. This garnet displays an anomalous increase in Zn, Ge, As, Y, Zr and Ni from the core of the garnet to the mineralised inner-ring. This suggests that the growth of the mineralised inner ring corresponded in time with the maximum mineralising activity in the Doornhoek

hydrothermal/metasomatic system. The unmineralised rim of the garnet probably crystallised at temperatures too high for mineralisation to occur. *The presence of up to 34.5ppm Au trapped in the mineralised inner ring of the garnet porphyroblast emphasises the epigenetic nature of the gold mineralisation, as well as the preference of gold for the metasomatic biotite-garnetiferous formation.*

ii) The REE study showed anomalous enrichment of Th<sup>232</sup> and U<sup>238</sup> in the metasomatic garnetiferous formation. The highly channelised altered lithologies have been enriched in light REE, such as La, Ce and Pr. It appears that this newly formed metasomatic formation acted as a trash-can for all the geochemical elements present in the Doornhoek mineralising system at the time of the mineralisation event. *This suggests that the biotite-garnetiferous formation represents a healed shear zone that acted as a channelway for the mineralising fluids.*

iii) The major elements study demonstrated that the newly formed metasomatic lithologies that acted as hosts for the mineralisation were highly enriched in Al<sub>2</sub>O<sub>3</sub> (14 times!), K<sub>2</sub>O, SiO<sub>2</sub> and TiO<sub>2</sub>. The depletion in CaO (greenstone belts terranes are often characterised by high secondary concentrations of carbonates) demonstrates that Au deposition took place at much higher temperatures at Doornhoek. *This data supports the suggestion that the highly metasomatised and hydrothermally altered lithologies (the biotite-garnetiferous formation and mineralised quartz veins) represent healed shear zones that were active during the M<sub>3</sub> regional metamorphic event. It is possible that the same fluids, at high crustal levels, were responsible for gold mineralisation and associated alteration in the adjacent Sutherland greenstone belt (fig. 4.13).*

iv) The trace elements show anomalous concentrations of Cu, As, Zr, Y, Rb, Ni, Cr, V, Ba, Mo and Au in the newly formed lithologies. These trace elements mark the pathway of the highly channelised mineralising solutions. A peculiar observation is the anomalous high concentration of Cr, V and Zr in the felsic granulite. This rock can not be easily classified based on mineralogical observations and the geochemical data also demonstrated its unusual features. From a geochemical point of view this lithology shows both felsic and ultramafic characteristics. The petrographic study suggested that this rock type represented a metapelite. If this was the case, the original sedimentary rock was probably derived from both a granite and a mafic/ultramafic precursor.



Stable isotope analyses were not done on lithologies from the Doornhoek deposit but a general discussion of the results of a whole rock/mineral O-isotope fractionation study from the metasomatised lithologies at Klipbank (Hoernes et al., 1995; Mokgatla, 1995) is summarised. The alteration at Klipbank, although only affecting Baviaanskloof gneiss (the other lithologies not being present) is very similar to that described at Doornhoek. The two localities are also only 2.5 km apart.

The purpose of the oxygen isotope study was to determine *i)* whether the alteration occurred under close or open system conditions and, *ii)* the temperature of alteration based on rock/mineral O-isotope fractionation (Javoy et al., 1970). Unfortunately, only the Baviaanskloof gneiss outcrops at Klipbank but this locality is a good example of the

high-temperature metasomatic process characterised by widespread K-metasomatism of the tonalitic Baviaanskloof gneiss accompanied by the growth of garnet+sillimanite+K-feldspar. The growth of sillimanite parallel to quartz stretching mineral lineations demonstrates the syn-tectonic nature of the alteration. The alteration process is very similar to that described from Doornhoek, but no sillimanite occurs at Doornhoek.

The fluid-rock exchange processes associated with the  $D_2$  shear zones of the Klipbank and Petronella localities investigated by Hoernes et al., (1995) can not be decoupled from the situation in the whole SMZ of the LB. Three aspects were investigated by Hoernes et al., (1995): the reconstruction of peak-temperatures, conditions of retrogression and nature and source of retrograde fluids.

#### 12.6.1 Reconstruction of peak-temperatures

**Fig. 12.9** illustrates the fractionation pattern of a coarse-grained pegmatitic band (the newly formed, metasomatic product at Klipbank). This product is the sensu-lato equivalent of the metasomatic biotite-garnetiferous formation at Doornhoek, the main product of alteration due to interaction between the hot, channelised hydrothermal fluid and wall-rock. Two stage isotopic equilibration characterise the aplitic band:

- firstly, K-feldspar, sillimanite and garnet-cores plot on a straight line, with a slope of 1.35 that corresponds to a temperature of  $890^{\circ}\text{C}$  (Mokgatla, 1995; Hoernes et al., 199).
- secondly, the next stage of isotopic evolution of the aplite is defined by plagioclase, muscovite and garnet outer rim that plot on a line corresponding to a temperature estimate of  $710^{\circ}\text{C}$  (Mokgatla, 1995).

- quartz and biotite continued to exchange oxygen to even lower temperature (530°C) (Mokgatla, 1995).

The high temperature estimates (890-710°C) suggests a very hot K-metasomatism alteration process (Mokgatla, 1995; Hoernes et al., 1995) and a magmatic origin of the pegmatite, that in return could represent the source of the potassium enrichment of altered rocks. On the other hand, this temperature could also represent the peak conditions of granulite-facies metamorphism. This second scenario agrees with Stevens and van Reenen (1992), who deduced a maximum temperature of 850°C from fluid-absent melting reactions preserved in selvages to leucosomes at the Bandelierkop Quarry in the granulite zone. In case this temperature range (around 850°C) really represents the regional heating during granulite metamorphism, traces of such an event should be preserved.





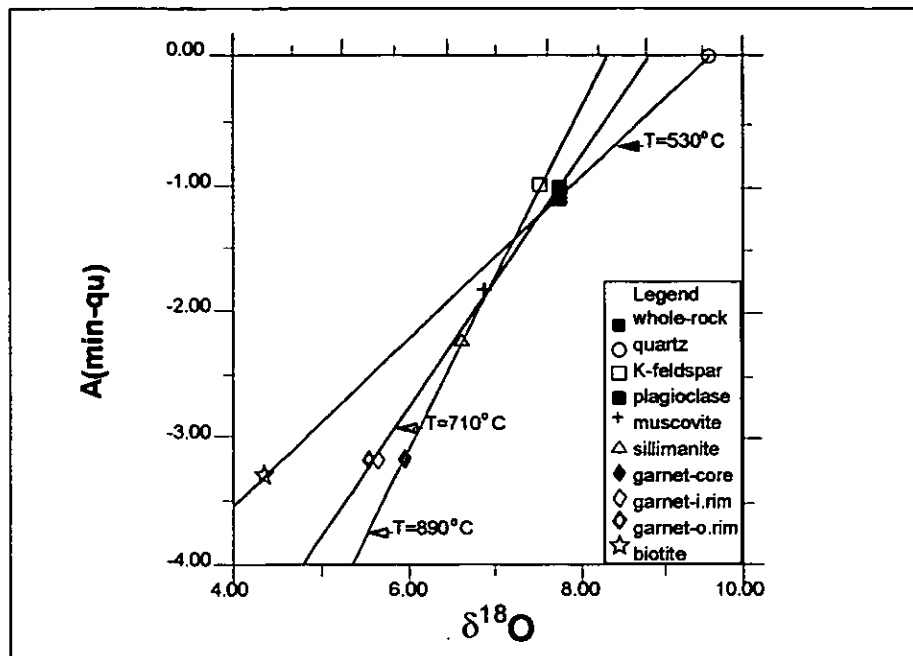


Figure 12.9: FCD graphical representation for isotopic equilibria in a sample of metasomatic aplitic band. The O-isotope fractionation is defined by garnet-core, sillimanite and K-feldspar and represents the peak-temperature of alteration of 890°C, under closed-system conditions (from Mokgatha, 1995).

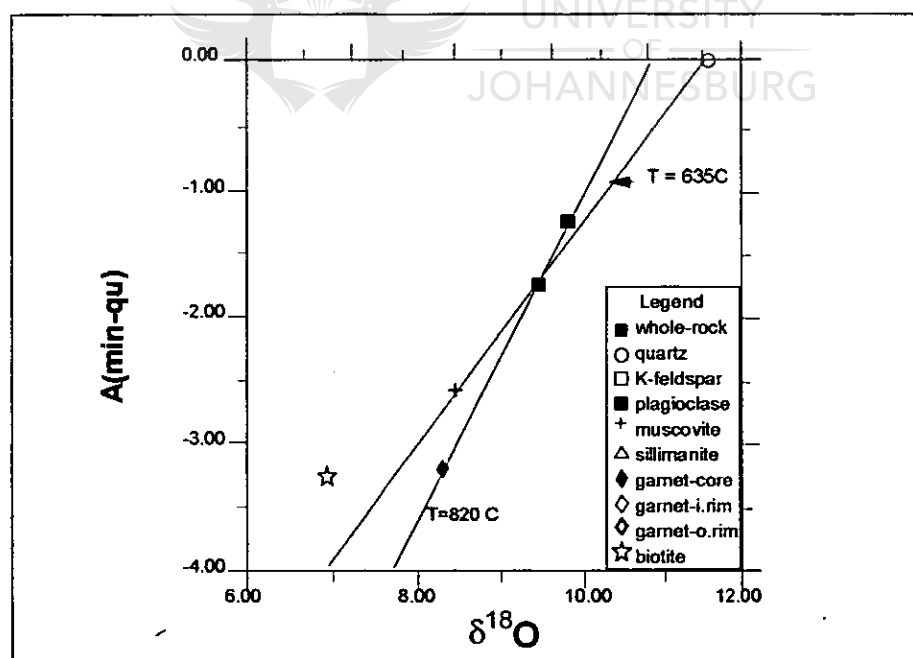
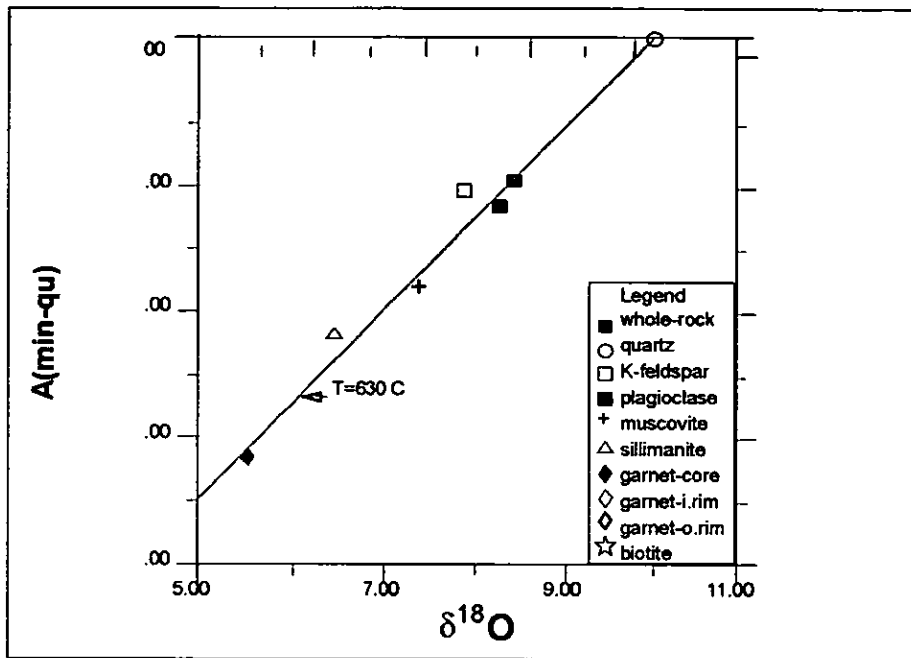


Figure 12.10: FCD diagram of metapelites from the SMZ derived from whole-rock/garnet fractionations. Data from Vennemann and Smith (1992). Example of near-peak temperature of 820°C defined by plagioclase, whole rock and garnet. Orthoamphibole, whole rock and quartz define a secondary linear array with a flatter slope corresponding to the formation temperature of orthoamphibole (635°C). The modal content of anthophyllite is 40% (from Hoernes et al., 1995).

### 12.6.2 Conditions of retrogression

Both quartz-garnet and quartz-ortho-amphibole O-isotope temperatures range between 700<sup>o</sup> and 750<sup>o</sup>C, suggesting therefore the formation of anthophyllite at near-peak conditions (Vennemann and Smith, 1992). This suggestion differs from the petrological calculations of van Reenen (1986) and Baker et al., (1992) which indicated temperatures not higher than 620<sup>o</sup>C for the orthoamphibole formation.

The question is how samples from shear zones would compare with samples from the rest of the SMZ in terms of O-isotope fractionation. It is considered that samples from shear zones (high fluid:rock ratio) should promote isotope re-equilibration, whereas samples provided from rocks blocked at different temperatures during closed-system cooling, should display a more diffuse fractionation pattern. In **fig. 12.11** a sample of strongly metasomatically altered gneiss from Klipbank is shown (Hoernes et al., 1995). With the exception of K-feldspar, all phases in this figure plot reasonable close to a straight line, the slope of which represents a temperature of 630<sup>o</sup>C, for the process of O-isotope equilibration. Since garnet closes to diffuse exchange at much higher temperatures, it can be concluded that this sample documents the influx of a new pulse of fluid at this temperature. This is in sharp contrast with the pattern preserved in a sample of pegmatite from the same Klipbank locality, exhibited in **fig. 12.9**. This sample is characterised by a continuous adjustment of mineral fractionations to lower temperatures, indicating O-isotope exchange in a close system. This means the pegmatite did not interact with an external fluid after its crystallisation.



**Figure 12.11:** FCD diagram of a metasomatically altered gneiss from Klipbank. Although the equilibrium is not so well defined, the fractionation pattern is remarkably different, in that it shows a tendency to equilibrate at lower temperatures. This is caused by infiltration of a new fluid. Note the correspondence of this temperature to that of orthoamphibole formation (fig. 12.10) (from Hoernes et al., 1995).

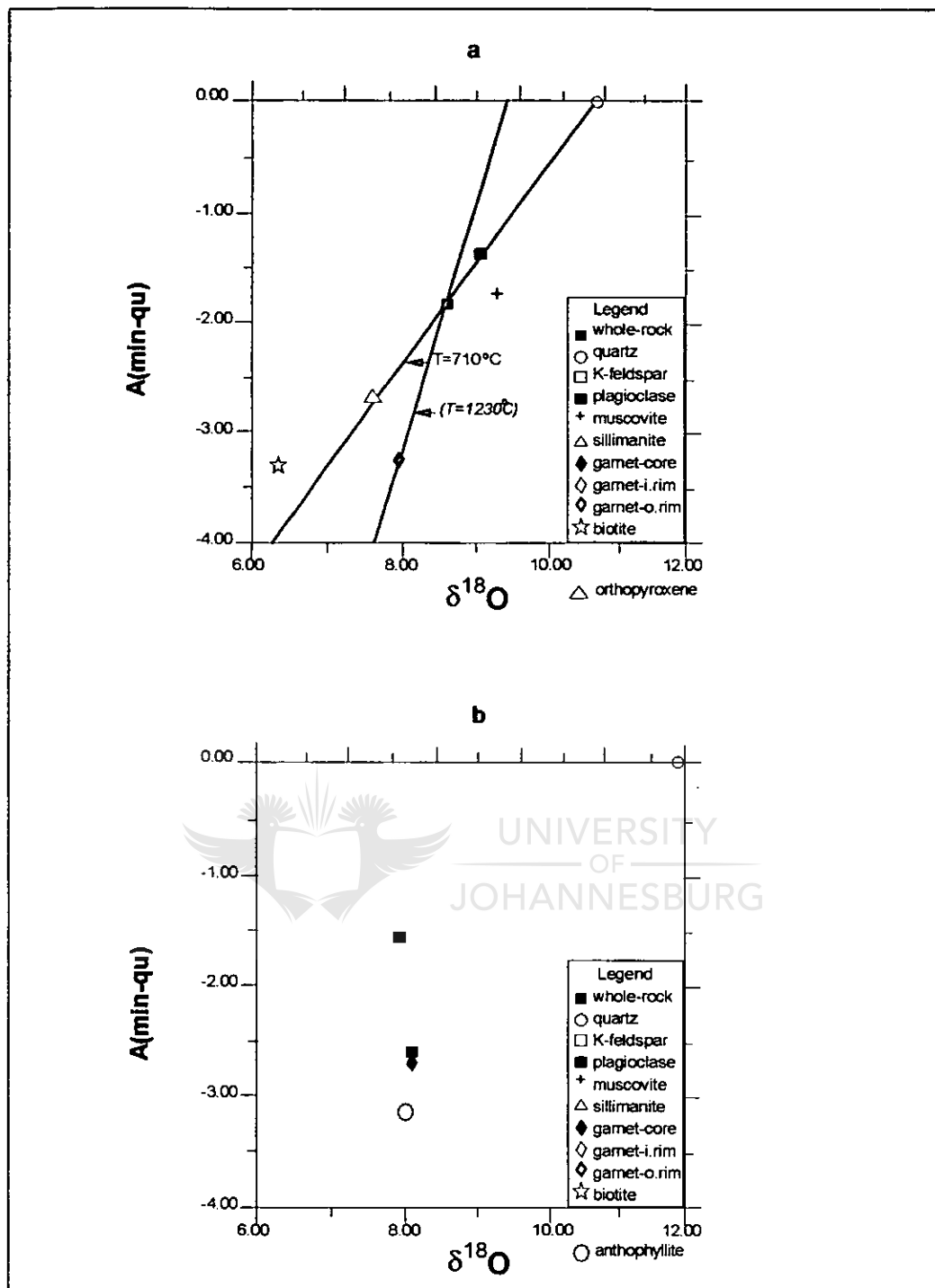
It is clear from **fig. 12.10** that although amphibole is not in isotopic equilibrium with garnet, the fractionation pattern still reflects closed system behaviour. The two linear arrays are balanced by the point which represents the whole-rock composition. In this sample, orthoamphibole, whole-rock and quartz plot on a straight line which indicates a temperature of 635°C, again suggesting formation of the retrograde phase orthoamphibole at this temperature (Hoernes et al., 1995). These examples confirm that within the shear zones both closed system conditions (**fig. 12.9**) and open system conditions (**fig. 12.12**) prevailed. The same is true for samples from outside the shear zone (Hoernes et al., 1995). And indeed, using the data of Vennemann and Smith (1992), it can be shown that whole-rock/garnet fractionations in metapelites indicate near-peak temperatures between 800° and 870°C (**fig. 12.10**), this indicating closed systems behaviour outside the shear zones. Hoernes and van

Reenen (1992), using O-isotope whole-rock data, also demonstrated that the amounts of fluid necessary to rehydrate a dry granulite-facies paragenesis is very small, and, if the invading fluid is not drastically different from the equilibrium fluid, the influx might be undetected.

**Fig. 12.12** represent samples from outside shear zones, but with obvious indications of fluid influx (**a** is a metapelite and **b** a mafic rock). The orthopyroxene-bearing metapelite (**fig. 12.12a**) displays evidence of partial re-equilibration at 670°C, although garnet apparently preserves isotopic reminiscence from an earlier higher temperature stage (Hoernes et al., 1995). If a temperature is calculated from the whole-rock/garnet fractionation as previously discussed, an unrealistically high value results ( $T > 1200^{\circ}\text{C}$ ). This indicates that one of the conditions of this model, i.e. closed system, has not been met (Hoernes et al., 1995). The partial equilibrium between quartz, plagioclase, whole-rock and orthopyroxene defined by the linear array of these phases can only be explained by equilibration with a new fluid. This is also in excellent agreement with the petrological data of van Reenen and Holister (1988) and Baker et al. (1992).

Even stronger proof for open system conditions is illustrated by the fractionation patterns of a mafic sample (**fig. 12.12b**). The nearly vertical alignment of most phases in this rock indicates that fluids were present during a long period of cooling.

Therefore, isotopic data suggest evidence for open and closed system behaviour *inside* and *outside* shear zones.



**Figure 12.12:** FCD diagrams representative for open-system conditions outside shear zones, proving the fluid-influx model of the SMZ. Data from Vennemann and Smith (1992).  
**a.** The linear array defined by quartz, plagioclase, whole rock and orthopyroxene corresponds to a temperature of 670°C - at which new fluid entered the system. Garnet represented a closed system at the time of fluid infiltration, yielding thus to an extremely small whole-rock/garnet fractionation.  
**b.** Vertical alignment of plagioclase, whole-rock, clinopyroxene and orthoamphibole can only be reached by interaction with fluid during a larger temperature interval (open system) (from Hoernes et al., 1995).

### 12.6.3 Nature and source of retrograde fluids

The source of fluids involved in the retrogression and metasomatic alteration of the granulite facies rocks of the SMZ of the LB remains an unsolved problem. Fluid inclusions studies (van Reenen and Hollister, 1988; van Reenen et al., 1993; Du Toit, 1994; Mokgatlha, 1995) documented the dominance of CO<sub>2</sub> in fluids entrapped in quartz in hydrated granulites outside shear zones, as well as in metasomatically altered rocks within shear zones. Baker et al., (1992) calculated water activities of between 0.6 and 0.1 for the hydrating fluids, but postulate the presence of additional gas species besides CO<sub>2</sub> and H<sub>2</sub>O. Hollister (1992) discussed the following three possible sources for the retrograde fluids:

i) the upper mantle, or mantle derived melts underplated to the lower crust (van Schalkwyk and van Reenen, 1992)

ii) anatectic melts that originated within the Limpopo Belt (Vennemann and Smith, 1992)

iii) the emplacement of hot granulite-facies rocks of the SMZ over the cooler low-grade greenschist facies rocks of the KVC. This process caused devolatilisation of the underlying rocks and hydration of the overlying granulites (van Reenen and Hollister, 1988). Since the first two sources are magmatic and the third is dominated by magmatic rocks, the O-isotope signature of the derived fluids will be more or less similar, meaning that the O-isotope data will not be able to define the ultimate source of the fluids. Hoernes et al., (1995), using isotopic data from two shear zone samples and two metapelitic samples from the SMZ with the partial equilibrium temperatures, succeeded to estimate the isotopic composition of the coexisting fluid as follows:

- pegmatite at Klipbank: 820°C  $\delta^{18}$  water = 8.5%
- pegmatite at Klipbank: 630°C  $\delta^{18}$  water = 7.6%
- metapelite: 670°C  $\delta^{18}$  water = 9.4%
- metapelite: 630°C  $\delta^{18}$  water = 10.1%

Not surprisingly, this points to a magmatic component in the shear zones and to a slightly more enriched magmatic-metamorphic fluid in the metapelites. The origin of the fluids can probably be solved using He-isotopes, as recently successfully demonstrated by Dunai (1994) in India for the Niligiri granulites (Hoernes et al., 1995).

In fig. 12.13 one can see the variation of the  $\delta^{18}$ O in Klipbank lithologies that underwent various alteration intensities. The higher the alteration, the higher the  $\delta^{18}$ O, although the trend is not very clear (Mokgatla, 1995). Furthermore, the whole rock O-isotope data at Klipbank is characterised by positive  $^{18}\text{O}/^{16}\text{O}$  ratios (Mokgatla, 1995).

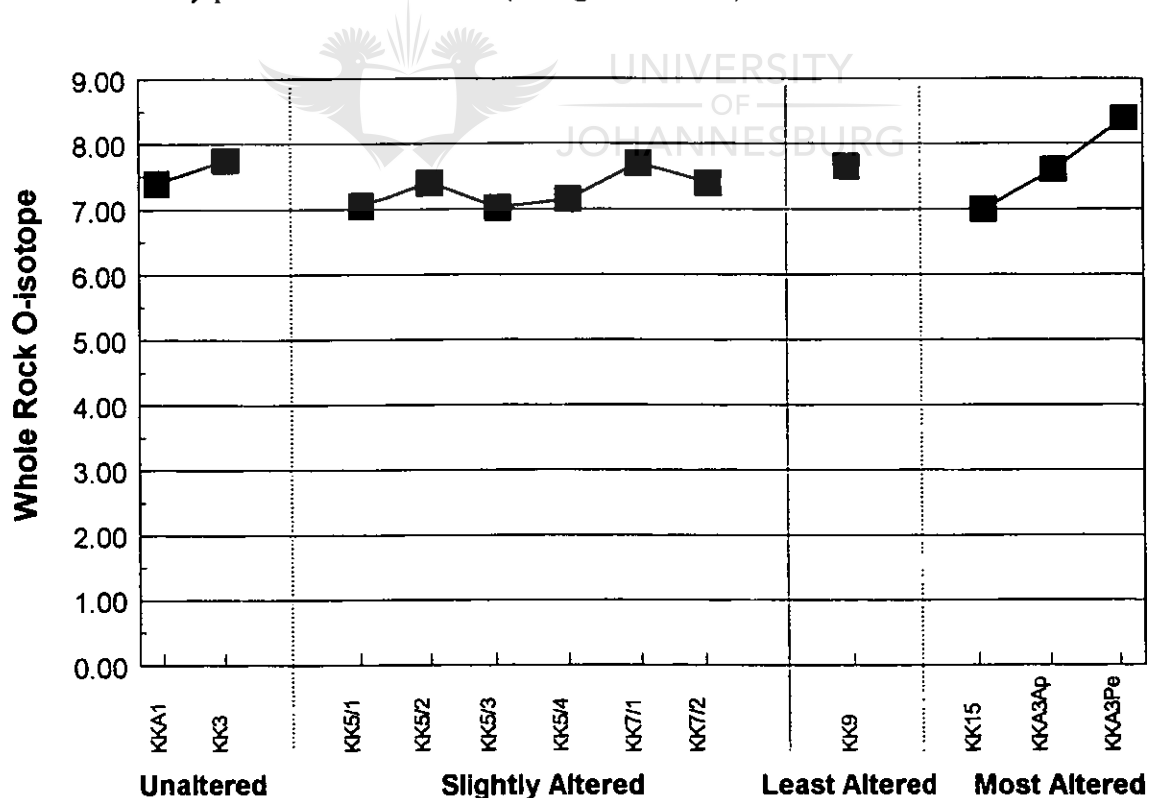


Figure 12.13: Whole rock O-isotopic (per mil) compositional changes plotted against increasing alteration (from Mokgatla, 1995). One can see a very weak increase of the  $^{18}\text{O}$  with the increasing of the alteration intensity, although it is also possible due to the mineral composition of the analysed material.

#### 12.6.4 Conclusion

The O-isotope fractionation patterns discussed by Hoernes et al., (1995) can be used to constrain the peak-temperature conditions to a range of 800<sup>o</sup> to 870<sup>o</sup> C, that agrees with the petrological considerations (Stevens and van Reenen, 1992). The retrogression of the SMZ granulites was probably triggered by the influx of external fluids into an existing north-to-south temperature gradient in the SMZ (Hoernes et al., 1995). Partial O-isotopic equilibria suggests that orthoamphibole formation has occurred at temperatures close to 600<sup>o</sup>C, whereas at higher temperatures the granulite-facies paragenesis (orthopyroxene and garnet) remained stable.

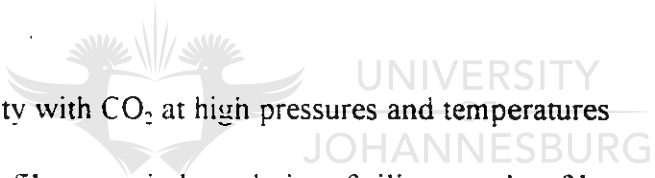
The quantity of fluids that penetrated the granulite terrane depended on the rock porosity. Along shear zones, fluid flux was, in part, accompanied by complete re-equilibration, whereas in most rocks outside the shear only partial re-equilibration was reached. Fluid/rock ratios in metapelites outside the shear zones were very small, often resulting in fractionation patterns typical for closed-system exchange. Open-system conditions were demonstrated in specific cases in metapelites and especially in the mafic rocks, based on fractionation patterns. The source of the retrograde fluids still remains an unsolved problem.

#### 12.6.5. Concentrated brines as high-grade metamorphic fluids

The newly described role of concentrated brines as high-grade metamorphic fluids (Newton et al., 1996) deserves some consideration here. Usually discarded by earth scientists, concentrated aqueous salt inclusions have been identified in a great diversity of igneous and

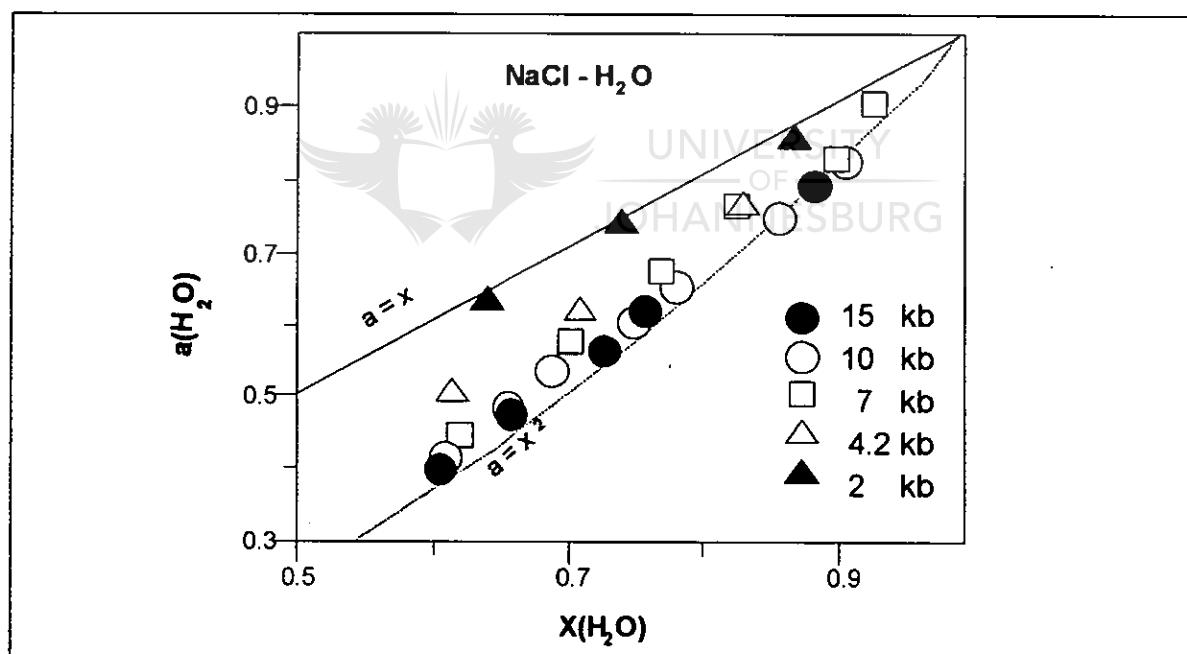


metamorphic settings (Newton et al., 1996). Hypersaline fluids are now believed to have played a major role in the evolution of alkaline volcanic rocks (Lowenstern, 1994), carbonatites (Samson et al., 1995), several gabbroic rocks (Pasteris et al., 1995), Alpine eclogites (Philippot and Silverstone, 1991) and the super high-pressure coesite-bearing metasediments (Philippot et al., 1995). Aranovich et al., (1987) suggested that concentrated brines as high-grade metamorphic fluids were able to satisfy the requirement of low-H<sub>2</sub>O activity combined with alkali mobility. Some recent studies (Newton et al., 1996) of brine-rock interactions at high temperatures and pressures demonstrate additional properties of concentrated NaCl solutions which support renewed consideration of such fluids as important agencies in the evolution of continental crust. These properties include (Newton et al., 1996):

- 
1. Immiscibility with CO<sub>2</sub> at high pressures and temperatures
  2. Ability to infiltrate grain boundaries of silicate rocks of low permeability, in contrast to dense CO<sub>2</sub>.
  3. Low H<sub>2</sub>O activity in concentrated brines at pressures above 5kbar, by virtue of pressure-induced ionic dissociation of NaCl.
  4. High affinity of Rb relative to biotite and K-feldspar, in contrast to granitic melts.

Thermodynamics-based reconstructions of the NaCl-H<sub>2</sub>O-CO<sub>2</sub> system (Bowers and Helgeson, 1983; Duan et al., 1995) show that concentrated brines with small CO<sub>2</sub>-content coexist stably with a nearly pure CO<sub>2</sub> phase at temperatures in the deep-crustal T and P range (500°-900° and pressures from 2 to 10kbar).

Although infrequently reported, brine solutions in granulites are increasingly recognised (Rollinson and Berger, 1995; Touret, 1995; Smit and van Reenen, 1997), and fluid immiscibility is generally accepted and cited as a basis for apparently coeval suites of hypersaline and  $\text{CO}_2$  inclusions in granulites (Crawford and Hollister, 1986; Touret, 1985). The much more abundant  $\text{CO}_2$  inclusions in granulites, reported by many authors, may result from greater propensity for capture in silicate minerals. Watson and Brenan (1987) showed experimentally that disseminated pure  $\text{CO}_2$  at elevated T and P forms high angle ( $>60^\circ$ ) contact angles in quartz aggregates and hence has low infiltration ability and greater tendency to be captured in secondary arrays along healed fractures.



**Figure 12.14:** At pressures above 3-4 kbar, the  $\text{H}_2\text{O}$  activity drops precipitously from values nearly equal to the  $\text{H}_2\text{O}$  mole fractions, to activities near the squares of the mole fractions in the deep-crustal pressure range. Thus, concentrated brines may have low enough  $\text{H}_2\text{O}$  activities (0.2-0.4) under deep-crustal conditions to coexist with the assemblage *orthopyroxene+K-feldspar* in charnockites, and that the low  $\text{H}_2\text{O}$  activities in such brines protect the rocks against melting even at temperatures  $>750^\circ\text{C}$  (from Newton *et al.*, 1996).

Water, in contrast, generally forms lower contact angles, and concentrated salt solutions have extraordinary wetting ability. Watson and Brenan (1987) stated that brines would have a very low tendency to be captured as fluid inclusions in the high-grade metamorphic regime; this property quite plausibly accounts for their rarity in granulites relative to CO<sub>2</sub>-rich inclusions. The importance of brines in high-grade metamorphism is therefore likely to have been underestimated from the fluid inclusion evidence. Aranovich and Newton (1995) have measured H<sub>2</sub>O activities in concentrated NaCl solutions at deep crustal temperatures and pressures by depression of the brucite dehydration equilibrium. Their results is shown in **fig. 12.14**.

Within the pressures range 4 to 15 kbar, the H<sub>2</sub>O activity drops precipitously from values nearly equal to the H<sub>2</sub>O mole fractions, to activities near the squares of the mole fractions in the deep-crustal pressure range (**fig. 12.14**). This behaviour is almost independent of temperature in the range 600°-900°C and is undoubtedly the result of pressure-induced ionic dissociation of NaCl as fluid densities approach those of condensed liquids. Predictable consequences are that concentrated brines may have low enough H<sub>2</sub>O activities (0.2-0.4) under deep-crustal conditions to coexist with the assemblage orthopyroxene plus K-feldspar in quartzo-feldspathic rocks, and that the low H<sub>2</sub>O activities in such brines protect the rocks against melting even at temperatures >750°C, although hyperfusible components (such as F) may provoke limited anatexis (Newton et al., 1996).

An important consideration for granulite fluids is significant solubility of silica with high alkali mobility. It is likely that quartz is substantially more soluble in alkaline aqueous solutions than in nearly pure CO<sub>2</sub>. The K-feldspar veining phenomenon in charnockites is

understood by simple exchange of  $K^+$  for  $Na^+$  in plagioclase, with the other major components being inert. A concentrated brine could most plausibly provide the observed high alkali mobility, as well as the high volatile mobilities. Thus, dehydration reactions and consequently the widespread LILE depletion in Precambrian granulite terranes would be favoured by elevated pressure in middle- to high-grade rocks in the presence of saline pore solutions. If Rb, U and Th extraction is accompanied by upward migrating brines during deep-crustal metamorphism, the fluids must have been fairly voluminous and pervasive and really extensive sources must be supposed (Newton et al., 1996). Several possible sources of brines for deep crustal metamorphism may be imagined, including connate waters in metasediments, meta-evaporite deposits and exhalations from deep-crustal mafic intrusions (Newton et al., 1996). The first possibility may be discounted because there are many Precambrian terranes with limited occurrences of metasediments. For the second possibility, to our knowledge, metamorphosed halite deposits are never found in granulite facies terrane. Mechanical buoyancy and high solubilities of salt beds prevent evaporites from reaching the deep crustal milieu. Regarding the third possibility, it seems the most reasonable (Newton et al., 1996) considering that some basaltic magmas, notably the alkalic suite, are inferred to be very rich in volatiles, alkalis and halogens (Bailey, 1980).

### 13. RELATIONSHIP BETWEEN DEEP CRUSTAL DEFORMATION AND FLUID ACTIVITY AT THE DOORNHOEK DEPOSIT: A THEORETICAL MODEL

As previously stated the Doornhoek Gold Deposit, with its unusual "interlayering" of lithologies that respectively display prograde and retrograde pattern characteristics is located on a shear zone. The texturally interlayered BIF, mafic, felsic and ultramafic granulite reacted as a trash-can for the mineralised fluids, because of its geochemical and rheological features which contrast drastically with that of the surrounding tonalitic gneiss.

Large volumes of fluids, channelised along shear zones through hydraulic micro-pumping were responsible for the in-situ formation of the mineralised metasomatic biotite-garnetiferous formation from the already retrogressed BIF and mafic lithologies, just after peak-metamorphic conditions. The deformation process was very ductile, a fact that almost eliminates friction as a source for heating during the shearing. Large volumes of arsenides, sulphides, oxides, quartz and gold were deposited in the shear zone as a result of this process. The horizons characterised by magnetite and pyrrhotite crosscutting the country rock are always orientated parallel to the shearing direction and represent an excellent testimony for the epigenetic source of the gold-related mineralisation. On a microscopic scale the development of kink-bands in orthopyroxene and clinopyroxene as a result of the shearing is a prominent feature in some of the lithologies (**fig. 13.1 and 13.2**).

In order to develop a model for the highly channelised high-temperature alteration/mineralisation at Doornhoek several observations need to be explained:

- i)* the fact that alteration/mineralisation occurred near granulite facies conditions
- ii)* close relationship between gold-related mineralisation and the formation of biotite-garnetiferous formation
- iii)* evidence for localised heat transfer (prograde growth of garnet porphyroblasts), and
- iv)* high fluid:rock ratio as demonstrated by the quartz vein system

In the upper crust, generally a cool and brittle environment, fluid-filled cracks might extend to depths of 3 km (for indurated sediments), or down to 15 km (for crystalline rocks) (Thompson and Connolly, 1992). The upper crustal fluid pressure is hydrostatic in nature with  $P_{\text{fluid}}$  approx.  $1/3$  of  $P_{\text{rock}}$  (**fig. 13.3**).

By contrast, in the lower crust, the rheologic response is plastic, at least at geological strain-rates (Sibson, 1983; Kirby, 1984; Kirby, 1985; Thompson and Connolly, 1992). It is assumed at such depths the crustal porosity is not connected and the fluid pressure is similar to the lithostatic pressure, thus  $P_{\text{fluid}}$  approx  $P_{\text{rock}}$ .

Deep crustal fluids will flow very slowly and pervasively upwards, occasionally resulting in the formation of lower crustal veins and mineral deposits, and inducing, at the same time, metamorphic thermal anomalies (less than 10 km<sup>2</sup> in surface) (Connolly and Thompson, 1989, 1990, 1991; Fyfe et al., 1978; Kerrich, 1986; Kerrich and Feng, 1992). Thus, there are two distinct hydrothermal regimes in the lower crust: *i)* a low-permeability porous flow, *ii)* a high-permeability channelised-focussed flow and *iii)* the still relatively unknown transitional process connecting the two regimes.

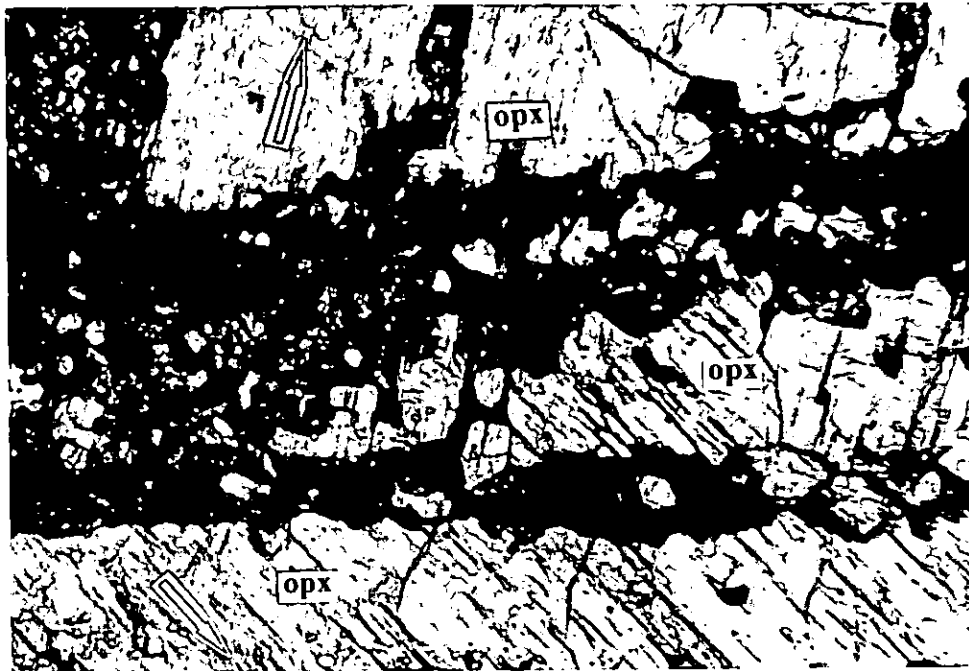


Figure 13.1: Large orthopyroxene crystal (opx) crosscut by epigenetic mineralisation (opaque). Due to the introduction of mineralisation into the Doornhoek system under ductile conditions, the opx underwent kink-band type of deformation (note the angle made by the cleavage direction at the top (red arrow) and bottom (yellow arrow) of the photo. Sample DD-2-2. 1cm=50µm

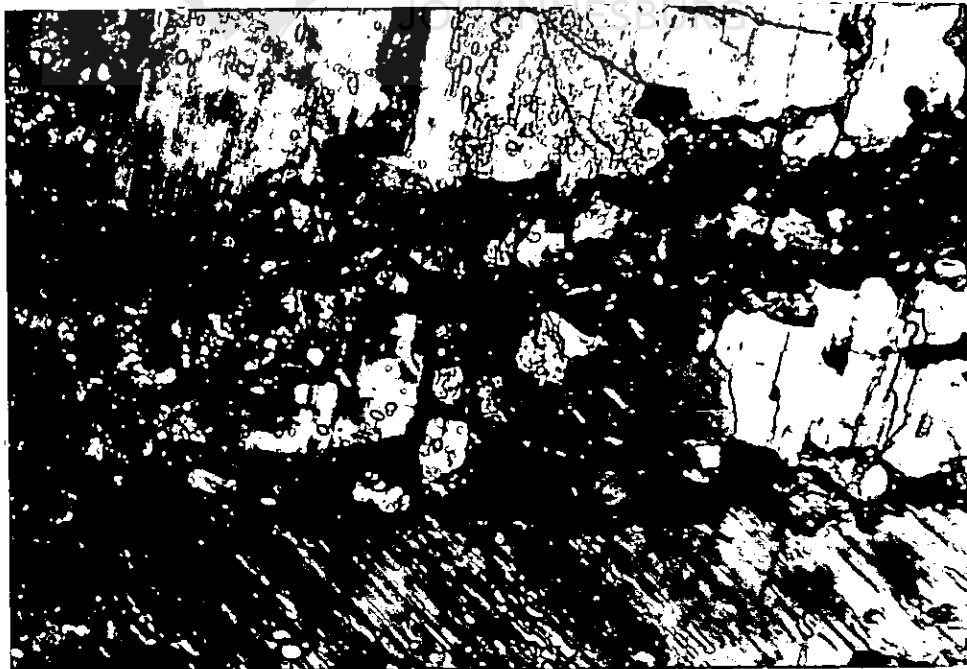
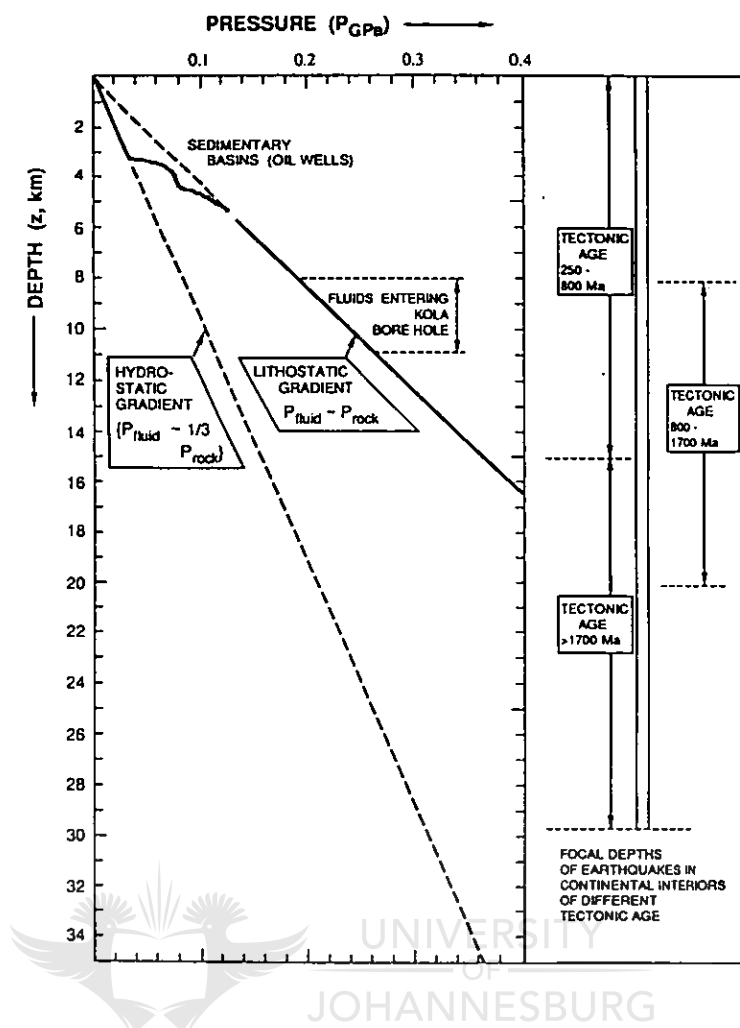


Figure 13.2: As fig. 13.1 but under crossed nicols. The kink-band type of deformation in the opx is better displayed, due to the variation of birefringence colours. Sample DD-2-2. 1cm=50µm



**Figure 13.3:** Pressure-depth relations for litho- and hydro-static gradients. The transition zone observed in oil-wells in sedimentary basins is from Fyfe et al. (1978) and Wood and Walther (1986) for fluids from the deep Kola Borehole from (Kozlovsky, 1987). The focal depth ranges of earthquakes in continental interiors of different tectonic-age is from Chen and Molnar (1983) and show deeper brittle behaviour in older and colder lithosphere (from Colvine et al. 1988).

### 13.1. PERVASIVE CIRCULATION OF FLUIDS (POROUS MEDIA FLOW)

The first step is to establish an order of magnitude for the fluid flux rate ( $q_f$  = the amount of fluid that percolates through a unit of surface during a time unit, measured in  $\text{m}^3\text{m}^{-2}\text{s}^{-1}$ ).

Walther and Orville (1982) calculated the advective behaviour of an average metamorphic fluid released by devolatilisation reactions in the metamorphic pile. A crustal column of



1m<sup>2</sup>x25km which releases 5wt per cent volatiles contains about 72x10<sup>6</sup> kg rock and about 3.6x10<sup>3</sup>m<sup>3</sup> H<sub>2</sub>O. Over 20 Ma the fluid flux rate ( $q_f$ ) it is about 3600 m<sup>3</sup>/20 Ma = 180 m<sup>3</sup>m<sup>-2</sup>s<sup>-1</sup> x 1 Ma (= 5.8 x 10<sup>-12</sup>m<sup>3</sup>m<sup>-2</sup>s<sup>-1</sup>) and over 100 Ma,  $q_f$  is about 36 m<sup>3</sup>m<sup>-2</sup>s<sup>-1</sup> x 1 Ma (aprox. 1.1 x 10<sup>-12</sup> m<sup>3</sup>m<sup>-2</sup>s<sup>-1</sup>) (Thompson and Connolly, 1992). This order of magnitude (10<sup>-11</sup>, 10<sup>-12</sup>m<sup>3</sup>m<sup>-2</sup>s<sup>-1</sup>) for the fluid (dehydration) flux rate ( $q_f$ ) is also accepted by Peacock (1989).

Considering that the fluid-flux rate is directly proportional to the permeability, and thus to the porosity, the next step is to determine the heat-advection during porous-media flow. An easy way is to view the fluid-advected heat as local heat-production compared to the radiogenic heat production - a continuous low and homogeneous long-term heat source in the crust. The amount of advective heat ( $H_a$  measured in Wm<sup>-3</sup>) of metamorphic fluid flow through a pervasive flow is the product of the above defined fluid-flux rate ( $q_f$ , m<sup>3</sup>m<sup>-2</sup>s<sup>-1</sup>), geothermal gradient ( $dT/dz$ , Km<sup>-1</sup>) and fluid heat capacity ( $\rho C_p$ , aprox. 3.5 x 10<sup>6</sup>, Jm<sup>-3</sup>K<sup>-3</sup>, e.g. England and Thompson, 1984, Thompson and Connolly, 1992).

Considering a wide range of thermal gradients (from 10 K/km - Archean shields - to 100K/km - young orogenes/volcanic belts) one can compare the advective heat with the radiogenic heat production from the crustal rocks (0.3 to 2.0  $\mu$ W m<sup>-3</sup>, e.g. England and Thompson, 1984). **Fig. 13.4** shows that only fluid fluxes in excess of 10<sup>-10</sup> m<sup>3</sup>m<sup>-2</sup>s<sup>-1</sup> (with an order or two of magnitude higher than the dehydration fluid-flux rate produced by the regional metamorphic heat supply) are required in order for the heat produced by fluid advection to be notably higher than the production of radiogenic heat. And also the heat regulated by the advected fluid is not particularly dependent on  $dT/dz$ .

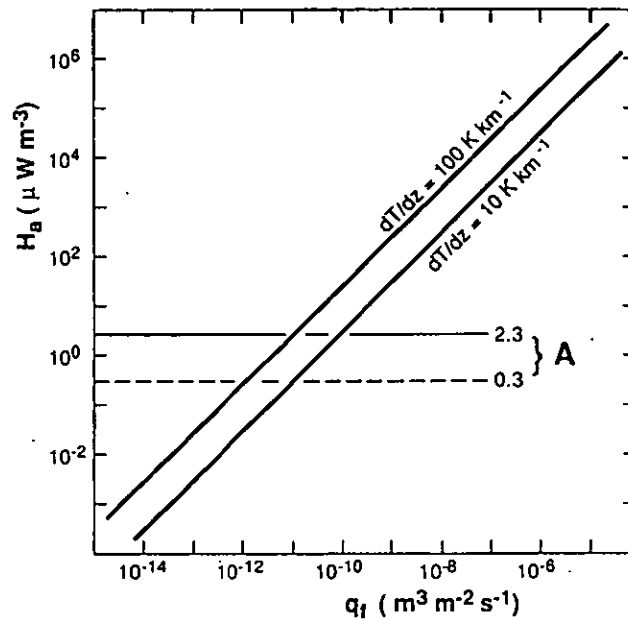


Figure 13.4: Heat production ( $H_a$ ,  $\mu W m^{-3}$ ) from advected fluids for various fluid-flux rates ( $q_f$ ,  $m^3 m^{-2} s^{-1}$ ) for  $\rho C_p = 3.5 \times 10^6 J/m^3$  and  $dT/dz = 10-100^0 K/km$ . Knowing that the radiogenic heat production for the crust ranges between  $0.03$  and  $2.3 \mu W/m^3$ , values of  $q_f$  higher than  $10^{-10} m^3/m^2 s^{-1}$  are required for advective heat production to exceed radiogenic heat production (from Thompson and Conolly, 1992).

Thus, the fluid advection in a possibly porous media in the lower crust will not dramatically increase the temperature of the country rock, unless impressive quantities of fluid can somehow become flow-channelised during a short interval of time (Brady, 1988; Peacock, 1989; Thompson and Connolly, 1992). As Bickle and McKenzie (1987) emphasised, only when fast volumes of fluid flow occur, advection becomes a very efficient process for both heat and mass-transfer (fig. 13.5).

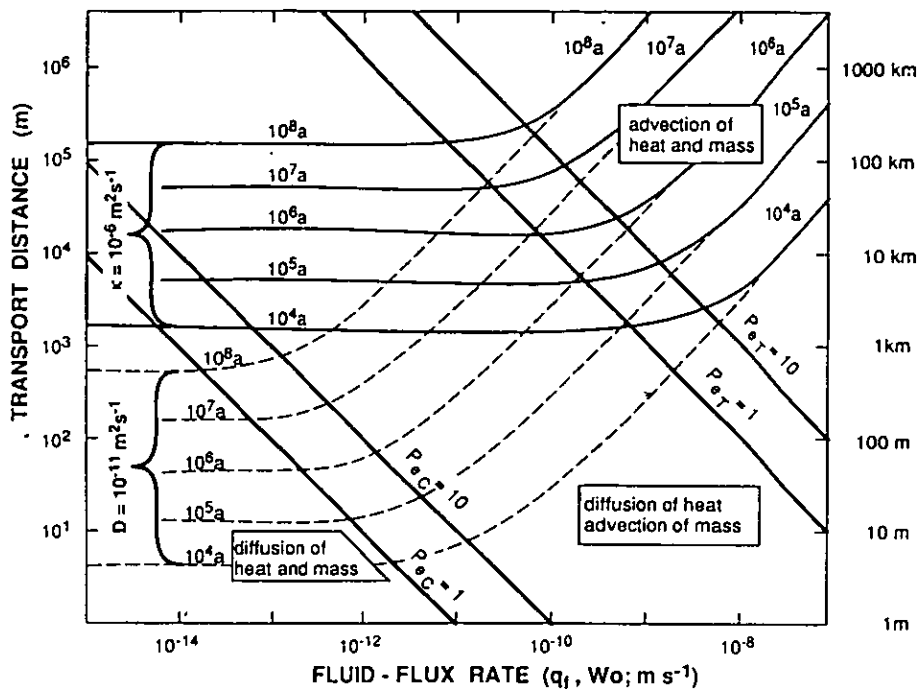


Figure 13.5: Transport distances for heat and mass transfer as a function of fluid-flux rates, for advective events of  $10^4$  a, 1 Ma and  $10^8$  a duration (modified from Bickle and McKenzie, 1987). Simple thermal and chemical Peclet numbers are defined as  $Pe_T = zW_o/k$  and  $Pe_C = zW_o/D$ , where  $z$  is lengthscale (m),  $W_o$  = fluid velocity ( $ms^{-1}$ ),  $k$  is a typical thermal diffusivity ( $10^{-6}m^2s^{-1}$ ), and  $D = 10^{-11}m^2s^{-1}$  is a simple chemical diffusivity ( $10^{-8}m^2$ ) for a porosity of  $10^{-3}$ . Such Peclet numbers are smaller by a factor of  $\pi^2$  (aprox. 10) than those defined by Bickle and McKenzie (1987) (from Thompson and Conolly, 1992).

## 13.2 MASS TRANSPORT

The mass-transport (dissolved material) by advecting fluids requires high fluid-fluxes (**fig. 13.4**), taking into account *i*) the low solubility of the ore minerals, and *ii*) the mineralogical nature of the host (quartz) in aqueous fluids at pressures below 10 kbar (the maximum pressure reached by the Doornhoek gold deposit was 8.21 kbar - see **Chapters 11 and 12**). A good example of the mass-transport regime is shown in **fig. 13.5**, where the relative

importance of diffusion versus advection of heat/mass is clearly illustrated for a wide range of fluid flux rates.

Transport distances are shown for geological time-scales for a mass-diffusivity of  $10^{-8} \text{ m}^2$  and porosity of  $10^{-3}$  (**fig. 13.5**) (Bickle and McKenzie, 1987; Thompson and Connolly, 1992). Knowing that the thermal diffusivity is orders of magnitude greater than mass diffusivity, there is a very large region of fluid-flux rates and length scales, in the middle of **fig. 13.5**, where diffusive mass transfer occurs in the absence of advective thermal perturbations (Thompson and Connolly, 1992).

### 13.3 CHANNELISED CIRCULATION OF FLUIDS (FRACTURE FLOW)

Although the long-term rheological behaviour of the lower crust is ductile, high fluid pressures ( $P_{\text{fluid}} \gg P_{\text{rock}}$ ) in the lower crust can definitely fracture (hydraulic microfracturing) and expel fluids (Spera, 1987; Thompson and Connolly, 1992; Roering et al., 1995 - see the emplacement of mantle-derived magmas). Fractures must be widely spaced in order to produce notable thermal effects (Peacock, 1989; Thompson and Connolly, 1992).

Consider the simplistic case when heat is to be conducted only laterally from the channel. In this case the diffusion distances ( $l$ ,  $m$ ) can be calculated for certain time scales ( $t$ ,  $s$ ) as  $l^2 = kt$  where the thermal diffusivity ( $k$ ,  $\text{m}^2\text{s}^{-1}$ ) is of an order of about  $10^{-6} \text{ m}^2\text{s}^{-1}$ .

*Thus, for a time scale of 1 million years ( $t=10^6$  a), the diffusion distance is  $l=5.6$  m. For a time of 10 million years ( $10^7$  a), the diffusion distance becomes  $l=17800$  m (Thompson and Connolly, 1992). Taking into account that the mineralised quartz veins and the metasomatic biotite-garnetiferous formation at Doornhoek has a maximum thickness of about 350m, the calculated  $\Delta t$  for the formation of the Ore Body at Doornhoek ranges between 1 Ma to 20 Ma.*

The difference in temperature between the core and the rim of the prograde garnet porphyroblast is about 250°C. To produce an increase of temperature above the ambient of at least 250°C, fluids just below the magmatic temperatures are required. Vennemann and Smith (1992), using an impressive amount of isotopic data suggested that temperatures of about 740°C prevailed at the time of hydration for the SMZ of the LB. Hoernes et al., (1995) showed that hydration occurred at about 600<sup>o</sup>-620<sup>o</sup>C, in accordance with petrological data (Baker et al., 1992). The calculated temperatures at Doornhoek showed temperatures of 570<sup>o</sup>-610<sup>o</sup>C at which ore minerals were trapped within the dark inner-ring of the garnet porphyroblast and temperatures of 720<sup>o</sup>-770<sup>o</sup>C for the fluid that formed the unmineralised rim of the garnet porphyroblast (**fig. 10.1** and **Chapter 10**). Only the combination between low H<sub>2</sub>O, high CO<sub>2</sub> and high salinity (brines) of the fluids involved (**Chapter 9**; van Reenen and Hollister, 1988; Newton et al., 1996) and the mainly mafic and BIF composition of the Doornhoek gold deposit prevented partial melting. And even in this case the fluxes of fluids must have been very high ( $10^{-9}$  to  $10^{-10}$  m<sup>3</sup>m<sup>-2</sup>s<sup>-1</sup>) in order to produce an ore deposit of Doornhoek scale.

The fluids were probably channelised along pre-existing shear zones formed since peak-metamorphic conditions during the  $D_2$  regional shear event (Smit and van Reenen, 1997). The system of fluid penetration through shear zones was further accelerated by propagating their own cracks (*hydraulic micropumping*), otherwise they would rapidly equilibrate thermally with the country rock (Knapp and Knight, 1977; Segall, 1984; Nishiyama, 1989; Thompson and Connolly, 1992). Such fluid fluxes can be facilitated by the reactivation of old heterogeneities (old lithological contacts, layers of different permeabilities, structural discontinuities) since it is mechanically easier to reactivate old heterogeneities rather than to initiate new ones in homogeneous rocks. A deep crustal shear zone is a suitable candidate for focussed fluid flow (Kerrick, 1986; Eisenlohr et al., 1989; Thompson and Connolly, 1992). These shear zones exist in the SMZ of the LB and are represented by the syn-tectonically emplaced  $D_2$  shear zones formed during the thrusting of the SMZ of the LB over the northern margin of the KC (Smit and van Reenen, 1997). Therefore, the migrating deep-crustal fluids used pre-existing shear zones to escape and during propagation further caused the formation of the shear zones and initiated deformation (Fyfe and Kerrich, 1985; Thompson and Connolly, 1992; Roering et al., 1995).

The Doornhoek deposit is mainly associated with BIF and mafic lithologies surrounded by hydrated tonalitic gneiss and localised within an old shear zone system that was probably reactivated (the  $D_2$  event was reactivated during  $D_3$  and the old discontinuities were used as a plumbing system for the highly channelised fluids). These fluids probably have a major contribution at the formation of the Doornhoek gold deposit.

The physical mechanism controlling the focussing of pervasive low-flux flowing fluid into high-velocity channels (shear zones, fractures etc) is still not fully understood. If a build-up of fluid pore-pressure can induce hydrofracturing, then fluid flow will become rapidly focussed, even in the ductile-regime of the lower crust (Fischer and Paterson, 1989; Roering et al., 1995).

#### 13.4 SOURCE OF METAMORPHIC FLUIDS

Geophysics is a very useful tool to investigate the lower crust. Electrical conductivity studies (Shankland and Ander, 1983) and particularly seismic reflection studies (Matthews, 1986; Matthews and Cheadle, 1986) suggest that fluid accumulation is a common phenomenon in the lower crust (Hyndmann, 1988; Thompson and Connolly, 1992).

High-electrical conductivity and low-velocity seismic layers can reflect "aquitards" (Thompson and Connolly, 1990) which require fluid-filled porosities in the order of 0.1% to 0.4% (Matthews, 1986; Matthews and Cheadle, 1986; Shankland and Ander, 1983; Thompson and Connolly, 1992).

During regional metamorphism, pervasive and transient porosities of up to 1% are predicted (Connolly and Thompson, 1989), but in certain tectonically thickened crust porosities can be higher and constant long enough for geological times. These metamorphic "aquitards" can store accumulated fluids for 60 to 120 Ma after thickened crust has isostatically been returned to the normal dimension (Thompson and Connolly, 1990, 1992). During this "storing",

isostatic readjustments following crustal thickening or normal overthrusting exercised along crustal shear zones, due to continental collision, can depressurise the "aquiferes" and channel them through and along deep structural discontinuities.

This accurately reflects the geological setting of the Doornhoek gold deposit within the highly ductile tectonised environment of the SMZ of the LB, a root zone of an old continental collision event between the Kaapvaal and Zimbabwean Craton, 2.7 Ga ago (Roering et al., 1992a; de Wit et al., 1992).

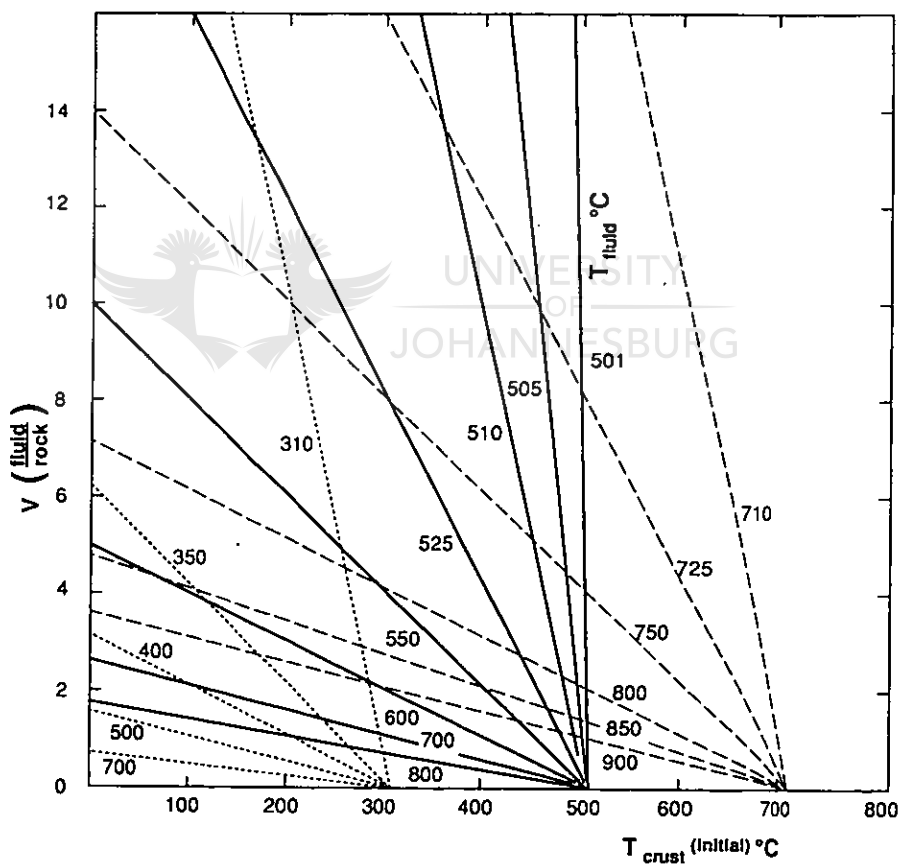


Figure 13.6: Variation of volumetric fluid-rock ratios required to cause crustal heating, for different initial values for  $T_{crust}$ . Various values of initial  $T_{fluid}$  are shown for selected values of  $T_{fluid}$  of 700°, 500° and 300°. Heat conservation was assumed to be given by:  $C_p fluid/C_p rock = \text{Volume}^{(fluid/rock)} \cdot \Delta T^{fluid}/\Delta T^{rock}$ , with equal values from volumetric heat-capacities (from Thompson and Connolly, 1992).



### 13.5 DEEP CRUSTAL EMBRITTLEMENT AND FLUID FLOW DURING GRANULITE FACIES IN THE SMZ OF THE LB AND FLUID:ROCK CONDITIONS AT DOORNHOEK

Roering et al. (1995) described and quantified the phenomenon of brittle failure and hydraulic fracture processes in the deep crustal rocks of the SMZ of the LB. The conclusion of their study is that despite the high metamorphic grade of the rocks in the SMZ of the LB which implies low permeabilities and low fluid:rock ratios, hydraulic micropumping occurred and channelised fluid flow was possible. This also implies that the possibility of forming mineral deposits, due to high concentration of mineralised fluids, such as Doornhoek, in the SMZ of the LB is relatively high.

Roering et al. (1995) using structural evidence in the SMZ of the LB (i.e. strike-slip faulting in the central part of the SMZ as opposed to thrust faulting in the western part - **fig. 4.1** and **4.2**), the existence of hydraulic fractures preserved as breccias in pelitic gneisses, enderbite veinlets crosscutting the foliation of tonalitic gneisses or opx-bearing en echelon veinlets crosscutting the D<sub>2</sub> fabric) concluded that strike-slip faulting is much more favourable for fluid flow than thrust faulting or normal faulting. This probably explains the fact that the zone of hydration is better developed in areas dominated by strike-slip faulting in the SMZ (**fig. 4.1** and **4.2**).

The relationship of style of faulting (shear failure), hydraulic fracture and the ratio fluid pressure:overburden pressure ( $P_{\text{fluid}}/P_{\text{rock}}$ ) are (Behrmann, 1991):

$$\lambda_v = P/\sigma_{\text{vertical}} = P/\rho gh, \text{ where } P = \text{density and } h = \text{depth}$$

Conditions for hydraulic fracturing during *thrust faulting* are:

$$\lambda_v = 1 + t/\rho gh$$

for *strike-slip faulting*:

$$\lambda_v = 1 - \left( \frac{KC - t/2(K2+1)}{\rho gh} \right)$$

and for *normal faulting*:

$\lambda_v = 1 - \left( \frac{2KC - K2t}{\rho gh} \right)$ , where  $K = \frac{1+\mu^2}{2} + \mu$ ,  $\mu$  is the coefficient of friction,  $C$  the cohesion and  $t$  the tensile strength of the hydraulic fracture.

For the retrograde isograd Roering et al. (1995) assumed that fluids were responsible for metamorphic reactions on a regional scale, and that these fluids gained access to the high-grade terrane along the Hout River Shear Zone terrane boundary. Roering et al. (1995) also associated hydraulic fracturing with regional compressional faulting (thrust faulting - D<sub>2</sub>) that allows an estimate of the  $\lambda_v$  ratio. For all the styles of faulting at deep crustal levels, however, the value of the ratio tends toward one because as the depth increases the denominator gets much larger than the numerator.

Accepting that the crust is essentially granitic, the following values to estimate the  $\lambda_v$  values were used (Roering et al., 1995):

- $\rho_{gh}$  = 700Mpa (based on mineral equilibria from the LB, Stevens and van Reenen, 1992)  
 $t$  = 40Mpa (Johnson, 1970)  
 $\mu$  = 0.6 Byerlee's law of rock friction for deep crustal levels (Byerlee, 1977, 1978)  
 $C$  = 50Mpa (Byerlee, 1977)

Employing these values, the following ratios were obtained (Roering et al., 1995):

for *thrust faulting*:  $\lambda v = 1.057$ ,  $P_{fluid} = 740Mpa$ ,  $P_{rock} = 700 Mpa$   
 for *strike-slip faulting*:  $\lambda v = 0.963$ ,  $P_{fluid} = 674Mpa$ ,  $P_{rock} = 700 Mpa$

This would imply that at the same deep crustal level, equivalent to a lithostatic load of 7kbar, thrust faulting environments would buffer, in a structural sense, the fluid pressure at 7.4 kbar, while strike-slip faults would buffer the fluid pressure at a value of 6.7 kbar. It would therefore be relatively easier for a fluid to move through a zone of strike-slip faulting than a zone of thrust faulting (Roering et al., 1995). Thus, hydraulic fracturing occurs in the SMZ of the LB and is mainly associated to the large strike-slip faulting zones (lateral ramps) associated with the Hout River Terrane Boundary (**fig. 4.1** and **4.2**). Considering the emplacement of the Doornhoek gold deposit along a similar strike-slip shear zone, in a zone of lateral ramps (**fig. 4.3**) associated with the Doornfontein and N'tabalala shear zones, the intense hydration and metasomatism present at Doornhoek are probably due to deep crustal embrittlement caused by fluid flow.

At Doornhoek, available data including structural evidence, mineral reactions and textures, and the crosscutting features of some of the mineralised veins support suggestions that the mineralised metasomatic fluid had a high fluid-rock ratio at the time of ore mineral deposition. Knowing that temperatures of at least 720°C were reached at the time of mineral

deposition, volumetric fluid/rock ratios of at least 5 (fig. 13.6) dominated the channelised mineral deposition and metasomatism at Doornhoek at least within the zones of quartz-sulphide veining and metasomatic garnet porphyroblasts, where thermobarometric data have been recorded.

The fluids pre-existed in a "captured" aquitard for million of years, accumulated during the  $M_1$  granulitic event. The isotopic component shows externally derived fluids with magmatic contamination (mantle provenance). The deep seated magmatic fluid, highly overpressurised, would become mixed with the metamorphic aquitard and could give rise to an effective plumbing system at the terrane boundary. The  $D_2$  shearing and deformation event related to the exhumation of the granulite terrane of the SMZ (Smit and van Reenen, 1997) created channelways for fluids that were responsible for both the regional hydration and the channelised alteration. The propagation of mineralised fluids occurred along strike-slip shear zones at high fluid:rock ratios, that caused intermittent hydraulic fracturing. Due to the geochemical contrast between the surrounding rocks and the predominantly BIF and mafic lithologies of Doornhoek, the channelised fluids, although still very hot, deposited some of their metallic load in this geochemical trap which today is the Doornhoek Gold Deposit.

Very favourable factors (proximity to the source aquitard, repeated reactivated pure shearing deformation on pre-existing major and auxiliary  $D_2$  discontinuities, geochemical contrast,  $CO_2$ -rich fluids that did not allow the host rock to melt etc) contributed to the formation of this interesting occurrence of gold deposition under near granulite facies conditions.

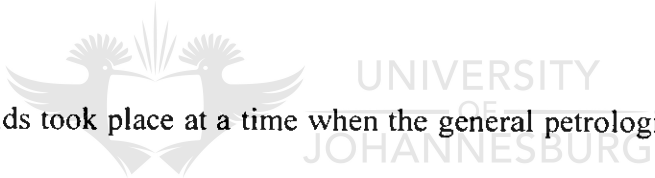
## 14. CONCLUSION

The deep-seated Doornhoek shear zone is a typical structural system of conjugated shear zones that were active during high-grade granulitic metamorphism and deformation. The deformation recorded by the filling of the shear zone system and by the wall rock is mainly ductile, as is suggested by the plastic-type of mechanical deformation. The shear zone started being active during  $D_2$  times which represents the main phase of exhumation of the Limpopo granulite facies terrane.

What is seen today outcropping on surface actually represent the deep seated roots of a massive collisional tectonic system formed between the greenstone dominated lithologies of the Kaapvaal Craton and the Zimbabwean Craton. The crustal thickening which occurred between the two cratons at that stage (2.67 Ga) was accompanied by isostatic re-equilibration and as a result steeply dipping shear zones became active. The mineral and mechanical lineations are testimonies of material escaping down-dip, almost vertically, along the shear zones planes. Strike-slip displacement also took place, as shown by the displacement of the orthoamphibole isograd and by the main structural movements inside the Doornhoek Gold Deposit. Penecontemporaneously with the intense, granulitic facies deformation, fluids derived from an external source mixed with fluids from regional aquitards, were depressurised.

At Doornhoek, the huge reservoirs contaminated with magmatic fluid, were depressurised due to strike-slip fracturing, and the hot fluids, mainly CO<sub>2</sub>-rich but also with some hypersaline component, started their long journey towards surface.

One of the main obstacles was represented by the BIF, mafic and ultramafic lithologies encountered at Doornhoek. Although these lithologies have already undergone the regional hydration event as most of the lithologies in the SMZ of the LB, the massive flushing of fluids generated through and by strike-slip fracturing changed even more severe the local appearance of the Doornhoek environment. The hot fluids have probably been trapped by the geochemical contrast of the Doornhoek lithologies surrounded by a sea of Baviaanskloof Gneiss.

The logo of the University of Johannesburg, featuring two stylized birds facing each other with a sunburst above them, and the text 'UNIVERSITY OF JOHANNESBURG' in a light grey font.

The introduction of fluids took place at a time when the general petrologic trend in the SMZ of the LB was retrograde (testimony being the retrograde pattern in the garnets hosted by the wall-rock lithologies of the mineralised sequences at Doornhoek). The fluid introduction was highly channelised and probably characterised by high fluid:rock ratios as compared to the general trend in the SMZ which usually displayed slow, pervasive alterations. Where the hot fluids penetrated the system two new rock types were formed: mineralised quartz veins and mineralised biotite-garnetiferous formation. According to petrologic calculations the core of the garnet crystallised at about 500°C and the rim at about 720°C. Therefore, at Doornhoek, prograde and retrograde garnets occur in the same units, sometimes only centimetres apart: retrograde in the wall-rock and prograde in the mineralised horizons, as a result of channelised hot fluids flowing through already cooling lithologies.

The gold associated mineralisation was deposited in the quartz vein after a prograde pattern, starting with sphalerite at temperatures of about 500°C and ending with lollingite at temperatures well above 700°C. But is the biotite-garnetiferous mineralisation, heavily gold mineralised that reconstitutes precisely the film of events at Doornhoek. The prograde garnet porphyroblast and biotite represent the result of K- and Al-rich high-temperature metasomatism upon BIF and mafic lithologies. And due to the fact that the mineralising fluids showed an increased activity during the late stage of M<sub>3</sub>, the host rock became hotter, the environmental temperature increased accordingly and the garnet crystallised after a prograde pattern. Simultaneously to its crystallisation, the prograde garnet porphyroblasts entrapped the ore minerals and the fluids active at certain moments of time during the evolution of the Doornhoek hydrothermal system. Thus, mineralisation started being entrapped within the garnet porphyroblast as sphalerite, gold and As-poor arsenopyrite at about 500°C and ended with lollingite and electrum just above 700°C.

There is a good correlation between the paragenesis and order of deposition of the ore minerals in the quartz veins and that in the biotite-garnetiferous formation.

The analytical modelling for the formation of the Doornhoek gold deposit showed the following data:

- $\Delta T =$  500-750°C
- $\Delta \text{time} =$  > 1Ma, for 350m normal width
- Fluid flux =  $10^{-9} \text{m}^3 \text{m}^{-2} \text{s}^{-1}$
- Volumetric fluid:rock ratio = 5 at 720°C.

## REFERENCES:

- Anderson, D.E. and Buckley, G.R., 1973: Zoning in garnets - Diffusion models: *Contrib. Min. Petrol.*, 40, pp.87-104.
- Aranovich, L.Y. and Newton, R.C., 1995: Experimental determination of H<sub>2</sub>O-activity in concentrated aqueous sodium chloride solutions at high P and T. *Geol. Soc. Amer. Abstr. w/Programs*, 27, pp.A-155.
- Aranovich, L.Y., Schmulovich, K.I. and Fedkin, V.V., 1987: The H<sub>2</sub>O and CO<sub>2</sub> regime in regional metamorphism. *Int. Geol. Rev.*, 29: pp.379-1401.
- Aydin, A. and Nur, A., 1982: Evolution of pull-apart basins and their scale independence: *Tectonics*, 1, pp.91-105.
- Bailey, D.K., 1980: Volcanism, Earth degassing and replenished lithosphere mantle. *Phil. Trans. R. Soc. London*, A-297, pp.309-322.
- Baker, A.J., Van Reenen, D.D., Van Schalkwyk, J.F. and Newton, R.C., 1992: Constraints on the composition of fluids involved in retrograde anthophyllite formation in the Limpopo Belt, South Africa. *Precamb. Res.*, 55, pp.327-336.



Bakker, R.J. and Jansen, J.B.H., 1990: Preferential water leakage from fluid inclusions by means of mobile dislocations. *Nature*, 345, pp.58-60.

Bancroft, G.M. and Jean, G., 1982: Gold deposition at low temperature on sulphide minerals. *Nature*, 298, pp.730-731.

Barley, M.E. and Groves, D.I., 1990: Deciphering the tectonic evolution of Archaean greenstone belts: the importance of contrasting histories to the distribution of mineralisation in the Yilgarn Craton, Western Australia. *Precamb. Res.*, 46, pp.3-20.

Barnicoat, A.C., Fare, R.J., Groves, D.I. and McNaughton, N.J., 1991: Syn-metamorphic lode-gold deposits in high-grade Archean settings. *Geology*, 19, pp.921-924.



Barton, J.M., Jr., Du Toit, M. C., Van Reenen, D.D. and Ryan, B., 1983: Geochronologic studies in the Southern Marginal Zone of the Limpopo Mobile Belt, southern Africa. *Spec. Publ. Geol. Soc. S. Afr.*, 8, pp.55-64.

Barton, J. M., Jr. and Van Reenen, D.D., 1992: The significance of Rb-Sr ages of biotite and phlogopite for the thermal history of the Central and Southern Marginal Zones of the Limpopo belt of southern Africa and the adjacent portions of the Kaapvaal Craton. *Precamb. Res.*, 55: pp. 17-31.

Barton, J.M., Jr., Doig, R., Smith, C.B., Bohlender, F. and Van Reenen, D.D., 1992:  
Isotopic and REE characteristics of the intrusive charnoenderbite and enderbite  
geographically associated with the Matok Pluton, Limpopo belt, southern Africa. *Precamb.  
Res.*, 55, pp.451-467.

Behrmann, J.H., 1991: Conditions for hydrofracture and fluid permeability of  
accretionary wedges. *Earth Planet. Sci. Lett.*, 107, pp.550-558.

Bickle, M. and McKenzie, D., 1987: The transport of heat and matter by fluids during  
metamorphism. *Contrib. Min. Petrol.*, 97, pp.384-392.

Bohlen, S.R., Wall, V.J. and Boettcher, A.L., 1983: Experimental investigations and  
application of garnet granulite equilibria. *Contrib. Min. Petrol.*, 83, pp.52-61.

Bohlender, F., 1992: Igneous and metamorphic charnockitic rocks in the Southern  
Marginal Zone of the Limpopo Belt with special emphasis on the Matok enderbite-granitic  
suite. *Ph.D. thesis (unpubl.)*, Rand Afrikaans Univ., Johannesburg, 259pp.

Bohlender, F., Van Reenen, D.D. and Barton, J.M., Jr., 1992: Metamorphic and  
igneous charnockites in the Southern Marginal Zone of the Limpopo Belt, South Africa.  
*Precamb. Res.*, 55, pp.429-449.

Bohmke, F.C. and Varndell, B.J., 1986: Gold in granulites at Renco Mine, Zimbabwe. In: *Min. Dep. S. Afr.*, vol.I&II, Anhausser, C.R. and Maske, S. editors. *Geol. Soc. S. Afr.*, Johannesburg.

Bowers, T.S. and Helgeson, H.C., 1983: Calculation of the thermodynamic and geochemical consequences of nonideal mixing in the system  $H_2O-CO_2-NaCl$  on phase relations in geologic systems: Equation of state for  $H_2O-CO_2-NaCl$  fluids at high pressures and temperatures. *Geochim. Cosmochim. Acta.*, 47, pp.1247-1275.

Brady, J.B., 1988: The role of volatiles in the thermal history of metamorphic terranes. *J. Petrol.*, 29, pp.1187-1213.

Brown, P.E., 1989: Flicor: a microcomputer program for the reduction and investigation of fluid-inclusion data. *Am. Min.*, 74, pp.1390-1393.

Burnham, C.W. and Ohmoto, H. 1980: Late-stage processes of felsic magmatism. In: *Granitic Magmatism and Related Mineralization*, edited by S. Ishihara and S. Takenouchi, pp.1-11, *Soc. Min. Geol.of Japan*, Special Issue 8, 247pp.

Byerlee, J.D., 1977: Friction in rocks. In: Evernden, J.F., ed., *Experimental studies of rock friction with application to earthquake prediction*. *U.S. Geol. Survey Paper*, pp.55-77.

Byerlee, J.D., 1978: Friction of rocks. *Pure Appl. Geophys.*, 116, pp.615-626.

Carroll, M.R. and Rutherford, M.J., 1985: Sulphide and sulphate saturation in hydrous silicate melts. *J. Geophys. Res.*, 90 Supplement, pp.C601-C612.

Chen, W.P. and Molnar, P., 1983: Focal depths of intracontinental and intraplate earthquakes and their implications for the thermal and mechanical properties of the lithosphere. *J. Geophys. Res.*, 88, pp.4183-4214.

Chinner, G.A., 1962: *Cordierite in hornfels from Angus, Scotland*. *J. Petol.*, 3, pp.316. In: F.R.S.A. Deer, W.A., Howie, R.A. and Zussman, J., *An Introduction to the Rock Forming Minerals*, 1966, Longman Group Ltd., London, 528pp.

Colopietro, M.R. and Frieberg, L.M., 1987: Tourmaline-biotite as a potential geothermometer for metapelites, Black Hills, South Dakota. *Geol. Soc. of Am. Abstr. with Programs*, 19, pp.624.

Colvine, A.C., 1989: An empirical model for the formation of Archaean gold deposits: products of final cratonization of the Superior Province, Canada. In: Keays, R.R., Ramsay, W.R.H., Groves, D.I. (eds.), *The Geology of Gold Deposits: The Perspective in 1988*, *Econ. Geol. Monogr.*, 6, pp.37-53.

Colvine, A.C., Fyon, J.A., Heather, K.B., Marmont, S., Smith P.M. and Troop, D.G., 1988: Archaean lode gold deposits in Ontario. *Ontario Geol. Surv. Misc. Paper*, 139, 136pp.

Connolly, J.A.D. and Thompson, A.B., 1989: Fluid and Enthalpy production during regional metamorphism. *Contrib. Min. Petrol.*, 102, pp.347-366.

Connolly, J.A.D. and Thompson, A.B., 1990: Focussed fluid movement in the lower crust. *Trans. Am. Geophys. Union*, 71, pp.642.

Connolly, J.A.D. and Thompson, A.B., 1991: Focussed fluid movement in the lower crust. *Trans. Am. Geophys. Union*, 71, pp.642.

Corfu, F., 1987: Inverse age stratification in the Archean crust of the Superior Province: evidence for intra- and subcrustal accretion from high resolution U-Pb zircon and monazite ages. *Precamb. Res.*, 36, pp.259-275.

Corfu, F., 1988: Differential response of U-Pb systems in coexisting accessory minerals, Winnipeg River Subprovince, Canadian Shield: implications for Archean crustal growth and stabilisation.

Corfu, F., and Muir T.L., 1988: U-Pb geochronology for magmatism and mineralisation in the Helmo belt, Superior Province, northwestern Ontario [abstr.]. *In: Program with Abstracts, Geol. Assoc. Can.*, 13.

Coward, M.P., 1983: Some thoughts on the tectonics of the Limpopo Belt. *Spec. Publ. Geol. Soc. S. Afr.*, 8, pp.175-180.

Coward, M. P., James, P.R. and Wright, L. I., 1976: Northern margin of the Limpopo mobile belt, Southern Africa. *Geol. Soc. Am. Bull.*, 87, pp.601-611.

Crawford, M.L. and Hollister, L.S., 1986: Metamorphic fluids: the evidence from fluid inclusions. *In*: Walther, J.V. and Wood, B.J. (eds.). Fluid-rock interactions during metamorphism. Springer-Verlag, New York, pp.1-35.

De Beer, J. H. and Stettler, E. H., 1992: The deep structure of the Limpopo Belt. *Precamb. Res.*, 55, pp.173-186.

De Wit, M.J., Van Reenen, D.D. and Roering, C., 1992: Geologic observations across a tectono-metamorphic boundary in the Babangu area, Giyani (Sutherland) Greenstone Belt, South Africa. *Precamb. Res.*, 55, pp.111-122.

Duan, Z., Moller, N. and Weare, J.H., 1995: Equation of state for the NaCl-H<sub>2</sub>O-CO<sub>2</sub> system: Prediction of phase equilibria and volumetric properties. *Geochim. Cosmochim. Acta*, 59, pp.2869-2882.

Dunai, T.J., 1994: Mantle derived CO<sub>2</sub> and granulite genesis: evidence from noble gases. *Min. Mag.*, 58A, pp.245-246.

Du Toit, M.C., 1979: Die geologie en struktuur van die gebiede Levubu en Bandelierkop in Noord-Transvaal. Ph.D. thesis (unpubl.), Rand Afrikaans Univ., Johannesburg, South Africa, 241 pp.

Du Toit, R., 1994: High temperature metasomatic alteration associated with deep-crustal shear zones in the Limpopo Belt, South Africa. M.Sc. thesis (unpubl.), Rand Afrikaans Univ., Johannesburg, 304pp.

Du Toit, M.C., Van Reenen, D.D. and Roering, C., 1983: Some aspects of the geology, structure and metamorphism of the Southern Marginal Zone of the Limpopo Metamorphic Complex. *Spec. Publ. Geol. Soc. S. Afr.*, 8, pp.121-142.

Eisenlohr, B.N., Groves, D., Partington, G.A., 1989: Crustal scale-shear zones and their significance to Archean gold mineralisation on Western Australia. *Min. Dep.*, 24, pp.1-8.

Ellis, D.J. and Green, E.H., 1979: An experimental study of the effect of Ca upon garnet-clinopyroxene Fe-Mg exchange equilibria. *Contrib. Min. Petrol.*, 71, pp.13-22.

England, P.C. and Thompson, A.B., 1984: Pressure-temperature-time paths of regional metamorphism. Heat transfer during the evolution of regions of thickened continental crust. *J. Petrol.*, 25, pp.894-928.

Fare, R.J., 1989: Nature, timing and genesis of a granulite-facies gold deposit at Griffin's Find, Western Gneiss Terrain, Western Australia. B.Sc Thesis, (unpubl.). The University of Western Australia, Nedlands, 63pp.

Fischer, G.J. and Paterson, M.S., 1989: Dilatancy during rock deformation at high temperatures and pressures. *J. Geophys. Res.*, 9, pp.17,607-17,617.

Foster, R.P., 1989: Archaean gold mineralisation in Zimbabwe: implications for metallogensis and exploration. *Econ. Geol. Monogr.*, 6, pp.54-70.

Fripp, R.E.P., 1976: Stratabound gold deposits in Archaean banded iron formation, Rhodesia. *Econ. Geol.*, 71, pp.58-75.

Frost, B.R. and Frost, C.D., 1987: CO<sub>2</sub>, melts and granulite metamorphism. *Nature*, 327, pp.503-506.

Fyfe, W.S., Price, N.J., Thompson, A.B., 1978:  Fluids in the Earth's Crust. Elsevier, Amsterdam, 383pp.

Fyfe, W.S. and Henley, R.W., 1973: Some thoughts on chemical transport processes with particular reference to gold. *Min. Sci. Eng.*, 5, pp.295-303.

Fyfe, W.S. and Kerrich, R., 1984: Gold: Natural concentration processes. In: Proceedings of Gold '82: *The Geology, Geochemistry, and Genesis of Gold Deposits*, pp.99-127, R.P. Foster (eds.). *Geol. Soc. Zimbabwe, Spec. Publ.*, 1, 753pp.

Fyfe, W.S. and Kerrich, R., 1985: Fluids and thrusting. *Chem. Geol.*, 49, pp.353-362.



Fyon, J.A. and Crocket, J.H., 1982: Gold exploration in the Timmins district using field and lithogeochemical characteristics of carbonate zones. *In: Geology of Canadian gold deposits*, R.W. Hodder and W. Petruk (eds.), pp.113-29. *Can. Inst. Min. Met., Spec. Vol.*, 24.

Fyon, J.A., Schwarcz, H.P. and Crocket, J.H., 1984: Carbonatization and gold mineralization in the Timmins area, Abitibi greenstone belt: Genetic links with Archaean mantle CO<sub>2</sub>- degassing and lower crustal granulisation [abstr.], pp.65 *In: Program with Abstracts, Geol. Assoc. Can.*, 9, 128pp.

Gan, S. and Van Reenen, D.D., 1995: Geology of gold deposits in the Southern Marginal Zone of the Limpopo Belt and the adjacent Sutherland Greenstone Belt, South Africa-Franke Mine. *Trans. Geol. Soc. S. Afr.*, 98, pp.263-275.

Ganguly, J. and Saxena, S.K., 1984: Mixing properties of aluminosilicate garnets: constraints from natural and experimental data, and applications to geothermobarometry. *Am. Min.*, 69, pp.88-97.

Groves, D.I., 1993: The crustal continuum model for late Archaean lode gold deposits of the Yilgarn Block, Western Australia. *Min. Dep.*, 28, pp.366-374.

Groves, D.I., Phillips, G.N., Ho, S.E., Henderson, C.A., Clark, M.E. and Woad, G.M., 1984: Controls on distribution of Archaean Hydrothermal gold deposits in Western Australia. *In: Foster R.P. (eds.) Gold'82: The Geology Geochemistry and Genesis of Gold Deposits.* Balkema, Rotterdam, pp.689-712.

Groves, D.I. and Phillips, G.N., 1987: The genesis and tectonic control on Archaean gold deposits of the Western Australian Shield: a metamorphic-replacement model. *Ore. Geol. Rev.*, 2, pp.287-322.

Groves, D.I., Barley, M.E. and Ho, S., 1989: Nature, genesis and tectonic setting of mesothermal gold mineralisation in the Yilgarn Block, Western Australia. *Econ. Geol. Mono.*, 6, pp.71-85.

Groves, D.I., Barley, M.E., Cassidy, K.C., Haggeman, S.G., Ho, S.E., Hronsky, J.M.A., Mikucki, E.J., Mueller, A.G., McNaughton, N.J., Perring, C.S., Ridley, J.R., 1991: Archaean lode-gold deposits: the products of a crustal-scale hydrothermal system. *In*: Ladeira, E.A. (eds.). *Brazil Gold' 91*. Balkema, Rotterdam, pp.299-305.

Groves, D.I., Barley, M.E., Barnicoat, A.C., Cassidy, K.F., Fre, R.J., Haggeman, S.G., Ho, S.E., Hronsky, J.M.A., Mikucki, E.J., Mueller, A.G., McNaughton, N.J., Perring, C.S., Ridley, J.R., Vearncombe, J.R., 1992: Sub-greenschist to granulite-hosted Archean lode gold deposits of the Yilgarn Craton: a depositional continuum from deep sourced hydrothermal fluid sin-crustal scale plumbing systems. Geol. Dept., (Key Centre) and University Extension, *Univ. West. Austr., Publ.* 22, pp.325-337.

Groves, D.I., Ridley, J.R., Bloem, E.M.J., Gebre-Mariam, M., Haggeman, S.G., Hronsky, J.M.A., Knight, J.T., McNaughton, N.J., Ojala, J., Vielreichter, R.M., McCuaig, T.C. and Holyland, P.W., 1995: Lode-gold deposits of the Yilgarn block: products of Late Archaean crustal-scale overpressured hydrothermal systems. *In*: Early Precambrian

Processes, Coward, M.P. and Ries, A.C. (eds.), 1995. *Geol. Soc. Spec. Publ.*, 95, pp.155-171, Western Australia.

Hamilton, P.J., Evensen, N.M., O'Nions, R.K., Smith, H.S., and Erlank, A.J., 1979:  
Nd-Sm dating of Onverwacht volcanics, South Africa. *Nature*, 279, pp.298-300.

Harley, S.L. and Green, D.H., 1982: Garnet-orthopyroxene barometry for granulites and peridotites. *Nature*, 300, pp.697-701.

Hayama, Y., 1959: Some considerations on the colour of biotite and its relation to metamorphism. *J. Geol. Soc. Japan*, 65, pp.21.

Hobbs, B. E., Means, W. D. and Williams, P. F., 1976:  An Outline of Structural Geology. John Wiley & Sons, Inc., 477pp.

Hodges, K.V. and Spear, F.S., 1982: Geothermometry, geobarometry and the  $Al_2SiO_5$  triple point at Mt. Moosilauke, New Hampshire. *Am. Min.*, 67, pp.1118-1134.

Hodgson, C.J., and MacGeehan, P.J., 1982: Gold ore formation at the Campbell and Dickenson mines, Red Lake area. *Ontario Geol. Surv. Misc. Paper*, 98, pp.132-143.

Hoernes, D. and Van Reenen, D.D., 1992: The oxygen isotopic composition of granulites from the Limpopo Belt as a monitor of fluid rock interaction. *Precamb. Res.*, 55, pp.353-364.

Hoernes, S., Lichtenstein, U., van Reenen, D.D. and Mokgatlha, K., 1995:

Whole-rock/mineral O-isotope fractionations as a tool to model fluid-rock interaction in deep-seated shear zones of the Southern Marginal Zone of the Limpopo Belt, South Africa. *S. Afr. J. Geol.*, 98/4, pp.488-497.

Hollister, L.S., 1990: Enrichment of CO<sub>2</sub> in fluid inclusions in quartz by removal of H<sub>2</sub>O during crystal-plastic deformation. *J. Struct. Geol.*, 12, pp.895-901.

Hollister, L.S., 1992: Fluid flow during deep crustal metamorphism, an introduction to new data from the Southern Marginal Zone of the Limpopo Belt. *Precamb. Res.*, 55, pp.321-325.

Holloway, J.R., and Lewis, C.F. 1974: CO<sub>2</sub> solubility in hydrous albite liquid at 5 kbar [abstr.]; *EOS, Trans. Am. Geophys. Union*, 55, pp.483.

Hutchinson, R.W., Fyfe, W.S., and Kerrich, R., 1982: Deep fluid penetration and ore deposition. *Min. Sci. Eng.*, 12, 3, pp.107-120.

Hyndman, R.D., 1988: Dipping seismic reflectors, electrically conductive zones and trapped water in the crust over a subducting plate. *J. Geophys. Res.*, 93, pp.13,391-13, 405.

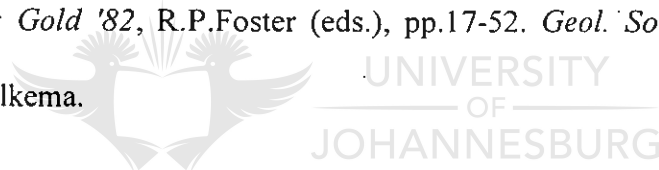
Javoy, M., Fourcade, S. and Allegre, C.J., 1970: Graphical method for examination of <sup>18</sup>O/<sup>16</sup>O fractionations in silicate rocks. *Earth and Planet. Sci. Lett.*, 10, pp.12-16.

Johnson, A.M., 1970: Physical Processes in Geology. San Francisco, Freeman, Cooper, 573pp.

Kadik, A.A. and Egger, D.H., 1975: Melt-vapour relations on the joint  $\text{NaAlSi}_3\text{O}_8\text{-H}_2\text{O-CO}_2$ . Yearbook of the Carnegie Institute of Washington, 74, pp.479-484.

Karvinen, W.O., 1982: Geology and evolution of gold deposits, Timmins area, Ontario. In: *Geology of Canadian gold deposits*, R.W. Hodder and W. Petruk (eds.), pp.101-120. *Can. Inst. Min. Met.*, Spec. Vol. 24.

Keays, R. R., 1984: Archaean gold deposits and their source rocks: the upper mantle connection. In: *Gold '82*, R.P.Foster (eds.), pp.17-52. *Geol. Soc. Zimbabwe, Spec. Publ. 1*, Rotterdam, Balkema.



Kerrick, R., 1986: Fluid infiltration into fault zones: chemical, isotopic and mechanical evidence. *PAGEOPH.*, 124, pp.225-268.

Kerrick, R., 1989a: Geodynamic setting and hydraulic regimes: shear zone hosted mesothermal gold deposits. In: Bursnall, J.T. (eds.), *Mineralisation and Shear zones. Geol. Assoc. Can. Short Course Notes*, 6, pp.89-128.

Kerrick, R., 1989b: Archaean gold: Relation to granulite formation or felsic intrusions? *Geology*, 17, pp.1011-1015.

Kerrich, R., 1990: Carbon-isotope systematics of Archaean Au-Ag vein deposits in the Superior Province. *Can. J. Earth Sci.*, 27, pp.40-56.

Kerrich, R., 1993: Preface: Perspectives on genetic models for lode gold deposits. *Min. Dep.*, 28, 6, pp.362-365.

Kerrich, R. and Fyfe, W.S., 1981: The gold carbonate association: Source of CO<sub>2</sub>. Fixation reactions in Archaean lode deposits. *Chem. Geol.*, 33, pp.265-294.

Kerrich, R., Fryer, B.J., King, R.W., Wilmore, L.M. and Van Hees, E., 1989: Crustal outgassing and LILE enrichment in major lithosphere structures, Archaean Abitibi greenstone belt: evidence on the source reservoir from strontium and carbone isotope tracers. *Contrib. Mineral. Petrol.*, 97, pp.156-168.



Kerrich, R. and Wyman, D., 1990: Geodynamic setting of mesothermal gold deposits: an association with accretionary tectonic regimes. *Geology*, 18, pp.882-885.

Kerrich, R. and Feng, R., 1992: Archaean geodynamics and the Abitibi-Pontiac collision; implications for advection of fluids at transpressive collisional boundaries and the origin of giant quartz vein systems. *Earth Sci. Rev.*, 32, 1/2, pp.33-60.

Kerrich, R. and Wyman, D., 1993: The mesothermal gold-lamprophyre association: significance for an accretionary geodynamic setting, supercontinental cycles, and metallogenic processes. *Min. Petrol.*

Kirby, S.H., 1984: Introduction and digest to the special issue on chemical effects of water on the deformation and strength of rocks. *J. Geophys. Res.*, 89, pp.3991-3995.

Kirby, S.H., 1985: Rock mechanics observations pertinent to the rheology of the continental lithosphere and the localisation of strain along shear zones. *Tectonophysics*, 119, pp.1-27.

Knapp, R.B., and Knight, J.E., 1977: Differential thermal expansion of pore fluids: Fracture propagation and microearthquake production in hot pluton environments. *J. Geophys. Res.*, 82, pp.2515-2522.

Kozlovsky, Y.A., 1987: The Superdeep Well of Kola Peninsula. Springer, Berlin, 558pp.



UNIVERSITY  
OF  
JOHANNESBURG

Krogh, T.E., Heaman, L.M. and Muchado, N., 1988: Detailed U-Pb chronology of successive stages of zircon growth at medium and deep level using parts of single zircon and titanite grains. *In: Project Lithoprobe, Kapuskasing Structural Zone Transect.*, p.243, Workshop, Toronto, Univ. of Toronto, 252pp.

Lindgren, W., 1928: Mineral deposits, 3rd edn., New York, McGraw Hill.

Loomis, T.P., 1983: Compositional zoning of crystals: Record of growth and reaction history. *In: Saxena, S.K., (eds.), Kinetics and Equilibrium in Mineral Reactions. Adv. Phys. Geochem.*, 3, pp.1-60. Springer-Verlag, New York.

Lowenstern, J.B., 1994: Chlorine, fluid immiscibility, and degassing in peralkaline magmas from Pantelleria, Italy. *Am. Min.*, 79, pp.353-369.

Macdonald, A.J., 1984: Gold mineralisation in Ontario, I: the role of banded iron formation. pp.412-430 *In: Chibougamau - Stratigraphy and Mineralization*. J. Guha and E.H. Chown, (eds.), *Can. Inst. Min. Met., Spec. Vol.*, 34, 534pp.

Masliwec, A., McMaster, D. and York, D., 1986: The dating of Ontario's gold deposits. pp.107-114 *In: Geosc. Res. Grant Program, Summary of Research, 1985-86*, edited by V.G. Milne, *Ontario Geol. Surv.*, Misc. paper 130, 235pp.

Mason, R., 1973: The Limpopo Mobile Belt - Southern Africa. *Philos. Trans. R. Soc. London*, A-273, pp.463-485.



UNIVERSITY  
OF  
JOHANNESBURG

Mason, R. and Melnik, N., 1986: The anatomy of Archean gold system. The McIntyre- Hollinger complex at Timmins, Ontario, Canada. pp. 40-55 *In: Proceedings of Gold '86, an International Symposium on the Geology of Gold*, A.J. MacDonald (eds.), Konsult International Inc, Toronto, 517pp.

Matthews, D.H., 1986: Seismic reflections from the lower crust around Britain. *In: J.B. Dawson, D.A. Carswell, J. Hall and K.H. Wedepohl (eds.), The Nature of the Lower Continental Crust*, 24, *Geol. Soc. Spec. Publ.*, pp.11-22.



Matthews, D.H. and Cheadle, M.J., 1986: Deep reflections from the Caledonites and Variscides west of Britain and comparison with the Hymalayas. *Geodynamics*, 13, pp.5-19.

McCourt, S. and van Reenen, D.D., 1992: Structural geology and tectonic setting of the Sutherland Greenstone Belt, Kaapvaal Craton, South Africa. *Precamb. Res.*, 55, pp.93-110.

McCuaig, T.T., Kerrich, R., Groves, D.I. and Archer, N., 1993: The nature and dimensions of regional and local gold-related hydrothermal alteration in tholeiitic metabasalts in the Norseman goldfield: the missing link in a crustal continuum of gold deposits. *Min.Dep.*, 28, 6, pp.420-435.



Means, W. D., 1963: Mesoscopic structures and multiple deformation in the Otago schist. *New Zealand J. Geol. Geophys.*, 6 (5), pp.801-816.

Mikucki, E.J. and Ridley, J.R., 1993: The hydrothermal fluid of Archaean lode-gold deposits of different metamorphic grades: compositional constraints from ore and wallrock alteration assemblage. *Min.Dep.*, 28, 6, pp.469-481.

Miyano, T., Tsunogae, T. and van Reenen., 1990: Fluid behaviour in Archaean granulite facies terrain of the Limpopo Belt. *EOS*, 71, pp.971.

Miyano, T. and van Reenen, D.D., 1987: Metamorphic conditions of the Rhenosterkoppies iron-formation in the Southern Marginal Zone of the Limpopo Belt, South Africa. *Ann. Rep. Inst. Geosci., Univ. Tsukuba*, 13, pp.119-122.

Mokgatla, K.P.B., 1995: Transformation of tonalitic gneiss into potassic garnet-sillimanite gneiss in a deep crustal shear zone in the Limpopo Belt. M.Sc. thesis (unpubl.), Rand Afrikaans Univ., Johannesburg, 163pp.

Mysen, B.O., 1976: The role of volatiles in silicate melts: solubility of carbon dioxide and water in feldspar, pyroxene and feldspatoid melts to 30 kb and 1625°C. *Am. J. Sci.*, 276, pp.969-996.

Nash, J.T., 1976: Fluid inclusion petrology - data from porphyry copper deposits and applications to exploration; *U.S. Geol. Surv., Professional Paper* 907-D, 16pp.

Newton, R.C., Smith, J.V. and Windley, B.F., 1980: Carbonic metamorphism granulites and crustal growth. *Nature*, 288, pp.45-50.

Newton, R.C., Aranovich, L.Ya., Hansen, E.C. and Vandenheuvel, B.A., 1996: Hypersaline fluids in Precambrian deep-crustal metamorphism. *Precamb. Res.*, 1996 (*in press*).

Niggli, P., 1926: *Lehrbuch der Mineralogie II (Spezielle Mineralogie)*. Berlin.

Nisbet, E.G., 1987: The Young Earth. An introduction to Archaean Geology. Boston, Allen & Unwin. Lon. Syd. Wellington.

Nisbet, E.G., J.F. Wilson and Bickle, M.J., 1981: The evolution of the Rhodesian Craton and adjacent Archaean terrain. *In: Precambrian plate tectonics*, A. Kroner (eds.), pp.161-83. Amsterdam: Elsevier.

Nishiyama, T., 1989: Kinetics of hydrofracturing and metamorphic veining. *Geology*, 17, pp.1068-1072.

Ojala, V.J., Ridley, J.R., Groves, D.I. and Hall, G.C., 1993: The Granny Smith gold deposit: the role of heterogenous stress distribution at an irregular granitoid contact in a greenschist facies terrane. *Min. Dep.*, 28, 6, pp.409-419.

Paradis, S., Ludden, J. and Gelinas, L., 1988: Evidence for contrasting compositional spectra in comagmatic intrusive and extrusive rocks of the late Archean Blake River Group, Abitibi, Quebec. *Can. J. Earth Sci.*, 25, pp.134-144.

Pasteris, J.D., Harris, T.N. and Sassari, D.C., 1995: Interactions of mixed volatile-brine fluids in rocks of the southwestern footwall of the Duluth Complex, Minnesota - evidence from aqueous fluid inclusions. *Amer. J. Sci.*, 295, pp.125-172.

Peacock, S.M., 1989: Numerical constraints on rates of metamorphism, fluid production and fluid flux during regional metamorphism. *Geol. Soc. Am. Bull.*, 101, pp.476-485.

Pearson, T.N., 1984: The role of carbonate alteration in Archaean gold mineralization. In: *Gold '82*, R.P. Foster (eds.), 687. *Geol. Soc. Zimbabwe, Spec. Publ.* 1.

Percival, J. A. and Krogh, T.E., 1983: U-Pb zircon geochronology of the Kapuskasing structural zone and vicinity in the Chapleau-Foley area, Ontario. *Can. J. Earth Sci.*, 20, 5, pp.830-843.

Petrakakis, K., 1986: Metamorphism of high-grade gneisses from the Moldanubian zone, Austria, with particular reference to the garnets. *J. Met. Geol.*, 4, pp.323-344.

Philippot, P. and Selverstone, J., 1991: Trace-element-rich brines in eclogitic veins: Implications for fluid composition and transport during subduction. *Contrib. Min. Petrol.*, 106, pp.417-430.

Philippot, P., Chevallier, P., Chopin, C. and Dubessy, J., 1995: Fluid composition and evolution in coesite-bearing rocks (Dora Maira massif, western Alps): Implications for element recycling during subduction. *Contrib. Min. Petrol.*, 121, pp.29-41.

Phillips, G.N. and Groves, D.I., 1983: The nature of Archaean gold bearing fluids as deduced from gold deposits of Western Australia. *J. Geol. Soc. Australia*, 30, pp.25-39.

Poldervaart, A. and Hess, H.H., 1951: Pyroxenes in the crystallisation of basaltic magmas. *J. Geol.*, 59, pp.472-489.

Potgieter, G.A. and de Villiers, J.P.R., 1986: Controls of mineralization at the Fumani gold deposit, Sutherland greenstone belt, 197-203. In: Anhaeusser, C.R. & Maske, S. (eds.), *Mineral Deposits of Southern Africa*, 1, *Geol. Soc. S. Afr.*, Johannesburg, 1020pp.

Pretorius, A.I., van Reenen, D.D. and Barton, J.M., Jr., 1988: BIF-hosted gold mineralization at the Fumani Mine, Sutherland greenstone belt, South Africa. *S. Afr. J. Geol.*, 91, 4, pp.429-438.

Pride, C. and Muecke, G.K., 1980: Rare earth element geochemistry of the Scourian Complex NW Scotland - evidence for the granite-granulite link. *Contrib. Min. Petrol.*, 73, pp.403-412.

Ramberg, H., 1963: Fluid dynamics of viscous buckling applicable to folding of layered rocks. *Am. Assoc. Petrol. Geol. Bull.*, 47, pp.484-505.

Ramdohr, P., 1980: The ore minerals and their intergrowths. 2 vol. International Series in Earth Sci., 35, 2<sup>nd</sup> edition, Pergamon Press Ltd., England.

Ramsay, J.G., 1960: The deformation of early linear structures in areas of repeated folding. *J. Geol.*, 68, pp.75-93.

Rich, R.A., 1979: Fluid inclusion evidence of Silurian evaporites in southeastern Vermont. *Bull. Geol. Soc. Am.*, 90, pp.1628-1643.

Robert, F. and Brown, A.C. 1986: Archaean gold-bearing quartz veins at the Sigma Mine, Abitibi Greenstone Belt, Quebec: Part I. Geological relations and formation of the vein system. *Econ. Geol.*, 81, pp.578-592.

Roedder, E., 1984: Fluid inclusions. *Min. Soc. Am.*, Reviews in Mineralogy, Vol. 12, 646pp.

Roering, C., Van Reenen, D.D., De Beer, J.H., Smit, C.A., Barton, J.M., Jr., De Wit, M.J., Stettler, E.G., Van Schalkwyk, J.F., Stevens, G. and Pretorius, S., 1992 a: Tectonic model for the evolution of the Limpopo Belt. *Precamb. Res.*, 55, pp.539-552.

Roering, C., Van Reenen D.D., de Wit, M.J., Smit, C.A., de Beer, J.H. and van Schalkwyk J.F., 1992 b: Structural, geological and metamorphic significance of the Kaapvaal Craton-Limpopo Belt contact. *Precamb. Res.*, 55, pp.69-80.

Roering, C., van Reenen, D.D., Smit, C.A. and du Toit, R., 1995: Deep crustal embrittlement and fluid flow during granulite metamorphism in the Limpopo Belt, South Africa. *J. Geol.*, 103, pp.673-686.

Rollinson, H.R. and Windley, B.F., 1980: An Archean granulite grade tonalite-trondhjemite- granite suite from Scourie, northwest Scotland: Geochemistry and origin. *Contrib. Min. Petrol.*, 72, pp.265-281.

Rollinson, H.R. and Berger, M., 1995: Geochemical constraints on Archaean Crustal Evolution from mafic granulites in the Limpopo Belt. Paper presented at Precambrian '95 Conference, Montreal, Aug.28-Sept.1.

Ruygrok, M., 1992: The tectono-metamorphic evolution of a portion of the Rhenosterkoppies greenstone belt in relation to the Limpopo geology, South Africa. M.Sc. Thesis (unpubl.), Rand Afrikaans Univ., Johannesburg, 226pp.

Sahama, T. G., 1936: Die Regelung von Quarz und Glimmer in den Gesteinen der Finnisch-Lappländischen Granulitformation. *Comm. Géol. de Finlande Bull.*, 113, pp.1-110.

Samson, I.M., Liu, W. and Williams-Jones, A.E., 1995: The nature of orthomagmatic fluids in the Oka carbonatite, Quebec, Canada: Evidence from fluid inclusions. *Geochem. Cosmochim. Acta*, 59, pp.1963-1977.

Sander, B., 1950: Einführung in die Gefügekunde der Geologischen Körper. Springer, Berlin, Vienna, 1950, 409pp.

Saxena, S.K. and Fei, Y., 1987: Fluids at crustal pressures and temperatures I. Pure species. *Contrib. Min. Petrol.*, 95, pp.370-375.

Schidlowski, M., Eichmann, R. and Junge, C.E., 1975: Precambrian sedimentary carbonates: C and O isotope geochemistry implications for the terrestrial oxygen budget. *Precamb. Res.*, 2, pp.1-69.

Scott, S.D., 1983: Chemical behaviour of sphalerite and arsenopyrite in hydrothermal and metamorphic environments. *Min. Magaz.*, Dec. 1983, 47, pp.427-435.

Segall, P., 1984: Rate-dependent extensional deformation resulting from crack growth in rock. *J. Geophys. Res.*, 89, pp.4185-4195.

Segall, P., 1989: Earthquakes triggered by fluid extraction. *Geology*, 17, pp.942-946.

Silverstone, J., Morteani, G. and Staude, J.-M., 1991: Fluid channelling during ductile shearing: transformation of granodiorite into aluminous schist in the Tauern Window, Eastern Alps. *J. Met. Geol.*, 9, pp.419-431.

Seward, T.M., 1984: The transport and deposition of gold in hydrothermal systems. pp.165-182 *In: Proceedings of Gold '82: the Geology, Geochemistry and Genesis of Gold Deposits*, R.P., Foster (eds.), *Geol. Soc. Zimbabwe, Spec. Publ. 1*, 753pp.

Shankland, T.J., and Ander, M.C., 1983: Electrical conductivity, temperatures and fluids in the lower crust. *J. Geophys. Res.*, 8, pp.9475-9484.



Sibson, R.H., 1983: Continental fault structure and the shallow earthquake source. *J. Geol. Soc.*, London, 140, pp.741-767.

Sibson, R.H., Robert, F., and Poulsen, H., 1988: High angle faults, fluid pressure cycling and mesothermal gold quartz deposits. *Geology*, 16, pp.551-555.

Sieber, T.J., 1991: Styles of hydrothermal alteration in Archaean rocks of the Northern Kaapvaal craton, South Africa, with implications for gold mineralization. Ph.D. Thesis (unpubl.), Rand Afrikaans Univ., Johannesburg, 263pp.

Smit, C.A., 1983: Petrochemistry and tectonic significance of a chromite-bearing ultramafic suite of rocks in the Limpopo metamorphic complex, South Africa. *Trans. Geol. Soc. S. Afr.*, 87, pp.303-314.



Smit, C.A., Roering, C., and Van Reenen D.D., 1992: The structural framework of the southern margin of the Limpopo Belt, South Africa. *Precamb. Res.*, 55, pp.51-58: 11-5.

Smit, C.A. and van Reenen, D.D., 1997: Deep crustal shear zones, high-grade tectonites, and associated metasomatic alteration in the Limpopo Belt, South Africa: Implications for deep crustal processes. *J. Geol.*, 105, pp.35-37.

Spera, F.J., 1987: Dynamics of Translithospheric Migration of Metasomatic fluid and Alkaline Magma. In: M.A. Menzies and C.J. Hawkesworth (eds.), *Mantle Metasomatism*. Academic Press, London, pp.1-20.

Spooner, E.T.C., Wood, P.C., Burrows, D.R., Thomas, A.V. and Noble, S.R., 1985:  
 Geological fluid inclusion, and isotopic (carbon and sulphur) studies of Au-quartz-carbonate  
 -pyrite-scheelite vein mineralisation and intrusion hosted Cu-(Au-Mo) mineralisation in the  
 Hollinger-McIntyre system, Timmins, Ontario. Grant 236, pp.229-246 *In: Geoscience  
 Research Grant Program, Summary of Research 1984-1985*, V.G. Milne, (eds.), *Ontario  
 Geol. Surv. Misc. Paper*, 127, 246pp.

Stern, C.R., Huang, W.L. and Wyllie, P.J., 1975: Basalt-andesite-rhyolite-H<sub>2</sub>O  
 crystallisation intervals with excess H<sub>2</sub>O and H<sub>2</sub>O-undersaturated liquidus surfaces to 35  
 kilobars, with implications for magma genesis. *Earth Planet. Sci. Lett.*, 28, pp.189-196.

Stevens, G. and Van Reenen, D.D., 1992: Constraints on the form of the P-T loop  
 in the Southern Marginal Zone of the Limpopo Belt, South Africa. *Precamb. Res.*, 55,  
 pp.279-296: 11-5.

Stevens, G., 1995: Melting carbonic fluids and water recycling in the deep crust:  
 an example from the Limpopo Belt, South Africa. *EGRU*, Univ. of the Witwatersrand,  
 Johannesburg, Inf. Cir. 290, 24pp.

Thompson, A.B., and Connolly, J.A.D., 1990: Metamorphic fluids and  
 anomalous porosities in the lower crust. *Tectonophys.*, 182, pp. 47-56.

Thompson, A.B. and Connolly, J.A.D., 1992: Migration of metamorphic fluid:  
 some aspects of mass and heat transfer. *Earth Sci. Rev.*, 32, pp.107-121, 1/2.

- Touret, J., 1981: Fluid inclusions in high-grade metamorphic rocks. pp.182-208  
*In: Short Course in Fluid Inclusions: Applications to Petrology*, L.S. Hollister and M.L. Crawford (eds.), *Min. Assoc. Can.*, 6, 304pp.
- Touret, J.L.R., 1985: Fluid regime in southern Norway: the record of fluid inclusion.  
*In: Tobi, A.C. and Touret, J.R.L. (eds.), The deep Proterozoic crust in the North Atlantic provinces*. Reidel, Dordrecht, pp.517-549.
- Touret, J.R.L., 1995: Brines in granulites: the other fluid (Abstract). *ECROFI* (European Conference on Fluid Inclusions): Barcelona, 1995.
- Touret, J., and Dietvorst, P., 1983: Fluid inclusions in high-grade anatectic metamorphites. *J. Geol. Soc. London*, 140, pp.635-649.
- Touret, J. and Hansteen, T.H., 1988: Geothermobarometry and fluid inclusions in a rock from the Dodola Betta charnockite complex, SW India. *Rendiconti della Societa Italiana di Mineralogia e Petrologia*, 43, pp.65-82.
- Tsunogae, T., Miyano, T. and Ridley, J., 1992: Metamorphic PT profiles from the Zimbabwean Craton to the Limpopo Belt, Zimbabwe. *Precamb. Res.*, 55, pp.259-277.
- Tuccillo, M.E., Essene, E.J. and van der Pluijm, B.A., 1990: Growth and retrograde zoning in garnets from high-grade metapelites: Implications for pressure-temperature paths. *Geology*, 18, pp.839-842.

Turner, F. J. and Verhoogen, J., 1960: Igneous and Metamorphic Petrology. McGraw-Hill, New York, pp.602.

Turner, F. J. and Weiss, L. E., 1963: Structural analysis of metamorphic tectonites. McGraw-Hill, New York, pp.545.

Van den Kerkhof, A.M., 1990: Isochoric phase diagrams in the systems CO<sub>2</sub>-CH<sub>4</sub> and CO<sub>2</sub>-N<sub>2</sub>: Applications to fluid inclusions. *Geochem. et Cosmochim. Acta*, 54, pp.621-629.

Van Reenen, D.D., 1978: Metamorfe studies van granoliete en verwante hoe-graadse gesteentes in die duideliete grenssone vandie Limpopo-metamorfekompleks in Suid-Afrika. Ph.D. Thesis, (unpublish.), Rand Afrikaans Univ. Johannesburg, South Africa.

Van Reenen, D.D., 1986: Hydration of cordierite and hypersthene and a description of the retrograde orthoamphibole isograd in the Limpopo Belt, South Africa. *Am. Min.*, 71, pp.900-915.

Van Reenen, D.D., Barton, J.M., Jr., Roering, C., Smit, C.A. and Van Schalkwyk, J.F., 1987: Deep crustal response to continental collisions: the Limpopo Belt of Southern Africa. *Geology*, 15, pp.11-14.

Van Reenen, D.D. and Hollister, L.S., 1988: Fluid inclusions in hydrated granulite facies rocks, Southern Marginal Zone of the Limpopo Belt, South Africa. *Geochem. Cosmochim. Acta*, 52, pp.1057-1064.

Van Reenen, D.D., Roering, C., Smit, C.A., Van Schalkwyk, J.F. and Barton, J.M., Jr., 1988: Evolution of the northern high-grade margin of the Kaapvaal craton, South Africa. *J. Geol.*, 96: pp.548-559.

Van Reenen, D.D., Roering, C., Brandl, G., Smit, C.A. and Barton, J.M., 1990: The granulite-facies rocks of the Limpopo Belt, Southern Africa. In: D. Vielzeuf and P. Vidal (eds.), *Granulites and Crustal Evolution. NATO Adv. Stud., Inst., Ser.*, 311. Kluwer, Dordrecht, pp.257-289.



Van Reenen, D.D., Du Toit, R., Hoernes, S., Roering, C. and Smit, C.A., 1993: CO<sub>2</sub>-rich fluids and potassium metasomatism associated with deep crustal (granulite-facies) shear zones in the Limpopo Belt, South Africa. *Abstr. USA*.

Van Reenen, D.D., Pretorius, A.I. and Roering, C., 1994: Characterization of fluids associated with gold mineralization and with regional retrogression of granulites in the Limpopo Belt, South Africa. *Geochem. Cosmochim. Acta*, 58, pp.1147-1159.

Van Reenen, D.D., McCourt, S. and Smit, C.A., 1995: Are the Southern and Northern Marginal Zones of the Limpopo Belt related to a single continental collisional event?. *S. Afr. J. Geol.*, 94/4, pp.489-504.

- Van Schalkwyk, J.F. and Van Reenen, D.D., 1992: High-temperature hydration of ultramafic granulites from the Southern Marginal Zone of the Limpopo Belt by infiltration of CO<sub>2</sub>-rich fluid. *Precamb. Res.*, 55, pp.337-352.
- Vearncombe, J.R., 1992: Archaean gold mineralisation in a normal-motion shear zone at Harbour Lights, Leonora, Western Australia. *Min. Dep.*, 27, pp.182-191.
- Vennemann, T.W. and Smith, H.S., 1992: Stable isotope profile across the amphibolite-granulite facies transition in the Southern Marginal Zone of the Limpopo Belt, South Africa. *Precamb. Res.*, 55, 1-4, pp.365-397.
- Viljoen, M.J. 1984: Archaean gold mineralisation and komatiites in southern Africa. In: *Gold '82*, R.P. Foster (eds.), pp.595-628. *Geol. Soc. Zimbabwe, Spec. Publ.* 1. Rotterdam, Balkema.
- Walther, J.V., and Orville, P.M., 1982: Volatile production and transport in regional metamorphism. *Contrib. Min. Petrol.*, 79, pp.252-257.
- Wang, L.G., McNaughton, N.J. and Groves. D.I., 1993: An overview of the relationship between granitoid intrusions and gold mineralisation in the Archaean Murchison Province, Western Australia. *Min. Dep.*, 28, 6, pp.482-494.
- Watson, E.D. and Brenan, J.M., 1987: Fluids in the lithosphere, 1. Experimentally-determined wetting characteristics of CO<sub>2</sub>-H<sub>2</sub>O fluids and their implications

for fluid transport, host-rock physical properties, and fluid inclusion formation. *Earth Planet. Sci. Lett.*, 85, pp.497-515.

Weilers, B.F., 1956: The geology of the Klein Letaba gold mine in the Sutherland range, northeastern Transvaal. *Ann. Univ. Stellenbosch.*, 33. Serie A, 6-11.

Wells, P.R.A., 1979: Chemical and thermal evolution of Archean sialic crust, southern west Greenland. *J. Petrol.*, 20, pp.187-226.

Whittaker, E.J.W., 1960: The crystal chemistry of amphiboles. *Acta Cryst.*, 13, pp.291-294.

Wood, B.J. and Walter, J.V., 1986: Fluid flow during metamorphism and its implications for fluid-rock ratios during greenschist facies metamorphism. In: J.V. Walter and B.J. Wood (eds.), *Fluid-Rock Interaction during Metamorphism*. Springer Verlag, New York, pp.89-108.

Wood, P.C., Thomas, A.V., Burrows, D.R., MacDonald, A.J., Noble, S.R. and Spooner, E.T.C., 1984: CO<sub>2</sub>-bearing low-moderate salinity fluids in Archean gold-quartz-carbonate-(W-Mo) vein deposits and magmatically derived Mo, W, Ta, and Sn mineralisation [abstr.], pp.700 in Abstracts with Programs, *Geol. Soc. Am. Bull.*, 16, pp.721.

Wood, P.C., Burrows, D.R., Thomas, A.V., and Spooner, E.T.C., 1986: The Hollinger-McIntyre Au-quartz vein system, Timmins, Ontario, Canada; Geologic

characteristics, fluid properties and light stable isotope geochemistry; pp.56-80 *In: Proceedings of Gold '86, an International Symposium on the Geology of Gold*, A.J. MacDonald (eds.), Konsult International Inc., Toronto, 517pp.

Woodsworth, G.J., 1977: Homogenization of zoned granets from pelitic schists. *Can. Min.*, 15, pp.230-242.

Wyman, D.A. and Kerrich, R., 1988: Alkaline magmatism, major structures and gold deposits: implications for greenstone belt metalogeny. *Econ. Geol.*, 83, pp.454-461.

Yardley, B.W.D., 1977: An empirical study of diffusion in garnet. *Am. Min.*, 62, pp.793-800.



UNIVERSITY  
OF  
JOHANNESBURG



**APPENDIX I:**

**DATA OF STRUCTURAL GEOLOGY**



UNIVERSITY  
OF  
JOHANNESBURG

**TABLE IA**  
**LONG AXIS OF QUARTZ BOUDINS DATA**

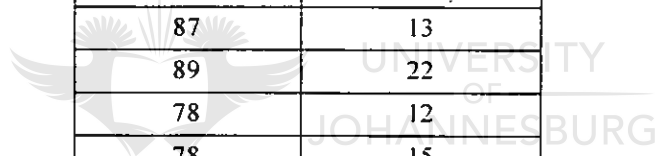
Long axis of boudine	Plunge of boudine
82	16
83	12
100	33
78	15
87	12
67	16
66	15
69	18
278	17
269	11
91	18
89	22
78	17
92	12
271	34
278	45
90	10
251	22
262	15
279	18
92	16
274	17
277	18
88	12
266	10
80	11
82	12
67	17
60	13
79	13
78	12
78	11
260	12
258	3
89	22
78	12
266	16
82	12
78	13

**TABLE IB  
LINEATION STRIKE DATA**

Lineation	Plunge
85	15
80	12
100	37
80	15
78	12
67	19
79	13
266	13
78	17
69	11
90	12
90	12
91	13
92	34
271	15
278	12
250	13
252	15
249	14
90	10
100	11
92	16
274	17
270	16
270	12
266	10
80	12
80	11
82	12
67	17
60	13
100	10
101	19
96	24
107	11
67	22
78	12
79	13

Lineation	Plunge
78	12
78	11
260	12
267	14
268	10
260	9
266	7
258	3
278	0
255	2
87	4
76	3
89	12
78	2
77	7
79	13
80	12
78	23
79	12
83	12
88	12
87	12
90	2
291	7
273	8
270	18
273	20
278	34
231	45
238	51
242	34
249	44
250	33
256	28
267	19
270	12
289	12
289	13

Lination	Plunge
273	45
267	16
78	12
78	34
77	23
84	12
89	13
90	12
85	11
81	12
82	22
83	15
83	12
86	12
86	21
87	12
87	12
87	13
89	22
78	12
78	15
100	12
101	17
103	45
100	12
90	7
278	23
267	13
267	16
270	8
271	18
266	16
267	13
256	12



**TABLE IC  
DIP DIRECTION DATA**

Dip	Plunge
350	78
345	82
356	56
359	67
349	59
348	78
337	88
349	88
348	87
331	67
328	76
333	67
332	74
328	65
355	76
360	88
2	88
5	76
12	69
360	77
345	56
351	66
356	72
345	69
359	78
347	66
357	65
344	45
345	67
327	87
161	89
160	78
178	45
189	87
160	63
154	45
131	67
178	67

Dip	Plunge
189	87
196	90
200	80
202	83
187	67
166	55
167	59
172	65
163	56
185	69
345	78
356	89
329	67
330	56
356	78
290	78
358	69
359	88
358	67
356	89
351	67
178	56
189	45
145	66
149	80
169	69
201	62
178	67
189	49
184	58
158	52
350	59
342	67
345	79
1	77
2	89
10	71
12	82

Dip	Plunge
359	59
342	65
345	28
333	68
354	76
357	90
355	90
345	89
310	45
301	67
345	78
312	76
338	80
328	77
345	82
333	65
309	45
328	87
339	67
336	45
22	67
23	90
349	76
352	78
345	76
345	67
333	87
345	78
360	90
1	82
355	79
351	79
342	60
358	89
356	79
345	48
34	67
352	89
339	89
8	88
10	89
45	49
67	67

Dip	Plunge
56	49
49	74
34	78
27	89
20	78
18	76
17	78
15	75
12	89
10	90
8	67
345	78
359	78
345	67
9	89
2	78
1	69
345	80
356	71
8	78
6	89
2	80
359	67
356	89
356	72
358	61
360	81
345	78
354	67
332	56
328	34
360	59
345	56
356	61
359	67
345	56
344	49
356	89
23	56
16	69
12	45
6	78
5	90

Dip	Plunge
1	68
0	67
331	49
345	67
348	65
176	78
176	45
165	78
156	76
145	58
165	77
180	87
178	79
193	78
187	69
169	69
134	56
124	57
128	35
110	23
145	58
157	34
137	89
156	47
167	78
189	56
194	89
210	89
200	79
203	67
194	78
180	90
183	67
187	72
198	75
189	70
175	78
178	77
179	86
173	71
168	45
356	87
360	57

Dip	Plunge
337	67
359	67
339	65
345	67
347	61
348	63
348	67
345	82
357	49
348	86
347	56
356	78
358	69
357	86
360	58
358	68
347	69
358	59
360	56
358	49
352	75
357	75
360	47
360	78
2	67
5	65
8	79
6	87
9	90
9	89
12	59
13	67
2	79
5	78
347	69
358	69
360	58
360	59
346	59
357	78
12	56
1	81
7	69

Dip	Plunge
5	79
348	79
358	65
279	59
354	69
358	54
348	67
3	78
12	89
7	85
345	78
352	68
356	59
351	67
354	76
360	47
2	69
349	69
342	76
351	72
360	56
348	67
357	49
2	78
342	56
347	63
348	68
347	56
346	73
341	73
356	72
348	65
341	59
353	49
162	78
356	67
173	69
182	67
183	49
187	78
169	65
167	59
167	78

Dip	Plunge
167	78
175	78
173	86
174	89
175	85
179	84
179	83
178	82
180	79
182	84
180	89
175	85
174	85
176	78
175	83
176	84
176	83
174	89
176	83
175	83
172	85
176	85
171	85
174	85
17	45
174	89
354	87
356	84
346	78
360	65
6	67
7	77
168	87
175	75
185	76
354	86
351	78
357	68
347	67
356	89
358	78
351	58
357	69



Dip	Plunge
353	76
351	78
354	67
354	78
357	69
354	79
356	87
354	68
352	78
351	78
352	71
354	76
352	79
351	75
7	82
345	72
358	59
356	79
346	72
349	67
348	62
349	67
359	69
348	59
358	87
352	76
354	79
354	69
358	83
357	84
356	86
354	76
346	58
354	38
359	58
5	67
4	89
167	79
176	78
186	79
190	65
189	67
178	87

Dip	Plunge
167	59
178	69
187	87
172	76
169	67
176	75
175	89
175	76
179	67
168	73
3	78
5	89
176	78
179	68
180	65
167	58
187	49
2	87
349	72
345	67
354	76
357	68
356	59
351	61
357	45
359	83

UNIVERSITI  
 OF  
 JOHANNESBURG

**APPENDIX II:**

**MICROPROBE ANALYSES (SILICATES &  
CARBONATES)**



**TABLE IIA: MICROPROBE GARNET ANALYSES**

	DH 2035-1	DH 2035-2	DH 2035-3	DH 2035-4	DH 2035-5	DH 2035-6	DH 2035-7	DH 2035-8	DH 2035-9	DH 2035-10	DH 2035-11	DH 2035-12*	DH 2035-13	DH 2035-14
SiO <sub>2</sub>	38.29	37.37	37.92	37.75	37.73	37.17	38.01	38.29	37.71	37.56	37.83	37.05	36.90	36.85
Al <sub>2</sub> O <sub>3</sub>	21.53	20.58	20.30	22.82	20.88	20.50	20.81	21.34	19.83	20.85	20.84	21.28	20.55	20.79
TiO <sub>2</sub>	0.36	-	0.07	-	0.05	0.08	-	0.02	0.11	-	0.07	0.02	-	0.10
Cr <sub>2</sub> O <sub>3</sub>	-	-	0.07	0.02	0.04	0.04	0.02	0.02	0.26	0.20	0.27	0.09	0.17	0.12
FeO	18.70	32.44	32.99	31.66	32.20	33.90	33.32	32.19	34.32	33.18	32.13	32.93	33.21	33.23
MnO	0.41	2.68	2.62	2.56	2.37	1.89	1.36	1.55	1.48	1.54	1.36	1.58	1.35	1.49
MgO	15.88	0.99	1.03	1.02	1.19	1.24	1.22	1.20	1.10	1.27	1.36	1.55	1.34	1.33
CaO	5.11	6.01	6.00	6.06	5.97	5.43	5.21	4.99	5.21	5.09	5.74	5.64	6.15	6.50
TOTAL	100.27	100.06	100.99	100.88	100.43	100.24	99.94	99.59	100.03	99.69	99.59	100.14	99.68	100.42
Si	5.73	6.04	6.08	5.94	6.05	6.01	6.11	6.14	6.11	6.07	6.09	5.96	5.99	5.95
Al	3.80	3.92	3.84	4.23	3.95	3.91	3.94	4.03	3.79	3.97	3.95	4.04	3.93	3.95
Ti	0.40	-	0.01	-	0.01	0.01	-	-	0.01	-	0.01	-	-	0.01
Cr	-	-	0.01	-	0.01	0.01	-	-	0.03	0.03	0.03	0.01	0.02	0.02
Fe	2.34	4.39	4.42	4.17	4.32	4.59	4.48	4.32	4.65	4.48	4.32	4.43	4.51	4.48
Mn	0.05	0.37	0.36	0.34	0.32	0.26	0.19	0.21	0.20	0.21	0.19	0.22	0.19	0.20
Mg	3.54	0.24	0.25	0.24	0.28	0.30	0.29	0.29	0.27	0.31	0.33	0.37	0.32	0.32
Ca	0.82	1.04	1.03	1.02	1.03	0.94	0.90	0.86	0.90	0.88	0.99	0.97	1.07	1.12
Andradite	0.9	-	0.2	-	0.1	0.2	-	-	0.3	-	0.2	-	-	0.2
Uwarovite	-	-	0.2	-	0.1	0.1	-	-	0.6	0.5	0.7	0.2	0.4	0.3
Almandine	46.2	77.0	77.1	76.6	76.9	79.6	81.1	80.6	80.8	80.4	78.5	78.8	78.7	77.7
Spessartine	1.0	6.4	6.1	6.2	5.7	4.4	3.3	3.9	3.5	3.7	3.3	3.8	3.2	3.5
Pyrope	39.2	2.4	2.4	2.5	2.8	2.9	3.0	3.0	2.6	3.1	3.3	3.7	3.2	3.1
Grossular	12.6	14.3	14.0	14.7	14.3	12.8	12.7	12.5	12.3	12.3	14.0	13.5	14.6	15.2

	DH 2035-15	DH 2035-16	DH 2035-17	DH 2035-18	DH 2035-19	DH 2035-20	DH 2035-21	DH 2035-22	DH 2035-23	DH 2035-24	DH 2035-25	DH 2035-26	DH 2035-27	DH 2035-28
SiO <sub>2</sub>	37.45	36.81	37.41	36.50	37.11	38.06	37.67	37.23	36.38	37.02	37.30	36.84	37.35	37.53
Al <sub>2</sub> O <sub>3</sub>	20.72	20.33	20.90	20.95	20.91	21.06	20.98	20.75	20.19	20.67	20.98	21.54	21.91	20.49
TiO <sub>2</sub>	-	-	0.09	0.05	-	0.09	0.01	-	-	-	0.01	0.06	0.23	0.04
Cr <sub>2</sub> O <sub>3</sub>	0.07	0.10	0.07	0.11	0.06	0.09	0.13	0.10	0.14	0.13	0.01	-	0.69	0.18
FeO	32.70	34.05	33.35	33.67	33.89	33.37	33.06	33.33	36.84	36.63	34.38	35.77	33.79	33.35
MnO	1.16	0.54	0.39	0.39	0.30	0.33	0.31	0.69	0.65	0.74	0.37	0.09	0.26	0.72
MgO	1.57	1.60	1.94	2.21	2.67	2.92	2.84	2.47	2.51	2.49	2.24	6.62	5.57	1.51
CaO	6.25	5.76	6.24	6.27	5.40	5.19	5.03	5.16	2.41	2.20	4.46	0.07	0.19	6.95
TOTAL	99.92	99.20	100.39	100.14	100.34	101.11	100.02	99.74	99.12	99.88	99.74	99.99	99.99	100.77

Si	6.03	6.00	5.99	5.89	5.95	6.02	6.02	6.00	5.97	5.78	6.01	5.83	5.91	6.01
Al	3.93	3.91	3.95	3.98	3.95	3.93	3.95	3.94	3.90	3.80	3.99	4.01	4.09	3.87
Ti	-	-	0.01	0.01	-	0.01	-	-	-	-	-	0.10	0.03	-
Cr	0.01	0.01	0.01	0.01	0.01	0.01	0.02	0.01	0.02	0.02	-	-	0.09	0.02
Fe	4.41	4.64	4.47	4.54	4.55	4.42	4.42	4.49	5.05	4.78	4.63	4.73	4.47	4.47
Mn	0.16	0.07	0.05	0.05	0.04	0.05	0.04	0.09	0.09	0.98	0.05	0.01	0.04	0.10
Mg	0.38	0.39	0.46	0.53	0.06	0.69	0.68	0.59	0.61	0.58	0.54	1.56	1.32	0.36
Ca	1.08	1.01	1.07	1.08	0.93	0.88	0.86	0.89	0.42	0.37	0.77	0.01	0.03	1.19

Anhydrite	-	-	0.2	0.1	-	0.2	-	-	-	-	-	0.1	0.6	0.1
Uvanovite	0.2	0.2	0.2	0.3	0.1	0.2	0.3	0.2	0.3	0.3	-	-	1.7	0.4
Almandine	78.3	81.0	79.3	78.9	80.1	79.5	79.9	79.8	86.6	86.8	82.9	83.4	83.0	78.0
Spessartine	2.8	1.3	0.9	0.9	0.7	0.8	0.7	1.7	1.5	1.8	0.9	0.2	0.6	1.7
Pyrope	3.8	3.8	4.6	5.2	6.3	7.0	6.9	5.9	5.9	5.9	5.4	15.4	13.7	3.5
Grossular	15.0	13.7	14.8	14.7	12.8	12.4	12.2	12.4	5.7	5.2	10.8	0.2	0.5	16.3

	DII 2035-29	DII 2035-30	DII 2035-31	DII 2035-32	DII 2035-33	DII 2035-34	DII 2035-35	DII 2035-36	DII 2035-37	DII 2035-38	DII 2035-39	DII 2035-40	DII 2035-41	DII 2035-42
SiO <sub>2</sub>	36.72	37.49	36.11	37.80	37.01	36.98	36.33	38.50	41.77	38.37	38.39	38.68	36.83	38.23
Al <sub>2</sub> O <sub>3</sub>	20.97	21.00	20.75	20.98	21.07	20.93	20.87	20.95	22.61	21.85	21.88	21.68	21.96	21.69
TiO <sub>2</sub>	0.01	0.10	0.04	-	0.06	-	0.02	-	0.41	0.05	0.08	-	-	0.03
Cr <sub>2</sub> O <sub>3</sub>	0.08	0.13	0.03	0.18	0.18	0.10	0.06	0.14	0.02	0.14	0.14	0.18	0.08	0.04
FeO	33.75	32.56	33.44	32.39	32.40	32.83	34.75	33.79	12.02	31.77	31.53	31.42	32.42	31.63
MnO	0.45	0.30	0.82	0.74	0.57	0.49	0.48	0.57	0.45	0.63	0.44	0.35	0.40	0.33
MgO	1.80	2.06	1.51	1.61	1.68	2.38	2.10	2.44	17.38	2.94	3.09	3.02	2.80	2.58
CaO	6.62	6.28	6.82	6.40	6.49	6.07	5.70	3.53	5.28	5.04	4.99	5.21	5.58	5.52
TOTAL	100.40	99.90	99.52	100.11	99.46	99.78	100.31	99.93	99.94	99.99	100.54	100.55	100.08	100.05

Si	5.91	6.01	5.89	6.05	5.98	5.96	5.88	6.15	6.03	6.04	6.04	6.09	5.89	6.06
Al	3.98	3.97	3.99	0.40	4.01	3.97	3.98	3.94	3.85	4.05	4.06	4.02	4.14	4.05
Ti	-	0.01	0.01	-	0.01	-	-	-	0.05	0.01	0.01	-	-	-
Cr	0.01	0.02	-	0.02	0.02	0.01	0.01	0.02	-	0.02	0.02	0.02	0.01	-
Fe	4.55	4.37	4.56	4.34	4.38	4.42	4.70	4.51	1.45	4.18	4.15	4.13	4.33	4.19
Mn	0.06	0.04	0.11	0.10	0.08	0.07	0.07	0.08	0.06	0.08	0.06	0.05	0.05	0.05
Mg	0.43	0.49	0.37	0.38	0.41	0.57	0.51	0.58	3.74	0.69	0.73	0.71	0.67	0.61
Ca	1.14	1.08	1.19	1.10	1.12	1.04	0.99	0.60	0.82	0.85	0.84	0.88	0.96	0.94

Andradite	-	0.2	0.1	-	0.1	-	-	-	1.2	0.1	0.2	-	-	-
Uvarovite	0.2	0.3	-	0.4	0.4	0.2	0.1	0.3	-	0.3	0.3	0.4	0.2	0.1
Almandine	79.0	78.5	78.4	78.4	78.3	78.4	80.6	83.5	33.8	78.3	78.3	78.2	78.5	78.9
Spessartine	1.1	0.7	1.9	1.8	1.4	1.2	1.1	1.4	1.3	1.6	1.1	0.9	1.0	0.8
Pyrope	4.2	5.0	3.5	3.9	4.1	5.7	4.9	6.0	48.9	7.2	7.7	7.5	6.8	6.4
Grossular	15.5	15.1	16.0	15.5	15.7	14.5	13.2	8.7	14.9	12.4	12.4	13.0	13.5	13.8

	DH 2035-43	DH 2035-44	DH 2035-45	DH 2035-46	DH 2035-47	DH 2035-48	DH 2035-49	DH 2035-50	DH 2035-51	DH 2035-52	DH 2035-53	DH 2035-54	DH 2035-55	DH 2035-56
SiO <sub>2</sub>	36.93	36.80	37.64	37.05	37.65	33.07	36.75	36.93	37.32	37.09	36.59	36.86	36.43	38.25
Al <sub>2</sub> O <sub>3</sub>	21.75	20.56	21.11	21.66	21.58	20.61	20.47	21.31	21.58	21.96	21.29	21.03	21.01	21.06
TiO <sub>2</sub>	-	-	-	-	0.07	0.09	0.22	-	-	-	-	0.03	-	0.01
Cr <sub>2</sub> O <sub>3</sub>	0.14	0.10	0.08	0.12	0.16	0.20	0.17	0.16	0.08	0.17	0.11	0.18	0.10	0.19
FeO	32.78	33.97	32.76	32.19	31.84	33.94	33.12	32.54	32.60	33.21	33.00	31.66	32.24	31.88
MnO	0.46	0.54	0.50	0.32	0.37	0.39	0.45	0.40	0.40	0.27	0.75	1.52	1.81	1.58
MgO	2.51	3.54	2.21	2.83	2.88	5.54	5.35	2.62	3.65	3.36	1.76	1.11	1.06	1.11
CaO	5.17	4.19	5.17	5.52	5.36	5.49	4.94	5.06	4.74	3.73	6.64	7.18	6.55	6.06
TOTAL	99.73	99.70	99.47	99.68	99.90	99.33	99.47	99.02	99.78	99.79	100.15	99.57	99.18	100.15

Si	5.93	5.94	6.05	5.95	6.00	5.44	5.82	5.96	5.93	5.93	5.90	5.97	5.94	6.12
Al	4.11	3.91	4.00	4.10	4.05	4.00	3.82	4.06	4.04	4.14	4.04	4.01	4.04	3.97
Ti	-	-	-	-	0.01	0.01	0.03	-	-	-	-	-	-	-
Cr	0.02	0.01	0.01	0.02	0.02	0.03	0.02	0.02	0.01	0.02	0.01	0.02	0.01	0.02
Fe	4.40	4.59	4.40	4.33	4.24	4.67	4.39	4.40	4.33	4.44	4.45	4.29	4.40	4.26
Mn	0.06	0.07	0.07	0.04	0.05	0.05	0.06	0.05	0.05	0.04	0.10	0.21	0.25	0.21
Mg	0.60	0.85	0.53	0.68	0.68	1.36	1.26	0.63	0.87	0.80	0.42	0.27	0.26	0.26
Ca	0.89	0.72	0.89	0.95	0.92	0.97	0.74	0.88	0.81	0.64	1.15	1.24	1.14	1.04

Andradite	-	-	-	-	0.2	0.2	0.5	-	-	-	-	-	-	-
Uvarovite	0.3	0.2	0.2	0.3	0.4	0.4	0.4	0.4	0.2	0.4	0.3	0.4	0.2	0.5
Almandine	79.8	80.2	80.5	78.6	78.3	74.3	74.8	79.8	78.6	81.5	78.1	76.0	77.2	78.1
Spessartine	1.1	1.3	1.2	0.8	0.9	0.9	1.0	1.0	1.0	0.7	1.8	3.6	4.3	3.9
Pyrope	6.1	8.4	5.4	6.9	7.1	12.1	12.1	6.4	8.8	8.2	4.2	2.7	2.5	2.7
Grossular	12.6	9.9	12.7	13.5	13.2	12.0	11.2	12.4	11.4	9.2	15.7	17.2	15.7	14.8

	DH 2035-57	DH 2035-58	DH 2035-59	DH 2035-60	DH 2035-61	DH 2035-62	DH 2035-63	DH 2035-64	DH 2035-65	DH 2035-66	DH 2035-67	DH 2035-68	DH 2035-69	DH 2035-70
SiO <sub>2</sub>	37.93	37.37	37.60	37.91	37.41	37.27	37.65	37.72	36.00	37.59	37.52	37.29	37.81	38.13
Al <sub>2</sub> O <sub>3</sub>	21.25	20.61	20.86	21.40	20.68	20.68	20.73	20.45	19.76	20.70	20.68	20.91	20.91	22.03
TiO <sub>2</sub>	0.07	0.15	-	-	0.11	-	0.07	-	3.64	-	0.14	0.08	0.07	0.05
Cr <sub>2</sub> O <sub>3</sub>	0.14	0.26	0.02	0.17	0.05	0.04	0.05	0.15	0.23	0.13	0.08	0.08	0.13	0.08
FeO	32.46	33.96	32.44	30.91	32.62	32.06	32.02	33.77	31.37	33.57	33.56	32.63	33.38	31.16
MnO	1.74	1.73	2.29	2.64	2.59	2.51	2.41	1.81	1.83	1.55	1.53	1.12	0.80	0.46
MgO	1.56	1.10	0.97	0.94	0.95	1.01	0.99	1.09	1.78	1.12	1.28	1.63	1.60	2.01
CaO	5.12	5.06	5.62	6.01	5.48	6.13	5.74	5.00	5.45	5.27	5.09	5.95	5.22	5.59
TOTAL	100.26	100.25	99.80	99.97	99.88	99.71	99.66	100.01	100.06	99.93	99.87	99.69	99.91	99.51

Si	6.06	6.03	6.07	6.08	6.05	6.04	6.08	6.10	5.80	6.07	6.06	6.01	6.07	6.07
Al	4.00	3.92	3.97	4.04	3.94	3.95	3.95	3.90	3.75	3.94	3.94	3.98	3.96	4.13
Ti	0.01	0.02	-	-	0.01	-	0.01	-	0.44	-	0.02	0.01	0.01	0.01
Cr	0.02	0.03	-	0.02	0.01	-	0.01	0.02	0.03	0.02	0.01	0.01	0.02	0.01
Fe	4.34	4.59	4.38	4.14	4.41	4.34	4.33	4.56	4.23	4.53	4.53	4.40	4.48	4.15
Mn	0.24	0.24	0.31	0.36	0.36	0.35	0.33	0.25	0.25	0.21	0.21	0.15	0.11	0.06
Mg	0.37	0.27	0.23	0.22	0.23	0.24	0.24	0.26	0.43	0.27	0.31	0.39	0.38	0.48
Ca	0.88	0.88	0.97	1.03	0.95	1.06	0.99	0.87	0.94	0.91	0.88	1.03	0.90	0.95

Andradite	0.2	0.4	-	-	0.3	-	0.2	-	8.2	-	0.3	0.2	0.2	0.1
Uvarovite	0.3	0.6	-	0.4	0.1	0.1	0.1	0.4	0.5	0.3	0.2	0.2	0.3	0.2
Almandine	79.0	80.4	78.5	76.0	78.0	76.8	77.6	80.8	70.8	80.6	80.5	78.6	81.0	79.2
Spessartine	4.2	4.1	5.5	6.5	6.2	6.0	5.8	4.3	4.1	3.7	3.7	2.7	1.9	1.2
Pyrope	3.8	2.6	2.3	2.3	2.3	2.4	2.4	2.6	4.0	2.7	3.1	3.9	3.9	5.1
Grossular	12.5	12.0	13.6	14.8	13.1	14.7	13.9	12.0	12.3	12.7	12.2	14.3	12.7	14.2

	DH 2035-71	DH 2035-72	DH 2035-73	DH 2035-74	DH 2035-75	DH 2035-76	DH 2035-77	DH 2035-78	DH 2035-79	DH 2035-80	DH 2035-81	DH 2035-82	DH 2035-83	DH 2035-84
SiO <sub>2</sub>	36.61	37.89	37.59	36.76	37.33	36.24	36.51	38.76	38.59	37.03	37.00	37.10	37.20	37.78
Al <sub>2</sub> O <sub>3</sub>	21.00	21.95	21.74	21.74	21.42	23.51	23.48	22.05	22.28	21.85	22.12	21.98	22.15	22.02
TiO <sub>2</sub>	-	0.11	-	0.02	0.12	0.67	0.46	-	0.03	0.05	-	-	-	0.04
Cr <sub>2</sub> O <sub>3</sub>	0.07	0.02	0.19	0.13	0.04	-	0.05	0.12	0.03	0.14	0.10	0.12	0.15	0.20
FeO	32.19	31.02	31.91	32.34	33.32	32.19	32.80	32.33	32.98	31.80	31.69	30.73	31.50	30.61
MnO	0.39	0.46	0.27	0.53	0.23	0.36	0.37	0.59	0.40	0.38	0.19	0.24	0.58	0.40
MgO	3.46	2.88	3.18	2.38	2.37	2.65	2.51	2.54	2.47	3.48	3.36	1.90	2.62	3.39
CaO	5.53	4.91	4.83	5.50	4.32	4.19	4.17	3.81	3.45	5.24	5.53	7.92	5.76	5.58
TOTAL	99.25	99.24	99.70	99.40	99.16	99.80	100.35	100.18	100.22	99.28	100.55	99.98	99.96	100.02

Si	5.91	6.04	5.99	5.92	6.01	5.77	5.79	6.12	6.10	5.90	5.89	5.92	5.93	5.98
Al	3.99	4.12	4.08	6.45	4.07	4.41	4.39	4.10	4.15	4.10	4.15	4.13	4.16	4.11
Ti	-	0.01	-	-	0.02	0.08	0.06	-	-	0.01	-	-	-	0.01
Cr	0.01	-	0.02	-	-	-	0.01	0.01	-	0.02	0.01	0.02	0.02	0.03
Fe	4.34	4.13	4.25	4.35	4.49	4.29	4.35	4.27	4.36	4.24	4.22	4.10	4.20	4.05
Mn	0.05	0.06	0.04	0.07	0.03	0.05	0.05	0.08	0.05	0.05	0.03	0.03	0.08	0.05
Mg	0.83	0.68	0.76	0.57	0.57	0.63	0.59	0.60	0.58	0.83	0.80	0.45	0.62	0.80
Ca	0.96	0.84	0.82	0.95	0.75	0.72	0.71	0.64	0.58	0.89	0.94	1.35	0.98	0.95

Andradite	-	0.3	-	-	0.3	1.7	1.1	-	-	0.1	-	-	-	0.1
Uvarovite	0.2	-	0.5	0.3	0.1	-	0.1	0.3	-	0.3	0.2	0.3	0.4	0.5
Almandine	77.3	78.8	79.0	79.1	82.5	80.4	81.3	82.1	83.9	77.4	77.5	75.1	77.6	76.1
Spessartine	0.9	1.2	0.7	1.3	0.6	0.9	0.9	1.5	1.0	0.9	0.5	0.6	1.4	1.0
Pyrope	8.3	7.3	7.9	5.8	5.9	6.6	6.2	6.4	6.3	8.5	8.2	4.6	6.5	8.4
Grossular	13.3	12.5	12.0	13.5	10.7	10.5	10.3	9.7	8.8	12.8	13.5	19.4	14.2	13.9



	DH 2035-85	DH 2035-86	DH 2035-87	DH 2035-88	DH 2035-89	DH 2035-90	DH 2035-91	DH 2035-92	DH 2035-93	DH 2035-94	DH 2035-95	DH 2035-96	DH 2035-97	DH 2035-98
SiO <sub>2</sub>	37.56	36.00	36.76	37.22	37.40	37.36	36.83	37.00	37.45	37.07	37.32	36.50	36.82	36.72
Al <sub>2</sub> O <sub>3</sub>	22.20	22.77	22.41	22.22	22.17	22.13	22.48	22.35	22.11	22.53	22.22	22.54	22.05	22.30
TiO <sub>2</sub>	0.01	-	0.02	0.05	0.07	0.02	-	-	-	0.05	0.01	0.02	-	0.03
Cr <sub>2</sub> O <sub>3</sub>	0.27	0.04	0.17	0.14	0.04	0.13	0.24	0.23	0.13	0.11	0.07	0.22	0.17	0.06
FeO	30.87	31.84	31.35	31.38	31.82	31.95	32.11	31.46	31.75	31.27	31.85	31.55	34.63	32.07
MnO	0.33	0.37	0.59	0.21	0.33	0.50	0.28	0.34	0.32	0.50	0.26	0.28	0.68	0.02
MgO	3.54	3.20	2.93	3.56	3.58	2.79	3.45	3.19	3.30	2.83	3.40	3.18	2.60	3.40
CaO	5.33	5.78	5.76	5.21	4.57	5.13	4.53	5.25	4.77	5.63	4.87	5.70	3.00	5.40
TOTAL	100.12	100.00	99.98	100.00	100.00	100.00	99.92	99.81	99.83	100.00	100.00	99.98	99.97	100.00

Si	5.94	5.75	5.86	5.91	5.93	5.96	5.86	5.89	5.92	5.89	5.93	5.82	5.91	5.85
Al	6.14	4.29	4.21	4.16	4.15	4.16	4.22	4.19	4.14	4.22	4.16	4.23	4.17	4.19
Ti	-	-	-	0.01	0.01	-	-	-	-	0.01	-	-	-	-
Cr	0.03	0.01	0.02	0.02	0.01	0.02	0.03	0.03	0.02	0.01	0.01	0.03	0.02	0.01
Fe	4.08	4.26	4.18	4.16	4.22	4.27	4.28	4.19	4.22	4.16	4.23	4.21	4.65	4.27
Mn	0.05	0.05	0.08	0.03	0.05	0.07	0.04	0.05	0.04	0.07	0.04	0.04	0.09	-
Mg	0.83	0.76	0.70	0.84	0.85	0.66	0.82	0.76	0.78	0.67	0.81	0.76	0.62	0.81
Ca	0.90	0.99	0.98	0.89	0.78	0.88	0.77	0.90	0.81	0.96	0.83	0.98	0.52	0.92

Andradite	-	-	-	0.1	0.2	-	-	-	-	0.1	-	-	-	-
Uvarovite	0.7	0.1	0.4	0.3	0.1	0.3	0.6	0.6	0.3	0.3	0.2	0.5	0.4	0.1
Almandine	76.5	77.2	76.8	77.4	78.7	78.9	79.1	77.7	78.8	77.4	78.7	77.1	84.3	78.4
Spessartine	0.8	0.9	1.4	0.5	0.8	1.2	0.7	0.8	0.8	1.2	0.6	0.7	1.7	-
Pyrope	8.8	7.8	7.2	8.8	8.9	6.9	8.5	7.9	8.2	7.0	8.4	7.8	6.3	8.3
Grossular	13.2	14.0	14.1	12.8	11.3	12.7	11.2	13.0	11.8	13.9	12.0	13.9	7.3	13.2

	DH 2035-99	DH 2035-100	DH 2035-101	DH 2035-102	DH 2035-103	DH 2035-104	DH 2035-105	DH 2035-106	DH 2035-107	DH 2035-108	DH 2035-109	DH 2035-110	DH 2035-111	DH 2035-112
SiO <sub>2</sub>	37.38	36.82	37.55	36.08	37.55	37.63	36.28	37.00	37.02	37.09	37.79	37.51	38.02	37.25
Al <sub>2</sub> O <sub>3</sub>	22.00	22.37	21.97	21.86	22.38	22.25	22.28	22.21	22.09	21.78	21.47	21.30	21.40	21.41
TiO <sub>2</sub>	-	0.05	0.06	-	-	-	-	0.02	-	-	0.01	0.08	-	0.01
Cr <sub>2</sub> O <sub>3</sub>	0.14	0.05	0.18	0.04	0.10	0.13	-	0.13	0.04	0.20	0.20	0.27	0.05	0.09
FeO	31.15	33.60	31.95	34.87	31.30	31.78	32.42	32.31	31.43	32.34	32.92	33.18	32.39	34.19
MnO	0.19	0.63	0.40	0.63	0.63	0.27	0.82	0.37	1.32	1.75	1.67	1.81	1.83	2.00
MgO	3.51	2.96	3.12	2.55	2.14	2.68	1.81	2.93	1.42	1.09	1.14	1.06	1.09	1.14
CaO	5.39	3.52	5.56	3.64	6.06	5.27	6.32	5.04	6.67	5.73	5.18	4.89	4.96	4.84
TOTAL	99.76	100.00	99.78	99.65	100.16	100.02	99.93	100.01	99.98	99.98	100.38	100.09	99.74	99.94

Si	5.94	5.89	5.93	5.84	5.96	5.97	5.84	5.93	5.93	5.97	6.05	6.03	6.10	5.97
Al	4.12	4.21	4.09	4.17	4.19	4.16	4.22	4.20	4.17	4.13	4.05	4.04	4.05	4.05
Ti	-	0.01	0.01	-	-	-	-	-	-	-	-	0.01	-	-
Cr	0.02	0.01	0.02	0.01	0.01	0.02	-	0.02	0.01	0.03	0.03	0.03	0.01	0.01
Fe	4.14	4.49	4.22	4.72	4.16	4.22	4.36	4.20	4.21	4.35	4.41	4.46	4.35	4.59
Mn	0.03	0.09	0.05	0.09	0.09	0.04	0.11	0.05	0.18	0.24	0.23	0.25	0.25	0.27
Mg	0.83	0.71	0.74	0.62	0.51	0.63	0.43	0.70	0.34	0.26	0.27	0.25	0.26	0.27
Ca	0.92	0.60	0.94	0.63	1.03	0.90	1.09	0.87	1.15	0.99	0.89	0.84	0.85	0.83

Andradite	-	0.1	0.1	-	-	-	-	-	-	-	-	0.2	-	-
Uvaovite	0.3	0.1	0.4	0.1	0.2	0.3	-	0.3	0.1	0.5	0.5	0.7	0.1	0.2
Almandine	77.1	82.3	77.4	83.6	77.8	79.2	78.4	79.2	76.9	78.7	80.0	80.4	80.3	80.9
Spessartine	0.5	1.5	1.0	1.5	1.6	0.7	2.0	0.9	3.2	4.3	4.1	4.4	4.5	4.7
Pyrope	8.7	7.3	7.6	6.1	5.3	6.7	4.4	7.2	3.5	2.7	2.8	2.6	2.7	2.7
Grossular	13.3	8.6	13.5	8.7	15.1	13.1	15.3	12.4	16.3	13.9	12.6	11.8	12.3	11.5

	DH 2035-113	DH 2035-114	DH 2035-115	DH 2035-116	DH 2035-117	DH 2035-118	DH 2035-119	DH 2035-120	DH 2035-121	DH 2035-122	DH 2035-123	DH 2035-124	DH 2035-125	DH 2035-126
SiO <sub>2</sub>	37.36	37.93	36.70	37.45	36.24	36.99	37.33	37.42	37.50	36.65	36.65	37.86	37.32	37.73
Al <sub>2</sub> O <sub>3</sub>	21.33	21.40	21.41	20.66	21.53	21.86	21.75	19.52	21.72	21.78	22.19	22.10	22.13	21.61
TiO <sub>2</sub>	-	-	0.03	-	0.12	-	0.19	0.05	0.02	0.02	0.01	0.04	0.13	0.01
Cr <sub>2</sub> O <sub>3</sub>	0.05	0.16	0.04	0.14	0.08	0.24	0.06	0.14	0.16	0.11	0.10	0.08	0.14	0.17
FeO	32.51	32.01	33.99	33.80	34.01	32.66	32.60	32.53	32.58	32.90	31.97	31.58	31.76	33.60
MnO	2.13	2.14	1.75	1.76	1.76	1.90	1.91	1.05	1.57	1.58	1.17	0.36	0.29	0.20
MgO	1.04	1.06	1.13	1.11	1.17	1.28	1.25	6.24	1.36	1.36	1.88	2.98	3.31	2.44
CaO	5.47	5.46	4.97	4.62	4.89	4.89	4.87	2.75	5.22	5.44	6.36	5.10	4.93	4.23
TOTAL	99.88	100.16	100.02	99.55	99.79	99.81	99.97	99.70	100.14	99.84	100.33	100.10	100.00	100.00

Si	6.02	6.07	5.92	6.08	5.89	5.96	6.00	5.99	6.01	5.92	5.86	6.00	5.93	6.02
Al	4.05	4.04	4.07	3.95	4.12	4.15	4.12	3.68	4.10	4.14	4.18	4.12	4.14	4.07
Ti	-	-	-	-	0.02	-	0.02	0.01	-	-	-	0.01	0.02	-
Cr	0.01	0.02	0.01	0.02	0.01	0.03	0.01	0.02	0.02	0.01	0.01	0.01	0.02	0.02
Fe	4.38	4.29	4.59	4.59	4.62	4.40	4.38	4.36	4.37	4.44	4.28	4.18	4.22	4.49
Mn	0.29	0.29	0.24	0.24	0.24	0.26	0.26	0.14	0.21	0.22	0.16	0.05	0.04	0.03
Mg	0.25	0.25	0.27	0.27	0.28	0.31	0.30	1.49	0.32	0.33	0.45	0.70	0.78	0.58
Ca	0.94	0.94	0.86	0.80	0.85	0.84	0.84	0.47	0.90	0.94	1.09	0.87	0.84	0.72

Andradite	-	-	-	-	0.3	-	0.5	0.1	-	-	-	0.1	0.3	-
Uvanovite	0.1	0.4	0.1	0.3	0.2	0.6	0.1	0.3	0.4	0.3	0.2	0.2	0.3	0.4
Almandine	78.9	78.4	81.2	81.6	80.9	79.7	79.7	76.1	79.7	79.5	77.1	78.7	78.3	82.7
Spessartine	5.2	5.2	4.2	4.2	4.2	4.6	4.7	2.5	3.8	3.8	2.8	0.9	0.7	0.5
Pyrope	2.5	2.6	2.7	2.7	2.8	3.1	3.1	14.6	3.3	3.3	4.5	7.4	8.2	6.0
Grossular	13.3	13.4	11.9	11.2	11.6	11.9	11.9	6.4	12.8	13.1	15.3	12.7	12.2	10.4

	DH 2035-127	DH 2035-128	DH 2035-129	DH 2035-130	DH 2035-131	DH 2035-132	DH 2035-133	DH 2035-134	DH 2035-135	DH 2035-136	DH 2035-137	DH 2035-138	DH 2035-139	DH 2035-140
SiO <sub>2</sub>	37.47	37.24	38.28	37.14	37.94	36.54	38.11	38.83	36.89	36.23	36.17	36.55	37.05	37.05
Al <sub>2</sub> O <sub>3</sub>	21.47	22.33	21.93	21.98	20.40	21.96	21.74	21.95	21.68	22.64	22.39	22.78	22.11	21.70
TiO <sub>2</sub>	-	0.14	-	0.04	0.05	0.06	-	0.06	0.01	0.09	-	0.02	-	0.04
Cr <sub>2</sub> O <sub>3</sub>	-	0.05	0.07	0.08	0.20	0.16	0.08	0.33	0.05	0.13	0.06	0.14	0.10	0.20
FeO	35.93	31.83	32.03	31.48	33.26	33.79	32.28	34.25	32.12	32.31	32.13	31.42	34.00	35.63
MnO	0.52	0.32	0.72	1.36	1.45	1.42	1.32	1.62	0.67	0.70	0.34	0.44	0.71	0.51
MgO	2.66	3.37	2.02	1.48	1.10	1.36	1.39	1.12	2.11	1.76	3.19	3.19	2.59	2.67
CaO	1.96	4.70	5.95	6.15	5.52	4.73	4.72	5.17	6.17	5.87	4.91	5.51	3.87	2.10
TOTAL	100.00	99.97	100.00	99.72	99.92	100.02	99.64	100.34	99.68	99.72	100.18	100.05	100.43	99.91

Si	6.02	5.91	6.04	5.96	6.12	5.90	6.10	6.05	5.93	5.82	5.82	5.81	5.91	5.96
Al	4.06	4.18	4.08	4.16	3.88	4.18	4.10	4.03	4.11	4.29	4.25	4.27	4.16	4.11
Ti	-	0.02	-	0.01	0.01	0.01	-	0.01	-	0.01	-	-	-	0.01
Cr	-	0.01	0.01	0.01	0.03	0.02	0.01	0.04	0.01	0.02	0.01	0.02	0.01	0.03
Fe	4.83	4.23	4.22	4.23	4.49	4.56	4.32	4.46	4.32	4.34	4.32	4.18	4.54	4.79
Mn	0.07	0.04	0.10	0.19	0.20	0.19	0.18	0.21	0.09	0.10	0.05	0.06	0.10	0.07
Mg	0.64	0.80	0.48	0.35	0.26	0.33	0.33	0.26	0.51	0.42	0.77	0.76	0.62	0.64
Ca	0.34	0.80	1.01	1.06	0.95	0.82	0.81	0.86	1.06	1.01	0.85	0.94	0.66	0.36

Andradite	-	0.3	-	0.1	0.1	0.1	-	0.1	-	0.2	-	-	-	0.1
Uvarovite	-	0.1	0.2	0.2	0.5	0.4	0.2	0.8	0.1	0.3	0.1	0.3	0.2	0.5
Almandine	87.5	78.8	78.5	77.6	80.0	81.4	81.1	80.5	78.1	79.1	79.1	77.2	82.4	86.6
Spessartine	1.3	0.8	1.8	3.4	3.5	3.4	3.3	3.8	1.6	1.7	0.8	1.1	1.7	1.2
Pyrope	6.5	8.3	5.0	3.6	2.6	3.3	3.5	2.6	5.1	4.3	7.9	7.8	6.3	6.5
Grossular	4.8	11.6	14.6	15.2	13.3	11.4	11.9	12.2	15.0	14.4	12.1	13.5	9.4	5.1

	DH 2035-141	DH 2035-142	DH 2035-143	DH 2035-144	DH 2035-145	DH 2035-146	DH 2035-147	DH 2035-148	DH 2035-149	DH 2035-150	DH 2035-151	DH 2035-152	DH 2035-153	DH 2035-154
SiO <sub>2</sub>	36.00	37.31	36.92	36.10	36.69	36.00	37.44	36.00	37.37	36.93	36.30	37.00	37.36	36.19
Al <sub>2</sub> O <sub>3</sub>	22.09	21.61	21.91	22.66	22.21	22.20	21.93	22.27	21.82	21.76	21.82	21.82	21.48	21.95
TiO <sub>2</sub>	0.09	-	0.11	0.03	-	0.06	0.06	-	0.16	0.10	-	-	0.03	-
Cr <sub>2</sub> O <sub>3</sub>	0.11	0.16	0.09	0.04	0.09	0.09	0.10	0.14	0.04	0.16	0.14	0.14	0.18	0.14
FeO	35.97	36.70	34.39	32.20	31.39	31.80	31.67	33.83	32.37	32.08	32.09	32.56	32.98	33.65
MnO	0.38	0.55	0.78	0.19	1.43	1.58	1.63	1.40	1.36	1.96	2.84	2.22	1.71	1.72
MgO	2.71	2.93	2.69	3.02	1.42	1.19	1.19	1.47	1.54	1.39	1.04	1.07	1.13	1.18
CaO	2.00	0.74	2.85	5.06	6.47	6.94	5.97	4.92	5.14	5.63	5.70	5.29	4.96	4.85
TOTAL	99.34	100.00	99.73	99.30	99.71	99.87	99.99	100.03	99.80	100.00	99.94	100.09	99.03	99.68

Si	5.82	6.00	5.93	5.80	5.90	5.82	5.99	5.82	5.99	5.94	5.88	5.96	6.02	5.87
Al	4.22	4.09	4.15	4.29	4.21	4.23	4.14	4.24	4.13	4.12	4.16	4.14	4.08	4.20
Ti	0.01	-	0.01	-	-	0.01	0.01	-	0.02	0.01	-	-	-	-
Cr	0.01	0.02	0.01	0.01	0.01	0.01	0.01	0.02	0.01	0.02	0.02	0.02	0.02	0.02
Fe	4.88	4.93	4.62	4.33	4.22	4.30	4.24	4.57	4.34	4.31	4.35	4.38	4.44	4.57
Mn	0.05	0.08	0.11	0.03	0.20	0.22	0.22	0.19	0.19	0.27	0.39	0.30	0.23	0.24
Mg	0.66	0.70	0.64	0.72	0.34	0.29	0.28	0.35	0.37	0.33	0.25	0.26	0.27	0.29
Ca	0.35	0.13	0.49	0.87	1.12	1.20	1.03	0.85	0.88	0.97	0.99	0.91	0.86	0.84

Anorthite	0.2	-	0.3	-	-	0.1	0.1	-	0.4	0.2	-	-	-	-
Uvarovite	0.3	0.4	0.2	0.1	0.2	0.2	0.2	0.3	0.1	0.4	0.3	0.3	0.4	0.3
Almandine	87.2	89.3	84.1	79.5	76.9	76.3	78.0	79.9	79.7	77.6	76.8	78.9	80.5	81.0
Spessartine	0.9	1.3	1.9	0.5	3.5	3.8	4.0	3.3	3.3	4.7	6.8	5.4	4.2	4.1
Pyrope	6.6	7.1	6.6	7.5	3.5	2.9	2.9	3.5	3.8	3.4	2.5	2.6	2.8	2.8
Grossular	4.8	1.8	7.0	12.5	15.9	16.7	14.7	11.6	12.7	13.6	13.6	12.8	12.1	11.7

	DH 2035-155	DH 2035-156	DH 2035-157	DH 2035-158	DH 2035-159	DH 2035-160	DH 2035-161	DH 2035-162	DH 2035-163	DH 2035-164	DH 2035-165	DH 2035-166	DH 2035-167	DH 2035-168
SiO <sub>2</sub>	37.12	37.97	37.25	38.24	37.90	37.67	37.08	36.27	37.85	37.27	36.91	36.20	37.15	37.48
Al <sub>2</sub> O <sub>3</sub>	21.68	21.36	21.71	21.73	21.78	22.04	22.00	21.90	21.31	21.42	21.17	21.68	21.14	21.18
TiO <sub>2</sub>	0.05	-	0.05	-	-	-	-	0.05	-	-	0.04	0.03	0.08	-
Cr <sub>2</sub> O <sub>3</sub>	0.18	0.23	0.15	0.12	0.07	0.12	0.12	0.05	0.11	0.08	0.20	0.05	0.03	0.14
FeO	33.66	33.06	32.07	30.98	31.33	31.57	32.09	33.48	32.74	32.71	33.50	33.95	33.40	31.31
MnO	1.53	1.55	1.50	1.00	0.33	0.70	0.63	0.69	1.55	1.98	2.15	2.04	1.56	1.38
MgO	1.13	1.21	1.12	1.60	3.03	1.60	1.80	1.83	1.29	1.12	1.08	1.13	1.10	1.53
CaO	4.57	4.58	6.14	6.34	5.23	6.25	5.82	5.70	5.11	5.42	5.24	4.92	5.58	6.95
TOTAL	99.92	99.95	100.00	100.00	99.67	99.95	99.55	99.98	99.96	100.00	100.00	100.00	100.00	99.96

Si	5.98	6.09	5.98	6.08	6.02	6.01	5.95	5.85	6.07	6.00	5.96	5.87	6.00	6.01
Al	4.12	4.04	4.11	4.07	4.08	4.14	4.16	4.16	4.03	4.07	4.03	4.15	4.02	4.00
Ti	0.01	-	0.01	-	-	-	-	0.01	-	-	0.01	-	0.01	-
Cr	0.02	0.03	0.02	0.02	0.01	0.02	0.02	0.01	0.01	0.01	0.03	0.01	-	0.02
Fe	4.54	4.43	4.31	4.12	4.17	4.21	4.31	4.52	4.39	4.41	4.53	4.61	4.51	4.20
Mn	0.21	0.21	0.20	0.14	0.05	0.10	0.09	0.09	0.21	0.27	0.29	0.28	0.21	0.19
Mg	0.27	0.29	0.27	0.38	0.72	0.38	0.43	0.44	0.31	0.27	0.26	0.27	0.27	0.37
Ca	0.79	0.79	1.06	1.08	0.89	1.07	1.00	0.99	0.88	0.94	0.91	0.86	0.97	1.19

Andradite	0.1	-	0.1	-	-	-	-	0.1	-	-	0.1	-	0.2	-
Uxarowite	0.4	0.6	0.4	0.3	0.2	0.3	0.3	0.1	0.3	0.2	0.5	0.1	-	0.3
Almandine	79.9	80.9	78.2	77.4	78.3	78.5	79.3	80.1	80.2	79.2	79.4	80.7	80.1	75.8
Spessartine	3.6	3.8	3.7	2.5	0.8	1.7	1.6	1.7	3.8	4.8	5.1	4.8	3.7	3.3
Pyrope	2.7	3.0	2.7	4.0	7.6	4.0	4.4	4.4	3.2	2.7	2.6	2.7	2.6	3.7
Grossular	10.9	11.2	15.0	15.8	13.1	15.5	14.4	13.6	12.5	13.1	12.4	11.7	13.4	16.8

	DH 2035-169	DH 2035-170	DH 2035-171	DH 2035-172	DH 2035-173	DH 2035-174	DH 2035-175	DH 2035-176	DH 2035-177	DH 2035-178	DH 2035-179	DH 2035-180	DH 2035-181	DH 2035-182
SiO <sub>2</sub>	37.30	38.11	38.14	38.16	37.60	37.31	37.09	37.52	37.07	38.02	37.81	37.48	37.70	37.45
Al <sub>2</sub> O <sub>3</sub>	21.76	21.11	21.05	21.13	21.42	21.25	20.97	21.26	21.25	21.05	20.76	21.57	21.87	21.39
TiO <sub>2</sub>	0.03	-	-	0.01	-	0.04	0.02	0.04	-	0.07	-	0.03	-	0.05
Cr <sub>2</sub> O <sub>3</sub>	0.09	0.15	0.11	0.05	0.03	0.08	0.03	0.07	0.07	0.11	0.16	0.03	0.10	0.20
FeO	32.12	32.26	31.75	30.59	32.61	31.94	31.96	31.96	31.81	31.67	33.20	32.40	31.79	30.61
MnO	0.27	0.51	0.60	1.35	0.24	1.21	1.40	0.62	1.40	1.40	1.43	0.37	1.17	1.63
MgO	3.21	2.33	2.20	1.18	3.27	1.60	1.22	1.97	1.49	1.14	1.09	3.11	1.76	1.21
CaO	5.17	5.83	6.36	7.13	4.74	6.63	6.86	6.41	6.91	6.52	5.31	5.08	6.61	7.47
TOTAL	99.97	100.3	100.22	99.59	99.90	100.06	99.56	99.84	100.00	99.98	99.75	100.07	100.00	100.00

Si	5.94	6.06	6.07	6.11	6.00	5.88	6.00	6.01	5.96	6.09	6.10	5.97	5.97	6.00
Al	4.09	3.96	3.95	3.99	4.03	4.02	4.00	4.01	4.03	3.97	3.95	4.05	4.09	4.04
Ti	-	-	-	-	-	0.01	-	0.01	-	0.01	-	-	-	0.01
Cr	0.01	0.02	0.01	0.01	-	0.01	-	0.01	0.01	0.01	0.02	-	0.01	0.03
Fe	4.28	4.29	4.23	4.10	4.35	4.29	4.32	4.28	4.28	4.24	4.48	4.32	4.21	4.10
Mn	0.04	0.07	0.08	0.18	0.03	0.17	0.19	0.08	0.19	0.19	0.20	0.05	0.16	0.22
Mg	0.76	0.55	0.52	0.28	0.78	0.38	0.29	0.47	0.36	0.27	0.26	0.74	0.42	0.29
Ca	0.88	0.99	1.09	1.22	0.81	1.14	1.19	1.10	1.19	1.12	0.92	0.87	1.12	1.28

Andradite	-	-	-	-	-	0.1	-	0.1	-	0.2	-	-	-	0.1
Uxarosite	0.2	0.4	0.3	0.1	-	0.2	-	0.2	0.2	0.3	0.4	-	0.2	0.5
Abundine	78.6	78.5	77.4	75.9	79.8	77.0	77.1	77.8	76.3	77.4	80.6	79.1	76.7	74.4
Spessartine	0.7	1.2	1.5	3.3	0.6	2.9	3.4	1.5	3.4	3.4	3.5	0.9	2.8	4.0
Pyrope	7.9	5.7	5.4	2.9	8.0	3.9	2.9	4.8	3.6	2.8	2.6	7.6	4.2	2.9
Grossular	12.7	14.2	15.5	17.7	11.6	16.0	16.6	15.6	16.6	15.9	12.9	12.4	16.0	18.1

	DH 2035-183	DH 2035-184	DH 2035-185	DH 2035-186	DH 2035-187	DH 2035-188	DH 2035-189	DH 2035-190	DH 2035-191	DH 2035-192	DH 2035-193	DH 2035-194	DH 2035-195	DH 2035-196
SiO <sub>2</sub>	37.32	38.01	37.67	37.15	36.56	37.50	37.00	37.04	38.36	37.18	38.26	36.71	37.60	37.11
Al <sub>2</sub> O <sub>3</sub>	21.27	20.84	20.83	21.01	21.32	21.08	21.21	21.19	20.89	21.07	20.89	21.34	21.60	21.37
TiO <sub>2</sub>	0.06	0.03	0.01	0.12	-	0.13	0.15	-	0.07	-	-	-	-	0.01
Cr <sub>2</sub> O <sub>3</sub>	-	0.13	0.24	0.17	0.16	0.11	0.16	0.09	0.24	0.06	0.07	0.14	0.09	0.10
FeO	31.88	33.01	32.89	32.95	32.68	31.08	31.84	32.77	32.68	33.59	32.16	32.00	31.43	34.53
MnO	1.71	1.51	1.54	1.96	2.12	2.79	2.81	1.77	1.16	1.47	1.56	1.53	0.47	0.53
MgO	1.09	1.24	1.33	1.40	1.37	1.14	1.03	1.37	1.49	1.44	1.26	1.40	3.01	2.74
CaO	6.66	4.96	4.73	5.17	5.75	6.15	5.90	5.70	5.18	5.27	5.97	6.92	5.80	3.61
TOTAL	99.98	99.74	99.23	99.94	99.96	99.99	100.10	99.90	100.07	100.08	100.18	100.04	100.00	100.00

Si	6.00	6.12	6.10	6.00	5.92	6.03	5.95	5.98	6.13	6.00	6.12	5.92	5.98	5.96
Al	4.03	3.95	3.97	4.00	4.07	4.00	4.02	4.03	3.94	4.01	3.94	4.06	4.05	4.05
Ti	0.01	-	-	0.02	-	0.02	0.02	-	0.01	-	-	-	-	-
Cr	-	0.02	0.03	0.02	0.02	0.01	0.02	0.01	0.03	0.01	0.01	0.02	0.01	0.01
Fe	4.29	4.44	4.45	4.45	4.42	4.18	4.28	4.42	4.37	4.53	4.30	4.31	4.18	4.64
Mn	0.23	0.21	0.21	0.27	0.29	0.38	0.38	0.24	0.16	0.20	0.21	0.21	0.06	0.07
Mg	0.26	0.30	0.32	0.34	0.33	0.27	0.25	0.33	0.36	0.35	0.30	0.34	0.71	0.66
Ca	1.15	0.86	0.82	0.89	1.00	1.06	1.02	0.99	0.89	0.91	1.02	1.20	0.99	0.62

Andradite	0.1	-	-	0.3	-	0.3	0.4	-	0.2	-	-	-	-	-
Uvarovite	-	0.3	0.6	0.4	0.4	0.3	0.4	0.2	0.6	0.1	0.2	0.3	0.2	0.2
Almandine	77.0	80.8	80.8	78.9	77.7	75.1	76.0	78.6	80.1	80.3	78.4	76.2	77.0	83.2
Spessartine	4.1	3.7	3.8	4.7	5.0	6.7	6.7	4.2	2.8	3.5	3.8	3.6	1.2	1.3
Pyrope	2.6	3.0	3.3	3.4	3.3	2.8	2.5	3.3	3.7	3.4	3.1	3.3	7.4	6.6
Grossular	16.1	12.1	11.6	12.4	13.7	14.9	14.1	13.7	12.7	12.6	14.6	16.5	14.2	8.7



	DII 2035-197	DII 2035-198	DII 2035-199	DII 2035-200	DII 2035-201	DII 2035-202	DII 2035-203	DII 2035-204	DII 2035-205	DII 2035-206	DII 2035-207	DII 2035-208	DII 2035-209	DII 2035-210
SiO <sub>2</sub>	36.00	36.40	37.20	37.00	37.45	37.00	37.00	37.21	36.30	37.99	36.68	37.60	36.25	36.89
Al <sub>2</sub> O <sub>3</sub>	21.63	21.32	21.14	21.35	21.42	21.40	21.07	21.00	21.03	20.99	20.99	21.49	21.26	21.51
TiO <sub>2</sub>	0.09	-	0.16	0.08	0.05	0.01	0.05	0.22	0.06	0.03	0.06	0.07	0.07	-
Cr <sub>2</sub> O <sub>3</sub>	0.14	0.01	0.08	0.02	0.04	0.03	0.14	-	0.29	0.04	0.23	0.10	0.09	0.19
FeO	32.45	32.58	32.55	33.00	32.30	33.00	32.31	33.11	34.13	33.93	33.47	31.51	35.41	32.23
MnO	0.53	1.32	1.45	0.29	0.35	0.19	1.55	1.30	1.62	0.62	0.59	0.41	0.46	0.53
MgO	3.18	1.27	1.31	3.29	3.17	3.00	1.29	1.29	1.28	3.11	2.79	2.61	2.44	2.48
CaO	5.95	7.09	5.97	5.02	5.19	5.14	6.59	5.85	5.33	3.29	5.53	6.25	3.98	6.42
TOTAL	99.98	100.00	99.87	100.05	99.97	99.76	100.00	100.00	100.05	100.00	99.95	100.05	99.90	100.02

Si	5.79	5.89	6.00	5.92	5.97	5.94	5.97	6.00	5.90	6.07	5.89	5.99	5.87	5.90
Al	4.10	4.07	6.02	4.03	4.03	4.05	4.01	3.99	4.03	3.95	3.97	4.03	4.06	4.06
Ti	0.01	-	0.02	0.01	0.01	-	0.01	0.03	0.01	-	0.01	0.01	0.01	-
Cr	0.02	-	0.01	-	0.01	-	0.02	-	0.04	0.01	0.03	0.01	0.01	0.02
Fe	4.36	4.41	4.39	4.42	4.31	4.43	4.36	4.46	4.64	4.53	4.50	4.20	4.80	4.31
Mn	0.07	0.18	0.20	0.04	0.05	0.03	0.21	0.18	0.22	0.08	0.08	0.06	0.06	0.07
Mg	0.76	0.31	0.32	0.78	0.75	0.72	0.31	0.31	0.31	0.74	0.67	0.62	0.59	0.59
Ca	1.03	1.23	1.03	0.86	0.89	0.88	1.14	1.01	0.93	0.56	0.95	1.07	0.69	1.10

Andradite	0.2	-	0.4	0.2	0.1	-	0.1	0.5	0.1	-	0.1	0.2	0.2	-
Uvarovite	0.3	-	0.2	-	0.1	-	0.3	-	0.7	0.1	0.5	0.2	0.2	0.5
Almandine	76.6	77.1	78.4	79.3	79.3	79.8	77.1	79.3	79.9	82.8	78.4	76.9	83.4	77.0
Spessartine	1.3	3.1	3.5	0.7	0.9	0.5	3.7	3.1	3.8	1.5	1.4	1.0	1.1	1.3
Pyrope	7.5	3.0	3.2	7.9	7.8	7.3	3.1	3.1	3.0	7.6	6.5	6.4	5.7	5.9
Grossular	14.1	16.8	14.4	12.1	12.7	12.4	15.7	14.0	12.5	8.0	13.0	15.3	9.4	15.3

	DH 2035-211	DH 2035-212	DH 2035-213	DH 2035-214	DH 2035-215	DH 2035-216	DH 2035-217	DH 2020-1	DH 2020-2	DH 2020-3	DH 2020-4	DH 2020-5	DH 2020-6	DH 2020-7
SiO <sub>2</sub>	37.47	37.03	37.62	37.40	37.65	37.52	37.21	36.64	38.23	37.36	37.47	37.48	38.34	37.91
Al <sub>2</sub> O <sub>3</sub>	20.87	21.54	21.02	21.08	21.00	21.34	21.17	20.40	20.30	19.92	20.00	20.81	21.15	20.71
TiO <sub>2</sub>	-	-	0.06	0.08	0.03	-	0.05	-	0.01	-	0.04	0.01	0.08	0.02
Cr <sub>2</sub> O <sub>3</sub>	0.20	0.10	0.13	0.05	0.12	0.07	0.10	0.07	0.04	0.02	-	0.05	0.10	0.08
FeO	32.89	35.06	31.43	32.27	32.14	31.54	32.42	32.13	31.06	31.98	32.49	30.50	29.20	31.26
MnO	0.40	0.29	0.25	0.60	0.49	1.42	1.42	2.52	2.43	2.24	2.44	2.54	2.68	2.30
MgO	2.32	2.14	3.06	1.89	2.16	1.12	1.10	0.72	0.66	0.61	0.62	0.58	0.47	0.59
CaO	5.77	3.75	5.96	6.28	6.27	6.97	6.17	7.67	7.70	7.25	7.18	7.68	7.75	7.09
TOTAL	99.92	99.91	99.53	99.67	99.87	99.18	99.64	100.15	100.44	99.39	100.26	99.65	99.77	99.95

Si	6.01	5.96	6.02	6.01	6.03	6.02	6.10	5.95	6.13	6.09	6.07	6.05	6.13	6.10
Al	3.95	4.09	3.96	3.99	3.96	4.04	4.03	3.91	3.84	3.83	3.82	3.96	3.99	3.93
Ti	-	-	0.01	0.01	-	-	0.01	-	-	-	0.01	-	0.01	-
Cr	0.03	0.01	0.02	0.01	0.02	0.01	0.01	0.01	0.01	-	-	0.01	0.01	0.01
Fe	4.41	4.72	4.20	4.34	4.31	4.23	4.38	4.37	4.17	4.36	4.40	4.12	3.91	4.21
Mn	0.05	0.04	0.03	0.08	0.07	0.19	0.19	0.35	0.33	0.31	0.34	0.35	0.36	0.31
Mg	0.56	0.51	0.73	0.45	0.52	0.27	0.27	0.18	0.16	0.15	0.15	0.14	0.11	0.14
Ca	0.99	0.65	1.02	1.08	1.08	1.20	1.07	1.34	1.32	1.27	1.25	1.33	1.33	1.22

Andradite	-	-	0.1	0.2	-	-	0.1	-	-	-	0.1	-	0.2	-
Uxanovite	0.5	0.2	0.3	0.1	0.3	0.2	0.2	0.2	0.1	-	-	0.1	0.2	0.2
Almandine	79.1	84.8	76.9	78.4	78.0	76.7	78.6	74.5	74.1	76.0	77.2	73.8	72.5	75.7
Spessartine	1.0	0.7	0.6	1.5	1.2	3.5	3.4	5.8	5.8	5.3	5.8	6.1	6.7	5.6
Pyrope	5.6	5.2	7.5	4.6	5.2	2.7	2.7	1.7	1.6	1.4	1.5	1.4	1.2	1.4
Grossular	13.9	9.1	14.6	15.3	15.2	17.0	15.0	17.8	18.4	17.2	17.1	18.6	19.2	17.2

	DH 2020-8	DH 2020-9	DH 2020-10	DH 2020-11	DH 2020-12	DH 2020-13	DH 2020-14	DH 2020-15	DH 2020-16	DH 2020-17	DH 2020-18	DH 2020-19	DH 2020-20	DH 2020-21
SiO <sub>2</sub>	36.81	37.23	36.07	36.89	36.78	38.30	36.54	36.88	36.76	36.41	36.41	36.98	36.01	36.13
Al <sub>2</sub> O <sub>3</sub>	21.15	20.36	21.95	19.89	19.91	20.01	21.90	20.03	20.00	20.09	20.85	20.17	21.06	20.81
TiO <sub>2</sub>	0.14	-	-	-	0.04	0.47	0.56	-	-	0.02	-	0.03	-	0.12
Cr <sub>2</sub> O <sub>3</sub>	0.05	0.02	0.07	-	-	-	-	0.01	0.04	-	0.01	0.03	0.02	0.12
FeO	30.71	31.52	32.95	31.53	32.05	30.52	30.99	31.97	32.29	32.64	32.11	32.50	32.05	31.41
MnO	2.41	2.76	2.73	2.96	2.89	3.36	3.33	2.96	2.68	2.56	2.67	2.51	2.70	2.94
MgO	0.60	0.41	0.51	0.39	0.55	0.07	0.07	0.52	0.63	0.68	0.67	0.64	0.62	0.45
CaO	7.31	7.68	7.86	8.32	7.82	8.20	7.18	8.05	7.70	7.55	7.47	7.30	7.71	8.03
TOTAL	99.18	99.98	100.15	99.97	100.05	99.94	99.57	100.42	100.00	99.95	100.19	100.16	100.17	100.01

Si	5.98	6.04	5.77	6.01	5.99	6.13	5.88	5.99	5.99	5.95	5.91	6.01	5.86	5.88
Al	4.05	3.89	4.14	3.82	3.82	3.77	4.15	3.83	3.84	3.87	3.99	3.86	4.04	3.99
Ti	0.02	-	-	-	0.01	0.06	0.07	-	-	-	-	-	-	0.02
Cr	0.01	-	0.01	-	-	-	-	-	0.01	-	-	-	-	0.02
Fe	4.17	4.27	4.41	4.30	4.37	4.09	4.17	4.34	4.40	4.46	4.36	4.41	4.36	4.28
Mn	0.33	0.38	0.37	0.41	0.40	0.46	0.45	0.41	0.37	0.35	0.37	0.35	0.37	0.41
Mg	0.15	0.10	0.12	0.10	0.13	0.02	0.02	0.13	0.15	0.17	0.16	0.16	0.15	0.11
Ca	1.27	1.33	1.35	1.45	1.37	1.41	1.24	1.40	1.34	1.32	1.30	1.27	1.34	1.40

Andradite	0.3	-	-	-	0.1	1.1	1.3	-	-	-	-	0.1	-	0.3
Uvarovite	0.1	-	0.2	-	-	-	-	-	0.1	-	-	0.1	-	0.3
Almandine	74.5	74.4	74.7	73.0	73.9	71.6	73.6	73.5	74.5	75.2	74.8	75.6	74.4	72.9
Spessartine	5.8	6.5	6.2	6.9	6.7	7.9	7.9	6.8	6.2	5.9	6.2	5.8	6.3	6.8
Pyrope	1.5	1.0	1.2	0.9	1.3	0.2	0.2	1.2	1.5	1.6	1.6	1.5	1.4	1.0
Grossular	17.7	18.1	17.8	19.3	18.0	19.2	17.0	18.5	17.8	17.4	17.4	17.0	17.9	18.6

	DH 2020-22	DH 2020-23	DH 2020-24	DH 2020-25	DH 2020-26	DH 2020-27	DH 2020-28	DH 2020-29	DH 2020-30	DH 2020-31	DH 2020-32	DH 2020-33	DH 2020-34	DH 2020-35
SiO <sub>2</sub>	36.84	36.86	36.22	36.00	36.29	36.93	36.29	35.99	36.79	36.52	36.08	36.04	36.00	37.40
Al <sub>2</sub> O <sub>3</sub>	20.98	19.89	20.49	20.55	20.00	20.10	19.80	20.06	20.31	20.24	20.19	21.07	20.67	20.03
TiO <sub>2</sub>	-	-	0.04	-	-	0.01	0.08	-	0.05	0.05	-	-	-	0.05
Cr <sub>2</sub> O <sub>3</sub>	0.02	0.01	-	-	0.04	0.01	0.04	-	0.01	-	-	-	0.04	0.02
FeO	31.24	31.52	31.72	32.23	32.17	31.66	31.31	32.72	31.65	32.67	32.99	32.25	32.85	32.90
MnO	2.98	2.96	2.82	2.83	3.25	2.74	3.21	3.06	3.04	2.47	2.50	2.40	2.37	2.39
MgO	0.49	0.49	0.44	0.46	0.39	0.44	0.44	0.45	0.44	0.73	0.78	0.59	0.75	0.67
CaO	7.87	8.02	8.07	7.95	7.88	7.92	8.24	8.05	7.62	7.46	6.91	7.65	7.17	6.56
TOTAL	100.42	99.74	99.80	100.00	100.01	99.80	100.41	100.33	99.91	100.15	99.45	100.00	99.86	100.04

Si	5.95	6.01	5.92	5.88	5.94	6.01	5.96	5.89	5.99	5.95	5.93	5.87	5.88	6.07
Al	3.99	3.83	3.94	3.96	3.86	3.86	3.83	3.87	3.90	3.88	3.91	4.04	3.98	3.83
Ti	-	-	0.01	-	-	-	0.01	-	0.01	0.01	-	-	-	0.01
Cr	-	-	-	-	0.01	-	0.01	-	-	-	-	-	0.01	-
Fe	4.22	4.30	4.33	4.40	4.40	4.31	4.30	4.48	4.31	4.45	4.53	4.39	4.49	4.47
Mn	0.41	0.41	0.39	0.39	0.45	0.38	0.45	0.42	0.42	0.34	0.35	0.33	0.33	0.33
Mg	0.12	0.12	0.11	0.11	0.10	0.11	0.11	0.11	0.11	0.18	0.19	0.14	0.18	0.16
Ca	1.36	1.40	1.41	1.39	1.38	1.38	1.45	1.41	1.33	1.30	1.22	1.33	1.26	1.14

Andradite	-	-	0.1	-	-	-	0.2	-	0.1	0.1	-	-	-	0.1
Uvarovite	-	-	-	-	0.1	-	0.1	-	-	-	-	-	0.1	-
Almandine	73.4	73.3	73.6	74.1	73.6	74.0	72.3	73.9	73.9	75.3	76.4	75.2	76.1	77.3
Spessartine	7.0	6.9	6.5	6.5	7.4	6.4	7.4	6.9	7.1	5.7	5.8	5.6	5.5	5.6
Pyrope	1.2	1.1	1.0	1.1	0.9	1.0	1.0	1.0	1.0	1.7	1.8	1.4	1.7	1.6
Grossular	18.5	18.7	18.7	18.3	18.0	18.5	19.0	18.2	17.8	17.2	16.0	17.8	16.6	15.4

	DH 2020-36	DH 2020-37	DH 2086-1	DH 2086-2	DH 2086-3	DH 2086-4	DH 2086-5	DH 2086-6	DH 2086-7	DH 2086-8	DH 2086-9	DH 2086-10	DH 2086-11	DH 2086-12
SiO <sub>2</sub>	37.10	36.99	36.38	36.24	36.19	36.28	36.49	36.58	36.27	36.79	36.84	36.95	36.05	38.00
Al <sub>2</sub> O <sub>3</sub>	19.61	20.49	21.11	20.38	21.48	21.57	21.19	20.31	21.67	20.25	21.12	21.00	21.28	21.07
TiO <sub>2</sub>	-	0.12	-	0.05	0.07	0.07	-	0.03	0.02	0.04	0.07	-	-	-
Cr <sub>2</sub> O <sub>3</sub>	0.11	0.11	0.09	0.03	0.06	0.06	0.07	0.10	0.02	0.25	0.21	0.32	0.22	0.21
FeO	32.21	31.71	35.06	35.23	37.40	34.93	33.76	34.86	33.84	34.95	33.25	33.51	34.07	33.00
MnO	2.51	2.33	0.37	0.39	0.36	0.22	0.40	0.30	0.46	0.33	0.41	0.36	0.37	0.59
MgO	0.73	0.70	2.01	2.00	1.97	2.12	2.05	1.81	2.09	1.89	2.87	2.51	2.27	1.73
CaO	7.07	7.49	4.95	5.07	4.80	4.93	5.70	5.70	5.76	4.93	4.96	5.23	5.22	5.39
TOTAL	99.34	99.93	99.98	99.40	99.72	100.16	99.65	99.70	100.13	99.43	99.73	99.88	99.49	100.00

Si	6.07	5.99	5.89	5.92	5.78	5.86	5.91	5.95	5.85	5.99	5.93	5.95	5.86	6.08
Al	3.78	3.91	4.03	3.93	4.05	4.10	4.04	3.90	4.12	3.89	4.01	3.98	4.07	3.97
Ti	-	0.01	-	0.01	0.01	0.01	-	-	-	-	0.01	-	-	-
Cr	0.01	0.01	0.01	-	0.01	0.01	0.01	0.01	-	0.03	0.03	0.04	0.03	0.03
Fe	4.41	4.30	4.75	4.82	5.00	4.71	4.57	4.75	4.56	4.76	4.48	4.51	4.63	4.42
Mn	0.35	0.32	0.05	0.05	0.05	0.03	0.05	0.04	0.06	0.05	0.06	0.05	0.05	0.08
Mg	0.18	0.17	0.49	0.49	0.47	0.51	0.50	0.44	0.50	0.46	0.69	0.60	0.55	0.41
Ca	1.24	1.30	0.86	0.89	0.82	0.85	0.99	0.99	0.99	0.86	0.85	0.90	0.91	0.92

Andradite	-	0.3	-	0.1	0.2	0.2	-	0.1	-	0.1	0.2	-	-	-
Uvanovite	0.3	0.3	0.2	0.1	0.1	0.1	0.2	0.2	-	0.6	0.5	0.8	0.5	0.5
Almandine	75.6	74.7	82.5	82.4	83.7	82.5	80.4	81.4	80.3	82.4	79.6	79.9	80.1	80.6
Spessartine	5.9	5.5	0.9	0.9	0.8	0.5	1.0	0.7	1.1	0.8	1.0	0.9	0.9	1.4
Pyrope	1.7	1.6	4.7	4.7	4.4	5.0	4.9	4.2	5.0	4.5	6.9	6.0	5.4	4.2
Grossular	16.6	17.6	11.7	11.9	10.7	11.6	13.6	13.3	13.7	11.6	11.9	12.5	12.4	13.2

	DH 2036-1	DH 2036-2	DH 2036-3	DH 2036-4	DH 2036-5	DH 2036-6	DH 2036-7	DH 2036-8	DH 2036-9	DH 2036-10	DH 2036-11	DH 2036-12	DH 2036-13	DH 2036-14
SiO <sub>2</sub>	36.77	36.35	36.65	36.79	36.13	36.64	36.94	37.00	37.36	36.87	37.81	36.59	37.04	38.23
Al <sub>2</sub> O <sub>3</sub>	20.68	22.00	21.49	21.23	21.81	21.51	19.13	20.89	20.08	20.33	20.08	19.67	19.68	19.95
TiO <sub>2</sub>	-	0.49	0.58	0.44	0.63	0.48	0.06	0.03	-	0.22	0.08	-	0.13	0.04
Cr <sub>2</sub> O <sub>3</sub>	0.08	0.03	0.08	0.10	0.02	0.07	0.23	0.13	0.15	0.02	0.01	0.16	0.17	0.16
FeO	33.39	33.37	32.07	31.28	31.70	31.63	32.95	32.49	33.20	32.90	33.61	35.87	35.35	34.16
MnO	1.26	1.41	1.31	1.37	0.28	0.32	1.48	1.30	1.12	0.65	1.13	1.05	1.22	1.19
MgO	1.34	4.02	2.79	3.54	6.39	5.11	0.70	0.76	0.63	0.47	0.46	0.41	0.55	0.56
CaO	6.32	5.40	4.97	4.19	4.00	4.08	7.67	7.08	7.14	8.31	6.73	5.91	5.40	5.02
TOTAL	99.83	100.07	99.93	99.95	99.96	99.84	99.14	99.68	99.68	99.77	99.91	99.67	99.53	99.31

Si	5.96	5.69	5.88	5.93	5.69	5.83	6.07	6.00	6.07	5.99	6.12	6.02	6.07	6.21
Al	3.95	4.06	4.06	4.03	4.05	4.03	3.70	3.99	3.85	3.89	3.83	3.81	3.80	3.82
Ti	-	0.06	0.07	0.05	0.07	0.06	0.01	-	-	0.03	0.01	-	0.02	-
Cr	0.01	-	0.01	0.01	-	0.01	0.03	0.02	0.02	-	-	0.02	0.02	0.02
Fe	4.53	4.37	4.30	4.21	4.18	4.21	4.53	4.40	4.51	4.47	4.55	4.93	4.84	4.64
Mn	0.17	0.19	0.18	0.19	0.04	0.04	0.21	0.18	0.15	0.09	0.15	0.15	0.17	0.16
Mg	0.32	0.94	0.67	0.85	1.50	1.21	0.17	0.18	0.15	0.11	0.11	0.10	0.13	0.14
Ca	1.10	0.91	0.85	0.72	0.67	0.70	1.35	1.23	1.24	1.45	1.17	1.04	0.95	0.87

Andradite	-	1.1	1.4	1.1	1.5	1.2	0.1	0.1	-	0.5	0.2	-	0.3	0.2
Uvarovite	0.2	0.1	0.2	0.2	-	0.2	0.5	0.3	0.4	-	-	0.4	0.4	0.4
Almandine	78.8	74.6	76.7	76.4	73.7	75.9	76.5	77.7	78.6	77.3	80.0	82.6	82.6	83.1
Spessartine	3.0	3.2	3.1	3.3	0.7	0.8	3.4	3.1	2.7	1.5	2.7	2.4	2.8	2.9
Pyrope	3.2	9.0	6.7	8.7	14.9	12.3	1.6	1.8	1.5	1.1	1.1	0.9	1.3	1.4
Grossular	14.9	12.1	11.9	10.2	9.3	9.8	17.8	16.9	16.9	19.5	16.0	13.6	12.6	12.2

	DH 2036-15	DH 2036-16	DH 2036-17	DH 2036-18	DH 2036-19	DH 2036-20	DH 2036-21	DH 2036-22	DH 2036-23	DH 2036-24	DH 2036-25	DH 2036-26	DH 2036-27	DH 2036-28
SiO <sub>2</sub>	37.20	37.46	36.81	36.23	37.21	38.54	36.99	37.10	37.65	37.34	36.50	37.67	36.44	36.01
Al <sub>2</sub> O <sub>3</sub>	20.17	20.10	19.97	19.90	20.93	20.15	20.51	20.33	19.94	20.55	20.62	20.18	20.56	20.48
TiO <sub>2</sub>	-	-	0.04	0.06	-	-	-	0.08	-	-	0.04	-	0.12	-
Cr <sub>2</sub> O <sub>3</sub>	0.05	0.14	0.06	0.14	0.17	0.07	0.15	0.13	0.18	0.11	0.16	0.08	0.11	0.09
FeO	33.75	32.39	36.02	33.88	31.08	32.25	32.24	32.28	32.52	33.30	32.86	32.91	32.88	33.93
MnO	1.14	1.20	1.16	1.06	1.26	1.17	1.58	1.49	1.35	1.74	1.67	1.54	1.74	1.31
MgO	0.48	0.50	0.52	0.59	0.73	0.71	0.82	0.86	0.78	0.68	0.81	0.78	0.67	0.78
CaO	6.68	7.43	4.67	7.75	7.65	7.00	7.71	8.02	7.60	7.43	7.29	7.73	7.41	7.39
TOTAL	99.47	99.22	99.26	99.59	99.03	99.89	100.00	100.29	100.01	100.15	99.97	100.88	99.93	99.99

Si	6.07	6.10	6.05	5.94	6.04	6.19	5.99	5.99	6.09	6.00	5.93	6.05	5.93	5.88
Al	3.88	3.86	3.87	3.85	4.00	3.82	3.91	3.87	3.80	3.89	3.95	3.82	3.94	3.94
Ti	-	-	-	0.01	-	-	-	0.01	-	-	-	-	0.01	-
Cr	0.01	0.02	0.01	0.02	0.02	0.01	0.02	0.02	0.02	0.01	0.02	0.01	0.01	0.01
Fe	4.60	4.41	4.95	4.65	4.22	4.34	4.37	4.36	4.40	4.47	4.47	4.42	4.48	4.64
Mn	0.16	0.17	0.16	0.15	0.17	0.16	0.22	0.20	0.18	0.24	0.23	0.21	0.24	0.18
Mg	0.12	0.12	0.13	0.14	0.18	0.17	0.20	0.21	0.19	0.16	0.20	0.19	0.16	0.19
Ca	1.17	1.30	0.82	1.36	1.33	1.21	1.34	1.39	1.32	1.28	1.27	1.33	1.29	1.29

Andradite	-	-	0.1	0.1	-	-	-	0.2	-	-	0.1	-	0.3	-
Uvarovite	0.1	0.3	0.1	0.3	0.4	0.2	0.4	0.3	0.4	0.3	0.4	0.2	0.3	0.2
Almandine	80.2	77.7	84.8	77.9	76.0	78.3	75.9	75.3	76.6	77.0	76.7	76.5	76.6	78.0
Spessartine	2.7	2.9	2.7	2.4	3.1	2.8	3.7	3.5	3.2	4.0	3.9	3.6	4.1	3.0
Pyrope	1.1	1.2	1.2	1.4	1.8	1.7	1.9	2.0	1.8	1.6	1.9	1.8	1.6	1.8
Grossular	15.9	17.8	11.0	17.8	18.7	17.0	18.1	18.7	17.9	17.2	17.0	18.0	17.3	17

	DH 2033B-1	DH 2033B-2	DH 2033B-3	DH 2033B-4	DH 2033B-5	DH 2033B-6	DH 2033B-7	DH 2033B-8	DH 2033B-9	DH 2033B-10	DH 2033B-11	DH 2033B-12	DH 2033B-13	DH 2033B-14
SiO <sub>2</sub>	36.36	36.20	36.18	36.73	36.89	36.34	37.03	36.63	36.48	36.79	37.40	36.18	37.08	36.65
Al <sub>2</sub> O <sub>3</sub>	21.61	21.68	21.55	21.39	21.64	21.35	21.51	21.58	21.49	21.57	21.61	21.59	21.31	21.36
TiO <sub>2</sub>	-	0.02	-	-	-	0.01	-	-	-	-	-	-	0.08	0.12
Cr <sub>2</sub> O <sub>3</sub>	0.25	0.42	0.41	0.40	0.37	0.32	0.52	0.33	0.42	0.42	0.41	0.42	0.36	0.38
FeO	34.67	33.05	33.64	33.83	32.28	34.29	33.26	33.64	33.78	33.26	32.55	34.11	33.96	34.15
MnO	0.41	0.48	0.43	0.26	0.36	0.26	0.25	0.31	0.25	0.27	0.22	0.30	0.36	0.27
MgO	1.88	2.43	2.65	2.65	2.62	2.48	2.23	2.60	2.72	2.69	2.65	2.39	1.93	1.74
CaO	4.74	4.68	5.00	4.77	4.90	4.91	5.03	4.92	4.82	5.15	5.16	4.98	4.85	5.21
TOTAL	99.93	99.97	99.86	100.03	100.06	99.97	99.83	100.01	99.98	100.14	100.00	99.97	99.97	99.89

Si	5.88	5.87	5.84	5.90	5.94	5.87	5.95	5.89	5.87	5.90	5.97	5.84	5.97	5.92
Al	4.12	4.15	4.10	4.05	4.11	4.06	4.07	4.09	4.08	4.07	4.06	4.11	4.04	4.06
Ti	-	-	-	-	-	-	-	-	-	-	-	-	0.01	0.01
Cr	0.03	0.05	0.05	0.05	0.05	0.04	0.07	0.04	0.05	0.05	0.05	0.05	0.05	0.05
Fe	4.69	4.48	4.54	4.55	4.35	4.63	4.47	4.52	4.55	4.46	4.34	4.60	4.57	4.61
Mn	0.06	0.07	0.06	0.04	0.05	0.04	0.03	0.04	0.03	0.04	0.03	0.04	0.05	0.04
Mg	0.45	0.59	0.64	0.63	0.63	0.60	0.53	0.62	0.65	0.64	0.63	0.58	0.46	0.42
Ca	0.82	0.81	0.86	0.82	0.85	0.85	0.87	0.85	0.83	0.88	0.88	0.86	0.84	0.9

Andradite	-	-	-	-	-	-	-	-	-	-	-	-	-	0.2
Uxanovite	0.6	1.0	1.0	1.0	0.9	0.8	1.3	0.8	1.0	1.0	1.0	1.0	0.9	0.9
Almandine	82.6	80.5	79.8	80.7	79.6	81.1	80.6	80.5	80.4	79.4	79.4	80.8	81.8	81.6
Spessartine	1.0	1.2	1.0	0.6	0.9	0.6	0.6	0.7	0.6	0.6	0.6	0.7	0.9	0.6
Pyrope	4.5	5.9	6.3	6.3	6.5	5.9	5.4	6.2	6.5	6.4	6.5	5.7	4.6	4.2
Grossular	11.3	11.4	11.9	11.4	12.1	11.6	12.2	11.8	11.5	12.3	12.6	11.8	11.7	12.4



	DH 2033B-15	DH 2033B-16	DH 2033B-17	DH 2033B-18	DH 2033B-19	DH 2033B-20	DH 2033B-21	DH 2033B-22	DH 2033B-23	DH 2033B-24	DH 2033B-25	DH 2033B-26	DH 2033B-27	DH 2033B-28
SiO <sub>2</sub>	36.58	36.65	36.31	37.14	37.71	38.77	36.75	37.18	38.47	36.59	37.60	36.35	36.82	36.02
Al <sub>2</sub> O <sub>3</sub>	22.25	21.63	22.02	21.68	21.29	20.32	21.40	21.12	21.35	21.63	21.20	21.31	21.56	21.60
TiO <sub>2</sub>	0.02	0.02	0.06	0.05	-	0.05	0.04	-	-	0.12	-	-	0.05	-
Cr <sub>2</sub> O <sub>3</sub>	0.29	0.22	0.19	0.31	0.09	0.17	0.22	0.27	0.24	0.17	0.16	0.16	0.13	0.27
FeO	33.04	32.97	32.87	32.48	32.65	32.55	32.45	32.59	31.50	32.98	33.68	34.52	33.94	34.30
MnO	0.57	0.42	0.39	0.56	0.82	0.99	0.93	0.79	0.74	0.46	0.62	0.64	0.31	0.45
MgO	1.59	2.22	2.46	2.33	2.22	2.05	2.18	2.31	2.11	2.15	1.68	1.86	2.18	1.92
CaO	5.40	5.18	5.14	5.25	5.05	4.86	5.37	5.48	5.54	5.68	5.01	5.08	4.85	4.31
TOTAL	99.73	99.31	99.44	99.81	99.83	99.77	99.34	99.74	99.95	99.78	99.95	99.92	99.84	99.78

Si	5.89	5.92	5.85	5.95	6.04	6.20	5.94	5.98	6.11	5.89	6.04	5.87	5.93	5.88
Al	4.22	4.12	4.18	4.09	4.02	3.83	4.07	4.00	4.00	4.10	4.01	4.07	4.09	4.15
Ti	-	-	0.01	0.01	-	0.01	-	-	-	0.01	-	-	0.01	-
Cr	0.04	0.03	0.02	0.04	0.01	0.02	0.03	0.03	0.03	0.02	0.02	0.02	0.02	0.03
Fe	4.45	4.45	4.43	4.35	4.37	4.35	4.38	4.38	4.19	4.44	4.52	4.68	4.57	4.68
Mn	0.08	0.06	0.05	0.08	0.11	0.13	0.13	0.11	0.10	0.06	0.08	0.09	0.04	0.06
Mg	0.38	0.53	0.59	0.56	0.53	0.49	0.53	0.55	0.50	0.52	0.40	0.45	0.52	0.47
Ca	0.93	0.90	0.89	0.90	0.87	0.83	0.93	0.94	0.94	0.98	0.86	0.88	0.84	0.75

Andradite	-	-	0.1	0.1	0.1	0.1	0.1	-	-	0.3	-	-	0.1	-
Uvarovite	0.7	0.5	0.5	0.8	0.2	0.4	0.5	0.7	0.6	0.4	0.4	0.4	0.3	0.7
Almandine	80.8	80.4	80.0	79.3	80.0	80.0	78.8	78.6	78.5	79.4	81.8	81.7	81.9	83.2
Spessartine	1.4	1.0	0.9	1.4	2.0	2.4	2.3	1.9	1.8	1.1	1.5	1.5	0.7	1.1
Pyrope	3.9	5.4	6.0	5.7	5.4	5.0	5.3	5.6	5.3	5.2	4.1	4.4	5.3	4.7
Grossular	13.2	12.6	12.5	12.8	12.4	11.9	13.0	13.2	13.8	13.7	12.2	12.0	11.7	10.4

	DII 2031-1	DII 2031-2
SiO <sub>2</sub>	36.71	36.66
Al <sub>2</sub> O <sub>3</sub>	21.19	21.10
TiO <sub>2</sub>	-	-
Cr <sub>2</sub> O <sub>3</sub>	-	0.09
FeO	31.22	31.33
MnO	2.10	1.44
MgO	1.27	1.50
CaO	7.73	8.12
TOTAL	100.23	100.26

Si	5.92	5.90
Al	4.02	4.00
Ti	-	-
Cr	-	0.01
Fe	4.21	4.22
Mn	0.29	0.20
Mg	0.30	0.36
Ca	1.33	1.40

Andradite	-	-
Uvarovite	-	0.2
Almandine	73.8	73.8
Spessartine	5.0	3.4
Pyrope	3.0	3.5
Grossular	18.3	19.1



UNIVERSITY  
OF  
JOHANNESBURG

**TABLE IIB: AMPHIBOLE MICROPROBE ANALYSES**

	DH 2019-1	DH 2019-2	DH 2019-3	DH 2019-4	DH 2019-5	DH 2019-6	DH 2019-7	DH 2019-8	DH 2019-9	DH 2019-10	DH 2019-11	DH 2002-1	DH 2002-2	DH 2002-3
Na <sub>2</sub> O	0.02	0.01	0.01	0.02	-	0.07	0.02	0.03	0.05	0.07	0.04	1.74	-	1.22
SiO <sub>2</sub>	49.47	49.31	48.66	50.12	50.41	50.18	50.05	50.74	50.48	50.47	51.25	41.20	40.36	41.24
Al <sub>2</sub> O <sub>3</sub>	0.35	0.15	0.12	0.18	0.21	0.19	0.17	0.20	0.21	0.21	0.15	11.36	18.71	10.30
MgO	5.58	4.91	5.17	5.33	3.31	5.02	5.13	5.15	5.32	5.79	6.44	3.70	0.54	3.64
FeO	38.71	41.83	41.04	40.19	34.65	40.52	41.49	40.45	41.22	39.86	38.57	27.41	30.15	29.11
MnO	0.32	0.36	0.44	0.43	0.43	0.30	0.32	0.43	0.22	0.43	0.40	0.13	1.56	0.23
TiO <sub>2</sub>	-	-	0.04	0.04	0.09	0.05	0.14	-	-	0.07	0.02	0.74	-	0.72
K <sub>2</sub> O	-	-	-	0.04	-	0.01	0.01	-	-	0.03	0.01	1.79	0.04	1.67
CaO	1.70	0.74	0.55	0.72	7.40	0.61	0.56	0.59	0.64	0.68	0.64	9.22	6.72	9.23
Cr <sub>2</sub> O <sub>3</sub>	0.05	-	-	-	-	0.01	0.03	0.10	0.03	0.01	-	-	0.07	0.01
NiO	-	-	-	-	-	-	-	-	-	-	-	-	-	-
TOTAL	96.20	97.31	96.03	97.06	96.50	97.06	97.94	97.68	98.17	97.62	97.52	97.28	98.14	97.37

Na	-	-	-	-	-	0.02	-	0.01	-	0.02	0.01	0.51	-	0.36
Si	7.64	7.61	7.61	7.69	7.72	7.71	7.65	7.73	7.67	7.68	7.73	6.28	6	6.34
Al	0.06	0.02	0.02	0.03	0.03	0.03	0.03	0.03	0.03	0.03	0.02	2.04	3.3	1.9
Mg	1.28	1.12	1.2	1.21	0.75	1.15	1.16	1.17	1.2	1.31	1.44	0.84	0.12	0.83
Fe	5	5.39	5.37	5.15	4.44	5.2	5.3	5.15	5.24	5.07	4.87	3.5	3.74	3.72
Mn	0.04	0.08	0.05	0.05	0.05	0.03	0.04	0.05	0.02	0.05	0.15	0.01	0.19	0.03
Ti	-	-	-	-	0.01	0.01	0.01	-	-	-	-	0.04	-	0.08
K	-	-	-	0.01	-	-	-	-	-	0.01	-	0.34	-	0.33
Ca	0.28	0.12	0.09	0.11	1.21	0.1	0.09	0.09	0.1	0.11	0.1	1.5	1.06	1.51
Cr	0.01	-	-	-	-	-	0.01	-	-	-	-	-	0.01	-
Ni	-	-	-	-	-	-	-	-	-	-	-	-	-	-

Mg	19.5	16.9	18.3	18.7	11.7	17.8	17.7	18.2	18.3	20.2	22.5	14.4	2.4	13.7
Fe	76.2	81.3	80.6	79.6	69.3	80.6	80.9	80.4	80.1	78.1	76	60	76	61.4
Ca	4.3	1.8	1.1	1.7	19	1.6	1.4	1.4	1.6	1.7	1.5	25.6	21.6	24.9

	DII 2002-4	DII 2002-5	DII 2037-2	DII 2037-3	DII 2027-1	DII 2027-2	DII 2020-1	DII 2136-1	DII 2136-2	DII 2136-3	DII 2136-4	DII 2136-5	DD 2-1	DD 2-2
Na <sub>2</sub> O	1.05	0.68	0.88	0.74	0.33	0.91	1.19	1.31	0.04	1.12	0.10	0.75	0.06	-
SiO <sub>2</sub>	42.01	39.90	46.66	47.47	48.46	46.78	39.94	48.55	53.30	49.74	56.64	51.48	52.88	53.02
Al <sub>2</sub> O <sub>3</sub>	6.70	7.17	6.74	5.90	3.09	7.91	10.76	8.25	3.41	7.14	1.82	6.01	0.18	0.10
MgO	3.32	1.76	8.04	8.13	9.69	8.95	2.51	18.03	29.64	18.99	25.55	19.48	29.77	29.34
FeO	30.68	32.26	22.46	23.47	28.25	19.64	20.87	5.39	9.17	6.45	11.95	4.56	1.11	1.07
MnO	0.25	0.17	0.10	0.08	0.42	0.13	0.40	0.08	0.24	0.05	0.27	0.09	-	0.03
TiO <sub>2</sub>	0.78	0.28	0.50	0.34	0.09	0.51	0.09	0.53	0.15	0.44	0.05	0.49	-	0.01
K <sub>2</sub> O	1.70	3.28	0.37	0.31	0.22	0.40	1.77	0.15	-	0.11	-	0.09	-	0.01
CaO	11.21	11.14	11.07	10.92	6.97	11.59	10.93	12.30	0.51	10.89	0.48	12.13	0.92	0.78
Cr <sub>2</sub> O <sub>3</sub>	0.05	-	0.35	0.33	0.22	0.44	-	0.39	0.15	0.20	0.17	0.15	0.01	0.01
NiO	-	-	0.14	0.03	0.02	0.11	-	0.11	0.08	0.20	0.20	0.17	0.12	0.04
TOTAL	97.74	96.65	97.30	97.72	97.74	97.36	97.46	95.09	96.69	95.34	97.22	95.38	98.25	98.22

Na	0.31	0.21	0.25	0.21	0.09	0.25	0.37	0.35	0.01	0.03	0.02	0.21	0.01	-
Si	6.51	6.39	6.38	6.93	7.09	6.75	6.53	6.71	7.07	6.86	7.51	7.47	7.61	7.61
Al	1.22	1.35	1.16	1.01	0.53	1.34	2.07	1.34	0.53	1.16	0.28	0.17	0.03	-
Mg	0.76	0.41	1.75	1.77	2.1	1.92	0.61	3.72	5.68	3.9	5.05	4.21	2.83	2.96
Fe	3.98	4.31	2.74	2.86	3.46	2.37	2.85	0.62	1.02	0.74	1.33	0.06	3.58	3.52
Mn	0.03	0.02	0.01	0.01	0.05	0.02	0.05	0.01	0.03	0.01	0.03	0.01	0.13	0.02
Ti	0.09	0.03	0.05	0.02	0.1	0.06	0.01	0.05	0.15	0.02	-	0.03	-	-
K	0.33	0.67	0.68	0.06	0.04	0.02	0.35	0.02	-	0.02	-	0.01	-	-
Ca	1.85	1.91	1.73	1.71	1.09	1.79	1.91	1.82	0.07	1.61	0.07	1.89	0.14	0.01
Cr	0.01	-	0.04	0.04	0.02	0.05	-	0.04	0.02	0.02	0.01	0.02	-	-
Ni	-	-	0.02	-	-	0.01	-	0.01	0.01	0.02	0.02	0.02	0.01	-

Mg	11.5	6.2	28.1	27.9	31.7	31.5	11.4	60.4	84.3	62.4	78.3	68.3	43.2	45.6
Fe	60.4	65	44.1	45.1	52	38	53	10.1	14.7	11.8	20.6	1	54.7	54.2
Ca	28.1	28.8	27.8	27	16.3	29.6	35.6	29.5	1	25.8	1.1	30.6	2.1	0.2

**TABLE IIB: AMPHIBOLE MICROPROBE ANALYSES**

	DH 2031-1	DH 2031-2	DH 2031-3	DH 2112-1	DH 2010-1	DH 2010-2
Na <sub>2</sub> O	0.64	1.75	0.03	1.47	0.55	0.10
SiO <sub>2</sub>	45.80	39.23	44.76	43.98	48.16	51.08
Al <sub>2</sub> O <sub>3</sub>	5.36	10.15	7.27	8.39	2.80	0.59
MgO	9.36	3.81	10.76	5.42	9.60	11.46
FeO	27.54	30.83	30.09	26.48	29.10	24.97
MnO	0.24	0.13	0.39	0.33	0.94	0.65
TiO <sub>2</sub>	0.45	0.09	-	0.50	0.07	0.07
K <sub>2</sub> O	0.29	1.24	1.99	0.77	0.26	0.02
CaO	8.14	10.59	1.36	10.95	5.15	8.61
Cr <sub>2</sub> O <sub>3</sub>	0.14	0.01	0.07	0.06	-	-
NiO	-	0.09	-	0.06	-	-
TOTAL	97.90	97.92	96.72	98.40	96.63	95.54

Na	0.18	0.53	0.01	0.49	0.16	0.03
Si	6.78	6.27	6.71	5.89	7.2	7.43
Al	0.93	1.85	1.28	1.54	0.49	0.1
Mg	2.06	0.89	2.4	1.38	2.14	2.49
Fe	3.41	3.99	3.77	3.79	3.64	3.04
Mn	0.03	0.02	0.05	0.04	0.12	0.08
Ti	0.05	0.01	-	0.06	0.01	0.01
K	0.02	0.24	0.38	0.16	0.05	-
Ca	1.29	1.75	0.21	2	0.82	1.34
Cr	0.01	-	0.01	0.01	-	-
Ni	-	0.01	-	0.01	-	-

Mg	30.5	13.4	37.6	19.2	32.4	36.2
Ca	50.4	60.2	59.1	52.9	55.2	44.3
Fe	19.1	26.4	3.3	27.9	12.4	19.5

**TABLE IIC: PYROXENE MICROPROBE ANALYSES**

	DH 2019-1	DH 2019-2	DH 2019-3	DH 2002-1	DH 2002-2	DH 2037-1	DH 2037-2	DH 2037-3	DH 2027-1	DH 2019-1	DH 2019-2	DH 2019-3	DH 2020-1	DH2-1
Na <sub>2</sub> O	0.06	0.57	0.60	0.17	0.25	0.15	0.01	0.16	0.16	0.05	0.08	0.21	0.03	0.08
SiO <sub>2</sub>	50.90	48.63	49.33	50.37	49.41	50.94	51.37	51.26	49.97	48.69	48.60	48.71	46.90	51.35
Al <sub>2</sub> O <sub>3</sub>	0.05	4.38	4.65	-	0.37	1.00	0.27	0.72	0.26	0.45	0.53	0.89	0.30	0.18
MgO	5.63	4.53	4.72	5.93	3.97	7.04	11.16	10.38	13.25	3.92	3.81	3.94	4.07	8.23
FeO	31.45	31.35	28.87	21.00	23.51	35.99	34.42	34.30	34.40	23.72	23.80	23.07	45.89	19.99
MnO	0.13	0.05	0.10	0.45	0.39	0.58	0.52	0.47	0.34	0.36	0.40	0.40	1.27	0.68
TiO <sub>2</sub>	-	0.27	0.10	0.04	0.07	0.07	-	0.09	-	-	-	0.05	-	-
K <sub>2</sub> O	0.02	0.27	0.19	0.03	0.02	0.02	0.04	0.02	0.01	-	0.02	-	0.03	-
CaO	11.87	10.14	11.26	22.00	22.16	3.92	1.54	1.28	0.79	22.05	22.04	22.59	0.68	19.27
Cr <sub>2</sub> O <sub>3</sub>	0.06	-	0.19	0.01	-	0.07	0.09	-	0.05	0.09	0.04	-	0.02	0.02
NiO	-	-	-	0.12	-	-	0.12	-	0.01	-	0.08	0.03	0.06	0.08
TOTAL	100.15	100.19	100.01	100.12	100.16	99.79	99.55	98.67	99.24	99.34	99.40	99.89	99.24	99.88

Na	-	-	0.04	0.01	0.02	0.01	-	0.01	0.01	-	-	0.01	-	-
Si	2.05	1.95	1.95	2	1.98	2.05	2.04	2.05	2	1.98	1.98	1.96	2	2.15
Al	-	0.21	0.22	-	0.02	0.05	0.01	0.03	0.01	0.02	0.2	0.04	0.01	-
Mg	0.34	0.27	0.28	0.35	0.24	0.42	0.66	0.62	0.79	0.24	0.23	0.24	0.26	0.51
Fe	1.06	1.05	0.96	0.7	0.79	1.21	1.14	1.15	1.15	0.8	0.76	0.78	1.64	0.7
Mn	-	0.02	-	0.02	0.01	0.02	0.02	0.02	0.01	0.01	0.01	0.01	0.05	0.02
Ti	-	-	-	-	-	-	-	-	-	-	-	-	-	-
K	-	-	-	-	-	-	-	-	-	-	-	-	-	-
Ca	0.51	0.44	0.48	0.93	0.95	0.17	0.07	0.05	0.03	0.96	0.96	0.97	0.03	0.86
Cr	-	-	0.01	-	-	-	-	-	-	-	-	-	-	-
Ni	-	-	-	-	-	-	-	-	-	-	-	-	-	-

Mg	17.8	15.3	16.3	17.7	12.1	23.3	35.2	34.1	40.1	12	11.8	12.1	13.5	24.6
Fe	55.5	59.7	55.8	35.3	39.9	67.2	61	63.2	58.4	40	39	39.2	85	33.8
Ca	26.7	25	27.9	47	48	9.5	3.8	2.7	1.5	48	49.2	48.7	1.5	41.6

	D102-2	D102-3	D102-4	D11 2020-1	D11 2020-2	D11 2020-3	D11 2020-4	D11 2020-5	D11 2020-6	D11 2020-7	D11 2020-8	D11 2020-9	D11 2020-10	D11 2031-1
Na <sub>2</sub> O	0.11	0.04	-	-	-	-	-	-	-	-	-	-	-	0.07
SiO <sub>2</sub>	52.09	53.50	52.99	49.92	49.61	49.46	49.22	48.00	48.00	49.08	49.02	49.11	49.28	50.97
Al <sub>2</sub> O <sub>3</sub>	0.16	0.14	0.16	0.43	0.50	0.45	0.45	0.34	0.17	0.30	0.57	0.54	0.36	0.34
MgO	0.44	1.47	1.421	3.88	4.04	3.88	3.79	4.37	5.26	4.11	4.02	4.02	5.17	11.00
FeO	24.42	29.77	30.23	25.87	24.20	26.48	25.41	26.85	44.51	25.15	28.93	24.19	24.28	36.44
MnO	0.47	1.04	0.86	0.44	0.43	0.59	0.47	0.49	1.36	0.39	0.59	0.55	0.44	0.39
TiO <sub>2</sub>	-	0.05	0.05	0.16	-	0.09	-	0.02	0.17	0.12	-	-	-	0.02
K <sub>2</sub> O	-	-	-	-	-	-	-	-	-	-	-	-	-	-
CaO	21.58	0.87	0.85	19.63	21.20	18.17	20.33	20.00	0.56	21.18	17.14	21.54	20.43	0.79
Cr <sub>2</sub> O <sub>3</sub>	-	0.03	-	-	-	0.05	0.03	0.02	0.04	-	-	-	-	-
NiO	-	-	0.01	-	-	-	-	-	-	-	-	-	-	-
TOTAL	99.27	99.91	99.35	100.32	99.97	99.17	99.70	100.08	100.09	100.34	100.27	99.90	99.96	100.03

Na	-	-	-	-	-	-	-	-	-	-	-	-	-	-
Si	2.04	2.06	2.05	2	2	2.01	1.99	1.95	2	1.98	1.99	1.99	1.98	2.03
Al	-	-	-	0.02	-	0.02	0.02	0.02	-	0.01	0.03	0.03	0.02	0.02
Mg	0.03	0.83	0.82	0.23	0.24	0.23	0.23	0.26	0.33	0.24	0.24	0.24	0.31	0.65
Fe	0.8	0.96	0.98	0.87	0.82	0.89	0.86	0.91	1.56	0.85	0.98	0.82	0.82	1.21
Mn	0.02	0.03	0.03	0.01	0.01	0.02	0.02	0.02	0.05	0.01	0.02	0.02	0.01	0.01
Ti	-	0.01	-	-	-	-	-	-	-	-	-	-	-	-
K	-	-	-	-	-	-	-	-	-	-	-	-	-	-
Ca	0.91	0.03	0.03	0.87	0.92	0.79	0.88	0.87	0.02	0.91	0.74	0.94	0.93	0.03
Cr	-	-	-	-	-	-	-	-	-	-	-	-	-	-
Ni	-	-	-	-	-	-	-	-	-	-	-	-	-	-

Mg	1.7	45.6	44.8	11.7	12.1	12	11.7	12.7	17.3	12	12.2	12	25.4	34.4
Fe	46	52.7	53.6	44.2	41.4	46.6	43.7	44.6	81.7	42.5	50	41	67.2	64
Ca	52.3	1.7	1.6	44.1	46.5	441.4	44.6	42.7	1	45.5	37.8	47	7.4	1.6

**TABLE IIC: PYROXENE MICROPROBE ANALYSES**

	DH 2031-2	DH 2112-1	DH 2112-2	DH 2112-3	DH 2112-4	DH 2010-1	DH 2010-2	DH 2010-3
Na <sub>2</sub> O	0.06	0.36	0.29	0.11	0.18	0.16	0.30	0.24
SiO <sub>2</sub>	52.57	50.55	50.46	48.91	49.00	52.31	50.17	50.99
Al <sub>2</sub> O <sub>3</sub>	0.76	1.83	0.42	0.21	0.18	0.81	0.93	0.78
MgO	11.76	7.44	7.25	5.28	6.36	10.06	9.93	9.69
FeO	25.28	23.80	19.46	22.19	21.40	13.38	15.15	15.16
MnO	0.29	0.73	0.57	0.66	0.66	0.52	0.57	0.43
TiO <sub>2</sub>	0.21	0.15	0.07	-	0.12	-	0.11	0.01
K <sub>2</sub> O	0.01	0.21	0.01	0.01	0.01	-	-	-
CaO	9.16	14.49	21.59	21.12	22.11	22.69	22.55	22.85
Cr <sub>2</sub> O <sub>3</sub>	0.09	-	-	-	0.02	-	-	0.05
NiO	0.02	-	-	0.06	-	0.08	0.16	-
TOTAL	100.70	99.64	100.12	99.55	100.04	100.01	99.86	100.20

Na	-	0.03	0.02	-	0.01	0.01	0.02	0.02
Si	2.03	1.99	1.98	1.98	1.97	2.16	1.95	1.97
Al	0.03	0.08	0.02	-	-	-	0.04	0.04
Mg	0.68	0.44	0.42	0.32	0.38	0.62	0.57	0.56
Fe	0.81	0.78	0.64	0.75	0.72	0.46	0.49	0.49
Mn	0.01	0.02	0.02	0.02	0.02	0.02	0.02	0.01
Ti	0.02	-	-	-	-	-	-	-
K	-	-	-	-	-	-	-	-
Ca	0.38	0.61	0.91	0.92	0.91	1.01	0.94	0.94
Cr	-	-	-	-	-	-	-	-
Ni	-	-	-	-	-	-	-	-

Mg	36.4	24	21.3	16.1	18.9	29.7	28.5	28.2
Fe	43.3	42.6	32.5	37.7	35.8	22	24.5	24.6
Ca	20.3	33.4	46.2	46.2	45.3	48.3	47	47.2



**TABLE IID: FELDSPAR MICROPROBE ANALYSES**

	DII 2003-1	DII 2003-2	DII 2003-3	DII 2003-4	DII 2003-5	DII 2003-6	DII 2003-7	DII 2003-8	DII 2003-9	DII 2003-10	DII 2003-11	DII 2003-12	DII 2003-13	DII 2003-14
Na <sub>2</sub> O	11.07	12.51	10.18	10.22	12.65	9.17	11.55	11.72	10.76	11.80	6.21	5.76	11.92	12.72
SiO <sub>2</sub>	67.83	66.88	66.99	63.14	66.98	65.86	66.92	66.63	64.97	66.16	66.38	66.44	65.62	66.31
Al <sub>2</sub> O <sub>3</sub>	19.66	20.75	20.60	19.34	20.62	20.08	20.70	21.04	19.94	20.98	19.18	20.80	21.55	20.63
MgO	-	-	0.25	4.27	0.01	-	-	-	0.51	0.03	0.26	0.72	0.01	-
FeO	0.09	-	0.59	0.03	0.39	0.31	0.46	0.34	2.96	0.54	1.86	0.89	0.39	0.46
MnO	-	-	0.16	0.06	-	0.02	-	0.02	0.05	0.01	0.02	0.20	0.04	0.02
K <sub>2</sub> O	0.29	-	0.02	2.02	0.01	0.08	0.04	0.01	0.08	0.06	6.74	0.08	0.06	0.01
CaO	-	-	1.25	0.19	0.01	4.61	0.08	0.03	0.21	0.26	0.08	5.28	0.68	0.02
TiO <sub>2</sub>	-	-	-	-	-	-	-	-	-	-	-	-	-	-
Cr <sub>2</sub> O <sub>3</sub>	-	-	-	-	-	-	-	-	-	-	-	-	-	-
TOTAL	98.94	99.93	100.05	99.27	100.08	100.12	99.74	99.79	99.48	99.83	100.73	100.17	100.27	100.17
Na	3.78	4.9	3.44	3.54	4.28	3.12	4.9	3.98	3.72	4.03	2.15	1.95	4.06	4.33
Si	11.97	11.72	11.71	11.33	11.71	11.62	14.7	11.71	11.6	11.66	11.86	11.62	11.54	11.66
Al	4.09	4.28	4.26	4.09	4.25	4.17	3.06	4.35	4.19	4.35	4.04	4.29	4.47	4.28
Mg	-	-	0.07	1.14	-	-	-	-	0.14	0.01	0.07	0.19	-	-
Fe	0.01	-	0.09	-	0.06	0.05	0.08	0.05	0.44	0.08	0.28	0.13	0.05	0.07
Mn	-	-	0.09	-	-	-	-	-	0.01	-	-	0.03	0.01	-
K	0.06	-	-	0.46	-	-	0.01	-	0.02	0.01	1.53	0.02	0.01	-
Ca	-	-	0.23	0.04	-	0.87	0.02	-	-	0.05	0.02	0.99	0.13	-
Ti	-	-	-	-	-	-	-	-	-	-	-	-	-	-
Cr	-	-	-	-	-	-	-	-	-	-	-	-	-	-
Ab	98.4	100	93.7	87.6	100	78.2	99.4	100	99.5	98.5	58.1	65.9	96.7	100
Or	1.6	-	-	11.4	-	-	0.2	-	0.5	0.2	41.4	0.7	0.2	-
An	-	-	6.3	1	-	21.8	0.4	-	-	1.3	0.5	33.4	3.1	-

	DH 2003-15	DH 2003-16	DH 2003-17	DH 2003-18	DH 2003-19	DH 2003-20	DH 2003-21	DH 2003-22	DH 2003-23	DH 2003-24	DH 2003-25	DH 2003-26	DH 2003-27	DH 2003-28
Na <sub>2</sub> O	12.59	0.62	0.69	0.79	0.85	8.39	6.65	7.07	0.67	1.21	8.37	0.97	12.00	7.41
SiO <sub>2</sub>	65.23	63.70	63.39	63.13	63.63	64.92	57.48	56.27	58.05	63.68	59.14	63.13	67.56	57.03
Al <sub>2</sub> O <sub>3</sub>	21.26	19.47	20.11	19.46	19.21	19.14	26.40	27.06	28.40	19.71	25.42	19.52	20.49	27.47
MgO	-	-	-	0.01	-	-	0.09	0.01	0.29	0.01	0.01	-	-	-
FeO	0.55	0.01	0.07	0.24	0.21	0.07	0.67	0.31	1.34	-	0.12	0.10	0.29	0.20
MnO	0.02	-	0.04	0.12	-	-	0.10	-	0.07	-	-	0.07	-	-
K <sub>2</sub> O	-	16.04	14.72	15.99	15.62	0.11	2.03	0.15	10.12	15.06	0.06	15.85	-	0.14
CaO	0.02	-	-	0.01	-	6.17	6.81	9.13	0.47	-	7.02	0.02	-	8.36
TiO <sub>2</sub>	-	-	-	-	-	-	-	-	-	-	-	-	-	-
Cr <sub>2</sub> O <sub>3</sub>	-	-	-	-	-	-	-	-	-	-	-	-	-	-
TOTAL	99.67	99.84	100.02	99.74	99.51	99.79	100.22	99.49	99.41	99.67	100.14	99.66	100.34	100.62

Na	4.22	0.22	0.25	0.28	0.3	2.91	2.32	2.47	0.24	0.44	2.9	0.35	4.06	2.57
Si	11.28	11.81	11.75	11.75	11.82	11.64	10.35	10.15	10.58	11.68	10.57	11.75	11.79	10.19
Al	4.33	4.25	4.39	4.27	4.18	4.04	5.61	5.75	6.1	4.4	5.36	4.28	4.82	5.79
Mg	0.79	-	-	-	-	-	0.02	-	-	-	-	-	-	-
Fe	-	-	0.1	0.04	0.03	0.01	0.1	0.05	0.2	-	0.01	0.01	0.04	0.03
Mn	-	-	0.01	0.02	-	-	0.02	-	0.01	-	-	0.01	-	-
K	-	3.79	3.48	3.79	3.7	0.02	0.46	0.03	2.35	3.63	0.01	3.76	-	0.03
Ca	-	-	-	-	-	1.18	1.32	1.76	0.09	-	1.34	-	-	1.6
Ti	-	-	-	-	-	-	-	-	-	-	-	-	-	-
Cr	-	-	-	-	-	-	-	-	-	-	-	-	-	-

Ab	100	5.5	6.8	6.9	7.5	70.8	56.6	58	9	10.8	68.2	8.5	100	61.2
Or	-	94.5	93.2	93.1	92.5	0.5	11.2	0.7	87.7	89.2	0.3	91.5	-	0.7
An	-	-	-	-	-	28.7	32.2	41.3	3.3	-	31.5	-	-	38.1

**TABLE IID: FELDSPAR MICROPROBE ANALYSES**

	DH 2078-1	DH 2078-2	DH 2078-3	DH 2078-4	DH 2078-5	DH 2078-6	DH 2078-7	DH 2078-8	DH 2078-9	DH 2078-10	DH 2078-11	DH 2078-12	DH 2078-13	DH 2078-14
Na <sub>2</sub> O	6.23	6.45	6.16	6.15	6.28	6.22	6.18	6.09	3.60	6.19	6.30	6.21	6.37	6.15
SiO <sub>2</sub>	53.19	53.22	53.48	53.31	53.28	53.10	53.89	53.62	52.33	53.77	53.64	53.78	53.57	53.08
Al <sub>2</sub> O <sub>3</sub>	30.15	30.27	30.24	30.42	30.22	30.28	29.04	29.70	26.28	29.99	29.24	29.20	28.99	30.33
MgO	0.02	-	0.02	0.01	-	0.01	-	0.03	5.65	0.01	-	0.01	-	0.01
FeO	0.57	0.41	0.12	0.21	0.27	0.34	0.48	0.53	1.41	-	0.17	0.19	-	0.24
MnO	0.01	-	0.04	0.03	0.08	-	0.08	-	0.03	-	-	0.04	0.01	-
K <sub>2</sub> O	0.03	0.14	0.09	0.11	0.08	0.04	0.07	0.04	0.05	0.06	0.05	0.06	0.07	0.11
CaO	10.35	10.26	10.08	10.16	10.00	10.25	10.38	10.00	9.94	10.23	10.31	10.57	10.52	10.11
TiO <sub>2</sub>	-	-	-	-	-	-	-	-	-	-	-	-	-	-
Cr <sub>2</sub> O <sub>3</sub>	-	-	-	-	-	-	-	-	-	-	-	-	-	-
TOTAL	100.35	100.75	100.24	100.39	100.22	100.23	100.13	100.01	99.29	100.27	99.71	100.07	100.51	100.00

Na	2.18	2.25	2.15	2.15	2.2	2.24	2.17	2.13	1.27	2.16	2.22	2.18	2.24	2.16
Si	9.6	9.6	9.64	9.61	9.62	9.59	9.75	9.7	9.56	9.68	9.74	9.5	9.74	9.6
Al	6.41	6.43	6.42	6.46	6.44	6.44	6.19	6.33	5.66	6.37	6.26	6.23	6.21	6.47
Mg	-	-	-	-	-	-	-	-	1.53	-	-	-	-	-
Fe	0.09	0.06	0.02	0.03	0.04	0.05	0.07	0.08	0.22	-	0.03	0.03	-	0.04
Mn	-	-	-	-	0.01	-	0.01	-	-	-	-	-	-	-
K	-	0.03	0.01	0.02	0.01	-	0.01	-	0.01	0.01	0.01	0.01	0.01	0.02
Ca	2	1.98	1.95	1.96	1.94	1.98	2.01	1.94	1.96	1.97	2	2.05	2.05	1.96
Ti	-	-	-	-	-	-	-	-	-	-	-	-	-	-
Cr	-	-	-	-	-	-	-	-	-	-	-	-	-	-

Ab	52.2	52.8	52.3	52.1	53.1	53.1	51.8	52.3	39.2	52.2	52.5	51.4	52.1	52.2
Or	-	0.7	0.2	0.5	0.2	-	0.2	-	0.3	0.2	0.2	0.2	0.2	0.5
An	47.8	46.5	47.5	47.4	46.7	46.9	48	47.7	60.5	47.6	47.3	48.4	47.7	47.3

	DH 2078-15	DH 2078-16	DH 2086-1	DH 2086-2	DH 2086-3	DH 2034-1	DH 2034-2	DH 2034-3	DH 2034-4	DH 2034-5	DH 2034-6	DH 2034-7	DH 2034-8
Na <sub>2</sub> O	6.42	6.36	-	-	12.51	8.54	4.38	8.50	0.84	8.44	1.66	1.03	3.75
SiO <sub>2</sub>	53.47	53.41	65.35	66.82	66.88	61.27	63.80	64.93	63.23	64.99	63.98	63.35	65.05
Al <sub>2</sub> O <sub>3</sub>	29.86	29.46	19.20	18.69	20.25	25.55	20.85	19.32	19.66	20.01	19.81	19.63	12.12
MgO	0.02	0.02	0.02	0.02	-	0.18	-0.03	0.17	0.01	0.45	0.01	0.01	0.10
FeO	0.22	0.29	0.09	0.31	-	0.23	0.12	0.75	0.14	0.27	0.07	-	0.22
MnO	0.02	-	0.02	-	-	0.04	0.02	0.04	0.09	0.08	-	-	-
K <sub>2</sub> O	0.10	0.06	15.00	14.10	-	2.14	10.29	4.50	16.02	5.48	14.12	15.77	10.47
CaO	10.35	10.14	0.01	-	-	1.88	0.37	1.87	0.01	0.87	0.42	0.03	0.77
TiO <sub>2</sub>	-	-	-	-	-	-	-	-	-	-	-	-	-
Cr <sub>2</sub> O <sub>3</sub>	-	-	-	0.01	-	-	-	-	-	-	-	-	-
TOTAL	100.46	99.75	99.69	99.95	99.93	99.83	99.86	100.08	99.99	100.59	100.07	99.81	100.48

Na	2.24	2.24	-	-	4.27	2.94	1.54	2.96	0.3	2.92	0.59	0.37	1.43
Si	9.65	9.7	12	12.15	11.77	10.9	11.61	11.67	11.73	11.62	11.75	11.75	12.77
Al	6.35	6.31	4.15	4	4.21	5.36	4.47	4.09	4.3	4.22	4.29	4.29	2.8
Mg	-	-	-	-	-	0.05	-	-	-	0.12	-	-	0.03
Fe	0.03	0.01	0.01	0.05	-	0.03	0.02	0.11	0.02	0.04	-	-	0.04
Mn	-	-	-	-	-	-	-	-	0.01	0.01	-	-	-
K	0.02	0.01	3.51	3.27	-	0.48	2.39	1.04	3.79	1.25	3.31	3.73	2.62
Ca	2	1.97	-	-	-	0.36	0.07	0.36	-	0.17	0.08	-	0.16
Ti	-	-	-	-	-	-	-	-	-	-	-	-	-
Cr	-	-	-	-	-	-	-	-	-	-	-	-	-

Ab	52.6	53.1	-	-	100	77.8	38.5	67.9	7.3	67.3	14.8	9	34
Or	0.5	0.2	100	100	-	12.7	59.8	23.9	92.7	28.8	83.2	91	62.2
An	46.9	46.7	-	-	-	9.5	1.7	8.2	-	3.9	2	-	3.8

**TABLE III: TOURMALINE MICROPROBE ANALYSES**

	DH 2033B-1	DH 2033B-2	DH 2033B-3	DH 2033B-4	DH 2033B-5	DH 2033B-6	DH 2033B-7	DH 2033B-8	DH 2033B-9	DH 2033B-10
Na <sub>2</sub> O	2.00	2.12	1.98	2.12	2.17	2.10	2.09	2.03	1.85	2.67
SiO <sub>2</sub>	35.04	36.10	35.92	34.96	33.67	35.25	35.67	36.01	35.33	35.28
Al <sub>2</sub> O <sub>3</sub>	30.65	29.25	30.12	30.01	32.85	30.12	30.12	29.67	30.72	30.33
MgO	5.85	4.26	3.20	3.67	3.96	4.07	4.12	4.13	4.33	3.67
FeO	8.06	9.12	9.95	9.01	10.12	9.67	9.23	9.57	8.67	9.39
MnO	0.11	-	-	0.15	0.67	0.02	-	-	0.12	0.33
TiO <sub>2</sub>	1.05	0.96	1.67	1.22	1.17	1.16	0.85	0.67	1.01	1.12
K <sub>2</sub> O	0.02	0.12	-	0.01	0.67	-	-	-	0.33	0.27
CaO	1.81	1.65	1.15	1.15	1.83	1.60	1.22	1.35	1.42	2.22
Cr <sub>2</sub> O <sub>3</sub>	1.84	2.00	1.25	1.67	1.85	1.86	1.95	1.87	1.12	1.13
B <sub>2</sub> O <sub>3</sub> *	10.00	10.00	10.00	10.00	10.00	10.00	10.00	10.00	10.00	10.00
TOTAL	96.43	95.58	95.24	93.97	98.96	95.85	95.25	95.30	94.90	96.41

\* B<sub>2</sub>O<sub>3</sub> is averagely estimated not counted by the microprobe's spectrometers.

Na	0.69	0.74	0.7	0.75	0.75	0.73	0.73	0.58	0.65	0.93
Si	6.26	6.52	6.55	6.41	6.02	6.38	6.45	6.52	6.41	6.36
Al	6.45	6.23	6.48	6.49	6.93	6.43	6.42	6.33	6.57	6.45
Mg	1.56	1.15	0.87	1	1.06	1.1	1.1	1.11	1.17	0.09
Fe	1.2	1.38	1.52	1.38	1.51	1.46	1.4	1.45	1.32	1.42
Mn	0.02	-	-	0.02	0.1	-	-	-	0.02	0.05
Ti	0.14	0.13	0.23	0.17	0.16	0.16	0.12	0.1	0.14	0.15
K	-	0.02	-	-	0.15	-	-	-	0.08	0.06
Ca	0.36	0.32	0.22	0.23	0.35	0.24	0.32	0.26	0.22	0.43
Cr	0.26	0.28	0.18	0.24	0.29	0.28	0.28	0.27	0.16	0.16
B	3.08	3.12	3.15	3.16	3.09	3.12	3.12	3.12	3.13	3.11



	DH 2035-9
Na <sub>2</sub> O	-
SiO <sub>2</sub>	26.26
Al <sub>2</sub> O <sub>3</sub>	19.72
MgO	8.66
FeO	31.30
MnO	0.28
TiO <sub>2</sub>	0.04
K <sub>2</sub> O	10.33
CaO	0.06
Cr <sub>2</sub> O <sub>3</sub>	-
NiO	-
TOTAL	96.66

Na	-
Si	4.66
Al	4.12
Mg	2.29
Fe	4.64
Mn	0.04
Ti	-
K	2.33
Ca	0
Cr	-
Ni	-



UNIVERSITY  
OF  
JOHANNESBURG

**TABLE IIG: CARBONATE MICROPROBE ANALYSES**

	DII 2019-3	DII 2027-1	DII 2010-1	DD2-1	DII 2072-1	DII 2035-1	DII 2035-2	DII 2035-3	DII 2035-4	DII 2035-5
Na <sub>2</sub> O	0.05	0.18	-	0.36	0.06	0.06	0.07	-	-	-
SiO <sub>2</sub>	-	1.41	-	0.12	0.08	0.10	-	0.25	-	-
Al <sub>2</sub> O <sub>3</sub>	-	0.36	-	0.24	-	0.02	-	0.18	-	-
MgO	0.38	2.29	0.04	0.86	0.55	0.02	0.03	-	-	0.67
FeO	2.65	6.87	1.00	4.32	1.72	0.66	0.95	2.23	4.33	3.68
MnO	0.29	0.22	-	0.67	0.13	-	0.12	0.10	0.12	1.13
K <sub>2</sub> O	0.02	0.25	-	0.10	0.03	0.28	0.11	-	0.33	0.11
CaO	59.17	55.58	55.92	52.23	58.91	57.87	57.90	56.85	54.54	55.67
NiO	0.10	-	-	0.12	0.04	-	0.09	0.13	0.27	0.18
TOTAL	62.65	67.16	56.96	59.02	61.52	59.00	59.27	59.74	59.59	61.44

Na	-	0.03	-	0.07	-	0.01	0.01	-	-	-
Si	-	0.06	-	0.01	0.01	-	-	0.23	-	-
Al	-	0.05	-	0.03	-	-	-	0.02	-	-
Mg	0.05	0.29	-	0.12	0.07	-	-	-	-	0.09
Fe	0.2	0.48	0.08	0.35	0.1	0.05	0.08	0.18	0.35	0.28
Mn	0.02	0.02	-	0.05	0.01	-	0.01	0.01	0.01	0.09
K	-	0.03	-	0.01	-	0.03	0.01	-	0.04	0.01
Ca	5.72	5.01	5.91	5.37	5.76	5.9	5.89	5.73	5.6	5.51
Ni	0.07	-	-	0.01	-	-	0.01	0.01	0.02	0.01





**APPENDIX III:**

**MICROPROBE ANALYSES (ORE MINERALS)**



**TABLE IIIA: PYRITE MICROPROBE ANALYSES**

SAMPLE ELEMENT	WEIGHT % CONCENTRATION									
	DH 2005C-1	DH 2005C-2	DH 2005C-3	DH 2005C-4	DH 2005C-5	DH 2005C-6	DH 2005C-7	DH 2005C-8	DH 2072-1	DH 2072-2
Fe	47.42	44.24	43.84	47.00	48.49	47.94	63.59	48.25	44.07	44.00
S	50.28	51.18	51.07	50.30	50.95	49.14	37.86	51.21	51.70	51.72
Cu	0.57	0.32	0.03	0.43	0.11	3.10	0.08	0.08	0.09	-
Ni	0.23	4.22	5.90	1.73	0.99	0.57	0.36	1.42	4.27	4.07
As	1.56	0.03	0.12	0.13	0.15	-	0.06	0.05	-	-
TOTAL	100.06	99.99	100.96	99.59	100.69	100.75	101.95	99.96	100.13	99.79
	ATOMIC CONCENTRATION									
Fe	34.64	32.08	31.60	34.79	35.27	34.98	34.57	33.82	35.36	35.83
S	63.89	64.63	64.11	63.55	63.70	62.46	65.08	65.05	64.11	64.03
Cu	0.36	0.21	0.02	0.28	0.10	1.99	0.05	0.05	0.04	-
Ni	0.16	2.91	4.04	1.22	0.91	0.40	0.26	0.98	0.14	0.04
As	0.83	0.01	0.06	0.07	0.09	-	0.03	0.03	-	-
TOTAL	99.88	99.84	99.83	99.91	100.07	99.83	99.99	99.93	99.65	99.90

UNIVERSITY OF ANNAPOLIS

**TABLE IIIB: PYRRHOTITE MICROPOBE ANALYSES**

WEIGHT % CONCENTRATION

SAMPLE ELEMENT	DH 2005C-1	DH 2005C-2	DH 2005C-3	DH 2005C-4	DH 2005C-5	DII 1026-1	DH 1026-2	DH 1026-3	DII 2038-1	DH 2038-2	DH 2035-1	DII 2112-1	DH 2112-2
Pb	-	-	-	-	-	-	-	-	0.54	0.32	1.03	0.28	0.14
Fe	61.12	61.46	61.62	61.06	60.98	61.85	61.97	62.49	62.05	62.47	61.48	61.94	61.59
S	39.23	39.07	38.11	38.45	38.43	37.89	37.07	37.17	37.27	37.68	34.81	38.07	38.96
Ni	0.50	0.36	0.63	0.71	0.27	-	0.04	0.17	0.05	0.20	3.49	-	-
TOTAL	100.85	99.89	100.36	100.22	99.68	99.74	99.08	99.83	99.91	99.67	99.81	100.29	100.69

ATOMIC CONCENTRATION

SAMPLE ELEMENT	DH 2005C-1	DH 2005C-2	DH 2005C-3	DH 2005C-4	DH 2005C-5	DII 1026-1	DH 1026-2	DH 1026-3	DII 2038-1	DH 2038-2	DH 2035-1	DII 2112-1	DH 2112-2
Pb	-	-	-	-	-	-	-	-	0.11	0.06	0.17	0.05	0.02
Fe	46.88	47.59	47.74	47.77	47.95	50.25	49.69	48.63	50.81	48.15	56.35	49.44	50.51
S	52.40	51.85	51.61	51.05	51.68	49.60	49.95	50.92	49.05	51.61	37.34	50.34	49.18
Ni	0.37	0.26	0.44	0.52	0.21	-	0.03	0.12	0.03	0.14	5.56	-	-
TOTAL	99.65	99.70	99.79	99.34	99.84	99.85	99.67	99.67	100.00	99.96	99.42	99.83	99.71

**TABLE III.C: LÖLLINGITE MICROPROBE ANALYSES**

WEIGHT % CONCENTRATION													
SAMPLE ELEMENT	DII 2005C-1	DII 2005C-2	DII 2005C-3	DII 2005C-4	DII 2005C-5	DII 2005-5	DH 2005C-6	DH 2005C-7	DH 2005C-8	DH 2005C-9	DH 2005C-10	DH 2005C-11	
Fe	30.90	30.10	30.94	30.25	30.43	30.41	30.48	30.57	30.31	30.45	30.46	30.32	
S	1.82	1.52	1.47	1.75	1.48	1.94	1.86	2.03	2.20	1.84	1.64	1.81	
As	68.05	68.62	67.51	68.00	68.37	68.13	67.79	67.83	67.28	68.15	68.14	68.04	
TOTAL	100.77	100.24	99.92	100.00	100.28	100.48	100.13	99.93	99.79	100.44	100.24	100.17	
ATOMIC CONCENTRATION													
Fe	34.68	35.67	35.61	35.17	35.19	35.81	36.73	35.39	36.75	35.78	37.24	36.23	
S	3.44	2.94	2.86	3.43	2.90	3.72	3.55	3.84	4.10	3.54	3.17	3.54	
As	61.63	60.15	61.10	60.66	61.23	59.40	58.71	59.88	58.51	60.12	59.01	59.36	
TOTAL	99.75	98.76	99.57	99.26	99.32	98.93	98.99	99.11	99.36	99.44	99.42	99.13	
WEIGHT % CONCENTRATION													
SAMPLE ELEMENT	DII 2005C-12	DII 2005C-13	DII 2005C-14	DII 2005C-14	DII 2005C-15	DII 2005-16	DII 2005C-17	DII 2005C-18	DII 2005C-19	DD 2-2	DD 2-3	DD 2-4	
Fe	30.75	30.23	30.49	30.16	30.80	30.20	30.26	30.06	30.78	30.21	30.68	30.04	
S	1.20	1.97	2.22	1.61	2.31	1.67	1.62	1.90	1.89	1.85	1.97	1.86	
As	67.68	49.80	66.92	68.17	66.65	68.67	68.31	68.56	67.34	68.29	69.29	67.78	
TOTAL	99.63	100.00	99.63	99.94	99.76	99.54	100.19	100.52	100.01	100.35	99.94	99.68	
ATOMIC CONCENTRATION													
Fe	36.85	34.92	35.89	35.65	35.88	35.87	36.32	35.64	34.83	36.11	36.19	36.22	
S	2.43	31.77	4.26	3.11	4.54	3.35	3.19	3.69	3.72	3.30	3.47	3.35	
As	59.41	32.87	59.22	60.46	58.58	59.71	59.83	60.13	60.50	59.85	60.10	59.93	
TOTAL	98.69	99.56	99.37	99.22	99.00	98.93	99.34	99.46	99.05	99.26	99.76	99.5	

**TABLE IIC: LÖLLINGITE MICROPROBE ANALYSES**

SAMPLE ELEMENT	WEIGHT % CONCENTRATION																
	DD 2-5	DD 2-6	DD 2-7	DD 2-8	DD 2-9	DD 2-10	DD 2-11	DD 2-12	DD 2-13	DD 2-14	DD 2-15	DD 2-16	DD 2-17				
Fe	30.18	30.71	30.73	30.11	29.17	30.33	30.33	32.56	30.73	30.08	30.48	30.94	30.04				
S	1.99	1.63	2.15	1.78	1.12	1.83	1.84	1.90	1.67	1.57	1.80	1.83	1.96				
As	68.39	68.23	67.12	68.11	69.43	67.83	67.38	75.43	67.06	68.44	68.00	67.58	67.76				
TOTAL	100.56	100.57	100.00	100.00	99.72	99.99	100.55	99.89	100.46	100.09	100.28	100.35	99.76				

SAMPLE ELEMENT	ATOMIC CONCENTRATION																
	DD 2-5	DD 2-6	DD 2-7	DD 2-8	DD 2-9	DD 2-10	DD 2-11	DD 2-12	DD 2-13	DD 2-14	DD 2-15	DD 2-16	DD 2-17				
Fe	36.85	35.95	36.14	38.15	32.59	34.28	35.69	35.90	36.15	34.82	37.23	35.35	34.73				
S	3.44	2.85	4.40	3.47	2.43	3.48	3.42	3.55	3.11	2.80	3.38	3.43	3.71				
As	59.39	60.95	59.45	57.41	64.43	61.03	60.17	60.15	59.95	62.02	59.15	60.46	61.22				
TOTAL	99.68	99.75	99.99	99.03	99.45	98.79	99.28	99.60	99.21	99.64	99.76	99.24	99.66				

SAMPLE ELEMENT	WEIGHT % CONCENTRATION																
	DD 2-18	DD 2-19	DD 2-20	DD 2-21	DD 2-22	DD 2-23	DD 2-24	DD 2-25	DH 2062-1	DH 2062-2	DH 2033-1	DH 2033-2	DH 2033-3				
Fe	30.33	30.95	30.89	30.28	30.28	30.74	30.96	30.21	30.64	30.64	30.90	30.28	30.29				
S	1.85	1.87	1.97	2.07	1.85	1.96	1.92	1.93	1.87	1.67	1.83	1.91	1.69				
As	67.68	67.82	66.96	67.16	67.69	68.47	67.10	67.50	67.53	67.61	67.18	67.77	67.82				
TOTAL	99.86	99.64	99.82	99.51	99.82	100.17	99.98	99.64	100.04	99.92	99.91	99.96	99.80				

SAMPLE ELEMENT	ATOMIC CONCENTRATION																
	DD 2-18	DD 2-19	DD 2-20	DD 2-21	DD 2-22	DD 2-23	DD 2-24	DD 2-25	DH 2062-1	DH 2062-2	DH 2033-1	DH 2033-2	DH 2033-3				
Fe	34.77	34.06	34.18	34.22	35.88	34.57	36.25	35.69	36.09	35.48	35.90	35.72	35.87				
S	3.47	3.59	3.79	3.94	3.47	3.73	3.57	3.62	3.72	3.37	3.70	3.81	3.38				
As	60.69	61.38	61.83	61.29	60.03	61.26	59.76	60.49	59.98	60.94	60.25	60.23	60.52				
TOTAL	98.93	99.03	99.80	99.45	99.38	99.56	99.58	99.80	99.79	99.79	99.85	99.76	99.77				

**TABLE III C: LÖLLINGITE MICROPROBE ANALYSES**

		WEIGHT % CONCENTRATION													
SAMPLE		DH 2033-4	DH 2033-5	DH 2033-6	DH 2033-7	DH 2033-8	DH 2033-9	DH 2033-10	DH 2033-11	DH 2033-12	DH 2033-13	DH 2033-14	DH 2033-15	DH 2033-16	
ELEMENT															
Fe	30.65	30.47	30.63	31.17	30.21	30.33	30.45	30.45	30.45	30.58	30.59	30.89	30.21	30.21	
S	1.78	1.67	1.78	1.65	1.90	1.13	1.47	1.86	1.86	1.71	1.89	1.90	1.78	1.60	
As	67.51	68.00	67.13	66.99	68.19	67.02	67.74	67.38	67.38	67.90	67.44	67.21	68.19	67.87	
TOTAL	99.94	99.94	99.54	99.81	100.30	98.48	99.66	99.69	99.69	100.19	99.92	100.00	100.18	99.68	

ATOMIC CONCENTRATION

Fe	36.17	36.19	34.38	35.45	35.57	39.61	36.40	36.23	36.23	36.38	36.11	35.49	35.63	35.88
S	3.55	3.34	3.49	3.28	3.78	3.21	3.06	3.86	3.86	3.44	3.77	3.80	3.54	3.21
As	60.06	60.27	62.02	61.03	60.48	57.06	60.37	59.77	59.77	60.03	60.02	60.51	60.58	60.74
TOTAL	99.78	99.80	99.89	99.76	99.83	99.88	99.83	99.86	99.86	99.85	99.90	99.80	99.75	99.83

WEIGHT % CONCENTRATION

SAMPLE		DH 2033-17	DH 2033-18	DH 2033-19	DH 2033-20	DH 2033-21	DH 2033-22	DH 2033-23	DH 2033-24	DH 2033-25	DH 2033-26	DH 2033-27
ELEMENT												
Fe	30.35	30.37	30.23	31.66	28.56	30.59	29.23	29.23	29.94	30.27	30.49	30.46
S	1.77	1.89	1.94	1.49	4.11	1.62	1.69	1.69	1.74	1.87	1.76	1.22
As	67.73	67.36	67.44	66.00	67.33	68.18	69.44	69.44	68.52	67.30	68.12	69.53
TOTAL	99.85	99.62	99.61	99.15	100.00	100.39	100.36	100.36	100.00	99.44	100.37	100.21

ATOMIC CONCENTRATION

Fe	35.89	35.61	35.77	38.23	35.74	36.23	34.76	34.76	35.76	35.87	35.15	36.20
S	3.54	3.73	3.87	3.13	13.19	3.33	3.50	3.50	3.53	3.73	3.54	2.91
As	60.34	60.36	60.15	58.50	50.93	60.17	61.55	61.55	60.45	60.12	61.12	60.72
TOTAL	99.77	99.70	99.79	99.86	99.86	99.73	99.81	99.81	99.74	99.72	99.81	99.83

**TABLE IIID: ARSENOPYRITE MICROPROBE ANALYSES**

WEIGHT % CONCENTRATION

SAMPLE ELEMENT	DII 2005C-1	DII 2005C-2	DII 2005C-3	DII 2005C-11	DII 1026-1	DII 1026-2	DII 2038-1	DII 2038-2	DII 2038-3	DII 2038-4	DII 2038-5	DII 2038-6	DII 2038-7
Fe	35.80	36.61	35.37	35.44	35.53	32.46	36.26	36.41	35.62	35.58	35.92	35.24	35.91
S	19.62	19.22	20.04	16.36	20.39	20.21	18.89	20.06	20.24	18.89	18.17	18.77	18.67
Cu	-	-	-	-	0.43	0.17	0.12	0.44	0.24	-	0.06	0.09	0.09
Ni	0.08	-	-	0.06	0.10	0.04	0.47	0.41	0.07	0.45	0.90	0.29	0.07
As	44.84	44.56	44.50	48.32	44.04	46.94	44.33	42.91	44.10	44.70	45.00	45.58	45.17
TOTAL	100.34	100.39	99.91	100.18	100.49	99.82	100.07	100.23	100.27	99.62	100.05	99.97	99.91

ATOMIC CONCENTRATION

Fe	35.49	36.80	34.43	36.02	33.40	31.06	34.54	34.19	34.83	34.01	34.18	35.75	35.42
S	32.08	31.10	31.85	29.10	32.47	33.67	29.69	33.33	31.80	29.78	28.52	28.34	29.08
Cu	-	-	-	-	0.35	0.14	0.09	0.34	0.19	-	0.05	0.07	0.07
Ni	0.07	-	-	0.06	0.08	0.03	0.40	0.34	0.41	0.39	0.78	0.24	0.06
As	32.07	31.55	33.65	34.64	33.42	34.18	35.21	31.63	32.34	35.56	36.28	35.27	35.37
TOTAL	99.71	99.45	99.93	99.82	99.72	99.08	99.93	99.83	99.57	99.74	99.81	99.67	100.00

WEIGHT % CONCENTRATION

SAMPLE ELEMENT	DII 2112-1	DII 2112-2
Fe	35.61	36.20
S	19.85	19.94
Cu	0.36	0.16
Ni	-	-
As	44.28	44.17
TOTAL	100.10	98.31

ATOMIC CONCENTRATION

Fe	35.67	36.83	34.40	34.50
S	32.61	31.67	30.65	29.70
Cu	0.25	0.13	-	0.08
Ni	-	-	-	0.39
As	32.20	17.74	34.55	35.20
TOTAL	100.73	100.37	99.60	99.87



**TABLE IIIE: CHALCOPYRITE MICROPROBE ANALYSES**

SAMPLE ELEMENT	WEIGHT % CONCENTRATION			
	DII 1026-1	DII 1026-2	DII 2038-1	DII 2038-2
Pb	-	-	0.55	-
Fe	33.18	33.42	34.23	34.47
Zn	-	-	0.05	0.09
S	33.41	34.81	34.15	34.31
Cu	33.31	31.68	31.44	31.21
TOTAL	99.90	99.91	100.42	100.08
			99.73	99.98

SAMPLE ELEMENT	ATOMIC CONCENTRATION			
	DII 1026-1	DII 1026-2	DII 2038-1	DII 2038-2
Pb	-	-	0.12	-
Fe	25.63	27.32	27.73	28.11
Zn	-	-	0.03	0.07
S	49.41	49.63	48.18	48.75
Cu	24.86	22.72	23.80	22.73
TOTAL	99.90	99.67	99.86	99.66
			99.48	99.63

**TABLE IIIF: Ni - Co MINERAL MICROPROBE ANALYSES**

SAMPLE	WEIGHT % CONCENTRATION									
	Ni-Co PHASE DH 2005C-1	Ni-Co PHASE DH 2005C-2	Ni-Co PHASE DH 2005C-3	PENTLANDITE DH 2005C-1	PENTLANDITE DH 2005C-2	Ni-Co PHASE DH 2005C-4	DH 2035-1	DH 2035-2	DH 2035-3	DH 2035-4
ELEMENT										
Fe	7.74	8.00	7.23	32.03	32.38	7.55	15.70	16.43	17.85	21.97
Zn	0.09	0.03	-	-	-	0.25	3.94	1.75	6.10	1.53
S	18.30	18.74	18.52	32.13	32.22	19.47	20.57	19.86	19.07	19.82
Ni	11.03	11.78	11.41	35.84	35.78	11.44	12.46	12.19	11.68	11.51
As	46.24	46.02	44.54	-	0.07	46.12	47.19	49.73	45.05	45.42
Co	16.40	15.00	18.05	-	-	15.13	-	-	-	-
TOTAL	99.80	99.57	99.75	100.00	100.45	99.96	99.86	99.96	99.75	100.25
ATOMIC CONCENTRATION										
Fe	9.13	9.26	8.60	26.52	26.39	8.65	14.43	15.30	16.01	19.53
Zn	0.09	0.03	-	-	-	0.24	3.09	1.39	4.68	1.16
S	37.59	37.76	38.39	45.92	45.75	38.84	32.92	32.20	32.93	30.68
Ni	12.38	12.97	12.92	27.38	27.74	12.46	17.01	16.46	15.94	15.65
As	40.66	39.68	39.52	-	0.04	39.38	32.33	34.51	30.12	32.74
Co	-	-	-	-	-	-	-	-	-	-
TOTAL	99.85	99.70	99.43	99.82	99.92	99.57	99.78	99.86	99.68	99.76

UNIVERSITY  
OF  
NANBURG

**TABLE III G: GOLD (ELECTRUM) MICROPROBE ANALYSES**

WEIGHT % CONCENTRATION					
SAMPLE ELEMENT	DH 2038-1	DH 2038-2	DH 2038-3	DH 2038-4	DH 2038-5
Fe	0.44	1.05	0.40	11.05	7.73
Ag	29.12	25.10	27.83	15.17	4.89
Cu	0.69	0.37	0.05	-	0.39
Au	73.43	76.02	77.50	73.84	87.18
TOTAL	103.68	102.54	105.78	100.06	100.19
ATOMIC CONCENTRATION					
Fe	1.18	2.89	1.09	24.10	21.54
Ag	40.75	35.83	39.02	16.66	8.06
Cu	1.65	0.90	0.11	-	0.69
Au	56.27	59.43	59.50	58.91	69.71
TOTAL	99.85	99.05	99.72	99.67	100.00

**TABLE IIIH: SPHALERITE MICROPROBE ANALYSES**

SAMPLE ELEMENT	WEIGHT % CONCENTRATION						
	DII 2035-1	DII 2035-2	DII 2035-3	DII 2035-4	DII 2035-5	DII 2035-6	DII 2035-7
Fe	8.48	12.00	13.44	10.05	10.66	8.36	10.99
Zn	59.08	55.63	55.02	57.73	58.26	59.14	56.19
S	32.40	32.36	31.54	32.14	31.59	32.30	32.54
Ag	0.23	0.23	-	0.11	0.28	0.11	0.06
TOTAL	100.19	100.22	100.00	100.03	100.79	99.91	99.78
	ATOMIC CONCENTRATION						
Fe	7.21	10.37	11.34	8.81	9.18	7.43	9.43
Zn	44.39	42.40	42.18	44.61	42.85	43.43	41.19
S	48.00	46.90	46.33	45.86	47.37	48.50	48.63
Ag	0.10	0.10	-	0.05	0.13	0.05	0.03
TOTAL	99.70	99.77	99.85	99.33	99.53	99.41	99.28

**APPENDIX IV:**

**PROTON MICROPROBE ANALYSES (GARNET)**



**TABLE IV**

**Major and trace elements of one prograde garnet from sample 2035A (analysed by protonic microprobe)**

**Document Summary: concentration (ppm or wt%), uncertainty (1 sigma) and MDL (99% confidence)**

	Mn	Fe	Ni	Zn	Ca	Ge	As	Y	Zr	Au\LA
E38.1 G1	1.23 % 0.127 % 193	29.9 % 2.09 % 75.3	44.5 19.7 29.0	597 74.1 12.3	5.27% < 10.4	20.1 2.79 8.97	1.09 < 8.21	3.62 12.7 9.83	74.5 5.28 10.3	4.19 < 20.3
E38.2 G2	1.95 % 0.313 % 205	32.2 % 4.08 % 77.8	50.2 22.9 28.4	389 22.7 12.4	6.14% < 10.6	17.2 3.26 9.23	5.21 < 0.81	114 9.49 9.86	168 9.37 10.1	3.66 < 20.8
E38.3 G3	2.89 % 0.461 % 216	30.0 % 3.81 % 72.1	462 47.0 32.1	444 26.5 13.9	1.47% < 12.0	38.3 4.57 10.4	0.199% 59.1 9.37	65.4 4.95 9.37	170 7.55 9.85	34.5 0.85 23.5
E38.4 G4	3.32 % 0.561 % 234	29.1 % 3.69 % 75.7	40.5 14.6 28.1	396 23.5 12.3	6.38% < 10.5	48.7 3.78 9.09	12.6 3.06 8.30	99.8 6.44 7.79	64.5 4.93 8.36	2.88 < 20.6
E38.5 G5	4.46 % 0.713 % 256	29.5 % 3.75 % 82.8	62.1 21.1 30.3	460 26.6 13.0	2.68% < 11.6	83.1 5.12 10.0	1.70 < 9.16	627 14.3 9.89	13.8 5.02 10.3	2.27 < 22.7
E38.6 G6	3.89 % 0.623 % 242	29.9 % 3.80 % 77.6	22.0 < 29.2	531 31.0 12.5	5.08% < 10.8	73.5 4.49 9.50	63.08 < 8.81	38.4 3.65 7.08	67.61 < 7.91	1.06 < 21.4
E38.7 G7	2.49 % 0.398 % 204	31.2 % 3.96 % 66.0	24.3 < 29.3	496 28.7 12.3	5.14% < 10.7	37.8 3.87 9.46	- < 8.84	26.4 3.31 8.16	11.5 3.38 8.30	- < 21.3
E38.8 G.8	2.18 % 0.349 % 210	32.2 % 4.08 % 67.7	32.6 18.4 28.7	517 29.7 12.7	7.82% < 10.9	27.3 3.59 9.54	3.79 < 8.90	25.8 3.64 8.60	16.8 3.99 9.06	- < 21.5
E38.9 G.9	1.66 % 0.269 % 208	32.3 % 4.10 % 67.6	97.4 15.6 29.5	193 25.0 12.4	5.16% < 10.6	13.7 2.73 9.84	0.120% 8.40 9.02	68.8 4.83 9.65	364 10.8 10.1	4.45 < 21.4
E39.10 G10	1.71 % 0.273 % 210	32.2 % 4.09 % 68.0	35.0 15.3 30.9	412 24.0 12.9	3.38% < 11.0	4.22 < 9.33	86.5 4.61 8.76	179 10.4 9.56	191 8.26 9.92	- < 21.6
E38.11 G11	1.30 % 0.221 % 201	30.4 % 3.86 % 66.1	31.3 16.3 30.3	474 20.3 12.5	3.27% < 10.7	22.6 3.30 9.38	11.2 3.01 8.61	453 11.7 8.16	4.60 < 8.64	2.50 < 21.1
E39.12 G12	0.669 % 0.111 % 197	31.3 % 3.97 % 63.5	33.4 18.3 28.6	840 31.2 11.3	4.51% < 9.91	12.7 2.47 0.67	3.43 < 0.04	16.7 2.97 8.55	8.03 < 9.00	7.21 < 18.5
E38.13 E13	0.421 % 700 197	31.8 % 4.03 % 64.1	36.7 21.7 29.5	604 34.4 12.5	7.07% < 10.6	3.52 < 9.21	2.46 < 8.49	21.3 3.08 7.71	3.98 < 8.23	4.45 < 20.8
E38.14 G14	0.387 % 0.652 % 209	29.7 % 3.77 % 79.7	18.5 < 30.2	417 24.4 12.5	5.07% < 11.0	60.0 7.34 4.60	10.2 2.75 8.90	109 5.71 8.84	61.0 5.21 9.28	1.74 < 21.6

**APPENDIX V:**

**GEOCHEMICAL ANALYSES (REE, TRACE AND  
MAJOR ELEMENTS)**

UNIVERSITY OF  
JOHANNESBURG

**TABLE VA**

<b>RARE EARTH ELEMENTS, RADIOACTIVE ELEMENTS AND LEAD CONTENTS (PPM) IN SOME ROCKS FROM DOORNHOEK GOLD DEPOSIT</b>										
Sample	CC1	GF1	GF2	MIN1	MP1	MP2	MR1	MR2	QV1	UM1
Y 89	20.20	21.90	28.90	18.70	38.00	40.20	20.50	11.20	2.67	17.30
La 139	6.39	17.70	23.50	10.20	8.30	7.39	16.60	4.51	1.79	2.54
Ce 140	13.00	37.30	51.00	20.90	50.10	43.90	37.90	10.40	20.30	8.23
Pr 141	1.88	4.41	6.02	2.63	3.67	3.1	5.91	1.20	0.55	1.48
Nd 143	8.46	14.60	21.90	10.80	17.20	17.80	24.10	6.62	2.15	7.78
Nd 145	7.11	18.40	27.20	12.40	13.70	19.50	23.60	5.69	3.53	6.76
Nd 146	7.25	16.10	25.70	11.60	16.60	16.40	23.80	5.79	2.14	6.30
Nd AVG	7.61	16.37	24.93	11.60	15.83	17.90	23.83	6.03	2.61	6.95
Sm 147	1.45	5.38	6.68	3.10	6.30	6.19	7.36	2.85	1.30	3.49
Sm 149	2.25	6.79	7.03	3.62	6.15	4.97	7.67	2.63	1.86	2.98
Sm AVG	1.85	6.09	6.86	3.36	6.23	5.58	7.52	2.74	1.58	3.24
Eu 151	1.84	2.73	4.47	1.83	2.92	2.02	3.77	0.66	0.48	1.19
Eu 153	1.91	2.57	4.44	1.26	2.11	1.96	3.95	0.76	0.39	1.08
Eu AVG	1.88	2.65	4.46	1.55	2.52	1.99	3.86	0.71	0.43	1.14
Gd 155	3.34	8.36	9.73	4.39	8.35	8.68	8.51	2.41	1.56	3.37
Gd 157	2.56	4.16	8.66	4.66	6.9	6.84	7.04	2.38	1.54	2.76
Gd AVG	2.95	6.26	9.20	4.53	7.63	7.76	7.78	2.40	1.55	3.07
Tb 159	0.43	1.11	1.12	0.64	1.50	1.24	1.77	0.36	0.18	0.64
Dy 161	3.47	5.89	7.71	3.94	8.57	6.85	5.61	2.62	1.18	3.28
Dy 163	3.46	5.15	6.87	3.33	6.76	7.76	6.21	1.83	1.00	3.66
Dy AVG	3.47	5.52	7.29	3.64	7.67	7.31	5.91	2.23	1.09	3.47
Ho 165	0.78	1.18	1.45	0.74	1.60	1.81	2.04	0.57	0.14	0.89
Er 166	1.95	3.74	4.14	1.99	4.41	4.65	4.26	1.86	0.42	2.47
Er 167	2.31	3.44	4.2	2.39	5.08	4.92	3.51	1.78	0.80	2.82
Er AVG	2.13	3.59	4.17	2.19	4.75	4.79	3.89	1.82	0.61	2.65
Tm 169	0.33	0.81	0.64	0.18	0.9	0.82	1.68	0.25	0.12	0.50
Yb 171	1.78	5.13	4.81	2.29	3.98	4.97	4.59	1.46	0.41	2.23
Yb 172	1.83	4.01	4.67	2.26	4.33	4.55	3.56	1.85	0.33	1.76
Yb 173	2.21	4.06	3.92	2.70	5.17	5.37	4.37	2.25	0.81	2.94
Yb AVG	1.94	4.40	4.47	2.42	4.49	4.96	4.17	1.85	0.52	2.31
Lu 175	0.22	0.79	0.76	0.37	0.99	0.75	1.62	0.24	0.10	0.52
Pb 208	17.90	5.86	5.60	2.65	7.56	4.99	13.70	2.78	4.64	2.45
Th 232	0.12	3.53	3.68	0.44	0.92	0.64	3.44	0.32	0.34	0.74
U 235	11.70	37.20	34.60	20.90	34.10	47.80	37.20	26.70	31.20	33.00
U 238	0.08	1.14	0.95	0.34	0.59	0.48	1.97	0.20	0.30	0.39



**TABLE VB**

RARE EARTH ELEMENTS, RADIOACTIVE ELEMENTS AND LEAD CONTENTS (PPM) IN SOME ROCKS FROM DOORNHOEK GOLD DEPOSIT (repeat analyses)										
Sample	CC1B	GF1B	GF2B	MIN1B	MP1B	MP2B	MR1B	MR2B	QV1B	UM1B
Y 89	19.60	21.99	26.56	15.87	36.13	36.97	19.71	12.89	2.10	16.08
La 139	6.26	19.37	23.16	8.48	7.43	7.25	15.40	5.44	1.66	2.52
Ce 140	13.20	39.18	51.72	19.61	48.70	43.65	34.74	10.28	19.98	7.54
Pr 141	1.77	4.20	6.15	2.52	3.15	3.28	5.07	1.27	0.53	1.18
Nd 143	6.79	14.97	23.76	12.36	14.69	15.89	18.41	4.38	2.36	6.38
Nd 145	6.86	16.81	23.76	10.00	14.89	17.95	22.36	6.64	1.71	5.84
Nd 146	7.26	17.77	23.56	11.96	16.89	15.15	23.96	4.32	2.78	5.70
Nd AVG	6.97	16.52	23.70	11.44	15.49	16.33	21.58	5.11	2.28	5.97
Sm 147	1.97	5.12	7.91	4.02	6.53	7.01	6.39	1.84	1.47	2.46
Sm 149	2.22	5.20	6.33	2.28	6.19	4.78	7.99	2.62	1.27	3.44
Sm AVG	2.10	5.16	7.12	3.15	6.36	5.90	7.19	2.23	1.37	2.95
Eu 151	1.69	2.66	4.13	0.96	1.57	1.69	2.68	0.82	0.39	0.89
Eu 153	2.01	2.50	4.75	1.56	1.96	1.79	2.74	1.03	0.34	0.65
Eu AVG	1.85	2.58	4.44	1.26	1.76	1.74	2.71	0.92	0.37	0.77
Gd 155	2.33	6.56	9.13	4.40	6.91	6.61	6.39	2.72	1.27	2.92
Gd 157	3.19	4.04	6.63	3.10	6.59	6.93	5.51	2.26	1.06	2.94
Gd AVG	2.76	5.30	7.88	3.75	6.75	6.77	5.95	2.49	1.17	2.93
Tb 159	0.45	0.76	1.04	0.53	1.02	1.11	0.68	0.31	0.24	0.43
Dy 161	3.37	5.74	7.29	4.06	6.59	8.71	4.79	2.26	1.16	3.36
Dy 163	3.28	4.48	6.49	2.90	7.03	7.57	4.57	2.30	0.61	3.42
Dy AVG	3.33	5.11	6.89	3.48	6.81	8.14	4.68	2.28	0.88	3.39
Ho 165	0.82	1.12	1.20	0.70	1.50	1.58	0.82	0.41	0.14	0.73
Er 166	2.06	3.36	4.03	2.46	4.17	4.82	2.72	1.44	0.45	2.02
Er 167	2.26	3.84	4.25	2.18	4.13	5.66	3.35	2.38	0.65	2.76
Er AVG	2.16	3.60	4.14	2.32	4.15	5.24	3.04	1.91	0.55	2.39
Tm 169	0.44	0.63	0.59	0.37	0.60	0.62	0.42	0.38	0.10	0.36
Yb 171	1.72	4.06	5.05	2.56	3.89	4.30	3.10	2.18	0.53	2.30
Yb 172	1.97	3.44	3.93	1.77	3.87	4.34	2.98	1.95	0.30	2.82
Yb 173	1.71	5.18	4.43	2.38	3.57	4.98	3.04	1.75	0.41	2.34
Yb AVG	1.80	4.22	4.47	2.24	3.78	4.54	3.04	1.96	0.42	2.49
Lu 175	0.28	0.66	0.72	0.37	0.71	0.73	0.38	0.35	0.18	0.33
Pb 208	18.10	5.28	5.63	2.20	7.80	4.80	13.40	2.96	4.12	1.44
Th 232	0.19	3.64	3.55	0.41	0.75	0.64	1.65	0.34	0.29	0.12
U 235	14.30	43.98	27.56	20.61	5.75	13.37	13.64	11.78	23.18	22.60
U 238	0.16	1.26	1.01	0.30	0.35	0.27	0.64	0.18	0.18	0.18

**TABLE VC**

ONLY RARE EARTH ELEMENTS (PPM) IN SOME ROCKS FROM DOORNHOEK GOLD DEPOSIT (analysis made on duplicate samples)										
Sample	CC1	GF1	GF2	MIN1	MP1	MP2	MR1	MR2	QV1	UM1
La	6.33	18.54	23.33	9.34	7.86	7.32	16.00	4.97	1.72	2.53
Ce	13.10	38.24	51.36	20.25	49.40	43.75	36.32	10.34	20.14	7.89
Pr	1.83	4.30	6.09	2.58	3.41	3.19	5.49	1.23	0.54	1.33
Nd	7.29	16.44	24.31	11.52	15.66	17.11	22.71	5.57	2.44	6.46
Sm	1.97	5.62	6.99	3.26	6.29	5.74	7.35	2.48	1.48	3.09
Eu	1.86	2.61	4.45	1.40	2.14	1.86	3.28	0.82	0.40	0.95
Gd	2.86	5.78	8.54	4.14	7.19	7.27	6.86	2.44	1.36	3.00
Tb	0.44	0.94	1.08	0.58	1.26	1.17	1.23	0.33	0.21	0.54
Dy	3.40	5.31	7.09	3.56	7.24	7.72	5.30	2.25	0.99	3.43
Ho	0.80	1.15	1.33	0.72	1.55	1.70	1.43	0.49	0.14	0.81
Er	2.15	3.59	4.16	2.26	4.45	5.01	3.46	1.86	0.58	2.52
Tm	0.39	0.72	0.62	0.28	0.75	0.72	1.05	0.31	0.11	0.43
Yb	1.87	4.31	4.47	2.33	4.14	4.75	3.60	1.91	0.47	2.40
Lu	0.25	0.72	0.74	0.37	0.85	0.74	1.00	0.29	0.14	0.43

- CC = monomineral calcite vein  
 GF = prograde garnetiferous formation  
 MIN = mineralisation in quartz vein (mainly pyrrhotite)  
 MP = "metapelite"  
 MR = mafic rock (mafic calc-silicate rock)  
 QV = quartz vein  
 UM = ultramafic rock

**TABLE VI: TRACE ELEMENTS FOR REPRESENTATIVE SAMPLES FROM DOORNHOEK GOLD DEPOSIT**

SAMPLE ELEMENT	2033 MP	2003 MP	2065 MP	2035 MP	2020 MR	2091 MR	2022 MR	2035 MR	2035 / PP1 MR	2035 / PP2 MP	2039 / PP3 MP	2047 / PP4 MP
Nb(ppm)	17	10	17	15	7	5	6	6	9	9	12	12
Y	45	32	29	99	21	14	17	15	47	25	43	39
Rb	100	86	97	113	6	<5	<5	<5	112	85	99	101
Sr	312	298	285	301	32	35	31	29	28	13	47	34
Zr	117	113	108	99	17	9	13	12	112	93	100	112
Cu	82	71	68	97	52	45	48	47	187	109	143	167
Ba	512	441	533	487	64	39	58	47	232	164	279	233
Ni	183	135	165	113	52	17	48	21	387	235	483	531
Co	48	55	47	52	39	41	40	36	48	40	47	46
Zn	127	118	119	131	207	134	181	192	726	415	679	498
Pb	15	14	12	18	<5	<5	<5	<5	18	10	23	22
W	17	14	9	18	28	46	37	31	12	9	15	18
Mo	<5	<5	<5	7	<5	<5	<5	<5	18	11	17	21
As	212	200	231	217	31	16	23	27	487	190	675	548
Cr	313	289	293	301	72	35	68	39	872	491	723	432
V	345	321	318	333	31	15	18	27	189	157	193	181
Au (ppb)	20	28	67	18	320	645	399	426	8620	3290	3870	4920

2033 MP :- Felsic granulite

2020 MR :- BIF - mafic granulite

2035 / PP1MR:- Metasomatic biotite-garnetiferous formation formed as the chemical interaction between the fluids and the BIF analysed in 2035 MR

2035 / PP2MP:- Metasomatic biotite-garnetiferous formation formed as the chemical interaction between the fluids and the felsic granulite analysed in 2035 MP

SAMPLE	2120 UR	2132 UR	2136 UR	2137 UR	Mineralised vein 2011	Mineralised vein 2035	Mineralised vein 2061	Calcite vein 2191	Bay. Gneiss 2100	Bay. Gneiss 2101	Metasomatic vein 2102
ELEMENT											
Nb(ppm)	<5	<5	<5	<5	7	8	12	<5	7	8	5
Y	18	13	17	21	22	23	31	22	6	5	9
Rb	<5	<5	<5	<5	7	6	8	<5	44	49	100
Sr	8	5	7	11	76	83	91	479	496	612	326
Zr	24	19	21	27	20	19	18	<5	70	81	<5
Cu	6	8	7	9	243	3136	4875	<5	12	18	11
Ba	30	32	31	29	28	29	31	27	308	499	2160
Ni	546	676	587	601	<5	<5	<5	<5	15	17	10
Co	46	48	52	61	29	31	33	<5	8	7	<5
Zn	49	51	47	39	69	112	118	24	44	61	24
Pb	<5	<5	<5	<5	<5	<5	<5	14	16	12	31
W	<5	<5	<5	<5	6	8	<5	29	12	14	10
Mo	<5	<5	<5	<5	9	8	7	<5	<5	<5	7
As	<5	<5	<5	<5	61	1131	1281	10	<5	<5	5
Cr	1106	1128	1312	1092	50	72	68	27	88	101	84
V	175	212	187	191	9	12	13	<5	14	19	<5
Au (ppb)	<10	12	<10	<10	13620	11680	12870	265	<10	<10	<10

2120 UR :- Ultramafic granulite

**TABLE VII: MAJOR ELEMENTS FOR REPRESENTATIVE SAMPLES FROM DOORNHOEK GOLD DEPOSIT**

SAMPLE ELEMENT	2033 MP	2003 MP	2065 MP	2035 MP	2020 MR	2091 MR	2022 MR	2035 MR	2035 / PP1 MR	2035 / PP2 MP	2039 / PP3 MP	2047 / PP4 MP
SiO <sub>2</sub>	59.04	53.50	62.36	68.31	38.49	35.38	40.68	41.15	47.50	53.09	54.11	52.15
TiO <sub>2</sub>	0.63	1.96	0.54	0.40	0.03	0.03	0.02	0.04	0.61	0.46	0.51	0.37
Al <sub>2</sub> O <sub>3</sub>	17.30	18.89	14.71	9.59	1.12	0.20	-	0.72	14.54	12.93	13.21	14.35
FeO	7.89	9.02	6.08	0.06	42.5	46.33	46.29	46.10	24.78	18.15	19.01	19.33
Fe <sub>2</sub> O <sub>3</sub>	3.00	1.55	0.65	11.47	4.29	7.95	9.22	4.52	2.31	3.21	1.88	3.07
MnO	0.17	0.18	0.03	0.02	0.94	0.50	0.59	0.85	0.35	0.36	0.65	0.81
MgO	2.49	2.47	2.15	0.79	3.74	2.43	3.44	4.04	2.03	4.52	4.51	4.62
CaO	1.64	9.25	1.23	0.98	3.14	2.40	2.97	3.87	3.83	2.58	2.36	3.67
Na <sub>2</sub> O	0.79	2.11	1.14	1.52	0.05	0.05	0.05	0.07	0.18	0.08	0.07	0.06
K <sub>2</sub> O	6.01	2.56	8.52	3.27	0.06	0.05	-	0.01	3.75	1.28	1.19	1.35
P <sub>2</sub> O <sub>5</sub>	0.08	0.14	0.12	0.06	0.22	0.14	0.15	0.53	0.17	0.12	0.11	0.15
Cr <sub>2</sub> O <sub>3</sub>	0.09	0.08	0.10	0.05	-	-	-	-	0.09	0.05	0.04	0.03
NiO	0.03	0.02	0.07	0.04	0.01	0.01	0.01	0.01	0.04	0.02	0.02	0.02
S	-	0.07	-	-	3.20	0.22	-	-	-	-	-	-
H <sub>2</sub> O	0.22	0.10	0.18	0.10	0.06	0.05	0.05	0.09	0.17	0.17	0.17	0.18
LOI	0.17	-1.94	1.97	2.79	2.09	4.05	-3.69	-2.00	-0.53	2.24	2.15	0.06
TOTAL	99.55	99.96	99.85	99.45	99.94	99.79	99.78	99.99	99.82	99.27	99.99	100.22

2033 MP :- Felsic granulite

2020 MR :- BIF - mafic granulite

2035 / PP1MR:- Metasomatic garnetiferous formation formed as the chemical interaction between the fluids and the BIF analysed in 2035 MR

2035 / PP2MP:- Metapelite analysed in 2035 MP

SAMPLE	2120 UR	2132 UR	2136 UR	2137 UR	Mineralised vein 2011	Mineralised vein 2035	Mineralised vein 2061	Calcite vein 2191	Hav. Cineiss 2100	Bav. Cineiss 2101	Pygmatic vein 2102
ELEMENT											
SiO <sub>2</sub>	48.08	47.83	43.62	49.22	53.11	52.67	48.39	32.94	72.79	72.13	72.13
TiO <sub>2</sub>	0.57	0.53	0.25	0.19	0.46	0.83	0.33	0.05	0.19	0.15	0.05
Al <sub>2</sub> O <sub>3</sub>	10.85	11.25	10.05	11.73	11.29	5.35	4.31	0.89	15.57	15.83	15.38
FeO	10.17	8.51	7.90	6.05	27.14	22.71	27.65	3.5	3.31	3.71	0.15
Fe <sub>2</sub> O <sub>3</sub>	0.98	0.75	0.80	1.04	1	2.27	1.23	0.23	1.56	0.77	0.01
MnO	0.18	0.15	0.15	0.14	0.43	0.15	0.12	0.31	0.05	0.06	0.05
MgO	18.09	16.97	22.42	17.59	2.92	1.12	0.98	0.97	0.55	0.67	0.50
CaO	11.25	10.08	7.35	10.24	2.53	1.85	1.50	59.26	2.19	2.21	0.97
Na <sub>2</sub> O	0.92	1.10	0.53	1.34	0.05	0.01	0.03	-	5.59	5.20	4.03
K <sub>2</sub> O	0.12	0.16	1.06	0.24	2.04	0.35	0.40	0.05	1.23	1.63	5.48
P <sub>2</sub> O <sub>5</sub>	0.05	0.02	0.01	0.02	0.14	0.11	0.10	0.05	0.06	-	0.09
Cr <sub>2</sub> O <sub>3</sub>	0.03	0.13	0.11	0.12	-	-	-	-	-	-	-
NiO	0.18	0.08	0.11	0.03	0.08	0.69	0.83	-	-	-	-
S	0.03	-	-	-	1.08	20.07	21.33	0.06	0.03	0.03	0.03
H <sub>2</sub> O	0.12	0.12	0.23	0.13	0.11	0.11	0.12	0.08	0.03	0.03	0.05
LOI	-1.90	1.67	4.92	1.78	-1.18	-6.78	-7.23	-28.70	-3.24	-3.20	-0.44
TOTAL	99.72	99.35	99.51	99.86	100.20	101.51	100.09	69.69	99.91	99.22	98.48

2120 UR:- Ultramafic granulite

**APPENDIX VI:**



**Table VIII A: Tf and Th for High-Density Fluid Inclusions (type 1a)**

Number	Tf °C	Tmf °C	Th °C	Size (when measured) μm
Sample : 2035 B quartz inclusions in garnet				
1	-97.8	-56.6	-48.3	11.5
2	-98.3	-56.8	-48.3	11
3	-95.3	-56.5	-48.9	10
4	-94.2	-56.7	-49.3	12.5
5	-99.2	-56.9	-50.3	13
6	-96.3	-56.9	-52.5	10
7	-92.5	-57.2	-51.8	17
8	-96.6	-58.3	-52.3	8
9	-96.5	-56.7	-45.8	7
10	-98.7	-56.6	-46.2	8.5
11	-97.3	-56.5	-46.3	8.5
12	-98.3	-56.2	-45.8	12.5
13	-98.9	-56.3	-45.2	10
14	-92.2	-56.1	-46.8	10
15	-86.8	-56.6	-37.3	13
16	-98.3	-56.6	-37.5	16
17	-99.9	-56.6	-34.2	6
18	-98.2	-56.5	-34.8	10
19	-93.2	-56.4	-30.2	12
20	-97.6	-56.2	-34.8	8
21	-98.3	-56.0	-26.8	8
22	-96.3	-56.2	-28.9	10
23	-96.5	-56.6	-29.0	14
24	-96.8	-56.9	-52.8	45
25	-95.4	-58.8	-50.6	8
26	-95.6	-59.2	-52.8	9
27	-95.4	-59.8	-53.7	12
28	-96.7	-59.7	-52.1	8
29	-96.4	-58.8	-50.0	7



Number	Tf °C	Tmf °C	Th °C	Size (when measured) μm
Sample : quartz vein 2035 B				
1	-96.3	-56.0	-8.0	10
2	-96.4	-56.4	-8.2	12
3	-96.5	-56.6	-19.3	13
4	-96.0	-56.3	-16.2	8
5	-92.8	-56.6	-14.7	13
6	-92.7	-56.7	-11.3	6.8
7	-98.3	-56.6	-20.1	7
8	-96.2	-56.5	-15.8	8.2
9	-96.5	-56.7	-20.3	9.5
10	-96.8	-56.8	-17.1	10
11	-96.5	-56.6	-48.2	5
12	-96.5	-56.6	-48.7	16.5
13	-96.5	-56.6	-48.9	10
14	-97.2	-56.7	-50.3	8
15	-96.5	-56.6	-49.2	
16	-96.4	-56.7	-48.3	
17	-98.3	-56.5	-47.2	
18	-98.5	-56.6	-46.8	
19	-97.3	-56.8	-46.7	
20	-98.3	-56.6	-46.8	
21	-96.6	-56.6	-46.9	
22	-95.4	-56.6	-48.2	
23	-95.8	-56.7	-47.5	
24	-95.7	-56.8	-48.3	
25	-95.6	-56.6	-48.0	
26	-95.6	-56.6	-48.0	
27	-95.8	-56.7	-49.2	
28	-96.4	-56.8	-50.2	
29	-96.5	-56.9	-51.3	
30	-96.4	-56.6	-46.0	14
31	-95.3	-56.7	-46.7	23
32	-98.7	-56.8	-48.0	6
33	-98.9	-56.6	-47.3	6
34	-89.6	-56.5	-47.1	7.5
35	-99.9	-56.6	-47.1	8.3

Number	Tf °C	Tmf °C	Th °C	Size (when measured) μm
36	-99.8	-56.7	-47.1	8.0
37	-98.3	-56.6	-46.3	6
38	-92.3	-56.5	-46.5	6
39	-96.5	-56.8	-46.3	9
40	-98.5	-56.6	-46.8	11
41	-98.9	-56.7	-46.3	8
42	-98.7	-56.5	-47.8	8
43	-98.3	-56.3	-48.1	10
44	-99.3	-56.2	-47.9	6
45	-96.6	-56.7	-46.7	6
46	-96.3	-56.6	-46.5	6
47	-96.8	-56.4	-46.3	7
Sample : DH 2033 B quartz vein				
1	-96.3	-56.9	-50.3	14.5
2	-98.7	-57.3	-52.1	14.5
3	-96.8	-56.8	-51.8	19
4	-96.4	-58.3	-52.3	18
5	-96.5	-59.2	-50.7	20
6	-96.4	-60.3	-52.2	18
7	-96.3	-58.7	-51.8	21
8	-96.8	-57.5	-50.7	14
9	-96.5	-58.9	-51.3	12
10	-96.7	-59.9	-52.0	8.5
11	-96.8	-59.9	-52.9	7.5
Sample : 2035 B quartz vein				
1	-98.9	-56.5	-44.6	10
2	-98.7	-56.3	-46.0	8.5
3	-97.3	-56.2	-45.0	8
4	-100.1	-56.1	-45.9	8
5	-99.9	-56.0	-44.3	11
6	-98.7	-56.2	-45.2	11
7	-98.6	-56.6	-44.3	10
8	-90.3	-56.0	-26.5	7
9	-81.7	-56.4	-27.3	8.5
10	-92.3	-56.0	-28.0	9.3
11	-87.2	-56.3	-22.3	12

Number	Tf °C	Tmf °C	Th °C	Size (when measured) μm
12	-79.6	-55.9	-27.0	12
13	-88.5	-55.7	-23.7	9.5
14	-86.6	-56.3	-24.6	8.7
15	-92.3	-56.2	-25.8	7
16	-97.6	-56.6	-40.3	13
17	-92.3	-56.6	-20.2	11
18	-96.4	-55.9	-21.3	12
19	-98.5	-56.3	-41.3	25
20	-92.4	-56.3	-28.9	4
21	-98.6	-56.4	-41.8	9
22	-97.3	-56.7	-41.2	8
23	-98.6	-56.2	-40.3	7.5
24	-97.6	-56.1	-41.8	8
25	-96.5	-56.1	-29.7	7
26	-97.8	-56.2	-30.3	13
27	-98.7	-56.6	-31.7	7
28	-97.7	-56.7	-34.3	9
29	-96.3	-56.6	-34.8	8.5
30	-96.4	-56.6	-38.7	7
Sample : 2033 A quartz vein near garnet				
1	-98.5	-56.7	-38.6	9
2	-96.7	-56.5	-38.3	10
3	-98.5	-56.3	-39.7	8
4	-97.3	-56.6	-44.5	9
5	-96.5	-56.6	-46.7	10
6	-96.4	-56.6	-48.3	11
7	-99.9	-58.7	-53.9	12

**Table VIII B: Tf and Th for Low-Density Fluid Inclusions (type 1b)**

Number	Tf °C	Tmf °C	Th °C	Size (when measured) μm
Sample : 2033 C quartz inclusions in garnet				
1		-58.3	25.3	
2		-56.7	-0.5	
3		-56.9	30.2	
4		-58.7	6.9	
5		-59.1	23.6	
6		-57.3	29.9	
7		-56.5	22.1	
8		-56.6	12.8	
9		-56.3	14.5	
10		-58.2	1.2	
11		-56.3	0.9	
12		-56.2	0.7	
13		-57.2	13.7	
14		-56.2	18.7	
15		-56.4	18.9	
Sample : 2059 - DH 23 quartz inclusions in garnet				
1	-79.8	-57.1	7.0	
2	-95.2	-56.4	10.6	
3	-95.5	-56.3	18.3	
4	-94.1	-56.6	23.6	
5	-96.5	-56.8	18.8	
6	-92.4	-56.7	11.9	
7	-92.7	-56.6	27.4	
8	-93.5	-56.7	19.2	
9	-94.3	-56.3	17.5	
10	-94.7	-56.4	29.3	
11	-93.8	-57.4	20.8	
12	-95.5	-56.8	22.5	
13	-94.9	-56.7	21.4	
14	-76.8	-56.9	19.8	
15	-95.4	-56.7	15.3	

Number	Tf °C	Tmf °C	Th °C	Size (when measured) μm
Sample : 2035 - B quartz inclusions in garnet				
1	-78.3	-57.0	18.5	
2	-92.9	-56.6	27.7	
3	-76.5	-57.8	24.5	
4	-70.7	-59.8	28.9	
5	-69.8	-59.3	30.3	
6	-72.8	-58.7	30.5	
7	-68.6	-59.6	30.6	
8	-66.7	-58.8	30.5	
9	-69.3	-59.2	30.7	
10	-92.8	-56.6	27.2	
11	-75.8	-57.4	24.3	
12	-94.3	-56.8	23.8	
13	-69.7	-57.1	23.5	
14	-93.2	-56.6	21.8	
15	-94.6	-56.5	19.7	
Sample : 2033 - A quartz vein				
1	-91.1	-56.6	15.3	
2	-95.3	-56.7	23.9	
3	-97.6	-56.3	19.9	
4	-95.8	-56.6	23.9	
5	-95.8	-56.5	20.7	
6	-95.6	-56.4	20.0	
7	-84.8	-56.7	22.2	
8	-71.3	-56.6	23.2	
9	-82.4	-56.6	24.8	
10	-92.9	-56.7	24.5	
11	-79.0	-56.6	23.7	
12	-77.6	-56.6	23.0	
13	-73.3	-56.7	25.3	
14	-89.1	-56.6	16.9	
15	-63.2	-57.2	30.3	
16	-97.8	-56.8	25.0	
17	-94.9	-56.8	20.5	
18	-94.5	-56.7	20.1	
19	-92.9	-56.6	27.6	

Number	Tf °C	Tmf °C	Th °C	Size (when measured) μm
20	-94.8	-56.5	29.3	
21	-95.7	-56.4	29.8	
22	-94.3	-56.4	26.7	
23	-95.2	-56.5	28.7	
24	-92.8	-56.3	29.7	
25	-94.3	-56.5	28.6	
26	-94.8	-57.2	27.3	
27	-95.3	-56.8	29.2	
28	-95.4	-56.2	28.7	
29	-94.9	-56.3	29.3	
30	-78.6	-56.2	30.2	
Sample : 2035 - AB quartz vein				
1	-78.1	-56.7	26.8	
2	-82.3	-56.6	27.3	
3	-82.4	-56.7	28.3	
4	-94.2	-56.4	29.2	
5	-82.3	-56.7	30.1	
6	-70.6	-57.2	28.7	
7	-72.3	-57.4	29.2	
8	-78.6	-57.8	27.6	
9	-76.3	-57.2	28.3	
10	-71.2	-57.3	29.2	
11	-74.4	-57.0	29.3	
12	-68.2	-57.8	28.7	
13	-69.3	-57.6	29.2	
14	-69.8	-57.3	29.0	
15	-70.0	-57.5	20.0	
Sample : 2033 AB quartz vein				
1	-95.3	-56.7	23.8	
2	-94.3	-56.6	27.6	
3	-92.1	-56.7	19.2	
4	-96.2	-56.6	22.3	
5	-96.5	-56.6	23.5	
6	-96.4	-56.4	24.7	
7	-96.7	-56.5	26.2	
8	-96.3	-56.4	27.1	

Number	Tf °C	Tmf °C	Th °C	Size (when measured) μm
9	-96.2	-56.5	26.2	
10	-92.3	-56.6	27.1	
11	-78.6	-56.3	26.3	
12	-72.3	-56.3	25.2	
13	-89.3	-56.3	26.9	
14	-91.9	-56.4	27.0	
15	-91.0	-56.5	27.3	



UNIVERSITY  
OF  
JOHANNESBURG

Table VIII C : Tf and Th for Mixed H<sub>2</sub>O-CO<sub>2</sub> Fluid Inclusions (type 3)

Number	Tf °C	Tmf °C	Th °C	Size (when measured) μm
Sample : 2033 AB				
1	-93.3	-58.8	8.6	
2	-95.6	-58.0	21.6	
3	-95.4	-57.1	13.9	
4	-89.8	-57.0	14.7	
5	-84.7	-58.8	12.8	
6		-59.7	10.1	
7	-68.7	-57.4	6.8	
8	-84.4	-58.4	15.0	
Sample : 2035 - A				
1	-94.3	-58.1	11.3	
2	-95.7	-59.3	14.9	
3	-93.0	-57.9	11.9	
4	-92.8	-57.9	14.1	
5	-92.0	-58.9	13.2	
6	-94.6	-57.9	8.7	
7	-94.6	-58.8	12.8	
8	-92.1	-56.8	23.7	
9	-93.2	-56.5	10.6	
10	-95.5	-56.6	8.5	
11	-89.1	-56.7	22.5	
12	-84.7	-56.5	14.8	
13	-86.2	-56.5	13.9	
14	-92.3	-56.5		
15	-94.5	-56.7		
16	-97.4	-56.7		
17	-96.9	-56.6	16.1	
18	-87.5	-56.7	12.2	
19	-83.8	-56.8	15.3	
20	-85.4	-56.6	10.8	



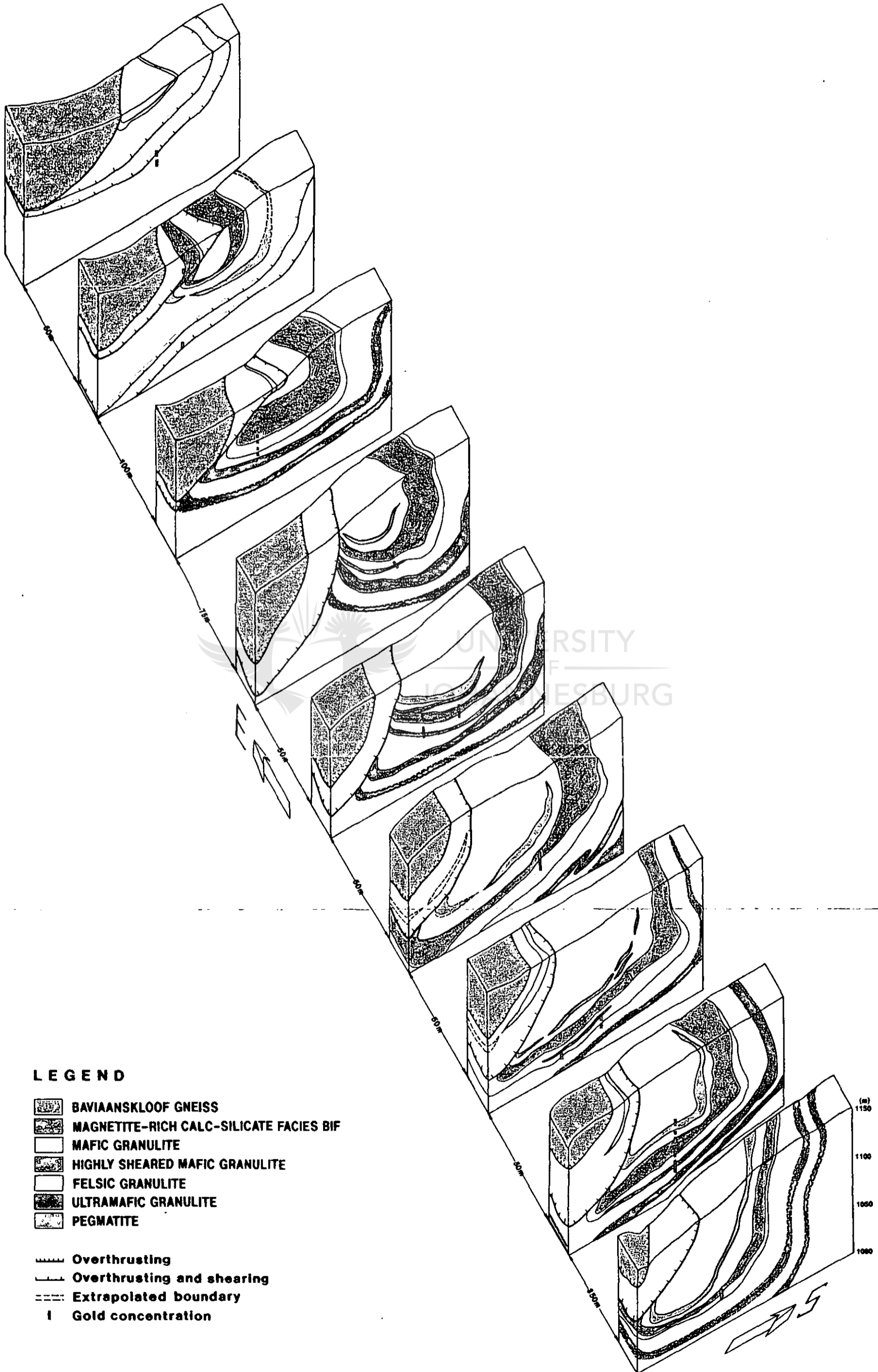
Number	Tf °C	Tmf °C	Th °C	Size (when measured) μm
21		-56.6	13.0	
22	-95.6	-56.6	-8.6	
23	-49.0	-13.1	173.1	
24	-72.7	-14.8	197.7	
25	-79.3	-26.1	168.1	
26	-79.6	-26.0	164.5	
27	-77.6	-26.2	159.8	
28	-74.5	-25.6	169.1	
29	-77.4	-27.1	151.8	
30	-78.2	-25.6	171.2	
31	-77.7	-28.0	156.8	
32	-86.1	-26.8	237.3	
Sample : 2035 B				
1	-52.1	-23.7		12
2	-55.6	-22.9	158.0	8
3	-55.6	-22.3	177.7	9
4	-53.7	-24.1	133.6	12
5	-49.8	-14.0	231.6	6
6	-43.0	-11.5	169.3	17
7	-56.6	-22.1		8
8	-48.9	-13.1	185.7	8
9	-56.3	-23.0	180.0	7
10	-54.7	-14.0	186.8	6
11	-73.6	-23.1	191.3	9
Sample : 2033 - A				
1	-50.9	-14.8		10
2	-52.0	-15.1	231.0	10
3	-49.1	-13.6	230.6	10

**APPENDIX VII:**




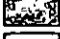
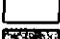

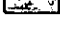
**BLOCK DIAGRAM THROUGH  
DOORNHOEK GOLD DEPOSIT**


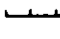
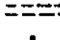
UNIVERSITY  
JOHANNESBURG

# DOORNHOEK GOLD OCCURRENCE



## LEGEND

-  BAVIAANSKLOOF GNEISS
-  MAGNETITE-RICH CALC-SILICATE FACIES BIF
-  MAFIC GRANULITE
-  HIGHLY SHEARED MAFIC GRANULITE
-  FELSIC GRANULITE
-  ULTRAMAFIC GRANULITE
-  PEGMATITE

-  Overthrusting
-  Overthrusting and shearing
-  Extrapolated boundary
- I** Gold concentration